



1

DTIC
FI ECTE
JAN 23 1992
S D D

AD-A245 416



K-PULSE ESTIMATION AND TARGET IDENTIFICATION

Gönlü Turhan
David L. Moffatt

The Ohio State University
ElectroScience Laboratory

Department of Electrical Engineering
Columbus, Ohio 43212

Technical Report 719710-3
Contract N00014-87-K-2011
August 1988

This document has been approved
for public release and sale; its
distribution is unlimited.

Naval Research Laboratory
4555 Overlook Ave., S.W.
Washington, D.C. 20375

92-01818

92 1 22 052

NOTICES

When Government drawings, specifications, or other data are used for any purpose other than in connection with a definitely related Government procurement operation, the United States Government thereby incurs no responsibility nor any obligation whatsoever, and the fact that the Government may have formulated, furnished, or in any way supplied the said drawings, specifications, or other data, is not to be regarded by implication or otherwise as in any manner licensing the holder or any other person or corporation, or conveying any rights or permission to manufacture, use, or sell any patented invention that may in any way be related thereto.

Accession For	
NTIS CRA&I	<input checked="" type="checkbox"/>
DTIC TAB	<input type="checkbox"/>
Unannounced	<input type="checkbox"/>
Justification	
By	
Distribution/	
Availability Codes	
Dist	Availability
A-1	



REPORT DOCUMENTATION PAGE	1. REPORT NO.	2.	3. Recipient's Accession No.
4. Title and Subtitle K-PULSE ESTIMATION AND TARGET IDENTIFICATION		5. Report Date August 1988	
7. Author(s) Gönül Turhan and D.L. Moffatt		8. Performing Organization Rept. No. 719710-3	
9. Performing Organization Name and Address The Ohio State University ElectroScience Laboratory 1320 Kinnear Road Columbus, Ohio 43212		10. Project/Task/Work Unit No.	
		11. Contract(C) or Grant(G) No (C) N00014-87-K-2011 (G)	
12. Sponsoring Organization Name and Address Naval Research Laboratory 4555 Overlook Ave., S.W. Washington, D.C. 20375		13. Type of Report & Period Covered Technical	
		14.	
15. Supplementary Notes			
<p>16. Abstract (Limit: 200 words)</p> <p>The unique K-pulse of a finite electromagnetic scatter is conceptually defined as a time-limited excitation of minimal duration which produces time-limited response waveforms for that specific object at all possible combinations of aspect and radar polarization. As a result of the aspect and polarization invariant feature of the K-pulse, it is a useful tool in target identification. In practical applications, to obtain the unique K-pulse is not feasible but generally useful K-pulse approximations are in order. The K-pulse estimation technique suggested in this dissertation is based on the annihilation of the target's natural resonances under K-pulse excitation. This technique basically addresses a simultaneous optimization problem in order to minimize the late-time energy content of the target response at several combinations of aspect and polarization. The K-pulse waveform is modeled as an impulse function at the initiation time and then a continuous time-limited function which can be mathematically represented by discrete or continuous basis functions. The suggested K-pulse synthesis technique is quite general in the sense that it can be applied to both geometrically simple and complicated targets upon the availability of some band-limited theoretical or measured scattering data. Also, estimation of the target poles from the synthesized K-pulse spectrum is an important by-product of this technique. Target identification, even at reasonably low signal-to-noise ratio levels, is successfully demonstrated for various classes of targets such as conducting thin-wires, conducting spheres, aircraft, ships and land vehicles using the K-pulse concept.</p>			
<p>17. Document Analysis</p> <p>a. Descriptors</p> <p>b. Identifiers/Open-Ended Terms</p> <p>c. COSATI Field/Group</p>			
18. Availability Statement Approved for public release; distribution is unlimited.		19. Security Class (This Report) Unclassified	21. No of Pages 364
		20. Security Class (This Page) Unclassified	22. Price

Prologue

The results presented in the main text of this report demonstrate that the K-pulse can be successfully exploited for the identification of realistic targets such as aircraft, ships and land vehicles. The practicality of the K-pulse technique in terms of the required bandwidth and frequency span (target electrical size) required can be questioned. Such questions are refuted in Appendix F where it is shown that full scale measurements of a real aircraft over a severely limited bandwidth (S-band) can also be exploited for K-pulse purposes.

TABLE OF CONTENTS

Prologue	iii
List of Tables	vii
List of Figures	viii
I INTRODUCTION	1
II AN OVERVIEW OF RESEARCH ON K-PULSE TECHNIQUES	7
III THEORIES AND FORMULATIONS	14
A. K-PULSE ESTIMATION	14
B. K-PULSE ESTIMATION USING LEGENDRE POLYNOMIALS	24
C. TARGET IDENTIFICATION	28
IV APPLICATIONS TO GEOMETRICALLY SIMPLE TARGETS	33
A. APPLICATIONS TO CONDUCTING LINEAR THIN-WIRE	34
1. K-Pulse Estimation Using a Discrete Representation ..	34
2. K-Pulse Estimation Using a Legendre Polynomial Representation	36
3. Target Identification	38
B. APPLICATIONS TO CONDUCTING SPHERE	40
1. K-Pulse Estimation Using a Discrete Representation ..	40
2. K-Pulse Estimation Using a Legendre Polynomial Expansion	43
3. Target Identification	44
V APPLICATIONS TO SHIPS	101
A. K-PULSE ESTIMATION FOR THE MODEL SHIP SH₁	102
B. K-PULSE ESTIMATION FOR THE MODEL SHIP SH₂	104
C. TARGET IDENTIFICATION	106
VI APPLICATIONS TO LAND VEHICLES	171
A. K-PULSE ESTIMATION FOR THE MODEL TARGET LV₁	172
B. K-PULSE ESTIMATION OF THE MODEL TARGET LV₂	173
C. TARGET IDENTIFICATION	173
VII APPLICATIONS TO AIRCRAFT	213
A. K-PULSE ESTIMATION FOR MODEL AIRCRAFT A₁	213

B.	K-PULSE ESTIMATION FOR MODEL AIRCRAFT A_2	215
C.	K-PULSE ESTIMATION FOR MODEL AIRCRAFT A_3	215
D.	TARGET IDENTIFICATION	217
VIII CONCLUSIONS		303
APPENDICES		
A	ESTIMATION OF THE K-PULSE DURATION AND CUT-OFF TIMES	308
	A. ESTIMATION OF K-PULSE DURATION	308
	B. ESTIMATION OF CUT-OFF TIMES	311
B	INTERPRETATION OF NORMALIZED ENERGY CURVES IN TARGET IDENTIFICATION	315
C	EXTRACTION OF TARGET POLES FROM THE K-PULSE	319
D	ORIGINAL AND MODIFIED LEGENDRE POLYNOMIALS	322
E	SIMULATION OF NOISY DATA	325
REFERENCES		327

LIST OF TABLES

Table 4.1	CNR Frequencies (Poles) of the Conducting Thin-Wire W_1 ($L/d_1=2000$) in sL_1/c Scale	47
Table 4.2	Legendre Polynomial Coefficients Used to Construct the K-Pulse Waveform Shown in Figure 4.5	47
Table 4.3	CNR Frequencies (Poles) of the Conducting Thin-Wire W_1 ($L_1/d_1 = 2000$) in sL_1/c Scale	48
Table 4.4	CNR Frequencies (Poles) of the Conducting Sphere S_2 ($2r_2=10$ inches) in sr_2/c Scale	48
Table 4.5	Legendre Polynomial Coefficients Used to Construct the K-Pulse Shown in Figure 4.16	49
Table 4.6	CNR Frequencies (Poles) of the Conducting Sphere S_2 ($2r_2=10$ inches) in sr_2/c Scale	49
Table 5.1	Poles of the Model Ship SH_1 Extracted from the K-pulse Shown in Figure 5.1	108
Table 5.2	Legendre Polynomial Expansion Coefficients for the Continuous Part of the K-pulse shown in Figure 5.12	109
Table 5.3	Poles of the Model Ship SH_2 Extracted from the K-pulse Shown in Figure 5.12	109
Table 6.1	Poles of the Model Tank LV_1 Extracted from the K-pulse Shown in Figure 6.1	176
Table 6.2	Poles of the Model Carrier LV_2 Extracted from the K-pulse shown in Figure 6.7	176
Table 7.1	Poles of Model Aircraft A_1 As Extracted from the K-pulse shown in Figure 7.1	221
Table 7.2	Poles of Model Aircraft A_2 As Extracted from the K-pulse shown in Figure 7.9	222
Table 7.3	Poles of Model Aircraft A_3 As Extracted from the K-pulse shown in Figure 7.16	223

LIST OF FIGURES

Figure 4.1.	An approximate K-pulse waveform for the conducting cylindrical thin-wire W_1 (with $L=12m$ and $L/d=2000$) estimated from the theoretical backscattered data at $\phi=30^\circ$, ϕ -polarization using a discrete representation for the continuous part of the K-pulse.	50
Figure 4.2.	Normalized impulse response (.....) and K-pulse response (——) waveforms and their energy curves for the wire W_1 (due to the K-pulse shown in Figure 4.1) at $\phi=30^\circ$, ϕ -polarization.	51
Figure 4.3.	Normalized impulse response (.....) and K-pulse response (——) waveforms of the wire W_1 at $\phi=60^\circ$, ϕ -polarization due to the K-pulse shown in Figure 4.1.	53
Figure 4.4.	Normalized impulse response (.....) and K-pulse response (——) waveforms of W_1 at $\phi=90^\circ$, ϕ -polarization due to the K-pulse shown in Figure 4.1.	54
Figure 4.5.	An approximate K-pulse waveform for the thin-wire W_1 estimated from the theoretical backscattered data at $\phi=60^\circ$, ϕ -polarization using a Legendre polynomial representation for the continuous part of the K-pulse.	55
Figure 4.6.	Normalized impulse response (.....) and K-pulse response (——) waveforms and their energy curves for the wire W_1 (due to the K-pulse shown in Figure 4.5) at $\phi=60^\circ$, ϕ -polarization.	56
Figure 4.7.	Normalized impulse response (.....) and K-pulse response (——) of W_1 at $\phi=30^\circ$, ϕ -polarization due to the K-pulse shown in Figure 4.5.	58
Figure 4.8.	Normalized impulse response (.....) and K-pulse response (——) of W_1 at $\phi=90^\circ$, ϕ -polarization due to the K-pulse shown in Figure 4.5.	59
Figure 4.9.	K-pulse waveforms of the thin-wires W_1 (——), W_2 (.....), and W_3 (— · — · —). All three wires have the same length-to-diameter ratio of 2000 with lengths $L_1=12m$, $L_2=10.8m$, and $L_3=13.2m$	60
Figure 4.10.	Normalized response waveforms and their energy curves for the wire W_1 produced by the K-pulses of library targets W_1 (——), W_2 (.....) and W_3 (— · — · —) at $\phi=30^\circ$, ϕ -polarization.	61

Figure 4.11. Normalized response waveforms and their energy curves for the wire W_1 produced by the K-pulses of library targets W_1 (—), W_2 (·····) and W_3 (— · — · —) at $\phi=60^\circ$, ϕ -polarization.	63
Figure 4.12. Normalized response waveforms and their energy curves for the wire W_1 produced by the K-pulses of library targets W_1 (—), W_2 (·····) and W_3 (— · — · —) at $\phi=90^\circ$, ϕ -polarization.	65
Figure 4.13. An approximate K-pulse waveform for the conducting sphere S_2 (with $2r_2=10$ inches) estimated from the theoretical backscattered data using a discrete representation for the continuous part of the K-pulse.	67
Figure 4.14. Normalized impulse response (---) and K-pulse response (—) waveforms and their energy curves for the sphere S_2 at the backscattered direction due to the K-pulse shown in Figure 4.13.	68
Figure 4.15. Normalized impulse response (---) and K-pulse response (—) waveforms of the sphere S_2 (due to the K-pulse shown in Figure 4.13) for the bistatic angle/radar polarization combinations of $30^\circ/HP$, $45^\circ/VP$, $60^\circ/HP$, $90^\circ/VP$, and $135^\circ/VP$	71
Figure 4.16. An approximate K-pulse waveform for the sphere S_2 estimated from the backscattered data using a Legendre polynomial representation for the continuous part of the K-pulse.	76
Figure 4.17. Normalized impulse response (---) and K-pulse response (—) waveforms and their energy curves for the sphere S_2 (due to the K-pulse shown in Figure 4.16) at the backscattered direction.	77
Figure 4.18. Normalized impulse response (---) and K-pulse response (—) waveforms of S_2 (due to the K-pulse shown in Figure 4.16) for the bistatic angle/radar polarization combinations of $30^\circ/HP$, $90^\circ/VP$ and $120^\circ/HP$	79
Figure 4.19. K-pulse waveform of the conducting sphere S_1 (with $2r_1=5$ inches) as constructed from the K-pulse of S_2 shown in Figure 4.16.	82
Figure 4.20. K-pulse waveform of the conducting sphere S_3 (with $2r_3=20$ inches) as constructed from the K-pulse of S_2 shown in Figure 4.16.	83

Figure 4.21.	Examples of target identification in the noise-free case using the K-pulse waveforms shown in Figures 4.16 (for the sphere S_2), 4.19 (for the sphere S_1) and 4.20 (for the sphere S_3).	84
Figure 4.22.	Normalized response waveforms and the corresponding energy curves of the test target S_2 due to the K-pulses of S_1 (---), S_2 (—) and S_3 (·—·) at the backscattered direction.	91
Figure 5.1.	An approximate K-pulse waveform of the model ship SH_1 estimated from the measured backscattered data at $0^\circ/VP$ and $80^\circ/VP$ using a discrete representation for the continuous part of the K-pulse.	110
Figure 5.2.	Normalized impulse response (· · · · ·) and K-pulse response (—) waveforms and their energy curves for the target SH_1 at $0^\circ/VP$	111
Figure 5.3.	Normalized impulse response (· · · · ·) and K-pulse response (—) waveforms and their energy curves for the target SH_1 at $15^\circ/VP$	113
Figure 5.4.	Normalized impulse response (· · · · ·) and K-pulse response (—) waveforms and their energy curves for the target SH_1 at $30^\circ/VP$	115
Figure 5.5.	Normalized impulse response (· · · · ·) and K-pulse response (—) waveforms and their energy curves for the target SH_1 at $45^\circ/VP$	117
Figure 5.6.	Normalized impulse response (· · · · ·) and K-pulse response (—) waveforms and their energy curves for the target SH_1 at $60^\circ/VP$	119
Figure 5.7.	Normalized impulse response (· · · · ·) and K-pulse response (—) waveforms and their energy curves for the target SH_1 at $80^\circ/VP$	121
Figure 5.8.	Normalized impulse response (· · · · ·) and K-pulse response (—) waveforms and their energy curves for the target SH_1 at $90^\circ/VP$	123
Figure 5.9.	Normalized impulse response (· · · · ·) and K-pulse response (—) waveforms and their energy curves for the target SH_1 at $100^\circ/VP$	125
Figure 5.10.	Normalized impulse response (· · · · ·) and K-pulse response (—) waveforms and their energy curves for the target SH_1 at $170^\circ/VP$	127

Figure 5.11. Normalized impulse response (.....) and K-pulse response (——) waveforms and their energy curves for the target SH ₁ at 180°/VP.	129
Figure 5.12. An approximate K-pulse waveform of the model ship SH ₂ estimated from the measured backscattered data at 30°/VP and 100°/VP using a Legendre polynomial representation for the continuous part of the K-pulse.	131
Figure 5.13. Normalized impulse response (.....) and K-pulse response (——) waveforms and their energy curves for the target SH ₂ at 0°/VP.	132
Figure 5.14. Normalized impulse response (.....) and K-pulse response (——) waveforms and their energy curves for the target SH ₂ at 10°/VP.	134
Figure 5.15. Normalized impulse response (.....) and K-pulse response (——) waveforms and their energy curves for the target SH ₂ at 30°/VP.	136
Figure 5.16. Normalized impulse response (.....) and K-pulse response (——) waveforms and their energy curves for the target SH ₂ at 45°/VP.	138
Figure 5.17. Normalized impulse response (.....) and K-pulse response (——) waveforms and their energy curves for the target SH ₂ at 60°/VP.	140
Figure 5.18. Normalized impulse response (.....) and K-pulse response (——) waveforms and their energy curves for the target SH ₂ at 80°/VP.	142
Figure 5.19. Normalized impulse response (.....) and K-pulse response (——) waveforms and their energy curves for the target SH ₂ at 90°/VP.	144
Figure 5.20. Normalized impulse response (.....) and K-pulse response (——) waveforms and their energy curves for the target SH ₂ at 100°/VP.	146
Figure 5.21. Normalized impulse response (.....) and K-pulse response (——) waveforms and their energy curves for the target SH ₂ at 170°/VP.	148
Figure 5.22. Normalized impulse response (.....) and K-pulse response (——) waveforms and their energy curves for the target SH ₂ at 180°/VP.	150
Figure 5.23. Normalized response energy curves of the test target SH ₁ produced by the K-pulses of library targets SH ₁ (——) and SH ₂ (.....) at 0°/VP.	152

Figure 5.24. Normalized response energy curves of the test target SH_1 produced by the K-pulses of library targets SH_1 (—) and SH_2 (.....) at $15^\circ/VP$	153
Figure 5.25. Normalized response energy curves of the test target SH_1 produced by the K-pulses of library targets SH_1 (—) and SH_2 (.....) at $30^\circ/VP$	154
Figure 5.26. Normalized response energy curves of the test target SH_1 produced by the K-pulses of library targets SH_1 (—) and SH_2 (.....) at $45^\circ/VP$	155
Figure 5.27. Normalized response energy curves of the test target SH_1 produced by the K-pulses of library targets SH_1 (—) and SH_2 (.....) at $80^\circ/VP$	156
Figure 5.28. Normalized response energy curves of the test target SH_1 produced by the K-pulses of library targets SH_1 (—) and SH_2 (.....) at $100^\circ/VP$	157
Figure 5.29. Normalized response energy curves of the test target SH_1 produced by the K-pulses of library targets SH_1 (—) and SH_2 (.....) at $170^\circ/VP$	158
Figure 5.30. Normalized response energy curves of the test target SH_2 produced by the K-pulses of library targets SH_1 (.....) and SH_2 (—) at $0^\circ/VP$	159
Figure 5.31. Normalized response energy curves of the test target SH_2 produced by the K-pulses of library targets SH_1 (.....) and SH_2 (—) at $30^\circ/VP$	160
Figure 5.32. Normalized response energy curves of the test target SH_2 produced by the K-pulses of library targets SH_1 (.....) and SH_2 (—) at $45^\circ/VP$	161
Figure 5.33. Normalized response energy curves of the test target SH_2 produced by the K-pulses of library targets SH_1 (.....) and SH_2 (—) at $60^\circ/VP$	162
Figure 5.34. Normalized response energy curves of the test target SH_2 produced by the K-pulses of library targets SH_1 (.....) and SH_2 (—) at $80^\circ/VP$	163
Figure 5.35. Normalized response energy curves of the test target SH_2 produced by the K-pulses of library targets SH_1 (.....) and SH_2 (—) at $90^\circ/VP$	164
Figure 5.36. Normalized response energy curves of the test target SH_2 produced by the K-pulses of library targets SH_1 (.....) and SH_2 (—) at $100^\circ/VP$	165

Figure 5.37.	Normalized response energy curves of the test target SH_2 produced by the K-pulses of library targets SH_1 ($\cdot\cdot\cdot\cdot$) and SH_2 (—) at $180^\circ/VP$	166
Figure 5.38.	Normalized response energy curves of the test target SH_1 produced by the K-pulses of library targets SH_1 (—) and SH_2 ($\cdot\cdot\cdot\cdot$) for some noisy backscattered data at $30^\circ/VP$	167
Figure 6.1.	An approximate K-pulse waveform for the model tank LV_1 estimated from the backscattered measurement data at $0^\circ/VP$ and $90^\circ/VP$ using a discrete representation for the continuous part of the K-pulse.	177
Figure 6.2.	Normalized impulse response ($\cdot\cdot\cdot\cdot$) and K-pulse response (—) waveforms and their energy curves for the model tank LV_1 at $0^\circ/VP$	178
Figure 6.3.	Normalized impulse response ($\cdot\cdot\cdot\cdot$) and K-pulse response (—) waveforms and their energy curves for the model tank LV_1 at $30^\circ/VP$	180
Figure 6.4.	Normalized impulse response ($\cdot\cdot\cdot\cdot$) and K-pulse response (—) waveforms and their energy curves for the model tank LV_1 at $45^\circ/VP$	182
Figure 6.5.	Normalized impulse response ($\cdot\cdot\cdot\cdot$) and K-pulse response (—) waveforms and their energy curves for the model tank LV_1 at $60^\circ/VP$	184
Figure 6.6.	Normalized impulse response ($\cdot\cdot\cdot\cdot$) and K-pulse response (—) waveforms and their energy curves for the model tank LV_1 at $90^\circ/VP$	186
Figure 6.7.	An approximate K-pulse waveform for the model carrier LV_2 estimated from the backscattered measurement data at $30^\circ/VP$ and $90^\circ/VP$ using a discrete representation for the continuous part of the K-pulse.	188
Figure 6.8.	Normalized impulse response ($\cdot\cdot\cdot\cdot$) and K-pulse response (—) waveforms and their energy curves for the model carrier LV_2 at $0^\circ/VP$	189
Figure 6.9.	Normalized impulse response ($\cdot\cdot\cdot\cdot$) and K-pulse response (—) waveforms and their energy curves for the model carrier LV_2 at $30^\circ/VP$	191
Figure 6.10.	Normalized impulse response ($\cdot\cdot\cdot\cdot$) and K-pulse response (—) waveforms and their energy curves for the model carrier LV_2 at $45^\circ/VP$	193

Figure 6.11.	Normalized impulse response (.....) and K-pulse response (—) waveforms and their energy curves for the model carrier LV ₂ at 60°/VP.	195
Figure 6.12.	Normalized impulse response (.....) and K-pulse response (—) waveforms and their energy curves for the model carrier LV ₂ at 90°/VP.	197
Figure 6.13.	Normalized response energy curves of the test target LV ₁ produced by the K-pulses of library targets LV ₁ (—) and LV ₂ (.....) at 0°/VP.	199
Figure 6.14.	Normalized response energy curves of the test target LV ₁ produced by the K-pulses of library targets LV ₁ (—) and LV ₂ (.....) at 30°/VP.	200
Figure 6.15.	Normalized response energy curves of the test target LV ₁ produced by the K-pulses of library targets LV ₁ (—) and LV ₂ (.....) at 45°/VP.	201
Figure 6.16.	Normalized response energy curves of the test target LV ₁ produced by the K-pulses of library targets LV ₁ (—) and LV ₂ (.....) at 60°/VP.	202
Figure 6.17.	Normalized response energy curves of the test target LV ₁ produced by the K-pulses of library targets LV ₁ (—) and LV ₂ (.....) at 90°/VP.	203
Figure 6.18.	Normalized response energy curves of the test target LV ₂ produced by the K-pulses of library targets LV ₁ (.....) and LV ₂ (—) at 0°/VP.	204
Figure 6.19.	Normalized response energy curves of the test target LV ₂ produced by the K-pulses of library targets LV ₁ (.....) and LV ₂ (—) at 30°/VP.	205
Figure 6.20.	Normalized response energy curves of the test target LV ₂ produced by the K-pulses of library targets LV ₁ (.....) and LV ₂ (—) at 45°/VP.	206
Figure 6.21.	Normalized response energy curves of the test target LV ₂ produced by the K-pulses of library targets LV ₁ (.....) and LV ₂ (—) at 60°/VP.	207
Figure 6.22.	Normalized response energy curves of the test target LV ₂ produced by the K-pulses of library targets LV ₁ (.....) and LV ₂ (—) at 90°/VP.	208
Figure 6.23.	Normalized response energy curves of the test target LV ₂ produced by the K-pulses of library targets LV ₁ (.....) and LV ₂ (—) from some noisy backscattered data at 90°/VP.	209

Figure 7.1.	An approximate K-pulse waveform for the model aircraft A_1 estimated from the backscattered measurement data at $0^\circ/VP$ and $90^\circ/VP$ using a discrete representation for the continuous part of the K-pulse.	224
Figure 7.2.	Normalized impulse response (.....) and K-pulse response (——) waveforms and their energy curves for aircraft A_1 at $0^\circ/VP$	225
Figure 7.3.	Normalized impulse response (.....) and K-pulse response (——) waveforms and their energy curves for aircraft A_1 at $30^\circ/VP$	227
Figure 7.4.	Normalized impulse response (.....) and K-pulse response (——) waveforms and their energy curves for aircraft A_1 at $45^\circ/VP$	229
Figure 7.5.	Normalized impulse response (.....) and K-pulse response (——) waveforms and their energy curves for aircraft A_1 at $60^\circ/VP$	231
Figure 7.6.	Normalized impulse response (.....) and K-pulse response (——) waveforms and their energy curves for aircraft A_1 at $90^\circ/VP$	233
Figure 7.7.	Normalized impulse response (.....) and K-pulse response (——) waveforms and their energy curves for aircraft A_1 at $120^\circ/VP$	235
Figure 7.8.	Normalized impulse response (.....) and K-pulse response (——) waveforms and their energy curves for aircraft A_1 at $180^\circ/VP$	237
Figure 7.9.	An approximate K-pulse waveform for the model aircraft A_2 estimated from the backscattered measurement data at $0^\circ/VP$ and $90^\circ/VP$ using a discrete representation for the continuous part of the K-pulse.	239
Figure 7.10.	Normalized impulse response (.....) and K-pulse response (——) waveforms and their energy curves for aircraft A_2 at $0^\circ/VP$	240
Figure 7.11.	Normalized impulse response (.....) and K-pulse response (——) waveforms and their energy curves for aircraft A_2 at $45^\circ/VP$	242
Figure 7.12.	Normalized impulse response (.....) and K-pulse response (——) waveforms and their energy curves for aircraft A_2 at $60^\circ/VP$	244

Figure 7.13. Normalized impulse response (.....) and K-pulse response (——) waveforms and their energy curves for aircraft A_2 at $90^\circ/VP$	246
Figure 7.14. Normalized impulse response (.....) and K-pulse response (——) waveforms and their energy curves for aircraft A_2 at $120^\circ/VP$	248
Figure 7.15. Normalized impulse response (.....) and K-pulse response (——) waveforms and their energy curves for aircraft A_2 at $180^\circ/VP$	250
Figure 7.16. An approximate K-pulse waveform for the model aircraft A_3 estimated from the backscattered measurement data at $0^\circ/VP$ and $90^\circ/VP$ using a discrete representation for the continuous part of the K-pulse.	252
Figure 7.17. Normalized impulse response (.....) and K-pulse response (——) waveforms and their energy curves for aircraft A_3 at $0^\circ/VP$	253
Figure 7.18. Normalized impulse response (.....) and K-pulse response (——) waveforms and their energy curves for aircraft A_3 at $30^\circ/VP$	255
Figure 7.19. Normalized impulse response (.....) and K-pulse response (——) waveforms and their energy curves for aircraft A_3 at $45^\circ/VP$	257
Figure 7.20. Normalized impulse response (.....) and K-pulse response (——) waveforms and their energy curves for aircraft A_3 at $60^\circ/VP$	259
Figure 7.21. Normalized impulse response (.....) and K-pulse response (——) waveforms and their energy curves for aircraft A_3 at $90^\circ/VP$	261
Figure 7.22. Normalized impulse response (.....) and K-pulse response (——) waveforms and their energy curves for aircraft A_3 at $120^\circ/VP$	263
Figure 7.23. Normalized impulse response (.....) and K-pulse response (——) waveforms and their energy curves for aircraft A_3 at $180^\circ/VP$	265
Figure 7.24. Normalized response energy curves of the test target A_1 produced by the K-pulses of the library targets A_1 (——), A_2 (.....) and A_3 (---) at $0^\circ/VP$ from a noisy backscattered data with SNR=11 dB.	267

- Figure 7.25. Normalized response energy curves (plotted on a magnified scale) of the test target A_1 produced by the K-pulses of the library targets A_1 (—), A_2 (.....) and A_3 (---) at $30^\circ/VP$ for three different SNR levels. 270
- Figure 7.26. Normalized response energy curves (plotted on a magnified scale) of the test target A_1 produced by the K-pulses of the library targets A_1 (—), A_2 (.....) and A_3 (---) at $45^\circ/VP$ from a noisy backscattered data with SNR=11 dB. 273
- Figure 7.27. Normalized response energy curves (plotted on a magnified scale) of the test target A_1 produced by the K-pulses of the library targets A_1 (—), A_2 (.....) and A_3 (---) at $60^\circ/VP$ for three different SNR levels. 274
- Figure 7.28. Normalized response energy curves (plotted on a magnified scale) of the test target A_1 produced by the K-pulses of the library targets A_1 (—), A_2 (.....) and A_3 (---) at $90^\circ/VP$ from a noisy backscattered data with SNR=11 dB. 277
- Figure 7.29. Normalized response energy curves (plotted on a magnified scale) of the test target A_1 produced by the K-pulses of the library targets A_1 (—), A_2 (.....) and A_3 (---) at $120^\circ/VP$ from a noisy backscattered data with SNR=11 dB. 278
- Figure 7.30. Normalized response energy curves (plotted on a magnified scale) of the test target A_1 produced by the K-pulses of the library targets A_1 (—), A_2 (.....) and A_3 (---) at $180^\circ/VP$ for two different SNR levels. 279
- Figure 7.31. Normalized response energy curves of the test target A_2 produced by the K-pulses of the library targets A_1 (.....), A_2 (—) and A_3 (---) at $0^\circ/VP$ from a noisy backscattered data with SNR=11 dB. 281
- Figure 7.32. Normalized response energy curves (plotted on a magnified scale) of the test target A_2 produced by the K-pulses of the library targets A_1 (.....), A_2 (—) and A_3 (---) at $45^\circ/VP$ from a noisy backscattered data with SNR=11 dB. 284
- Figure 7.33. Normalized response energy curves (plotted on a magnified scale) of the test target A_2 produced by the K-pulses of the library targets A_1 (.....), A_2 (—) and A_3 (---) at $60^\circ/VP$ from a noisy backscattered data with SNR=11 dB. 285

- Figure 7.34. Normalized response energy curves (plotted on a magnified scale) of the test target A_2 produced by the K-pulses of the library targets A_1 ($\cdot\cdot\cdot\cdot$), A_2 (—) and A_3 (---) at $90^\circ/VP$ from a noisy backscattered data with SNR=11 dB. 288
- Figure 7.35. Normalized response energy curves (plotted on a magnified scale) of the test target A_2 produced by the K-pulses of the library targets A_1 ($\cdot\cdot\cdot\cdot$), A_2 (—) and A_3 (---) at $120^\circ/VP$ from a noisy backscattered data with SNR=11 dB. 289
- Figure 7.36. Normalized response energy curves (plotted on a magnified scale) of the test target A_2 produced by the K-pulses of the library targets A_1 ($\cdot\cdot\cdot\cdot$), A_2 (—) and A_3 (---) at $180^\circ/VP$ for two different SNR levels. 290
- Figure 7.37. Normalized response energy curves of the test target A_3 produced by the K-pulses of the library targets A_1 ($\cdot\cdot\cdot\cdot$), A_2 (---) and A_3 (—) at $0^\circ/VP$ from a noisy backscattered data with SNR=11 dB. 292
- Figure 7.38. Normalized response energy curves (plotted on a magnified scale) of the test target A_3 produced by the K-pulses of the library targets A_1 ($\cdot\cdot\cdot\cdot$), A_2 (---) and A_3 (—) at $30^\circ/VP$ from a noisy backscattered data with SNR=11 dB. 295
- Figure 7.39. Normalized response energy curves (plotted on a magnified scale) of the test target A_3 produced by the K-pulses of the library targets A_1 ($\cdot\cdot\cdot\cdot$), A_2 (---) and A_3 (—) at $45^\circ/VP$ from a noisy backscattered data with SNR=11 dB. 296
- Figure 7.40. Normalized response energy curves (plotted on a magnified scale) of the test target A_3 produced by the K-pulses of the library targets A_1 ($\cdot\cdot\cdot\cdot$), A_2 (---) and A_3 (—) at $60^\circ/VP$ from a noisy backscattered data with SNR=11 dB. 297
- Figure 7.41. Normalized response energy curves (plotted on a magnified scale) of the test target A_3 produced by the K-pulses of the library targets A_1 ($\cdot\cdot\cdot\cdot$), A_2 (---) and A_3 (—) at $90^\circ/VP$ from a noisy backscattered data with SNR=11 dB. 298
- Figure 7.42. Normalized response energy curves (plotted on a magnified scale) of the test target A_3 produced by the K-pulses of the library targets A_1 ($\cdot\cdot\cdot\cdot$), A_2 (---) and A_3 (—) at $120^\circ/VP$ from a noisy backscattered data with SNR=11 dB. 299

Figure 7.43. Normalized response energy curves (plotted on a magnified scale) of the test target A_3 produced by the K-pulses of the library targets A_1 ($\cdot\cdot\cdot\cdot$), A_2 ($- \cdot - \cdot -$) and A_3 (---) at $180^\circ/\text{VP}$ for three different SNR levels. 300

CHAPTER I
INTRODUCTION

Estimation of the physical features of an object or medium from its interactions with electromagnetic waves is a challenging problem, and radar target identification is one of the most well-known applications of practical significance. The fundamental problem in radar target identification is to extract some characteristic information which is uniquely specified by the physical properties (size, shape and composition) of an "unknown" object from a restricted set of measurements.

The radar cross section (RCS) is a well-known measure of electromagnetic scattering properties of an object, but it cannot be used directly as a tool for identification purposes since the RCS of a radar target is not only a function of frequency but also a function of aspect and radar polarization. The earliest attempts to discriminate radar targets focused on variations of the received signal with choice of transmitter and receiver polarization at a single aspect and frequency but are found to be useful only for differentiating classes of targets with special geometrical or electrical symmetries [1]. The next idea was the determination of scattering centers on a target from the complex spectral density function. But, as discussed in [1], a discrete distribution of scattering centers is not sufficient to uniquely define a target.

Extensive use of linear system analysis in electromagnetic scattering problems was first introduced by Kennaugh and Cosgriff [2] in their 1958 paper. They proposed the concept of impulse response for three-dimensional electromagnetic scatterers and described the relationship between the geometry of a perfectly conducting target and its impulse response waveform. This approach was later formalized by Kennaugh and Moffatt [3] leading to very important results in transient analysis of electromagnetic scattering problems in terms of natural resonances of objects. In their 1965 paper, it is suggested that an electromagnetic scatterer can be approximately modeled as a linear time-invariant lumped parameter system, at sufficiently low frequencies. The implication of this statement is that the transfer function of an object can be approximated as a ratio of two polynomials where the zeros of the denominator give the complex natural resonant (CNR) frequencies of the system. Later, the complex natural resonance idea was extensively studied and formalized as the Singularity Expansion Method (SEM) by Baum [4,5]. Since then, a substantial amount of research has focused on the extraction of CNR frequencies of potential radar targets [6-10] for two reasons. First, the CNR frequencies are uniquely determined by the physical properties of an object. Secondly, these frequencies are independent of the aspect angle and polarization of the transmitted and received radar signals. In other words, the infinite set of CNR frequencies constitutes an aspect and polarization-independent descriptor of a finite electromagnetic scatterer as used in radar target identification. Although this idea sounds quite attractive from the theoretical point

of view, some crucial difficulties have been noticed in practice. An exact solution for the CNR frequencies is known to be possible for only spherical scatterers [11] and thin-circular disks [12] whose vector wave functions are separable. The CNR frequencies of other finite objects must be estimated using either the integral equation formulations, as in the Moment Method [13], or asymptotic techniques such as the geometrical theory of diffraction (GTD) [14,15]. But the usefulness of these approaches to estimate the CNR frequencies are limited by the restrictions on the electrical size and the geometrical complexity of radar targets. Another possibility is the numerical extraction of the system poles directly from the measured transient response (or from the corresponding frequency domain data) of the object [16-20]. Most of the methods using this approach are found to be highly sensitive to the signal-to-noise ratio of the measured signals. Consequently, a direct use of CNR frequency information in target identification does not seem to be adequate for identifying real-world radar targets of complicated geometries, especially when they are detected in noisy environments. On the other hand, the concept of natural resonances has been recognized as an important building block in the development of a new target identification method called the Kill-pulse or K-pulse method.

The K-pulse concept was first suggested by Kennaugh in the early 70's [21,22] to devise an inversion technique which utilizes as wide a frequency spectrum as possible but involves only a few aspects, in contrast to conventional imaging techniques. Later, he gave a formal

definition of a special time-limited excitation waveform called the "K-pulse waveform" for an isolated scatterer and introduced a K-pulse synthesized technique which employed the dominant CNR frequencies of the object in his 1981 paper [15]. He also stressed that the K-pulse waveform is an aspect and polarization independent descriptor of an object and can be effectively used for target identification. The need for new techniques of K-pulse synthesis, especially for low-Q and/or geometrically complicated targets, has been inevitable but the basic concept introduced by Kennaugh remains the main building block of the K-pulse method.

The purpose of this report is to develop a K-pulse synthesis technique which is sufficiently general to be applicable to realistically complicated target identification problems. Chapter II is devoted to an overview of the previously suggested K-pulse techniques in the literature, which are found to be useful in case of various objects with simple geometries. The extension of the K-pulse applications to low-Q and/or geometrically complicated radar targets is made possible by the contributions of this report as described in Chapter III. Presented also in this chapter are an alternative mathematical representation of a K-pulse waveform in terms of Legendre polynomials and a target identification scheme employing a normalized instantaneous energy concept, both introduced for the first time in this report. The applications of the proposed K-pulse synthesis and target identification techniques to two classes of geometrically simple conducting targets; linear thin-wires and spherical scatterers are demonstrated in Chapter IV. The K-pulse waveforms of these targets are

estimated using both the discrete sampling approach and the Legendre polynomial approach. Also demonstrated in this chapter is the advantage of using the normalized instantaneous energy function concept in target identification of low-Q objects such as a conducting sphere, especially under noisy conditions. The applications of both K-pulse estimation and target identification techniques are extended to three different classes of geometrically complicated and generally low-Q targets (ships, land vehicles and aircraft) in the next three chapters. Chapter V focuses on the applications to two model ships including also a demonstration of the K-pulse estimation technique using the Legendre polynomial approach. Chapter VI presents the results of applications to a model tank and a model personnel carrier. Applications to three different commercial aircraft models are given in Chapter VII. The noise performance of the target identification technique is tested for various levels of signal-to-noise ratio in Chapters V, VI and VII. Finally, Chapter VIII concludes the report with a discussion of the results obtained in the previous chapters together with the suggestions for future research in the K-pulse estimation and target identification studies.

Several appendices are provided at the end of the report. Several rules of thumb for the estimation of K-pulse duration and cut-off times are given in Appendix A. Appendix B discusses some important points related to the interpretation of the normalized response energy curves for the purpose of target identification. Extraction of the target poles (CNR frequencies) as a by-product of the proposed K-pulse synthesis technique is described in Appendix C. Definitions and

orthogonality properties of the original and modified Legendre polynomials are provided in Appendix D. Appendix E summarizes how to add random Gaussian noise to the original data to be used in noise performance testing of the suggested target identification scheme. Finally, the K-pulse estimation procedure from narrow band full-scale aircraft data is demonstrated in Appendix F as a pilot study towards the design of sophisticated (substructure-related) K-pulse waveforms.

CHAPTER II

AN OVERVIEW OF RESEARCH ON K-PULSE TECHNIQUES

As stated briefly in the previous chapter, the K-pulse concept was first suggested and formalized by Kennaugh. He introduced the idea of synthesizing a time-limited (TL) excitation waveform, called the K-pulse, for a target to produce TL responses regardless of the aspect and radar polarization [15,21,22]. In other words, this characteristic waveform is an aspect and polarization invariant descriptor of the corresponding target such that the target response can be TL under this special excitation waveform at all combinations of aspect and polarization. A similar problem was studied in the early 60's by Gerst and Diamond [23] for the purpose of reducing intersymbol interference in communication systems. Given a time-invariant linear system, they proved that there exist input pulses of arbitrary time duration such that the corresponding output of the system also turns out to be time-limited. In the following years, Campbell studied the problem of designing input waveforms to yield time-limited orthogonal outputs for the purpose of signal detection using matched filters in a communication system [24,25]. Kennaugh's K-pulse concept as well as the former studies just mentioned were based on the idea of input waveform shaping via insertion of zeros in the Laplace transform domain, at the same locations as the system poles, to produce time-limited system responses by pole-zero cancellation. The reasoning

behind this idea may be best explained in terms of complex natural resonances of an electromagnetic scatterer. When a scatterer is modeled as a linear time-invariant distributed parameter system [2,3], its transfer function, $H(s, \Omega)$, can be shown as a meromorphic function [34] in the complex frequency domain (s-domain) and can be factored as

$$H(s, \Omega) = \frac{N(s, \Omega)}{D(s)} \quad (2.1a)$$

where $N(s, \Omega)$ and $D(s)$ are entire functions and the parameter " Ω " implies the aspect and polarization dependency. Then, the scattered impulse response, $h(t, \Omega)$, is computed as

$$h(t, \Omega) = L^{-1}\{H(s, \Omega)\} \quad (2.1b)$$

or

$$h(t, \Omega) = L^{-1}\{N(s, \Omega)\} * L^{-1}\left\{\frac{1}{D(s)}\right\} \quad (2.1c)$$

where " L^{-1} " denotes the inverse Laplace operator and the asterisk "*" refers to the convolution operation. Thus, the impulse response can be decomposed, at least theoretically, as the convolution of two parts; one is excitation dependent and the other one is excitation invariant.

The response of the scatterer, to an arbitrary input waveform, $x(t)$, can be computed as

$$r(t, \Omega) = h(t, \Omega) * x(t) \quad (2.2a)$$

in time domain, or as

$$R(s, \Omega) = H(s, \Omega) X(s) \quad (2.2b)$$

in the Laplace transform domain. Using Equations (2.1a) and (2.2b), one can write

$$R(s, \Omega) = \frac{N(s, \Omega)}{D(s)} X(s) . \quad (2.2c)$$

As discussed in [23], [26] and [27], the Laplace transform of every TL function can be easily proved to be an entire function. Conversely, the inverse Laplace transform of a function, defined in the complex frequency domain, can be TL only if the function itself is entire and of exponential type. Then, one of the necessary conditions for having a TL system response is that the Laplace transform function, $R(s, \Omega)$, should be entire. This condition is satisfied when the function, $X(s)$, is also entire and its zeros cancel the zeros of $D(s)$ which are often called the system poles. Consequently, the K-pulse waveform, $k(t)$, of an object can be uniquely defined as a special TL excitation such that there is a one-to-one correspondence between the zeros of its Laplace transform and the poles of the object. It can easily be shown that the duration of the unique K-pulse waveform is shorter than the durations of all other TL input waveforms which also produce TL target outputs at all aspects and polarizations. As a matter of fact, those TL functions can be thought as convolutions of the unique K-pulse waveform with some arbitrary TL functions. At this point, it should be noted that the unique K-pulse as defined above is a completely theoretical concept, not a practically realizable one. This fact was also implied by the

thin-wire applications of the K-pulse method presented by Kennaugh [21,22] in that an approximate K-pulse waveform characterized only by some dominant target poles may be good enough for almost all practical purposes.

About four years after Kennaugh's introductory K-pulse paper, the K-pulse waveform for a conducting thin-circular loop was provided by Kim, Wang and Moffatt [28]. They utilized the dominant CNR frequencies of the object by inserting zeros into an exponential type entire Laplace transform expression given by Gerst and Diamond [23] to produce an approximate K-pulse waveform. Later, an application of the K-pulse approach to non-uniform transmission lines was studied by Kennaugh, Moffatt and Wang [29]. Meanwhile, Rothwell et al. [30,31] and Chen et al. [32] proposed a target identification approach called the Extinction-pulse (or E-pulse) method which appears to have originated from the basic K-pulse idea. As discussed by Fok and Moffatt [33], under certain conditions, the E-pulse method and the K-pulse method are completely equivalent in terms of the basic concepts and models they use.

Almost all of the references given so far share one important aspect; direct use of target CNR frequencies (poles) for K-pulse (or E-pulse) synthesis. Although this approach has proved to be successful for geometrically simple targets for which the dominant CNR frequencies can be estimated by various techniques, the difficulties of accurate pole extraction in the case of geometrically complicated targets and noisy radar measurements make such an approach difficult if not impossible to use in real-world target identification problems.

Consequently, it has been inevitable that a search for an alternative technique of K-pulse synthesis which does not need a priori information on the target CNR frequencies would occur. Remembering that the ultimate purpose of the K-pulse method is to generate (conceptually) a special TL excitation waveform which produces TL responses at all aspects and polarizations, a reasonable approach may be to solve this problem in the reverse direction. In other words, an optimal solution for an approximate K-pulse waveform may be obtained by forcing the target response to be time-limited. This approach was recently demonstrated by Fok, Moffatt and Wang [34,35] for geometrically simple, high-Q and low-Q targets. Since the K-pulse synthesis technique used in this report is based on the same basic idea, it will be useful to examine the approach introduced by Fok et al. in some detail. The K-pulse synthesis procedure described in [35] basically refers to an optimization problem where the first step is to assume a mathematical representation for the K-pulse waveform as

$$k(t) = \delta(t) + \sum_{n=1}^N a_n \delta(t-n\tau) \quad (2.3)$$

with $\tau=T/N$, where T is the duration of the K-pulse, N is the number of discrete delta functions in the model and the a_n 's are unknown real constants. The summation term in this expression approximates a continuous function whose equally-spaced sample values are represented by the weights of delta functions falling in the semi-closed time interval $(0,T]$. A cost function, J , is then defined as

$$J = \int_{T_R}^{T_C} [k(t)*h(t)]^2 dt ; \quad (2.4)$$

to be the natural resonance-related energy content of the target response after a cut-off time, T_R .

In this expression, $h(t)$ is the impulse response of the target at an arbitrary aspect and radar polarization, T_C represents an arbitrarily long time duration and the asterisk denotes convolution. By minimizing the cost function J , the unknown weights, a_n , of the impulsive basis functions can be estimated. It should be noted that the choice of this cost function is due to the following interpretation of the scattering mechanism from the systems theory point of view. When a finite object is excited by an aperiodic pulse, its response consists of first a time-limited forced response as the incident wavefront moves over the object and then a free or natural response which keeps ringing after the wavefront moves beyond the object. The amount of energy to be minimized must be related to these natural modes only. Otherwise, the zero-pattern of the K-pulse spectrum would be totally different from the pole-pattern of the target and the resultant waveform would not be a K-pulse. Consequently, the lower limit of the integral in Equation (2.4) must be chosen very carefully. As stated by Fok et al., the most important feature of their K-pulse synthesis technique is that it does not need a priori knowledge of the target poles. In fact, the target poles can be estimated as the zeros of the Laplace transform of the synthesized K-pulse waveform. The applications of this technique are successfully demonstrated in [34]

and [35] for simple geometries such as a grounded dielectric slab, linear thin-wire, thin-circular conductor, conducting sphere, conducting circular disk and circular waveguides. But for applications involving complicated target geometries as in the case of aircraft, ships, etc., this proposed approach is not found to be useful due to some important shortcomings of the problem formulation. It is one of the purposes of the next chapter to suggest several modifications of crucial importance to this existing K-pulse synthesis technique, which are basically related to the definition of the cost function.

CHAPTER III

THEORIES AND FORMULATIONS

This chapter introduces the theoretical aspects of a new K-pulse synthesis technique, mainly for geometrically complicated targets and the related target identification approach. First, the K-pulse synthesis technique will be described by stressing its similarities to and differences from the technique suggested by Fok et al. Secondly, an alternative mathematical representation of the K-pulse in terms of Legendre polynomials will be introduced. Finally, two versions of a target identification scheme will be described: one using the time-limited K-pulse response idea directly, and the other one employing the normalized instantaneous energy functions associated with the target responses.

A. K-PULSE ESTIMATION

As discussed in the previous chapter, almost none of the K-pulse synthesis techniques suggested in the literature to this point seem to be applicable to real-world target identification problems. But, among all the others, the technique suggested by Fok et al. should be given a special credit for developing a K-pulse synthesis procedure which is not dependent upon a priori target pole information. There are three important reasons why this technique works very well for simple target geometries as presented in [34] and [35], but fails for sophisticated

ones. First, the existence of target substructures complicates the natural resonance mechanisms so that estimation of time durations for the K-pulse waveforms turns out to be a very difficult problem. Secondly, the use of a target's impulse response at a single combination of aspect and radar polarizations is usually adequate for simple and highly symmetrical target geometries but does not provide sufficient information for complicated structures. The reason is that the target pole residues are known to be aspect and polarization dependent so that some of the natural modes might be excited very weakly for a specific experiment chosen for the K-pulse synthesis procedure. Consequently, the resultant approximate K-pulse waveform does not contain the characteristic features due to such target poles and may easily fail in producing time-limited responses at some other aspects and radar polarizations. Thirdly, in most real-world target identification problems, available scattered data are "incomplete" in the sense that the frequency range of radar measurements may not be spanning the early part of the resonance region. The loss of information at such frequencies means no access to at least several target pole-pairs falling in that range. Therefore, a K-pulse waveform synthesized from such an incomplete data set will be a relatively poor approximation to the true K-pulse.

The K-pulse synthesis technique introduced in this report is conceptually similar to the one suggested by Fok et al. Both techniques address an optimization problem to synthesize an approximate K-pulse waveform of a target from its scattered impulse response without using any pole information. Furthermore, both assume a similar

mathematical model for the K-pulse; a unit strength impulse function at the initiation time and then a continuous function of finite duration whose shape is to be estimated via minimization of the energy content of the target's natural response. The distinguishing feature of the technique suggested in this report is the use of a simultaneous "multi-combinational" system analysis in the following sense: the response of a geometrically complicated target is computed at several combinations of the aspect and/or polarization and the energy content of these responses beyond the corresponding K-pulse response durations is minimized simultaneously to obtain an optimal K-pulse waveform. This conceptually simple modification has been found to be substantially useful in extending the K-pulse applications to sophisticated target geometries [36]. As another important modification to the existing technique, a new cost function is employed in this report, whose effect on the performance of the K-pulse synthesis technique will be explained during the derivations.

The assumed time-domain model for the K-pulse consists of a unit strength impulse (Dirac delta) function, $\delta(t)$, and then a continuous time function $k^c(t)$, such that

$$k(t) = \delta(t) + k^c(t) \quad (3.1a)$$

for

$$t \in [0, T_k] \quad (3.1b)$$

where T_k is the K-pulse duration. The K-pulse response of a target can be computed as

$$r^i(t) = h^i(t) * [\delta(t) + k^c(t)] \quad (3.2a)$$

or

$$r^i(t) = h^i(t) + [h^i(t) * k^c(t)] \quad (3.2b)$$

where $h^i(t)$ is the scattered impulse response of the target, the asterisk "*" denotes the convolution operator, and the superscript "i" refers to an arbitrary combination of aspect and radar polarization. The right hand side of the last equation is composed of two functions: the impulse response and its convolution with the continuous part of the K-pulse. Theoretically, both of these functions are of infinite time duration but they must sum up to a time-limited function, $r^i(t)$, as a result of natural response annihilation. Then, the problem is to synthesize the function, $k^c(t)$, properly to meet this requirement. As mentioned earlier, the simultaneous multi-combinational analysis approach will be used in connection with an optimization problem for this purpose. The cost function to be minimized is defined as follows:

$$J = a J_1 + b J_2 \quad (3.3a)$$

with

$$J_1 = \sum_{i=1}^I \omega_i \frac{\int_{T_L^i}^{\infty} |r^i(t)|^2 dt}{\int_0^{T_L^i} |r^i(t)|^2 dt} \quad (3.3b)$$

and

$$J_2 = \sum_{i=1}^I g_i \int_{T_L^i}^{\infty} |r^i(t)|^2 dt \quad (3.3c)$$

where I is the number of combinations of aspect and radar polarization used in the K-pulse synthesis; T_L^i 's are the combination dependent cut-off times which represent the estimated time durations of the target's forced response at each combination; and the constants a , b , ω_i 's and g_i 's are weight factors. This cost function can be expressed in a compact form as

$$J = a \sum_{i=1}^I \omega_i \frac{\xi_L^i}{\xi_E^i} + b \sum_{i=1}^I g_i \xi_L^i \quad (3.4)$$

defining the early-time energy content such that

$$\xi_E^i = \int_0^{T_L^i} |r^i(t)|^2 dt \quad (3.5a)$$

and the late-time energy content given by

$$\xi_L^i = \int_{T_L^i}^{\infty} |r^i(t)|^2 dt \quad (3.5b)$$

where the target response is for the i^{th} combination of aspect and radar polarization. Ideally, ξ_L^i must represent the energy content of the natural target response only such that its minimization results in a correct zero insertion into the K-pulse spectrum. But the late portion of the forced response usually overlaps with the early portion of the natural response. Consequently, the cut-off time T_L^i must be

chosen in such a way that some part of the natural response energy is left unused for the sake of preventing the minimization of forced response energy. The use of simultaneous multi-combinational system analysis for K-pulse formulation is found to be very effective in spotting an improper pre-estimation of cut-off times such that a serious convergence problem occurs during the minimization if the cut-off times are assigned incorrectly. It should also be noted that the minimization of the ratio of ξ_L^1 to ξ_E^1 at each combination as implied by Equation (3.3b) is another precaution taken against the undesired minimization of forced response energy. In other words, the first part of the cost function tries to assure the concentration of the K-pulse response energy in the time interval $[0, T_L^1]$ at each combination used in the K-pulse synthesis procedure. The second part of the cost function directly helps the minimization of late-time response energy. As a matter of fact, the cost function suggested by Fok et al. is a special case of Equation (3.4) for $a=0$, $b=1$, $g_1=1$ and $I=1$. As the last comment on the cost function, it should be noted that using more than just one combination in the K-pulse synthesis procedure complicates the mathematical derivations and increases the computation time, but it is a vital necessity in the case of complicated targets such as aircraft, land vehicles and ships. Use of this approach leads to a self-correcting synthesis problem in the sense that an inaccurate cut-off time assumption or missing some weakly excited poles at one combination results in an improper zero pattern of the K-pulse spectrum and reflects on the other combinations as an excess late-time energy. A satisfactory convergence is obtained only when the K-pulse works well

at all of the synthesis combinations. Practically, it seems difficult to consider more than five combinations for K-pulse synthesis and two or three combinations are found to be sufficient in most of the applications when the aspect angles are chosen to be far apart.

To this point the problem is formulated in general terms without specifying the optimization variables explicitly. The next step is to choose a convenient mathematical representation for the continuous part of the K-pulse model. The representation suggested by Fok et al. was based on an expansion in terms of impulsive basis functions which was equivalent to approximating $k^c(t)$ by its equally-sampled values as indicated in Equation (2.3). In this report, two types of representation will be demonstrated; first a discrete representation which is conceptually the same as the one used by Fok et al., secondly a continuous representation in terms of Legendre polynomials which is suggested for the first time in this chapter.

The expression for the K-pulse response of a target was given in Equation (3.2). It can be rewritten in terms of the convolution integral as

$$r^i(t) = h^i(t) + \int_0^{\min[t, T_k]} k^c(z)h^i(t-z)dz . \quad (3.6)$$

If the function $k^c(t)$ is going to be represented in a discrete manner, the continuous-time expression given above should be approximated by its discrete counterpart to express the cost function

in terms of the sample values of $k^c(t)$. The discrete notation to be used in the rest of the derivations will be

$$x_j \stackrel{\Delta}{=} x(t) \Big|_{t=\tau(j-1)} \quad j=1,2,\dots ; \quad (3.7a)$$

where $x(t)$ stands for $k^c(t)$, $h^i(t)$ or $r^i(t)$; and

$$\tau = \frac{T_k}{N-1} \quad (3.7b)$$

with T_k being the K-pulse duration, and N the number of equally-spaced samples of the function $k^c(t)$. Using this notation, an arbitrary sample of the K-pulse response, r_j^i , can be approximated as

$$r_j^i = h_j^i + \tau \sum_{m=1}^{\min[N,j]} k_m^c h_{j-m+1}^i \quad (3.8)$$

where the summation term is simply a rectangular-segments approximation to the convolution integral given in Equation (3.6). This approximation can be improved using the trapezoidal rule or Simpson's rule [37]. While the use of Simpson's rule is not preferred for the sake of simplicity, the trapezoidal rule can be applied easily by dividing the end sample values of $k^c(t)$ and $h^i(t)$ by a factor of two in Equation (3.8).

The discrete approximation of the cost function, \bar{J} , can be expressed implicitly in terms of the unknown K-pulse samples, $k_1^c, k_2^c, \dots, k_N^c$ as

$$\bar{J} = a \sum_{i=1}^I \omega_i \left[\sum_{j=N_L^i}^{N_m} (r_j^i)^2 / \sum_{j=1}^{N_L^i-1} (r_j^i)^2 \right] + b \sum_{i=1}^I g_i \sum_{i=1}^m (r_j^i)^2 \quad (3.9a)$$

where

$$N_L^i = \frac{T_L^i}{\tau} + 1 \quad (3.9b)$$

and

$$N_m = \frac{T_{\max}}{\tau} + 1 \quad (3.9c)$$

with T_{\max} being a sufficiently long time duration beyond which the target response can be assumed to be zero for all practical purposes.

The K-pulse waveforms to be demonstrated in the next chapters are synthesized by minimizing this cost function using the Fletcher-Powell steepest descent algorithm [38] which requires the computation of a gradient vector as

$$\bar{G} = \left[\frac{\partial \bar{J}}{\partial k_1^c}, \frac{\partial \bar{J}}{\partial k_2^c}, \dots, \frac{\partial \bar{J}}{\partial k_N^c} \right]^T \quad (3.10)$$

where 'T' denotes the transpose operation. An arbitrary element of this vector can be expressed as

$$\frac{\partial \bar{J}}{\partial k_n^c} = 2a \sum_{i=1}^I \omega_i \frac{\xi_E^i \sum_{j=N_L^i}^{N_m} r_j^i \frac{\partial r_j^i}{\partial k_n^c} - \xi_L^i \sum_{j=1}^{N_L^i-1} r_j^i \frac{\partial r_j^i}{\partial k_m^c}}{(\xi_E^i)^2} +$$

$$+ 2b \sum_{i=1}^I g_i \sum_{j=N_L^i}^{N_m} r_j^i \frac{\partial r_j^i}{\partial k_n^c} \quad (3.11a)$$

where

$$\xi_E^i = \sum_{j=1}^{N_L^i-1} (r_j^i)^2 \quad (3.11b)$$

$$\xi_L^i = \sum_{j=N_L^i}^{N_m} (r_j^i)^2 \quad (3.11c)$$

and

$$\frac{\partial r_j^i}{\partial k_n^c} = \begin{cases} \tau h_{j-n+1}^i & , \text{ if } n \leq \min(N, j) \\ 0 & , \text{ otherwise} \end{cases} \quad (3.11d)$$

for $n=1, 2, \dots, N$.

Use of this discrete mathematical representation for the continuous part of the K-pulse leads to a relatively simple formulation which is also suitable for computer simulation. On the other hand, this representation may require a large number of optimization variables, which are equal to the number of K-pulse samples. This problem may be partially solved by using some other basis functions to

represent the function, $k^c(t)$. A possible approach in this direction will be described in the following section.

B. K-PULSE ESTIMATION USING LEGENDRE POLYNOMIALS

One of the basic features of a K-pulse waveform is that it is a time-limited function. Therefore, the continuous part of the K-pulse can be represented in terms of a basis of continuous functions defined on a compact support [39-41]. The set of Legendre polynomials [42] is such a candidate basis being a complete and orthogonal set of continuous functions over the closed interval $[-1,1]$. Since, the interval of definition in the K-pulse synthesis problem is $[0, T_k]$, a modified version of the Legendre polynomials will be utilized as

$$\bar{P}_n(t) = P_n(z) \Big|_{z = \frac{2}{T_k} t - 1} \quad (3.12a)$$

or

$$\bar{P}_n(t) = \sum_{m=0}^n \alpha_{nm} \left(\frac{2}{T_k} t - 1 \right)^m \quad (3.12b)$$

for

$$t \in [0, T_k] \quad (3.12c)$$

where $\{P_n(z)\}_{n=0}^{\infty}$ is the set of original Legendre polynomials and $\{\bar{P}_n(t)\}_{n=0}^{\infty}$ is that of modified Legendre polynomials obtained via the time-scaling rule

$$z = \frac{2}{T_k} t - 1 . \quad (3.12d)$$

The definition and the orthogonality properties of the original and modified Legendre polynomials are given in Appendix D.

The mathematical representation of the K-pulse can be given as

$$k(t) = \delta(t) + \sum_{n=0}^{\infty} D_n \bar{P}_n(t) \quad (3.13)$$

where the summation term stands for the function, $k^c(t)$, and the D_n 's are the expansion coefficients to be determined. Using Equations (3.2b), (3.12b) and (3.13), the K-pulse response is given as follows:

$$r^i(t) = h^i(t) + \sum_{n=0}^{\infty} D_n \sum_{m=0}^n \alpha_{nm} \left[h^i(t) * \left(\frac{2}{T_k} t - 1 \right)^m \right] \quad (3.14a)$$

or

$$r^i(t) = h^i(t) + \sum_{n=0}^{\infty} D_n \sum_{m=0}^n \alpha_{nm} B^i(t, m) \quad (3.14b)$$

where

$$B^i(t, m) = \int_0^{\min(T_k, t)} h^i(t-\eta) \left(\frac{2}{T_k} \eta - 1 \right)^m d\eta . \quad (3.14c)$$

Then, the unknown expansion coefficients can be estimated by minimizing the cost function, J , defined in Equation (3.3). The gradient vector

of this cost function with respect to the optimization variables, D_n 's, is given as

$$\bar{G} = \left[\frac{\partial J}{\partial D_1}, \frac{\partial J}{\partial D_2}, \dots, \frac{\partial J}{\partial D_p}, \dots \right]^T \quad (3.15)$$

where an arbitrary element $\partial J / \partial D_p$ of this vector can be computed as

$$\begin{aligned} \frac{\partial J}{\partial D_p} = & 2a \sum_{i=1}^I \omega_i \frac{1}{(\xi_E^i)^2} \left[\xi_E^i \int_{T_L^i}^{\infty} r^i(t) \frac{\partial r^i(t)}{\partial D_p} dt - \int_0^{T_L^i} r^i(t) \frac{\partial r^i(t)}{\partial D_p} dt \right] \\ & + 2b \sum_{i=1}^I g_i \int_{T_L^i}^{\infty} r^i(t) \frac{\partial r^i(t)}{\partial D_p} dt \end{aligned} \quad (3.16a)$$

with

$$\frac{\partial r^i(t)}{\partial D_p} = \sum_{m=1}^P \alpha_{pm} B^i(t,m) \quad (3.16b)$$

where ξ_E^i and ξ_L^t are defined in Equations (3.5a) and (3.5b), respectively. The expressions derived to this point need to be approximated by their discrete time counterparts for the purpose of computer simulation. Using the discrete notation defined in the previous section

$$r_j^i = h_j^i + \sum_{n=0}^{NP} D_n \sum_{m=0}^n \alpha_{nm} B^i(j,m) \quad (3.17a)$$

where

$$B^i(j,m) = \tau \sum_{q=1}^{\min(j,N)} h_{j-q+1}^i \left[\frac{2}{T_k}(q-1)\tau - 1 \right]^m \quad (3.17b)$$

and

$$\begin{aligned} \frac{\partial J}{\partial D_p} = & 2a \sum_{i=1}^I \omega_i \frac{1}{(\xi_E^i)^L} \left[\xi_E^i \sum_{j=N_L^i}^{N_m} r^i(t) \left(\frac{\partial r^i(t)}{\partial D_p} \right)_j - \sum_{j=1}^{N_L^i-1} r^i(t) \left(\frac{\partial r^i(t)}{\partial D_p} \right)_j \right] \\ & + 2b \sum_{i=1}^I \xi_i \sum_{j=N_L^i}^{N_m} r^i(t) \left(\frac{\partial r^i(t)}{\partial D_p} \right)_j \end{aligned} \quad (3.17c)$$

with

$$\left(\frac{\partial r^i(t)}{\partial D_p} \right)_j = \sum_{m=0}^P \alpha_{pm} B^i(j,m) \quad (3.17d)$$

and the approximate cost function, \bar{J} , is given by Equation (3.9). The approximate energy terms ξ_E^i and ξ_L^i are as defined in Equation (3.11) in the previous section. It should also be noted that the maximum order of the modified Legendre polynomials to be used in the synthesis procedure must be limited to a sufficiently large finite integer for practical purposes. This parameter is denoted as NP in Equation (3.17a). The K-pulse synthesis examples to be demonstrated in Chapters IV and V show that use of a highly truncated set of Legendre polynomials with NP=5 is sufficient for the K-pulse synthesis of thin wires and spheres; and for the case of a model ship, NP=9 turns out to be an adequate choice for satisfactory results. In other words, the related optimization problem generally requires a substantially smaller number of variables when a Legendre polynomial basis is utilized in the

K-pulse formation procedure as an alternative to a discrete basis described in Section A. Therefore, the Legendre polynomial approach leads to a faster K-pulse synthesis algorithm in most cases.

The problem of K-pulse synthesis is mathematically formulated and two types of representations for the K-pulse waveform are described. It is also noted that the K-pulse duration, T_k , and the cut-off times, T_L^i , need to be pre-estimated properly. There appears to be no straightforward way of estimating these parameters, especially for complicated target geometries. Several rules of thumb are discussed in Appendix A.

C. TARGET IDENTIFICATION

The target identification scheme employed in this report requires a "K-pulse library" which consists of the K-pulse waveforms of various candidate targets in a class of interest. All of these K-pulses must be synthesized in advance and stored in computer files to create this library. When an "unknown" object is detected by radar, the measured impulse response is digitally convolved with each of these K-pulse waveforms to compute the corresponding target responses. The object is identified as one of the library targets whose response exhibits the shortest time duration or more realistically for noisy data, has the lowest percentage of late-time response energy. The number and types of the targets included in the K-pulse library are determined by the specific needs of the target identification systems.

The most important feature of this identification approach is that it does not require sophisticated signal processing or information

extraction from the received radar signal. The identification procedure is simply the numerical computation of the outputs of a parallel bank of digital filters characterized by the pre-synthesized K-pulse waveforms. The identification decision can be made by comparing the plots of either the resulting response waveforms or the related normalized instantaneous energy functions.

Comparison of target responses for identification purposes naturally follows from the key idea of the K-pulse theory that the response of a target to its "matched" K-pulse should be time-limited at all aspects and radar polarizations. But, this condition can only be met theoretically if the "unique" K-pulse of the target is available. It has been repeatedly indicated that the K-pulse synthesis technique introduced in this report as well as the formerly suggested ones are useful to obtain approximate K-pulse waveforms as a result of partial natural mode annihilation, which may fail to produce absolutely time-limited target responses at all combinations. Consequently, it is more realistic to expect a reduced but non-zero amount of natural response energy under the K-pulse excitation at not all but most of the combinations of aspect and polarization. This situation occurs most frequently in the case of geometrically complicated targets due to the difficulties of cut-off time estimations as mentioned earlier. Also, in almost all of the practical cases, the measured unknown signal is contaminated by noise that may cause a substantial amount of uncertainty or even false results in target identification. Clearly, the signal-to-noise ratio (SNR) gets smaller at the tail of the target response where the noise energy is likely to be comparable to the

signal energy. In other words, the late-time portion of the target response, whose magnitude is expected to be minimized to very small finite values under the matched K-pulse excitation, is effected most in the existence of noise energy. For a low-Q target, this problem becomes much more serious because the natural response dies out very quickly providing only a small amount of natural response related energy for the late-time minimization. As a result, even a little noise energy becomes sufficient to make the identification of low-Q targets impossible on the basis of target response comparisons.

The use of normalized instantaneous response energy functions instead of response waveforms themselves is suggested and used in this report for the purpose of target identification. The definition of instantaneous energy function is given as

$$\xi^x(t) = \int_{-\infty}^t x(t) x^*(t) dt \quad (3.18a)$$

where $x(t)$ is an arbitrary time function and the superscript "*" denotes the complex conjugate operator. Assuming that $x(t)$ is real and causal, this expression can be rewritten as

$$\xi^x(t) = \int_0^t [x(t)]^2 dt \quad (3.18b)$$

and the total energy of $x(t)$ is

$$\xi_T^x = \lim_{t \rightarrow \infty} \xi^x(t) \quad (3.18c)$$

or

$$\xi_T^x = \int_0^{\infty} [x(t)]^2 dt . \quad (3.18d)$$

Obviously, $\xi^x(t)$ is a positive-valued increasing function and approaches the asymptotic maximum value of ξ_T^x . Furthermore, the energy distributions of different functions can be compared in the most convenient way when the corresponding instantaneous energy functions are normalized as

$$\bar{\xi}^x(t) = \frac{1}{\xi_T^x} \int_0^t [x(t)]^2 dt \quad (3.19a)$$

or

$$\bar{\xi}^x(t) = \frac{\int_0^t [x(t)]^2 dt}{\int_0^{\infty} [x(t)]^2 dt} \quad (3.19b)$$

where the total normalized energy, $\bar{\xi}_T^x$, becomes unity.

The target identification examples to be given in Chapters IV through VII for various classes of targets mostly utilize the comparison of the normalized response energy curves of the unknown target under the excitation of library K-pulse. The response energy curve that corresponds to the matched K-pulse is expected to lead other curves, especially at late times in the sense that it reaches high energy levels earlier than the normalized response energy curves which

correspond to the mismatched K-pulses. Appendix B provides further discussion on how to interpret the normalized energy curves in various situations to make an identification decision.

CHAPTER IV

APPLICATIONS TO GEOMETRICALLY SIMPLE TARGETS

Although the main goal of this report is to extend the K-pulse applications to geometrically complicated targets, the suggested K-pulse estimation and target identification techniques need to be tested first on simple targets for two reasons; first, the scattering mechanisms of targets such as a conducting sphere [43-47] and a conducting linear thin-wire [48-50] have been studied extensively in the literature. Their impulse response waveforms can be generated by computer programs, if not available via measurements, and their dominant pole values are already known. Therefore, such targets are valuable tools in justifying the validity of new proposed K-pulse techniques, especially through comparison of the actual pole values with those which are extracted as the zeros of the synthesized K-pulse spectra. Secondly, application of the K-pulse estimation and target identification techniques to simple geometries helps one to understand the basic phenomena and the limitations of these techniques apart from some specific complications that may be caused by complex geometrical features. In this chapter, two objects with simple geometries are considered as radar targets; a conducting linear thin-wire which is a very high-Q object, and a conducting sphere which shows the typical features of low-Q radar targets.

A. APPLICATIONS TO CONDUCTING LINEAR THIN-WIRE

In this section the test target is chosen to be a conducting linear thin-wire of length 12 meters and length-to-diameter ratio of 2000. The K-pulse estimation technique formalized in Chapter III is applied to this target, first using a discrete representation for the continuous part of the K-pulse waveform and then using a Legendre polynomial expansion. Finally, the K-pulse waveforms of two other conducting linear thin-wires, with different lengths but the same length-to-diameter ratios, will be generated to construct a K-pulse library and to demonstrate several identification examples. The original test wire is going to be referred to hereafter as W_1 with $L_1=12\text{m}$ and $L_1/d_1=2000$.

1. K-Pulse Estimation Using a Discrete Representation

The general model of the K-pulse was given in Equation (3.1) as

$$k(t) = \delta(t) + k^c(t) \quad \text{for } t \in [0, T_k] . \quad (4.1)$$

In this application, the K-pulse duration is estimated to be $2L_1/c = 80$ ns (nanoseconds); i.e., twice the length of the wire divided by the speed of light in vacuum. The function $k^c(t)$ is approximately represented by its equally-spaced sample values; $k_1^c, k_2^c, \dots, k_N^c$ for $N=100$. The initial estimate of each sample value is taken to be unity. The discrete cost function, \bar{J} , as specified in Equation (3.9), is minimized for $a=1$, $b=0$ and $I=1$ to determine the optimal values of the

K-pulse samples. Since the target has a simple geometry, a single-combinational analysis is found to be sufficient. The backscattered frequency data at $\phi=30^\circ$ (measured from the axis of the wire) for $\hat{\phi}$ -polarization are generated from a moment method solution [50] over the frequency range 2-(2)-256 MHz to be used for K-pulse estimation. The backscattered impulse response of W_1 at this combination is obtained using an inverse fast Fourier transformation (IFFT) after weighting the frequency data by a low-pass Hanning window function to reduce the Gibb's phenomena [51,52]. The cut-off time, T_L , of the cost function is set to 100 ns. Since the target is a substantially high-Q object, the initial amount of response energy beyond this cut-off time is reasonably large. The value of the cost function is reduced from about 0.26 to 2.4×10^{-3} in 20 iterations of the Fletcher-Powell optimization algorithm. The resultant approximate K-pulse waveform is shown in Figure 4.1*. The impulse response and the optimized K-pulse response of W_1 at $\phi=30^\circ$ are plotted together in Figure 4.2a where both waveforms are normalized to have unit total energy in the time interval [0,500 ns] to provide a meaningful comparison. As seen in this figure, the time span of the normalized K-pulse response is about 100 ns as dictated by the pre-estimated cut-off time. The normalized energy function of the impulse response and that of the K-pulse response are also plotted in Figure 4.2b to compare the time spans of these two waveforms on the basis of their energy distributions.

* All the figures and tables are collected at the end of the chapter for convenience.

To justify the claim that the K-pulse waveform presented in Figure 4.1 is indeed an aspect-invariant descriptor of the wire W_1 , the target response must also turn out to be time-limited at other aspect angles. Two of these cases are demonstrated in Figures 4.3 and 4.4 at aspect angles of 60° and 90° , respectively. Both of these figures show that the corresponding K-pulse responses are time-limited, as expected. The validity of the K-pulse synthesis result is also justified in a manner which does not leave any doubt via the comparison of two sets of wire poles; one is computed [2] from a moment method solution for the first six pole pairs of the wire with $L/d=2000$ and the other set is extracted as the zeros of the Laplace transform of the K-pulse shown in Figure 4.1. These sets of values are presented in Table 4.1 showing a very good agreement with each other.

2. K-Pulse Estimation Using a Legendre Polynomial Representation

The K-pulse estimation technique using an expansion in Legendre polynomials is formalized in this report for the first time and needs to be tested for targets of simple geometries before being applied to complicated cases. For this reason, application to the conducting linear thin-wire is pertinent.

The target and data to be used in this example are the same as those utilized in the previous demonstration. The K-pulse of the wire W_1 is going to be synthesized in the form

$$k(t) = \delta(t) + \sum_{n=0}^{\infty} D_n \bar{P}_n(t) \quad \text{for} \quad t \in [0, T_k] \quad (4.2)$$

where the \bar{P}_n 's are modified Legendre polynomials and the D_n 's are the expansion coefficients to be determined. The K-pulse duration is 80 ns as in the previous example. The infinite set of Legendre polynomials is truncated at the maximum order of five for practical reasons, as explained in Chapter III. The K-pulse synthesis aspect is chosen to be $\phi=60^\circ$ and the cut-off time is set at 115 ns. The cost function \bar{J} of Equation (3.9) is minimized for the case $a=0$, $b=1$ and $I=1$. The synthesis aspect and some of the optimization parameters are intentionally chosen to be different from those used in the previous example to see if they have any crucial effect on the synthesis procedure. As a result of only ten iterations of the minimization algorithm, the K-pulse waveform shown in Figure 4.5 is constructed from the optimized values of the expansion coefficients. As a matter of fact, only the first five of these coefficients are found to be important in the expansion as shown in Table 4.2 (higher order Legendre polynomials would be included in the expansion if any convergence problem occurred in the synthesis procedure indicating that the present representation was not adequate). The normalized impulse response and K-pulse response of W_1 at $\phi=60^\circ$, the synthesis aspect, are plotted together in Figure 4.6a. The corresponding normalized energy curves are shown in Figure 4.6b. The comparisons of the impulse response and K-pulse response at two non-synthesis aspects, 30° and 90° , are given in Figures 4.7 and 4.8, respectively. Although these results are not as perfect as those presented in Figures 4.2 through 4.4, they are still very satisfactory for all practical purposes. If a higher number of iterations was allowed in this example, better results could be

obtained, but the present results are quite satisfactory as they stand and it seems that there is no need to keep minimizing the cost function at the expense of more computer time. This conclusion is supported by the results presented in Table 4.3, where the pole values of the target as extracted from the K-pulse waveform of Figure 4.5 are found to be in a good agreement with those pole values calculated from a moment method solution. It should also be noted that the K-pulse waveform of the wire, W_1 , presented in Figures 4.1 and 4.5 are similar but not exactly the same, reflecting the fact that these waveforms are two different approximations to the theoretically "unique" K-pulse whose spectrum zeros are exactly the same as the poles of W_1 . In practice, any one of these approximate K-pulses is acceptable and useful in target identification as will be demonstrated next.

3. Target Identification

In this section, a K-pulse library of three conducting cylindrical thin-wires, to be called W_1 , W_2 and W_3 , is formed for target identification purposes. The geometrical features of these wire targets are summarized as

$$W_1: L_1 = 12 \text{ m.}, d_1 = 6 \text{ mm.}$$

$$W_2: L_2 = 10.8 \text{ m.}, d_2 = 5.4 \text{ mm.}$$

$$W_3: L_3 = 13.2 \text{ m.}, d_3 = 6.6 \text{ mm.}$$

where all have the same length-to-diameter ratio of 2000. The dimensions of the targets W_2 and W_3 differ from the dimensions of W_1 only by -10% and +10%, respectively. The first target, W_1 , is the one for which two approximate K-pulse waveforms were already synthesized via different approaches and presented in Figures 4.1 and 4.5. The latter K-pulse result which was synthesized using the Legendre polynomial approach is going to be utilized here for target identification. The K-pulse waveforms of the wires W_2 and W_3 can be directly constructed from the K-pulse of W_1 by re-scaling the time-axis and the K-pulse waveform amplitude since all three wires have the same basic geometry with $L_1/d_1 = L_2/d_2 = L_3/d_3 = 2000$. The resultant K-pulse waveforms $k_{W_2}(t)$ and $k_{W_3}(t)$ as well as the originally synthesized K-pulse waveform $k_{W_1}(t)$ are plotted together in Figure 4.9. The zeros of the Laplace transforms $K_{W_2}(s)$ and $K_{W_3}(s)$ on sL_2/c and sL_3/c scales, respectively have the same numerical values as the zeros of $K_{W_1}(s)$ which are tabulated on a sL_1/c scale in Table 4.3.

In the following identification examples, the "unknown" target is the wire W_1 . Figure 4.10a shows the response waveforms of W_1 , at 30° aspect angle, to the library K-pulse $k_{W_1}(t)$, $k_{W_2}(t)$ and $k_{W_3}(t)$. The corresponding normalized response energy curves are plotted in Figure 4.10b. The comparison of response waveforms clearly shows that the magnitude of the "matched" target response is much smaller than the magnitudes of the "mismatched" target responses beyond 80 ns. The corresponding energy plot makes the identification decision even easier

in favor of the library target W_1 whose K-pulse waveform leads to that normalized response energy curve which reaches the maximum energy level much earlier than the others. In the second identification example, the aspect angle is 60° . It is demonstrated in Figure 4.11a that responses of the "unknown" target to the K-pulses $k_{W_2}(t)$ and $k_{W_3}(t)$ keep ringing in time but its response to the K-pulse $k_{W_1}(t)$ becomes approximately zero beyond 110 ns. Consequently, the unknown target can be identified as W_1 . Also, the normalized energy curve related to $k_{W_1}(t)$ reaches the total energy level about 350 ns earlier than the "mismatched" energy curves as shown in Figure 4.11b. Similar identification results at a 90° aspect angle are demonstrated in Figure 4.12a comparing the responses of the target (W_1) to the library K-pulses, and in Figure 4.12b using the associated energy curves. Again the target is identified to be W_1 without any uncertainty.

B. APPLICATIONS TO CONDUCTING SPHERE

Most of the geometrically complicated targets to be studied later in this report are also low-Q objects for which the K-pulse estimation and target identification problems turn out to be very delicate. It is reasonable therefore to study these problems for a very low-Q but yet geometrically simple target such as a conducting sphere to isolate the practical difficulties caused only by the low-Q nature of radar targets.

1. K-Pulse Estimation Using a Discrete Representation

The target of this section is a conducting sphere whose diameter, d , equals ten inches. (It is referred to as the sphere, S_2 , in Section B.3 of Chapter IV.) An approximate K-pulse waveform is synthesized from the backscattered impulse response of the sphere where the original frequency data are generated by a computer program for the Mie series over the frequency band [0.05-10 GHz] with 0.05 GHz frequency steps. The K-pulse duration is chosen to be 2.8 ns which is approximately equal to $\pi d/c$, that is, the circumferential path length of the sphere divided by the speed of light in vacuum. The cut-off time is set at 3.5 ns which is roughly specified by the sum of K-pulse duration and the transit time, d/c , for the target diameter. The assumption here is that the forced response of the sphere to the K-pulse waveform ends before the cut-off time beyond which only the natural response may exist.

The continuous part of the K-pulse model in Equation (4.1) is represented by 146 equally-spaced samples which are all initially assumed to be unity. The cost function of Equation (3.9) is minimized to find the optimal values of these unknown samples, with $a=1$, $b=0$ and $I=1$. Since the conducting sphere is a very low- Q target, the initial percentage energy of the target response remaining beyond the cut-off time is found to be very small, on the order of 10^{-3} . This value of the cost function is decreased about one thousand times, to 1.15×10^{-6} , in fifty iterations of the Fletcher-Powell steepest descent algorithm. The resultant K-pulse waveform is shown in Figure 4.13. The impulse response and the optimized K-pulse response in the

backscatter direction are plotted in Figure 4.14a and a magnified version of this plot is presented in Figure 4.14b to show the important late-time variations in detail. These waveforms are both normalized to have unit total energies so that the comparison of their amplitudes is meaningful and reveals that the time span of the K-pulse response is about 3 ns shorter than that of the impulse response. Theoretically, the impulse response is of infinite duration but as seen in Figure 4.14b, it can practically be assumed zero beyond 6.4 ns. The energy content of the optimized backscattered K-pulse response is concentrated in a shorter time interval as implied by Figure 4.14c where the normalized energy curve of the K-pulse response reaches high energy levels (after 75%) earlier than the energy curve of the impulse response. This is the result of natural mode annihilation under K-pulse excitation. This statement is also verified by the agreement between the approximate sphere poles, extracted from the synthesized K-pulse waveform, and the true pole values of the sphere as presented in Table 4.4. The synthesized K-pulse waveform is also tested at some other combinations of aspect and radar polarization to justify the claim that it is an aspect and polarization invariant descriptor of the sphere. The pairs of normalized impulse response and the corresponding normalized K-pulse response waveforms are plotted (on a magnified scale) in parts (a) through (e) of Figure 4.15 for the bistatic angle/radar polarization combinations of 30°/horizontal polarization (HP), 45°/vertical polarization (VP), 60°/HP, 90°/VP and 135°/VP, respectively. In all these cases, the K-pulse response is found to have a shorter time span compared to the impulse response, as required.

2. K-Pulse Estimation Using a Legendre Polynomial Expansion

The target and scattering data employed in this demonstration are the same as those used in the previous example. This time, the continuous part of the K-pulse is represented by a truncated expansion of modified Legendre polynomials (up to order five) over the interval [0,2.8 ns]. With a cut-off time of 5 ns, the cost function is minimized to obtain the optimal values of the expansion coefficients. As a result of fifteen iteration steps, these values are optimized as shown in Table 4.5 where the coefficient of the fifth order modified Legendre polynomial is found to be negligible as compared to the others. The corresponding K-pulse waveform is constructed using Equation (4.2) and plotted in Figure 4.16. The normalized impulse response and K-pulse response waveforms in the backscattered direction are shown together (with a magnified scale) in Figure 4.17a where the latter waveform becomes zero about 3 ns earlier than the former one. The associated normalized energy curves are shown in Figure 4.17b, which are separated from each other at high energy levels with the energy curve of the K-pulse response leading that of the impulse response. In parts (a) through (c) of Figure 4.18, the synthesized K-pulse is tested for three combinations of bistatic angle/radar polarization, 30°/HP, 90°/VP and 120°/HP, respectively. Finally, Table 4.6 contains the approximate sphere poles which are estimated from the K-pulse shown in Figure 4.16. As compared to the results of pole estimation shown in Table 4.4, this new set of results approximates the dominant poles of the sphere much closer. On the other hand, the results of Table 4.4 for higher order poles look better. The choice of

the cut-off time seems to be the most important factor in determining how closely the zeros of the K-pulse spectrum approximate the actual target poles. The dominant poles are approximated much better if the cut-off time is chosen very late (5 ns for the results of Table 4.6) since the interference from the forced response component is almost completely avoided. However, the natural modes of the less dominant poles beyond such a late cut-off time are very small, so such pole values cannot be approximated as well as the dominant ones.

3. Target Identification

In this section, a K-pulse library of three conducting spheres, S_1 , S_2 and S_3 is formed for identification purposes. The diameters of these spheres are

$$S_1: d_1 = 5 \text{ inches}$$

$$S_2: d_2 = 10 \text{ inches}$$

$$S_3: d_3 = 20 \text{ inches.}$$

The target S_2 is the same one studied in the last two examples. The approximate K-pulse waveform shown in Figure 4.13 is used to characterize the sphere, S_2 . The K-pulse waveforms of the spheres, S_1 and S_3 , are constructed by re-scaling the K-pulse waveform of S_2 and are shown in Figures 4.19 and 4.20, respectively. The examples of target identification on the basis of "time-limited K-pulse response

criterion" are presented in Parts (a) through (g) of Figure 4.21 for different combinations of aspect and radar polarizations in the noise-free case. The "unknown" target in each demonstration is indicated in the figure caption. In all of these examples, the response of the test target to the "matched" K-pulse dies out at an earlier time, as expected. But as explained in Chapter III, Section C, this target identification scheme is very susceptible to noise in the case of low-Q targets such as the conducting spheres of this section. Therefore, the alternative target identification approach which is based on the comparison of normalized response energy curves is much more useful when the impulse response of the "unknown" target is contaminated by noise. The next group of examples demonstrate target identification for various levels of signal-to-noise ratio. The unknown target of these examples is the sphere, S_2 . The signal-to-noise ratio (SNR) level of its backscattered impulse response is adjusted by adding random Gaussian noise to the real and imaginary parts of the frequency spectrum independently. Parts (a), (c), (e), (g) and (i) of Figure 4.22 show the normalized responses of S_2 to the library K-pulses for the SNR of infinity (noiseless case), 20 dB, 15 dB, 10 dB and 5 dB, respectively. Parts (b), (d), (f), (h) and (j) of the same figure present the corresponding normalized response energy curves for the same noise levels. As the SNR decreases, comparison of target responses gives more and more ambiguous results; even at the SNR of 20 dB, it is very difficult to obtain a correct identification of sphere S_2 . On the other hand, it is clearly seen that the noise distortion of the energy curves is extremely slow; even at the SNR of 10 dB, the

energy plot is still very similar to that of the noiseless case, except for a downward shift of about five percent and an almost constant non-zero slope after 3.5 ns due to the added noise. In the extreme case of a SNR of 5 dB, target responses give no idea about identification but the associated energy curves are still useful to declare the unknown target to be S_2 .

Table 4.1

CNR Frequencies (Poles) of the Conducting Thin-Wire W_1
 $(L/d_1=2000)$ is SL_1/c Scale

<u>True Values Obtained by using the Moment Method [2]</u>	<u>Approximate Values Extracted from the K-Pulse Shown in Figure 4.1</u>
-0.161 ± j 3.013	-0.178 ± j 2.978
-0.219 ± j 6.133	-0.235 ± j 6.089
-0.262 ± j 9.256	-0.311 ± j 9.219
-0.294 ± j 12.383	-0.335 ± j 12.320
-0.320 ± j 15.512	-0.363 ± j 15.472
-0.343 ± j 18.642	-0.397 ± j 18.582
.	-0.398 ± j 21.710
.	-0.469 ± j 24.881
.	-0.437 ± j 28.008
	.
	.
	.

Table 4.2

Legendre Polynomial Coefficients Used to Construct
the K-Pulse Waveform Shown in Figure 4.5

<u>Order (m)</u>	<u>Coefficient (D_m)</u>
0	0.3019
1	-0.0508
2	0.0204
3	-0.0257
4	0.0162
5	-0.0016

Table 4.3

CNR Frequencies (Poles) of the Conducting Thin-Wire W_1
 $(L_1/d_1 = 2000)$ in sL_1/c Scale

<u>True Values obtained using the Moment Method [2]</u>	<u>Approximate Values Extracted from the K-pulse shown in Figure 4.5</u>
-0.161 ± j 3.013	-0.149 ± j 2.994
-0.219 ± j 6.133	-0.227 ± j 6.025
-0.262 ± j 9.256	-0.317 ± j 9.137
-0.294 ± j12.383	-0.376 ± j12.235
-0.320 ± j15.512	-0.427 ± j15.332
-0.343 ± j18.642	-0.474 ± j18.433
.	-0.514 ± j21.539
.	-0.563 ± j24.610
.	-0.604 ± j27.766
.	.
.	.
.	.

Table 4.4

CNR Frequencies (Poles) of the Conducting Sphere S_2
 $(2r_2=10 \text{ inches})$ in sr_2/c Scale

<u>True Values [15]</u>	<u>Extracted Values from the K-Pulse shown in Figure 4.13</u>
-0.500 ± j 0.866	-0.528 ± j 0.843
-0.702 ± j 1.807	-0.723 ± j 1.863
-0.843 ± j 2.758	-0.805 ± j 2.855
-0.954 ± j 3.715	-0.843 ± j 3.838
-1.048 ± j 4.676	-0.860 ± j 4.799
-1.129 ± j 5.642	-0.854 ± j 5.727
-1.201 ± j 6.610	-0.880 ± j 6.676
-1.267 ± j 7.580	-0.934 ± j 7.578
-1.327 ± j 8.552	-0.923 ± j 8.491
-1.382 ± j 9.526	-0.876 ± j 9.441
.	.
.	.
-1.613 ± j14.415	-0.773 ± j14.241
.	.
.	.
-1.796 ± j19.323	-0.879 ± j19.457
.	.
.	.
-1.949 ± j24.245	-0.779 ± j24.409
.	.
.	.
.	.

Table 4.5

Legendre Polynomial Coefficients Used to Construct the K-Pulse Shown in Figure 4.16

Order (m)	Coefficient (D _m)
0	0.2252
1	-0.1885
2	-0.1419
3	0.1475
4	-0.0532
5	0.0001

Table 4.6

CNR Frequencies (Poles) of the Conducting Sphere S₂ (2r₂=10 inches) in sr₂/c Scale

True Values [15]	Extracted Values from the K-Pulse shown in Figure 4.16
-0.500 ± j 0.866	-0.496 ± j 0.883
-0.702 ± j 1.807	-0.765 ± j 1.795
-0.843 ± j 2.758	-0.865 ± j 2.776
-0.954 ± j 3.715	-0.933 ± j 3.752
-1.048 ± j 4.676	-0.983 ± j 4.721
-1.129 ± j 5.642	-1.022 ± j 5.684
-1.201 ± j 6.610	-1.054 ± j 6.641
-1.267 ± j 7.580	-1.080 ± j 7.596
-1.327 ± j 8.552	-1.102 ± j 8.547
-1.382 ± j 9.526	-1.121 ± j 9.497
.	.
.	.
-1.613 ± j14.415	-1.191 ± j14.225
.	.
.	.
-1.796 ± j19.323	-1.229 ± j18.936
.	.
.	.
-1.949 ± j24.245	-1.271 ± j23.640
.	.
.	.
.	.

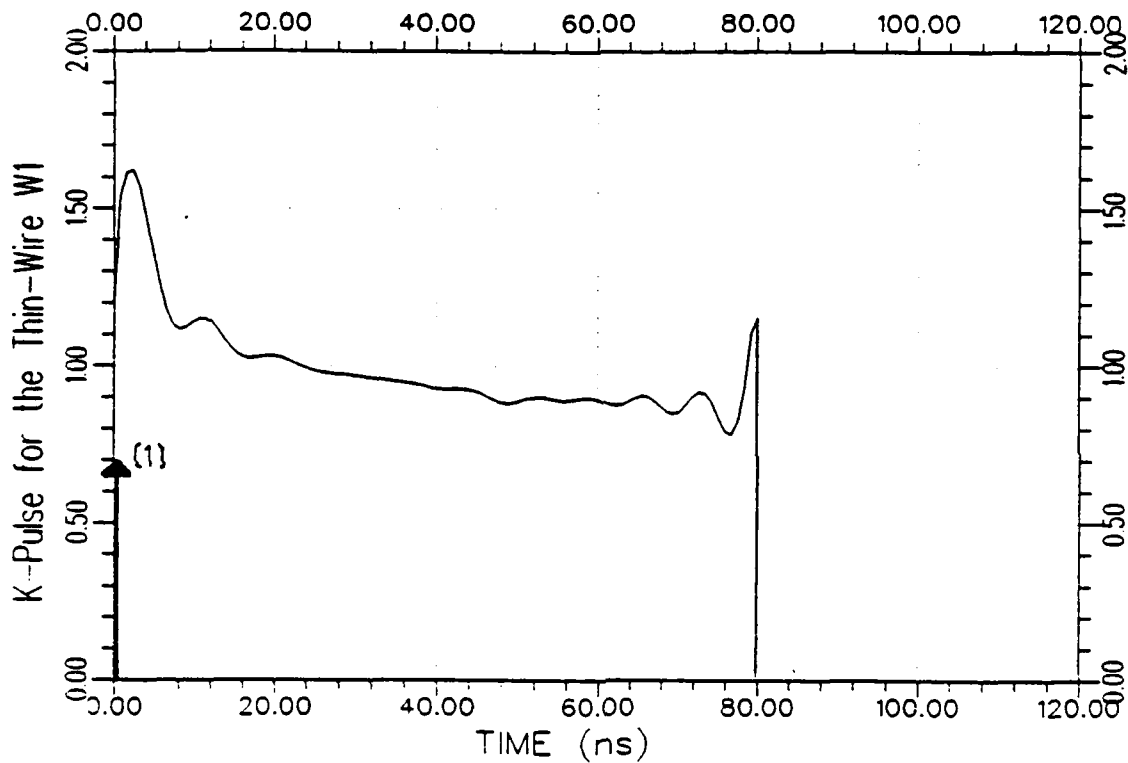
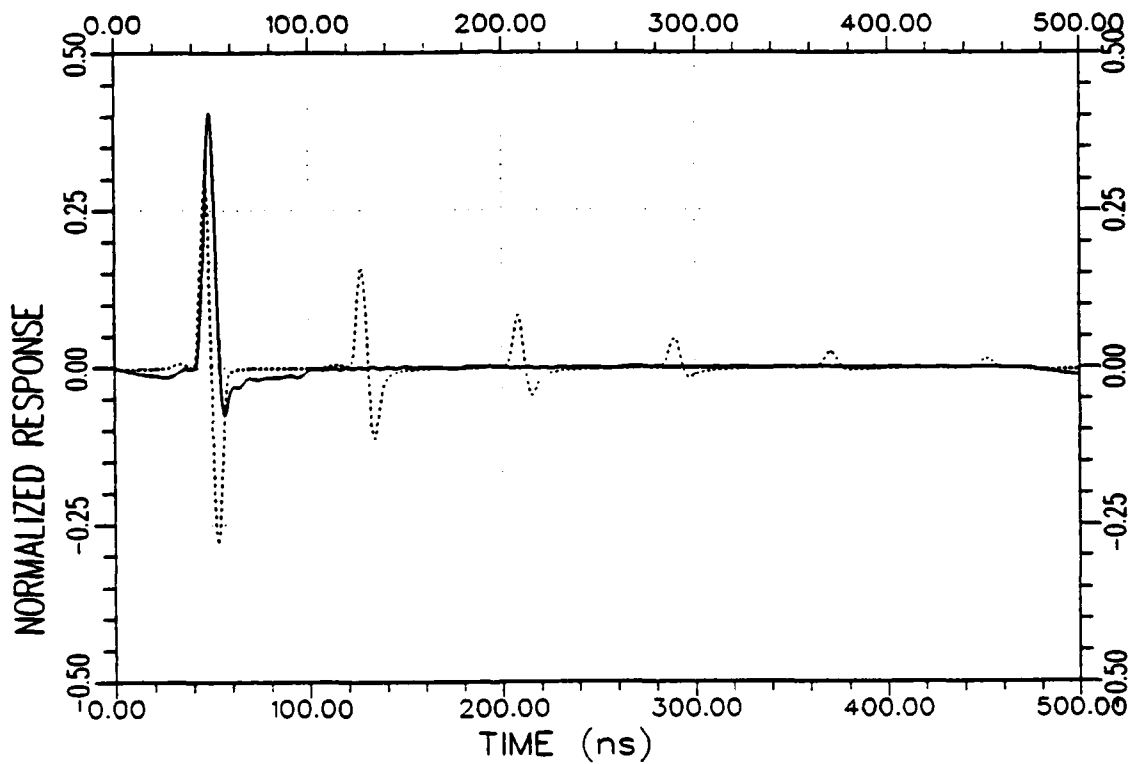
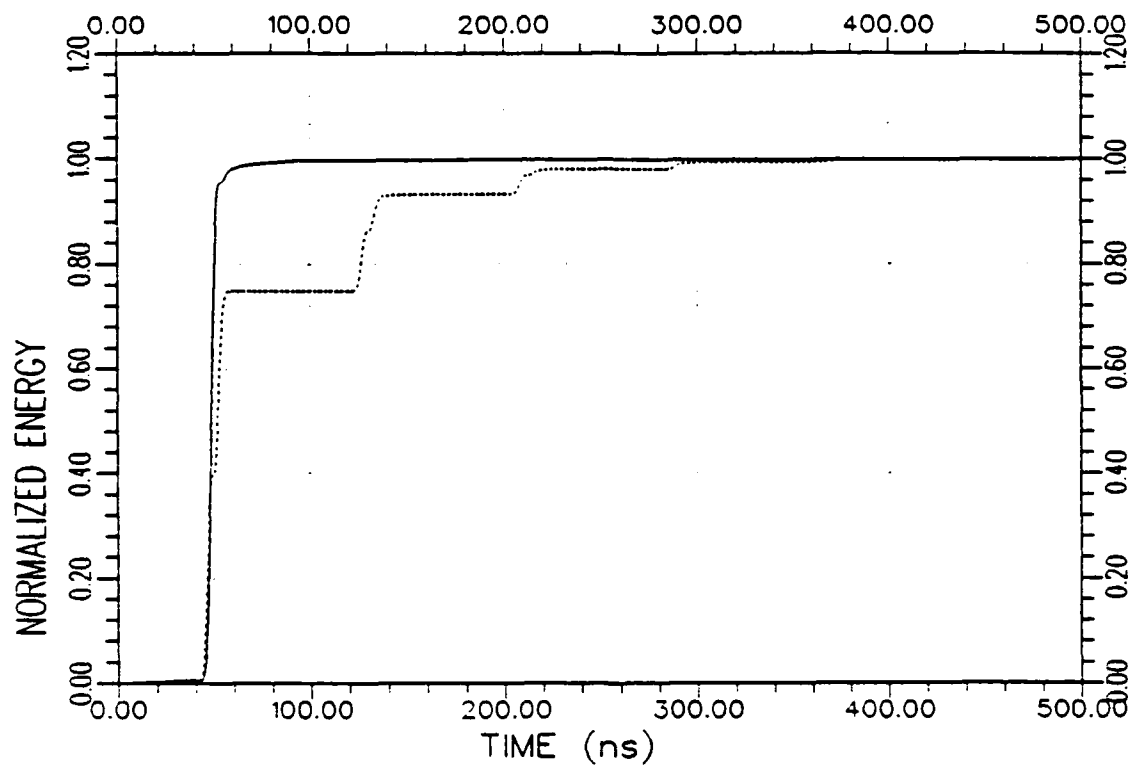


Figure 4.1. An approximate K-pulse waveform for the conducting cylindrical thin-wire W_1 (with $L=12m$ and $L/d=2000$) estimated from the theoretical backscattered data at $\phi=30^\circ$, ϕ -polarization using a discrete representation for the continuous part of the K-pulse. (The $\delta(t)$ term of the K-pulse is symbolically shown by the arrow at $t=0$.)



(a) Response waveforms

Figure 4.2. Normalized impulse response (·····) and K-pulse response (—) waveforms and their energy curves for the wire W_1 (due to the K-pulse shown in Figure 4.1) at $\phi=30^\circ$, $\hat{\phi}$ -polarization.



(b) Response energy curves

Figure 4.2. Continued.

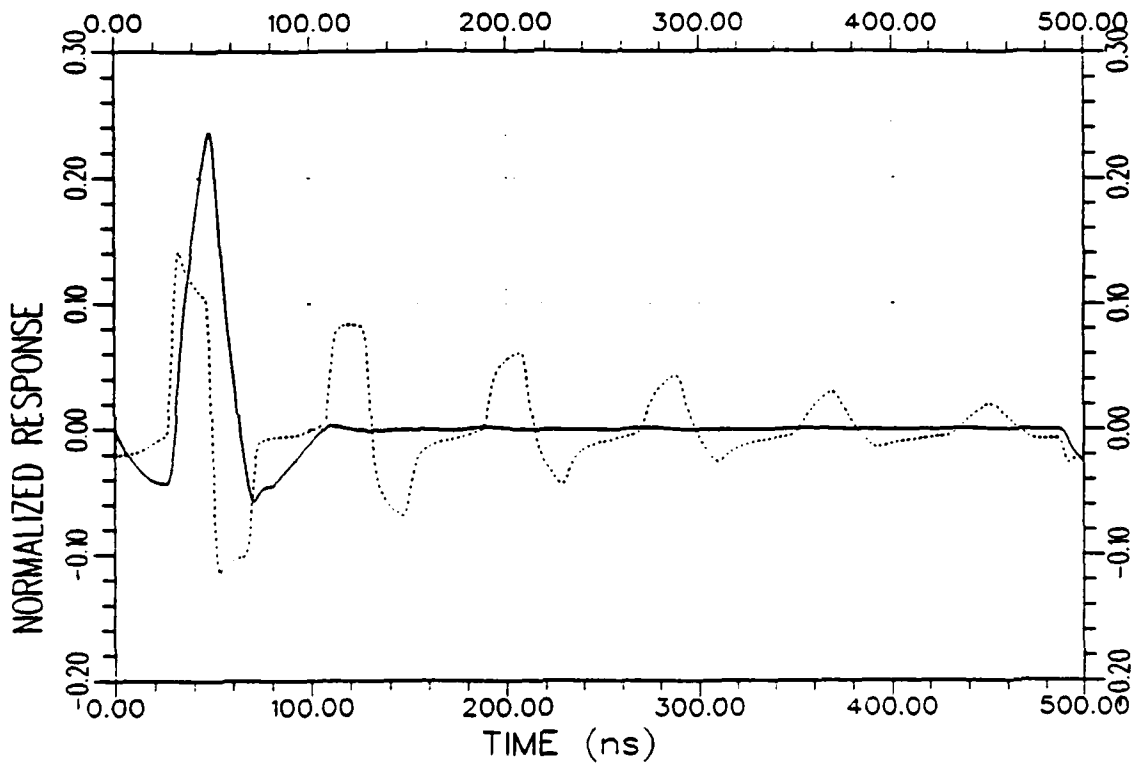


Figure 4.3. Normalized impulse response (·····) and K-pulse response (—) waveforms of the wire W_1 at $\phi=60^\circ$, ϕ -polarization due to the K-pulse shown in Figure 4.1.

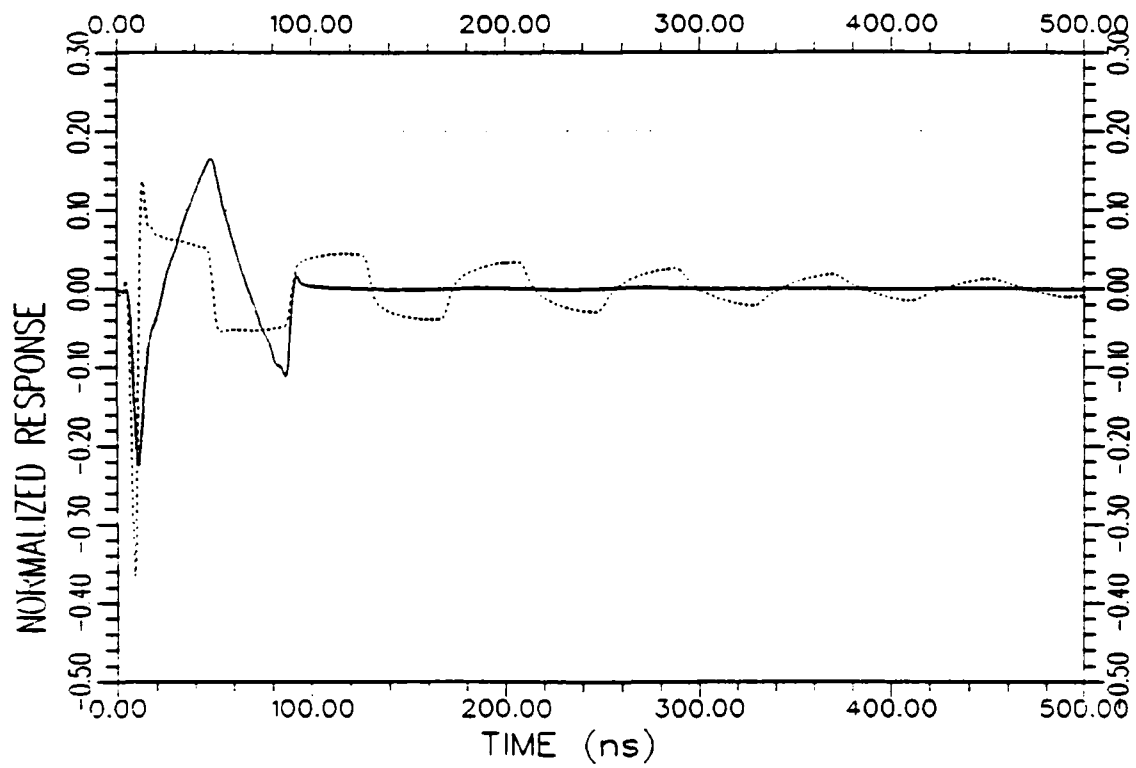


Figure 4.4. Normalized impulse response (.....) and K-pulse response (—) waveforms of V_1 at $\phi=90^\circ$. ϕ -polarization due to the K-pulse shown in Figure 4.1.

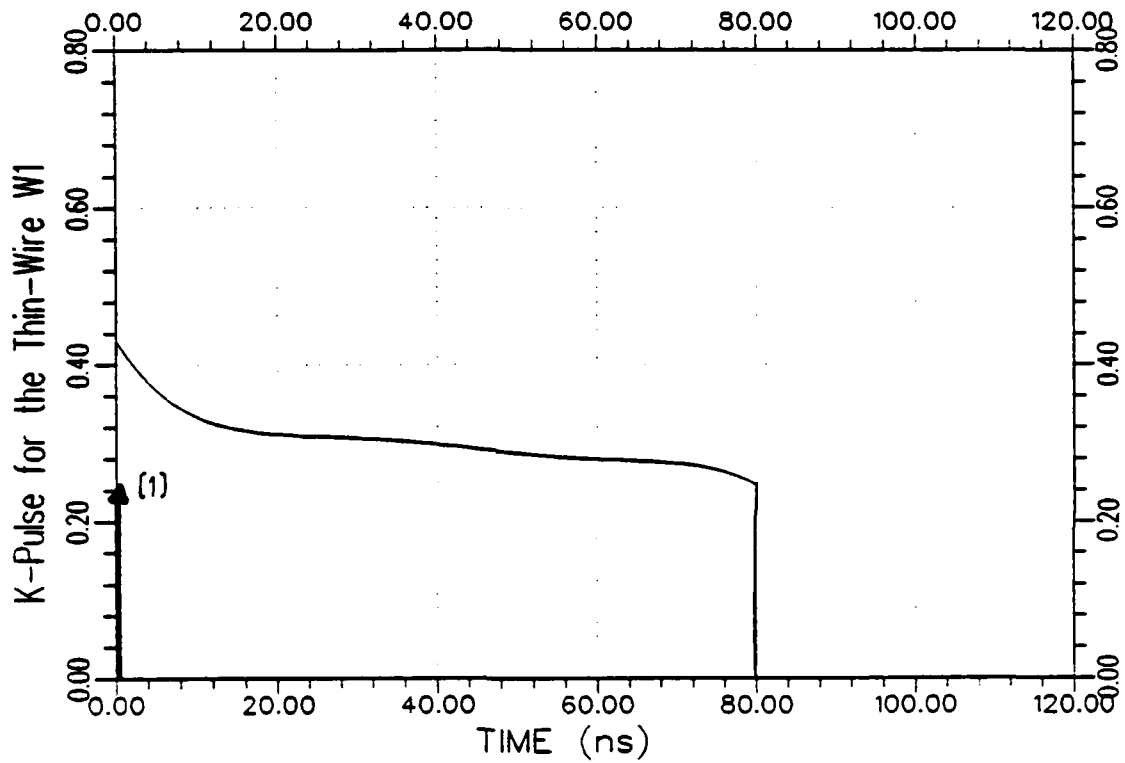
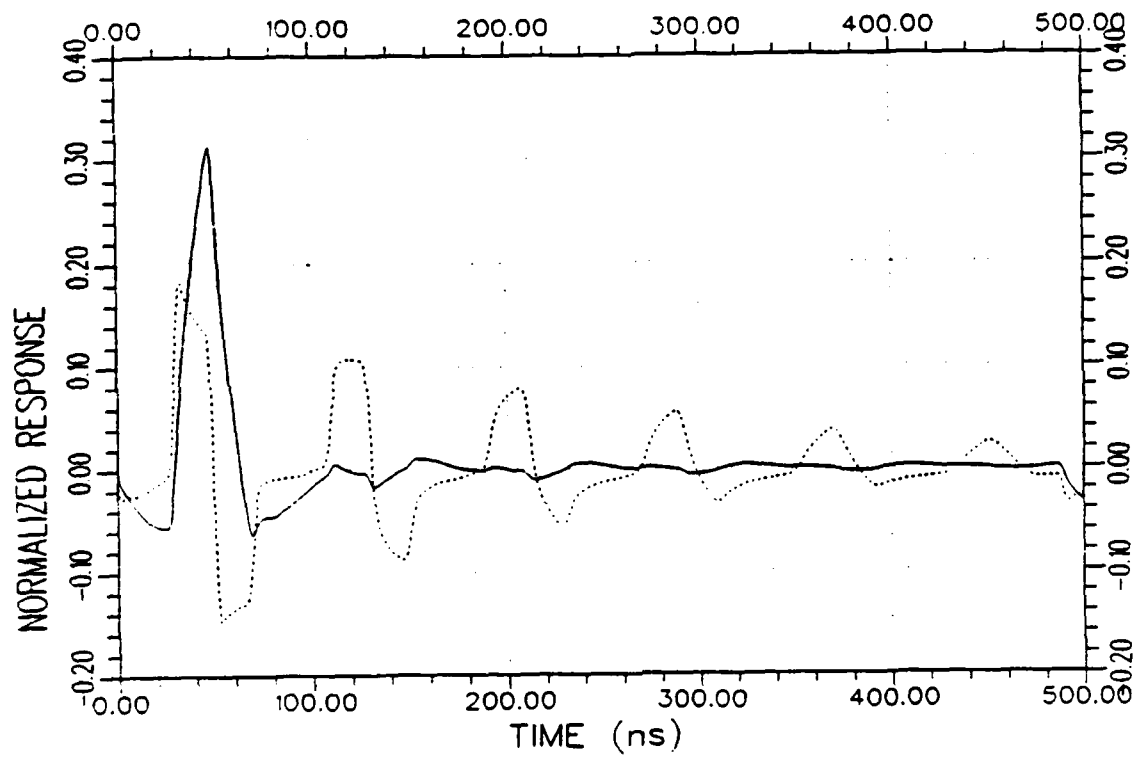
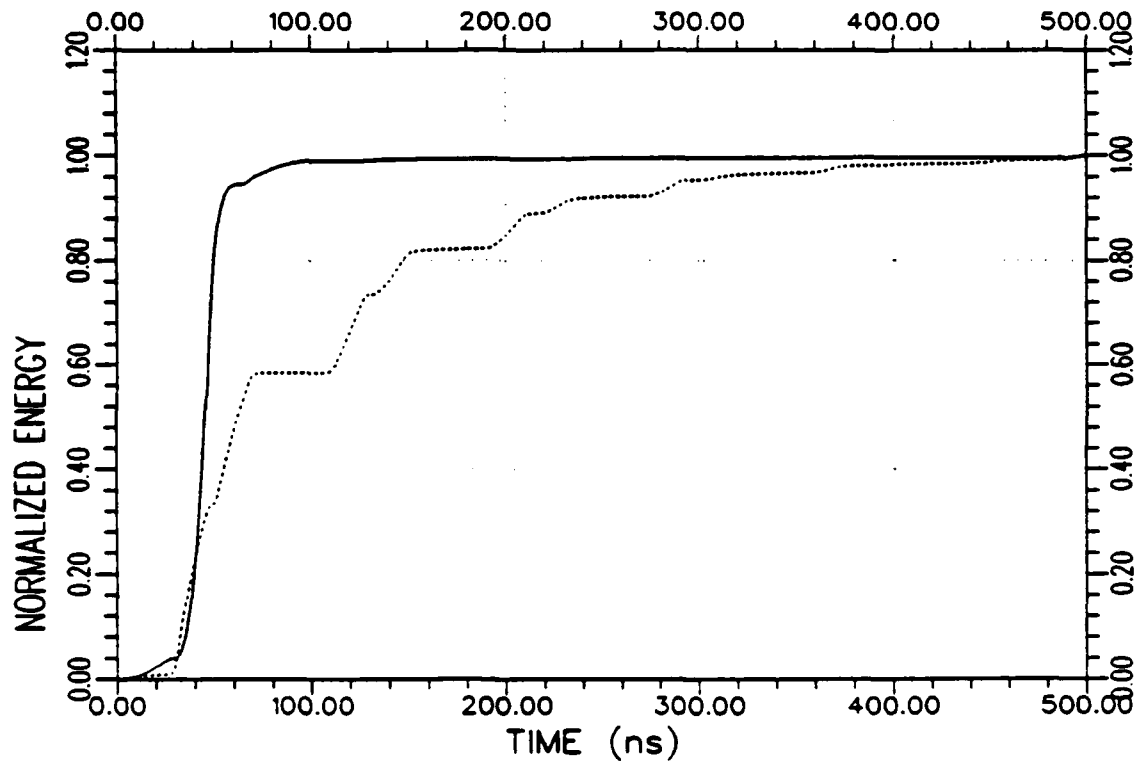


Figure 4.5. An approximate K-pulse waveform for the thin-wire W_1 estimated from the theoretical backscattered data at $\phi=60^\circ$, ϕ -polarization using a Legendre polynomial representation for the continuous part of the K-pulse. (The $\delta(t)$ term of the K-pulse is symbolically shown by the arrow at $t=0$.)



(a) Response waveforms

Figure 4.6. Normalized impulse response (.....) and K-pulse response (——) waveforms and their energy curves for the wire W_1 (due to the K-pulse shown in Figure 4.5) at $\phi=60^\circ$. ϕ -polarization.



(b) Response energy curves

Figure 4.6. Continued.

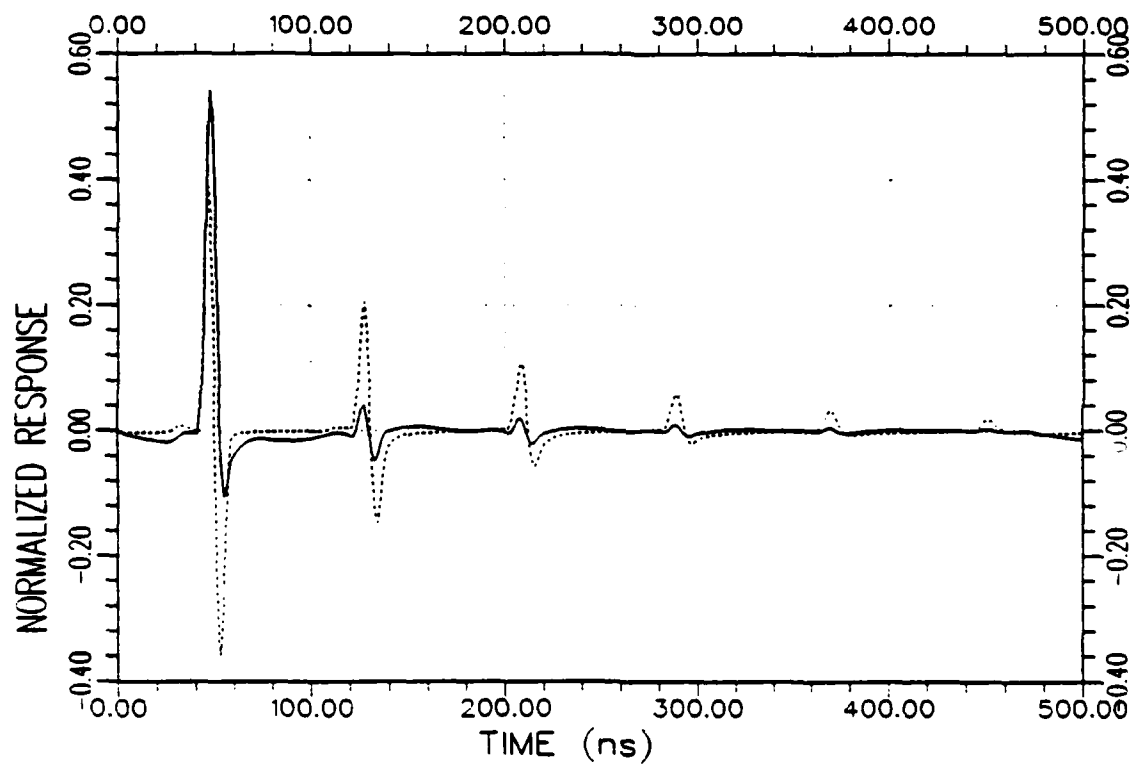


Figure 4.7. Normalized impulse response (.....) and K-pulse response (—) of W_1 at $\phi=30^\circ$, ϕ -polarization due to the K-pulse shown in Figure 4.5.

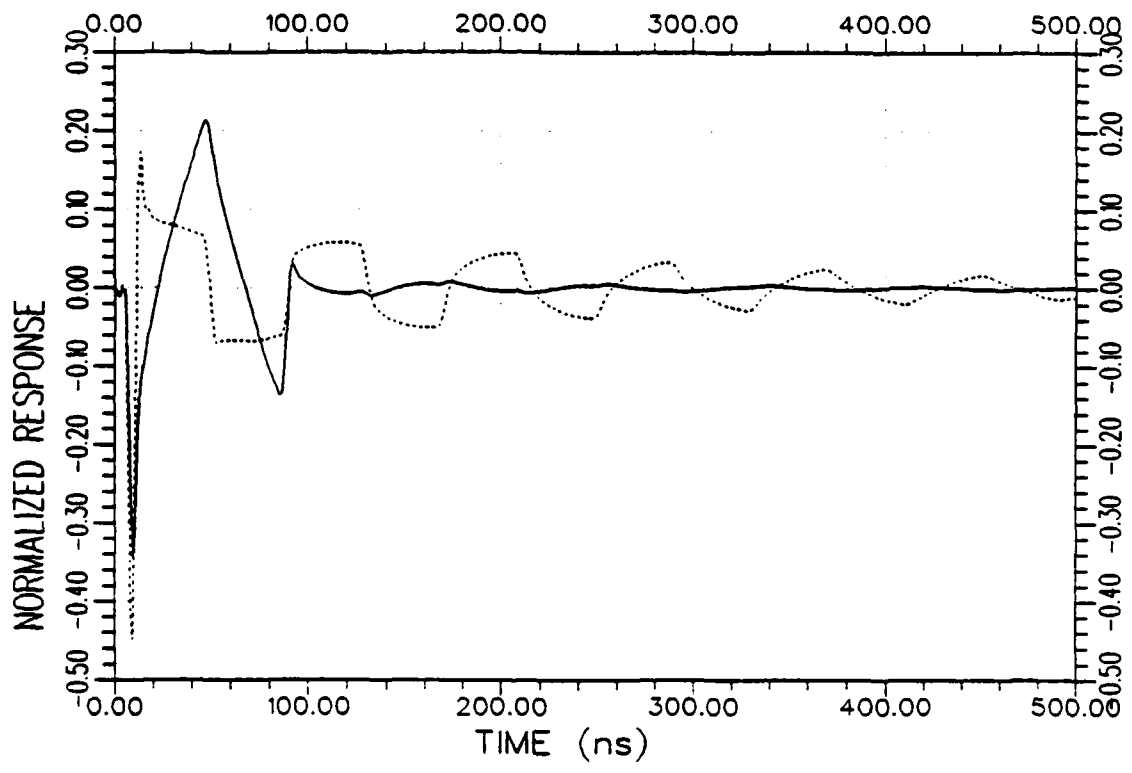


Figure 4.8. Normalized impulse response (·····) and K-pulse response (—) of W_1 at $\phi=90^\circ$, $\hat{\phi}$ -polarization due to the K-pulse shown in Figure 4.5.

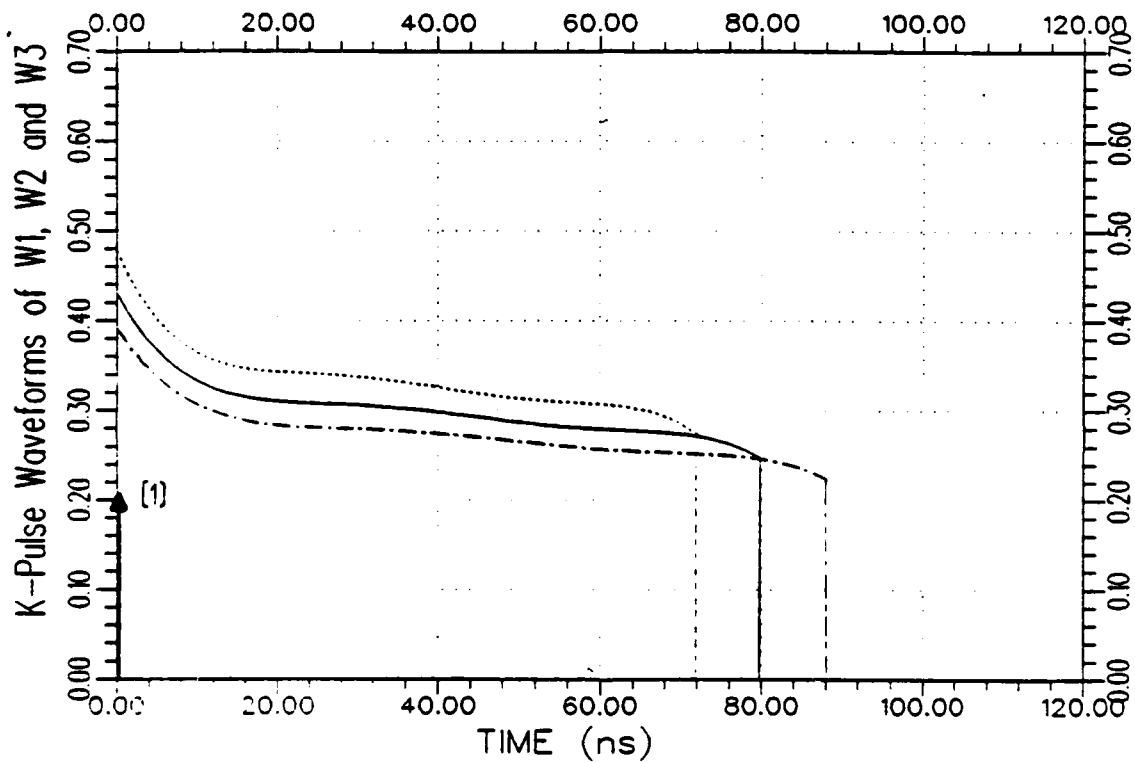
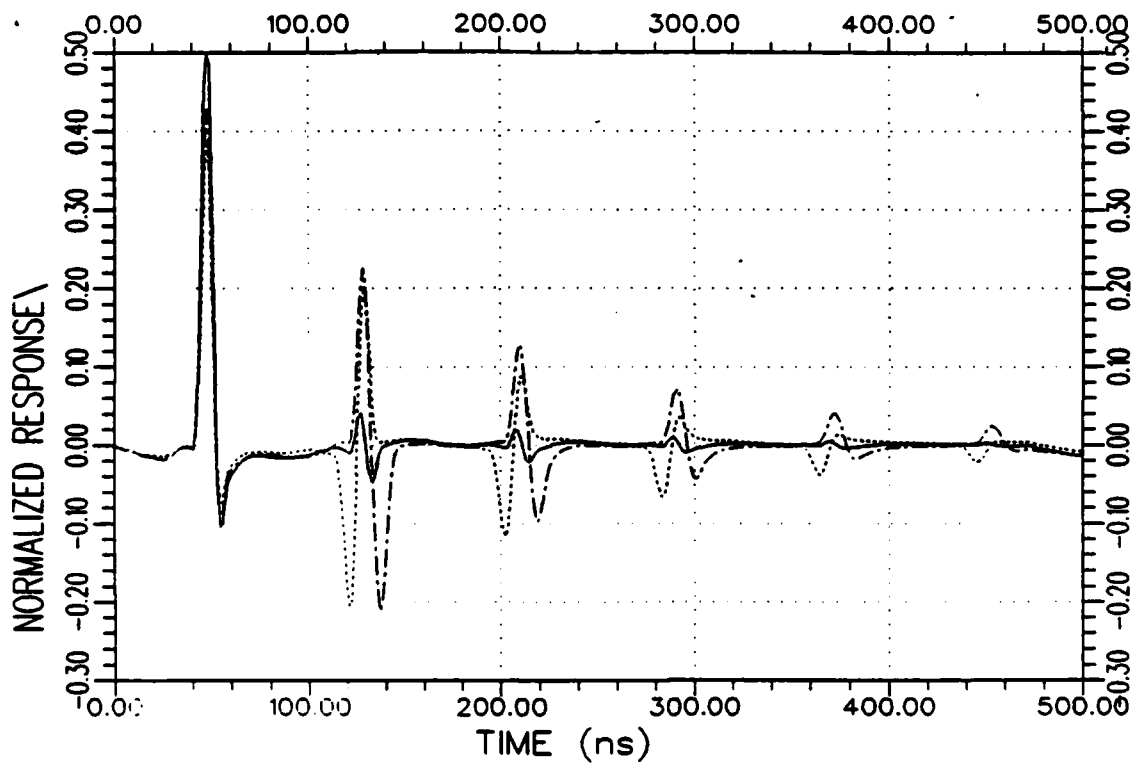
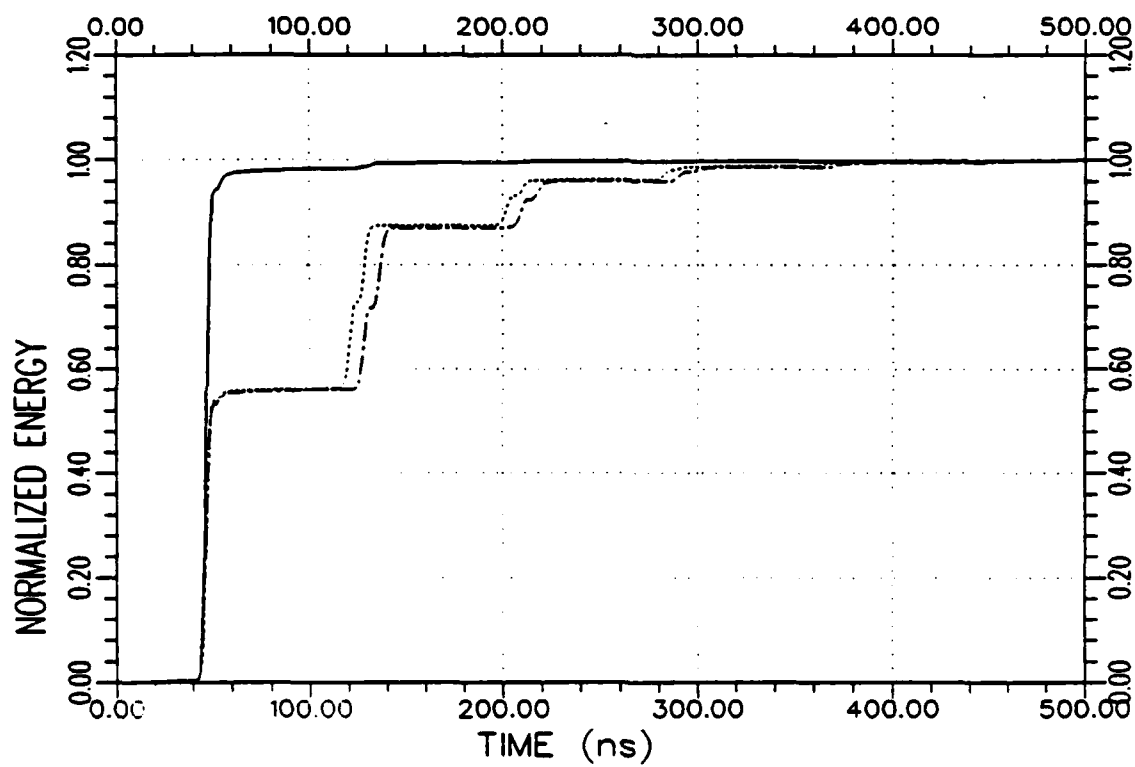


Figure 4.9. K-pulse waveforms of the thin-wires W_1 (—), W_2 (·····), and W_3 (---). All three wires have the same length-to-diameter ratio of 2000 with lengths $L_1=12\text{m}$, $L_2=10.8\text{m}$, and $L_3=13.2\text{m}$. (The $\delta(t)$ term of the K-pulse is symbolically shown by the arrow at $t=0$.)



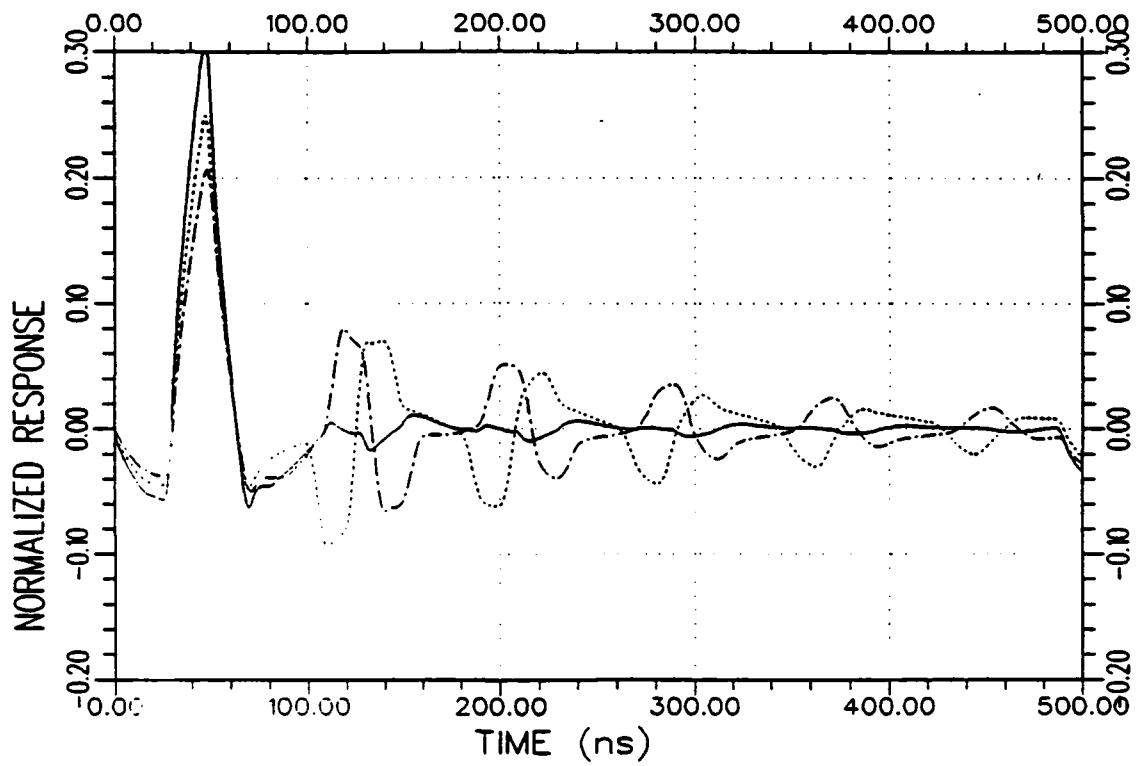
(a) Response waveforms

Figure 4.10. Normalized response waveforms and their energy curves for the wire W_1 produced by the K-pulses of library targets W_1 (—), W_2 (·····), and W_3 (—·—·—) at $\phi=30^\circ$, ϕ -polarization.



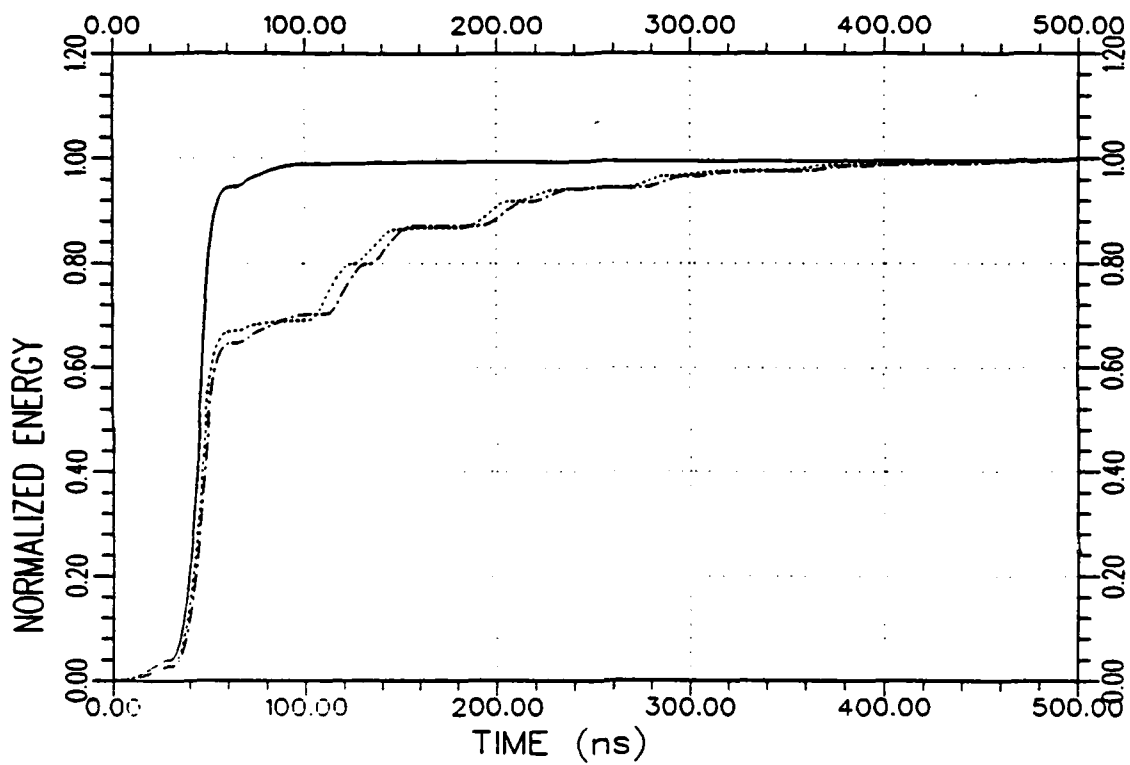
(b) Response energy curves

Figure 4.10. Continued.



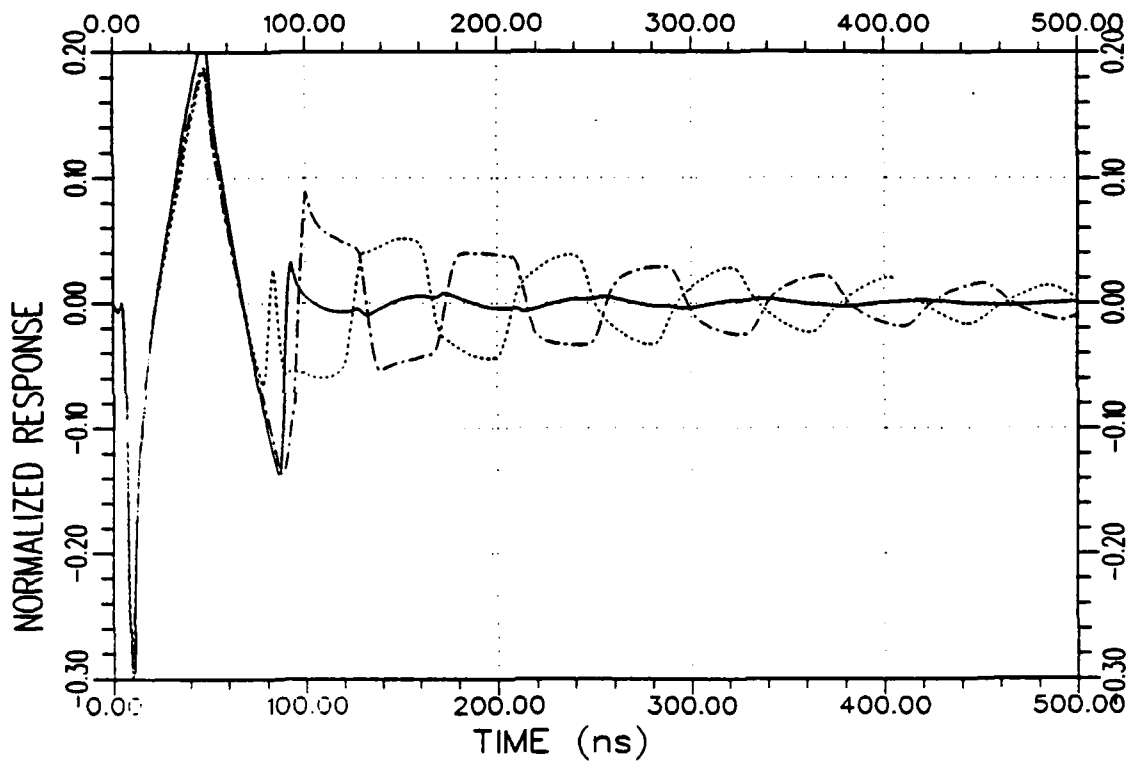
(a) Response waveforms

Figure 4.11. Normalized response waveforms and their energy curves for the wire W_1 produced by the K-pulses of library targets W_1 (—), W_2 (·····), and W_3 (-·-·-) at $\phi=60^\circ$, ϕ -polarization.



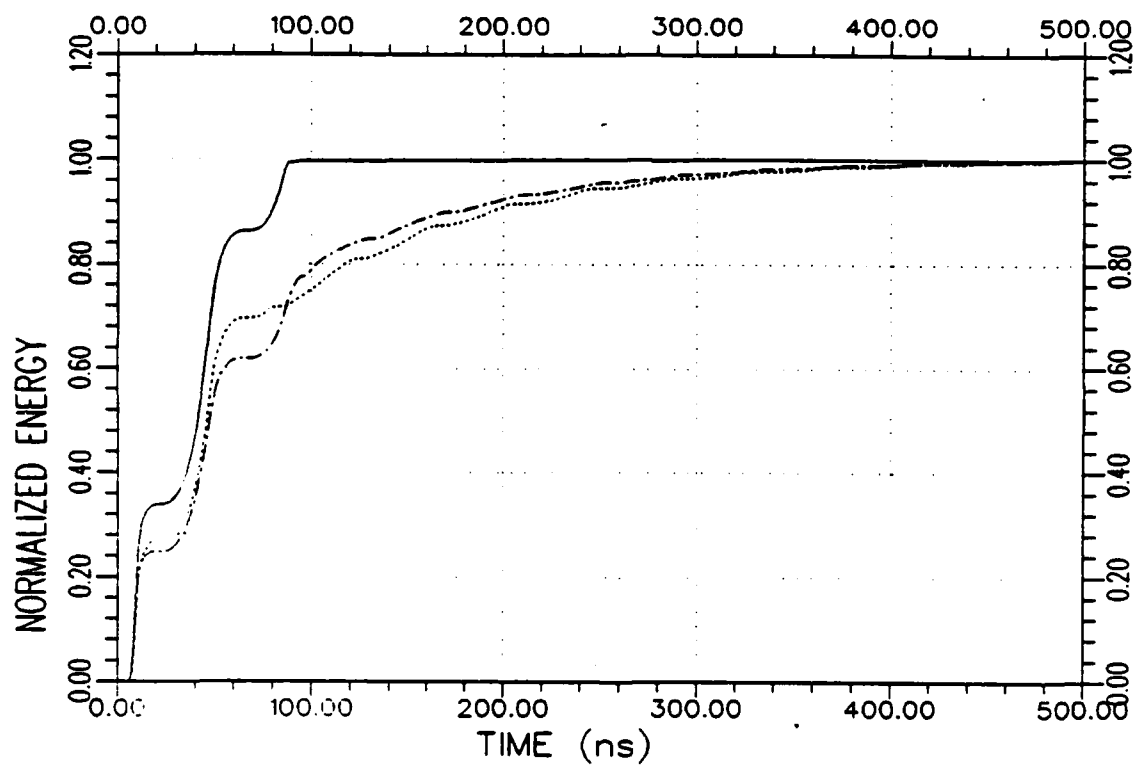
(b) Response energy curves

Figure 4.11. Continued.



(a) Response waveforms

Figure 4.12. Normalized response waveforms and their energy curves for the wire W_1 produced by the K-pulses of library targets W_1 (—), W_2 (·····), and W_3 (-·-·-) at $\phi=90^\circ$, ϕ -polarization.



(b) Response energy curves

Figure 4.12. Continued.

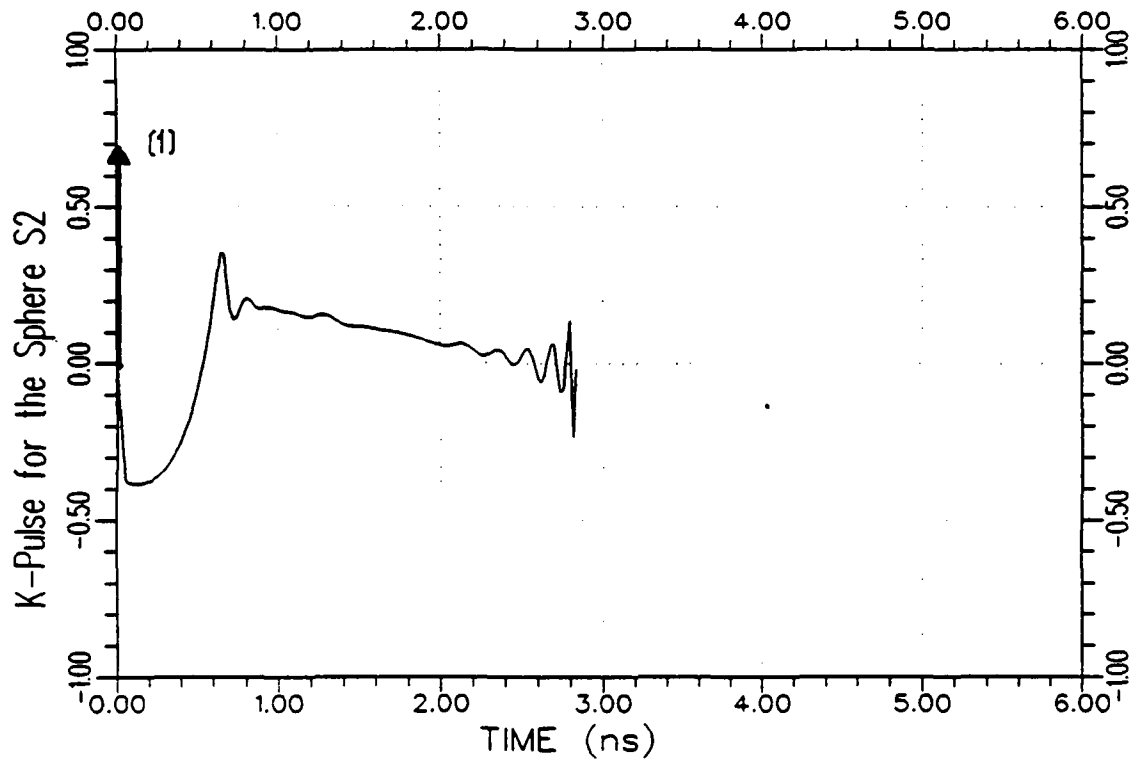
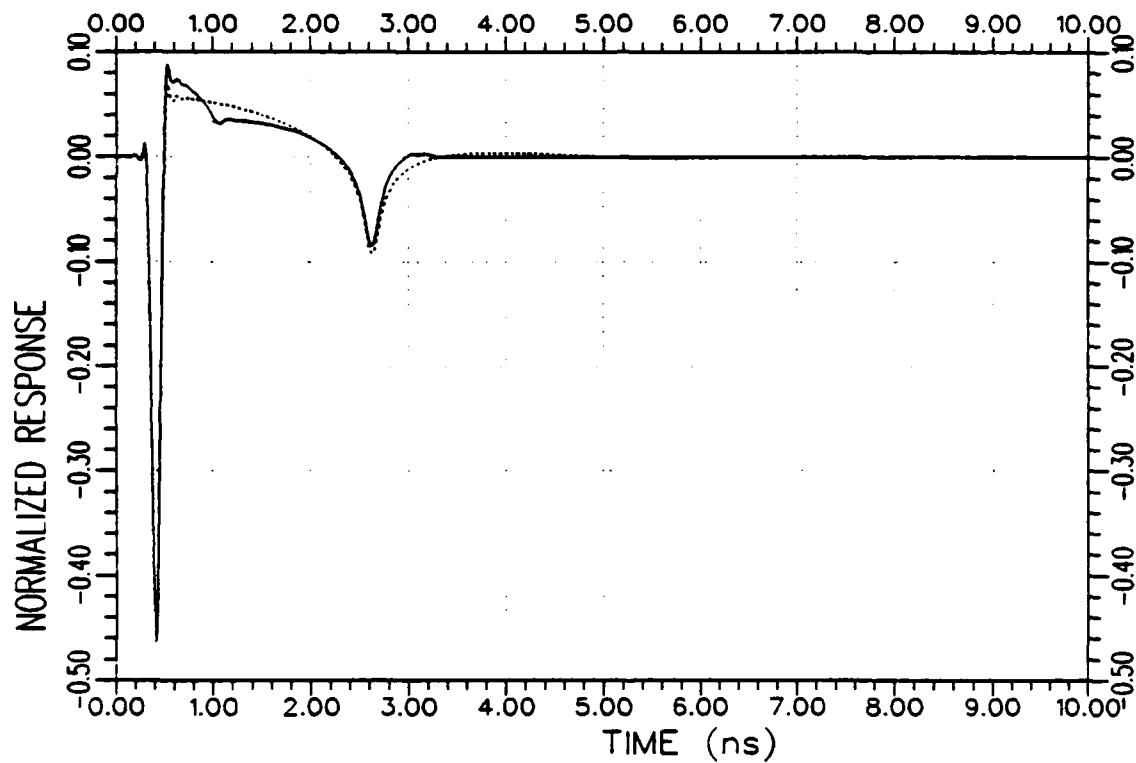
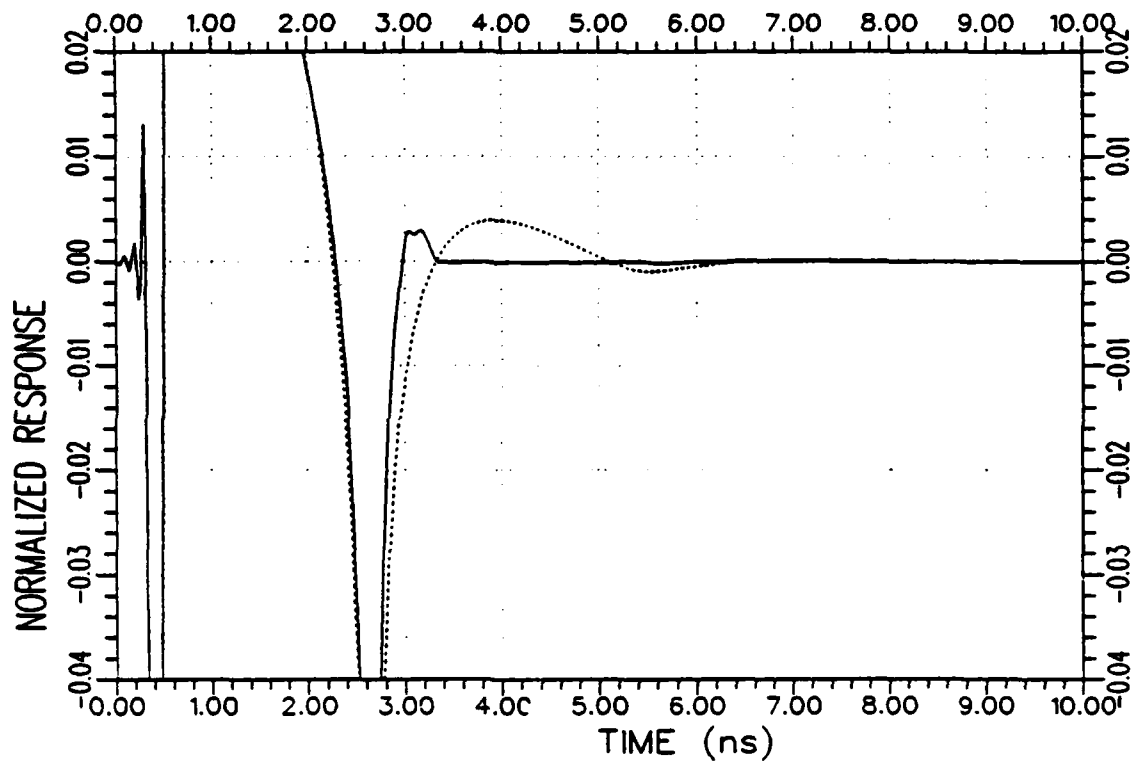


Figure 4.13. An approximate K-pulse waveform for the conducting sphere S_2 (with $2r_2=10$ inches) estimated from the theoretical backscattered data using a discrete representation for the continuous part of the K-pulse. (The $\delta(t)$ term of the K-pulse is symbolically shown by the arrow at $t=0$.)



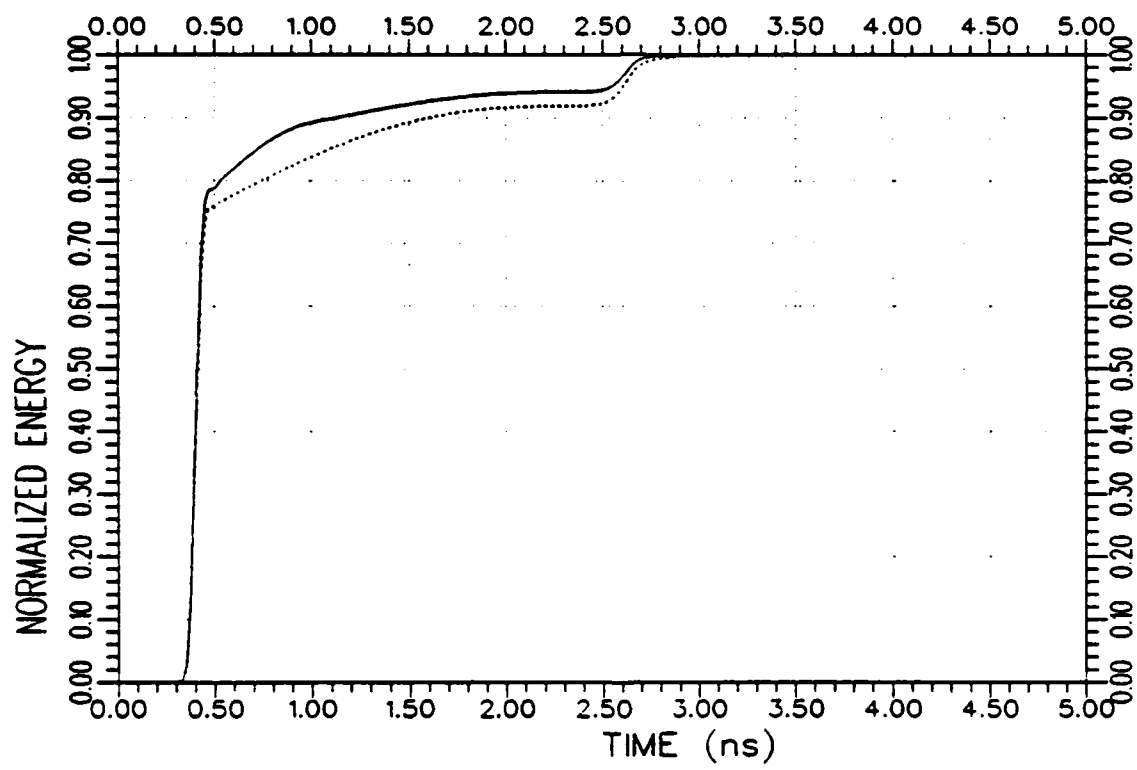
(a) Response waveforms

Figure 4.14. Normalized impulse response (·····) and K-pulse response (—) waveforms and their energy curves for the sphere S_2 at the backscattered direction due to the K-pulse shown in Figure 4.13.



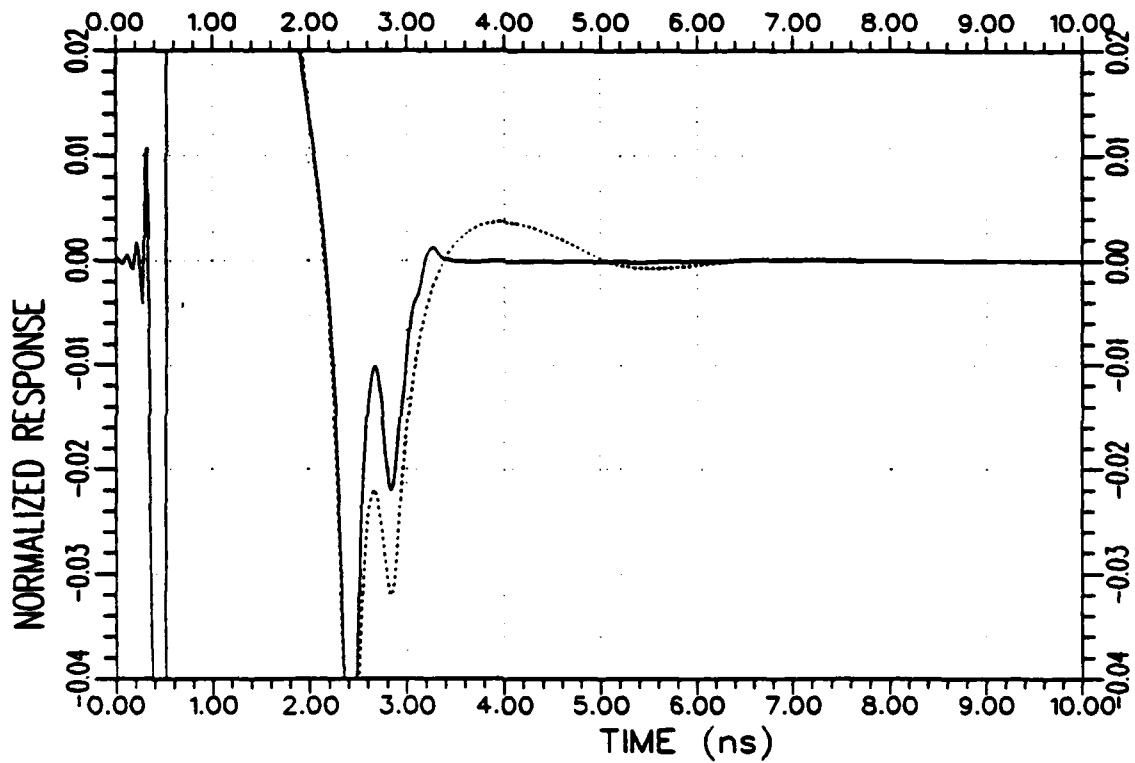
(b) A ten times magnified version of part (a)

Figure 4.14. Continued.



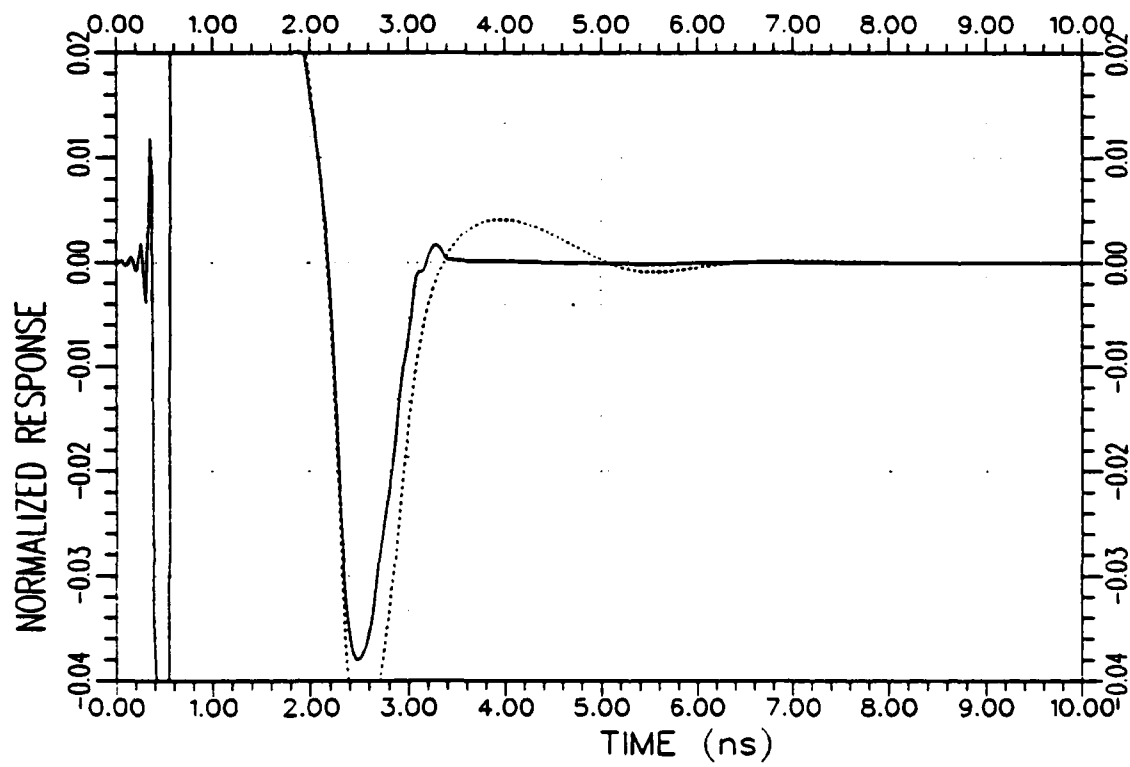
(c) Response energy curves

Figure 4.14. Continued.



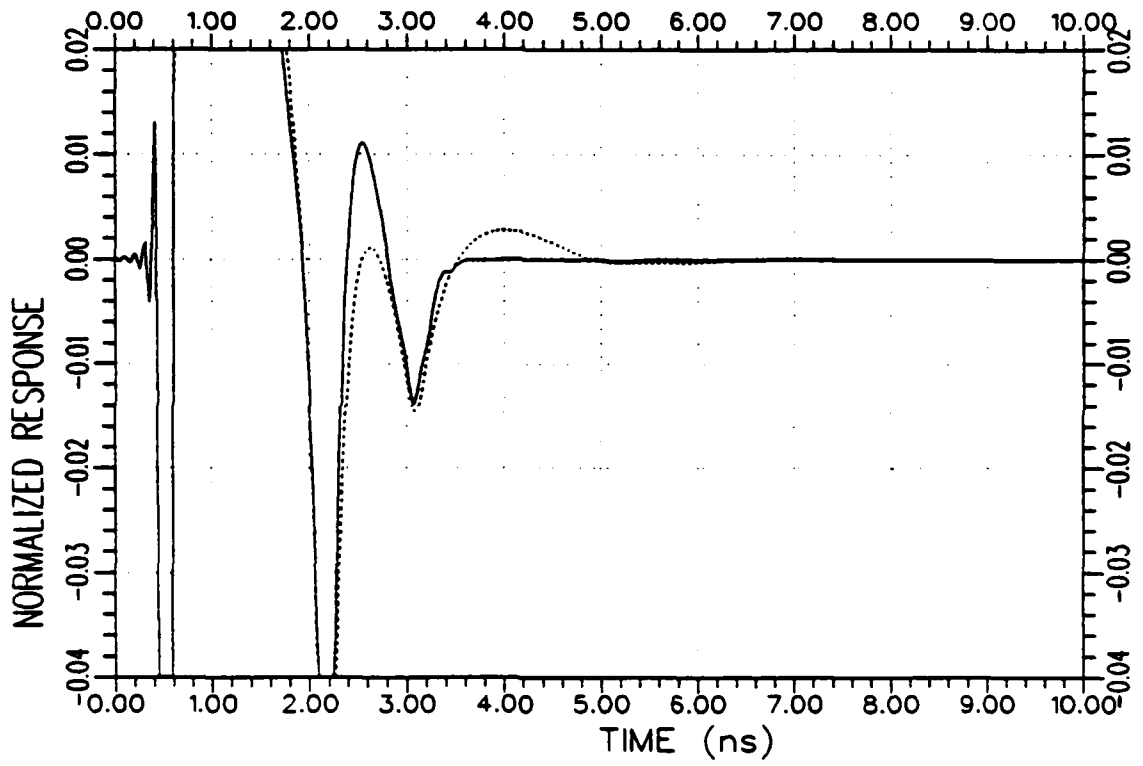
(a) 30°/Horizontal polarization

Figure 4.15. Normalized impulse response (.....) and K-pulse response (—) waveforms of the sphere S_2 (due to the K-pulse shown in Figure 4.13) for the bistatic angle/radar polarization combinations of 30°/HP, 45°/VP, 60°/HP, 90°/VP, and 135°/VP.



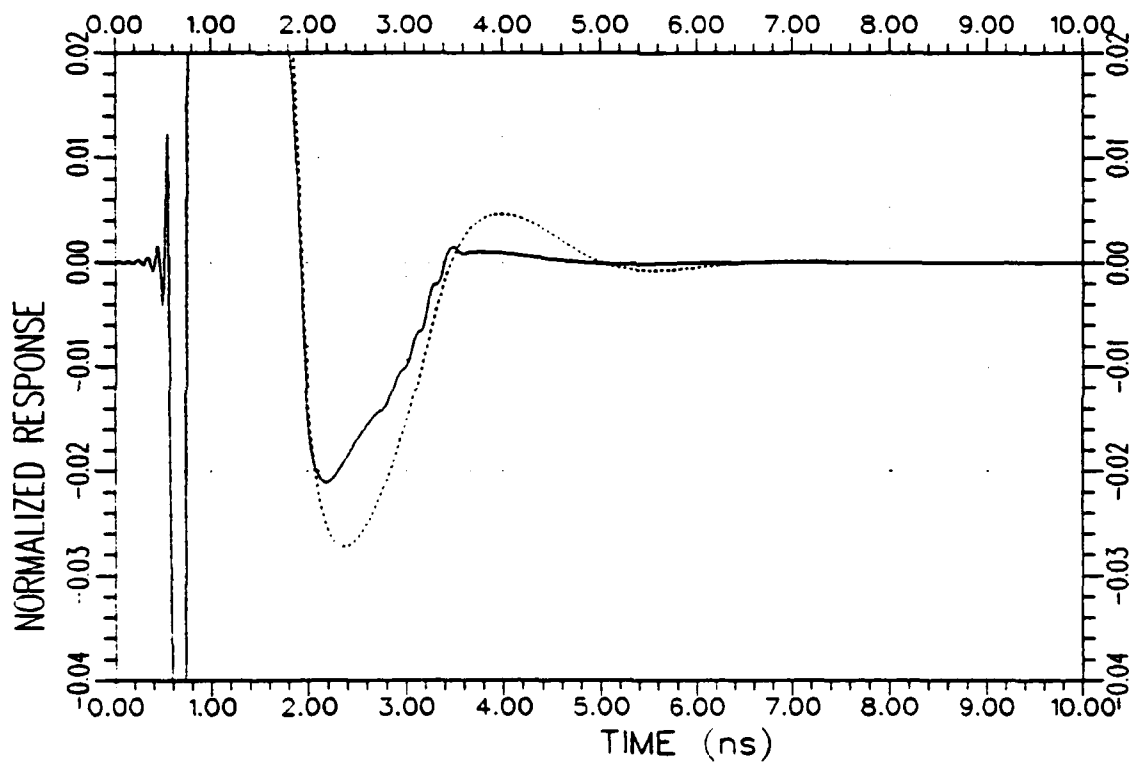
(b) 45°/Vertical polarization

Figure 4.15. Continued.



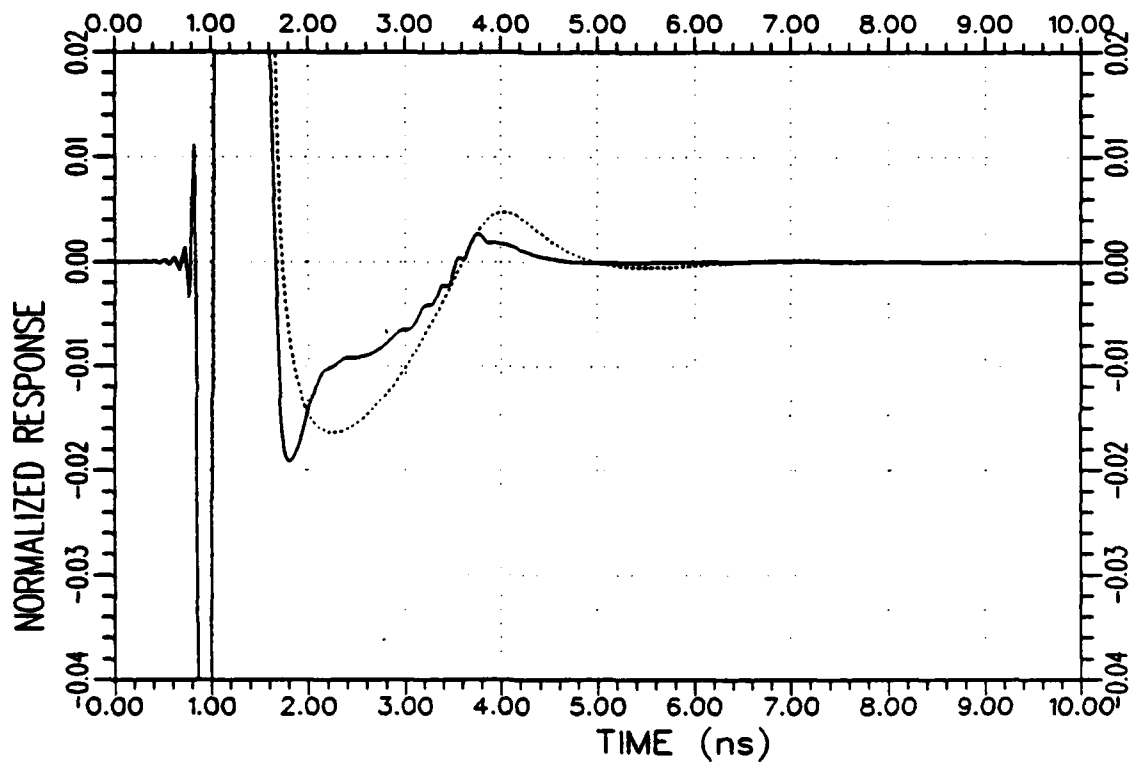
(c) 60°/Horizontal polarization

Figure 4.15. Continued.



(d) 90°/Vertical polarization

Figure 4.15. Continued.



(e) 135°/Vertical polarization

Figure 4.15. Continued.

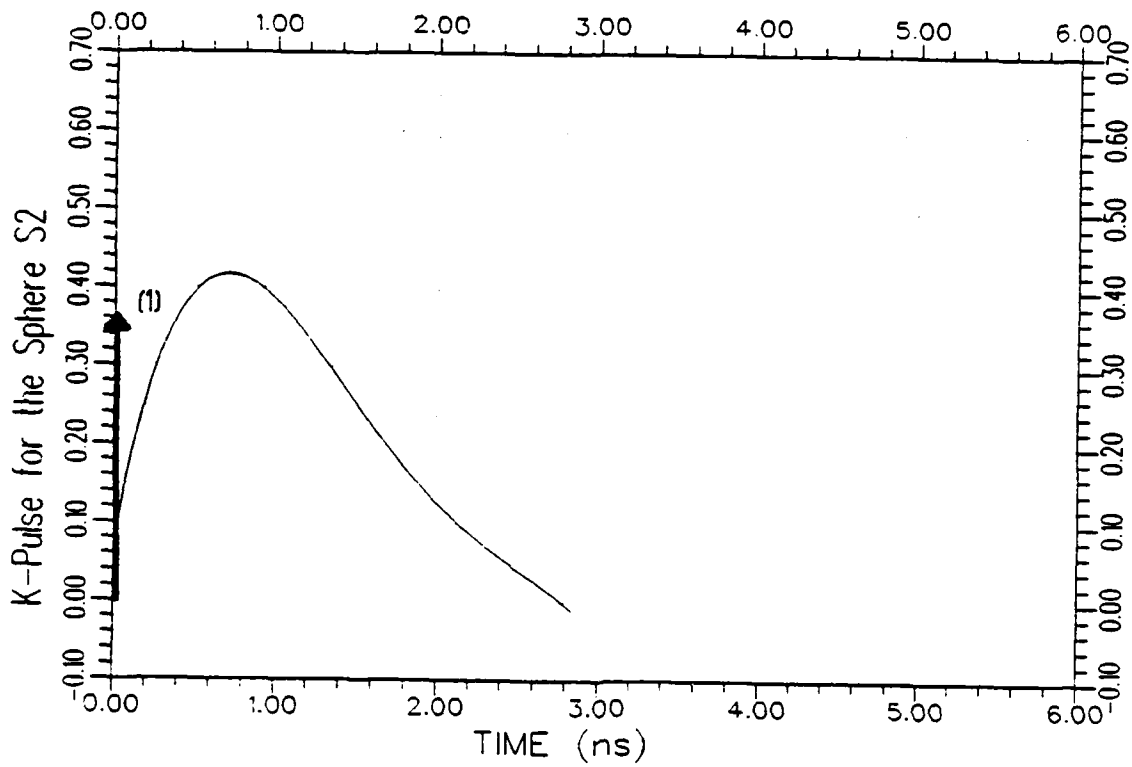
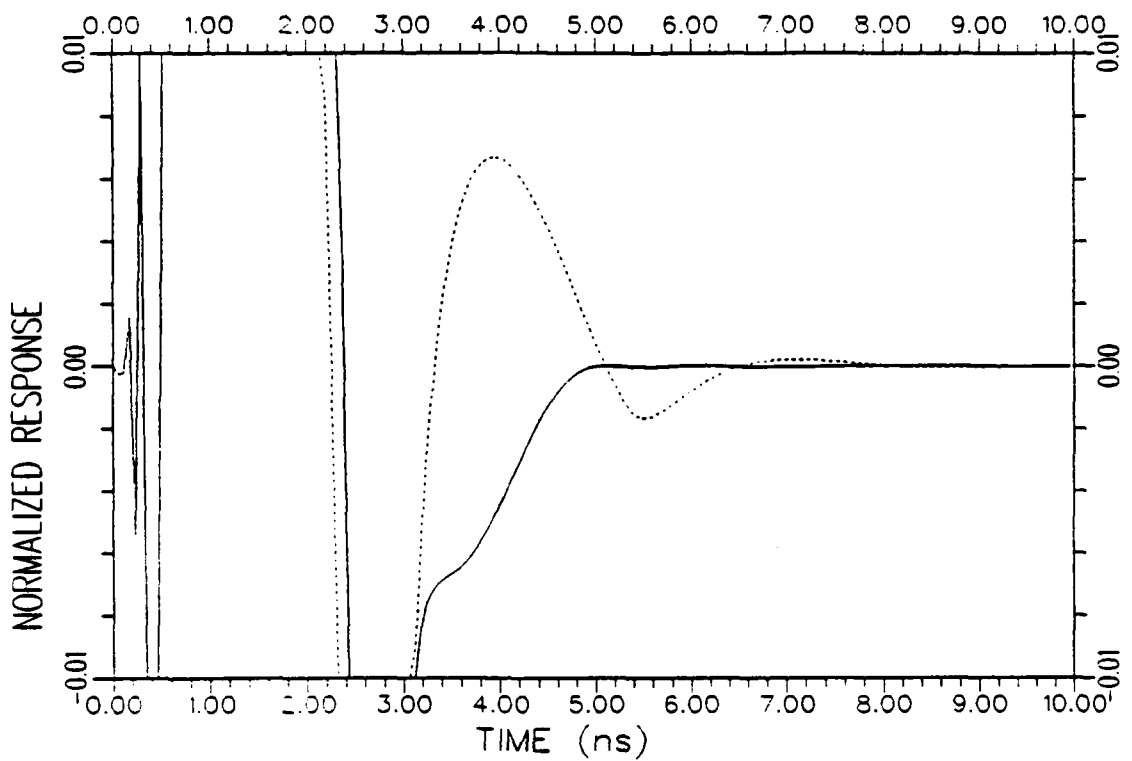
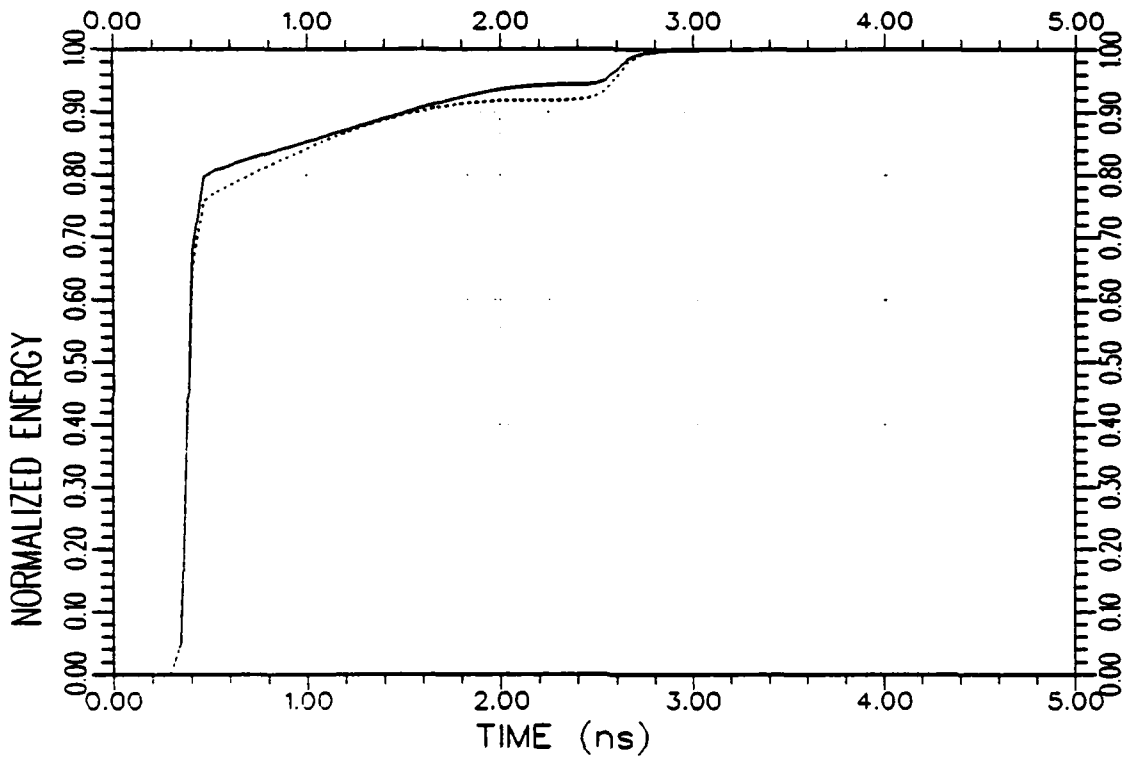


Figure 4.16. An approximate K-pulse waveform for the sphere S₂ estimated from the backscattered data using a Legendre polynomial representation for the continuous part of the K-pulse. (The $\delta(t)$ term of the K-pulse is symbolically shown by the arrow at $t=0$.)



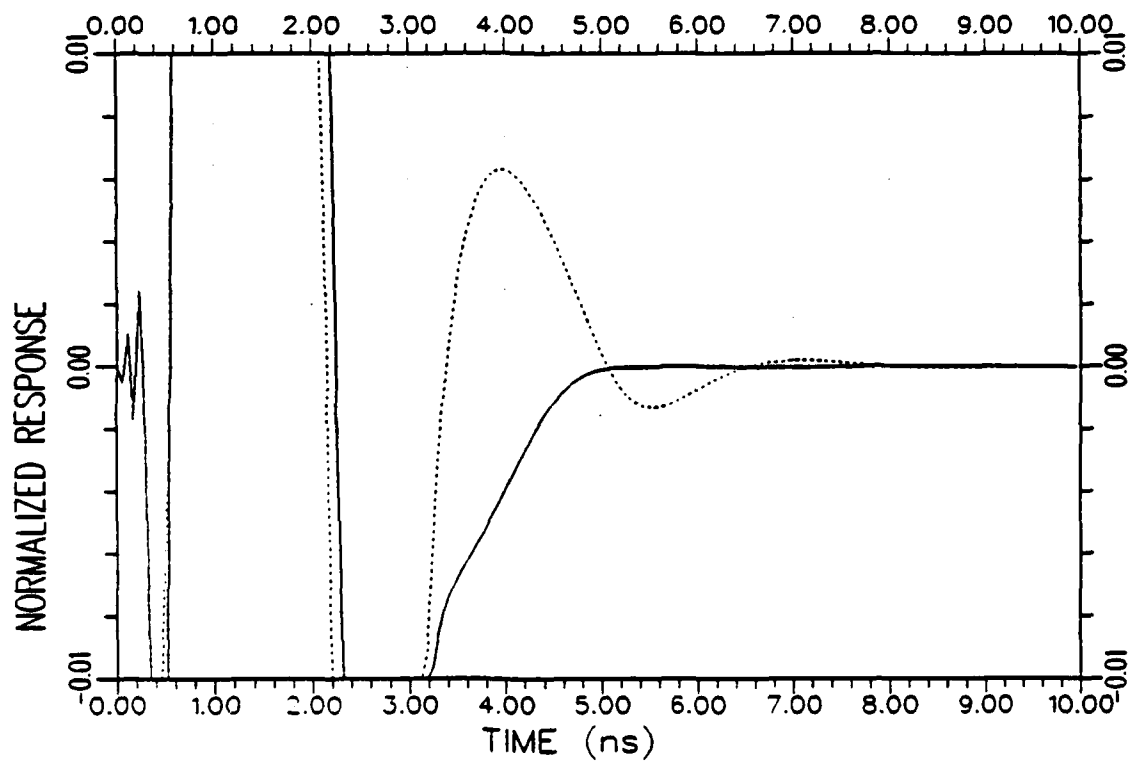
(a) Response waveforms

Figure 4.17. Normalized impulse response (.....) and K-pulse response (—) waveforms and their energy curves for the sphere S_2 (due to the K-pulse shown in Figure 4.16) at the backscattered direction.



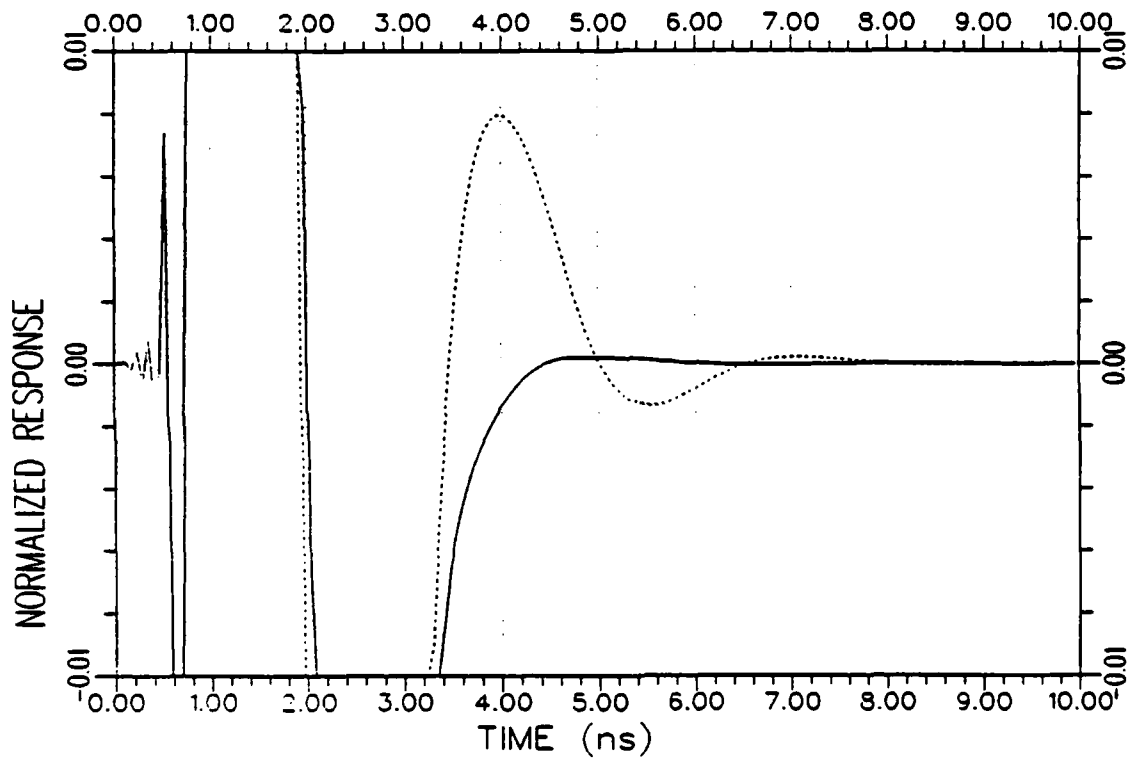
(b) Response energy curves

Figure 4.17. Continued.



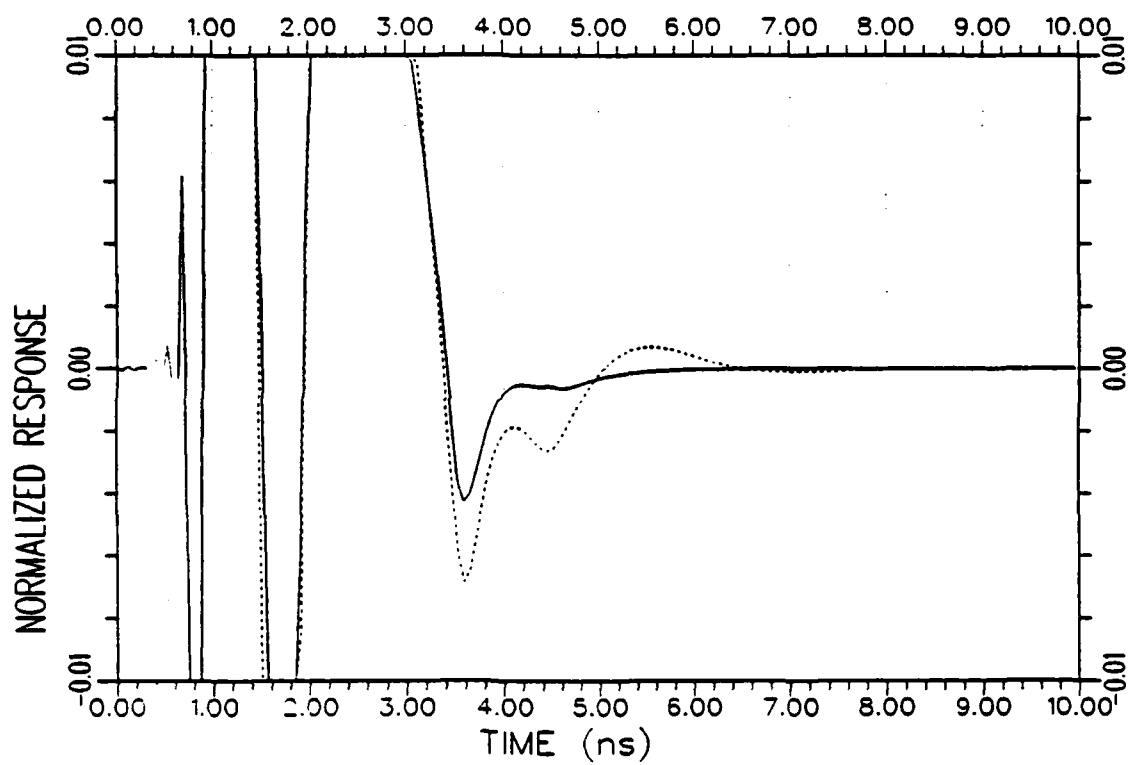
(a) 30°/Horizontal polarization

Figure 4.18. Normalized impulse response (.....) and K-pulse response (——) waveforms of S_2 (due to the K-pulse shown in Figure 4.16) for the bistatic angle/radar polarization combinations of 30°/HP, 90°/VP and 120°/HP.



(b) 90°/Vertical polarization

Figure 4.18. Continued.



(c) 120°/Horizontal polarization

Figure 4.18. Continued.

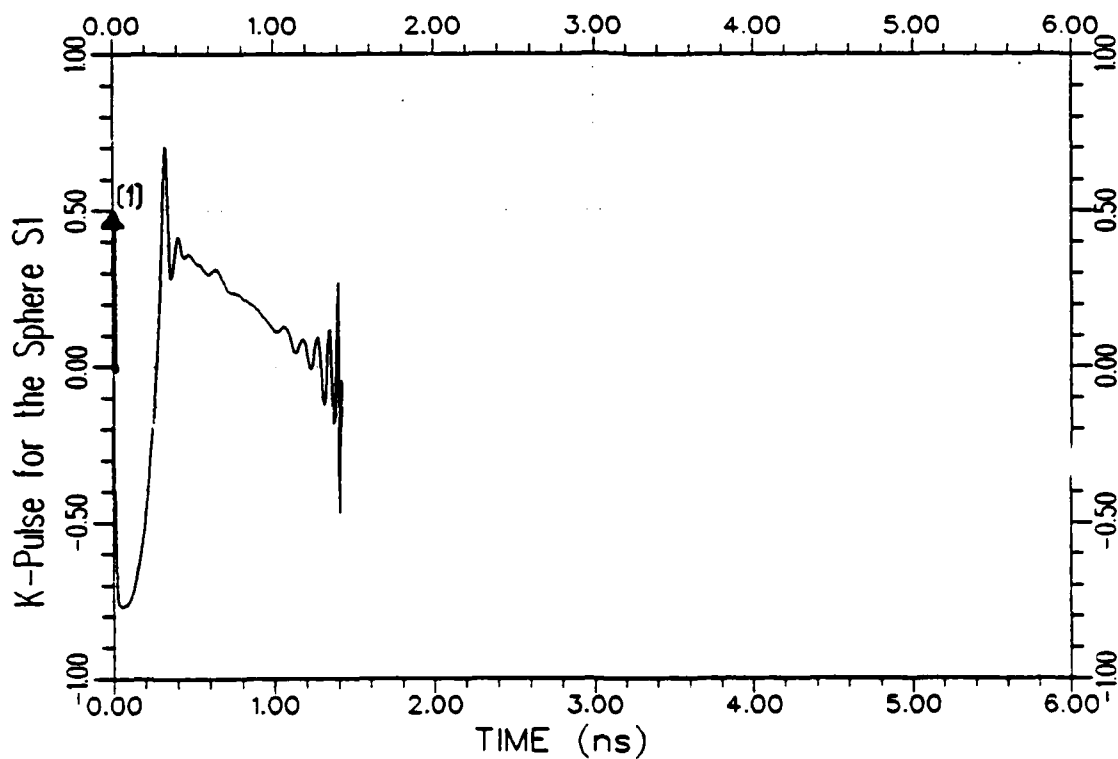


Figure 4.19. K-pulse waveform of the conducting sphere S_1 (with $2r_1=5$ inches) as constructed from the K-pulse of S_2 shown in Figure 4.16. (The $\delta(t)$ term of the K-pulse is symbolically shown by the arrow at $t=0$.)

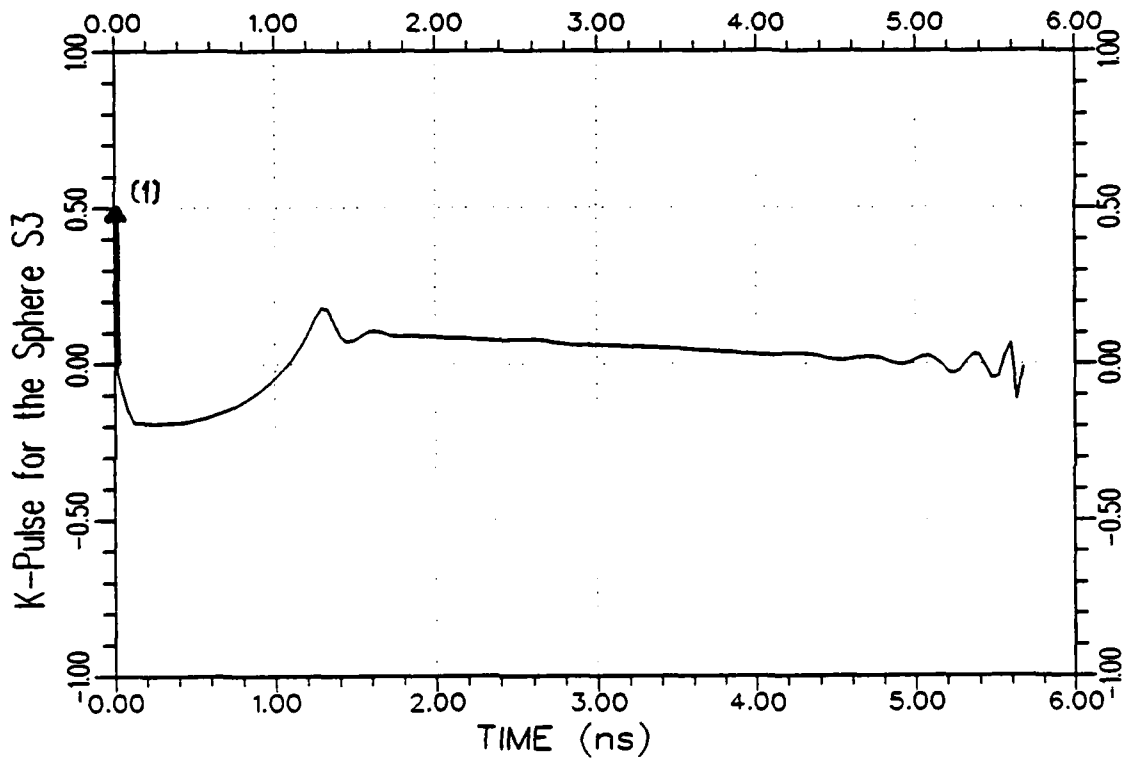
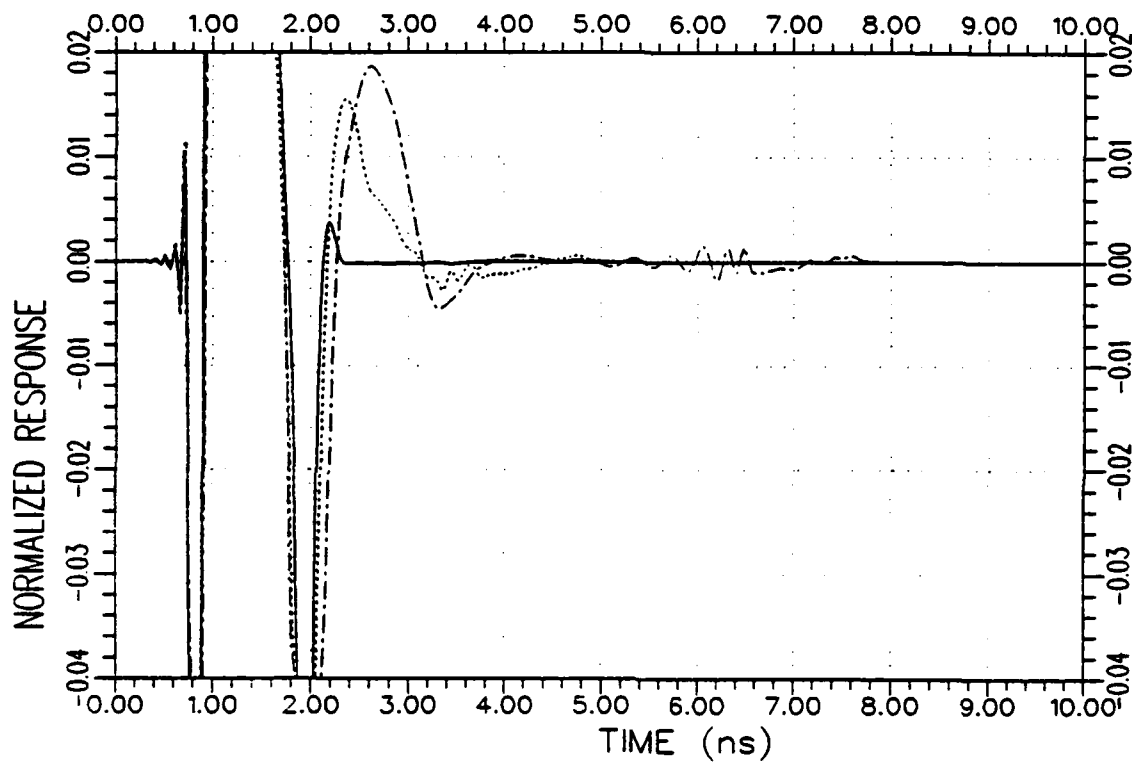
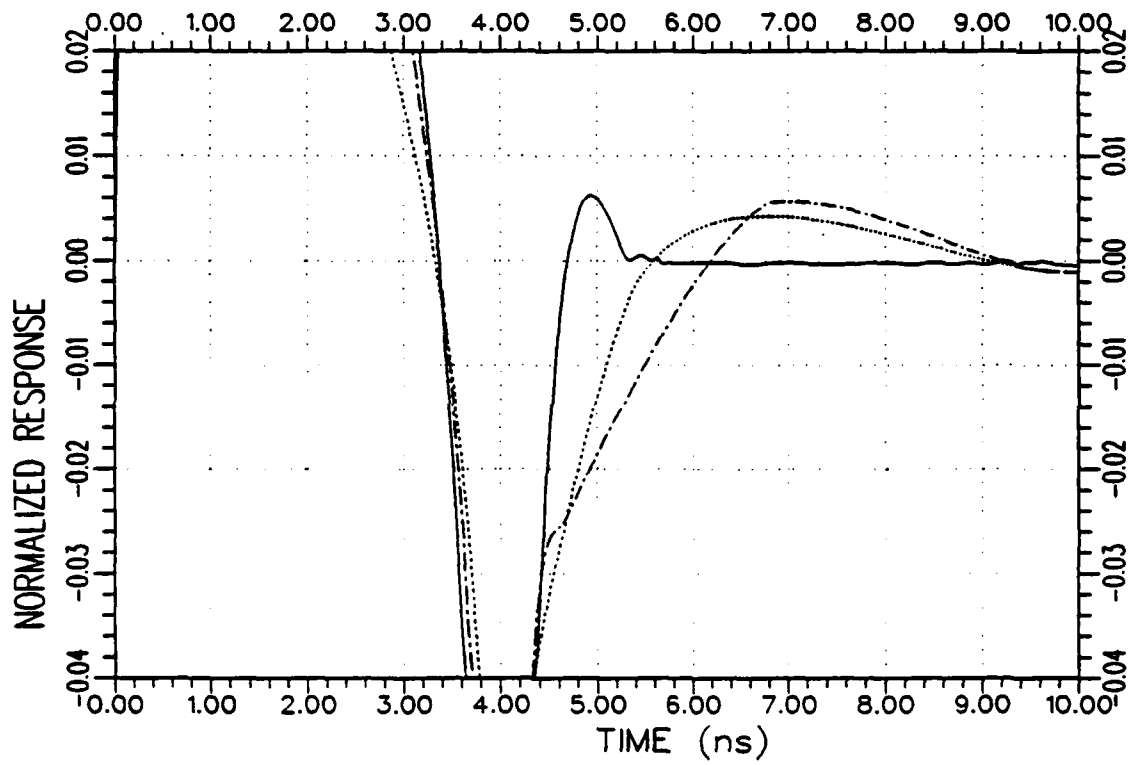


Figure 4.20. K-pulse waveform of the conducting sphere S_3 (with $2r_3=20$ inches) as constructed from the K-pulse of S_2 shown in Figure 4.16. (The $\delta(t)$ term of the K-pulse is symbolically shown by the arrow at $t=0$.)



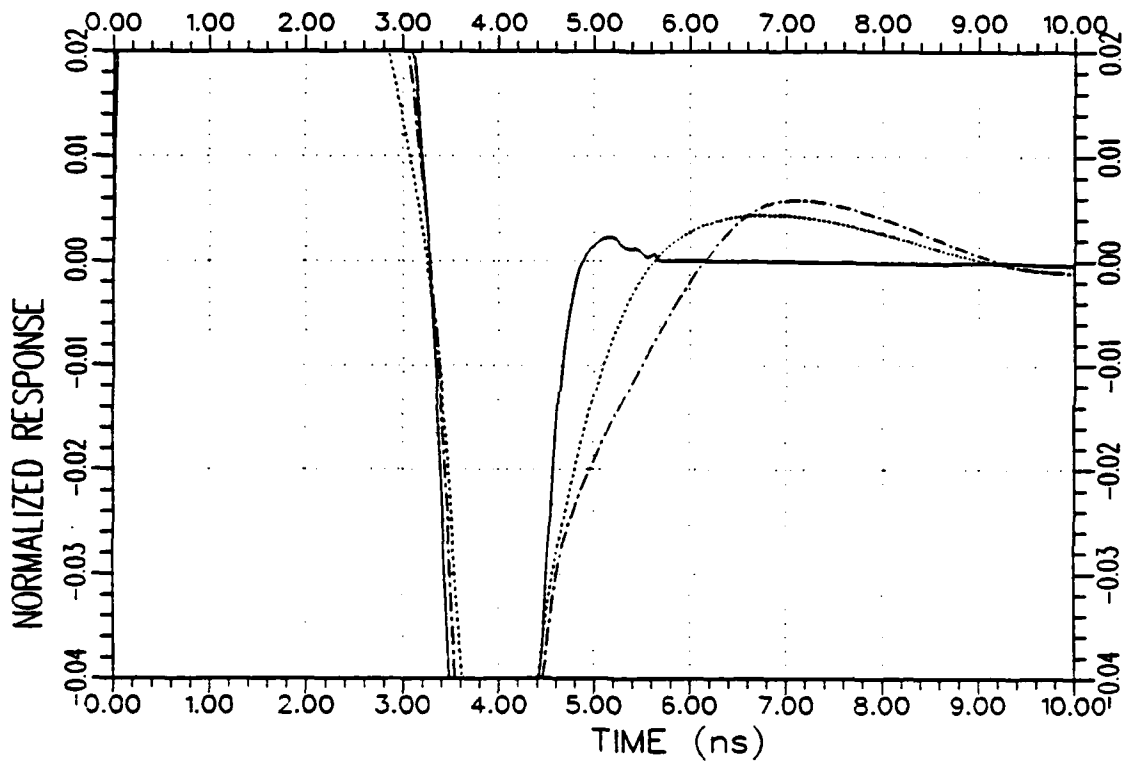
(a) Response of the test target S_1 to the K-pulses of S_1 (———), S_2 (·····) and S_3 (— · — · —) at the backscattered direction

Figure 4.21. Examples of target identification in the noise-free case using the K-pulse waveforms shown in Figures 4.16 (for the sphere S_2), 4.19 (for the sphere S_1) and 4.20 (for the sphere S_3).



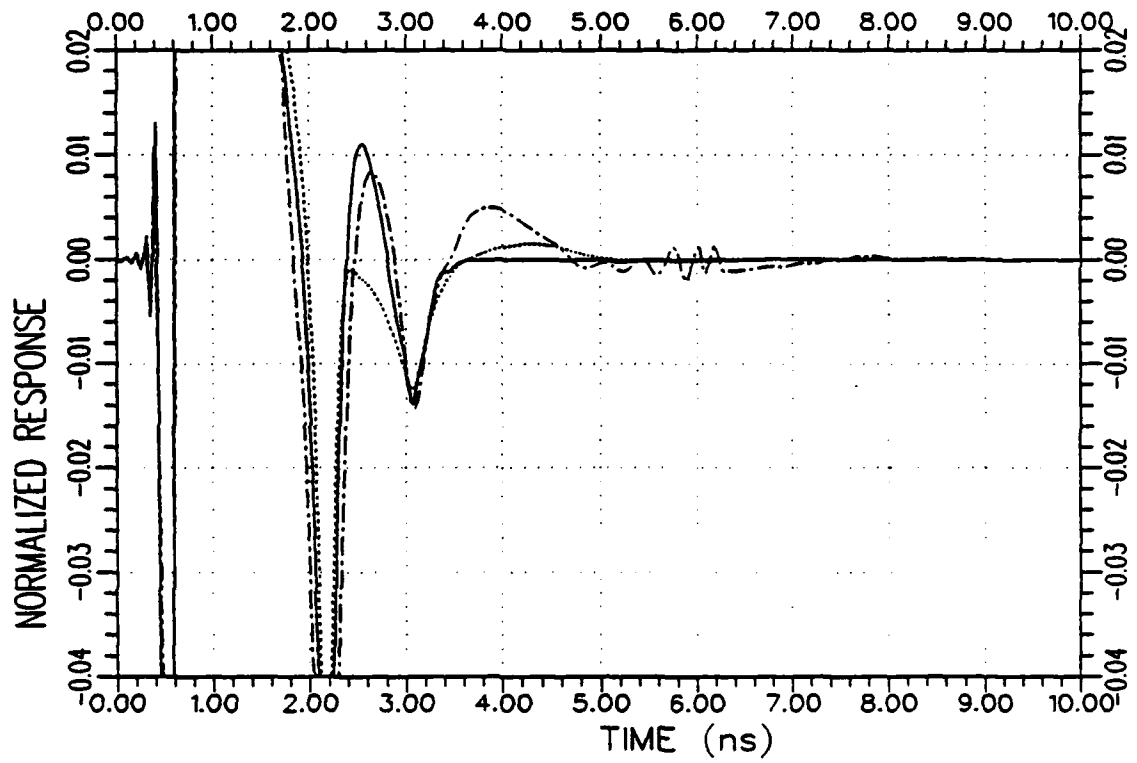
(b) Response of the test target S_3 to the K-pulses of S_1 (.....), S_2 (— · —) and S_3 (——) at the backscattered direction

Figure 4.21. Continued.



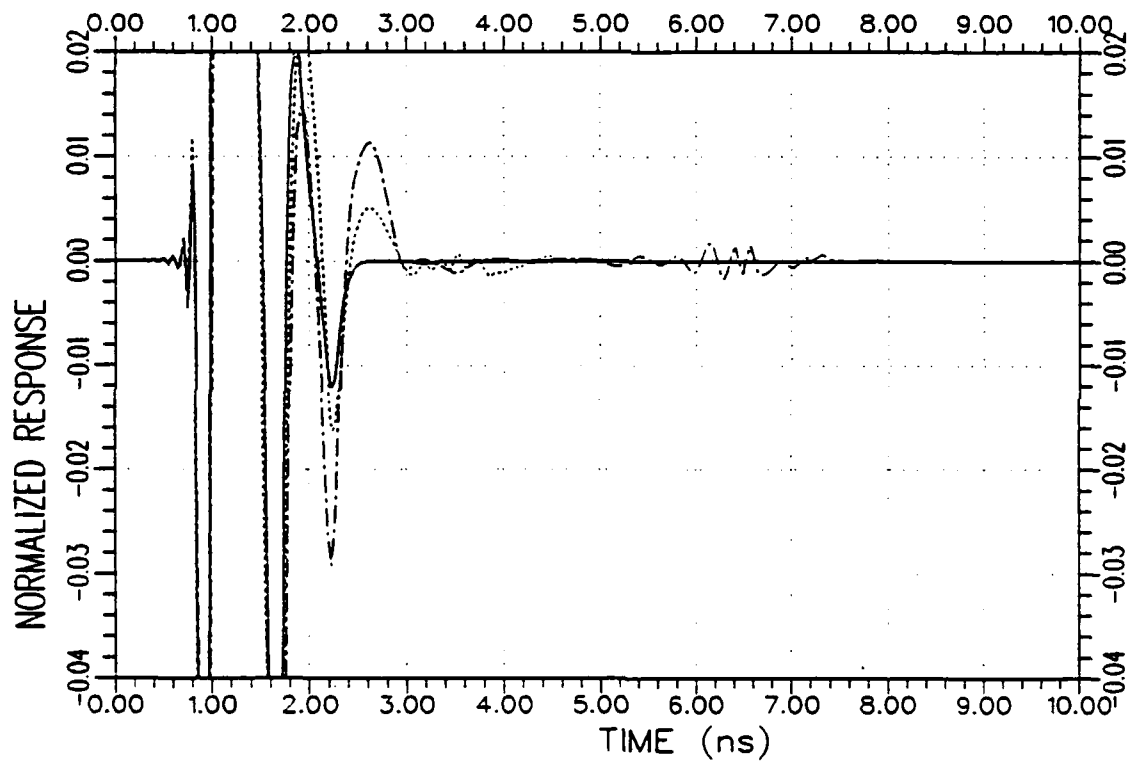
(c) Response of the test target S_3 to the K-pulses of S_1 (.....), S_2 (-.-.-) and S_3 (—) at 30° bistatic angle, vertical polarization

Figure 4.21. Continued.



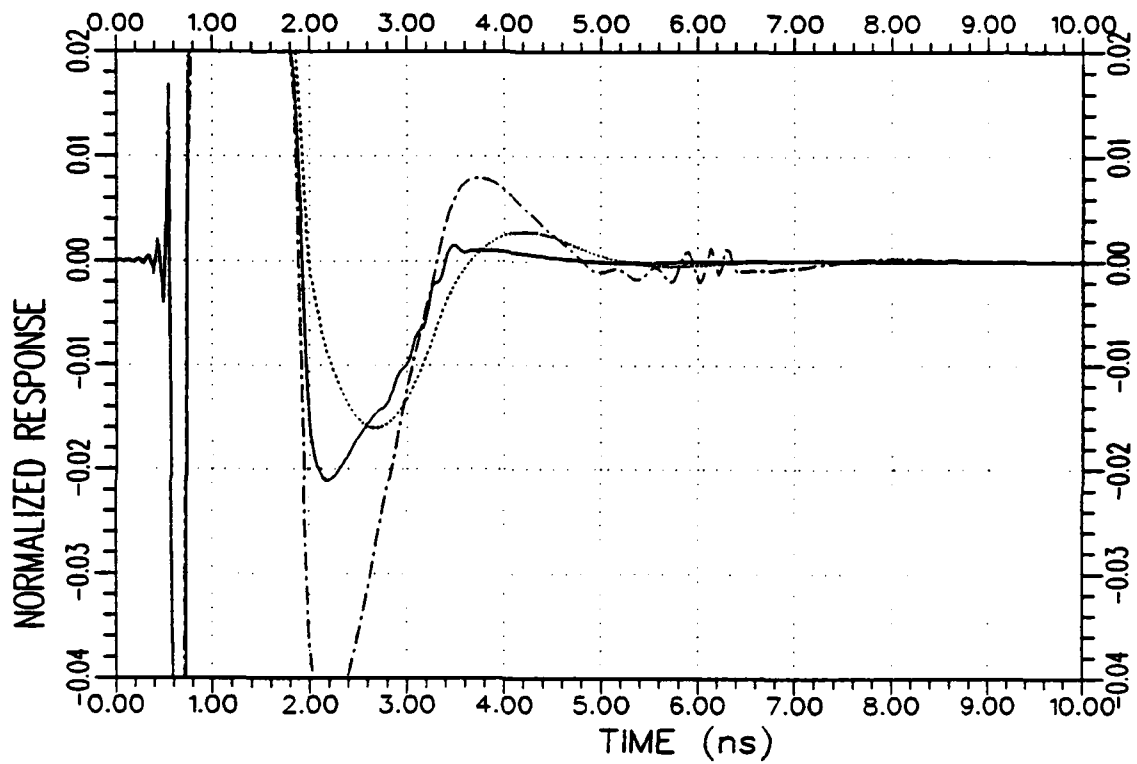
(d) Response of the test target S_2 to the K-pulses of S_1 (.....), S_2 (——) and S_3 (—·—·) at 60° bistatic angle, horizontal polarization

Figure 4.21. Continued.



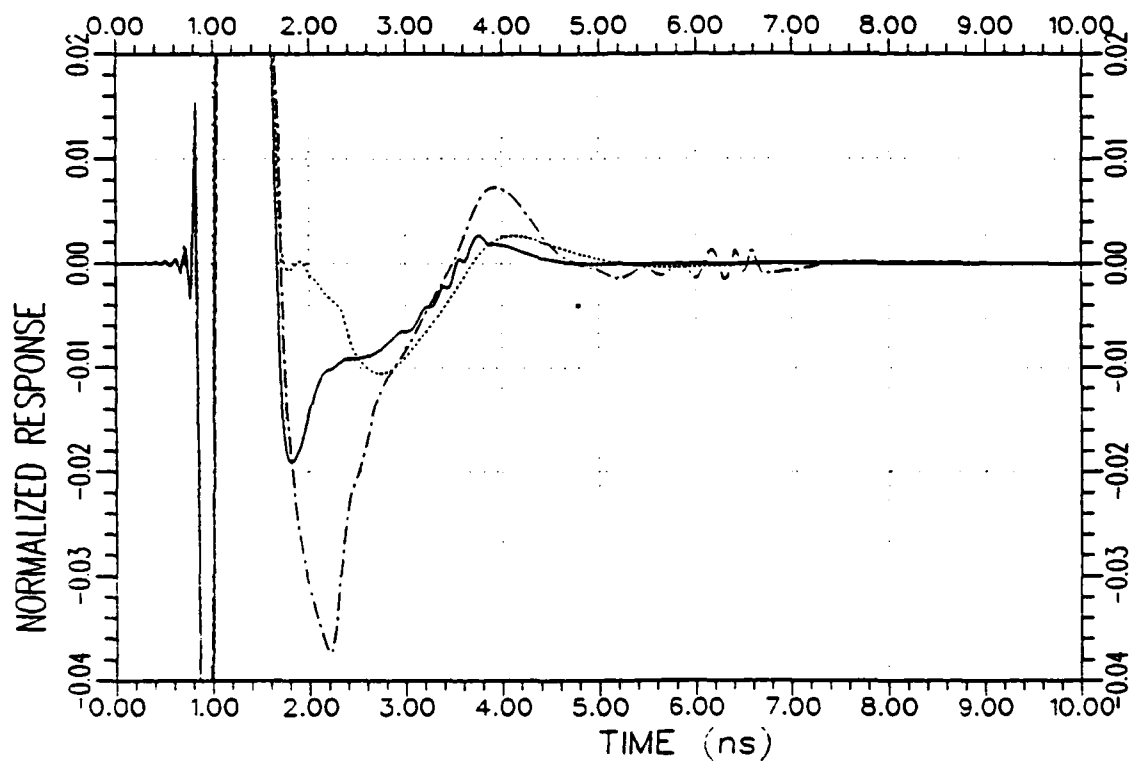
(e) Response of the test target S_1 to the K-pulses of S_1 (—), S_2 (.....) and S_3 (—·—·) at 175° bistatic angle, horizontal polarization

Figure 4.21. Continued.



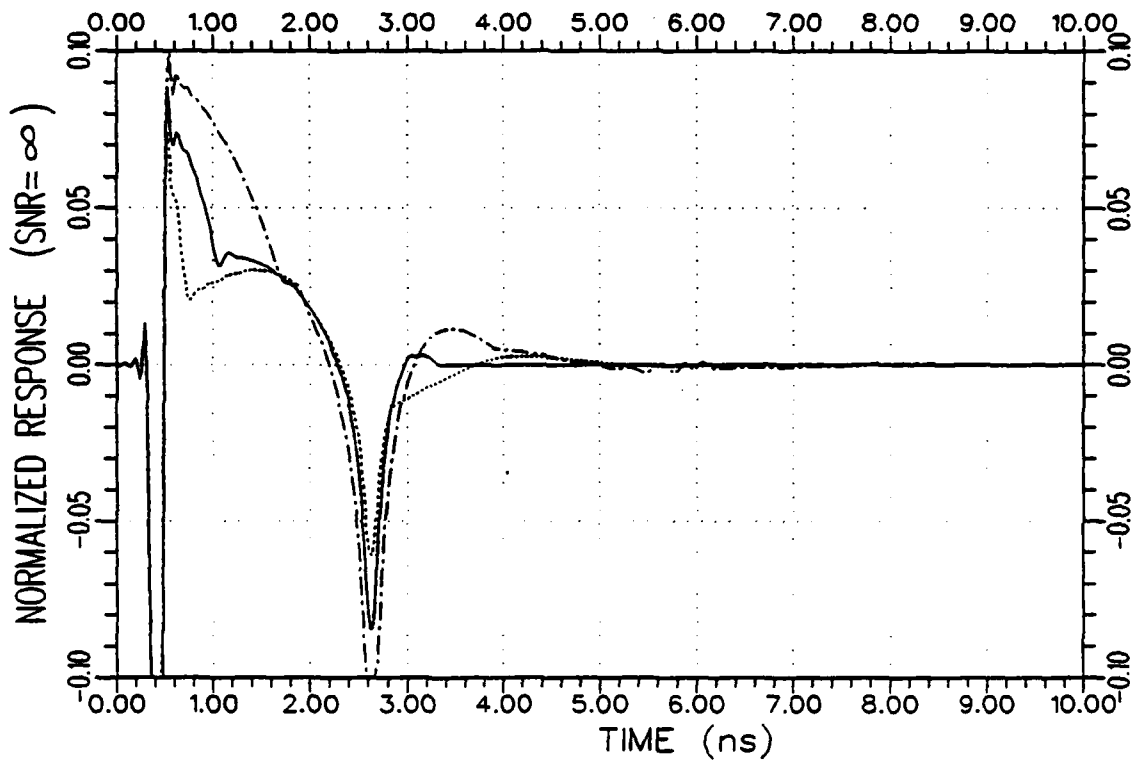
(f) Response of the test target S_2 to the K-pulses of S_1 (.....), S_2 (—) and S_3 (-·-·) at 290° bistatic angle, vertical polarization

Figure 4.21. Continued.



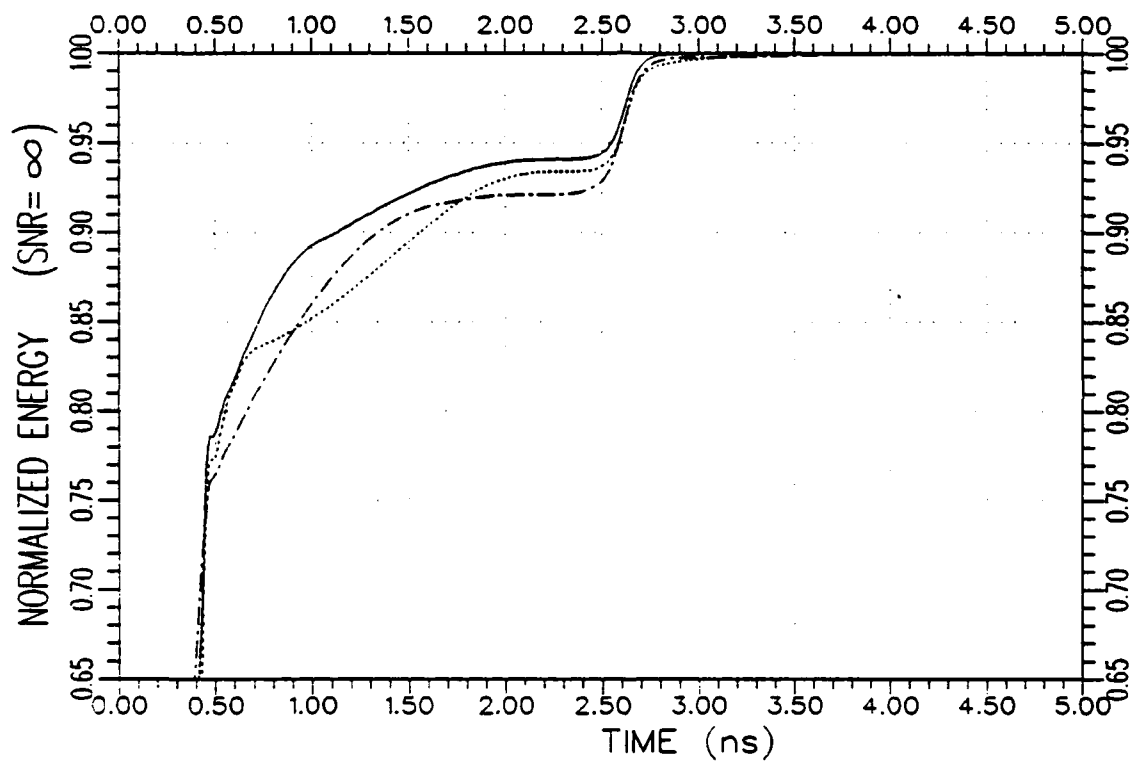
(g) Response of the test target S_2 to the K-pulses of S_1 (.....), S_2 (—) and S_3 (—·—) at 135° bistatic angle, vertical polarization

Figure 4.21. Continued.



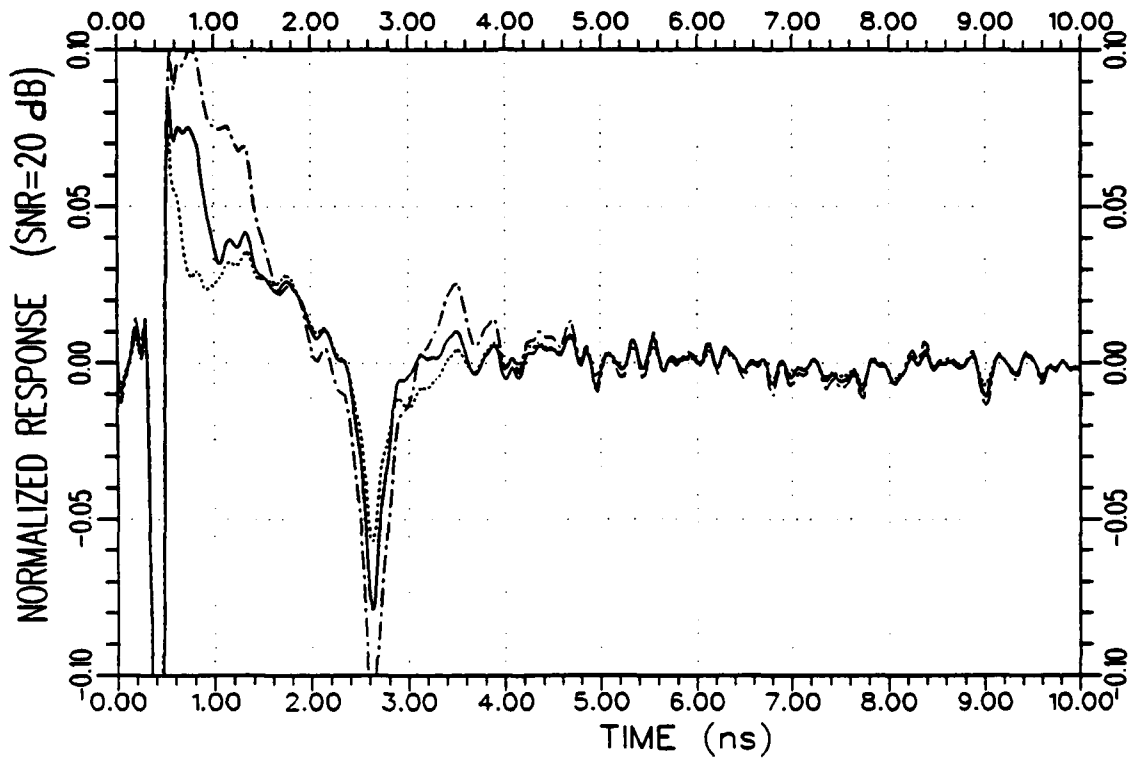
(a) Normalized response waveforms for the noiseless case ($SNR=\infty$)

Figure 4.22. Normalized response waveforms and the corresponding energy curves of the test target S_2 due to the K-pulses of S_1 (.....), S_2 (—) and S_3 (-.-.-) at the backscattered direction.



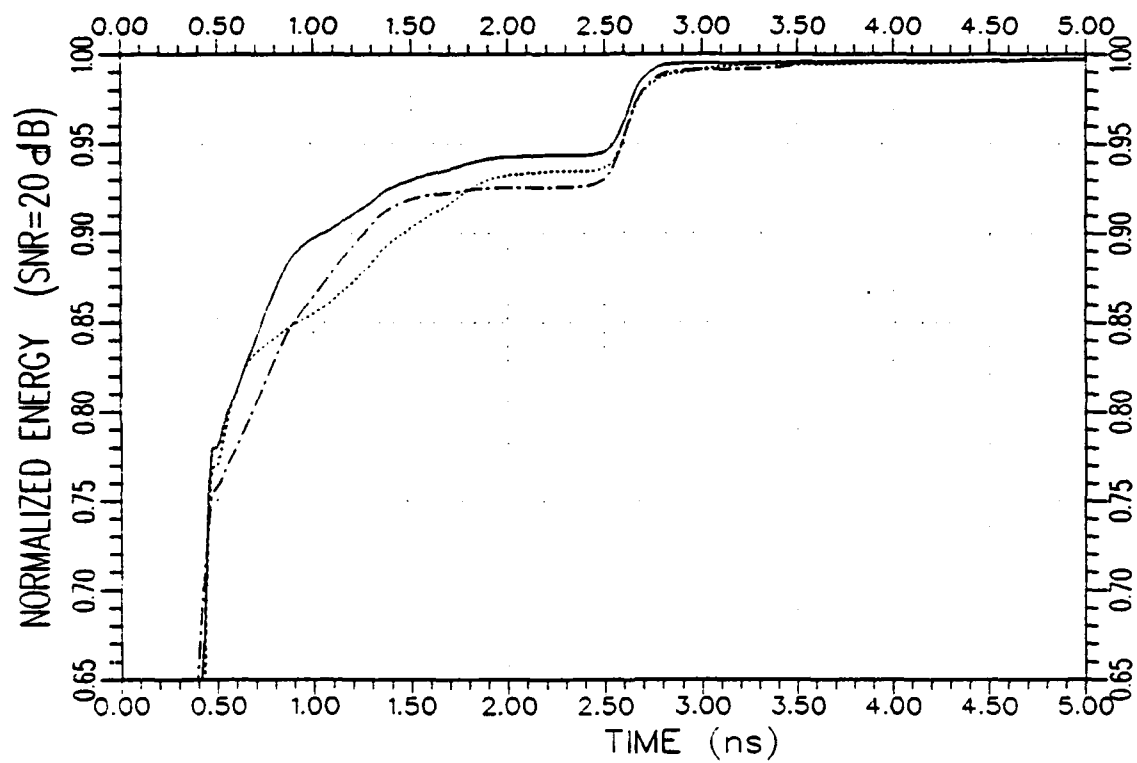
(b) Normalized response energy curves for the noiseless case (SNR=∞)

Figure 4.22. Continued.



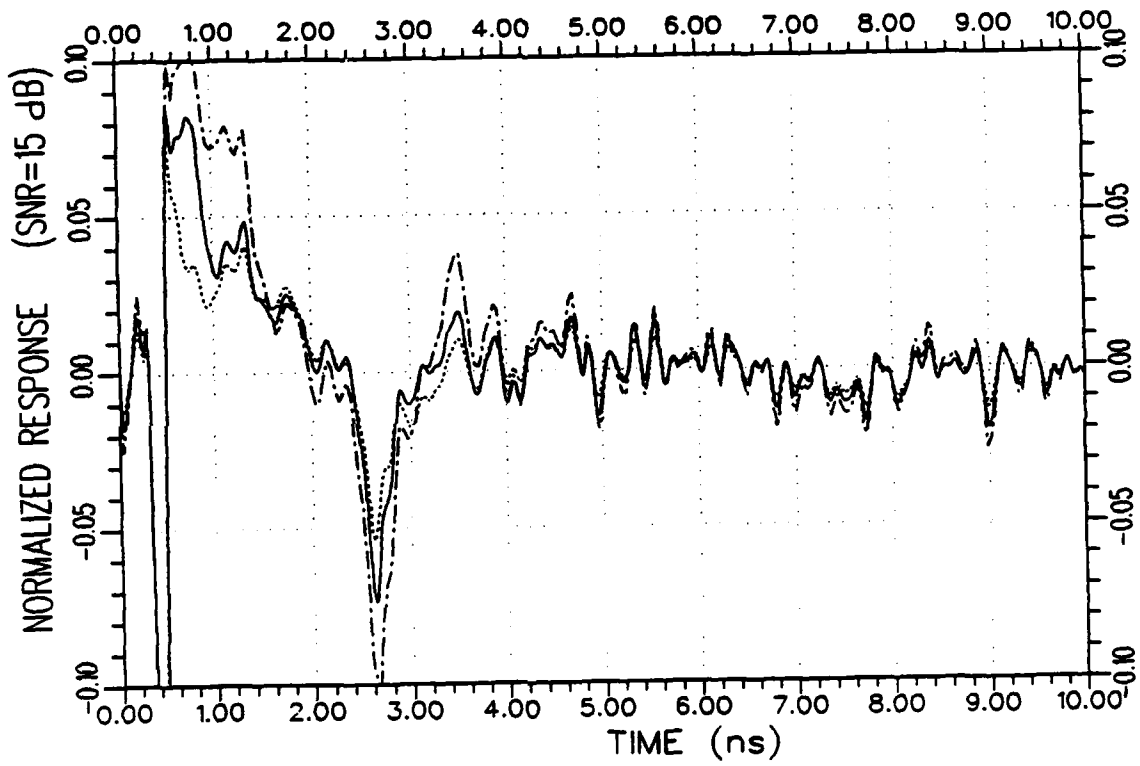
(c) Normalized response waveforms for SNR=20 dB

Figure 4.22. Continued.



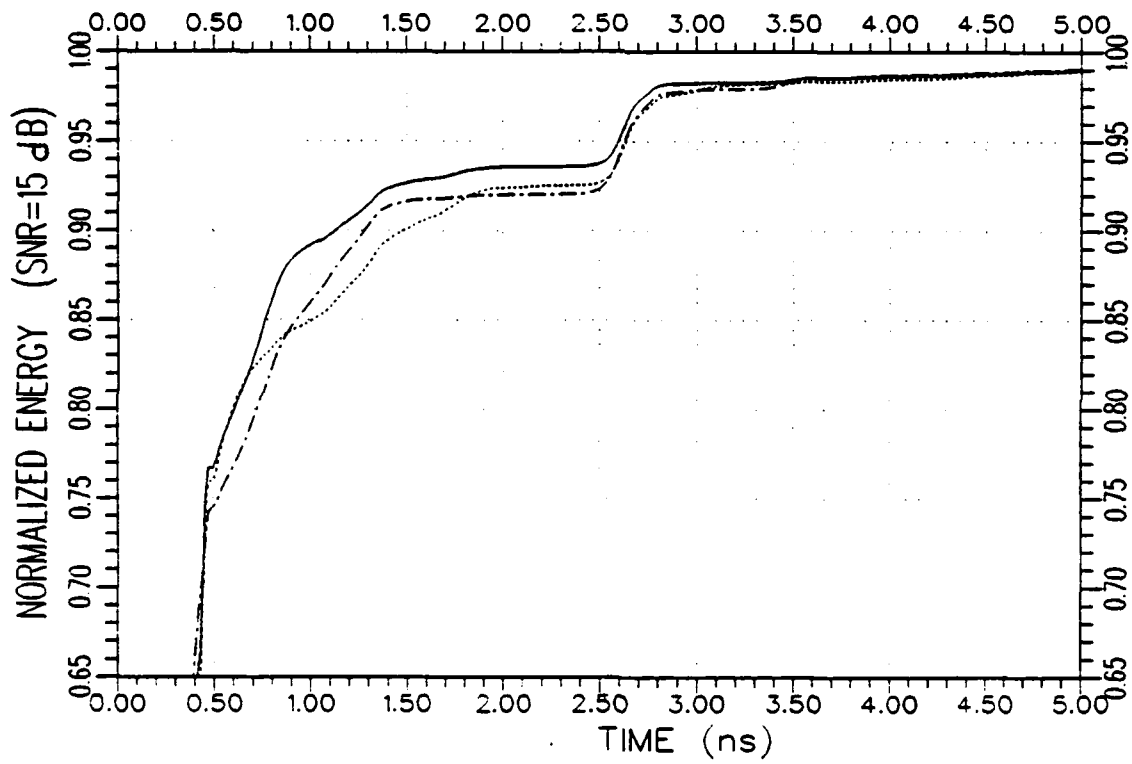
(d) Normalized response energy curves for SNR=20 dB

Figure 4.22. Continued.



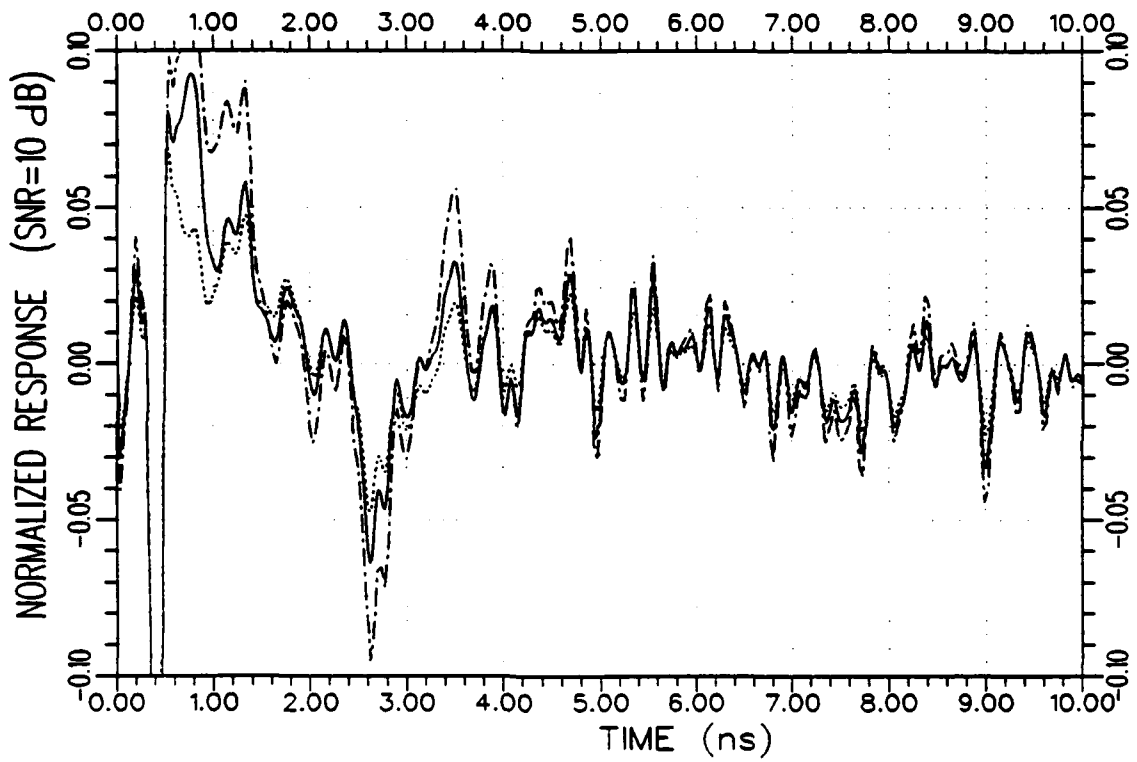
(e) Normalized response waveforms for SNR=15 dB

Figure 4.22. Continued.



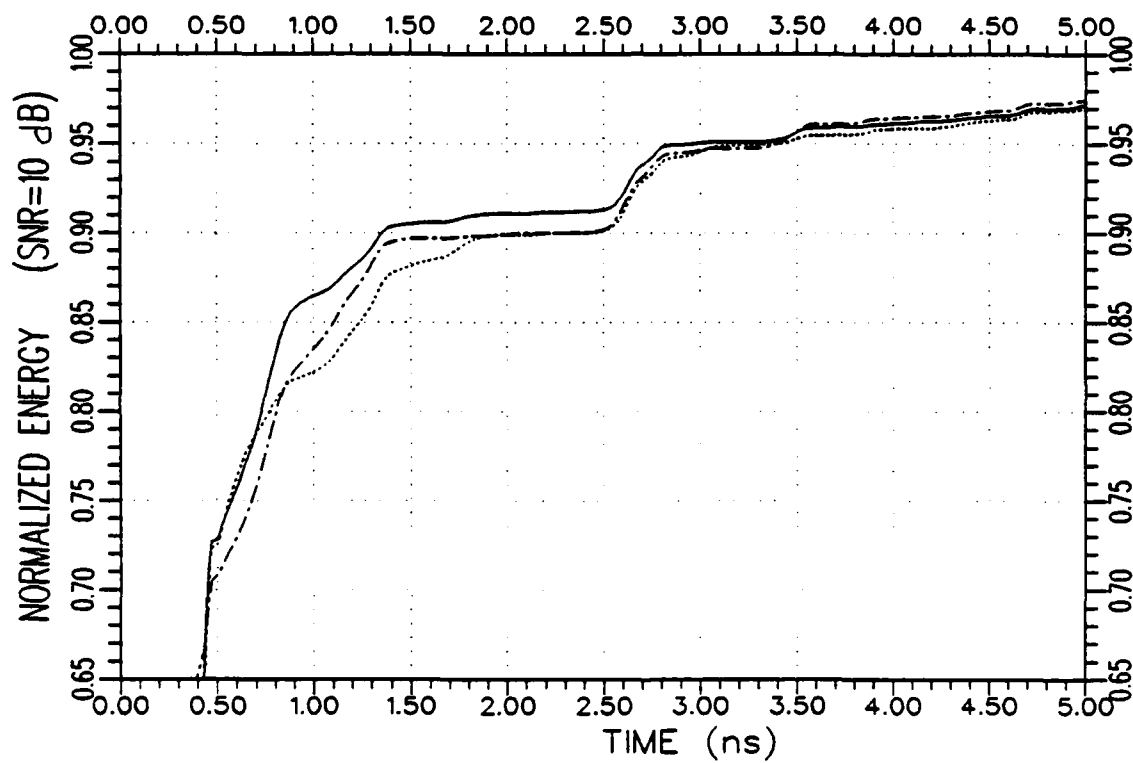
(f) Normalized response energy curves for SNR=15 dB

Figure 4.22. Continued.



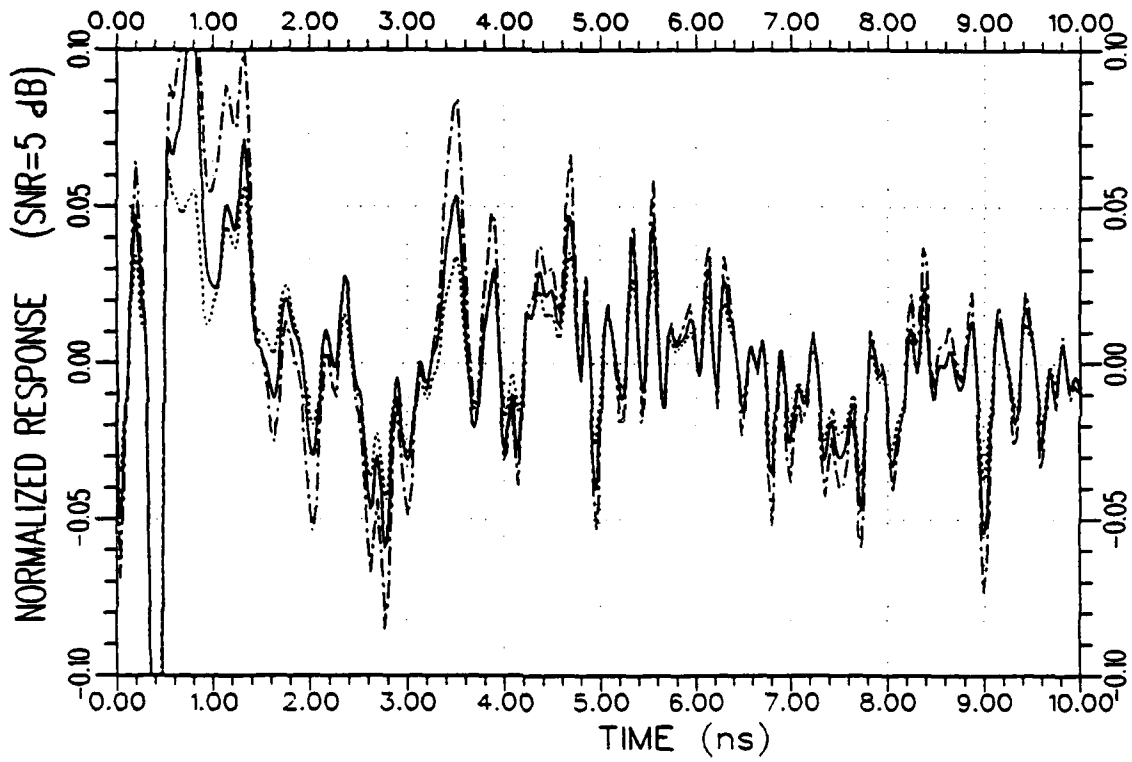
(g) Normalized response waveforms for SNR=10 dB

Figure 4.22. Continued.



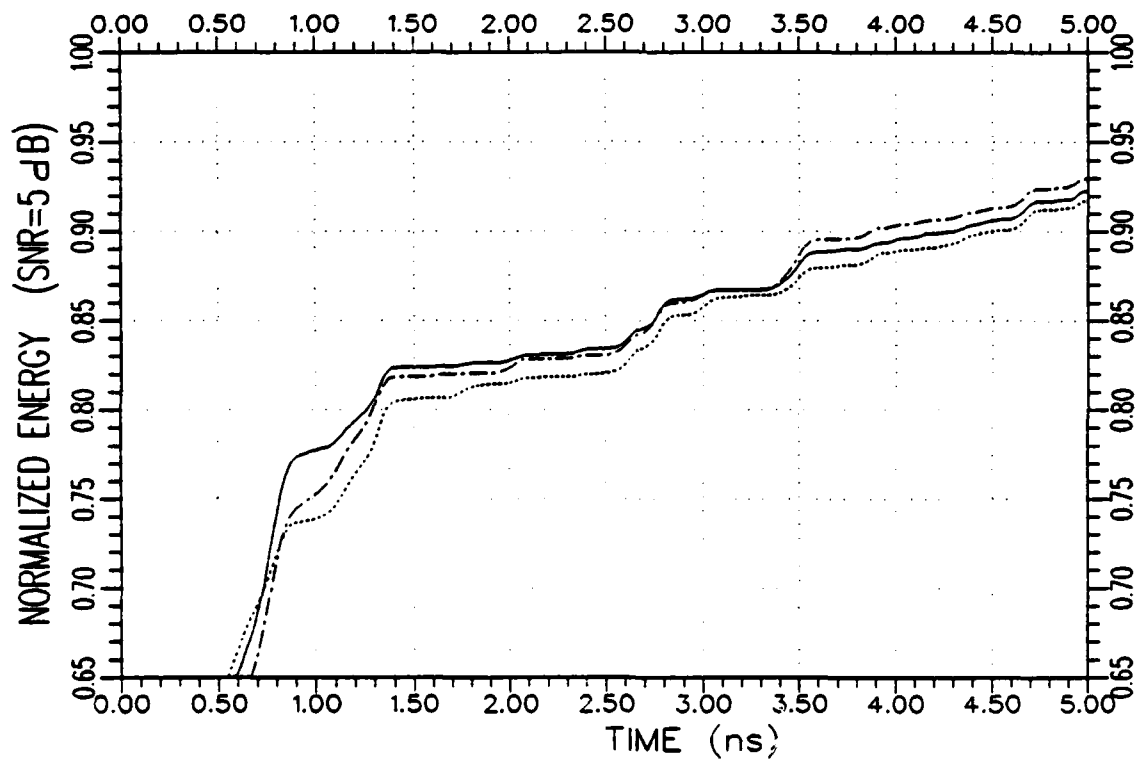
(h) Normalized response energy curves for SNR=10 dB

Figure 4.22. Continued.



(i) Normalized response waveforms for SNR=5 dB

Figure 4.22. Continued.



(j) Normalized response energy curves for SNR=5 dB

Figure 4.22. Continued.

CHAPTER V
APPLICATIONS TO SHIPS

In this chapter, attention will focus on the application of K-pulse techniques to naval targets. Two small-scale electroplated model ships are employed in the demonstrations where no geometrical features of the actual targets are simplified. The backscattered frequency data of the model ships, referred to as SH_1 and SH_2 hereafter, were measured on the Ohio State University Compact RCS Measurement Range [53] in the presence of a ground plane^{*}. The frequency span of the data used for both targets is 2 to 8 GHz. The wavelength at the lowest measurement frequency is 15 cm which is slightly larger than the lengths of targets SH_1 and SH_2 . This means that the available scattering data do not span the lower portion of the resonance region for either target. As discussed in Chapter III, such data are termed incomplete in this report and may cause uncertainties in K-pulse estimation. Furthermore, the targets SH_1 and SH_2 are relatively low-Q objects with complicated substructures. All these factors result in a challenging problem of K-pulse estimation and target identification. In Sections A and B of this chapter, the K-pulse estimation aspect of the problem is examined, first for the ship

* The ground plane configuration is described in [54].

SH_1 then for SH_2 . The synthesized K-pulse waveforms are used for target identification purposes in Section C. The K-pulse waveform of the target SH_2 is synthesized using the Legendre polynomial basis functions to demonstrate that this alternative K-pulse estimation technique can be applied successfully not only to simple targets as shown in Chapter IV but also to geometrically complicated and low-Q targets such as the model ship, SH_2 .

A. K-PULSE ESTIMATION FOR THE MODEL SHIP SH_1

The K-pulse estimation technique to be utilized in this section is based on a discrete representation of the continuous part of the K-pulse as described in Section A of Chapter III. The continuous function, $k^c(t)$, (see Equation (3.1)) is represented by discrete sample values $k_1^c, k_2^c, \dots, k_N^c$ where N is chosen to be 80. The combination of aspect and polarization used in the K-pulse synthesis procedure are $0^\circ/VP$ and $80^\circ/VP$. The backscattered impulse response waveforms at these combinations are obtained via inverse FFT of the measured frequency data which are weighted by a band-limited Hanning window function prior to transformation. As a result of several pilot runs of the synthesis program, the K-pulse duration is chosen to be $3L_1/c = 0.915$ ns where L_1 is the length of the model ship and c is the speed of light in a vacuum. The unknown sample values of $k^c(t)$ are estimated by minimizing the cost function \tilde{J} of Equation (3.9) with $a=1$, $b=0$ and $I=2$. The pre-estimated cut-off times are 0.65 ns and 0.60 ns at the aspect angles of 0° and 80° , respectively. The resultant K-pulse waveform is shown in Figure 5.1. Since there is no a priori information available

on the target poles to be compared with the zeros of the K-pulse spectrum, the only way of justifying the synthesis result is to check the K-pulse response at as many combinations as possible for the late-time response energy reduction. For this purpose, the normalized impulse response and K-pulse response pairs as well as the corresponding normalized energy curve pairs of the target SH_1 are plotted in Figure 5.2 through 5.11 at the aspect angles of 0° , 15° , 30° , 45° , 60° , 80° , 90° , 100° , 170° and 180° , respectively all for vertical polarization. Each of these figures has two parts; time waveforms are plotted in part (a), and the associated energy curves are shown in part (b). The common result observed in all these figures is that the K-pulse response of the target is not severely time-limited but its late-time energy content is reduced as compared to that of the corresponding impulse response. In other words, at each aspect angle, the energy content of the K-pulse response is concentrated in a shorter time interval with respect to the impulse response as a result of partial natural mode annihilation. The energy plots are particularly useful for viewing the late-time energy variations, where the normalized energy curves of the impulse response and K-pulse response follow a similar path up to a certain high energy level but then the energy curve of the K-pulse response reaches higher levels earlier than that of the impulse response. The energy level at which the two curves start separating from each other varies from one aspect to another, but remains in the range 0.7 to 0.9, where the value unity corresponds to the total normalized energy level.

In summary, the demonstrations presented in Figures 5.2 through 5.11 strongly support the claim that the K-pulse waveform shown in Figure 5.1 characterizes the target SH_1 in an aspect-invariant manner. As a by-product of the K-pulse estimation procedure, several pole-pairs of the target SH_1 are estimated as zeros of the Laplace transform of the K-pulse waveform shown in Figure 5.1. These approximate pole-pairs (CNR frequencies) are listed in Table 5.1.

B. K-PULSE ESTIMATION FOR THE MODEL SHIP SH_2

In this section, an approximate K-pulse waveform of the model target SH_2 will be synthesized using the Legendre polynomial approach as described in Section B of Chapter III. The K-pulse duration, T_k , for this complicated geometry is estimated to be $3L_2/c = 1.016$ ns where L_2 is the length of ship SH_2 . The combinations of aspect and polarization used for K-pulse synthesis are $30^\circ/VP$ and $100^\circ/VP$. The continuous part of the K-pulse model is represented by an expansion of modified Legendre polynomials in the interval $[0, 1.016$ ns] (see Equations (3.12) and (3.13)). The maximum order of the Legendre polynomials is restricted to five for the first test run of the synthesis computer program. The optimal values of the expansion coefficients D_0, D_1, \dots, D_5 were searched by minimizing the cost function \tilde{J} in Equation (3.9) for $a=1, b=0, I=2$ with the cut-off times being 1.55 ns and 1.20 ns at the combinations $30^\circ/VP$ and $100^\circ/VP$, respectively. A satisfactory convergence could not be obtained for these assumptions. The program was rerun by changing the cut-off time specifications which did not lead to any improvement. The last two

expansion coefficients were observed to attain much larger values than the others possibly indicating that several of the higher order Legendre polynomials should be included in the mathematical representation for better results. Then the maximum order of the Legendre polynomials used in Equation (3.13) was increased to nine leading to a satisfactory K-pulse estimation result. With the same parameters and the cut-off times as indicated earlier, minimization of the cost function generated the optimized values of expansion coefficients D_0, D_1, \dots, D_9 as listed in Table 5.2. The K-pulse waveform presented in Figure 5.12 is constructed using Equation (3.13). A subset of target poles extracted as zeros of the K-pulse spectrum is shown in Table 5.3. The pairs of the normalized impulse response and K-pulse response waveforms of the target SH_2 (under the K-pulse excitation of Figure 5.12) are given in part (a) of Figures 5.13 through 5.22 for aspects of $0^\circ, 10^\circ, 30^\circ, 45^\circ, 60^\circ, 80^\circ, 90^\circ, 100^\circ, 170^\circ$ and 180° , respectively for vertical polarization. Also, the associated normalized energy curve pairs are shown in part (b) of the same figures. In each of these figures except those for 80° and 90° cases, it is observed that the late-time energy content of the K-pulse response is not zero but definitely lower than that of the impulse response due to partial annihilation of the target's natural modes. This late-time energy reduction behavior is strongly reflected in the energy plots by the way that the normalized energy curves of the K-pulse response lead those of the corresponding impulse responses not only at high energy levels but at almost all energy levels. On the other hand, there is no obvious late-time natural response annihilation

observed at the 80° and 90° cases. It is very likely that the zero pattern of the synthesized K-pulse spectrum fails to include a complex pole-pair which is strongly excited at these aspects. However, in Section C of this chapter, it is demonstrated that identification of SH₂ on the basis of this K-pulse waveform is still possible at 80° and 90° aspect angles despite the relatively poor results of Figures 5.18 and 5.19.

C. TARGET IDENTIFICATION

The K-pulse library of this section is composed of the K-pulse waveforms of the targets SH₁ and SH₂ which are shown in Figures 5.1 and 5.12, respectively. Not only are the geometrical features of these targets quite similar, but their physical dimensions are also in close proximity. First, a group of demonstrations are presented for the practically noiseless case since the original data were measured in a noise-controlled chamber [53]. The unknown target of identification examples given in Figures 5.23 through 5.29 is the model ship SH₁ whose normalized response energy curves under the excitation of its own K-pulse (matched case) and the K-pulse of the other library target SH₂ (mismatched case) are plotted in pairs at 0°, 15°, 30°, 45°, 80°, 100°, and 170°, respectively for vertical polarization. In these figures, matched response energy curves are shown by solid lines and mismatched ones are drawn by dotted lines; the same representation is used in the rest of the identification examples of this section. At 0°, 15°, 30° and 45° aspect angles, the matched energy curve starts leading the mismatched one after the normalized energy level of about 86%. This

energy threshold is approximately 90%, 70% and 92% at the aspect angles 80°, 100° and 170°, respectively. Consequently, the target SH₁ is correctly identified in all these examples except the 170° case for which the result has a little ambiguity. It should be noted that in some cases, the matched energy curve may lead the mismatched one for a wide range of high energy levels but may fail to do so for a very narrow energy range just before the maximum (unity) energy level. Such situations are basically due to either partial natural response annihilation or noisy variations at the very tail of the impulse response data which may be coming from measurements or caused by the numerical data processing used to obtain the time domain data from the original frequency domain measurement data. An example of this situation occurs in Figure 5.28, i.e., at the 100°/VP combination where the mismatched energy curve leads the matched one very slightly after 96% energy level but does not cause an incorrect identification since the matched energy curve leads to a mismatched one very dominantly in the energy range from 70% to 96%. Next, the model ship SH₂ is used as the unknown target of the identification examples (for the practically noise-free case) demonstrated in Figures 5.30 through 5.37 at the backscattered aspect angles of 0°, 30°, 45°, 60°, 80°, 90°, 100° and 180°, respectively at vertical polarization. In all these figures, the matched normalized energy response leads the mismatched one not only at high energy levels but even at mid-energy levels. Therefore, the target, SH₂, can be identified correctly in all cases.

Finally, the noise performance of the target identification scheme is tested in several cases where the SNR of the impulse response is

decreased by adding random Gaussian noise to the real and imaginary parts of the corresponding frequency domain data independently. The unknown target of the following example is the model ship, SH₁, at 30°/VP combination; parts (a), (b) and (c) of Figure 5.38 show the matched and mismatched response energy curves of this target for 15 dB, 10 dB and 5 dB signal-to-noise ratio levels, respectively. (A similar plot for the noise-free case is given in Figure 5.25.) The phase and amplitude plots of the noisy frequency domain data is shown in part (d) of the same figure for SNR=5 dB. As the SNR decreases, identification results deteriorate very slowly and even at 5 dB noise level the target, SH₁, can be identified correctly. In part (c) of this figure, the matched energy curve starts lagging the mismatched one very slightly after about 0.75 ns since the K-pulse of the target cannot annihilate the random variations caused by added noise which determine the late-time behavior of the resultant noisy impulse response after the actual signal components die out.

Table 5.1

Poles of the Model Ship SH₁
 Extracted from the K-pulse Shown in Figure 5.1

10^9 Nepers/s, GHz Scale	sL/c Scale
-0.316 ± j 3.148	-0.605 ± j 6.029
-0.397 ± j 4.040	-0.760 ± j 7.737
-0.576 ± j 5.611	-1.103 ± j10.746
-0.518 ± j 6.743	-0.992 ± j12.914
-0.551 ± j 8.220	-1.055 ± j15.742

Table 5.2

Legendre Polynomial Expansion Coefficients
for the Continuous Part of the K-pulse shown in Figure 5.12

<u>Order (m)</u>	<u>D_m</u>
0	1.0852
1	-2.6250
2	0.7580
3	0.9085
4	-1.4577
5	5.6933
6	-6.6951
7	2.8000
8	0.1344
9	0.1040

Table 5.3

Poles of the Model Ship SH₂ Extracted from
the K-pulse Shown in Figure 5.12

<u>10⁹ Nepers/s, GHz Scale</u>	<u>in sL/c Scale</u>
-0.486 ± j 2.930	-1.034 ± j 6.235
-0.507 ± j 3.627	-1.079 ± j 7.718
-0.529 ± j 4.318	-1.126 ± j 9.188
-0.577 ± j 5.323	-1.228 ± j 11.327
-0.612 ± j 6.349	-1.302 ± j 13.510
-0.639 ± j 7.368	-1.360 ± j 15.678

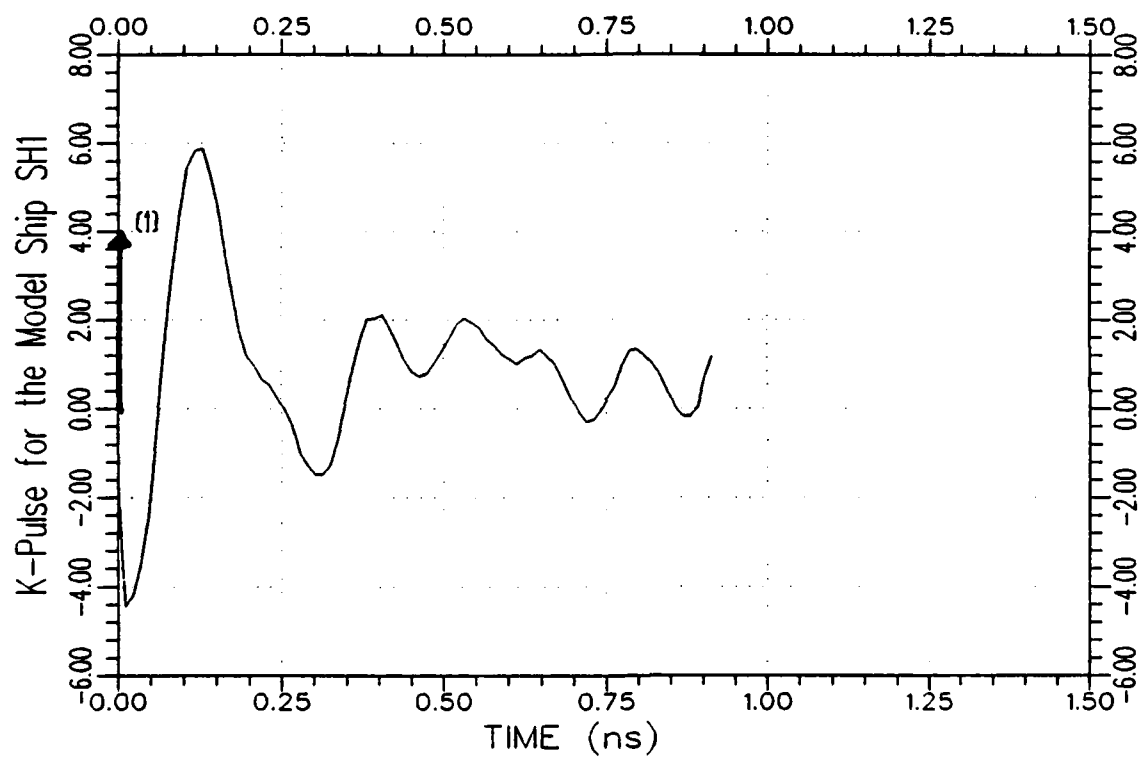
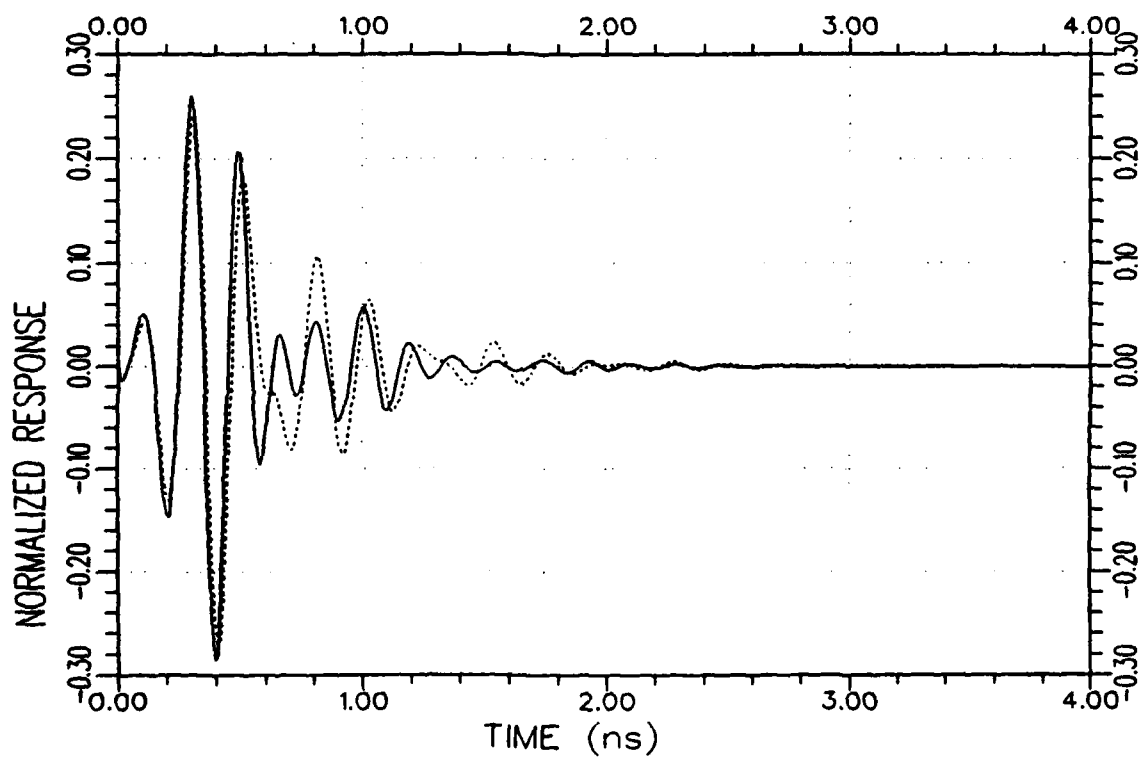
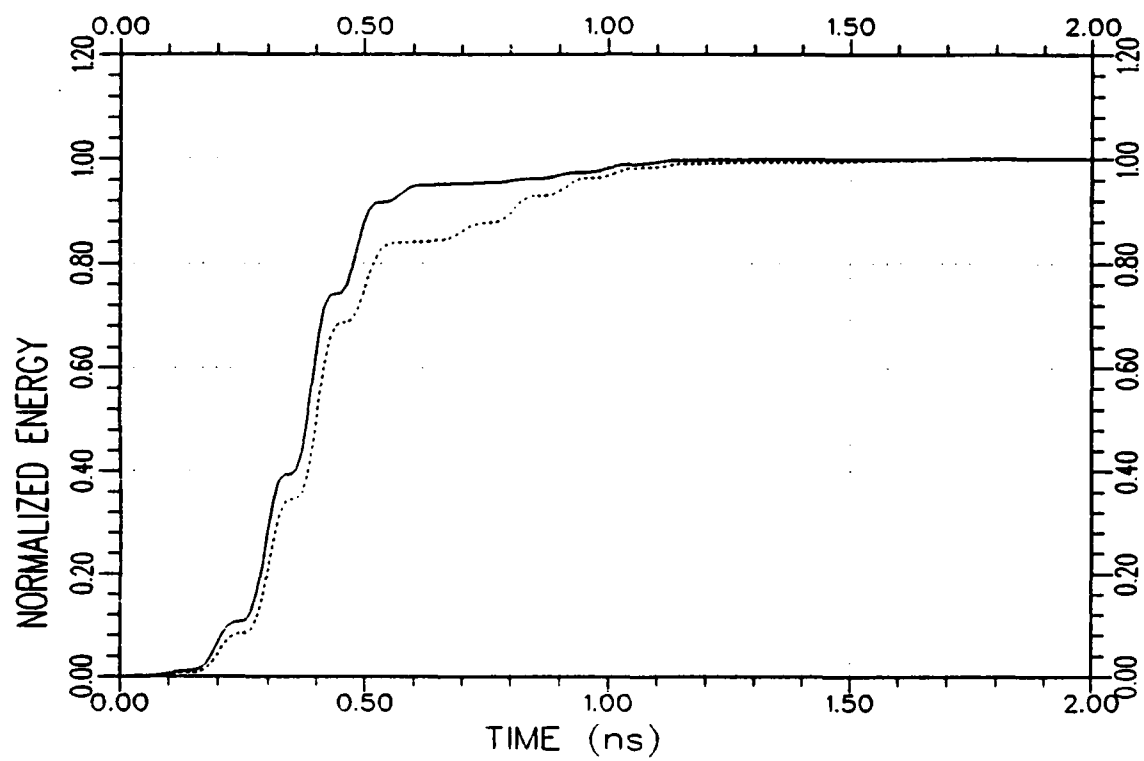


Figure 5.1. An approximate K-pulse waveform of the model ship SH₁ estimated from the measured backscattered data at 0°/VP and 80°/VP using a discrete representation for the continuous part of the K-pulse. (The $\delta(t)$ term of the K-pulse is symbolically shown by the arrow at $t=0$.)



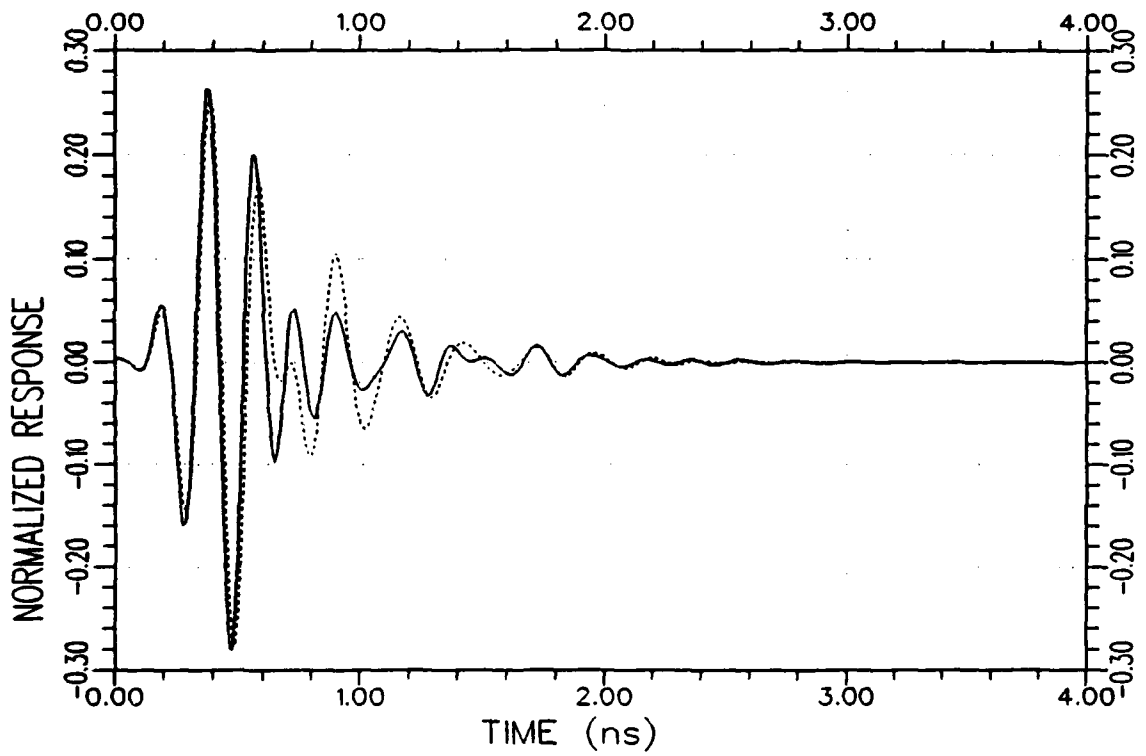
(a) Response waveforms

Figure 5.2. Normalized impulse response (.....) and K-pulse response (——) waveforms and their energy curves for the target SH_1 at $0^\circ/VP$.



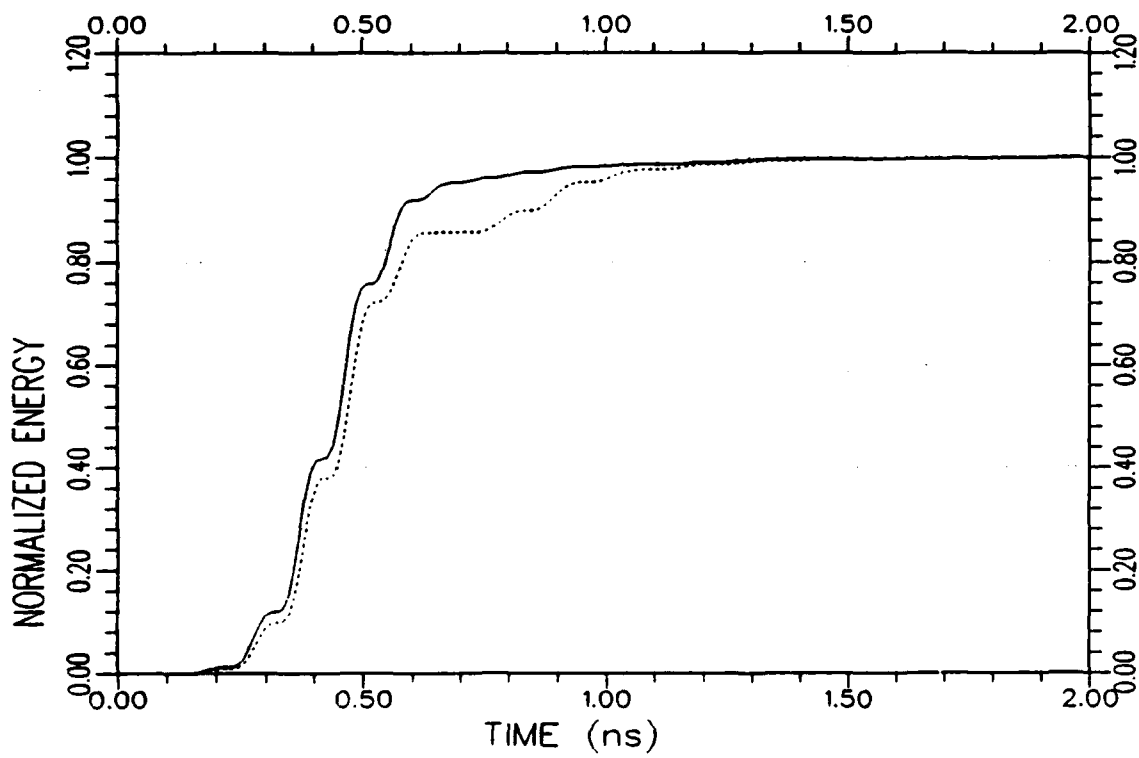
(b) Response energy curves

Figure 5.2. Continued.



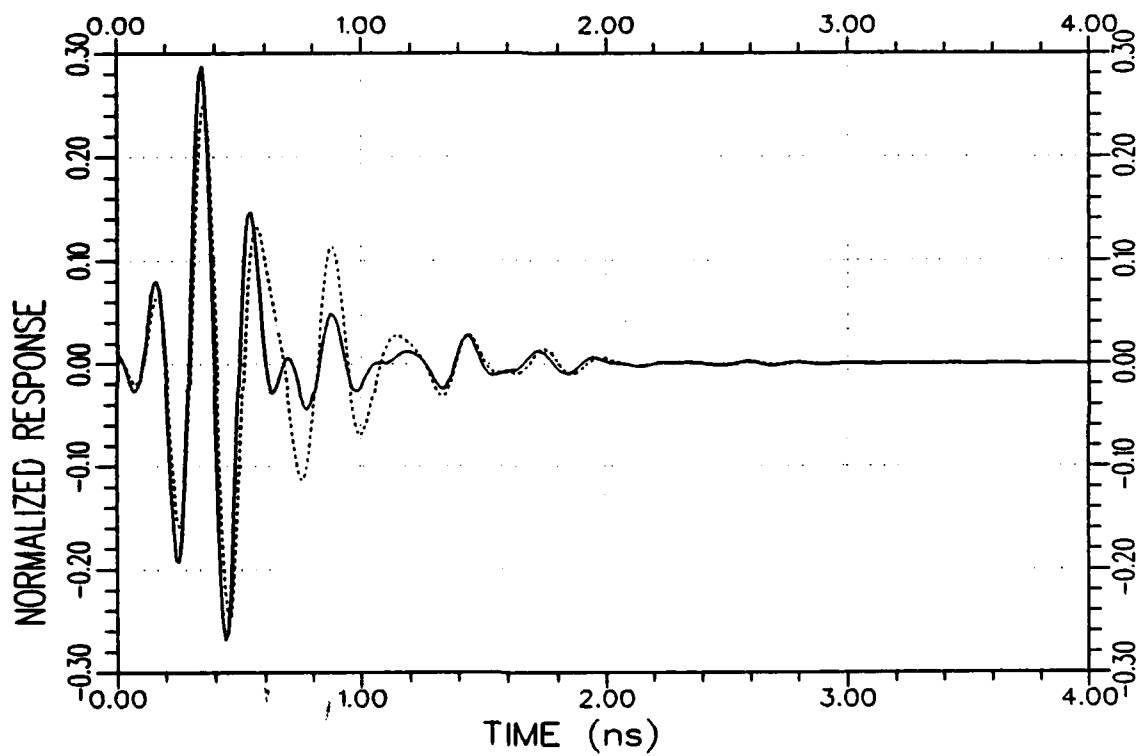
(a) Response waveforms

Figure 5.3. Normalized impulse response (.....) and K-pulse response (—) waveforms and their energy curves for the target SH_1 at $15^\circ/VP$.



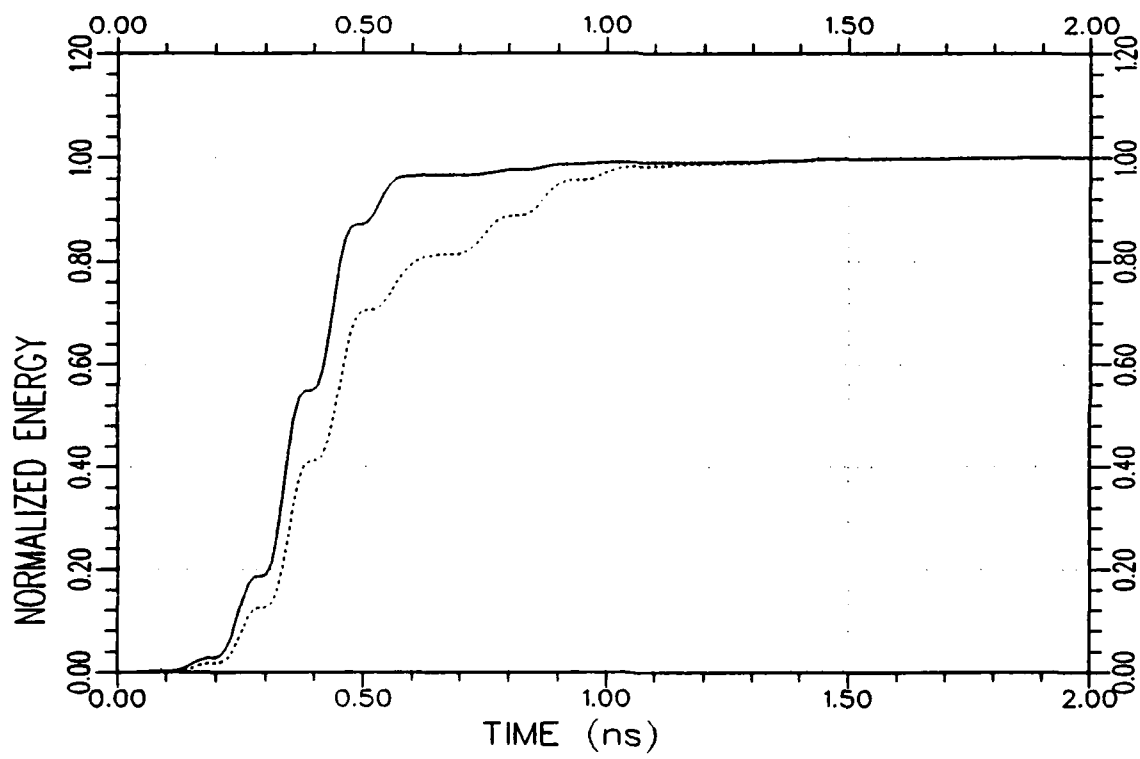
(b) Response energy curves

Figure 5.3. Continued.



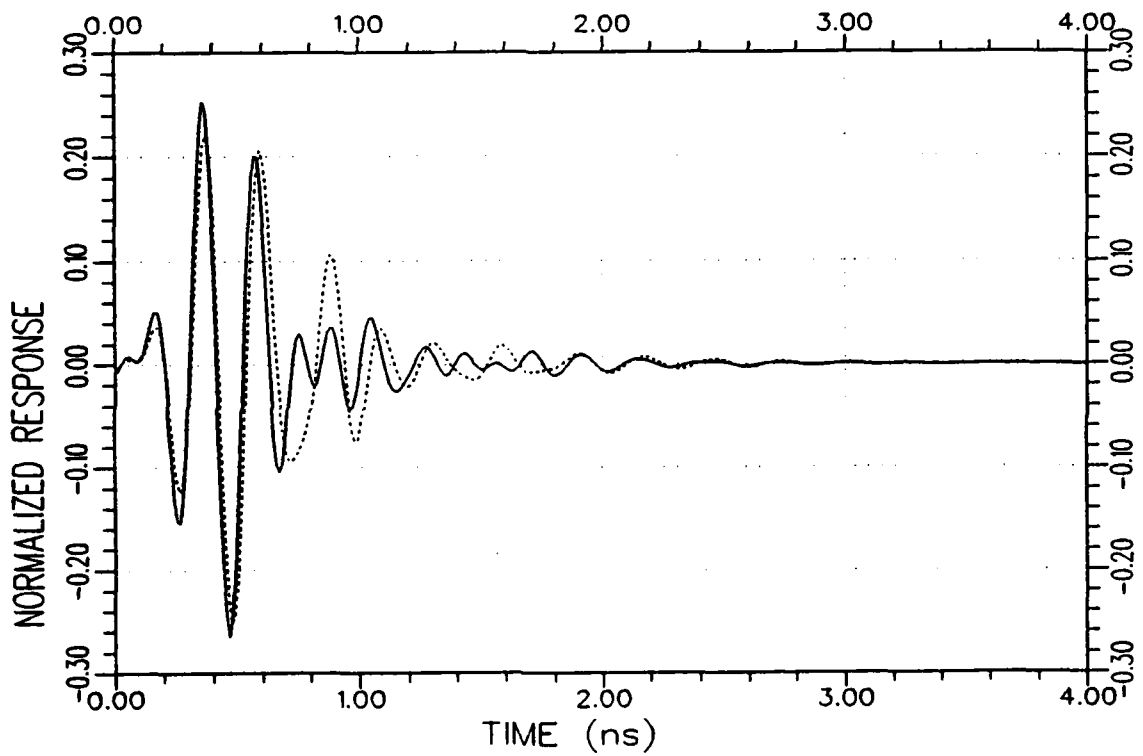
(a) Response waveforms

Figure 5.4. Normalized impulse response (.....) and K-pulse response (—) waveforms and their energy curves for the target SH_1 at $30^\circ/VP$.



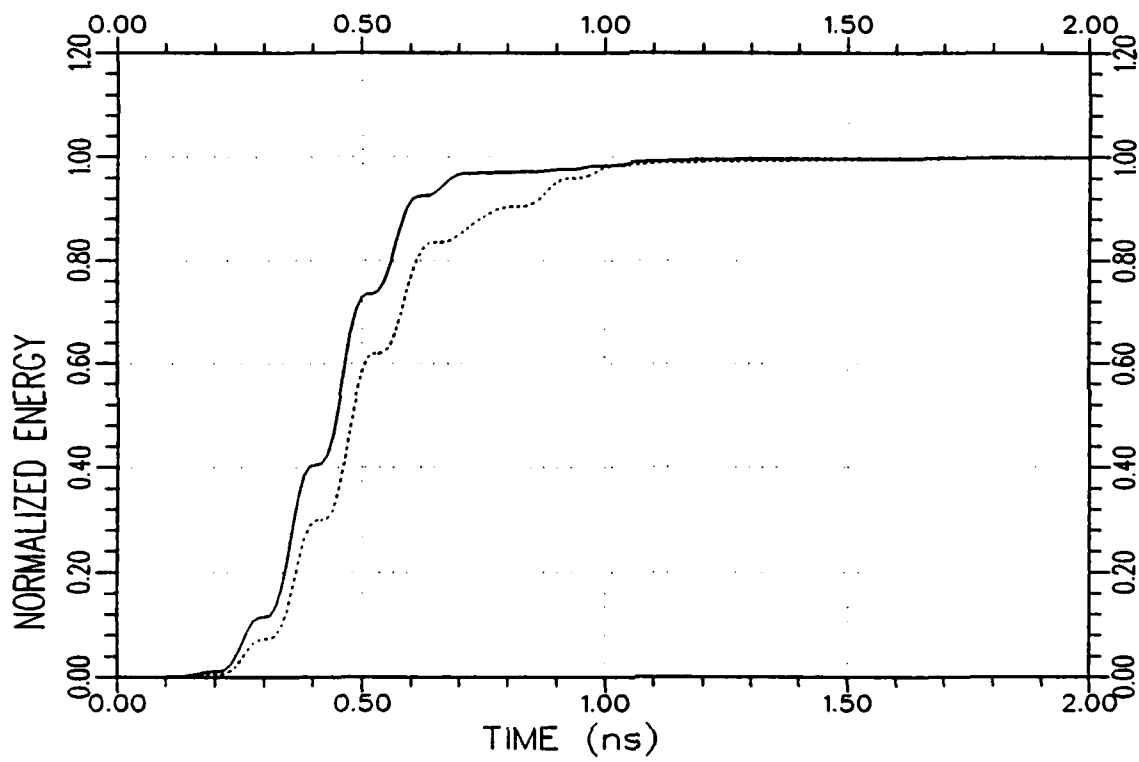
(b) Response energy curves

Figure 5.4 Continued.



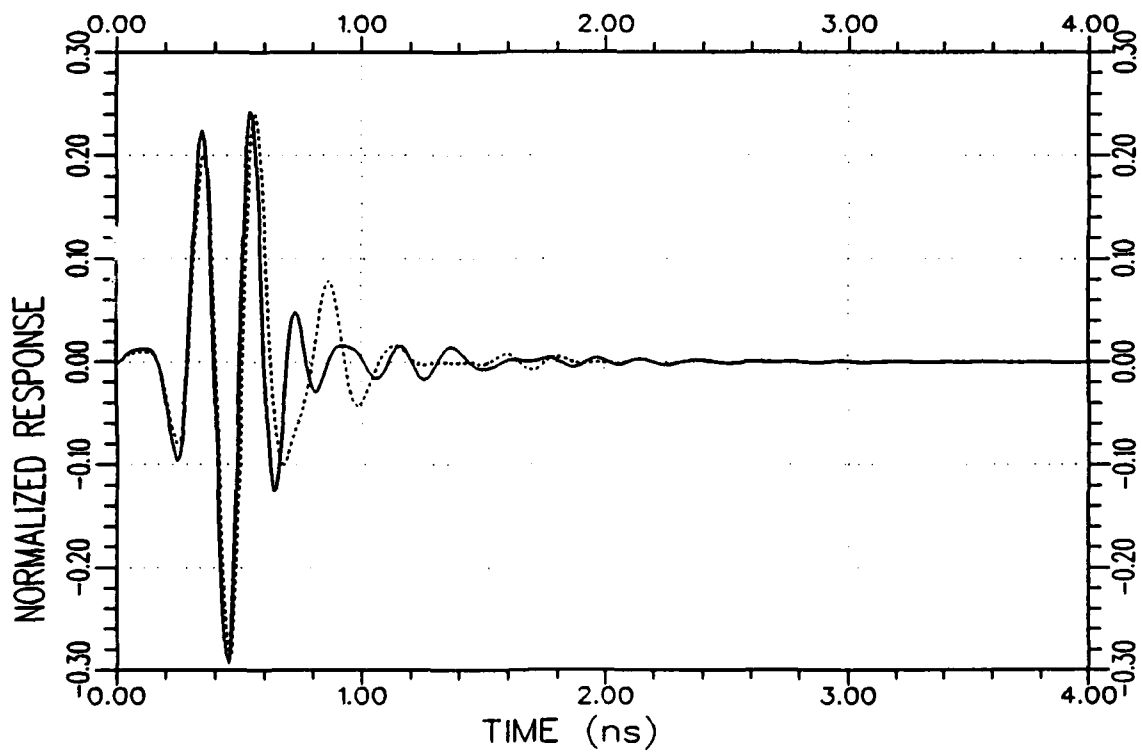
(a) Response waveforms

Figure 5.5. Normalized impulse response (.....) and K-pulse response (—) waveforms and their energy curves for the target SH_1 at $45^\circ/VP$.



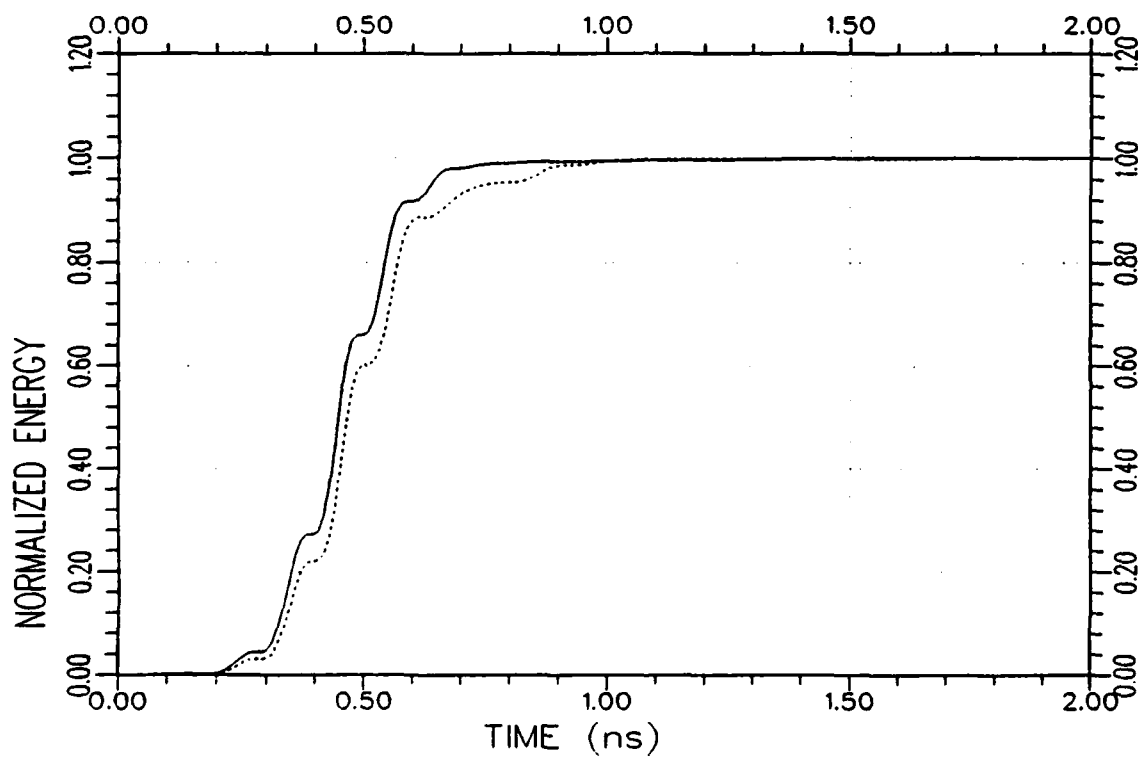
(b) Response energy curves

Figure 5.5. Continued.



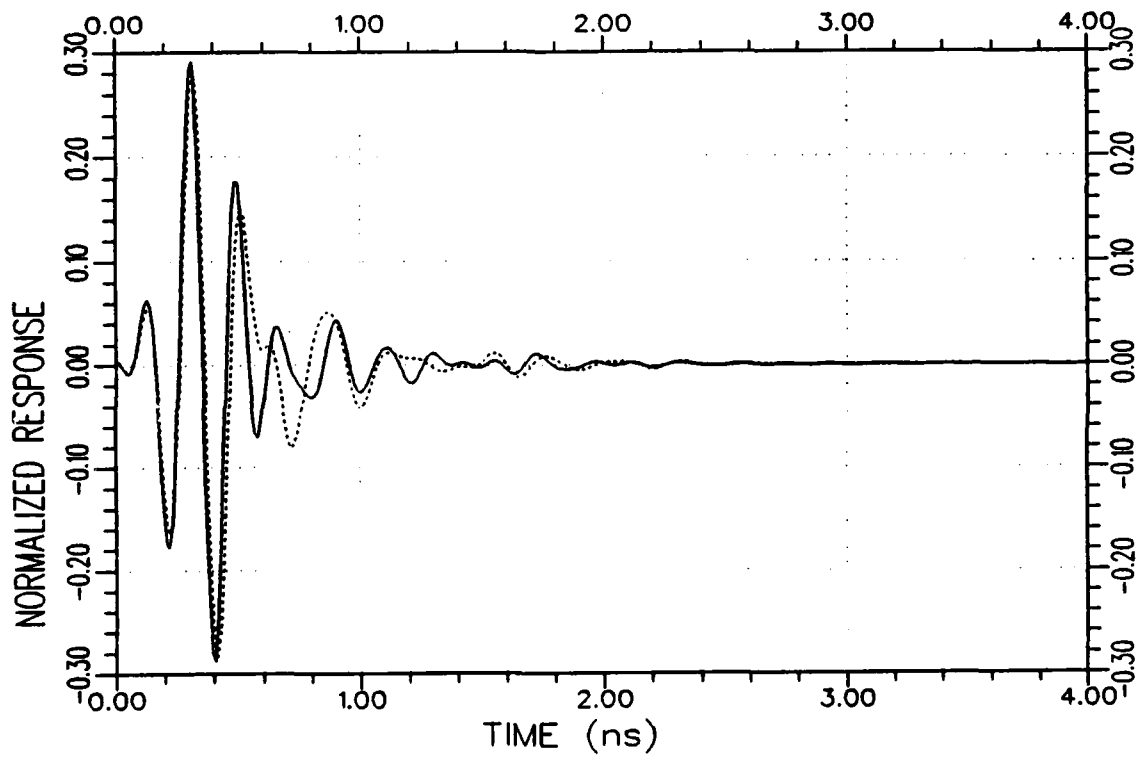
(a) Response waveforms

Figure 5.6. Normalized impulse response (.....) and K-pulse response (——) waveforms and their energy curves for the target SH_1 at $60^\circ/VP$.



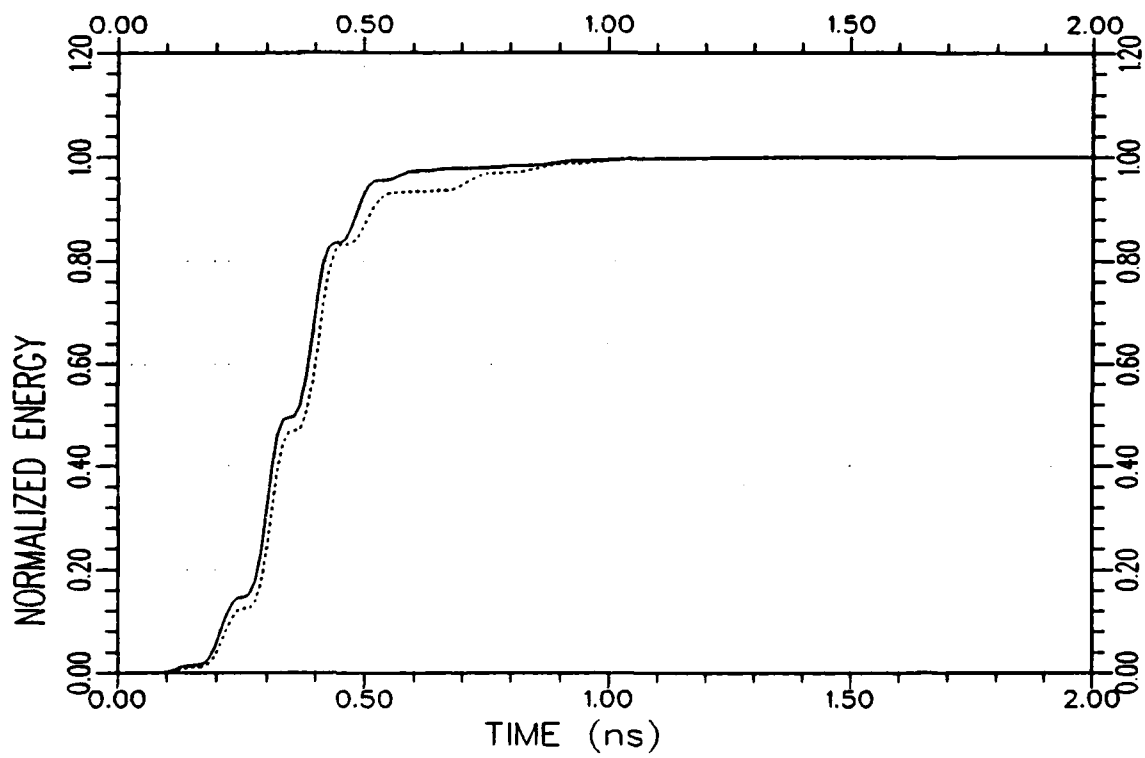
(b) Response energy curves

Figure 5.6. Continued.



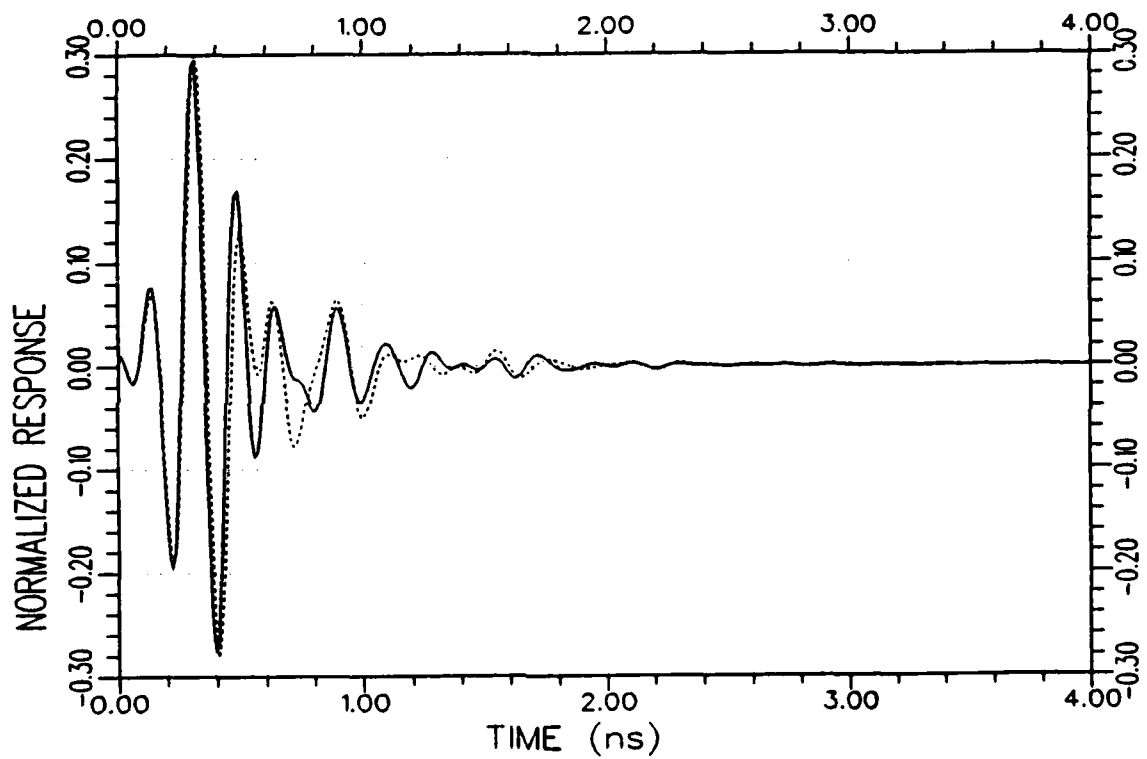
(a) Response waveforms

Figure 5.7. Normalized impulse response (.....) and K-pulse response (—) waveforms and their energy curves for the target SH_1 at $80^\circ/VP$.



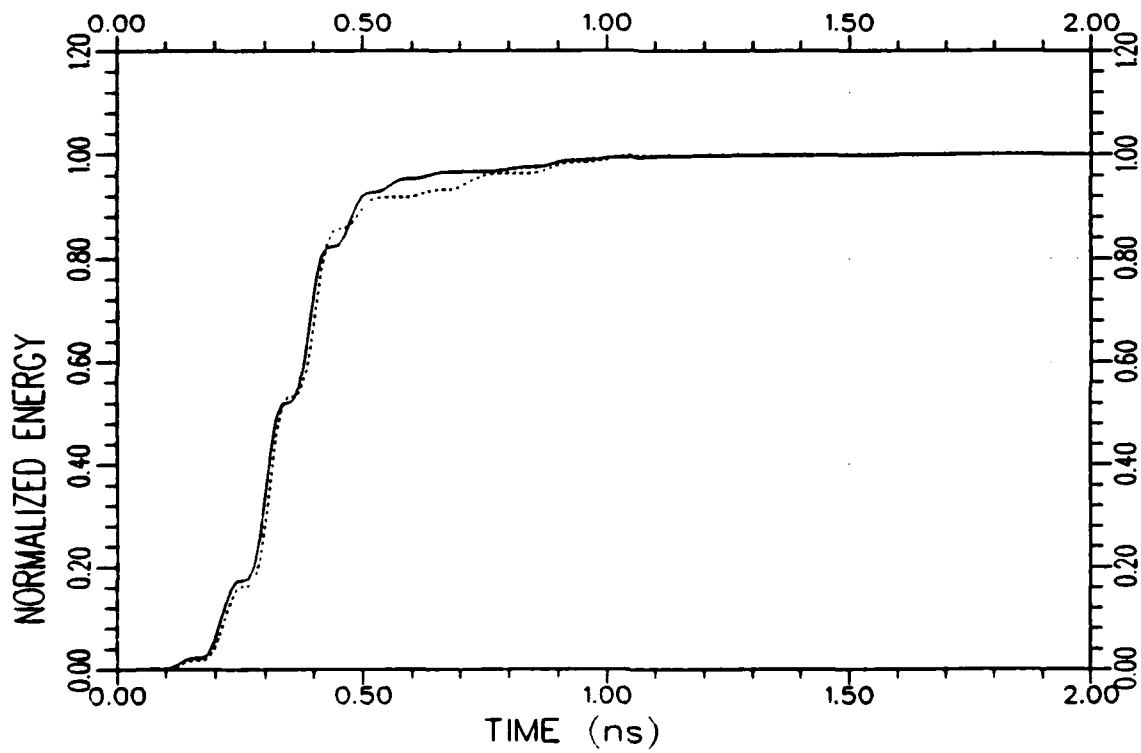
(b) Response energy curves

Figure 5.7. Continued.



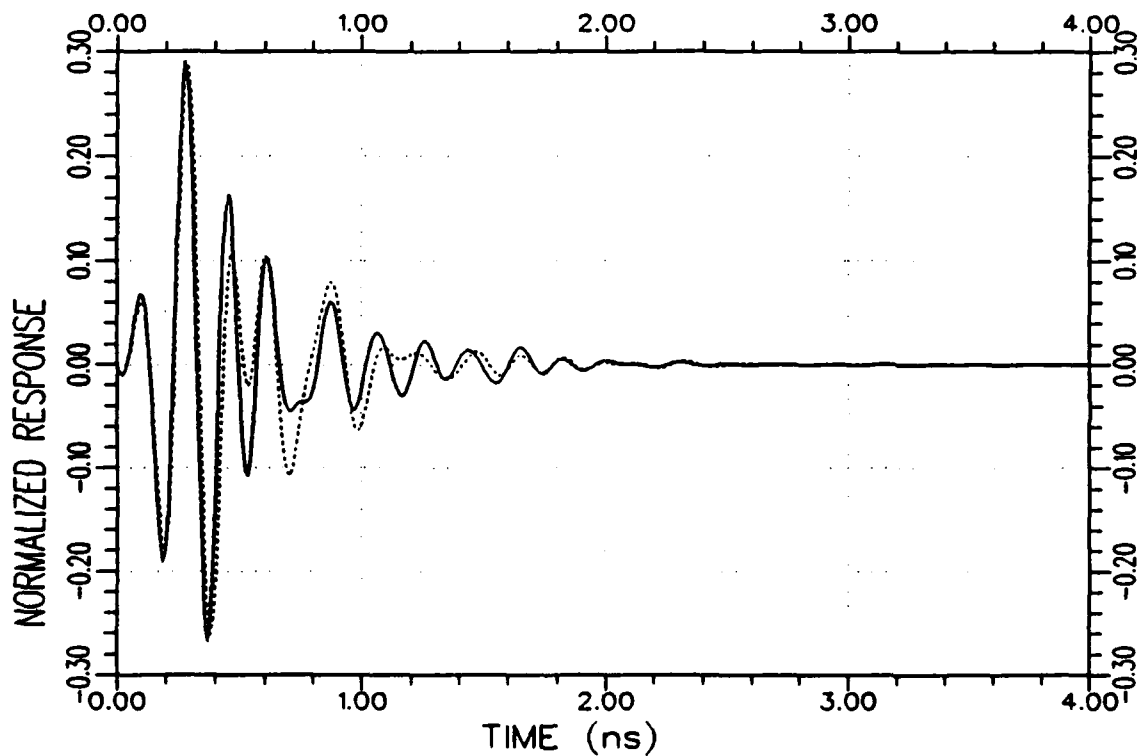
(a) Response waveforms

Figure 5.8. Normalized impulse response (.....) and K-pulse response (—) waveforms and their energy curves for the target SH_1 at $90^\circ/VP$.



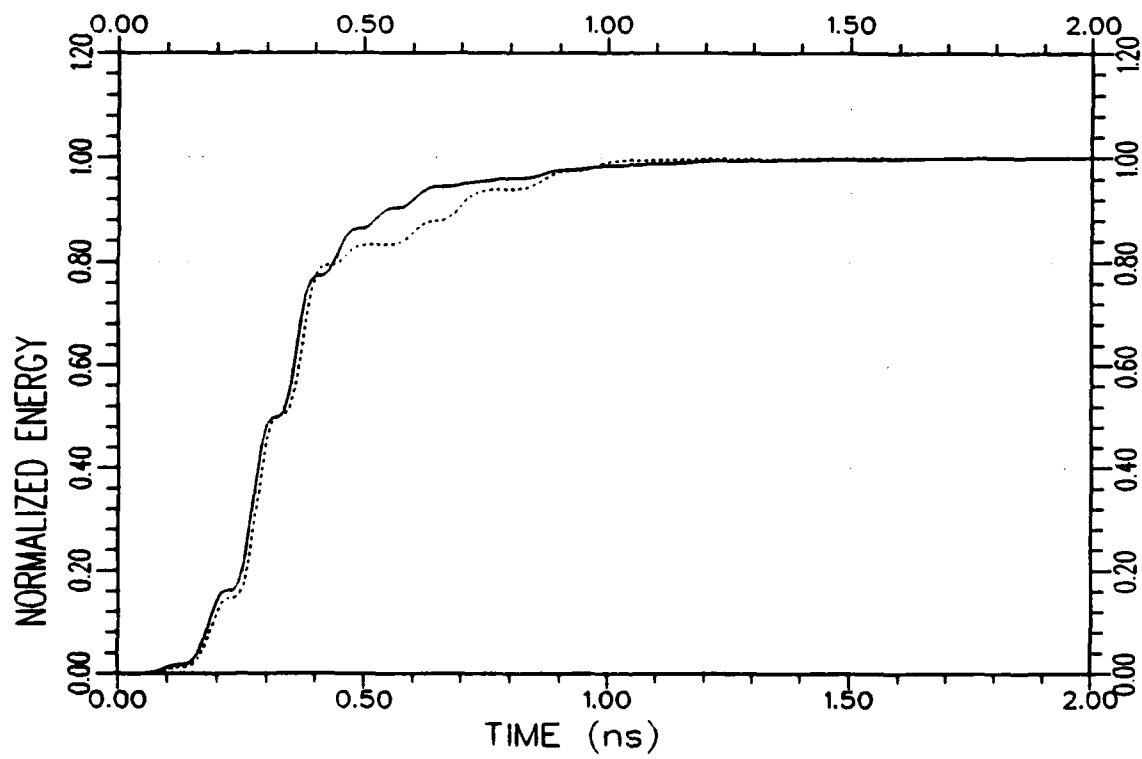
(b) Response energy curves

Figure 5.8. Continued.



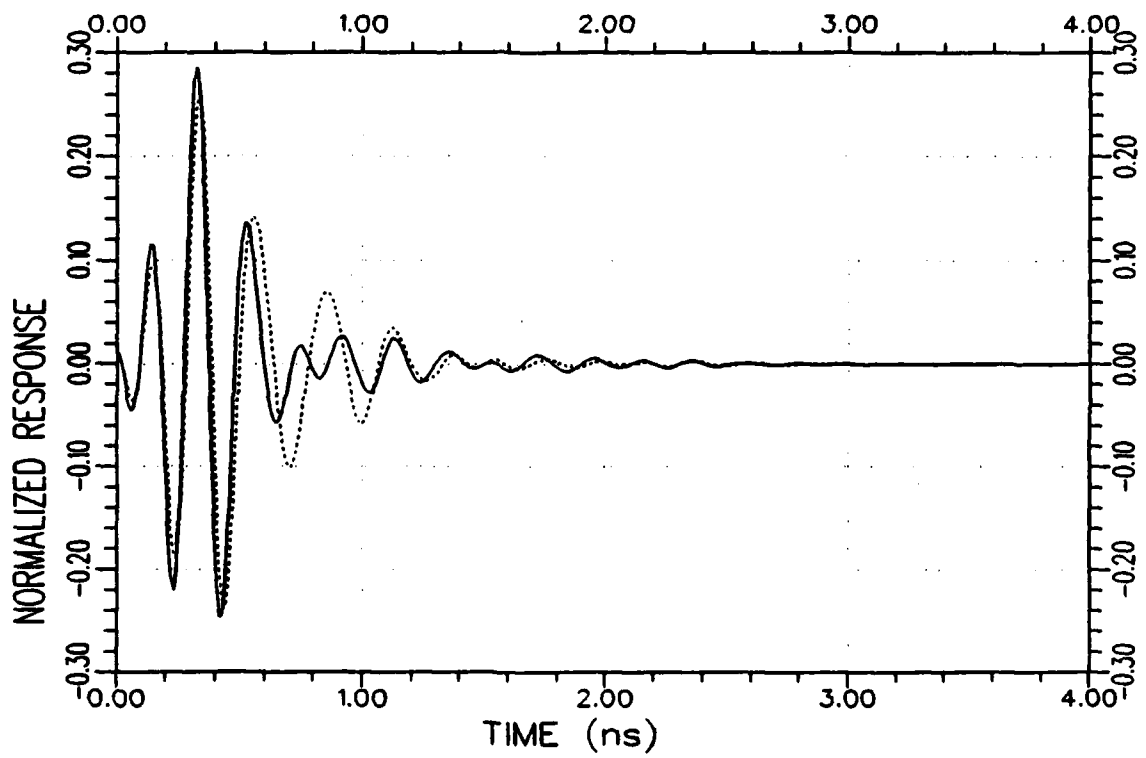
(a) Response waveforms

Figure 5.9. Normalized impulse response (.....) and K-pulse response (——) waveforms and their energy curves for the target SH_1 at $100^\circ/VP$.



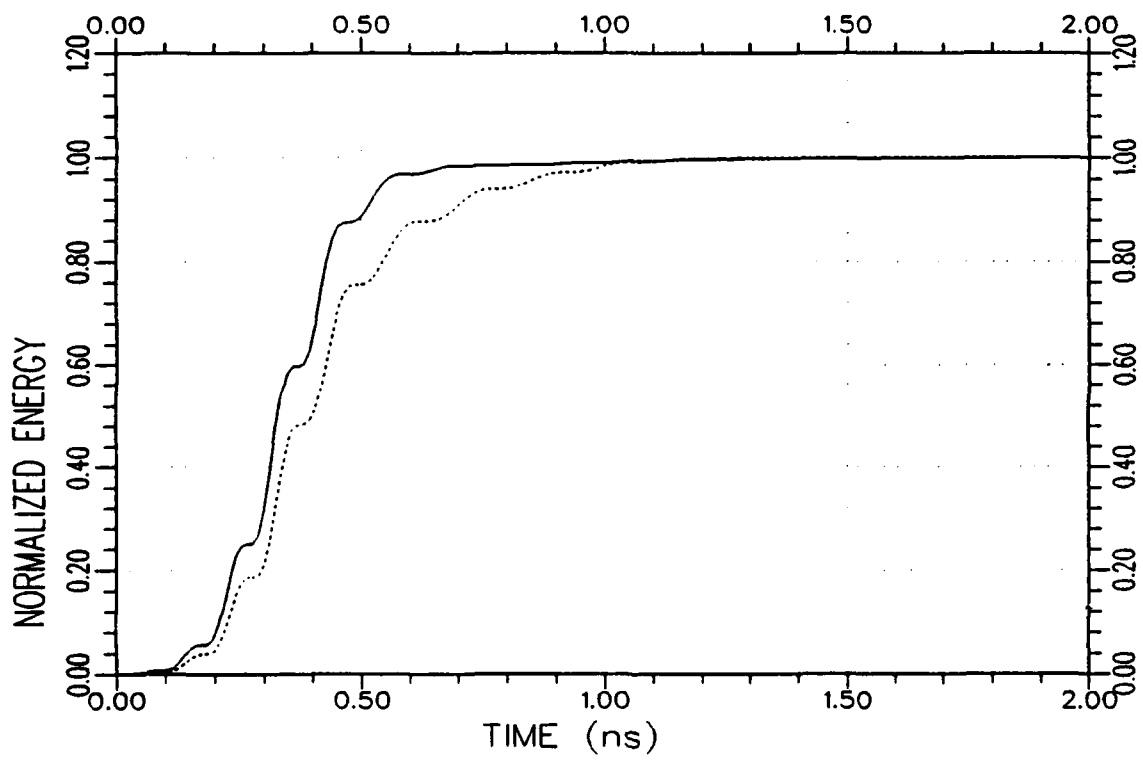
(b) Response energy curves

Figure 5.9. Continued.



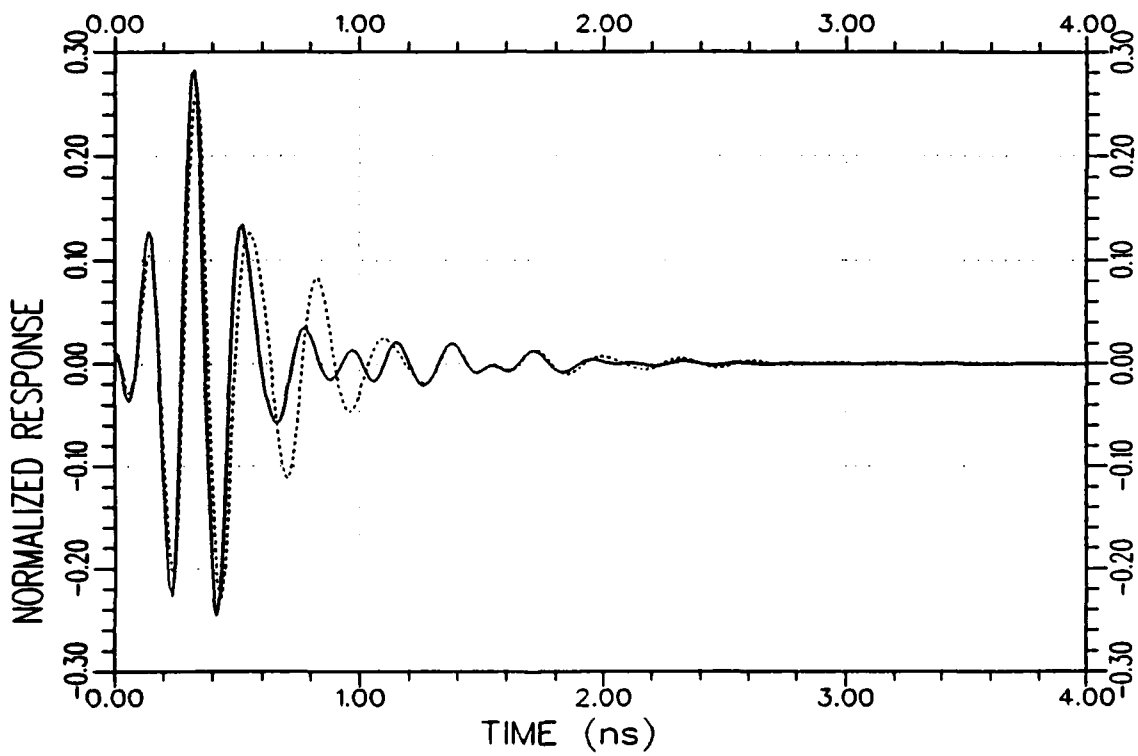
(a) Response waveforms

Figure 5.10. Normalized impulse response (.....) and K-pulse response (——) waveforms and their energy curves for the target SH_1 at $170^\circ/VP$.



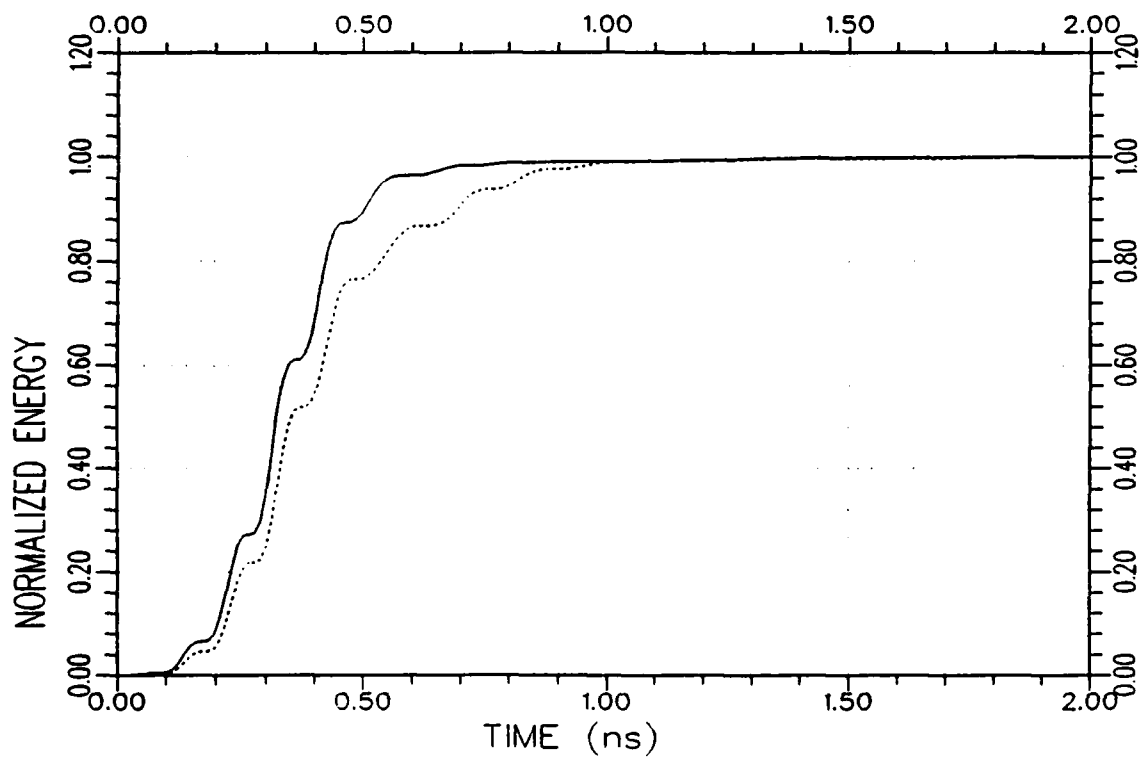
(b) Response energy curves

Figure 5.10. Continued.



(a) Response waveforms

Figure 5.11. Normalized impulse response (.....) and K-pulse response (—) waveforms and their energy curves for the target SH_1 at $180^\circ/VP$.



(b) Response energy curves

Figure 5.11. Continued.

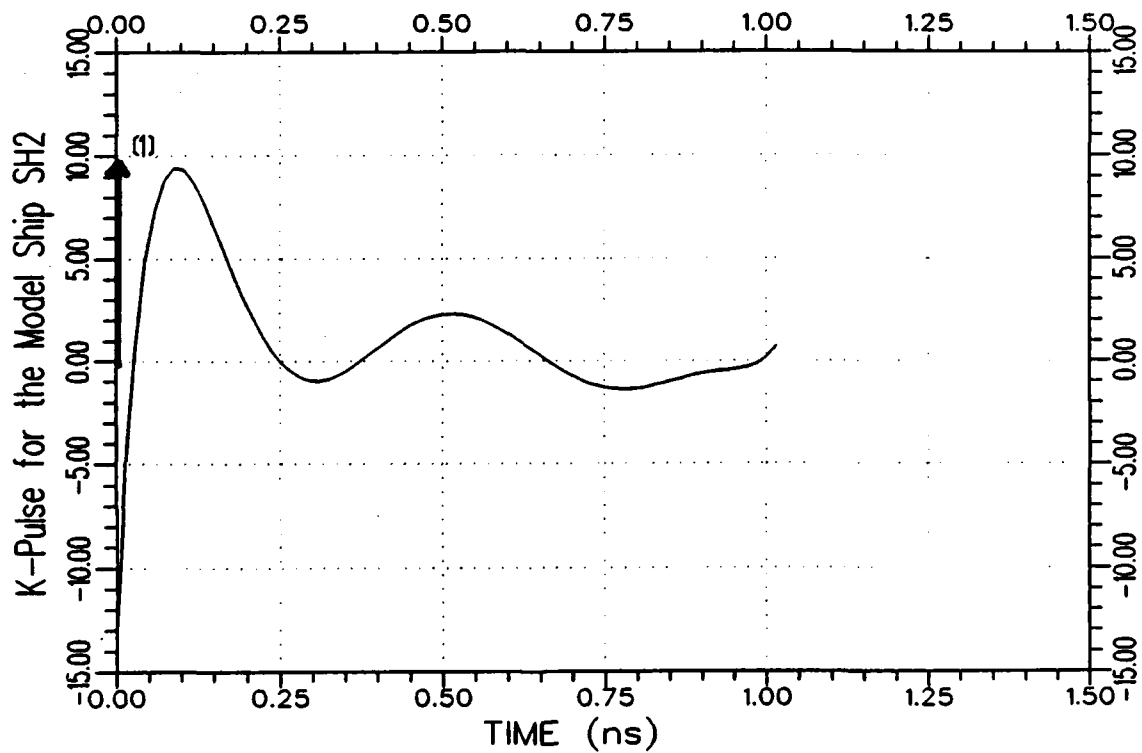
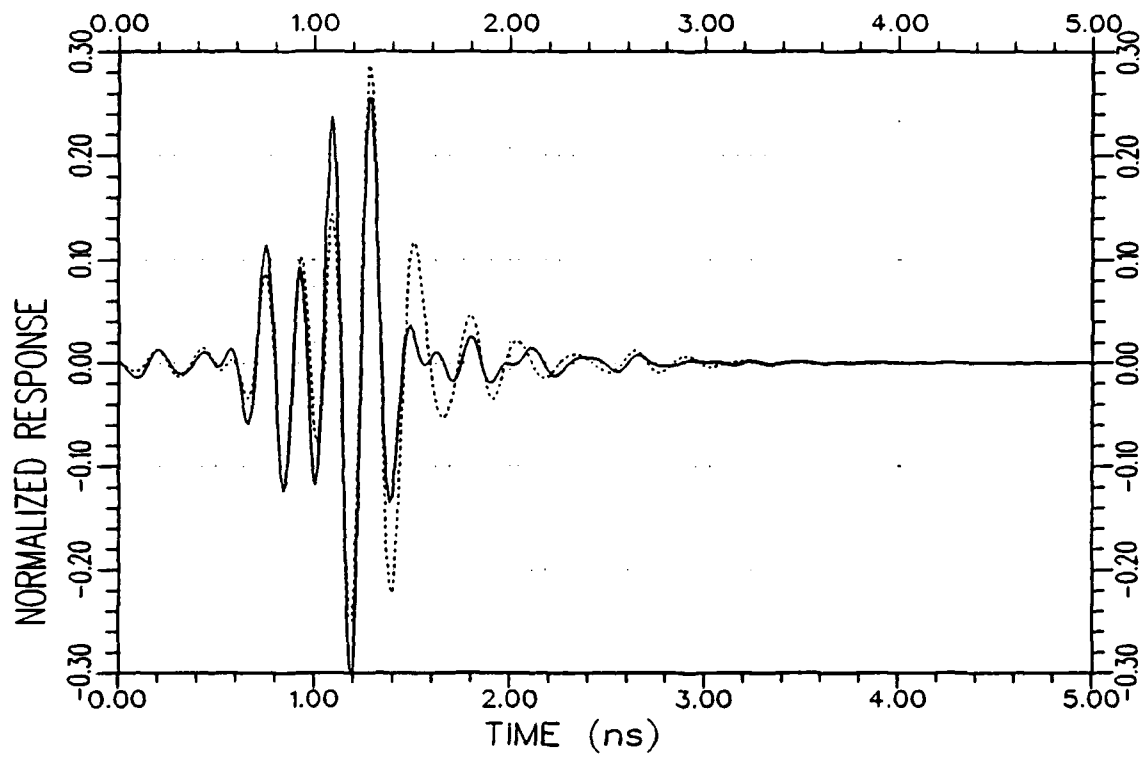
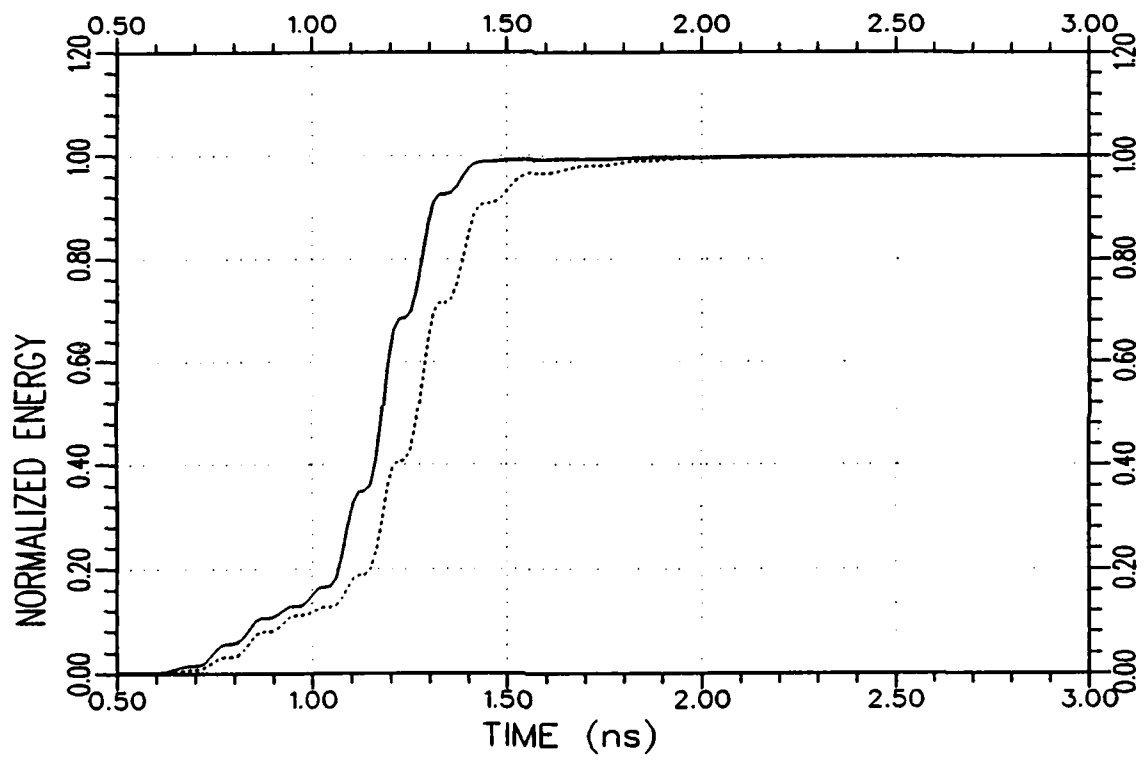


Figure 5.12. An approximate K-pulse waveform of the model ship SH₂ estimated from the measured backscattered data at 30°/VP and 100°/VP using a Legendre polynomial representation for the continuous part of the K-pulse. (The $\delta(t)$ term of the K-pulse is symbolically shown by the arrow at $t=0$.)



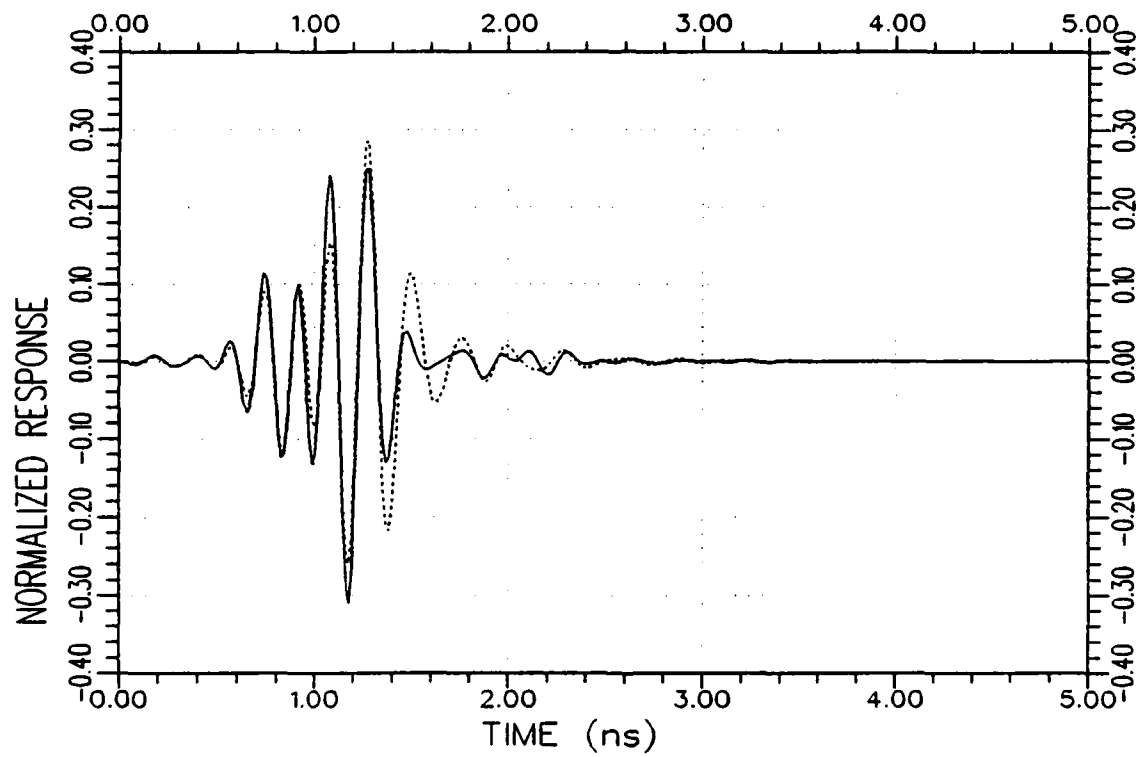
(a) Response waveforms

Figure 5.13. Normalized impulse response (.....) and K-pulse response (—) waveforms and their energy curves for the target SH_2 at $0^\circ/VP$.



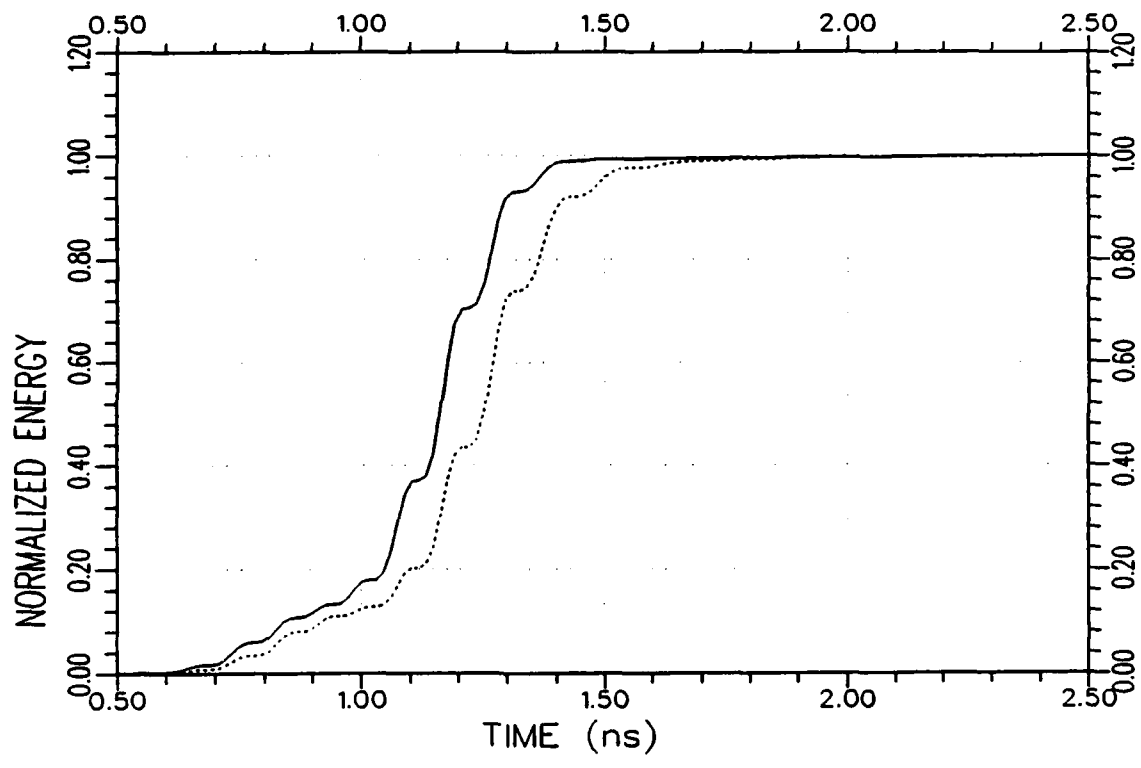
(b) Response energy curves

Figure 5.13. Continued.



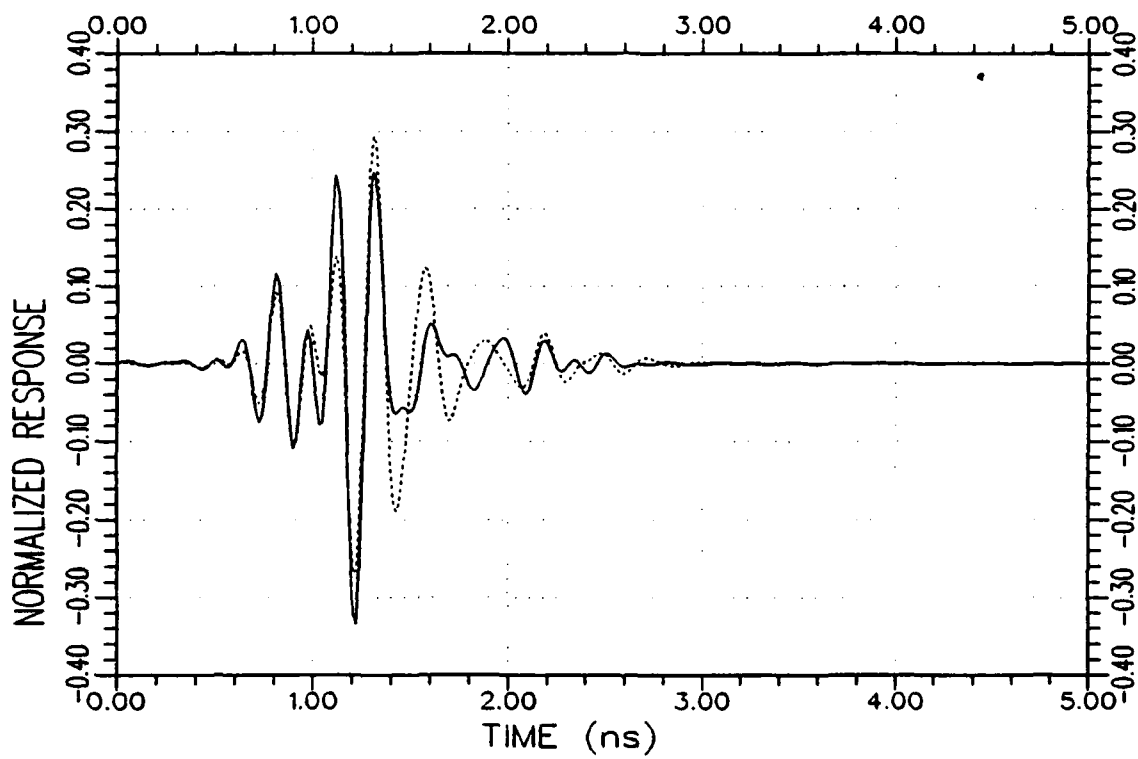
(a) Response waveforms

Figure 5.14. Normalized impulse response (.....) and K-pulse response (——) waveforms and their energy curves for the target SH_2 at $10^\circ/\text{VP}$.



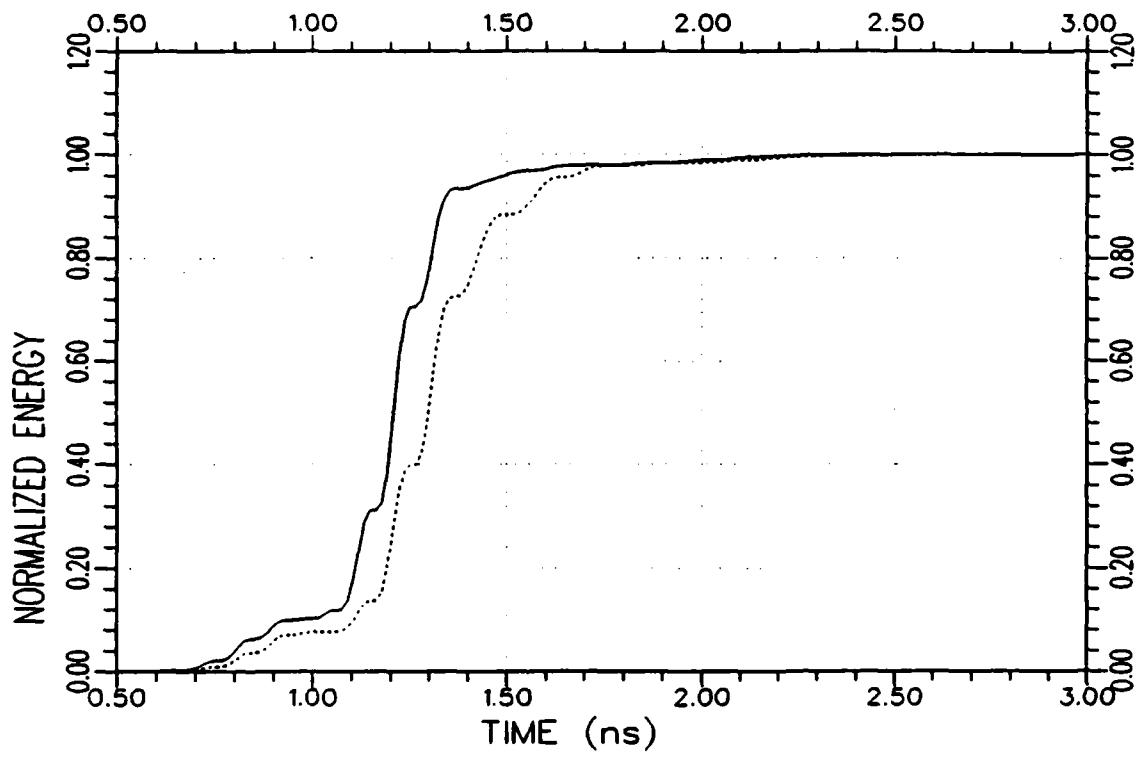
(b) Response energy curves

Figure 5.14. Continued.



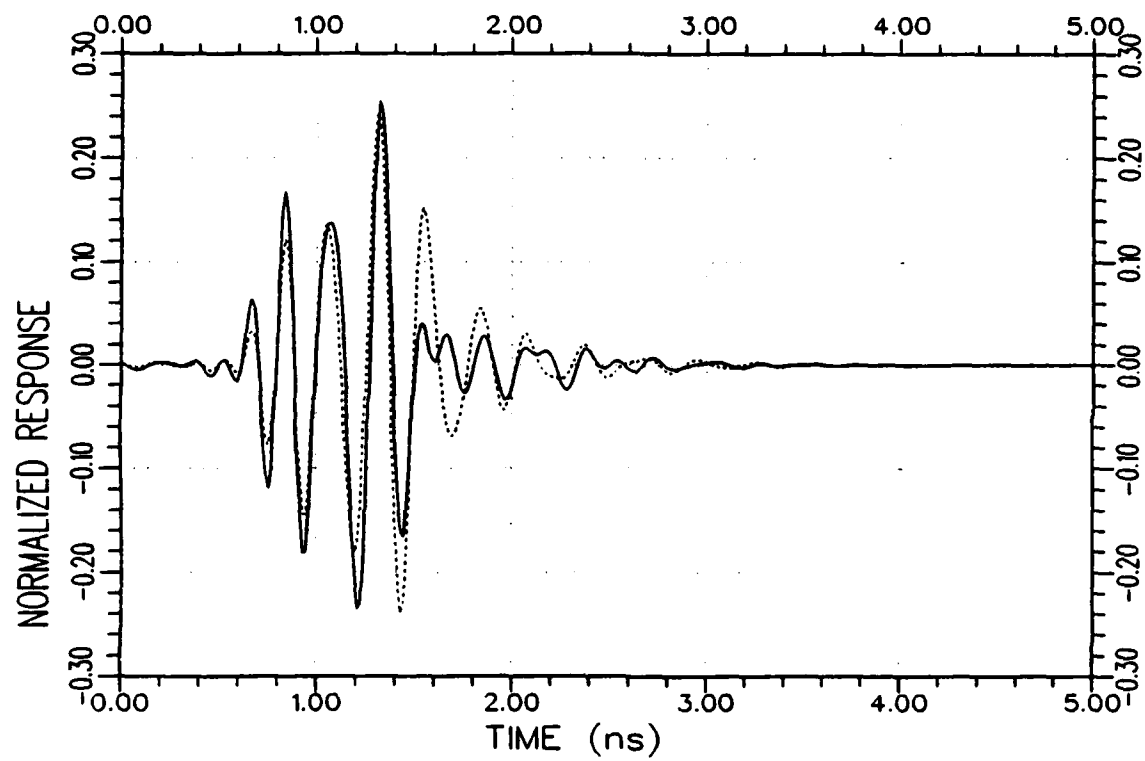
(a) Response waveforms

Figure 5.15. Normalized impulse response (.....) and K-pulse response (—) waveforms and their energy curves for the target SH_2 at $30^\circ/VP$.



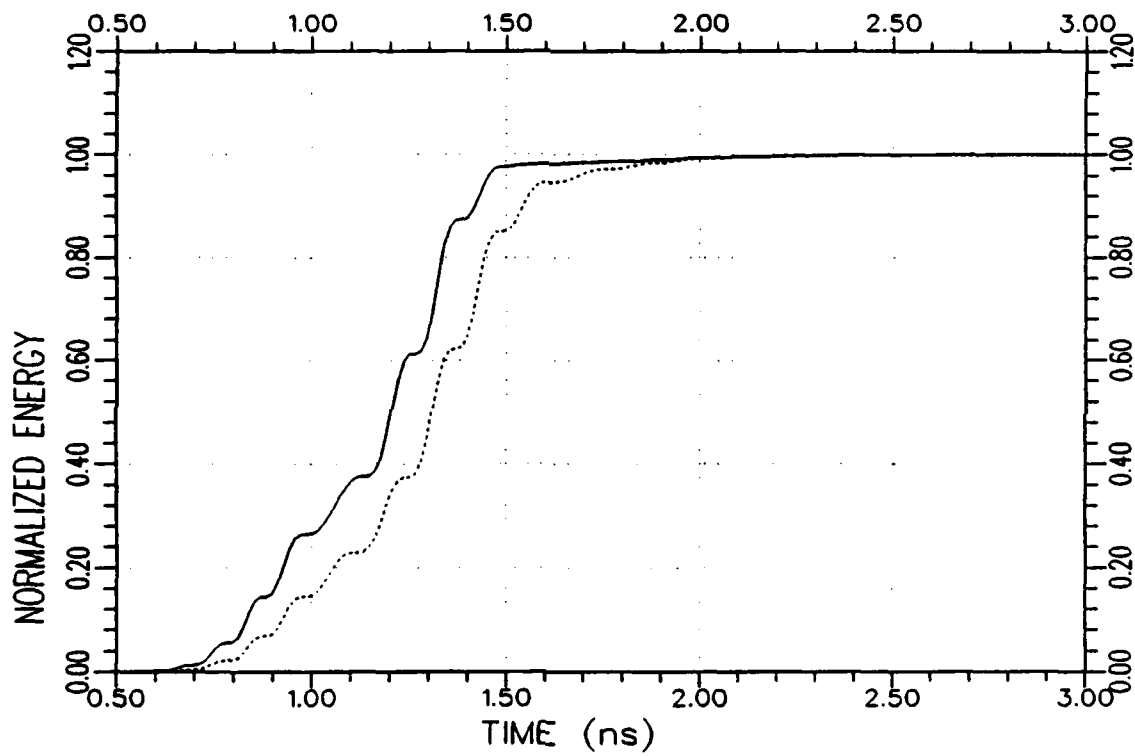
(b) Response energy curves

Figure 5.15. Continued.



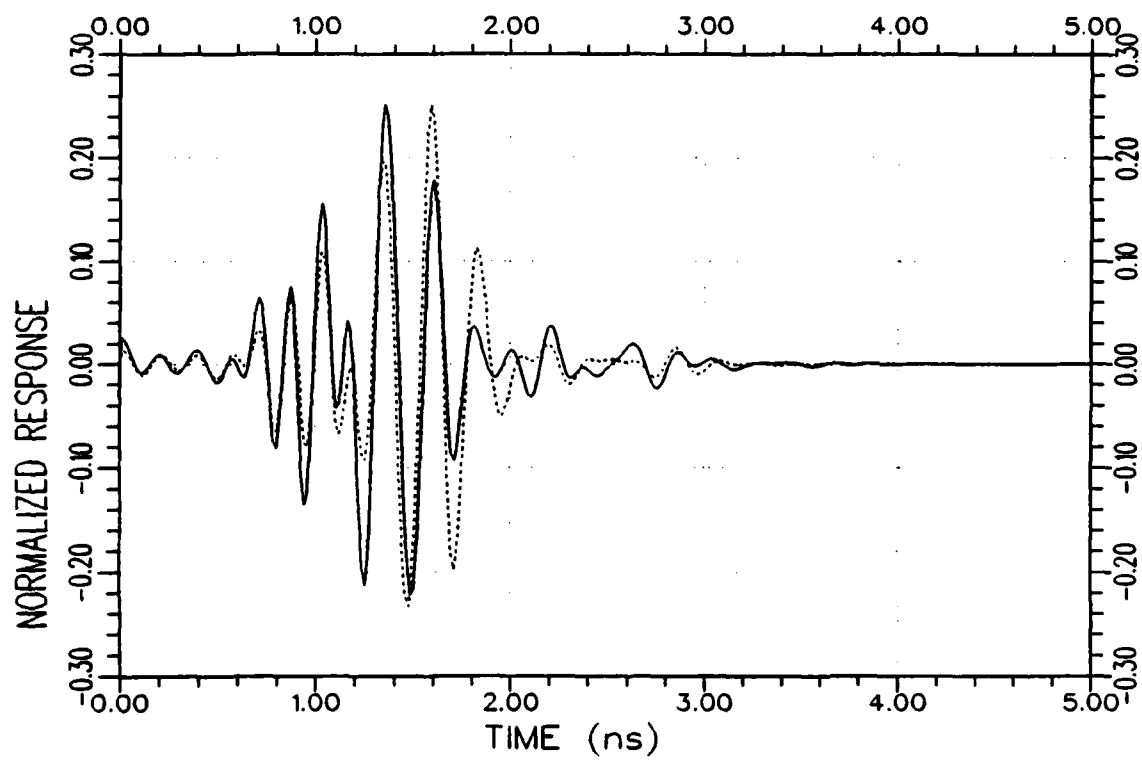
(a) Response waveforms

Figure 5.16. Normalized impulse response (.....) and K-pulse response (—) waveforms and their energy curves for the target SH_2 at $45^\circ/VP$.



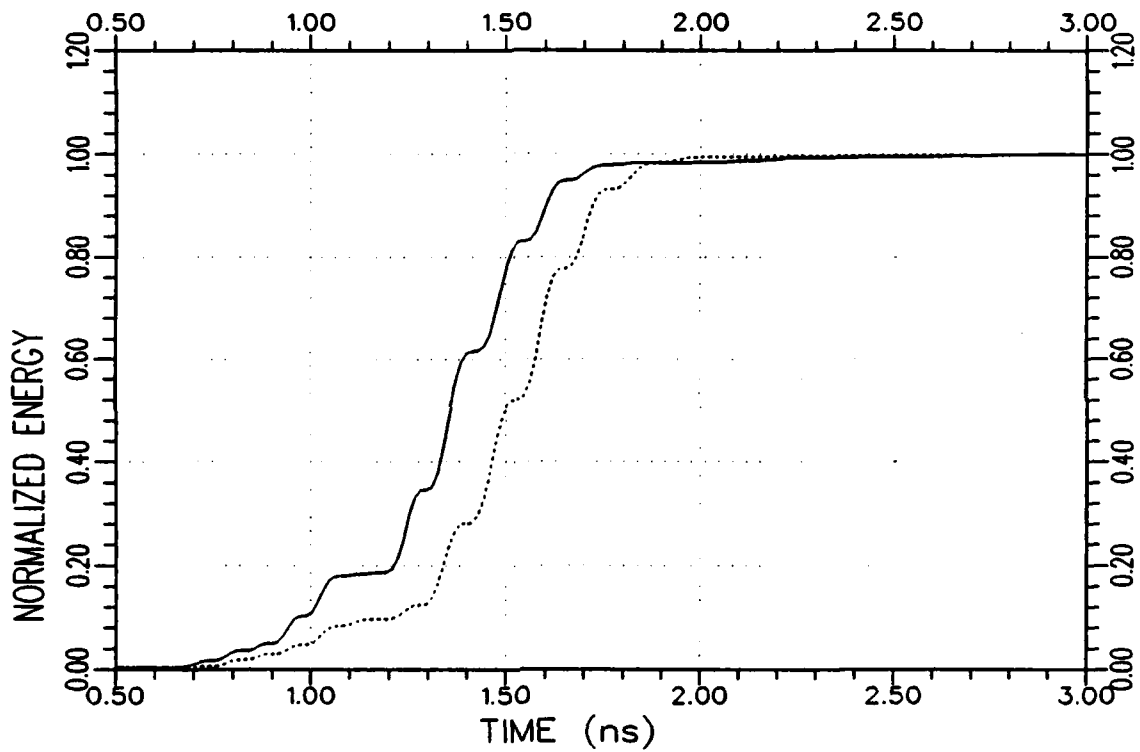
(b) Response energy curves

Figure 5.16. Continued.



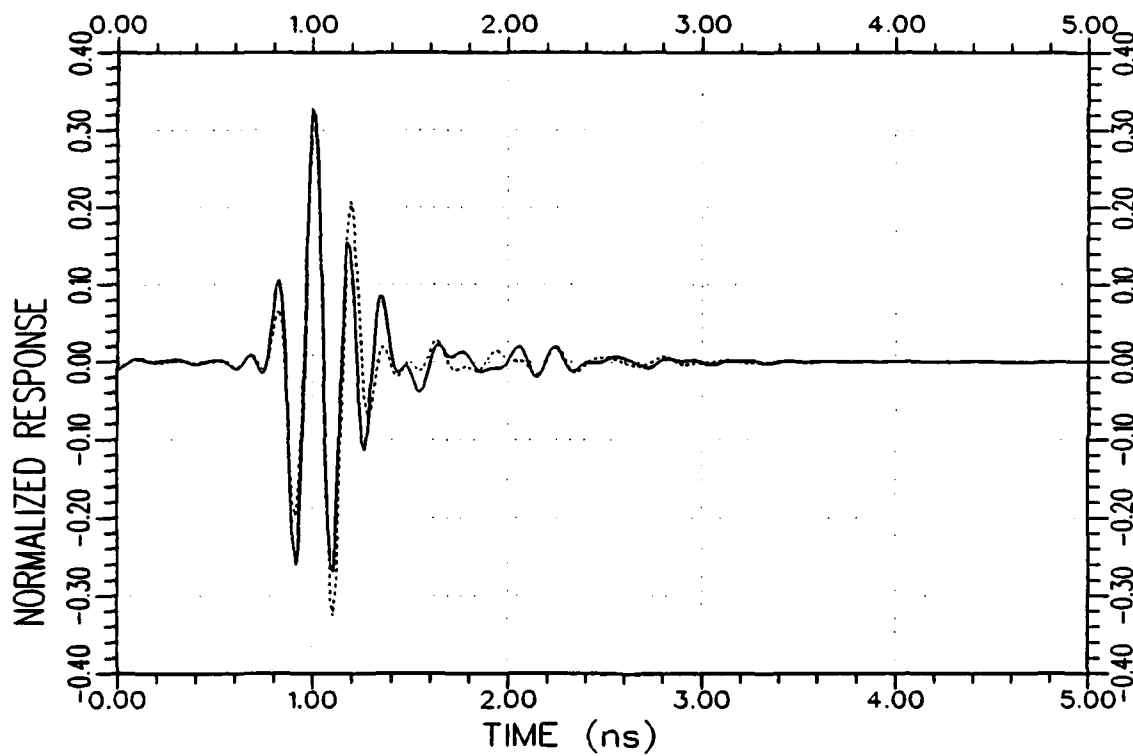
(a) Response waveforms

Figure 5.17. Normalized impulse response (.....) and K-pulse response (—) waveforms and their energy curves for the target SH_2 at $60^\circ/VP$.



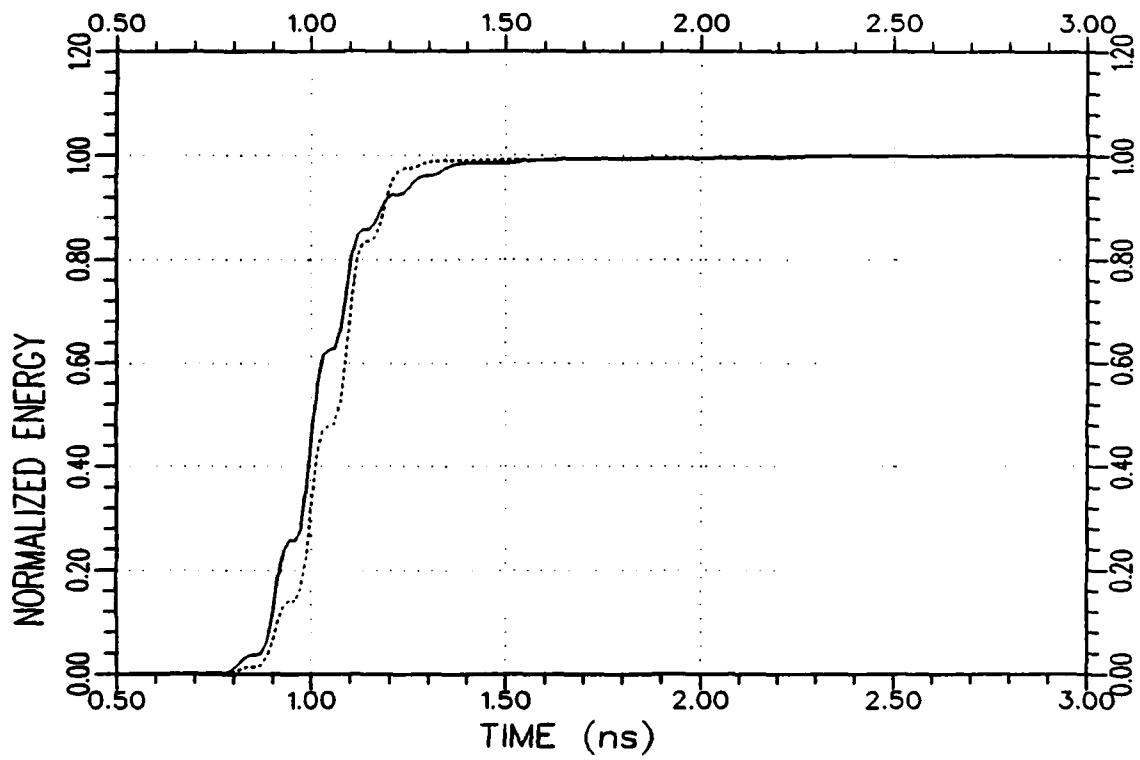
(b) Response energy curves

Figure 5.17. Continued.



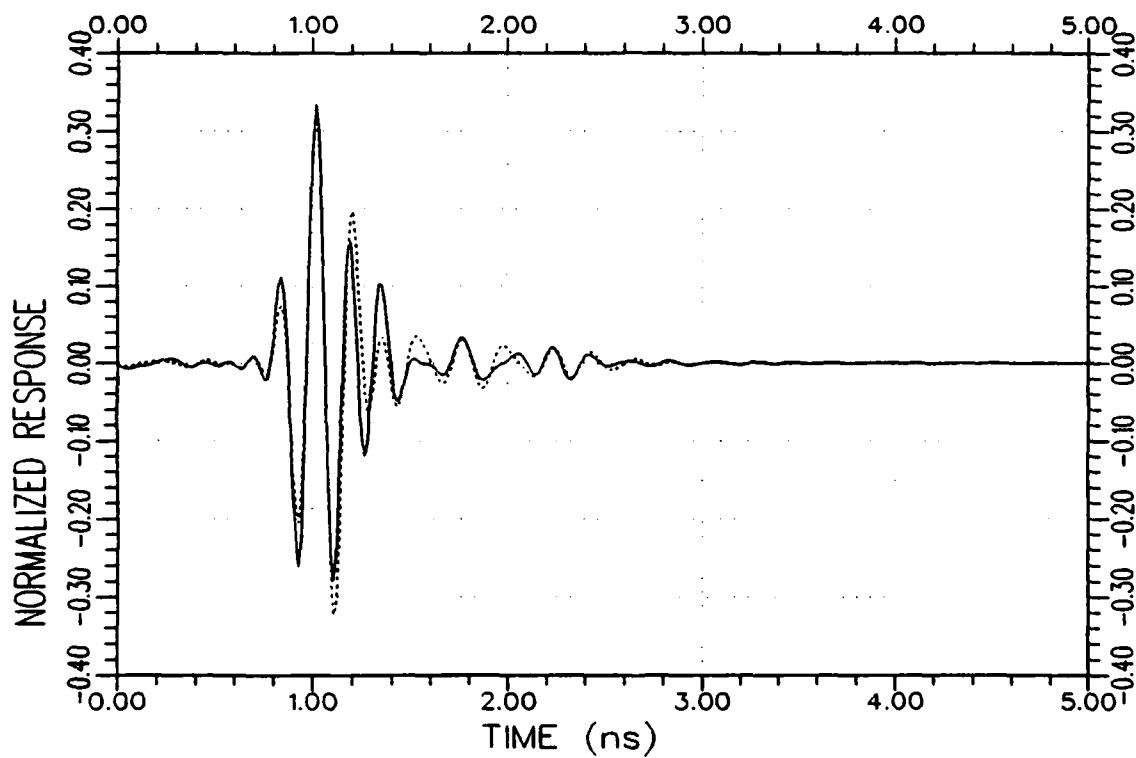
(a) Response waveforms

Figure 5.18. Normalized impulse response (.....) and K-pulse response (—) waveforms and their energy curves for the target SH_2 at $80^\circ/VP$.



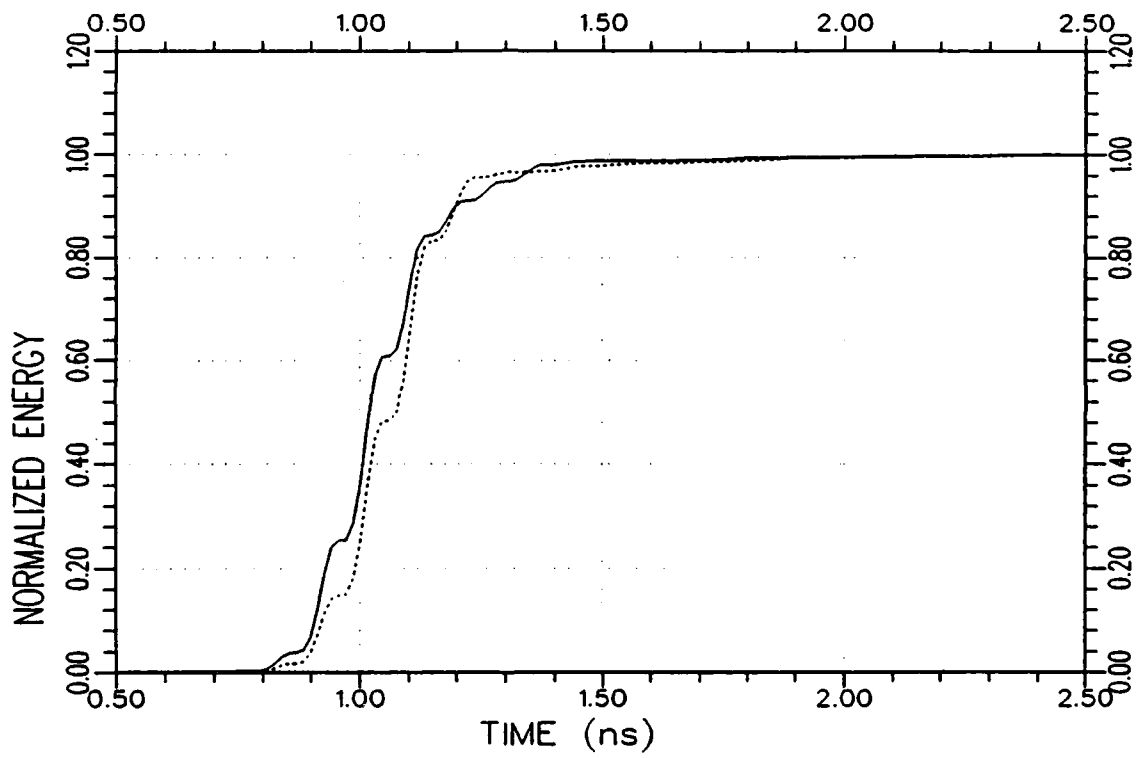
(b) Response energy curves

Figure 5.18. Continued.



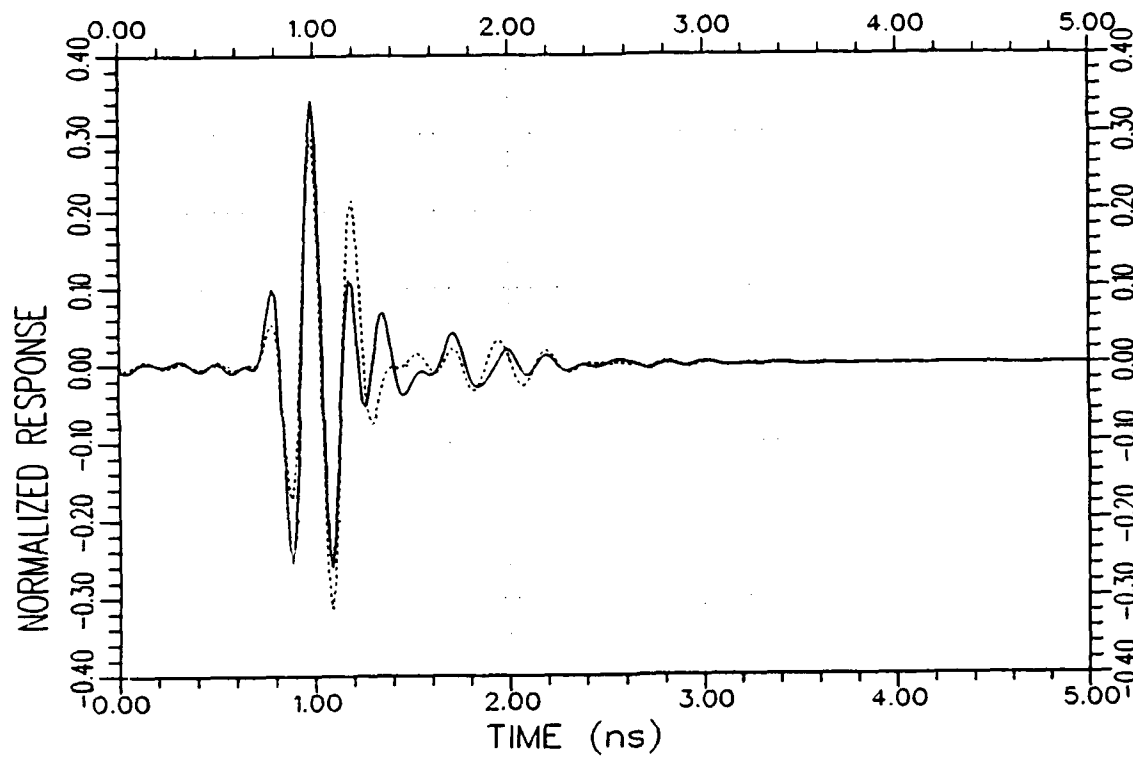
(a) Response waveforms

Figure 5.19. Normalized impulse response (.....) and K-pulse response (—) waveforms and their energy curves for the target SH_2 at $90^\circ/\text{VP}$.



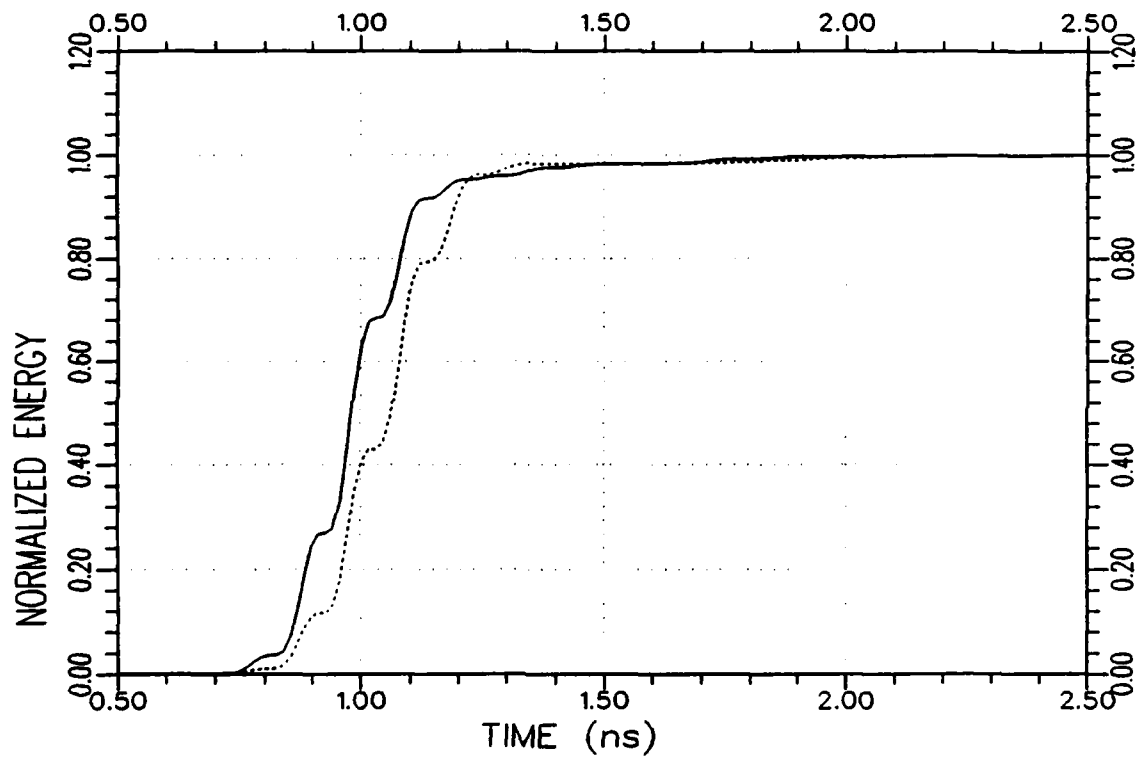
(b) Response energy curves

Figure 5.19. Continued.



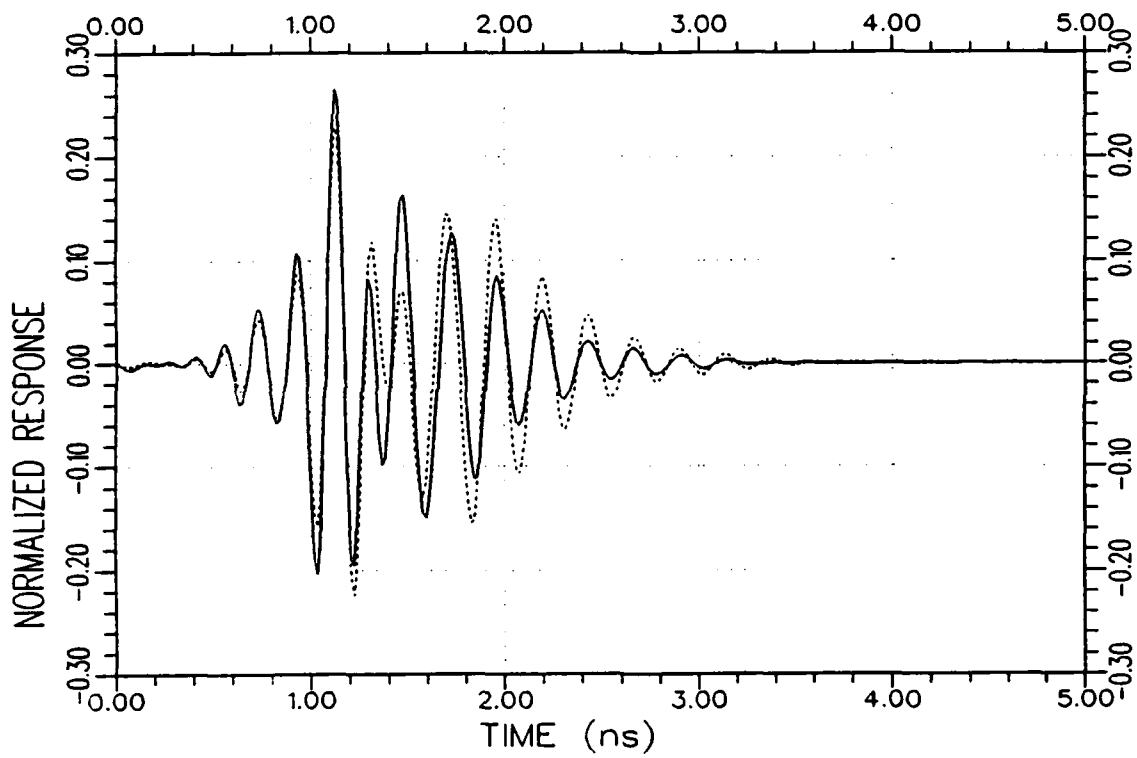
(a) Response waveforms

Figure 5.20. Normalized impulse response (·····) and K-pulse response (—) waveforms and their energy curves for the target SH_2 at $100^\circ/VP$.



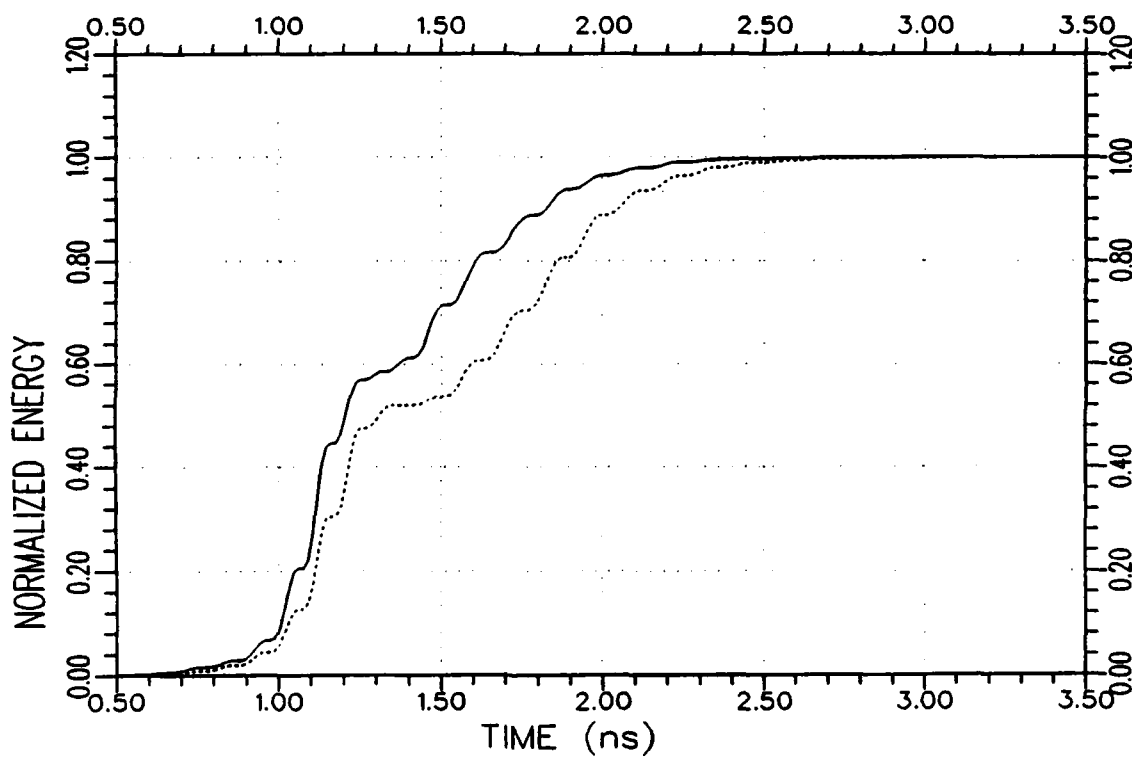
(b) Response energy curves

Figure 5.20. Continued.



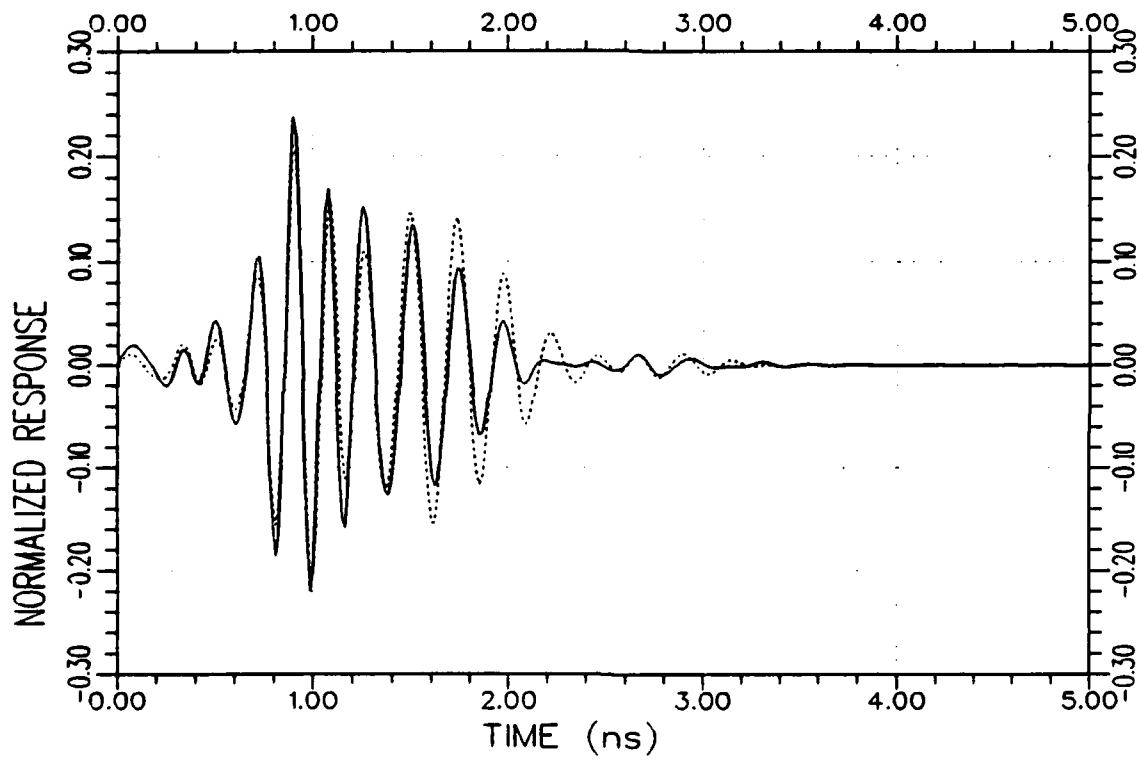
(a) Response waveforms

Figure 5.21. Normalized impulse response (.....) and K-pulse response (—) waveforms and their energy curves for the target SH_2 at $170^\circ/\text{VP}$.



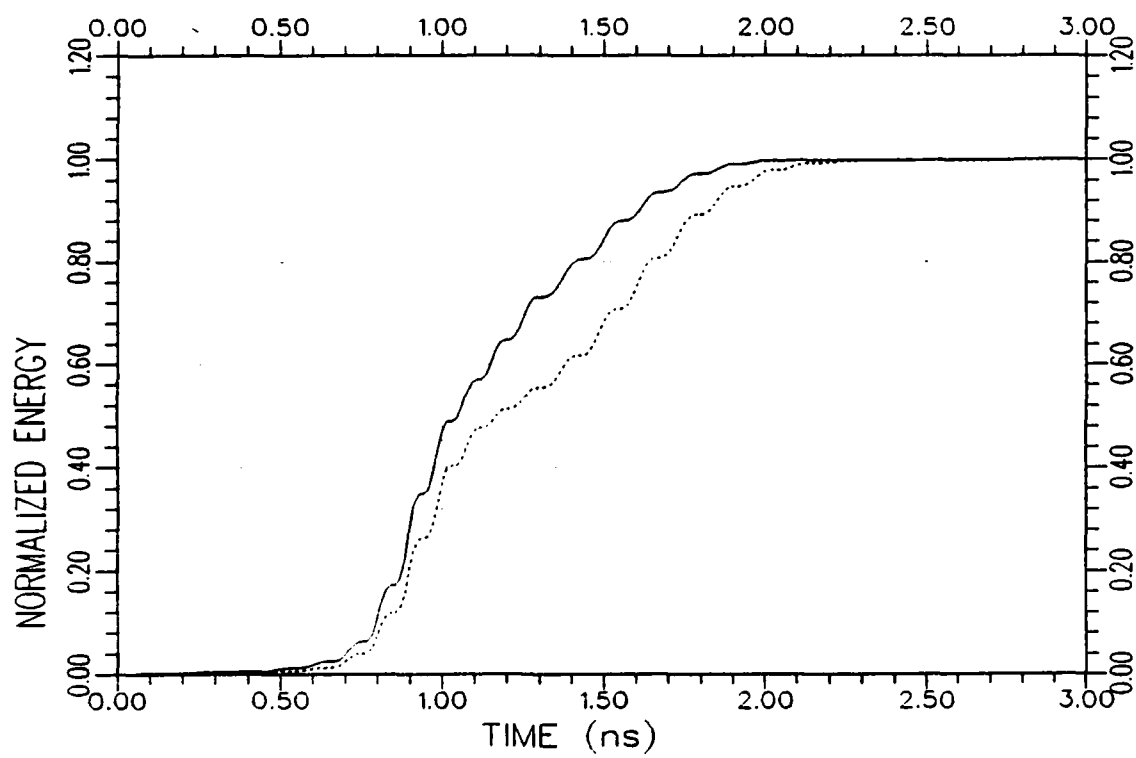
(b) Response energy curves

Figure 5.21. Continued.



(a) Response waveforms

Figure 5.22. Normalized impulse response (.....) and K-pulse response (——) waveforms and their energy curves for the target SH_2 at $180^\circ/VP$.



(b) Response energy curves

Figure 5.22. Continued.

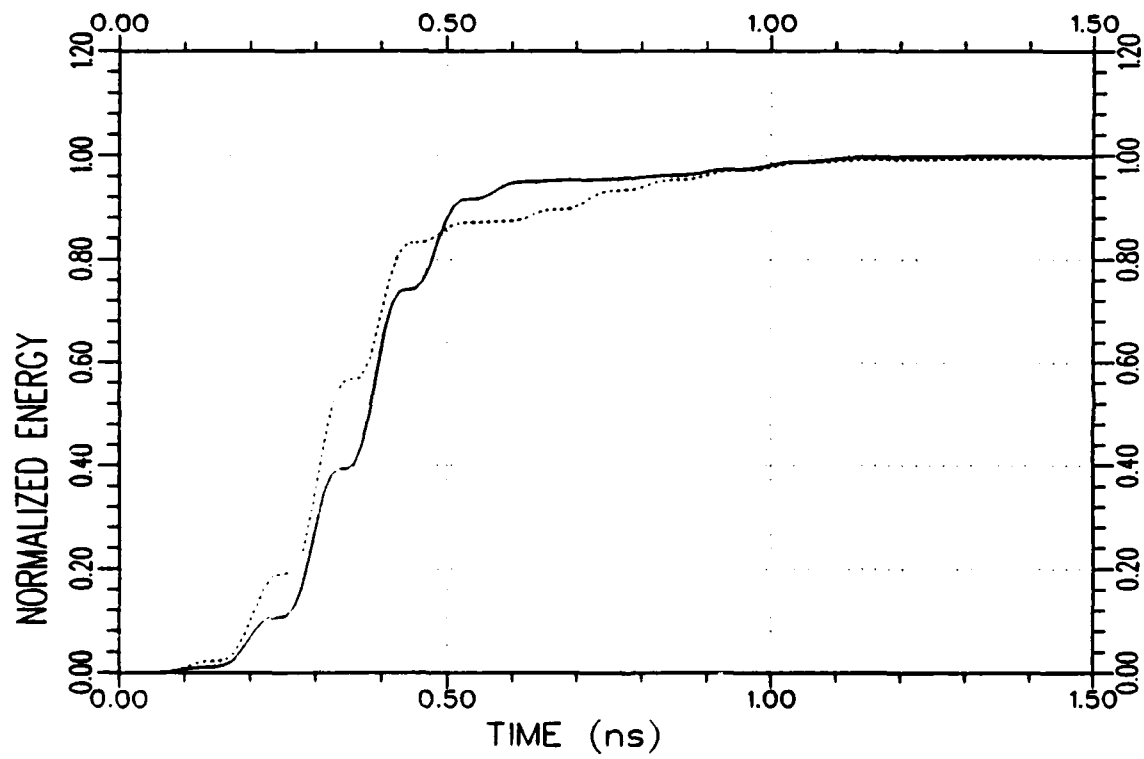


Figure 5.23. Normalized response energy curves of the test target SH₁ produced by the K-pulses of library targets SH₁ (—) and SH₂ (·····) at 0°/VP.

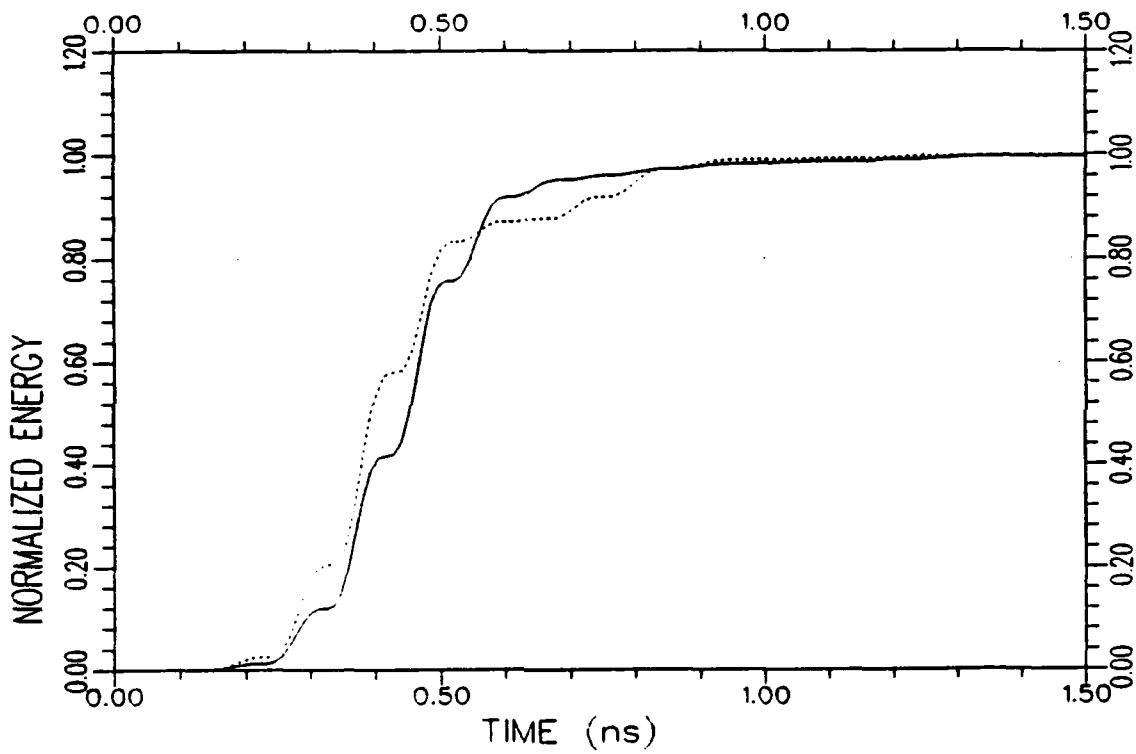


Figure 5.24. Normalized response energy curves of the test target SH₁ produced by the K-pulses of library targets SH₁ (—) and SH₂ (·····) at 15°/VP.

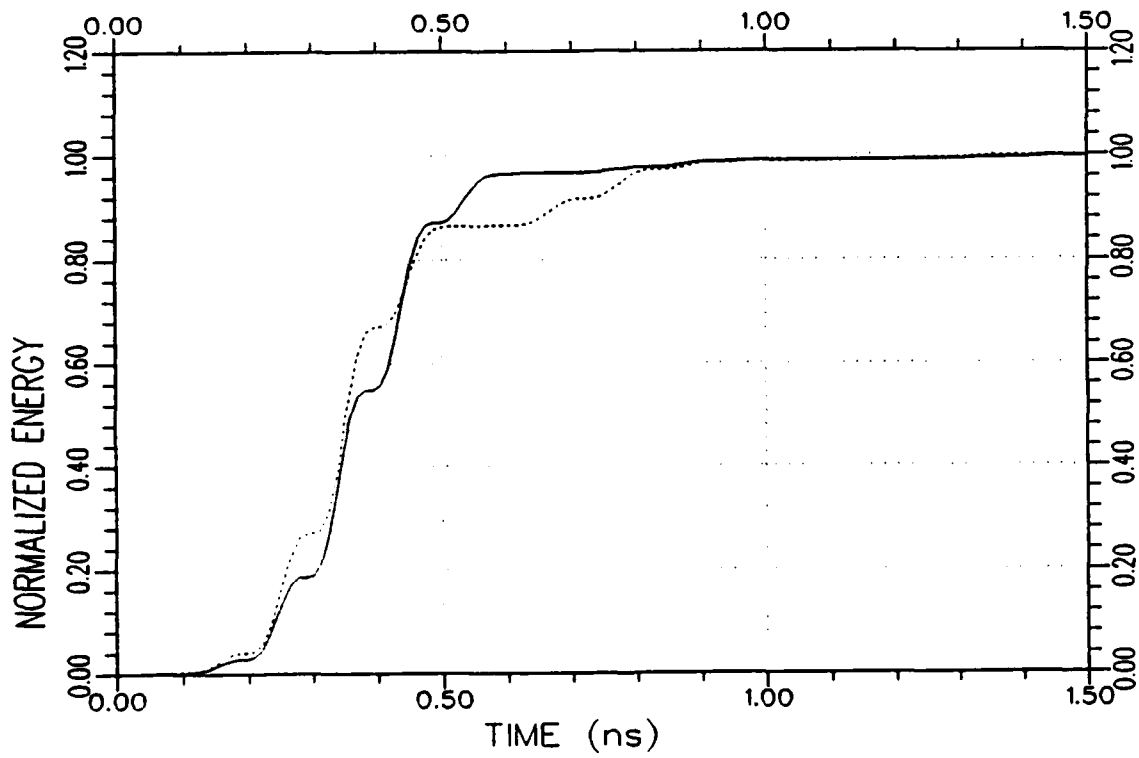


Figure 5.25. Normalized response energy curves of the test target SH₁ produced by the K-pulses of library targets SH₁ (—) and SH₂ (·····) at 30°/VP.

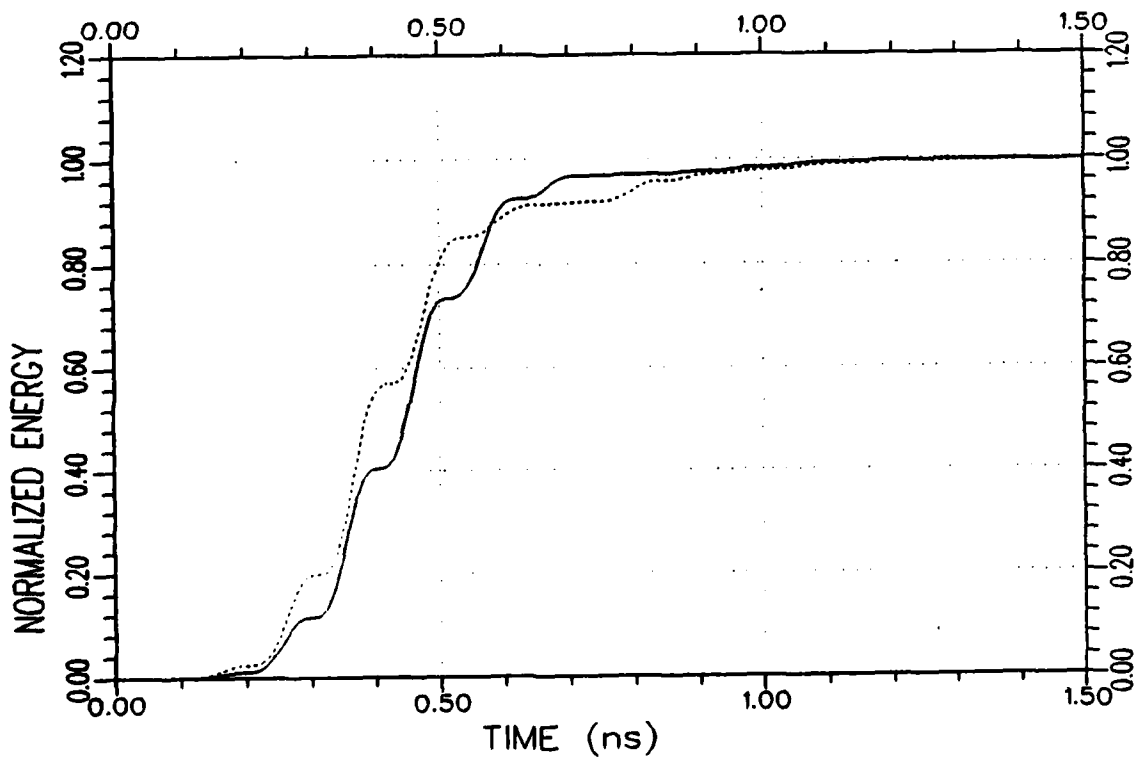


Figure 5.26. Normalized response energy curves of the test target SH_1 produced by the K-pulses of library targets SH_1 (—) and SH_2 (·····) at $45^\circ/VP$.

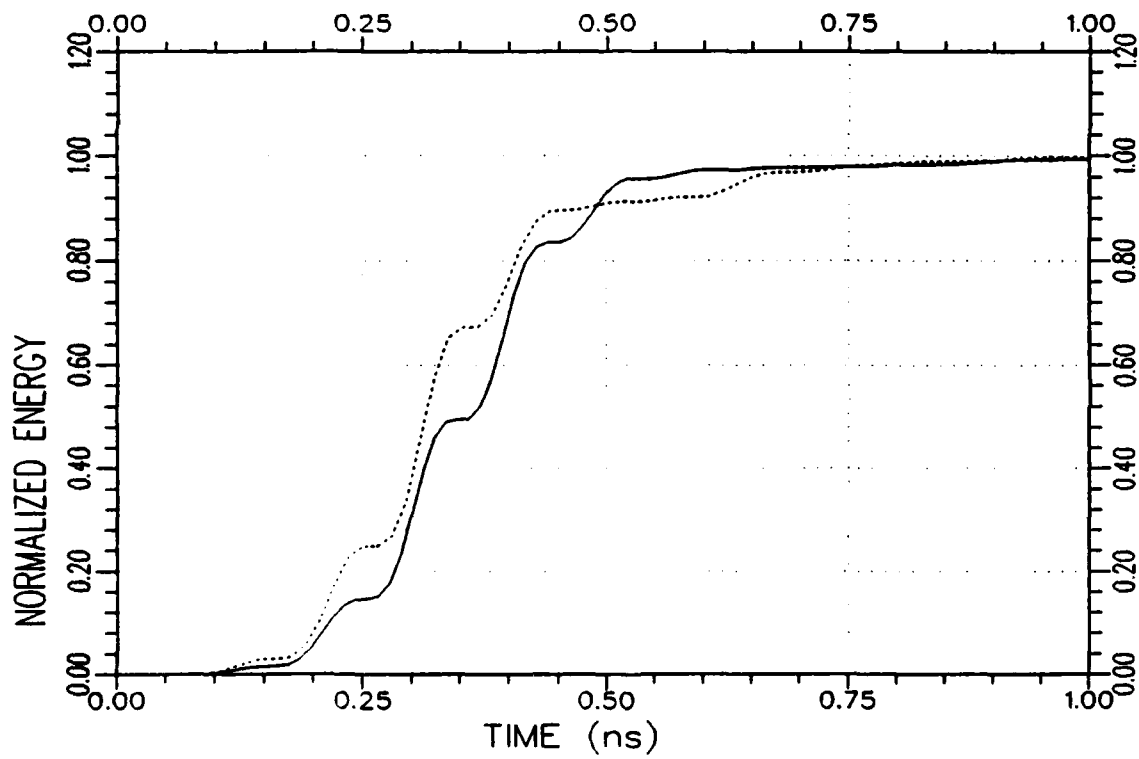


Figure 5.27. Normalized response energy curves of the test target SH₁ produced by the K-pulses of library targets SH₁ (—) and SH₂ (·····) at 80°/VP.

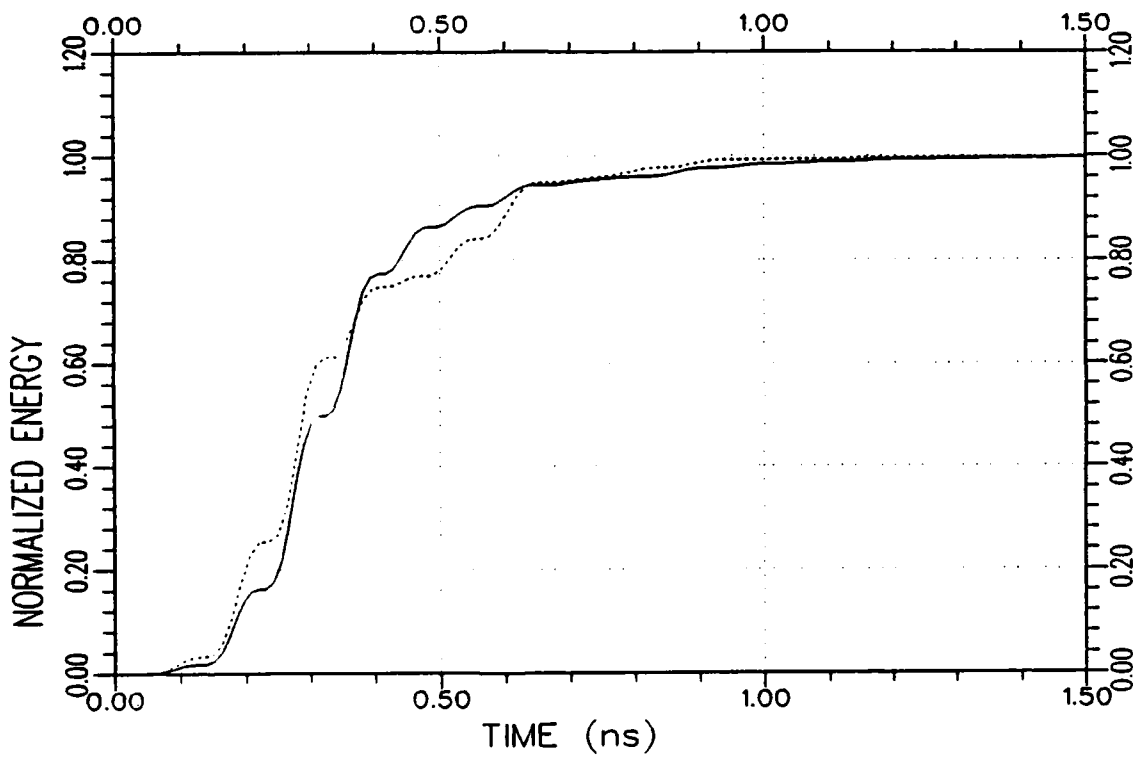


Figure 5.28. Normalized response energy curves of the test target SH₁ produced by the K-pulses of library targets SH₁ (—) and SH₂ (·····) at 100°/VP.

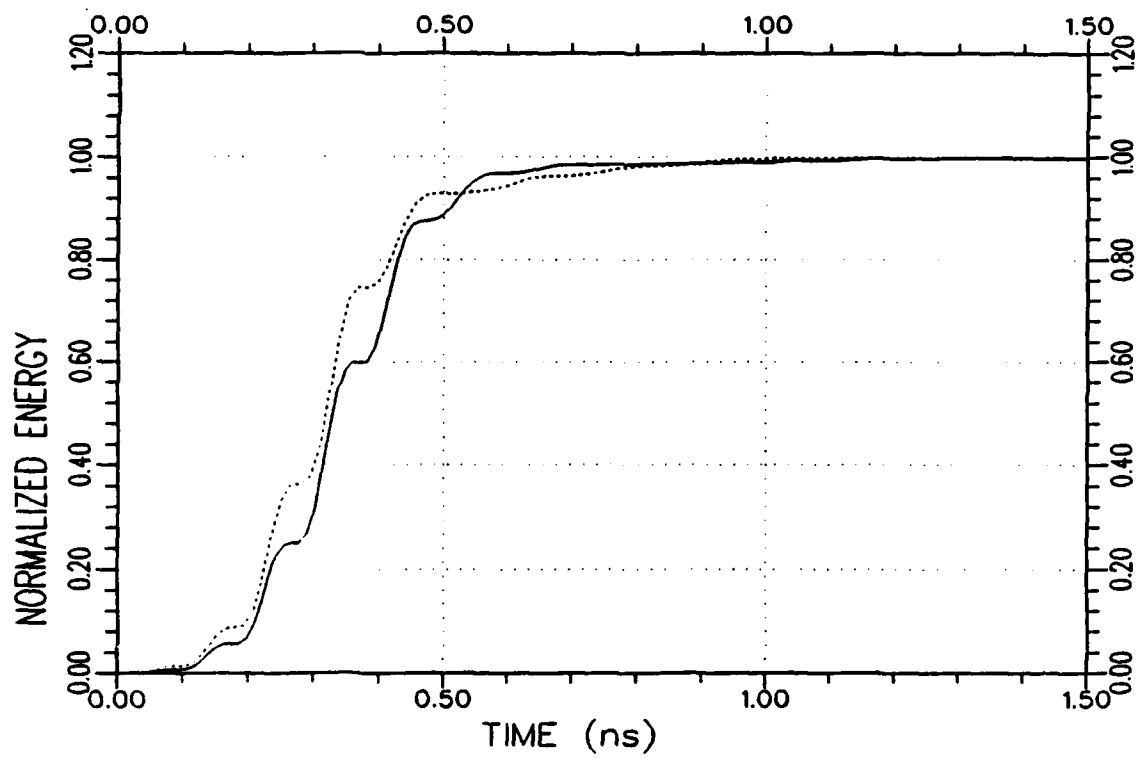


Figure 5.29. Normalized response energy curves of the test target SH_1 produced by the K-pulses of library targets SH_1 (—) and SH_2 (.....) at $170^\circ/VP$.

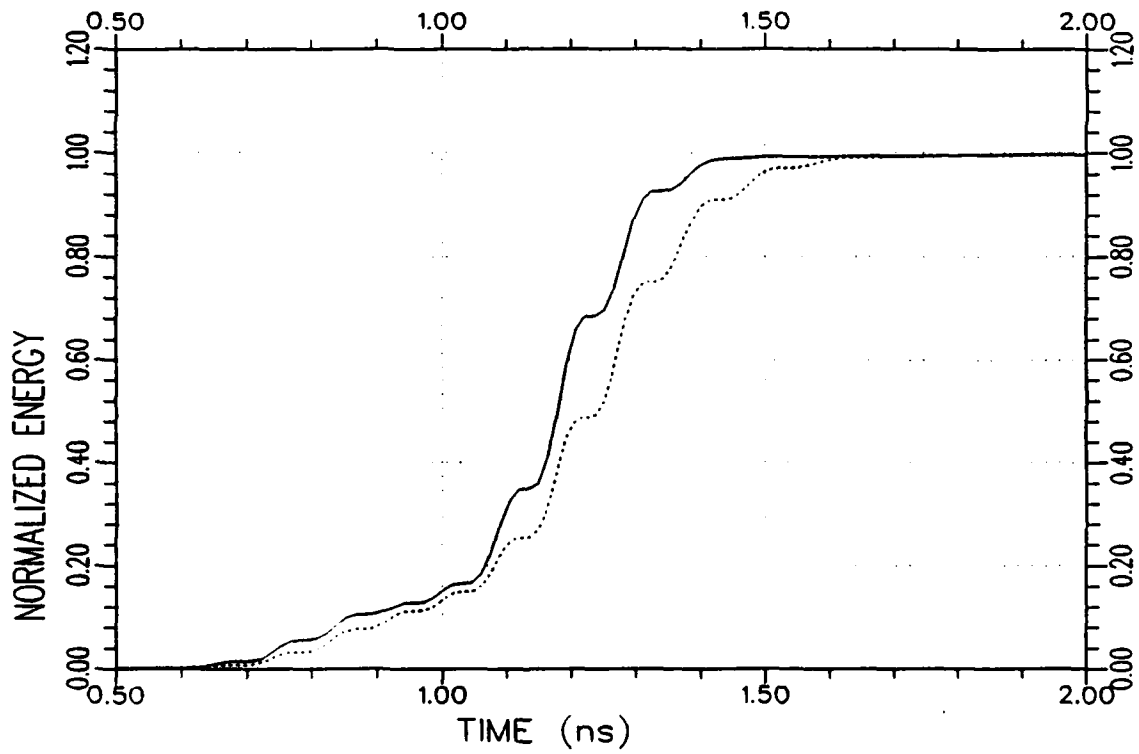


Figure 5.30. Normalized response energy curves of the test target SH₂ produced by the K-pulses of library targets SH₁ (.....)² and SH₂ (—) at 0°/VP.

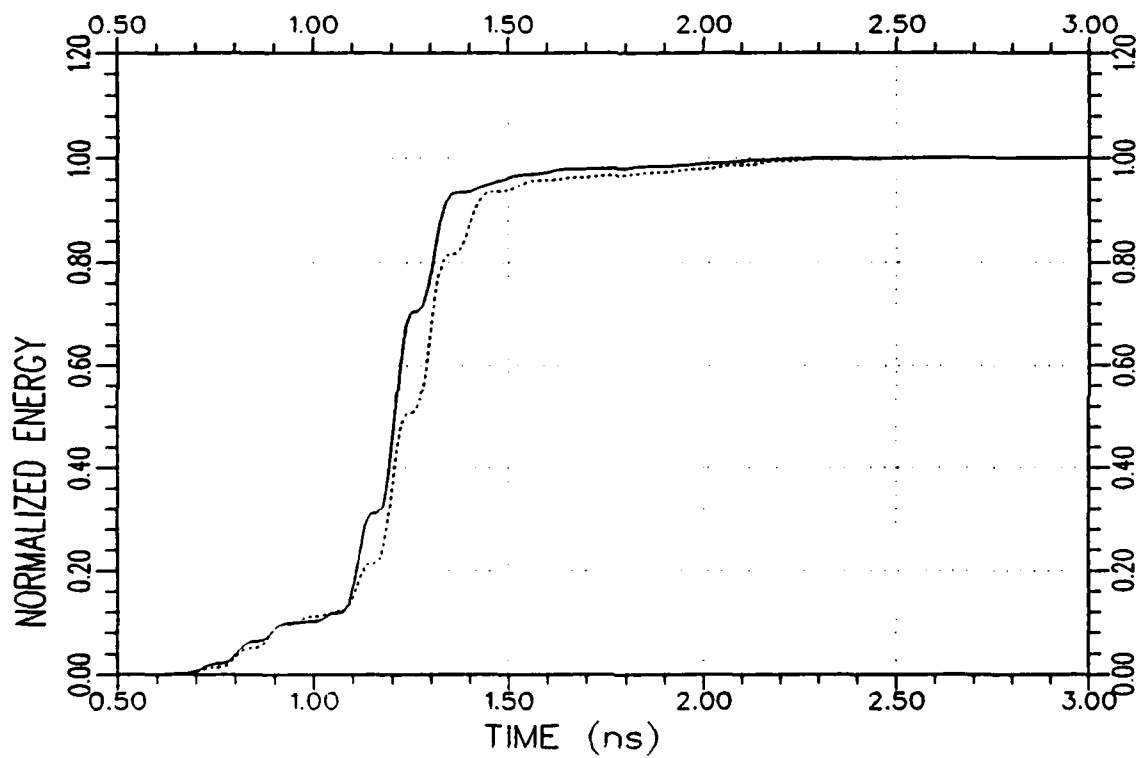


Figure 5.31. Normalized response energy curves of the test target SH₂ produced by the K-pulses of library targets SH₁ (.....) and SH₂ (—) at 30°/VP.

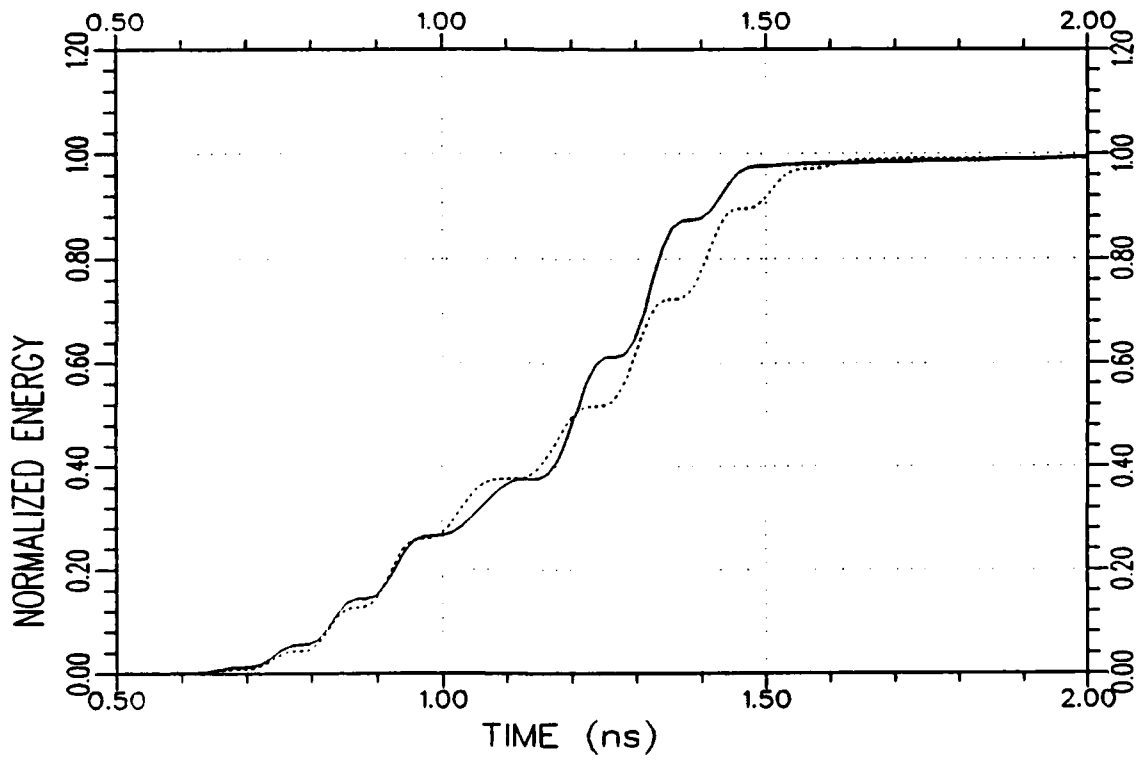


Figure 5.32. Normalized response energy curves of the test target SH₂ produced by the K-pulses of library targets SH₁ (.....) and SH₂ (—) at 45°/VP.

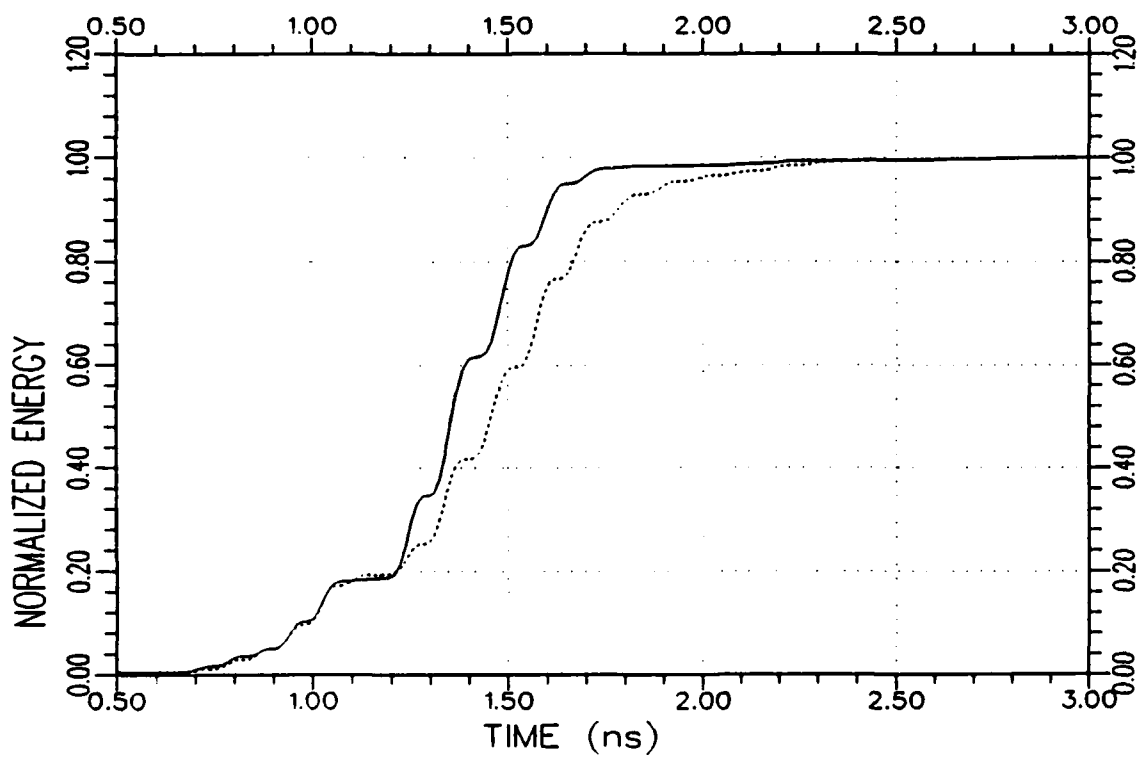


Figure 5.33. Normalized response energy curves of the test target SH₂ produced by the K-pulses of library targets SH₁ (.....)² and SH₂ (—) at 60°/VP.

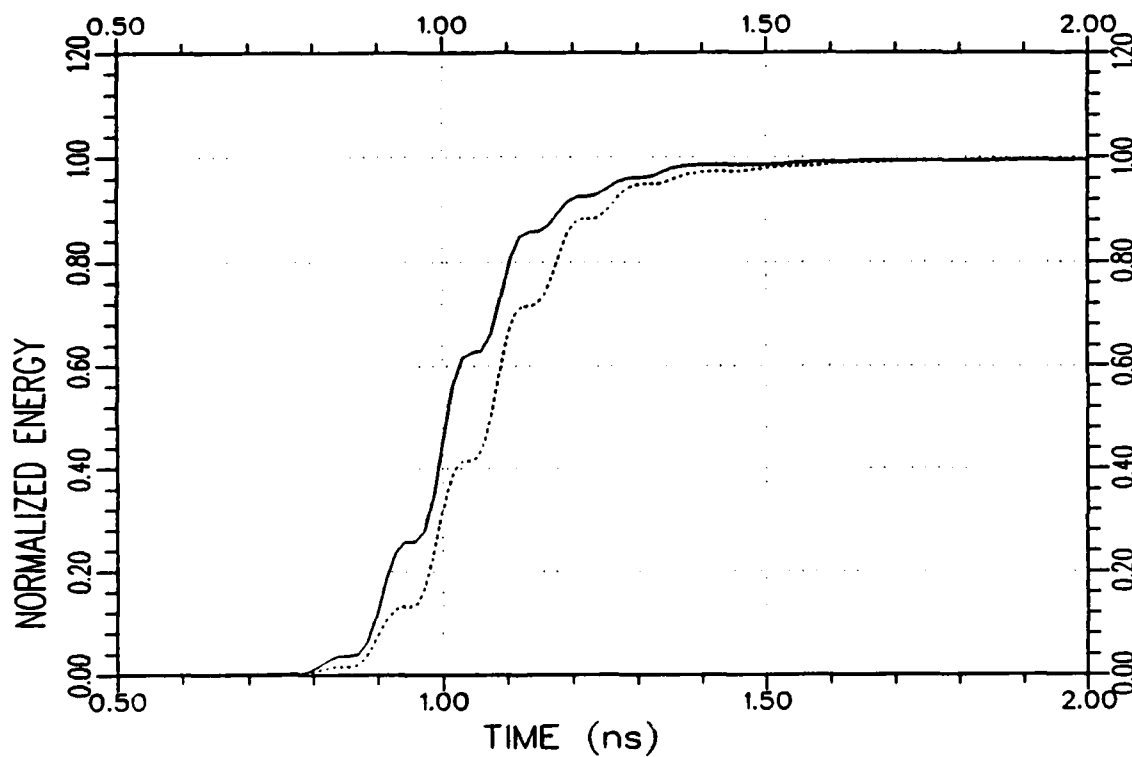


Figure 5.34. Normalized response energy curves of the test target SH₂ produced by the K-pulses of library targets SH₁ (·····) and SH₂ (—) at 80°/VP.

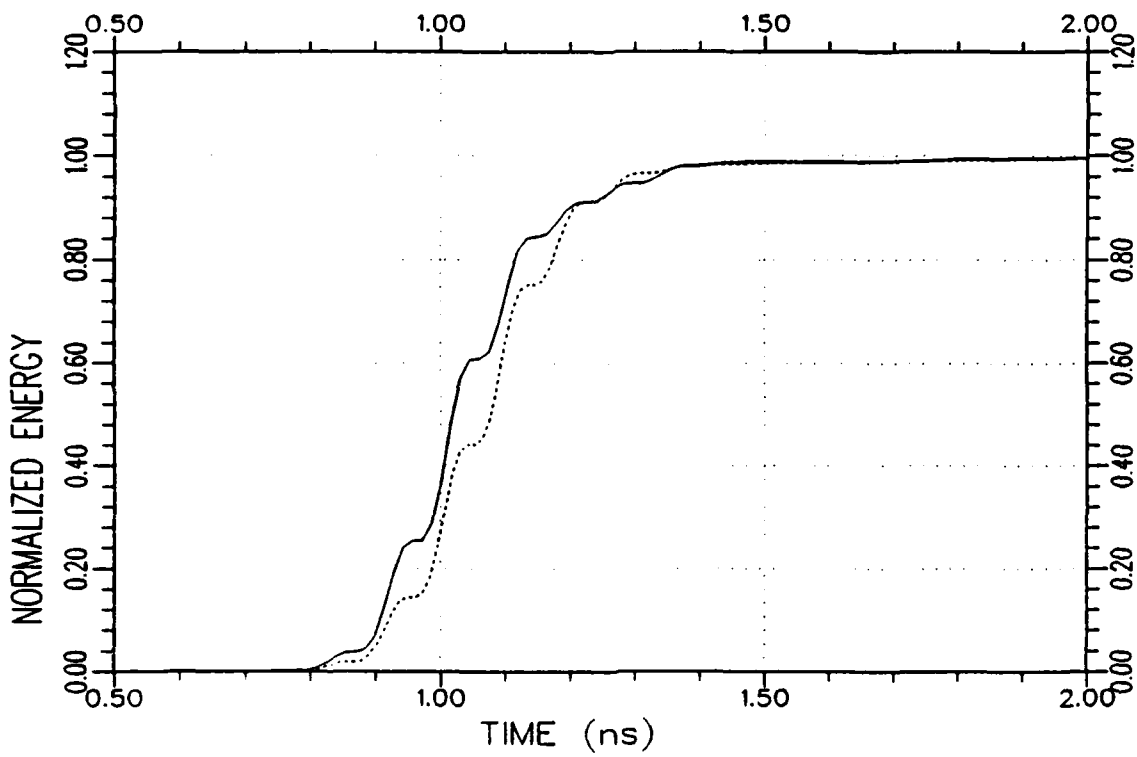


Figure 5.35. Normalized response energy curves of the test target SH₂ produced by the K-pulses of library targets SH₁ (.....)² and SH₂ (—) at 90°/VP.

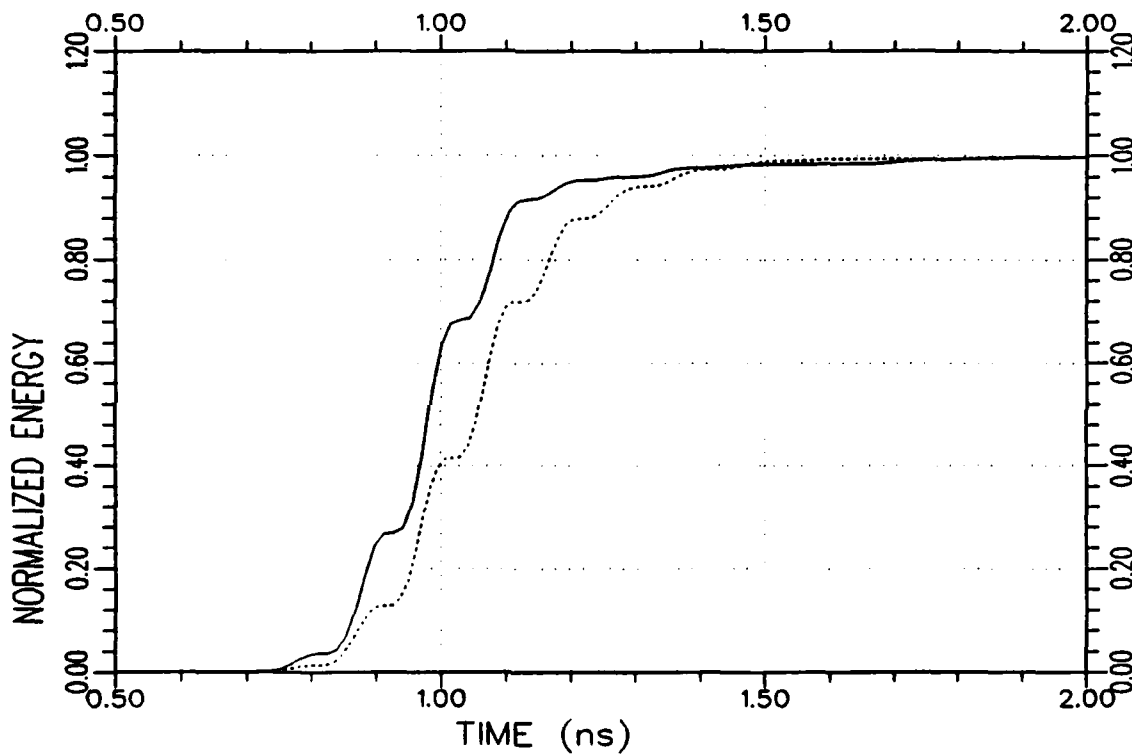


Figure 5.36. Normalized response energy curves of the test target SH₂ produced by the K-pulses of library targets SH₁ (.....) and SH₂ (—) at 100°/VP.

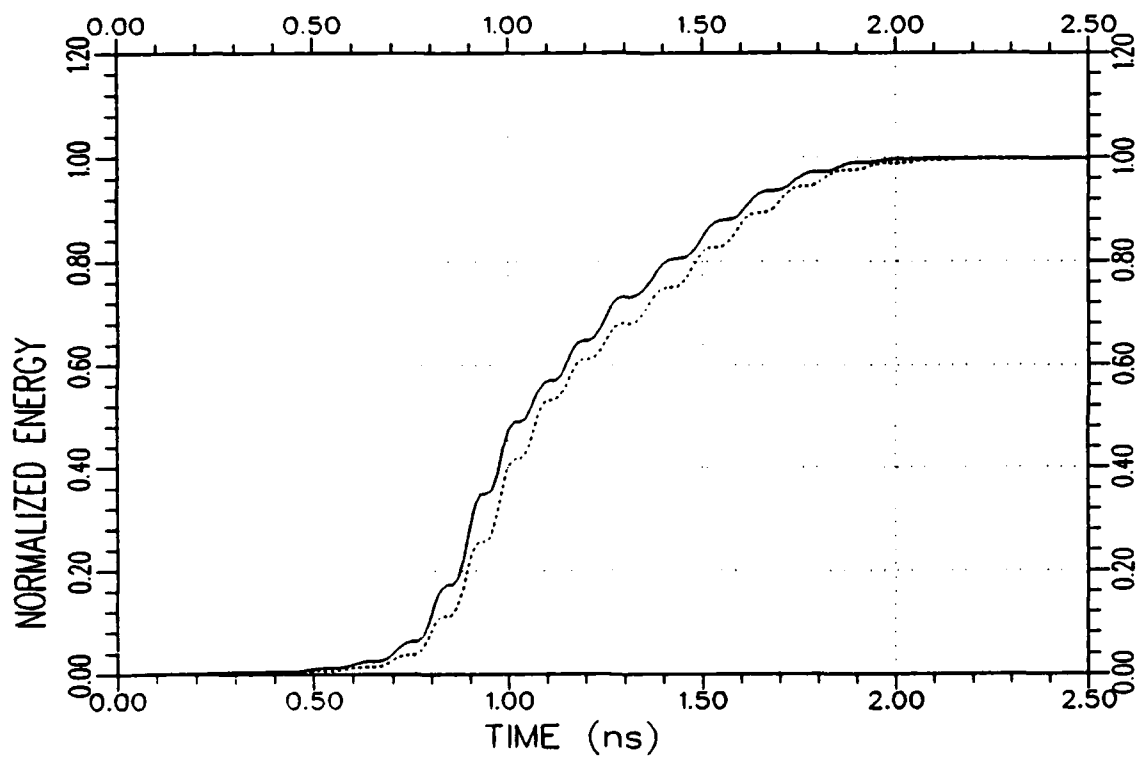
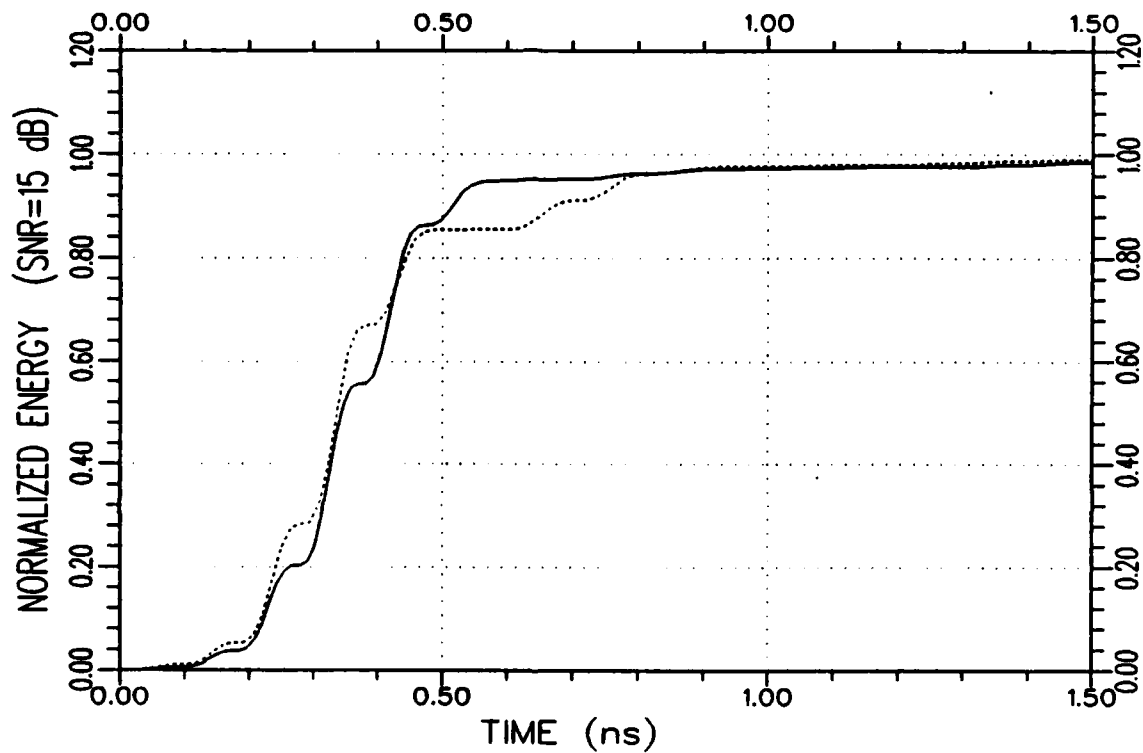
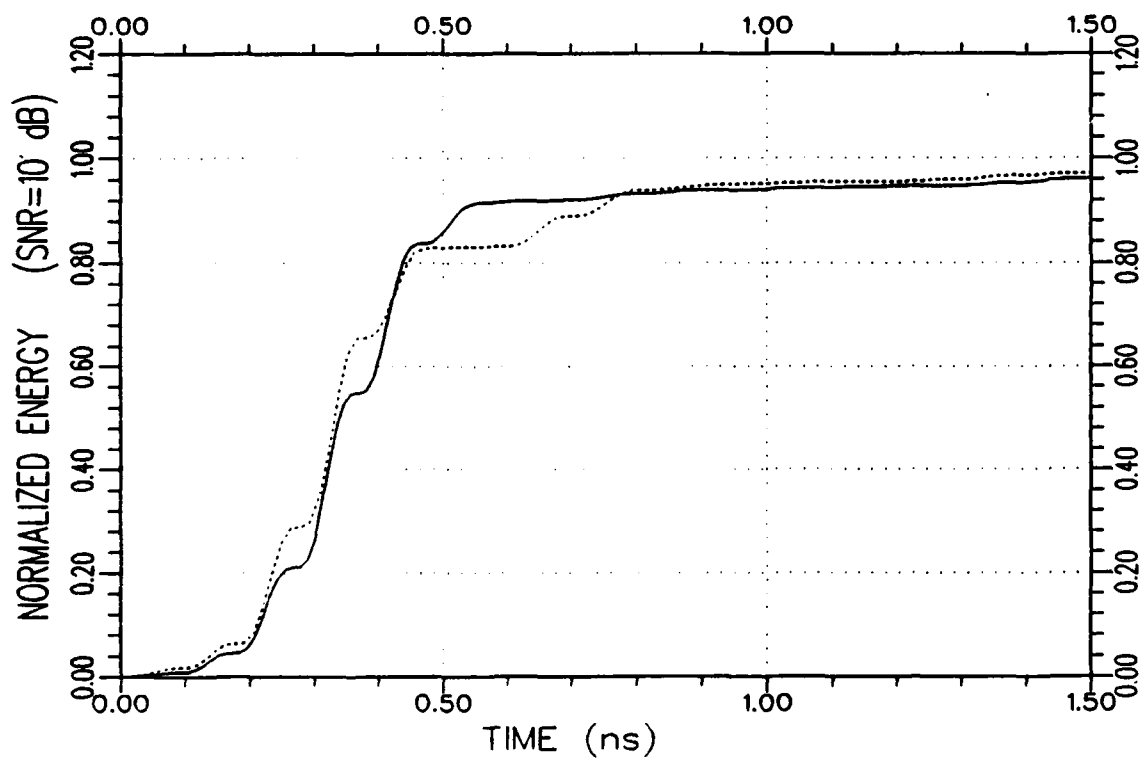


Figure 5.37. Normalized response energy curves of the test target SH₂ produced by the K-pulses of library targets SH₁ (.....) and SH₂ (—) at 180°/VP.



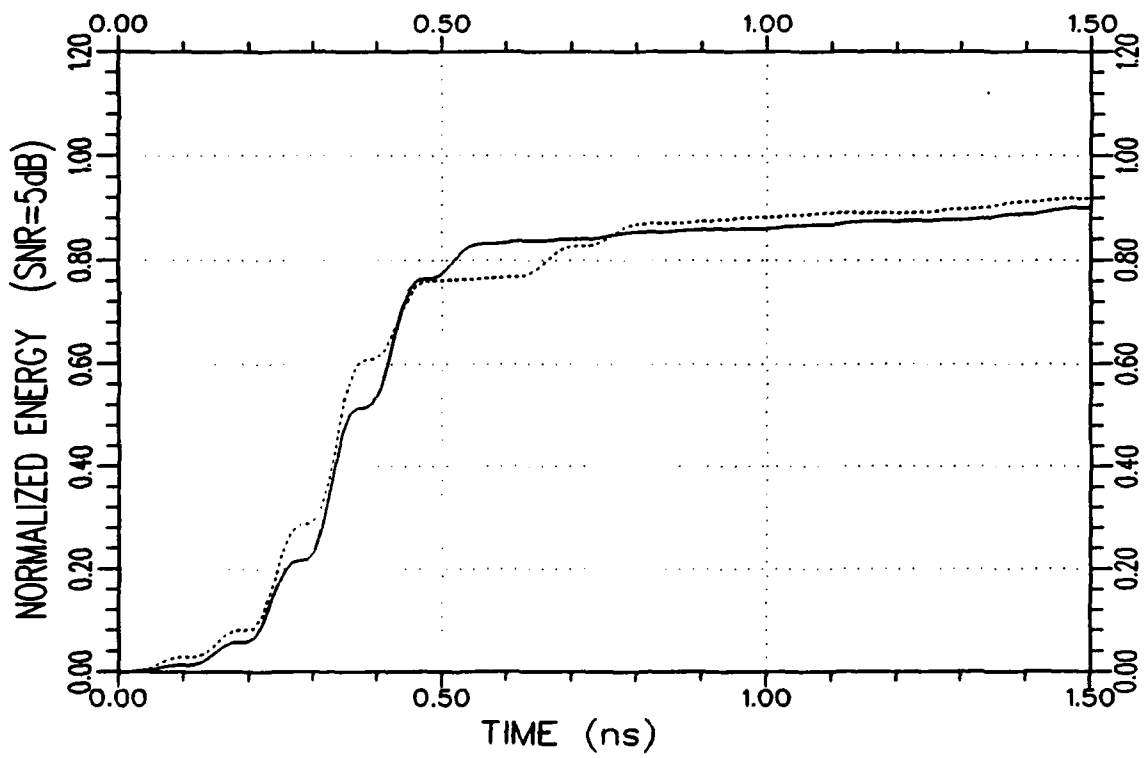
(a) SNR = 15 dB

Figure 5.38. Normalized response energy curves of the test target SH_1 produced by the K-pulses of library targets SH_1 (—) and SH_2 (····) for some noisy backscattered data at $30^\circ/VP$.



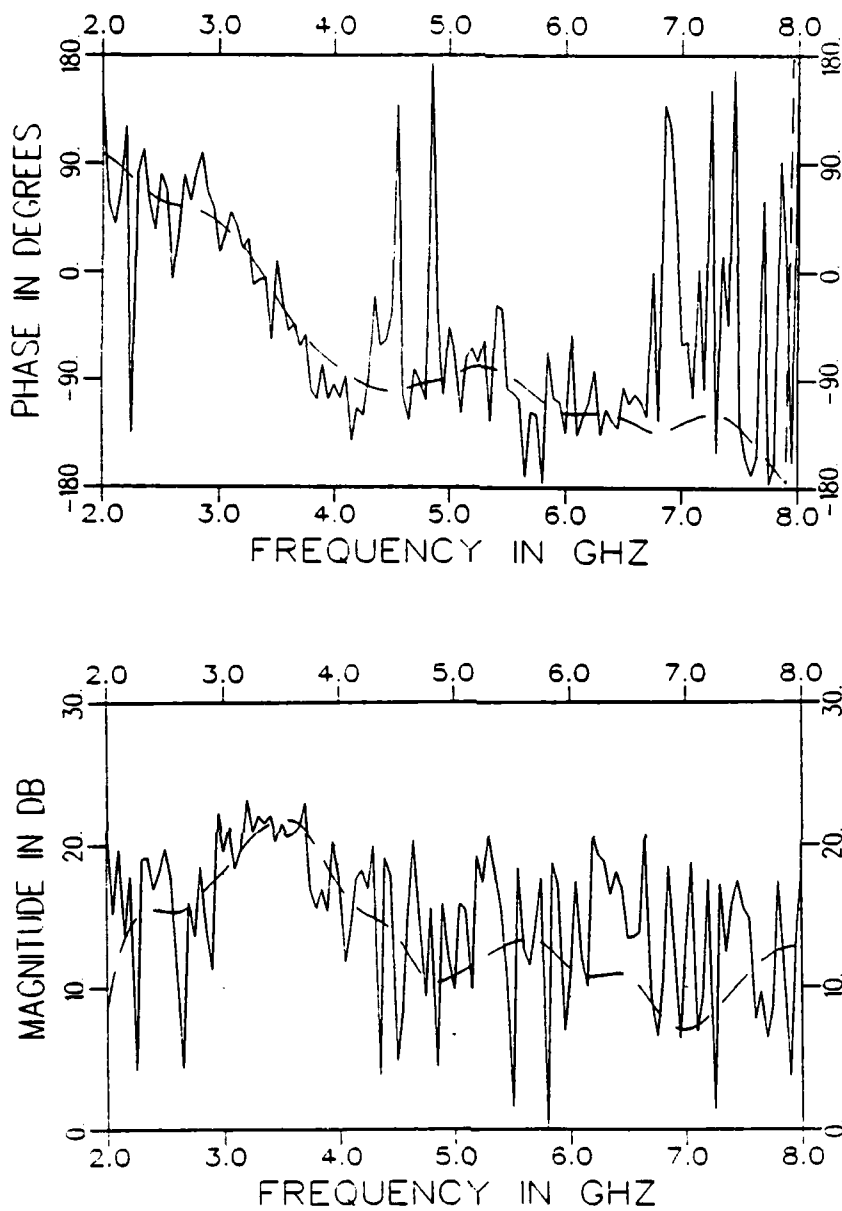
(b) SNR = 10 dB

Figure 5.38. Continued.



(c) SNR = 5 dB

Figure 5.38. Continued.



(d) The phase and amplitude plots for the noisy (—) and original (— —) backscattered data for SNR=5 dB

Figure 5.38. Continued.

CHAPTER VI
APPLICATIONS TO LAND VEHICLES

In this chapter, K-pulse applications are extended to land vehicles. The targets used for the demonstrations are electroplated small scale models of a tank and a personnel carrier which are referred to as LV_1 and LV_2 , respectively, in the remainder of this chapter. The geometrical features and overall size of these two model targets are quite similar except for the long gun barrel of the tank. In Sections A and B, a discrete representation for the K-pulse model is employed to estimate the K-pulse waveforms of the targets. The synthesized approximate K-pulses are utilized in the target identification demonstrations of Section C. The vertically polarized frequency domain backscattered data for both targets were measured on the Ohio State University compact RCS measurement range [53] in the presence of a ground plane [54] over the aspect angle range from 0° to 90° where the aspect angle is measured from the major (front-to-end) axes of the targets. The backscattered impulse response data are obtained via the standard IFFT of the frequency data which are weighted by a bandpass Hanning window function over the frequency range 2.0-(0,05)-8.0 GHz.

A. K-PULSE ESTIMATION FOR THE MODEL TARGET LV_1

An approximate K-pulse waveform of the target, LV_1 , is synthesized using the backscattered impulse response data at two combinations; $0^\circ/VP$ and $90^\circ/VP$. The K-pulse duration is estimated to be $3L_1/c=0.889$ ns where L_1 is the length of the target including the gun barrel. The continuous part of the K-pulse waveform is represented by equally-spaced samples $k_1^c, k_2^c, \dots, k_N^c$ with $N=77$. The optimal values of these samples are estimated via minimization of the cost function (Equation (3.9) with $a=1$, $b=0$, and $I=2$ for the cut-off times 0.9 ns and 0.6 ns at the synthesis combinations of $0^\circ/VP$ and $90^\circ/VP$, respectively. The resultant K-pulse waveform is shown in Figure 6.1 which also includes a unit strength impulse function $\delta(t)$, as stated in the general form of the K-pulse model of Equation (3.1). The zeros of the Laplace transform of the synthesized K-pulse waveform are listed in Table 6.1, which are expected to approximate a subset of the target poles in the frequency range 2 to 8 GHz. To test the aspect-invariant feature of the K-pulse, the pairs of normalized impulse response and K-pulse response waveforms as well as the corresponding normalized energy curve pairs are plotted in Figures 6.2 through 6.6 at the aspect angles of 0° , 30° , 45° , 60° and 90° , respectively for vertical polarization. Late-time response energy reduction is naturally expected at the 0° and 90° cases which are the synthesis aspect angles used. Indeed, the normalized energy curve of the K-pulse response leads that of the impulse response at almost all energy levels in part (b) of Figures 6.2 and 6.6. The late-time target response energy reduction is also observed in part (a) of all figures at varying extents. At 30° aspect angle, the result looks

quite satisfactory while for the 60° case, it turns out to be relatively poor. The best result is observed in Figure 6.4 at a 45° aspect angle although it is not one of the synthesis aspects used.

B. K-PULSE ESTIMATION OF THE MODEL TARGET LV_2

The K-pulse waveform of the target LV_2 is estimated using the backscattered data at $30^\circ/VP$ and $90^\circ/VP$. The K-pulse duration is estimated to be $3L_2/c = 0.572$ ns where L_2 is the length of the target. The continuous part of the K-pulse is represented by equally-spaced samples $k_1^C, k_2^C, \dots, k_N^C$ with $N=50$. The cut-off times are set to 0.85 ns at 30° aspect angle and 0.65 ns at 90° aspect angle. Minimization of the cost function, \tilde{J} , (with $a=1$, $b=0$ and $I=2$) led to the approximate K-pulse waveform shown in Figure 6.7. Laplace domain zeros of this K-pulse are numerically extracted and listed in Table 6.2. The normalized impulse response and K-pulse response pairs are plotted together in part (a) of Figures 6.8 through 6.12 at aspect angles 0° , 30° , 45° , 60° and 90° , respectively, for vertical polarization. The corresponding energy curve pairs are also shown in part (b) of the same figures. Results are found to be satisfactory in all these cases, especially at the 45° and 90° aspect angles.

C. TARGET IDENTIFICATION

The K-pulse library of this section is composed of the approximate K-pulse waveforms of the targets LV_1 and LV_2 . The test target of the identification examples shown in Figures 6.13 through 6.17 is the model tank, LV_1 , at aspect angles of 0° , 30° , 45° , 60° and 90° , respectively.

In all these demonstrations, the test target is identified correctly. The normalized energy curve of the matched target response leads that of the mismatched one over the energy range 82% to 98% at 0°; 76% to 99% at 30°; 75% to 97% at 45°; 52% to 90% at 60°; and 93% to 99% at 90° cases. The average energy difference of the matched and mismatched curves is about 2% at a 90° aspect angle but still enough for a correct identification since the mismatched curve never goes above the matched one at any energy level. On the other hand, the mismatched energy curve of the 60° case is observed to be leading the matched one starting from the 90% energy level by about 2% average energy difference. However, this variation is compensated by the reverse situation observed over the 52% to 90% energy range where the average difference between the energy curves is about 10% of the total energy.

Next, the model carrier, LV_2 , is chosen to be the test target of the demonstrations presented in Figures 6.18 through 6.22 at the aspect angles 0°, 30°, 45°, 60° and 90°, respectively for vertical polarization. At the 0° case, the matched and mismatched energy curves follow each other very closely causing an ambiguity in the identification. At 30° aspect angle, the matched energy curve reaches all energy levels earlier than the mismatched one with an average energy difference of about 6% over the energy range 88% to 98%. The best identification result is observed at 45° aspect angle as shown in Figure 6.20. Another satisfactory result is presented in Figure 6.21 for the 60° case. The target, LV_2 , is again identified with certainty in Figure 6.22 at 90° aspect angle where the matched energy curve reaches all energy levels earlier than the mismatched curve by an

average energy level difference of about 9% over the range 75% to 96%. In summary, the overall result of Figures 6.13 to 6.22 leads to a correct identification score of 90%.

Finally, the noise performance of the identification scheme is checked in Figure 6.23 where the test target is LV_2 at a $90^\circ/VP$ combination. A set of noisy data is simulated from the original (measured) scattered data as explained in Appendix E. Assuming the SNR of the original data to be infinite, the SNR of the noisy data is set to 15 dB, 10 dB and 5 dB in parts (a), (b) and (c) of Figure 6.23. Even at the 5 dB SNR level for which the noisy data spectrum is shown in part (d) of the same figure, a correct identification is still possible.

Table 6.1

Poles of the Model Tank LV₁
 Extracted from the K-pulse Shown in Figure 6.1

10^9 Nepers/s, GHz Scale	sL_1/c Scale
.	.
.	.
-0.282 ± j 3.522	-0.525 ± j 6.558
-0.483 ± j 4.445	-0.899 ± j 8.276
-0.384 ± j 5.638	-0.715 ± j 10.497
-0.271 ± j 6.762	-0.606 ± j 12.590
.	.
.	.
.	.

Table 6.2

Poles of the Model Carrier LV₂
 Extracted from the K-pulse shown in Figure 6.7

10^9 Nepers/s, GHz Scale	sL_2/c Scale
.	.
.	.
-0.275 ± j 2.843	-0.329 ± j 3.403
-0.288 ± j 4.068	-0.345 ± j 4.869
-0.442 ± j 5.628	-0.529 ± j 6.786
-0.358 ± j 6.941	-0.429 ± j 8.308
.	.
.	.
.	.

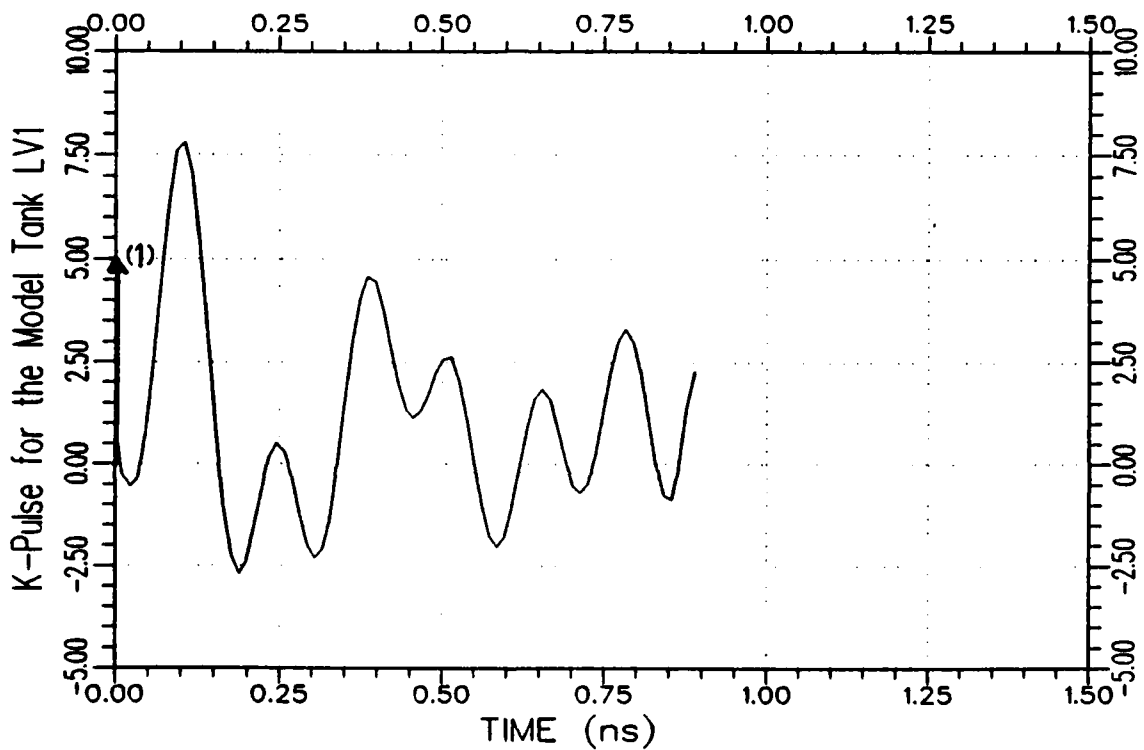
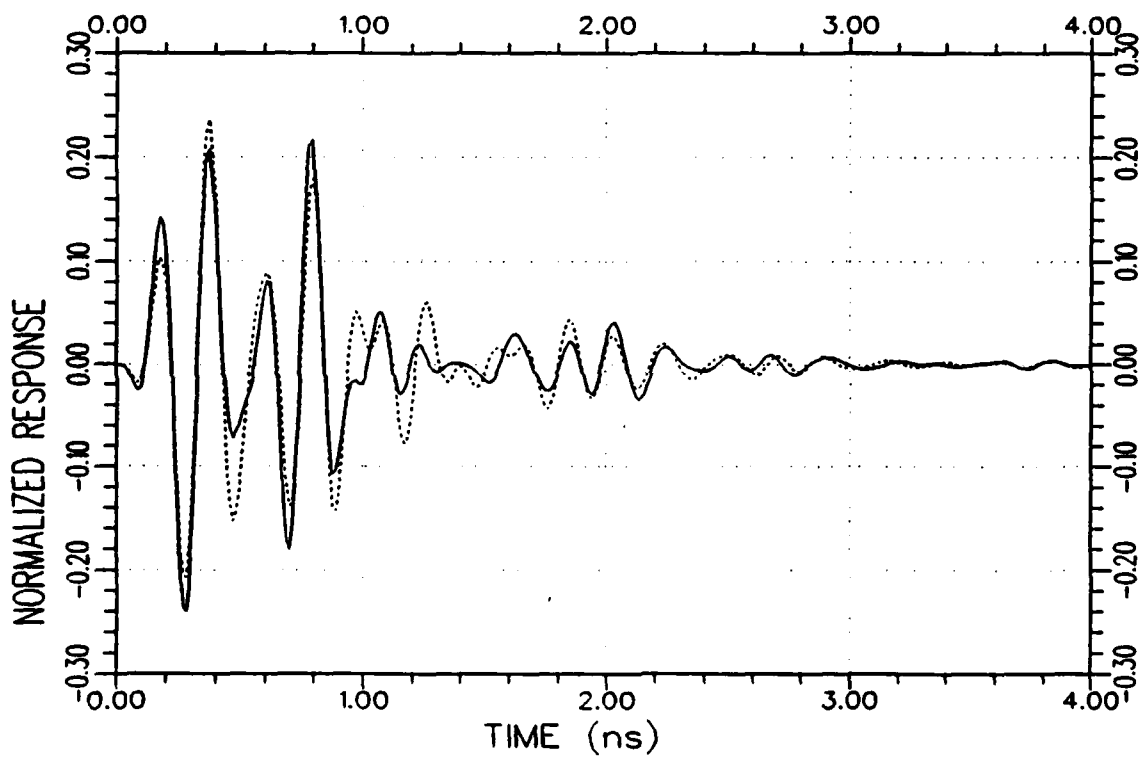
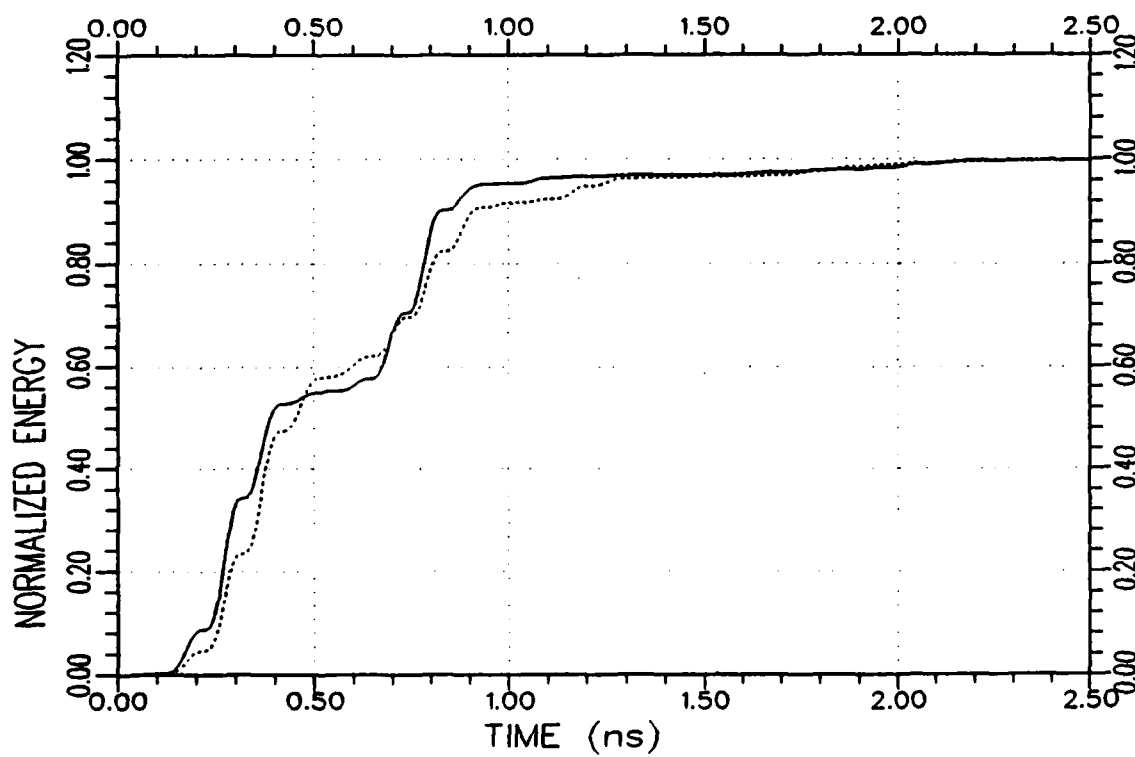


Figure 6.1. An approximate K-pulse waveform for the model tank LV_1 estimated from the backscattered measurement data at $0^\circ/VP$ and $90^\circ/VP$ using a discrete representation for the continuous part of the K-pulse. (The $\delta(t)$ term of the K-pulse is symbolically shown by the arrow at $t=0$.)



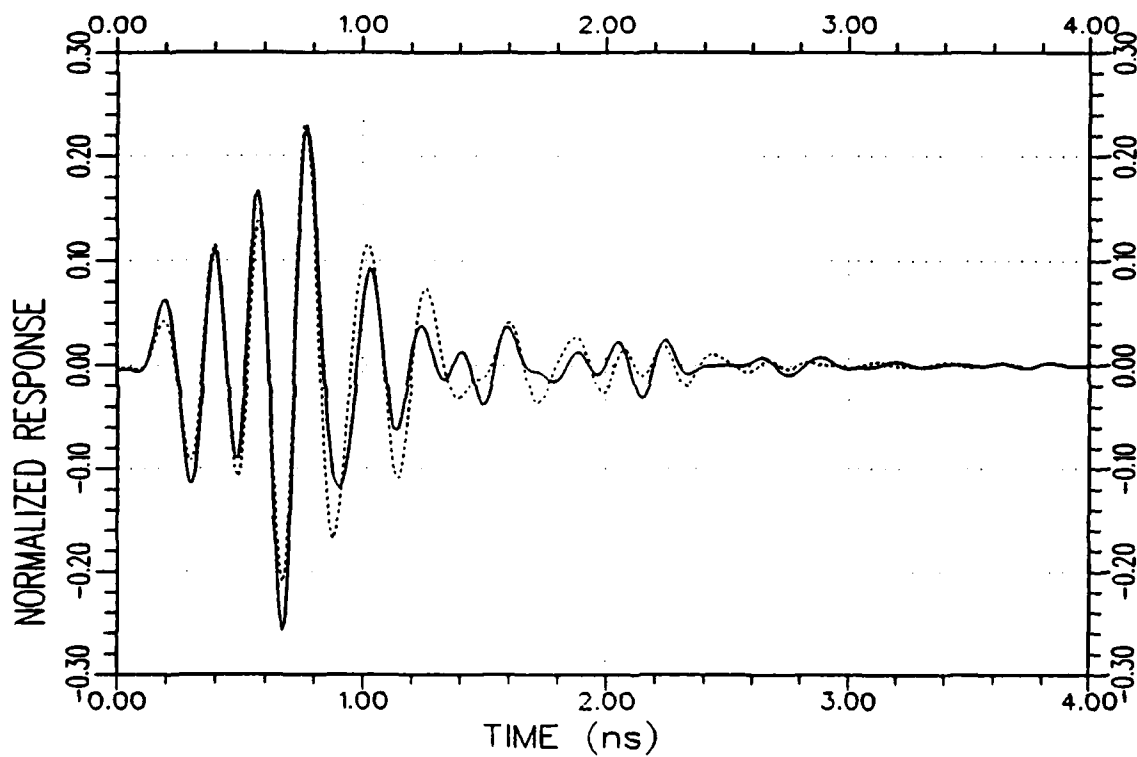
(a) Response waveforms

Figure 6.2. Normalized impulse response (.....) and K-pulse response (—) waveforms and their energy curves for the model tank LV_1 at $0^\circ/VP$.



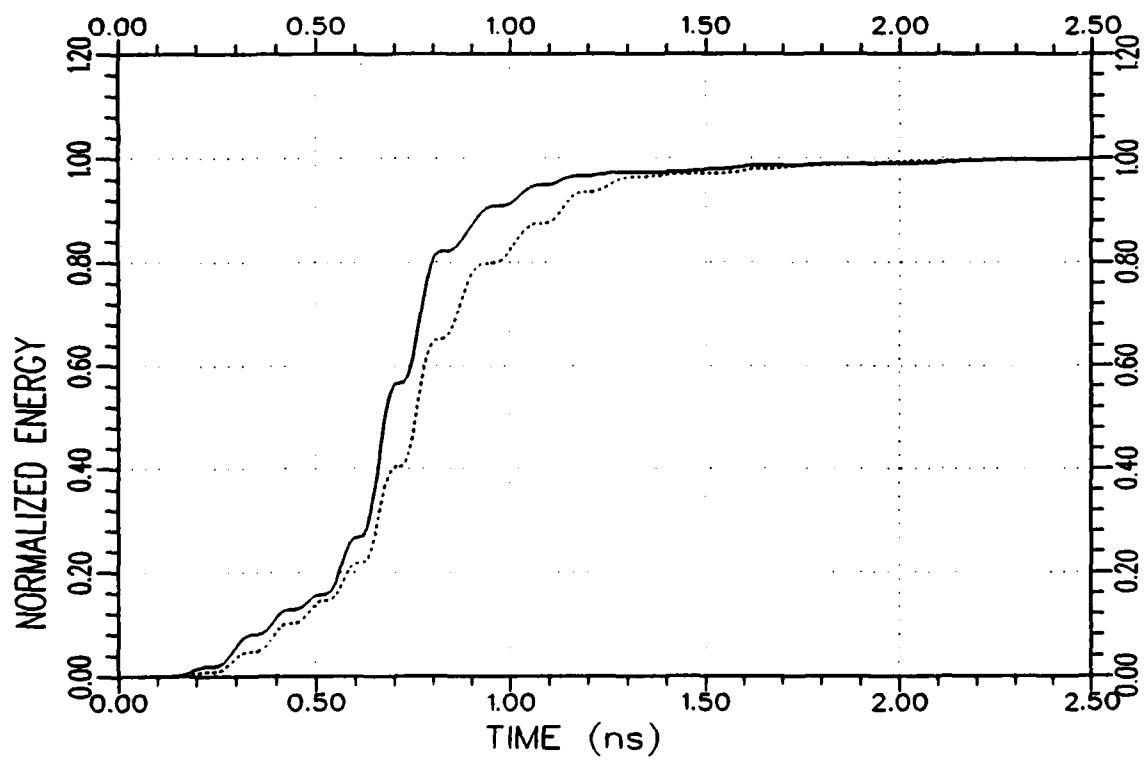
(b) Response energy curves

Figure 6.2. Continued.



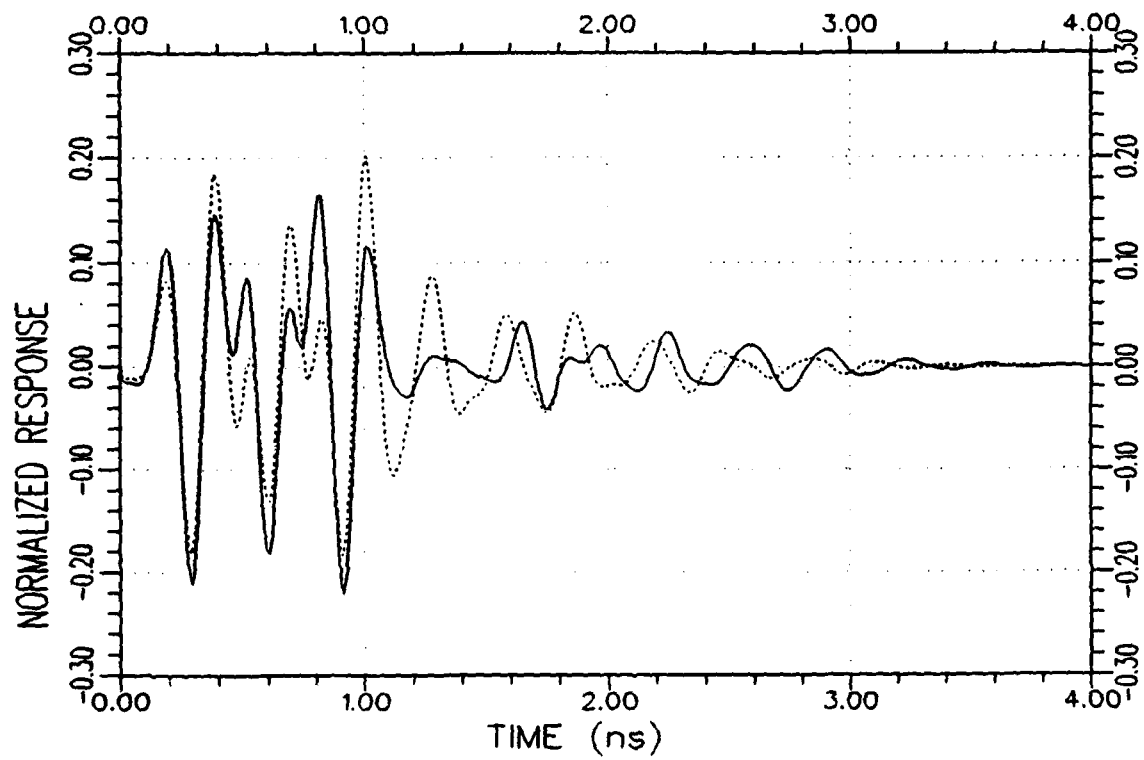
(a) Response waveforms

Figure 6.3. Normalized impulse response (.....) and K-pulse response (—) waveforms and their energy curves for the model tank LV_1 at $30^\circ/VP$.



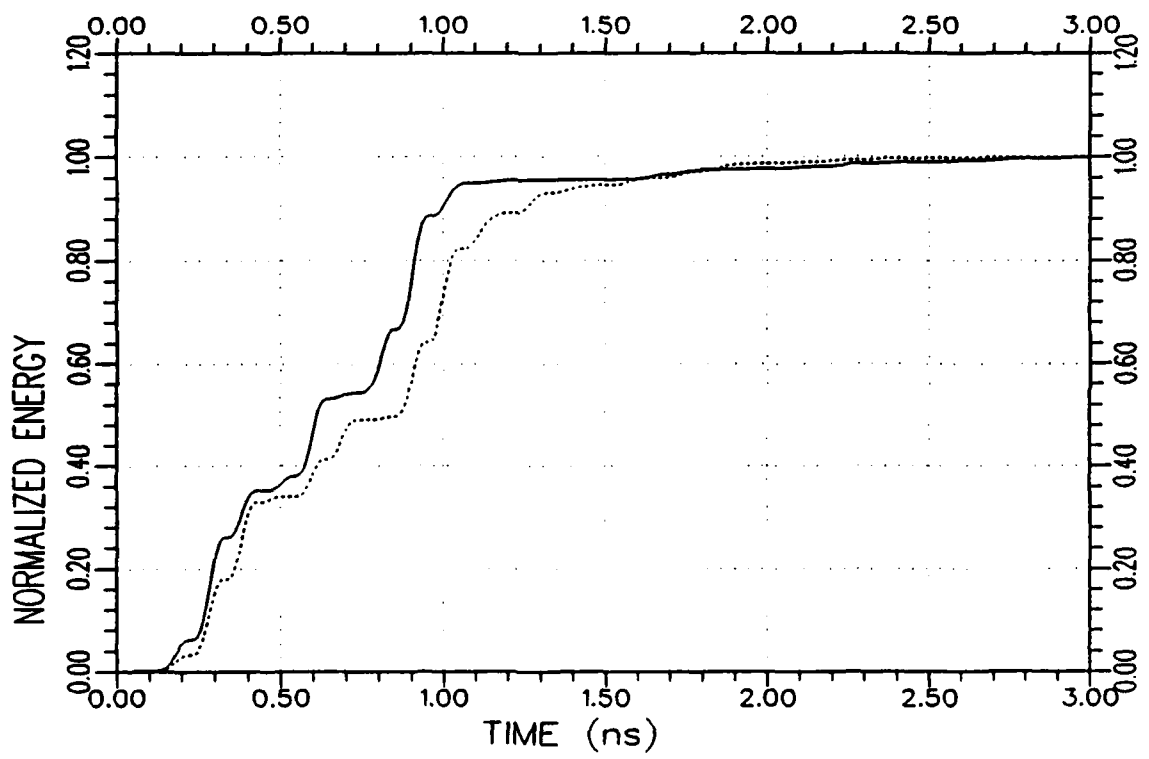
(b) Response energy curves

Figure 6.3. Continued.



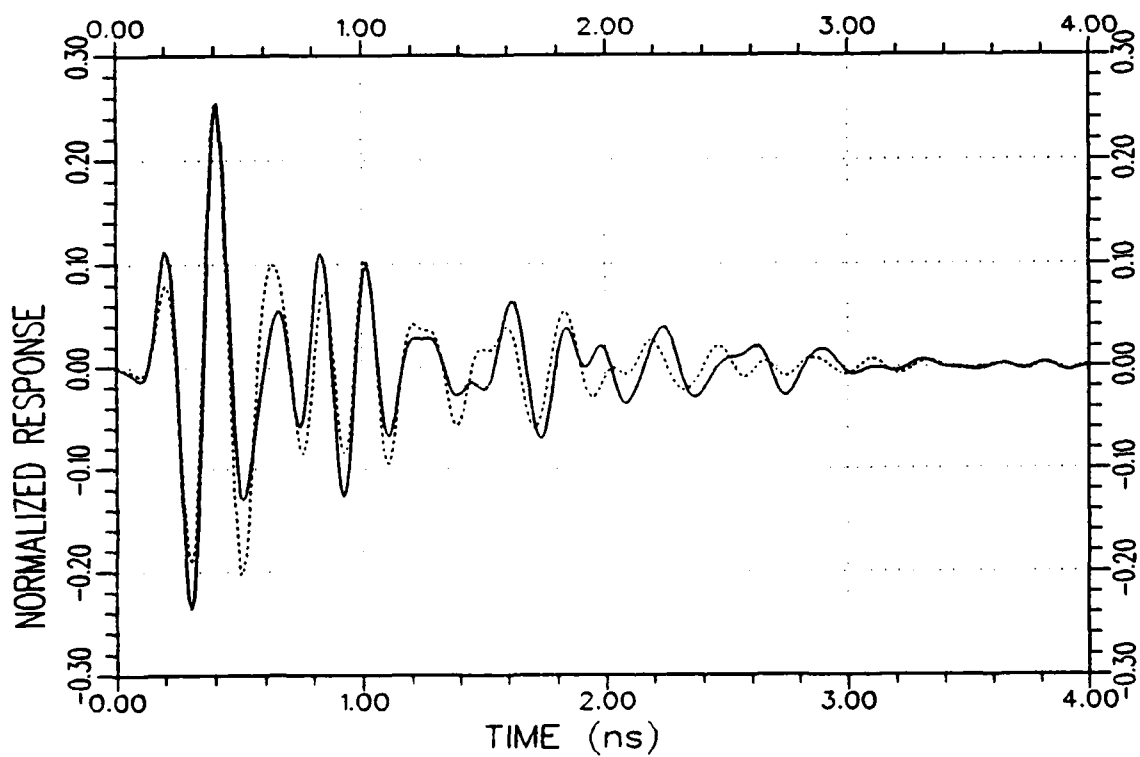
(a) Response waveforms

Figure 6.4. Normalized impulse response (·····) and K-pulse response (—) waveforms and their energy curves for the model tank LV_1 at $45^\circ/VP$.



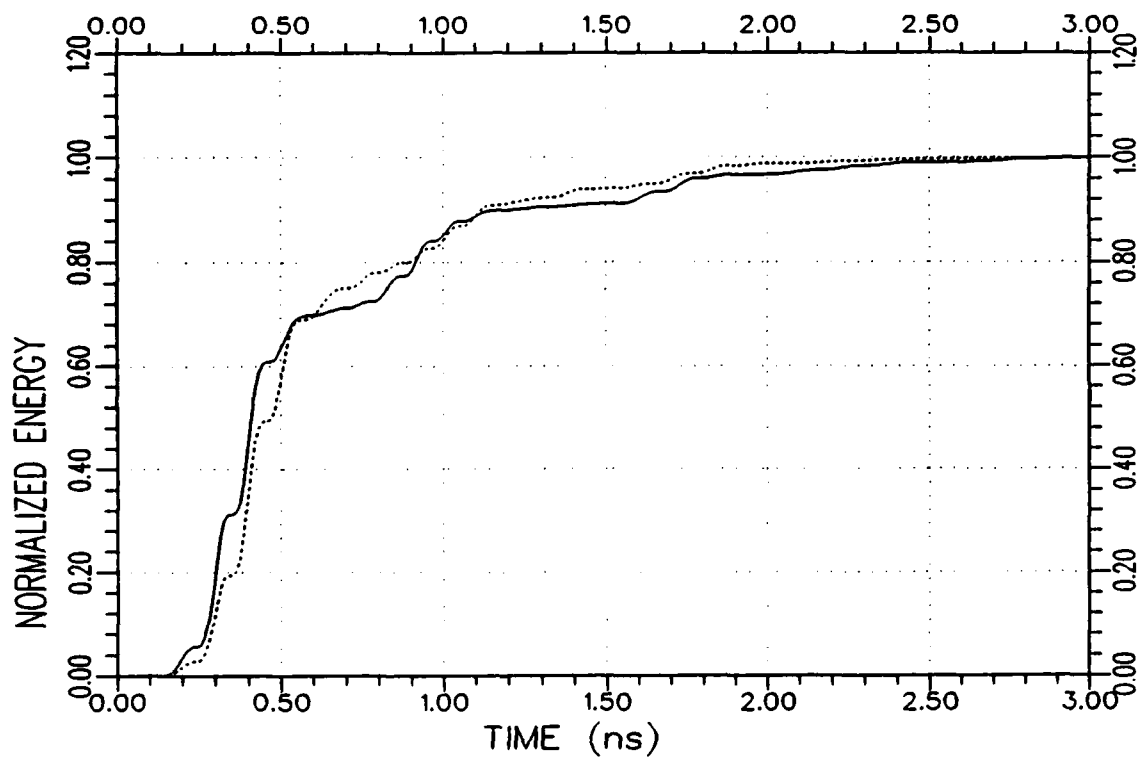
(b) Response energy curves

Figure 6.4. Continued.



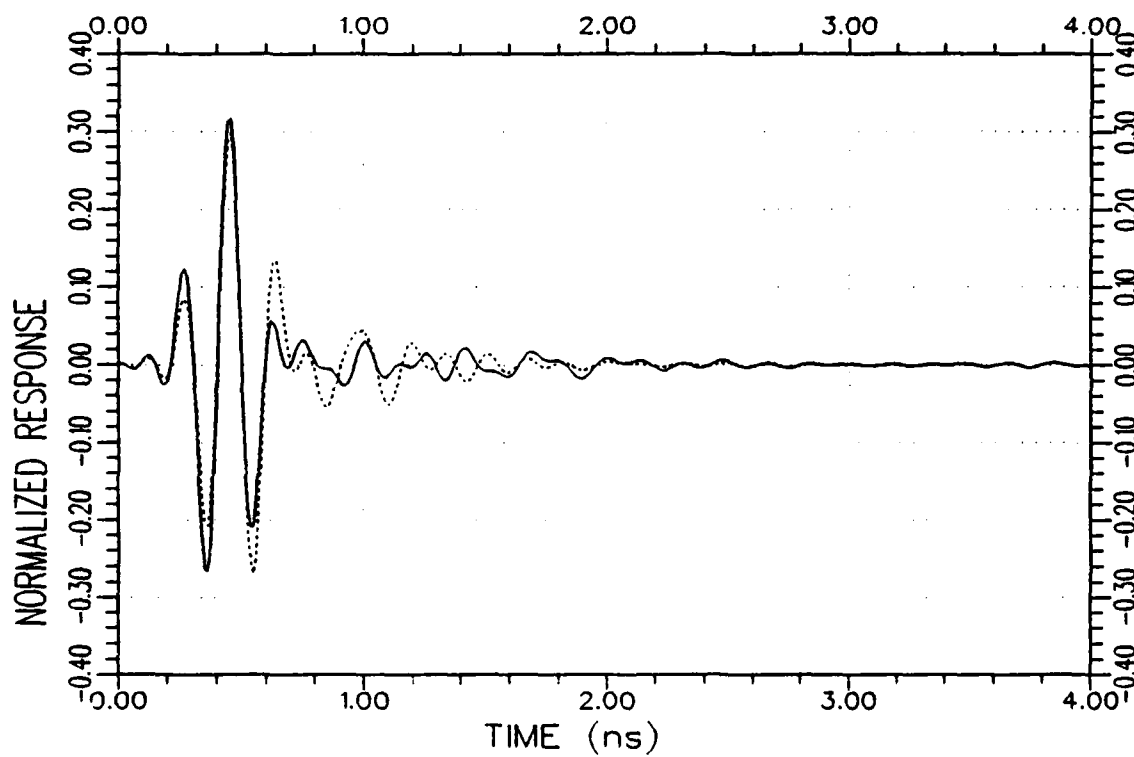
(a) Response waveforms

Figure 6.5. Normalized impulse response (.....) and K-pulse response (—) waveforms and their energy curves for the model tank LV_1 at $60^\circ/VP$.



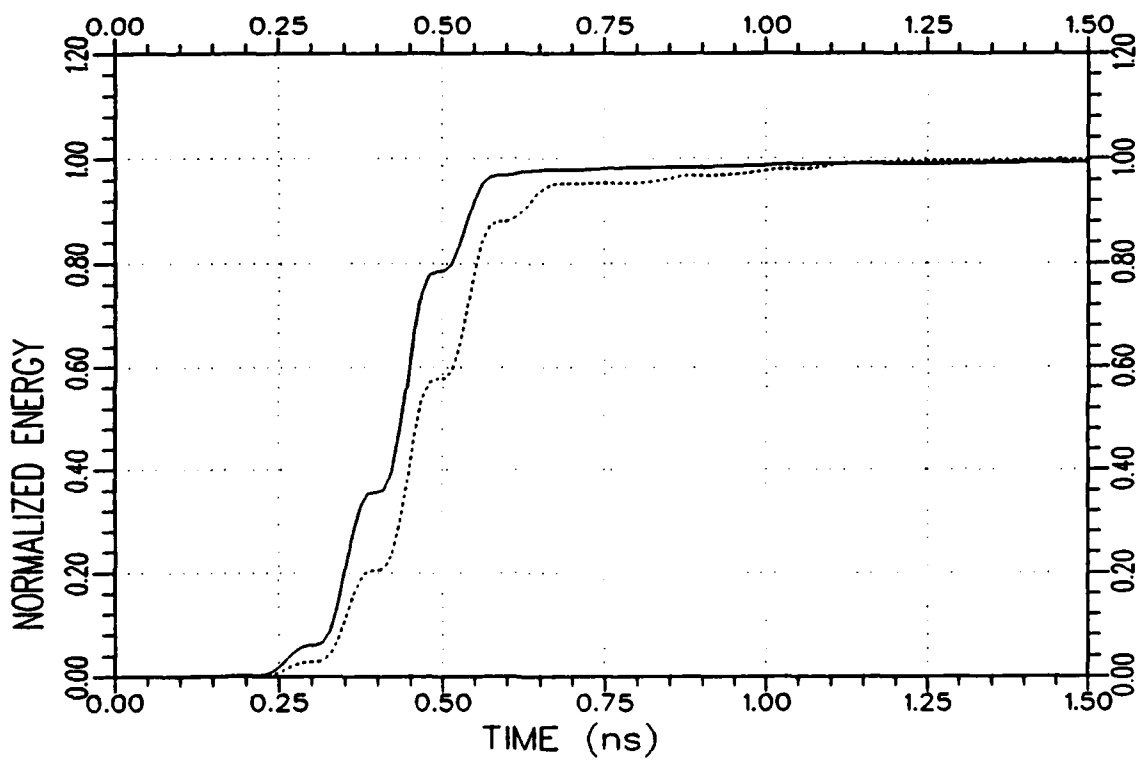
(b) Response energy curves

Figure 6.5. Continued.



(a) Response waveforms

Figure 6.6. Normalized impulse response (.....) and K-pulse response (—) waveforms and their energy curves for the model tank LV_1 at $90^\circ/VP$.



(b) Response energy curves

Figure 6.6. Continued.

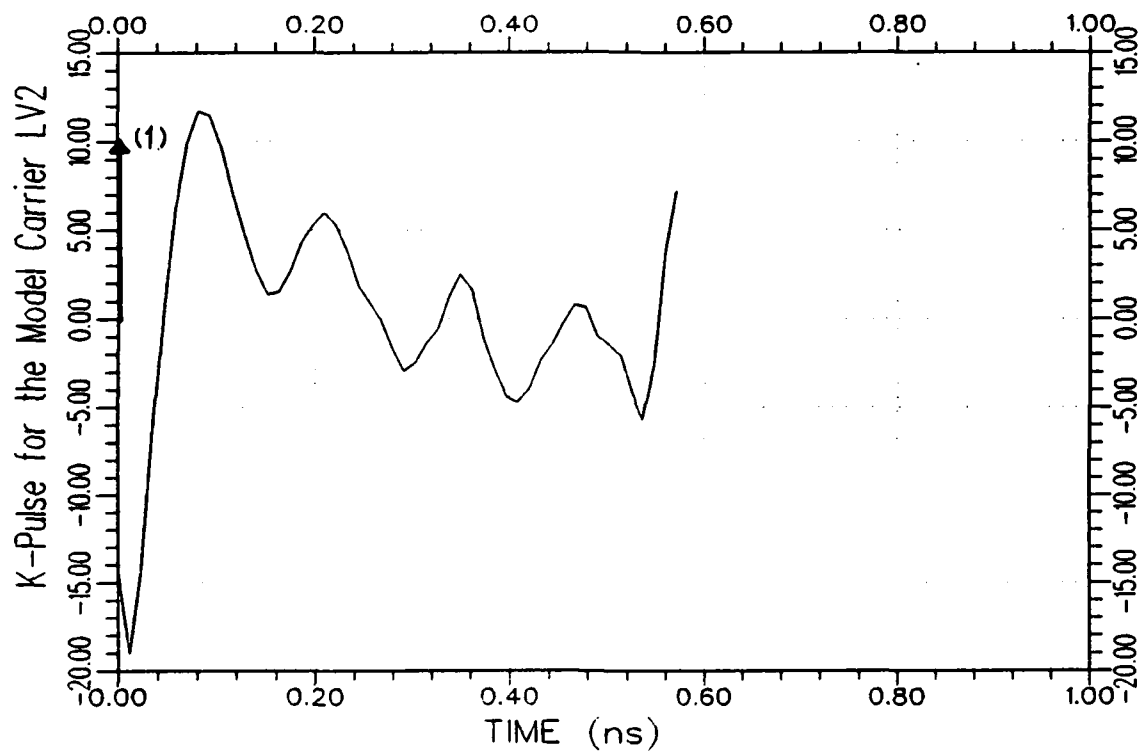
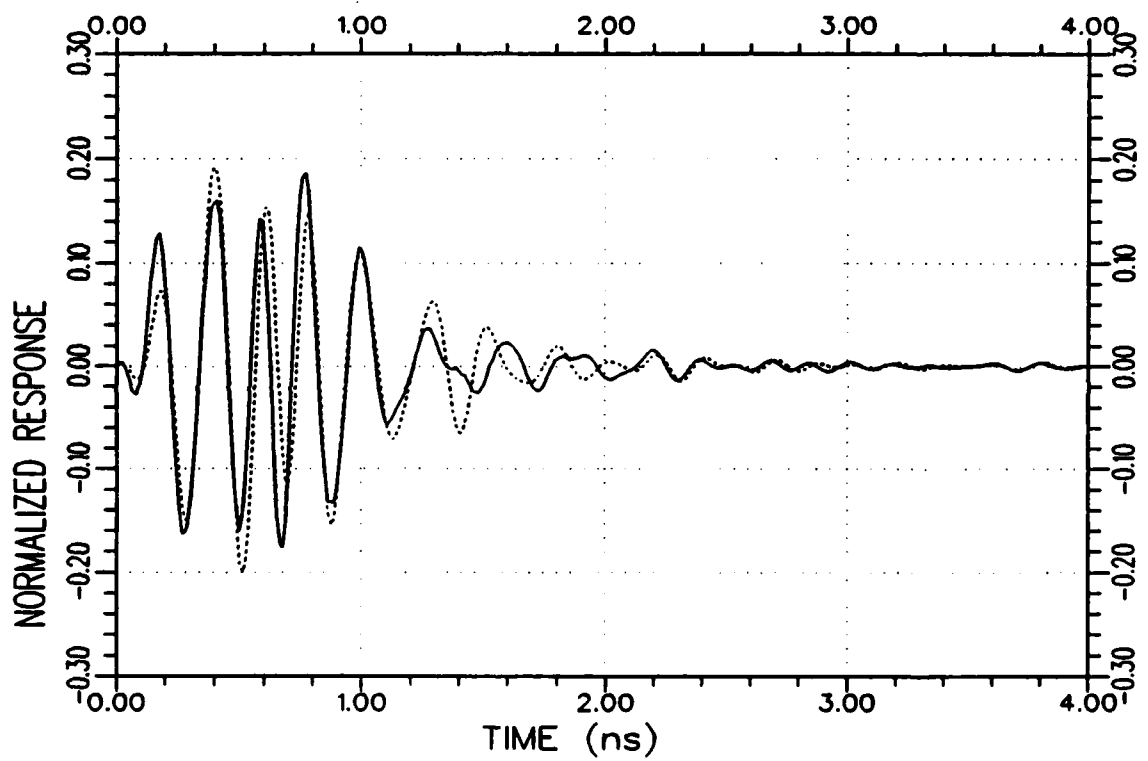
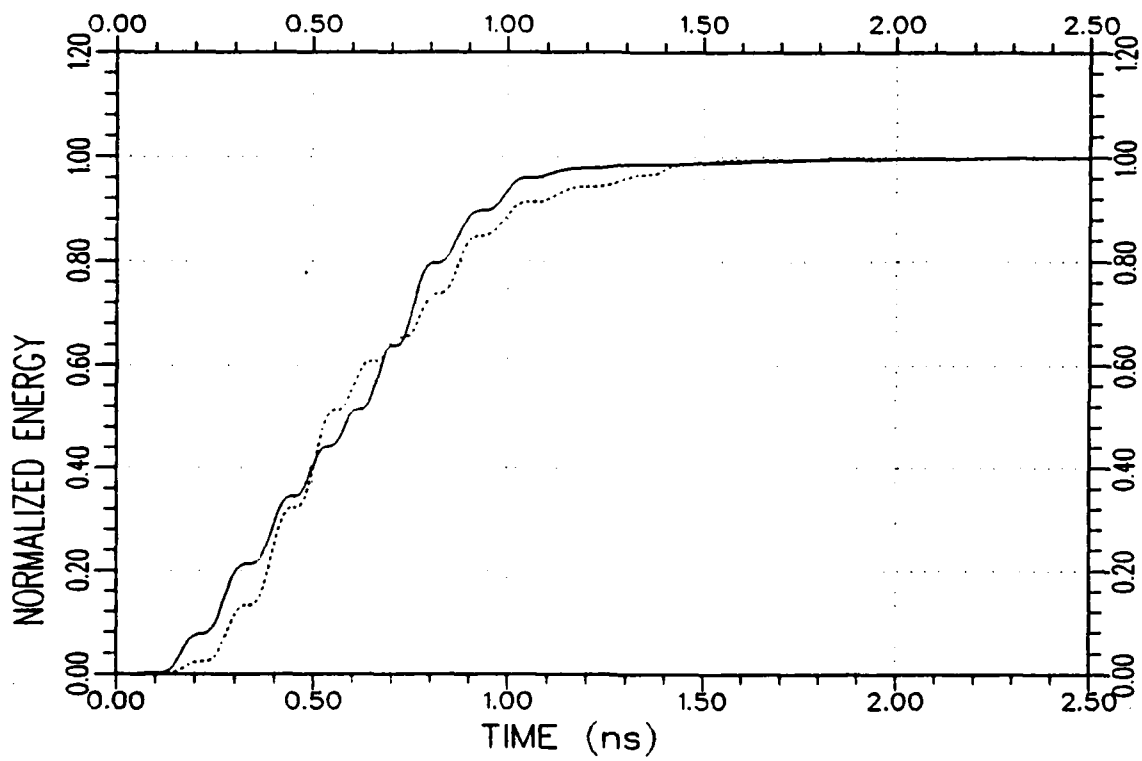


Figure 6.7. An approximate K-pulse waveform for the model carrier LV_2 estimated from the backscattered measurement data at $30^\circ/VP$ and $90^\circ/VP$ using a discrete representation for the continuous part of the K-pulse. (The $\delta(t)$ term of the K-pulse is symbolically shown by the arrow at $t=0$.)



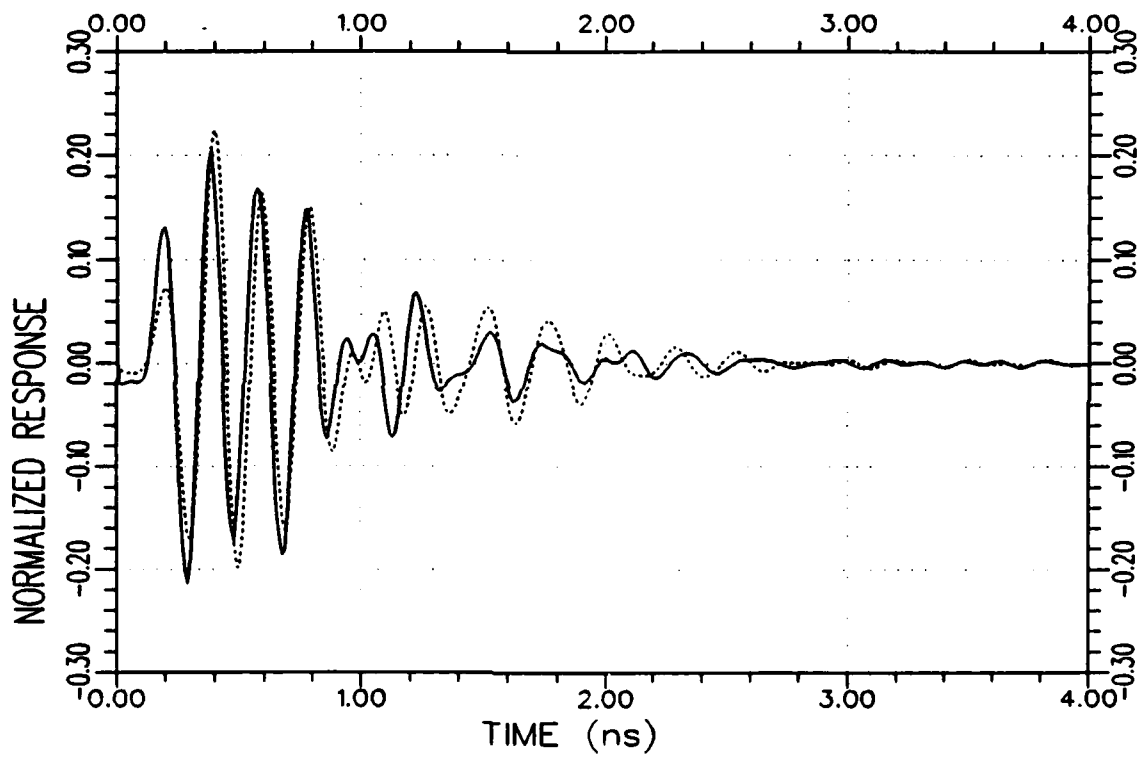
(a) Response waveforms

Figure 6.8. Normalized impulse response (.....) and K-pulse response (——) waveforms and their energy curves for the model carrier LV_2 at $0^\circ/VP$.



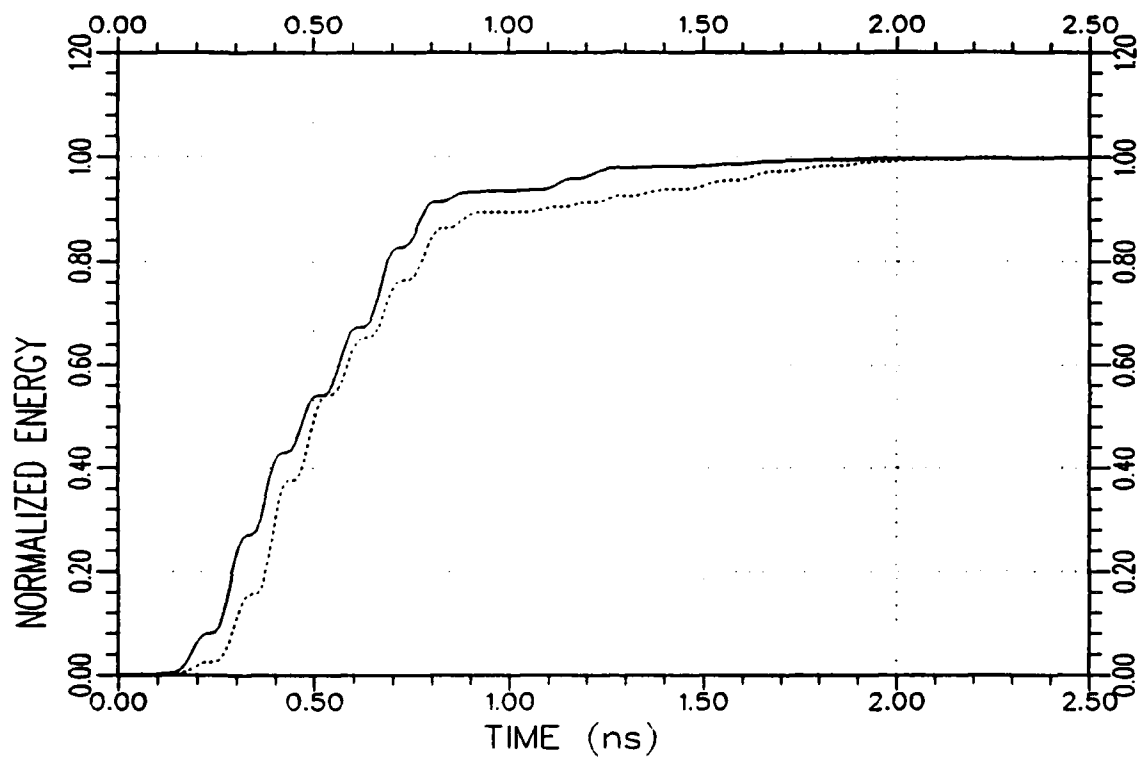
(b) Response energy curves

Figure 6.8. Continued.



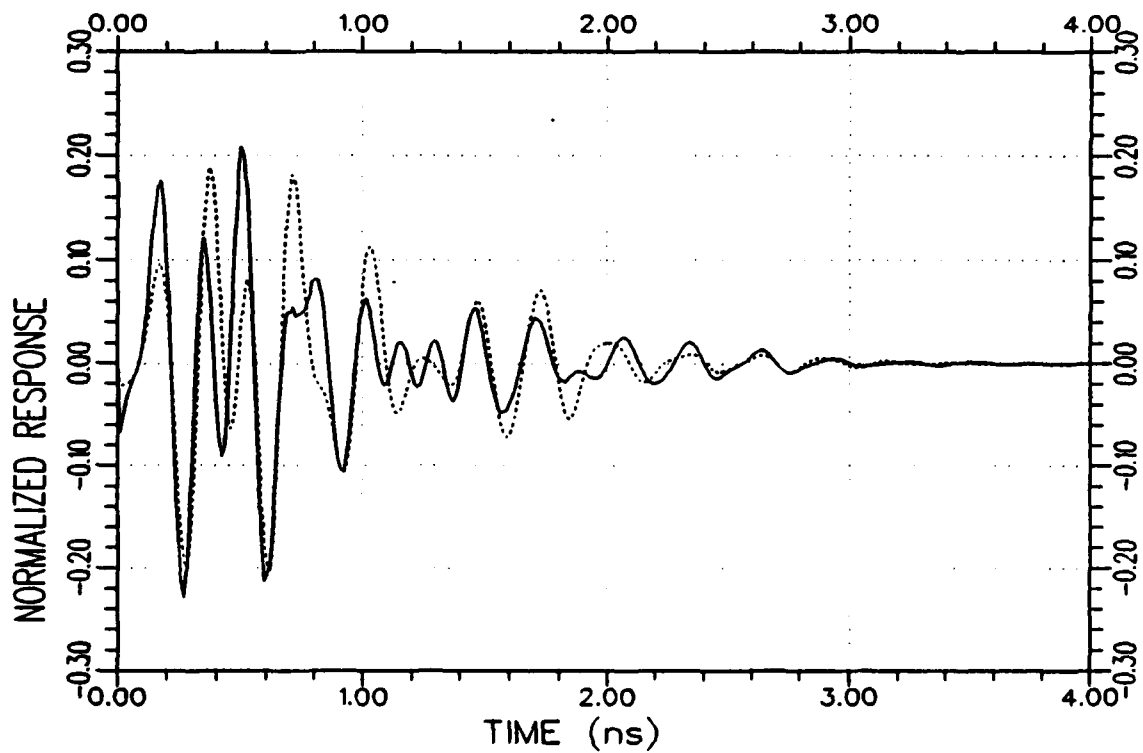
(a) Response waveforms

Figure 6.9. Normalized impulse response (.....) and K-pulse response (—) waveforms and their energy curves for the model carrier LV_2 at $30^\circ/VP$.



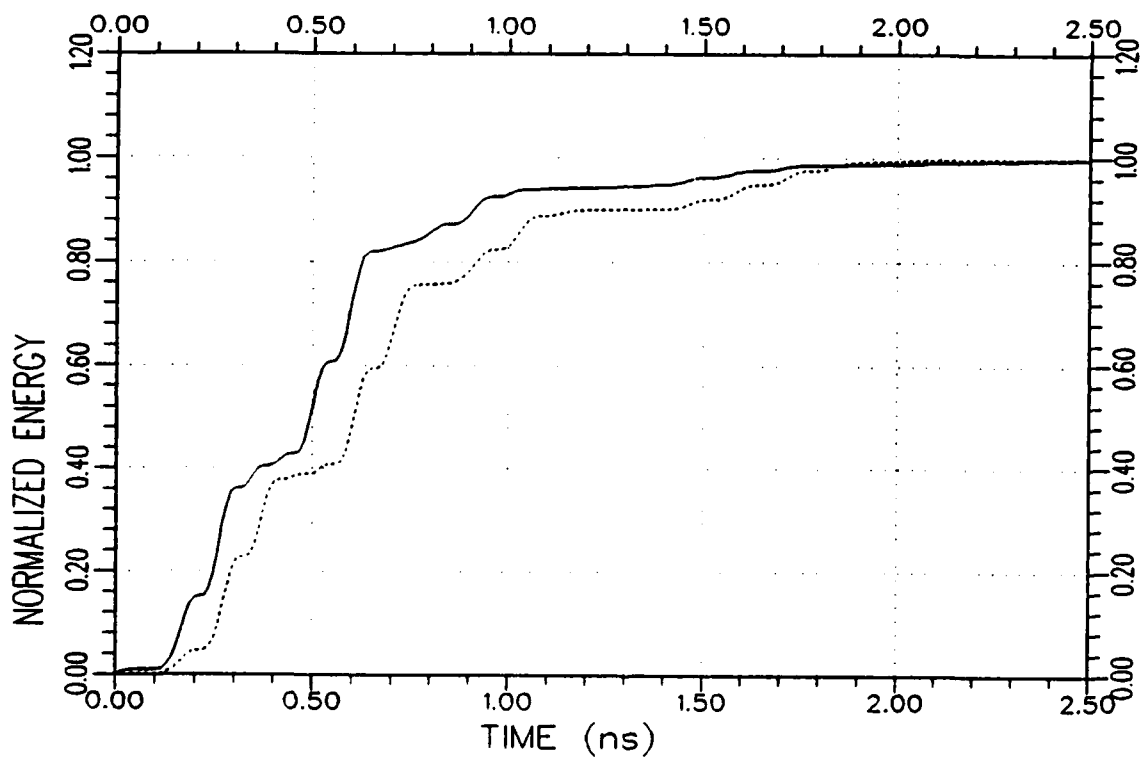
(b) Response energy curves

Figure 6.9. Continued.



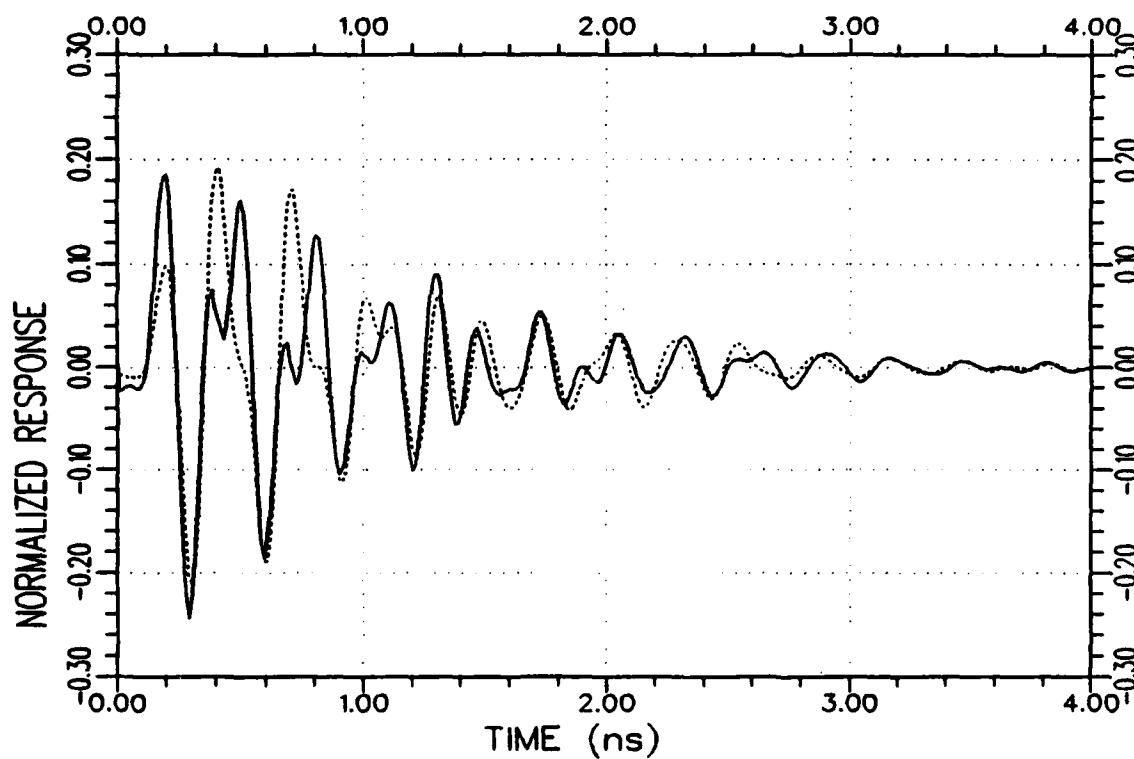
(a) Response waveforms

Figure 6.10. Normalized impulse response (·····) and K-pulse response (—) waveforms and their energy curves for the model carrier LV_2 at $45^\circ/VP$.



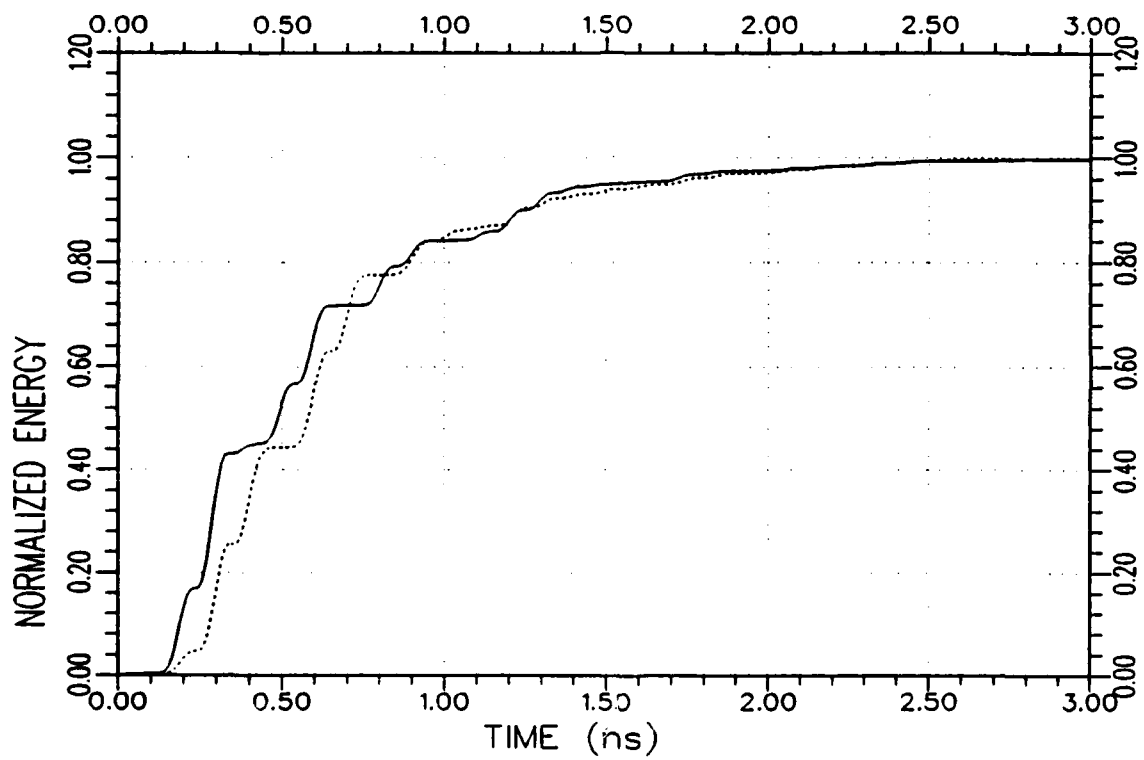
(b) Response energy curves

Figure 6.10. Continued.



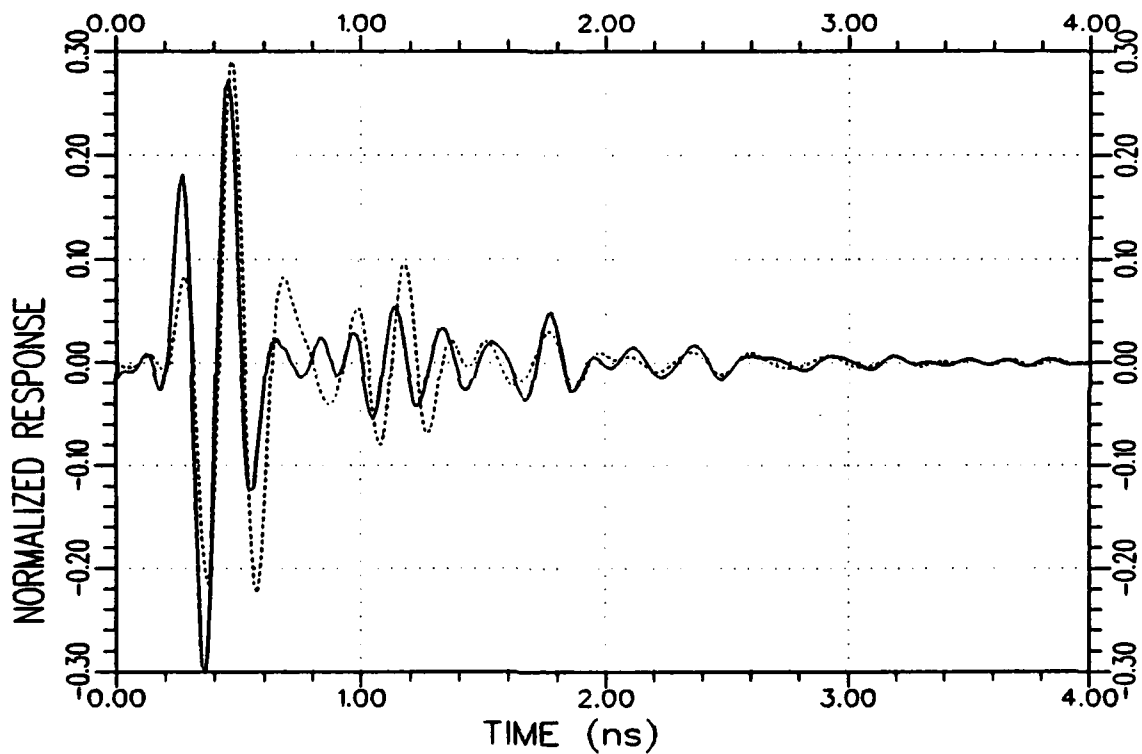
(a) Response waveforms

Figure 6.11. Normalized impulse response (.....) and K-pulse response (—) waveforms and their energy curves for the model carrier LV_2 at $60^\circ/VP$.



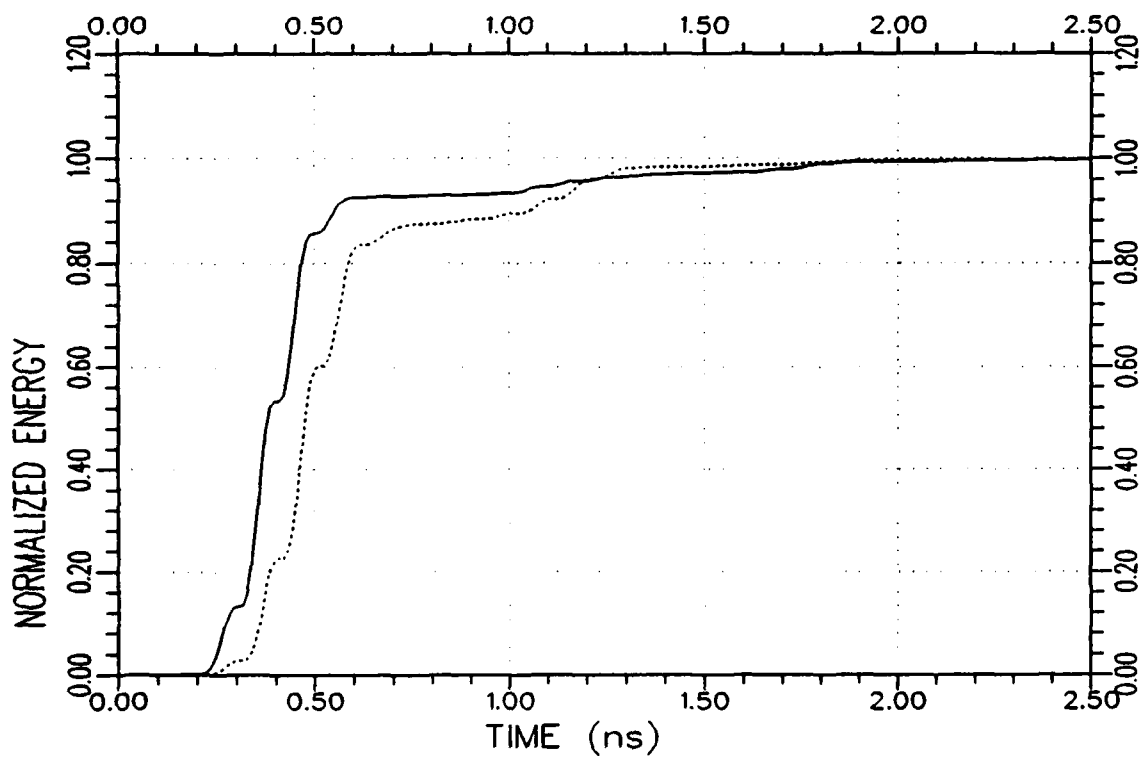
(b) Response energy curves

Figure 6.11. Continued.



(a) Response waveforms

Figure 6.12. Normalized impulse response (.....) and K-pulse response (—) waveforms and their energy curves for the model carrier LV_2 at $90^\circ/VP$.



(b) Response energy curves

Figure 6.12. Continued.

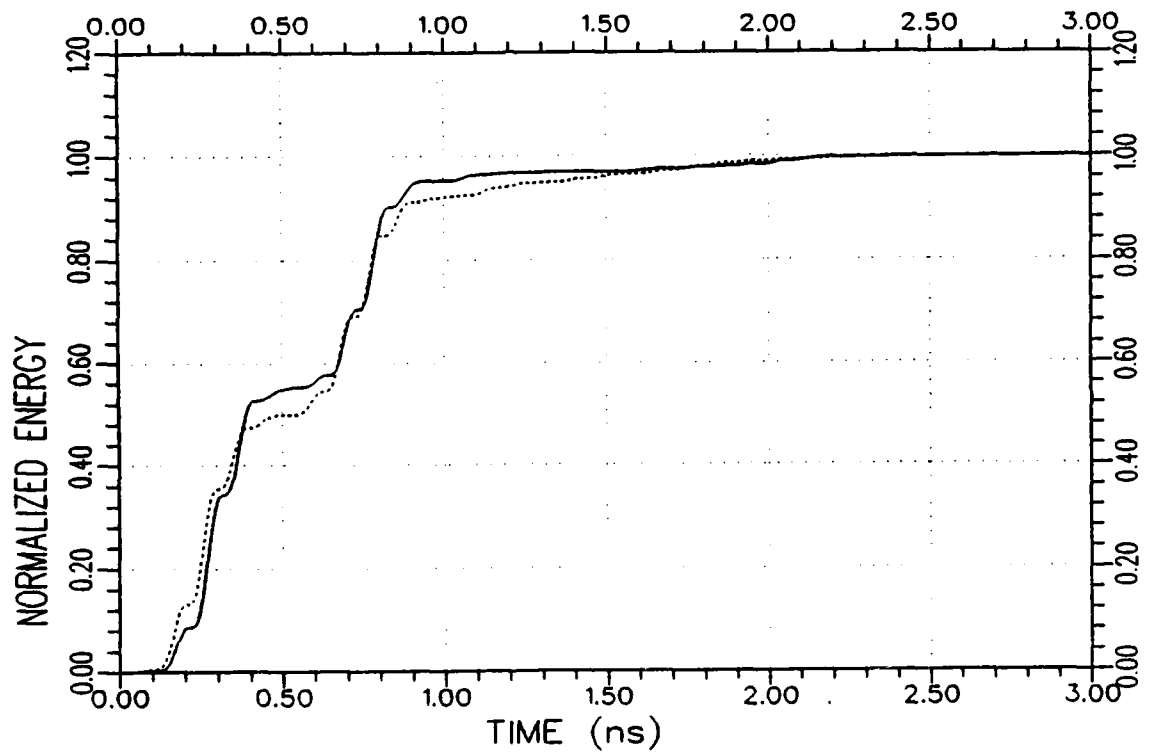


Figure 6.13. Normalized response energy curves of the test target LV₁ produced by the K-pulses of library targets LV₁ (—) and LV₂ (·····) at 100 VP.

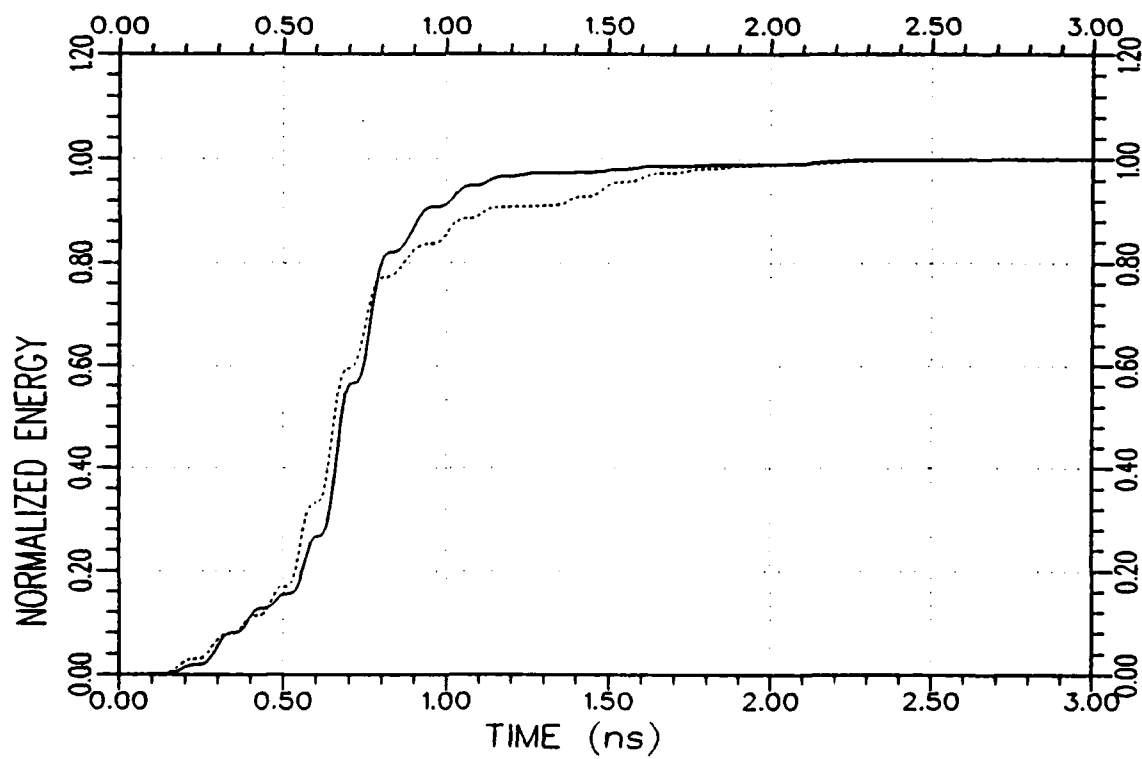


Figure 6.14. Normalized response energy curves of the test target LV₁ produced by the K-pulses of library targets LV₁ (—) and LV₂ (· · · · ·) at 30°/VP.

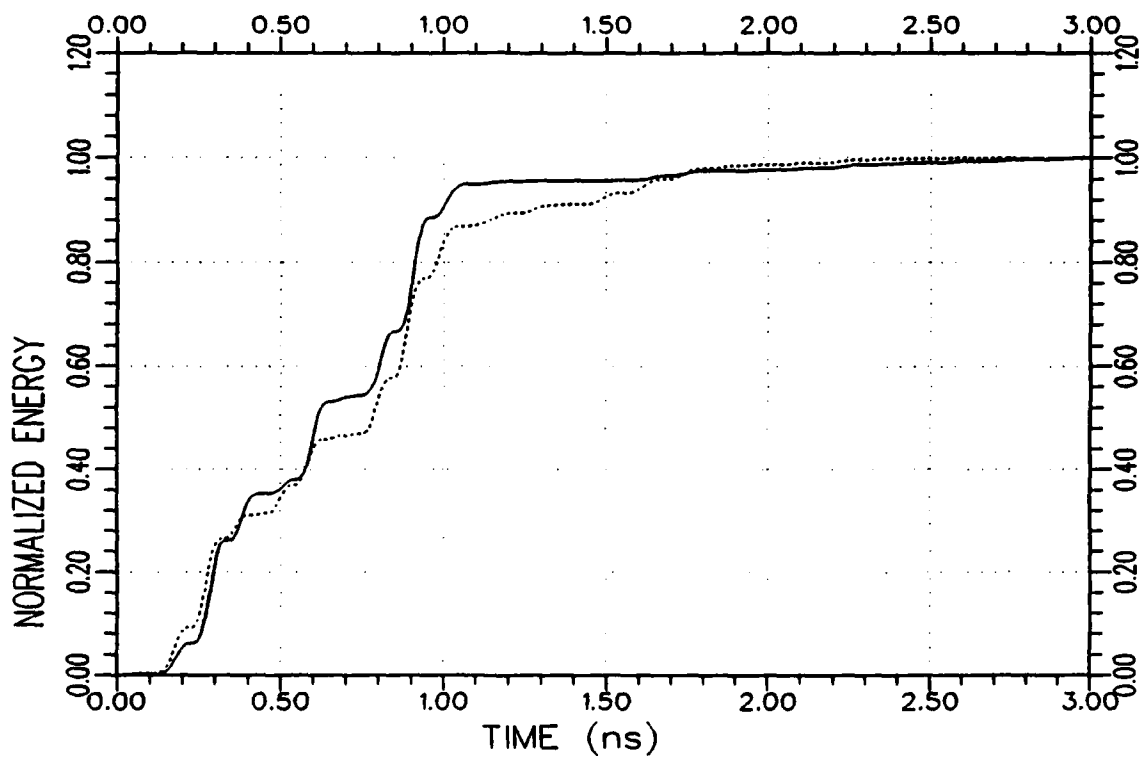


Figure 6.15. Normalized response energy curves of the test target LV_1 produced by the K-pulses of library targets LV_1 (—) and LV_2 (·····) at $45^\circ/VP$.

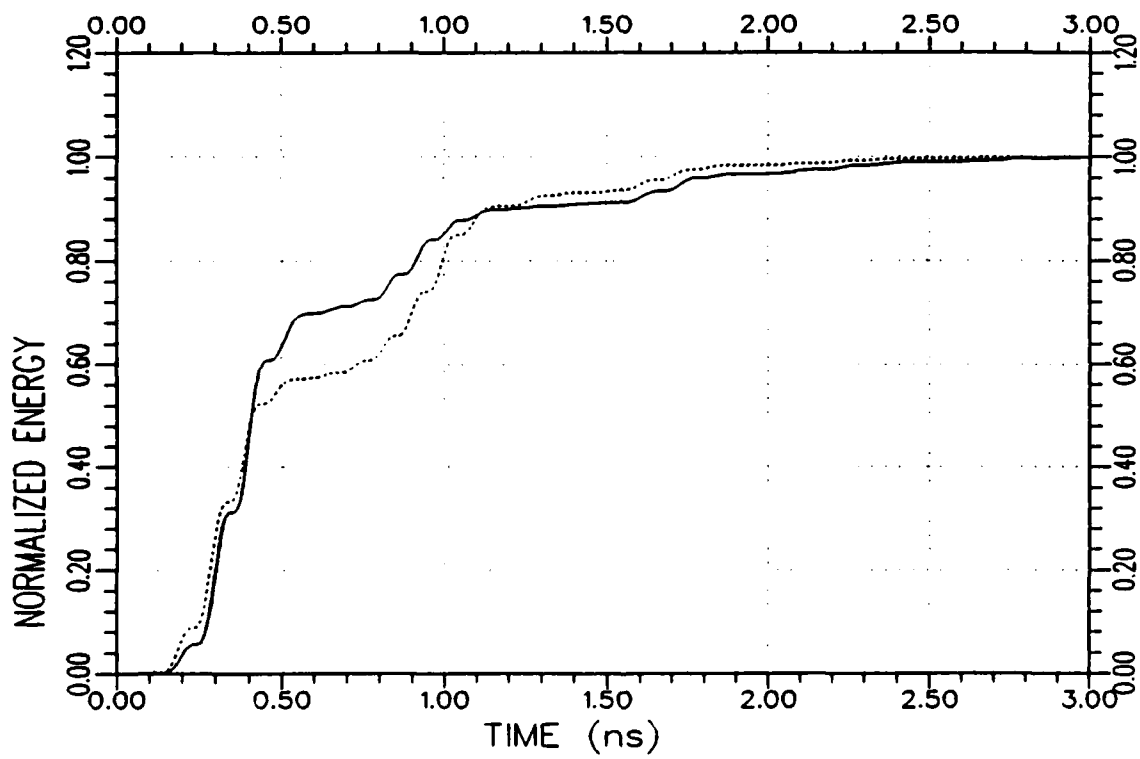


Figure 6.16. Normalized response energy curves of the test target LV₁ produced by the K-pulses of library targets LV₁ (—) and LV₂ (·····) at 60°/VP.

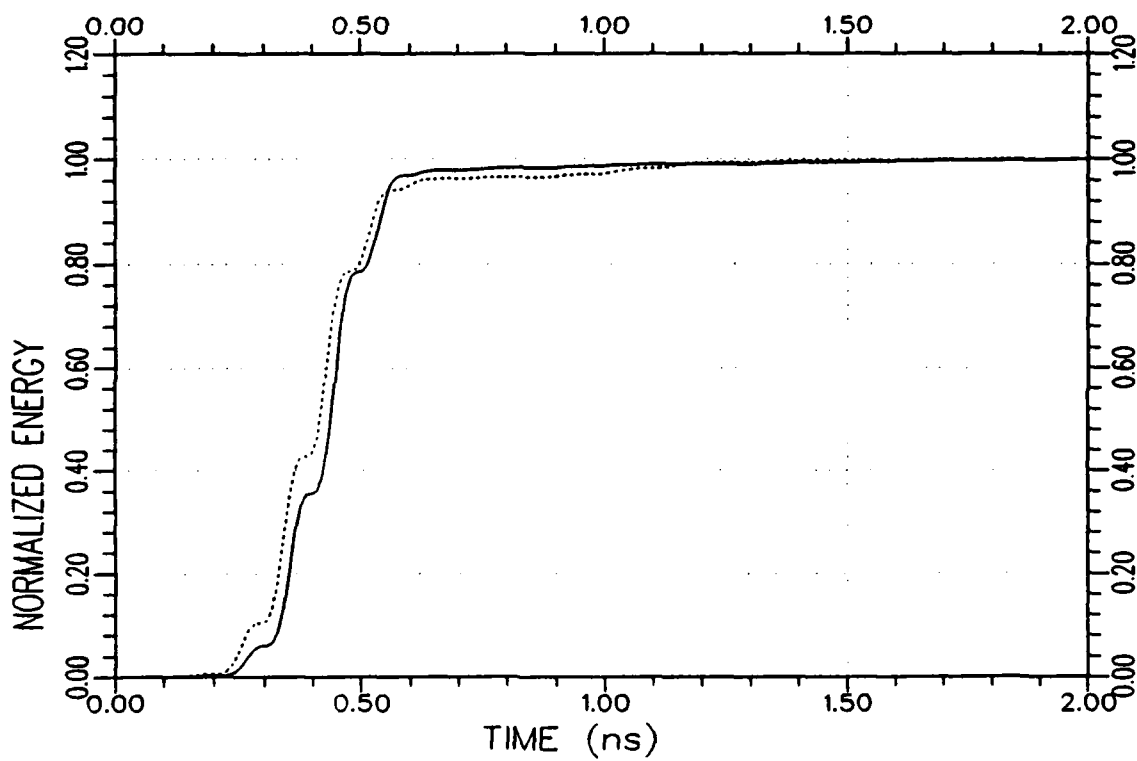


Figure 6.17. Normalized response energy curves of the test target LV₁ produced by the K-pulses of library targets LV₁ (—) and LV₂ (·····) at 90°/VP.

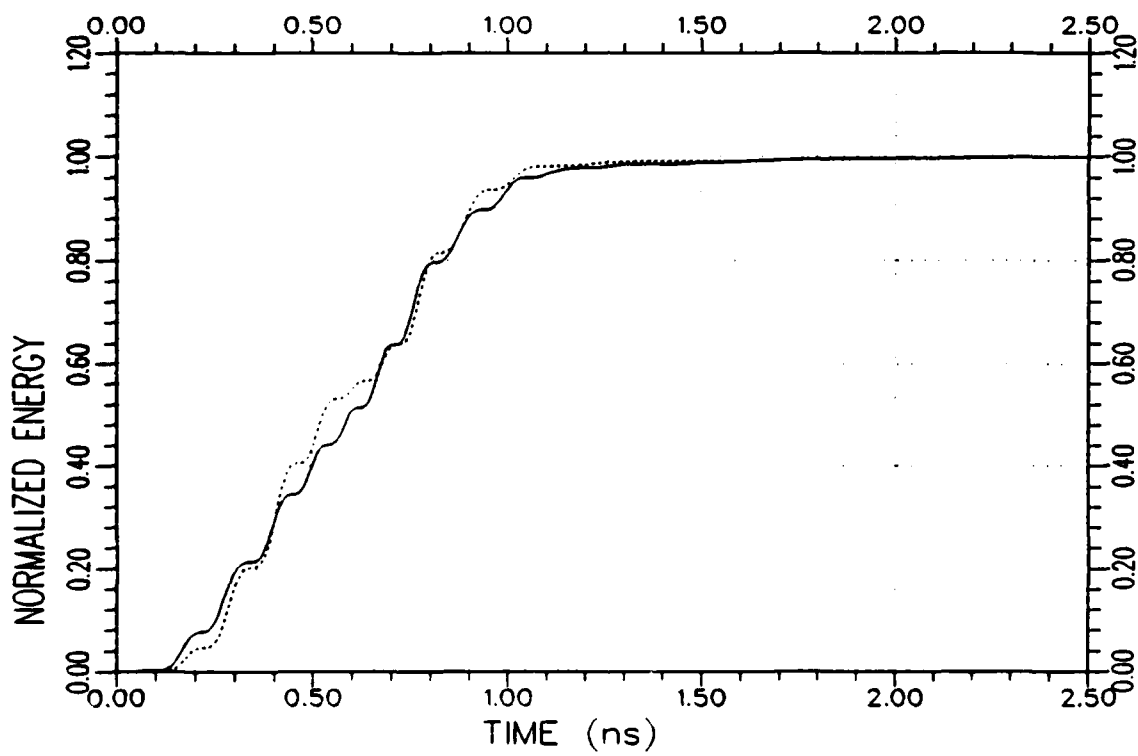


Figure 6.18. Normalized response energy curves of the test target LV₂ produced by the K-pulses of library targets LV₁ (.....)² and LV₂ (—) at 0°/VP.

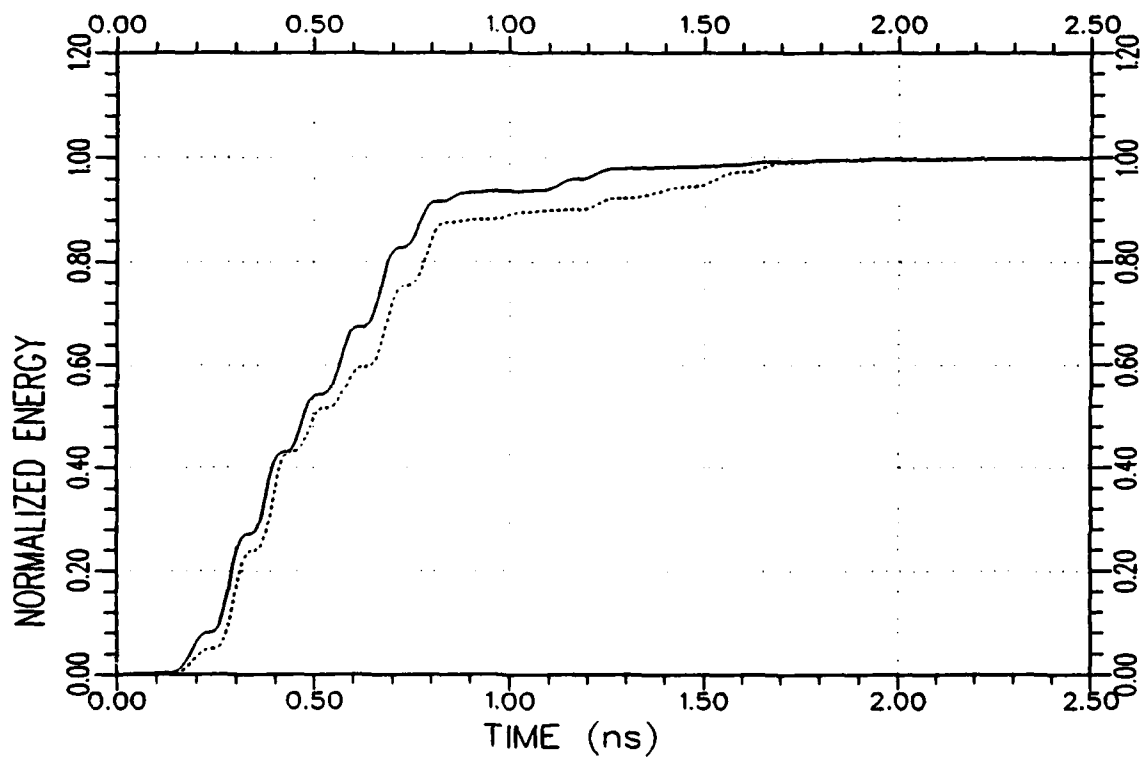


Figure 6.19. Normalized response energy curves of the test target LV₂ produced by the K-pulses of library targets LV₁ (.....) and LV₂ (—) at 30°/VP.

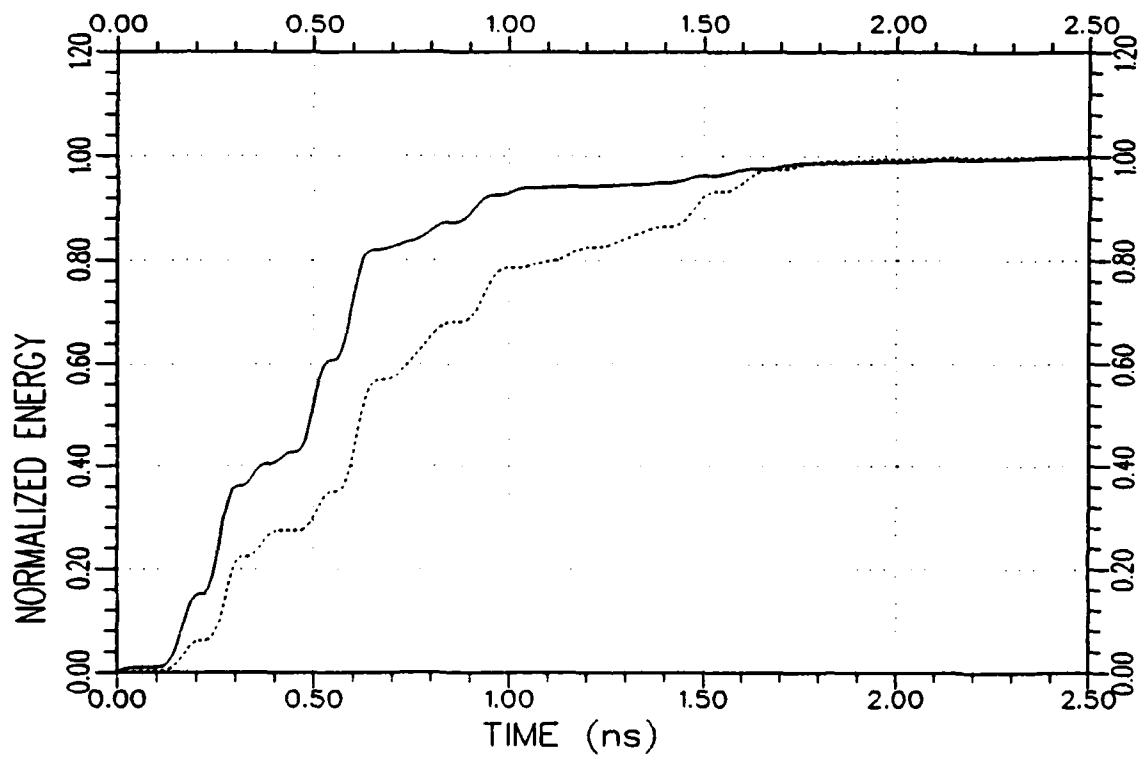


Figure 6.20. Normalized response energy curves of the test target LV₂ produced by the K-pulses of library targets LV₁ (.....) and LV₂ (—) at 45°/VP.

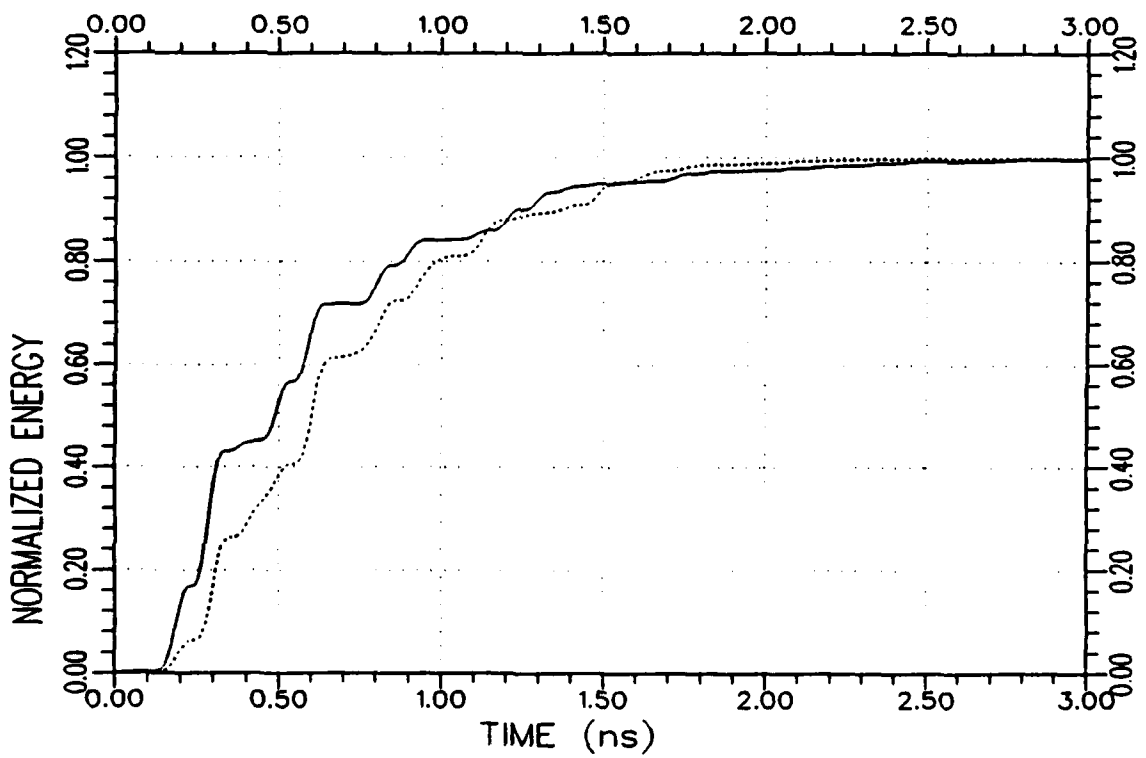


Figure 6.21. Normalized response energy curves of the test target LV₂ produced by the K-pulses of library targets LV₁ (.....)² and LV₂ (—) at 60°/VP.

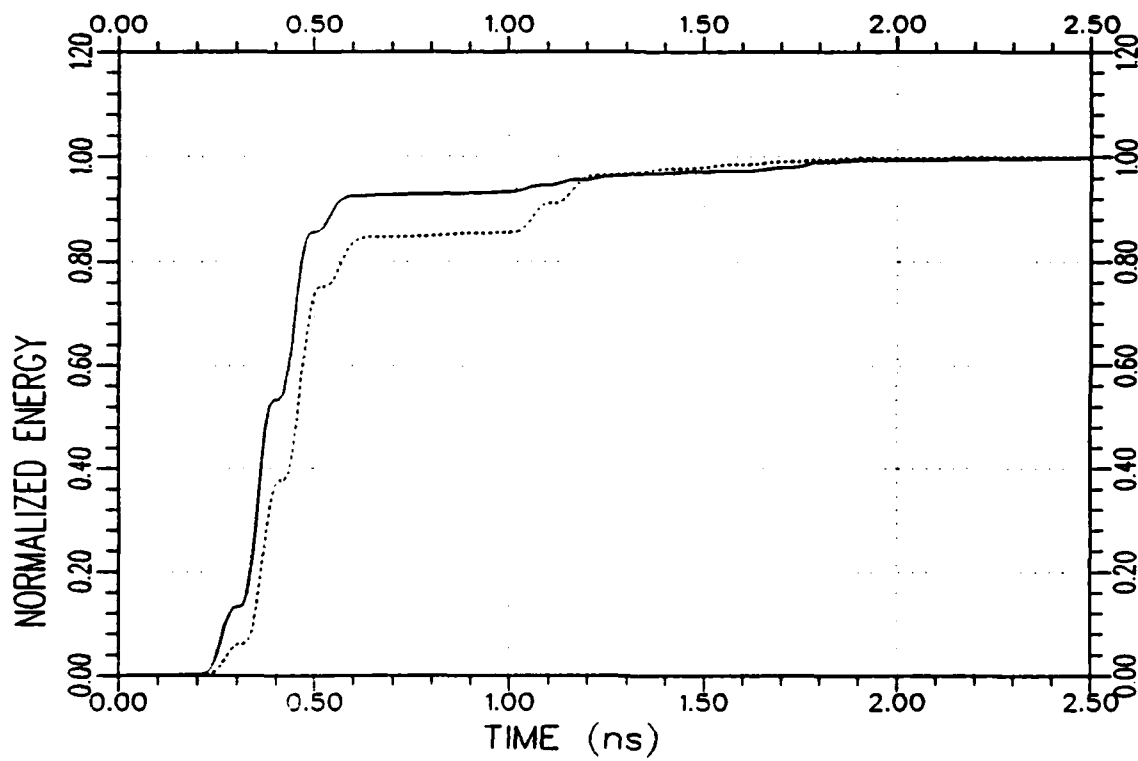
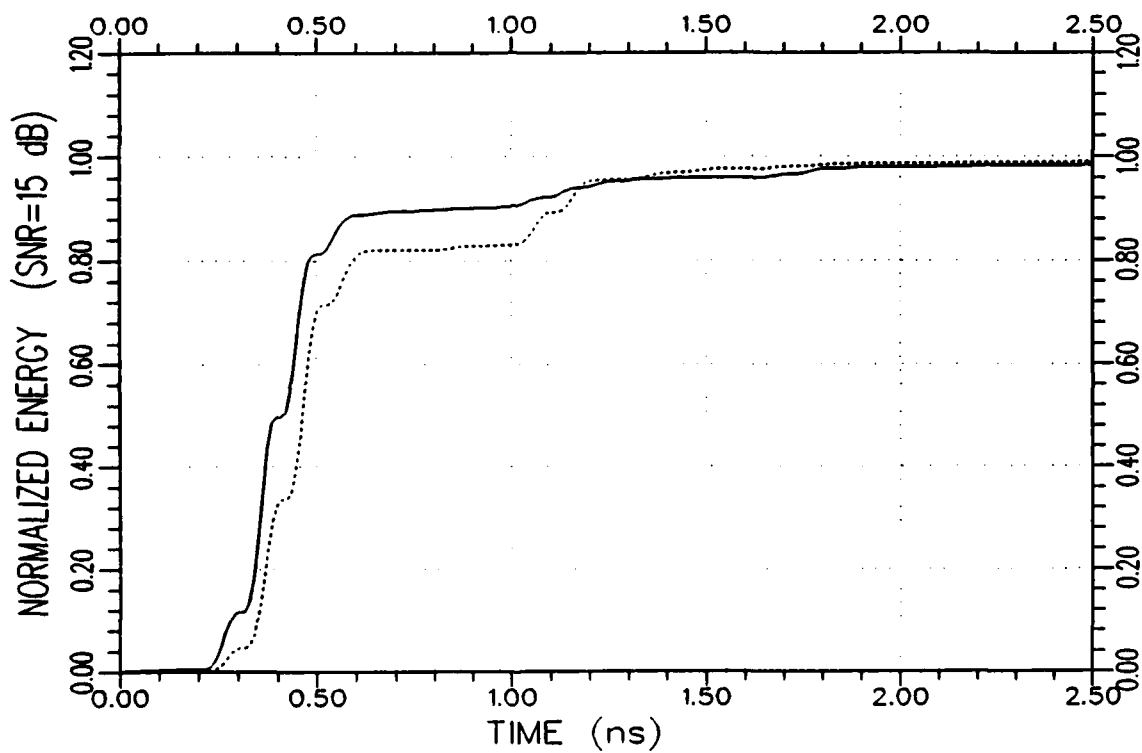
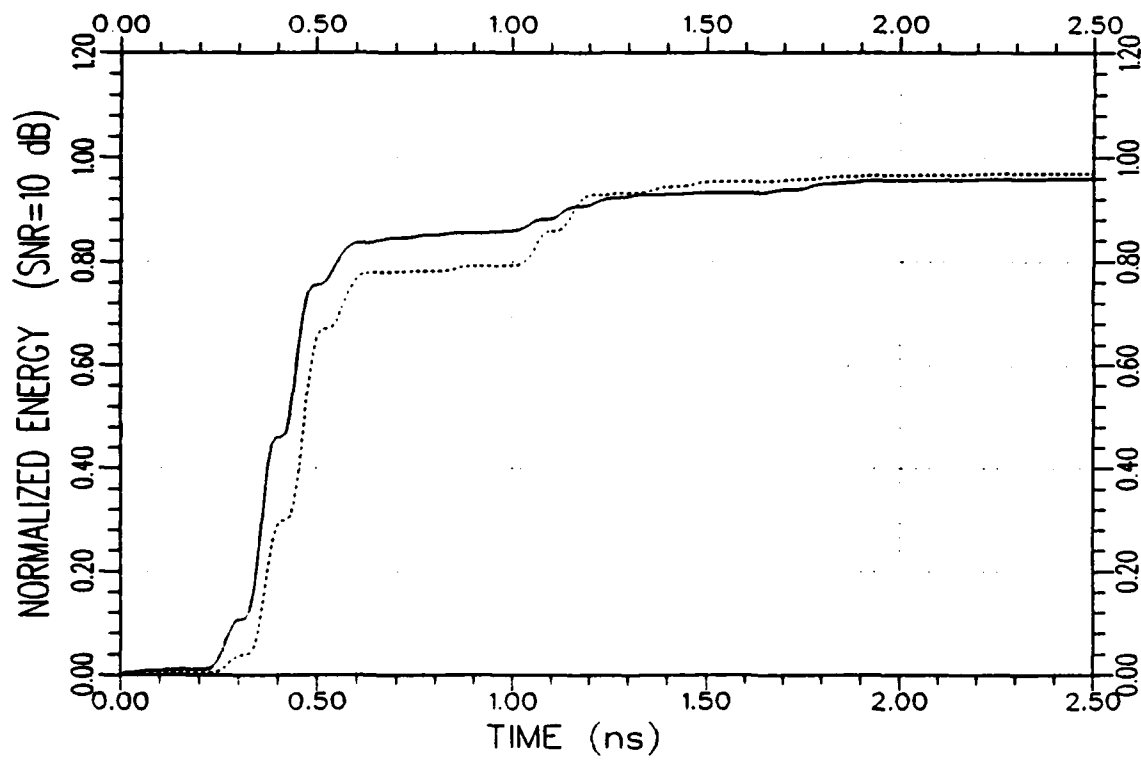


Figure 6.22. Normalized response energy curves of the test target LV₂ produced by the K-pulses of library targets LV₁ (.....) and LV₂ (—) at 90°/VP.



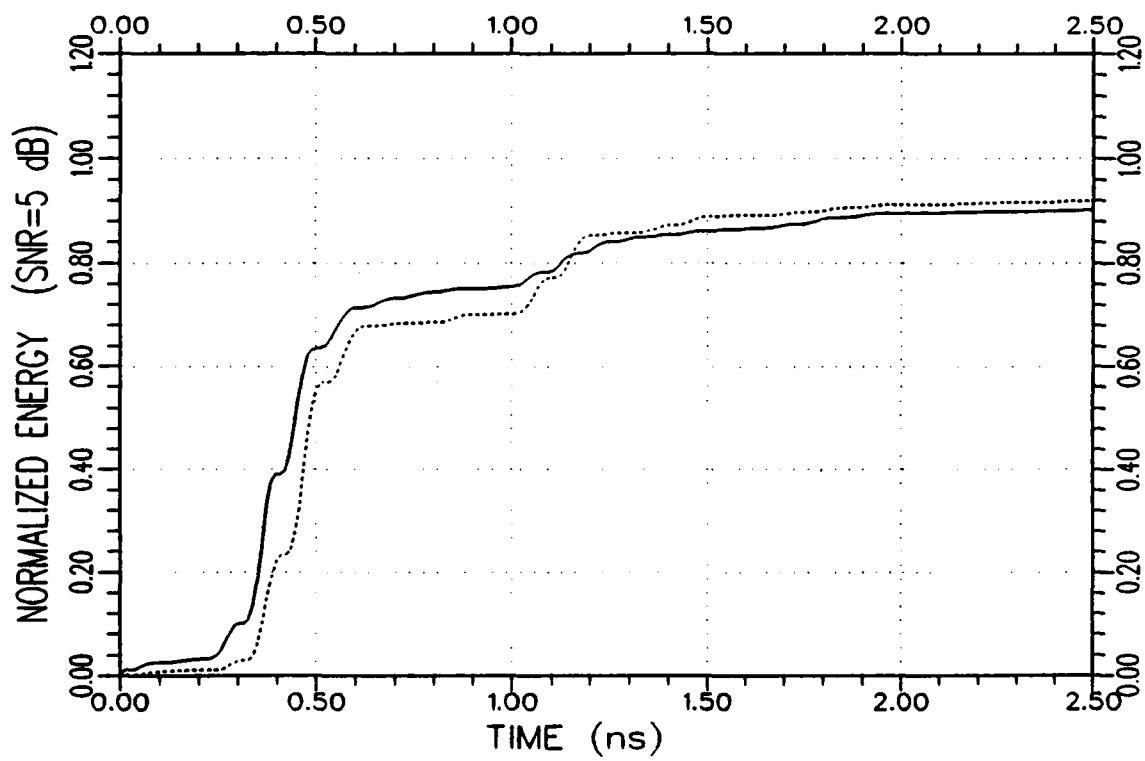
(a) for SNR = 15 dB

Figure 6.23. Normalized response energy curves of the test target LV_2 produced by the K-pulses of library targets LV_1 (.....)² and LV_2 (—) from some noisy backscattered data at $90^\circ/VP$.



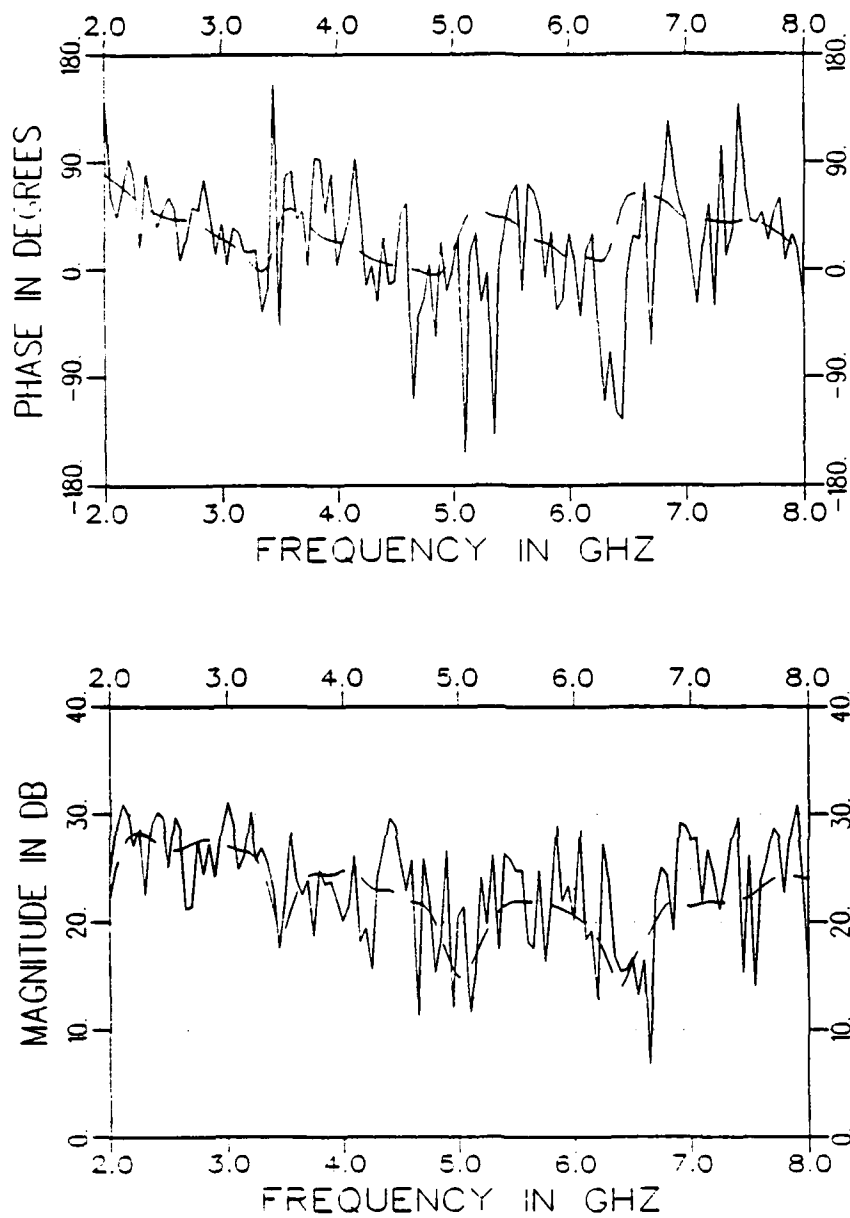
(b) for SNR = 10 dB

Figure 6.23. Continued.



(c) for SNR = 5 dB

Figure 6.23. Continued.



(d) The phase and amplitude plots of the noisy (—) and original (— —) backscattered data for SNR=5 dB

Figure 6.23. Continued.

CHAPTER VII
APPLICATIONS TO AIRCRAFT

In this chapter, applications of the proposed K-pulse estimation and target identification techniques are extended to aircraft targets. Approximate K-pulse waveforms of three small-scale electroplated commercial aircraft models, referred to as A_1 , A_2 and A_3 , are synthesized from their vertically-polarized backscattered measurement data in Sections A, B, and C of this chapter, respectively. Model frequency span of the data used in the following demonstrations is 1 to 8 GHz for all three targets and the data were measured on the Ohio State University compact RCS measurement range [53]. Demonstrations of target identification for aircraft models A_1 , A_2 and A_3 are presented in Section D for both (essentially) noise-free and noisy cases.

A. K-PULSE ESTIMATION FOR MODEL AIRCRAFT A_1

An approximate K-pulse waveform of target A_1 is synthesized using a discrete mathematical representation for the continuous function $k^c(t)$ (Equation (3.1)) whose time span is zero to 1.862 ns. The K-pulse duration is estimated to be $\frac{2L_1}{c}$ where L_1 is the length of the model aircraft. An optimal set of values for the equally-spaced samples $k_1^c, k_2^c, \dots, k_N^c$ ($N=60$) are obtained by minimizing the cost function (Equation (3.9)) with $a=1$, $b=0$ and $I=2$. The aspect/

polarization combinations used for K-pulse estimation are $0^\circ/VP$ and $90^\circ/VP$ where the aspect angles are measured from the nose-on direction. The cut-off times are set to 2.2 ns and 1.3 ns at aspect angles of 0° and 90° , respectively. The resultant K-pulse waveform is shown in Figure 7.1*. The complex zeros extracted from the Laplace transform of this K-pulse are listed in Table 7.1, and are expected to approximate a subset of the CNR frequencies of the model aircraft A_1 . The normalized impulse response and K-pulse response waveform pairs of target A_1 are plotted in part (a) of Figures 7.2 through 7.8 for aspect angles of 0° , 30° , 45° , 60° , 90° , 120° and 180° , respectively for vertical polarization. The corresponding normalized response energy curve-pairs are shown in part (b) of the same figures. Partial natural mode annihilation is easily observed at the aspect angles of 0° , 30° , 45° , 90° and 120° . Annihilation results at 60° and 180° are relatively poor, probably due to the fact that several complex pole-pairs of the target are strongly excited at these aspect angle/polarization combinations, but are not included in the zero pattern of the approximate K-pulse spectrum. However, these results are tolerable since the late-time energy content of the K-pulse response is not larger than that of the impulse response at neither the 60° nor the 180° cases (part (b) of Figures 7.5 and 7.8).

* All of the tables and figures are collected at the end of the chapter.

B. K-PULSE ESTIMATION FOR MODEL AIRCRAFT A_2

An approximate K-pulse waveform of the target, A_2 , is synthesized over the time interval zero to 2.117 ns. The duration of the K-pulse is estimated to be $\frac{2L_2}{c}$ where L_2 is the length of the model aircraft. As specified in Equation (3.1), the K-pulse waveform is composed of a unit strength impulse function $\delta(t)$ and then a continuous function $k^c(t)$ whose equally-spaced sample values $k_1^c, k_2^c, \dots, k_N^c$ ($N=68$) are estimated by minimizing the cost function of Equation (3.9). The backscattered data used for K-pulse estimation are measured at the aspect angles of 0° and 90° , both for vertical polarization. The corresponding cut-off times are set to 2.35 ns and 1.3 ns. The synthesized K-pulse waveform is shown in Figure 7.9. The normalized impulse response and K-pulse response pairs of the target, A_2 , are plotted in part (a) of Figures 7.10 through 7.15 at the aspect angles of $0^\circ, 45^\circ, 60^\circ, 90^\circ, 120^\circ$ and 180° , respectively for vertical polarization. These results show that the waveform given in Figure 7.9 is a generally useful approximation to the K-pulse of the target. The zeros of the Laplace transform of this K-pulse are extracted and listed in Table 7.2 as the approximate complex poles of the model aircraft, A_2 .

C. K-PULSE ESTIMATION FOR MODEL AIRCRAFT A_3

The K-pulse waveform of the model aircraft, A_3 , is estimated by using the same discrete mathematical representation for the K-pulse model as utilized in Sections A and B for targets A_1 and A_2 ,

respectively. The continuous part of the K-pulse waveform is represented by the sample values $k_1^c, k_2^c, \dots, k_N^c$ ($N=100$). The K-pulse duration is estimated as $\frac{2L_3}{c} \approx 2.88$ ns where L_3 is the length of the target. The data used for K-pulse synthesis are from $0^\circ/VP$ and $90^\circ/VP$; and the corresponding cut-off times are set to 2.3 ns and 1.25 ns. The unknown sample values of the K-pulse are estimated via minimization of the previously specified cost function, \tilde{J} , (Equation (3.9)) and the resultant approximate K-pulse waveform is shown in Figure 7.16. Figures 7.17 through 7.23 show the pairs of normalized K-pulse response and impulse response waveforms of the target, A_3 , as well as the associated normalized response energy curves at the aspect angles of $0^\circ, 30^\circ, 45^\circ, 60^\circ, 90^\circ, 120^\circ$ and 180° for vertical polarization. Both the response plots and the energy plots show that the estimated K-pulse waveform is useful in partially annihilating the late-time natural oscillations of the target's response at almost all test aspects. Results look especially good for the $0^\circ, 45^\circ, 60^\circ, 90^\circ$ and 120° cases. Estimated pole-pairs for the target, A_3 , are given in Table 7.3. It should also be noted that the K-pulse of model aircraft, A_3 , is estimated from a measurement data with a frequency span 1 GHz to 8 GHz. At the lowest measurement frequency, the wavelength is 30 cm which is about 70% of the overall target length. Therefore, there is a strong possibility that the list of extracted pole values given in Table 7.3 does not include some dominant pole-pairs related to the fuselage and perhaps the wings of the aircraft. The same argument is also valid for the pole extraction results of Sections A and B (for targets A_1 and A_2 ,

respectively) since this 30 cm wavelength at the lowest available measurement frequency is about 90% of the overall length of target A_2 and approximately equal to the length of target A_1 .

D. TARGET IDENTIFICATION

The K-pulse library of this section is composed of the K-pulse waveforms of model aircraft A_1 , A_2 and A_3 , which are shown in Figures 7.1, 7.9 and 7.16, respectively. All three targets are geometrically complicated low-Q objects. For low-Q targets, even small variations in the late-time response waveforms or in the corresponding normalized energy curves play an important role in target identification. The unknown target of the identification demonstrations is model aircraft A_1 in Figures 7.24 through 7.30; A_2 in Figures 7.31 through 7.36; and A_3 in Figures 7.37 through 7.43. The aspect angle and polarization combinations of the test data used in these examples are indicated in the figure captions. As previously mentioned, the data used in the demonstrations of this chapter were measured on the OSU Compact Range where the noise contributions were not absolutely zero but extremely small as compared, for example, to real-world radar measurements. To make the demonstrations more realistic, certain amounts of uncorrelated random Gaussian noise (generated from different seeds) are added to the real and imaginary parts of the backscattered frequency domain data which are used in Figures 7.24 through 7.43. In each case, the target identification procedure is repeated for three different values of SNR; infinite (without adding any noise to the original measurement data), 15 dB and 11 dB. All of the results for the SNR=11 dB case are shown

in Figures 7.24 through 7.43, while the results obtained for the SNR=15 dB and SNR= ∞ cases are presented only when they lead to different identification decisions as compared to the SNR=11 dB case, for the sake of brevity. Most of the figures are plotted on a magnified scale showing the important high energy level variations of the response energy curves in detail. Full scale versions of the energy plots and the phase-magnitude plots for the noise-free and noise-contaminated frequency domain data are included in only several cases in order to keep the number of figures at a reasonable value but yet to give the readers a general idea about what these plots look like.

The identification results for SNR= ∞ show that the unknown target can be identified correctly from the comparison of normalized response energy curves produced by the library K-pulses in seventeen cases (at all testing aspect angles for vertical polarization when the unknown target is A_1 or A_2 ; and at 0° , 30° , 45° and 60° when A_3 is the test target) out of twenty. There is no incorrect identification observed. At 90° , 120° and 180° aspect angles with A_3 being the unknown target, the identification decision remains ambiguous between library targets A_2 and A_3 while library target A_1 can be definitely eliminated as not being matched to the unknown target.

As the SNR is decreased to 15 dB, the identification results summarized in the previous paragraph deteriorate somewhat so that the unknown target in question cannot be identified anymore with certainty at 60° /VP when the test target is either A_1 or A_2 . In the former case, the result is totally ambiguous (Figure 7.27b) while in the latter case, the mismatched library target A_3 can be eliminated as not being

the unknown target but A_1 cannot be ruled out (Figure 7.33b). The rest of the identification results are not affected drastically by the added noise.

Finally, at the SNR of 11 dB, the number of cases for which the identification procedure yields correct results drops to twelve. These cases are demonstrated in Figures 7.24, 7.26, 7.28 and 7.29 for test target A_1 at the aspect angles of 0° , 45° , 90° and 120° , respectively; in Figures 7.31, 7.32, 7.34 and 7.35 for test target A_2 at 0° , 45° , 90° and 120° , respectively; and in Figures 7.37 through 7.40 for test target A_3 at 0° , 30° , 45° and 60° , respectively. The results are completely ambiguous at $180^\circ/VP$ for test targets A_1 (in Figure 7.30a) and A_2 (in Figure 7.36a). A false identification occurred in two cases: Aircraft A_1 is incorrectly identified as A_2 at $60^\circ/VP$ as shown in Figure 7.27a; and aircraft A_3 is identified as A_2 at $180^\circ/VP$ as shown in Figure 7.43a. In the remaining four cases, only one of the mismatched library targets can be ruled out by the identification scheme. The identification decision is ambiguous between library targets A_1^* and A_3 at $30^\circ/VP$ in Figure 7.25a; between A_1 and A_2^* at $60^\circ/VP$ in Figure 7.33a; between A_2 and A_3^* at $90^\circ/VP$ and $120^\circ/VP$ in Figures 7.41a and 7.42b, respectively. (The superscript '*' denotes the test target of these demonstrations.)

In summary, the correct identification score is observed to be 85%, 75% and 60% at the SNR values of infinity, 15 dB and 11 dB, respectively, while the false identifications occur only when SNR=11 dB with a score of about 10%. It should be noted that these identification scores do not show the actual performance limits of the suggested

identification scheme. The correct identification scores are expected to increase for better library K-pulse estimates.

Table 7.1

Poles of Model Aircraft A₁
 As Extracted from the K-pulse shown in Figure 7.1

10^9 Nepers/s; GHz scale	sL_1/c scale
.	.
.	.
-0.203 ± j 1.581	-1.188 ± j 9.252
-0.314 ± j 2.380	-1.837 ± j13.927
-0.253 ± j 2.583	-1.480 ± j15.115
-0.236 ± j 3.137	-1.381 ± j18.357
-0.339 ± j 3.754	-1.984 ± j21.967
-0.509 ± j 4.159	-2.979 ± j24.326
-0.329 ± j 4.643	-1.925 ± j27.170
-0.494 ± j 5.322	-2.891 ± j31.143
-0.397 ± j 5.768	-2.323 ± j33.753
-0.516 ± j 6.208	-3.109 ± j36.328
-0.295 ± j 6.674	-1.726 ± j39.055
-0.466 ± j 7.358	-2.727 ± j43.057
.	.
.	.

Table 7.2

Poles of Model Aircraft A_2
 As Extracted from the K-pulse shown in Figure 7.9

10^9 Nepers/s; GHz scale	sL_2/c scale
.	.
.	.
-0.209 ± j 1.564	-1.390 ± j10.400
-0.285 ± j 1.923	-1.895 ± j12.787
-0.299 ± j 2.511	-1.988 ± j16.697
-0.310 ± j 3.119	-2.061 ± j20.740
-0.438 ± j 3.374	-2.913 ± j22.436
-0.463 ± j 3.705	-3.079 ± j24.637
-0.240 ± j 4.307	-1.596 ± j28.690
-0.275 ± j 4.931	-1.829 ± j32.790
-0.320 ± j 5.619	-2.128 ± j37.365
-0.228 ± j 6.206	-1.516 ± j41.268
-0.214 ± j 6.705	-1.423 ± j44.586
-0.399 ± j 7.275	-2.653 ± j48.376
-0.382 ± j 7.787	-2.540 ± j51.781
.	.
.	.
.	.

Table 7.3

Poles of Model Aircraft A₃
 As Extracted from the K-pulse shown in Figure 7.16

10^9 Nepers/s; GHz scale	sL_3/c scale
.	.
.	.
.	.
-0.292 ± j 1.307	-2.641 ± j11.820
-0.161 ± j 1.832	-1.456 ± j16.568
-0.186 ± j 2.079	-1.682 ± j18.802
-0.203 ± j 2.424	-1.836 ± j21.922
-0.241 ± j 2.772	-2.180 ± j25.069
-0.236 ± j 3.257	-2.134 ± j29.455
-0.189 ± j 3.646	-1.709 ± j32.973
-0.209 ± j 4.042	-1.890 ± j36.554
-0.250 ± j 4.336	-2.261 ± j39.213
-0.226 ± j 4.642	-2.044 ± j41.980
-0.220 ± j 4.970	-1.990 ± j44.947
-0.188 ± j 5.317	-1.700 ± j48.085
-0.197 ± j 5.692	-1.782 ± j51.476
-0.192 ± j 6.099	-1.736 ± j55.476
-0.253 ± j 6.451	-2.288 ± j58.340
-0.239 ± j 6.793	-2.161 ± j61.433
-0.270 ± j 7.061	-2.442 ± j63.857
-0.257 ± j 7.345	-2.324 ± j68.425
.	.
.	.
.	.

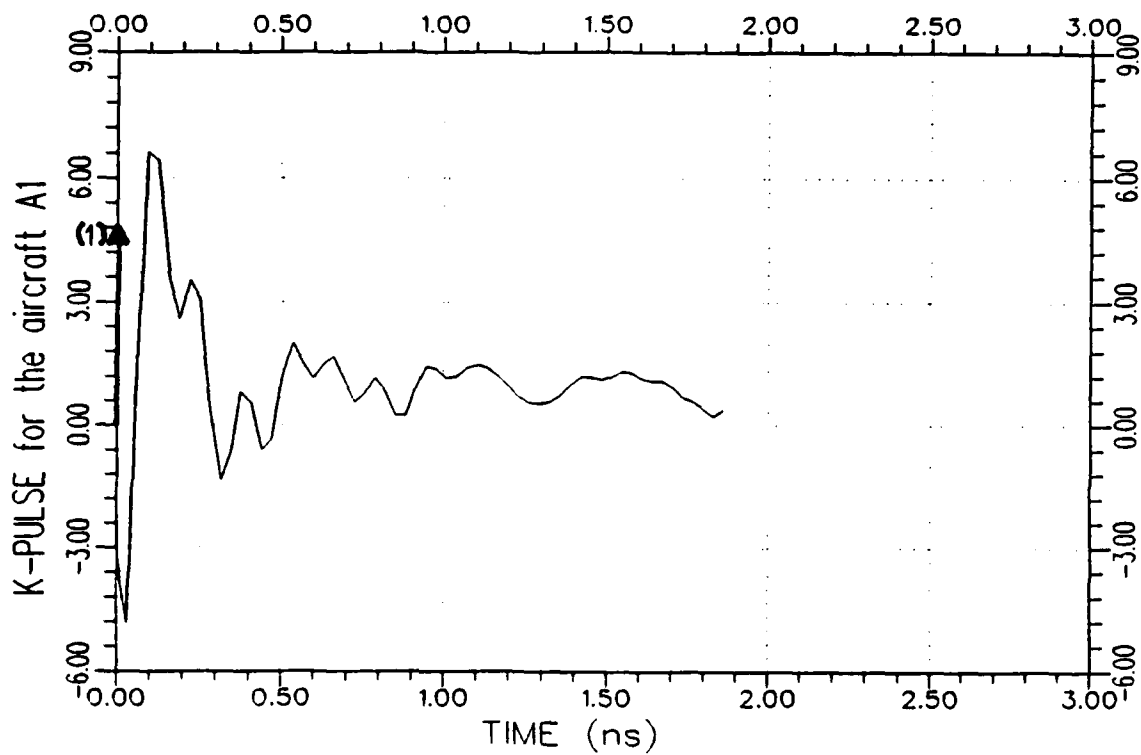
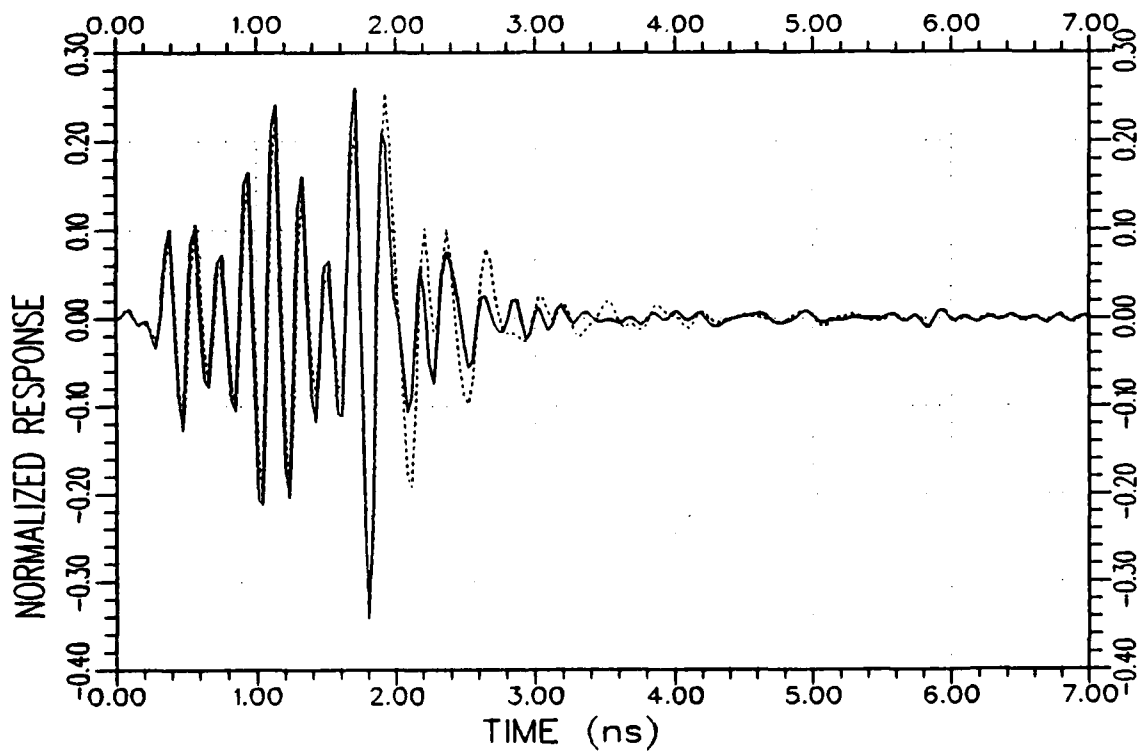
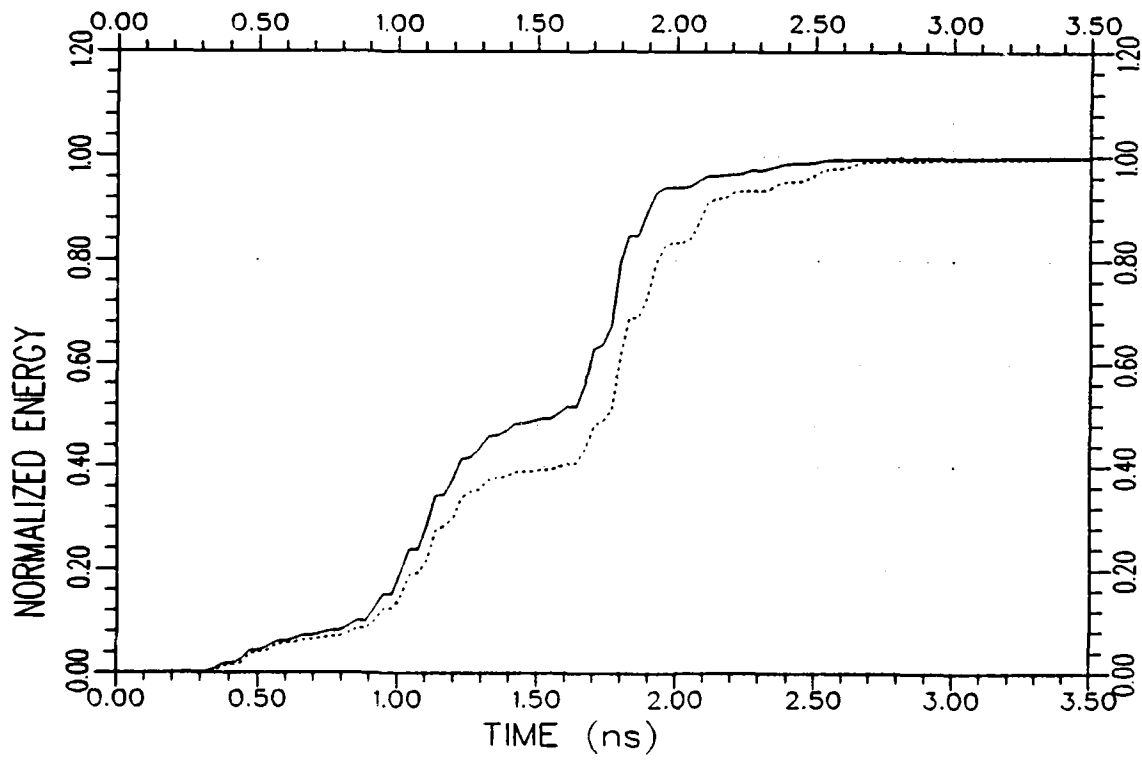


Figure 7.1. An approximate K-pulse waveform for the model aircraft A_1 , estimated from the backscattered measurement data at $0^\circ/VP$ and $90^\circ/VP$ using a discrete representation for the continuous part of the K-pulse. (The $\delta(t)$ term of the K-pulse is symbolically shown by the arrow at $t=0$.)



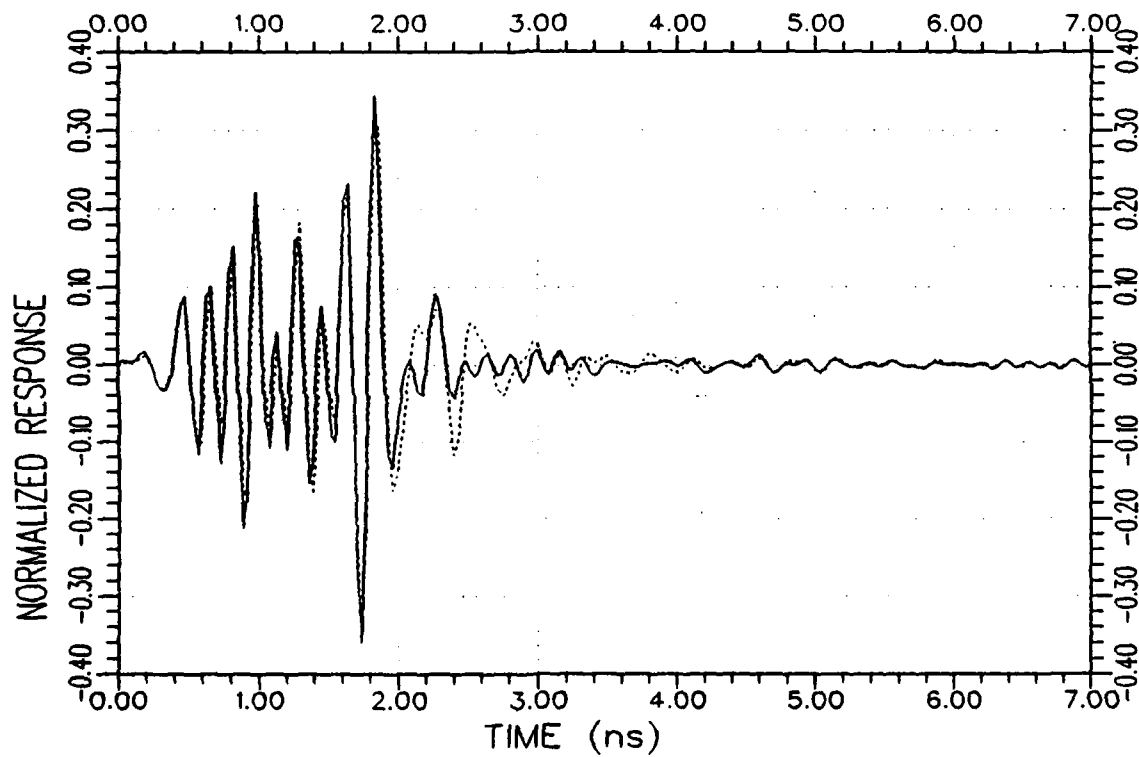
(a) Response waveforms

Figure 7.2. Normalized impulse response (.....) and K-pulse response (——) waveforms and their energy curves for aircraft A_1 at $0^\circ/VP$.



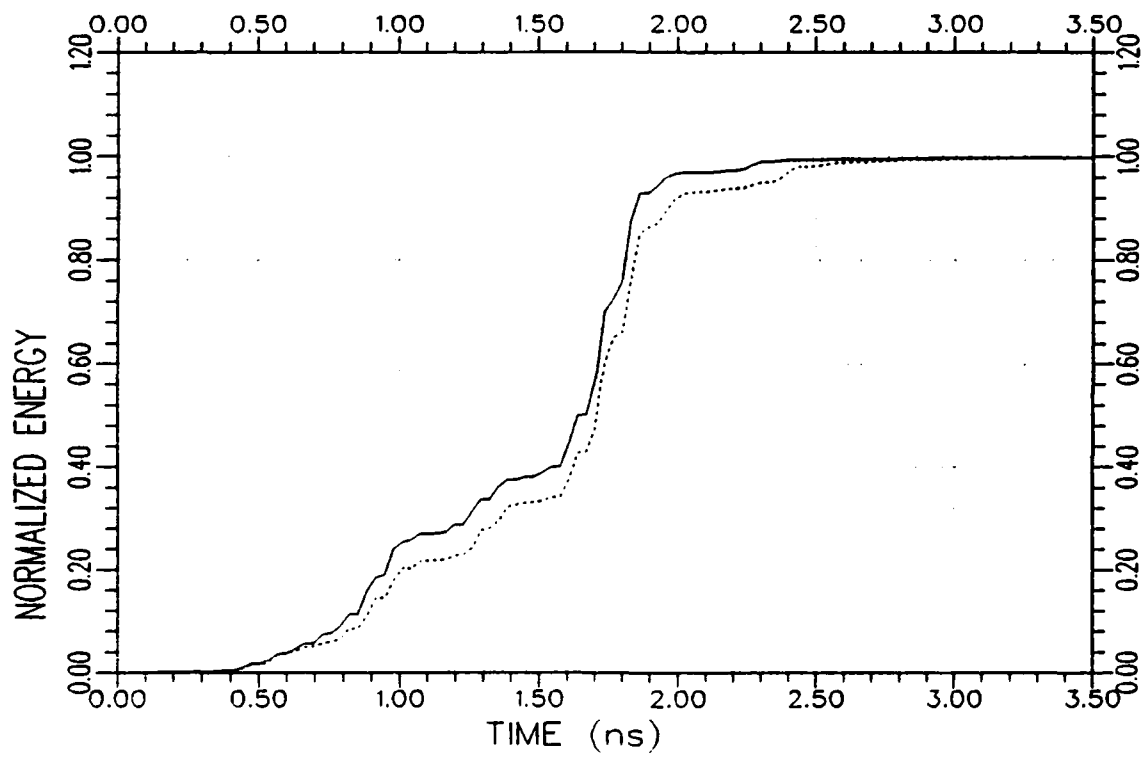
(b) Response energy curves

Figure 7.2. Continued.



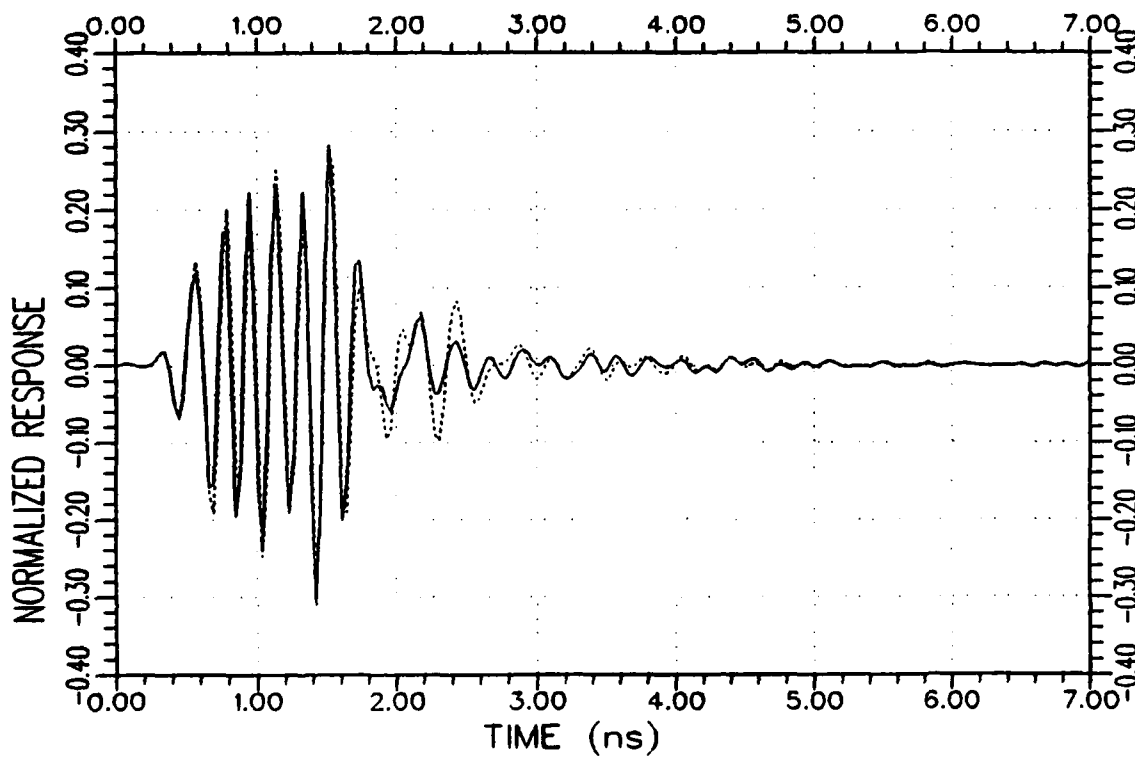
(a) Response waveforms

Figure 7.3. Normalized impulse response (.....) and K-pulse response (——) waveforms and their energy curves for aircraft A_1 at $30^\circ/VP$.



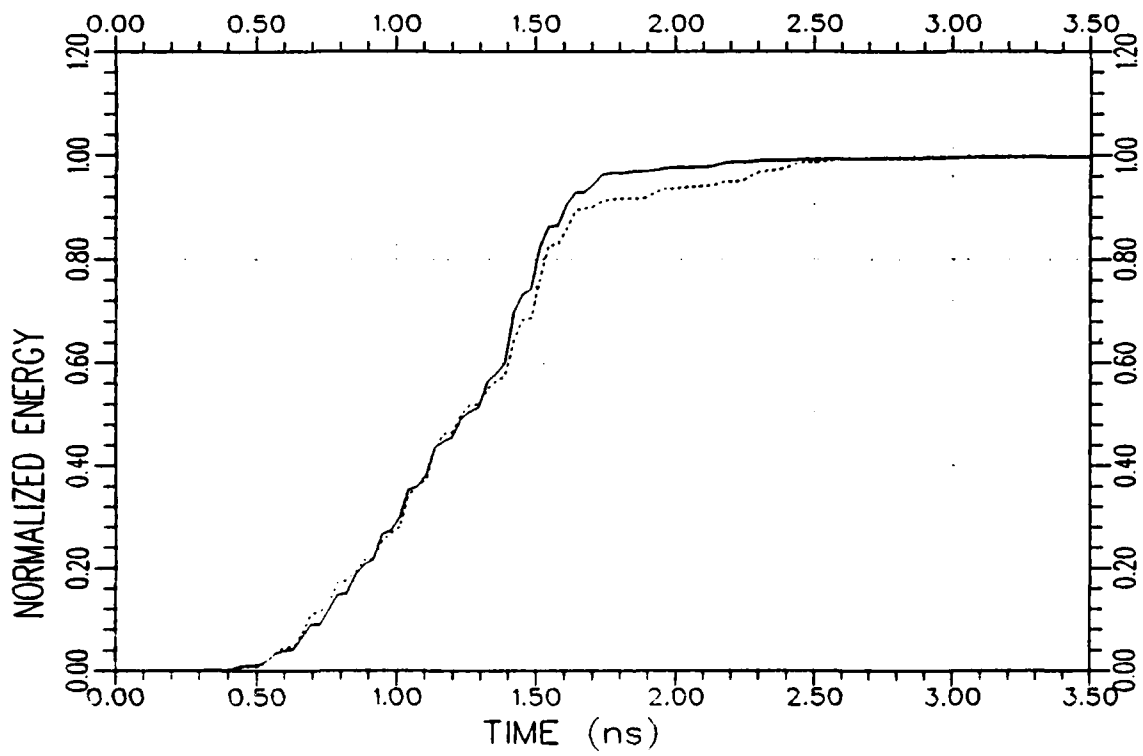
(b) Response energy curves

Figure 7.3. Continued.



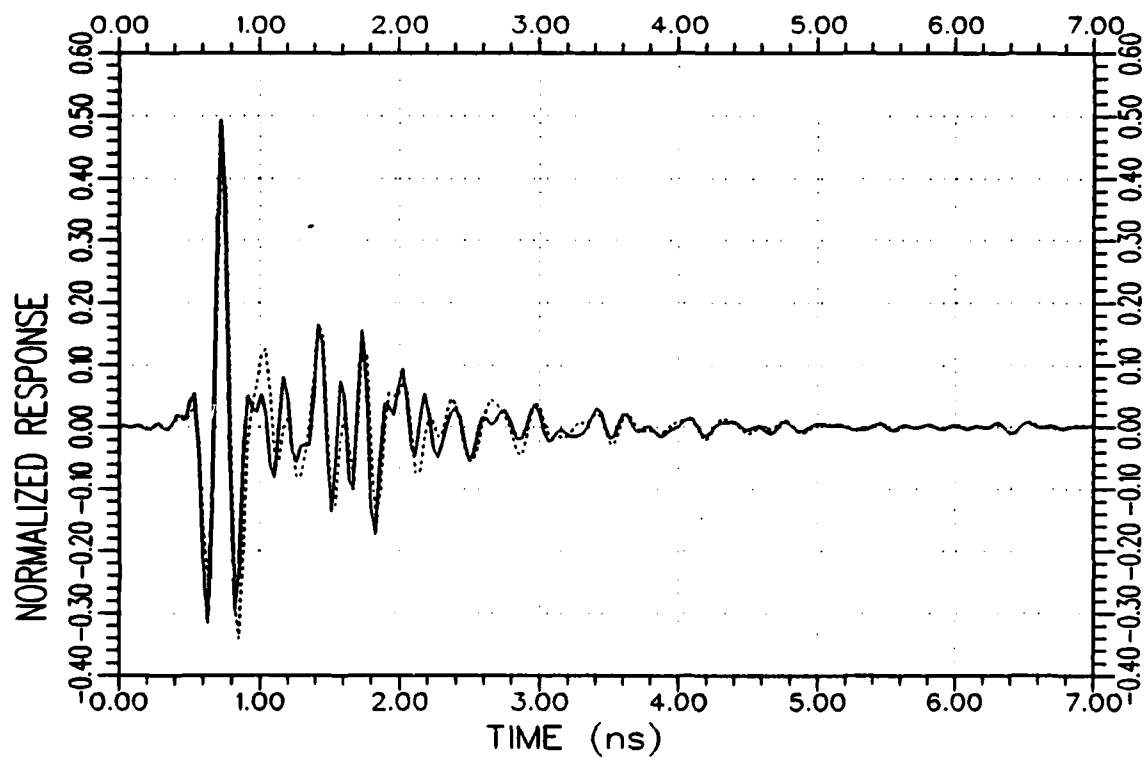
(a) Response waveforms

Figure 7.4. Normalized impulse response (.....) and K-pulse response (—) waveforms and their energy curves for aircraft A_1 at $45^\circ/VP$.



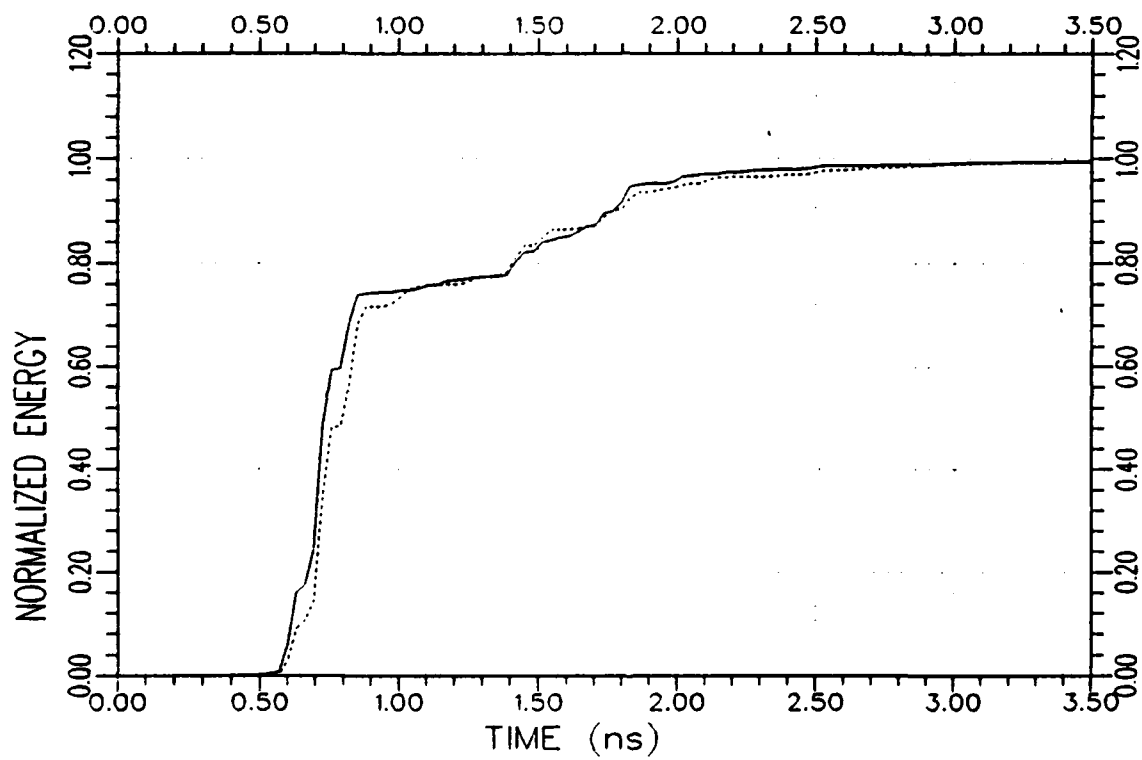
(b) Response energy curves

Figure 7.4. Continued.



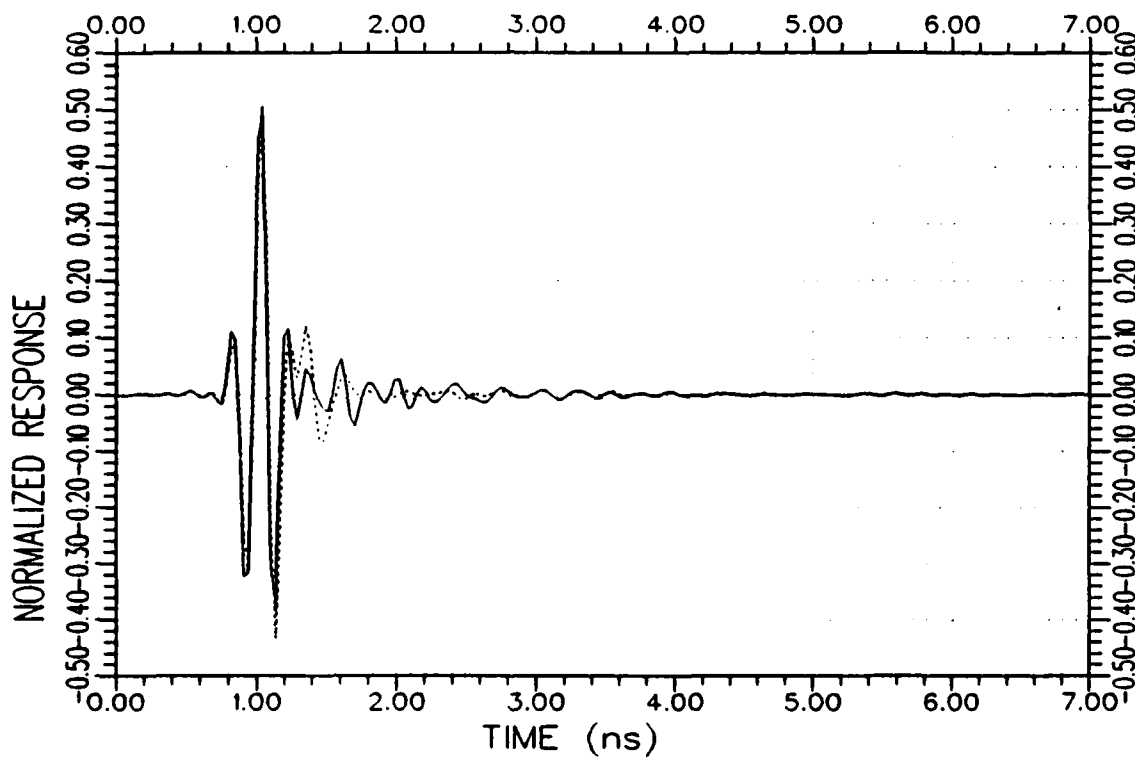
(a) Response waveforms

Figure 7.5. Normalized impulse response (.....) and K-pulse response (——) waveforms and their energy curves for aircraft A_1 at $60^\circ/VP$.



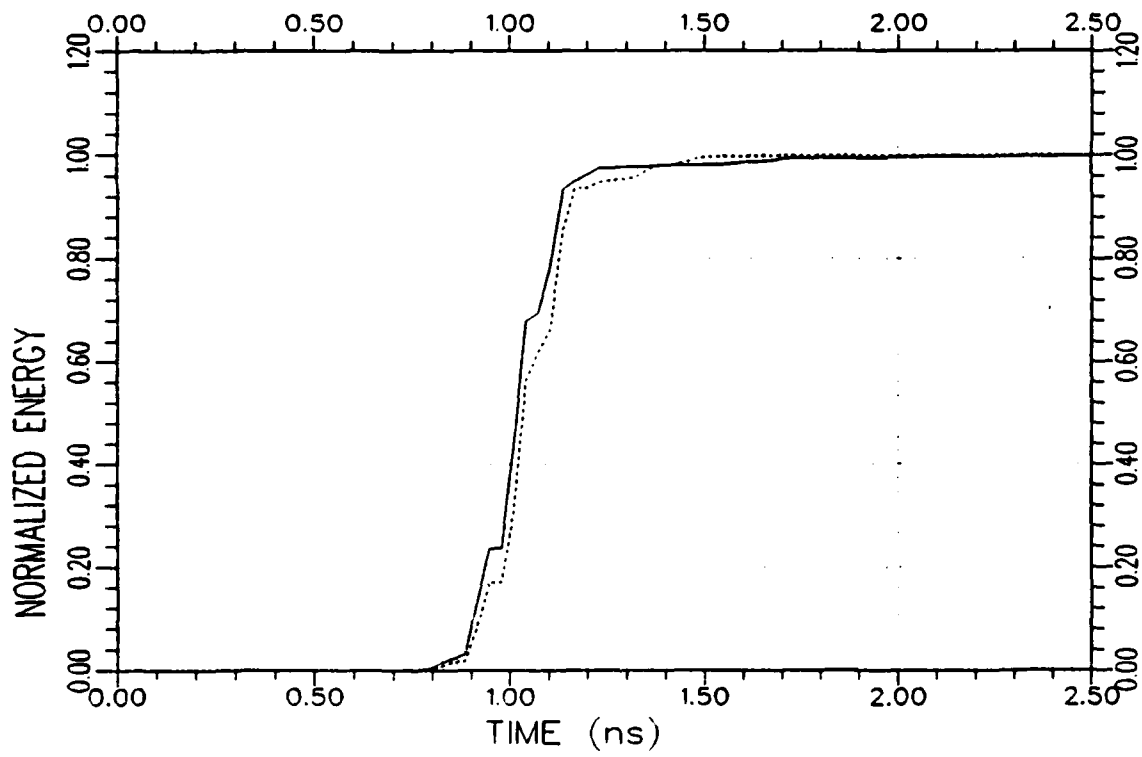
(b) Response energy curves

Figure 7.5. Continued.



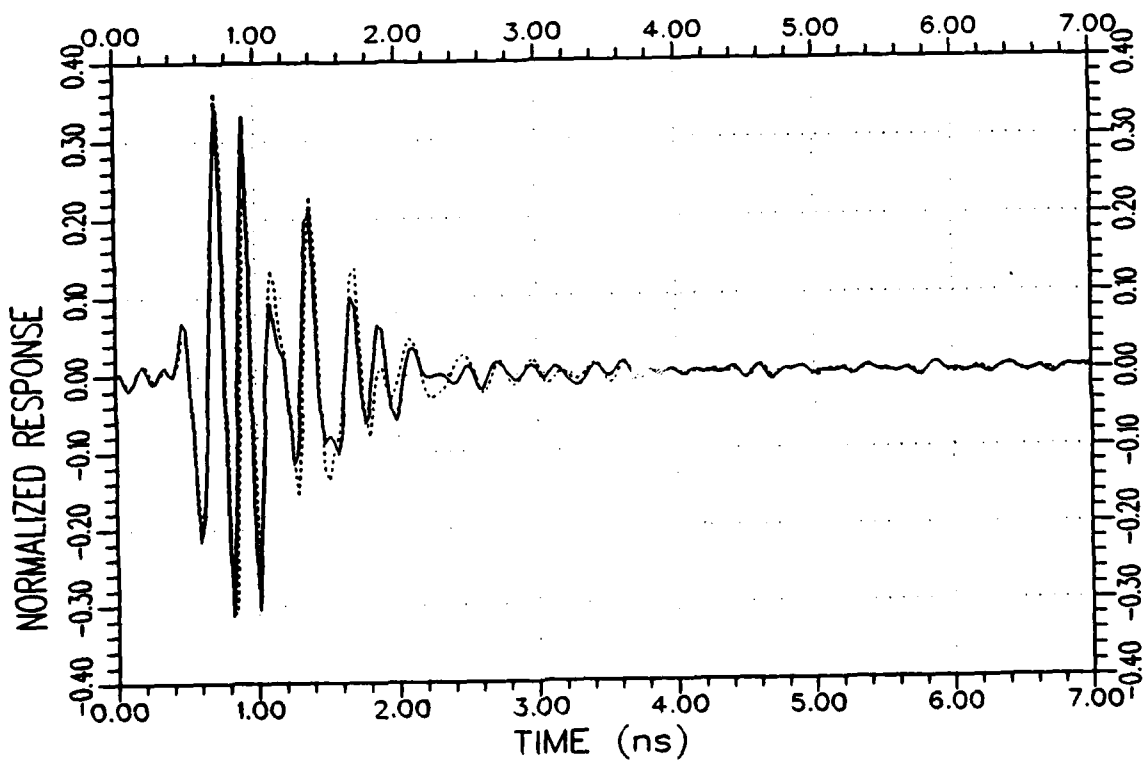
(a) Response waveforms

Figure 7.6. Normalized impulse response (.....) and K-pulse response (——) waveforms and their energy curves for aircraft A_1 at $90^\circ/VP$.



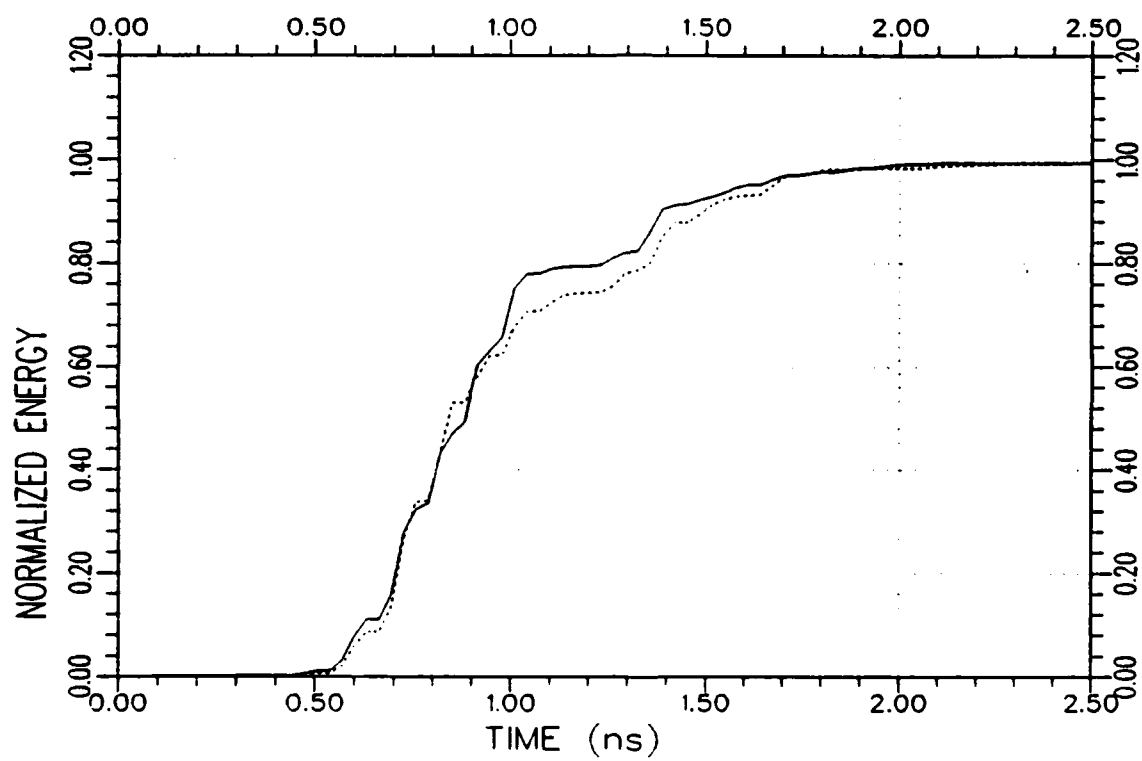
(b) Response energy curves

Figure 7.6. Continued.



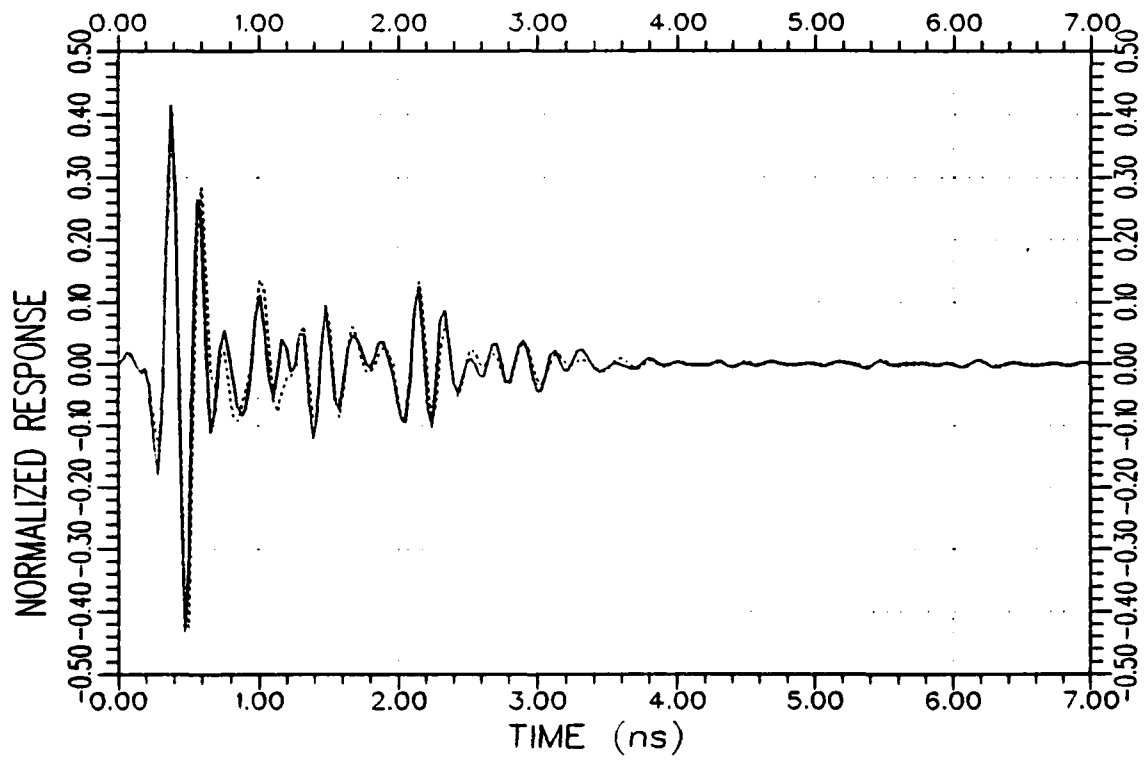
(a) Response waveforms

Figure 7.7. Normalized impulse response (.....) and K-pulse response (—) waveforms and their energy curves for aircraft A_1 at $120^\circ/VP$.



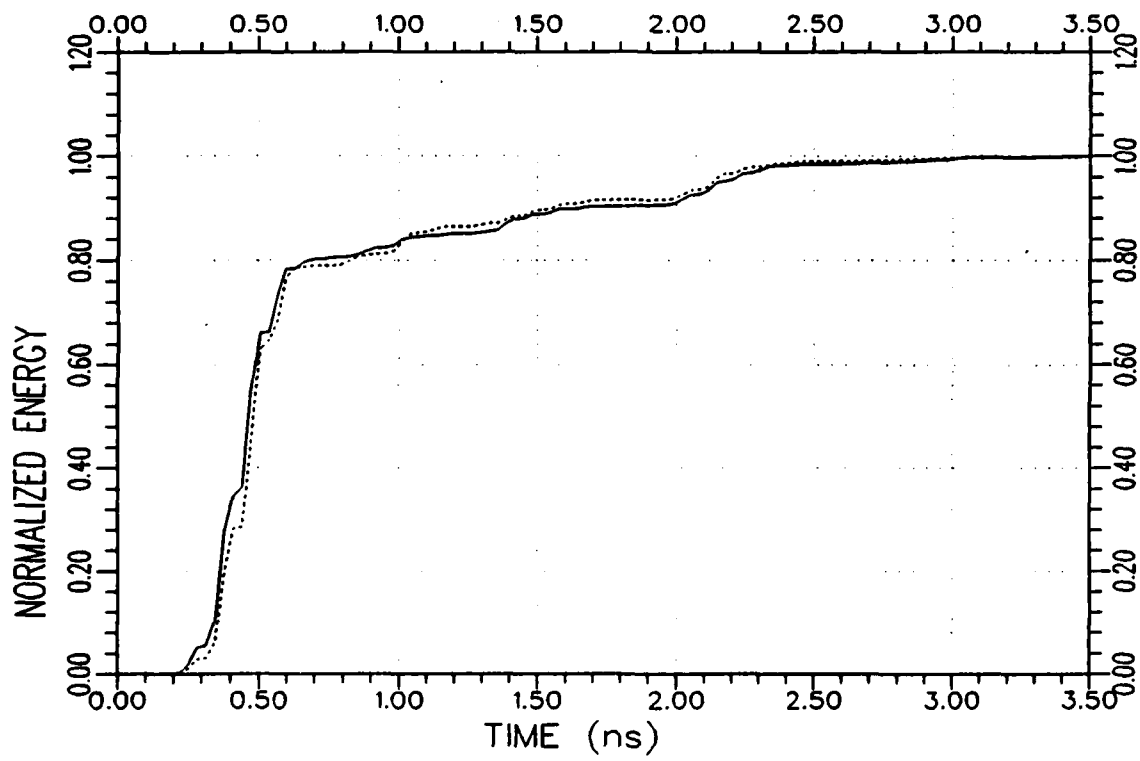
(b) Response energy curves

Figure 7.7. Continued.



(a) Response waveforms

Figure 7.8. Normalized impulse response (·····) and K-pulse response (—) waveforms and their energy curves for aircraft A_1 at $180^\circ/VP$.



(b) Response energy curves

Figure 7.8. Continued.

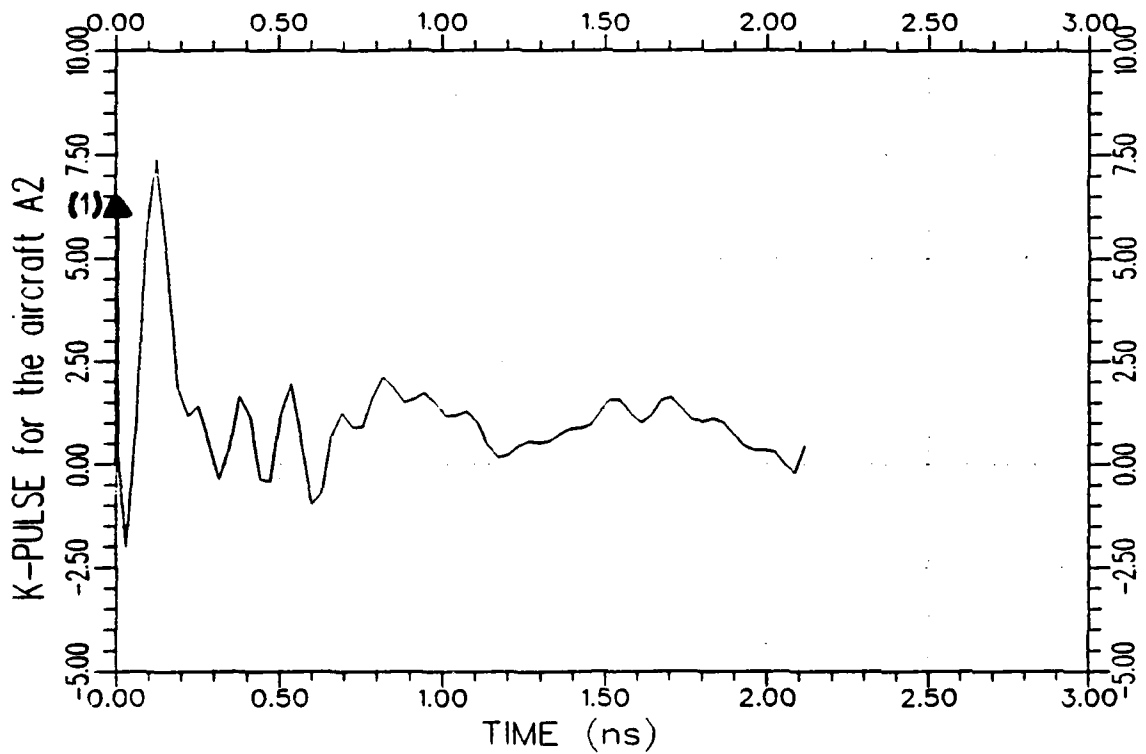
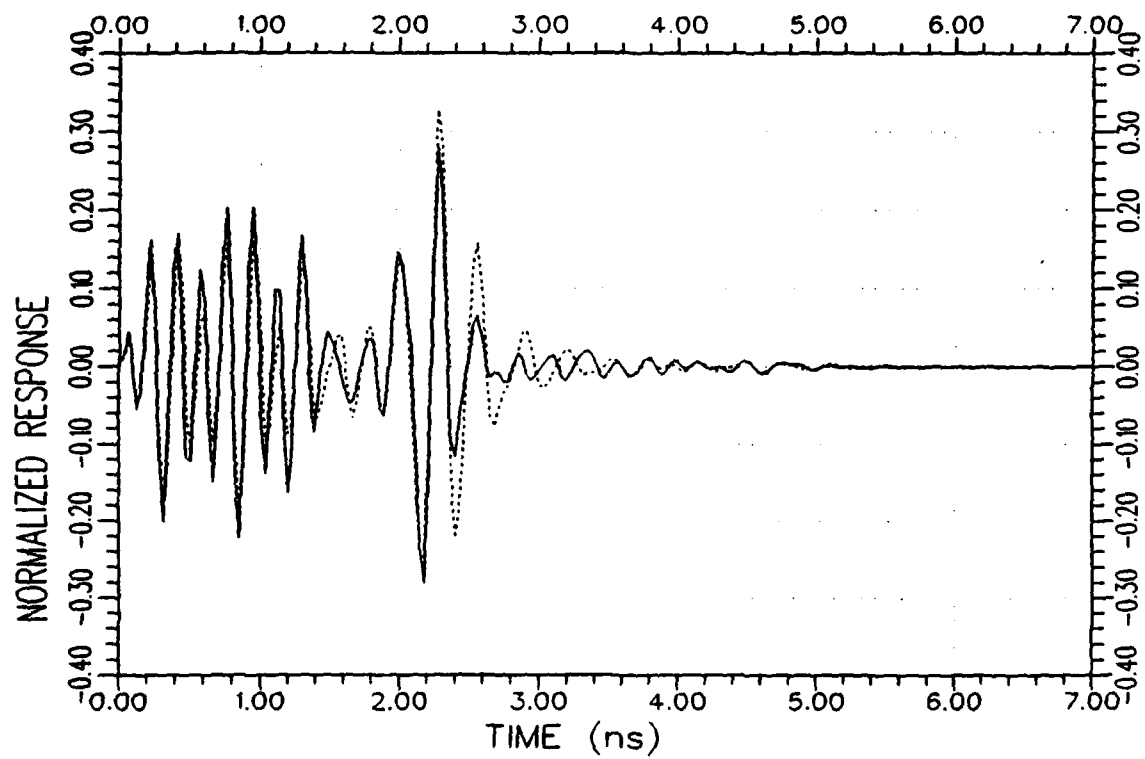
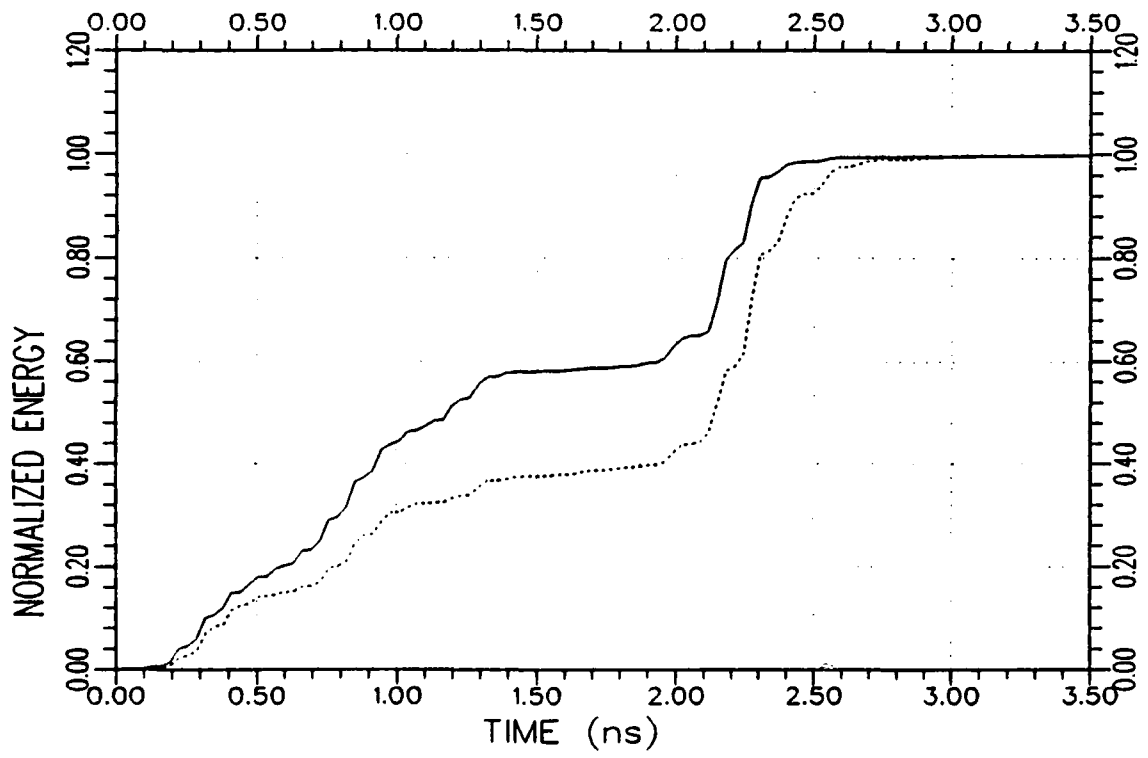


Figure 7.9. An approximate K-pulse waveform for the model aircraft A₂ estimated from the backscattered measurement data at 0°/VP and 90°/VP using a discrete representation for the continuous part of the K-pulse. (The $\delta(t)$ term of the K-pulse is symbolically shown by the arrow at t=0.)



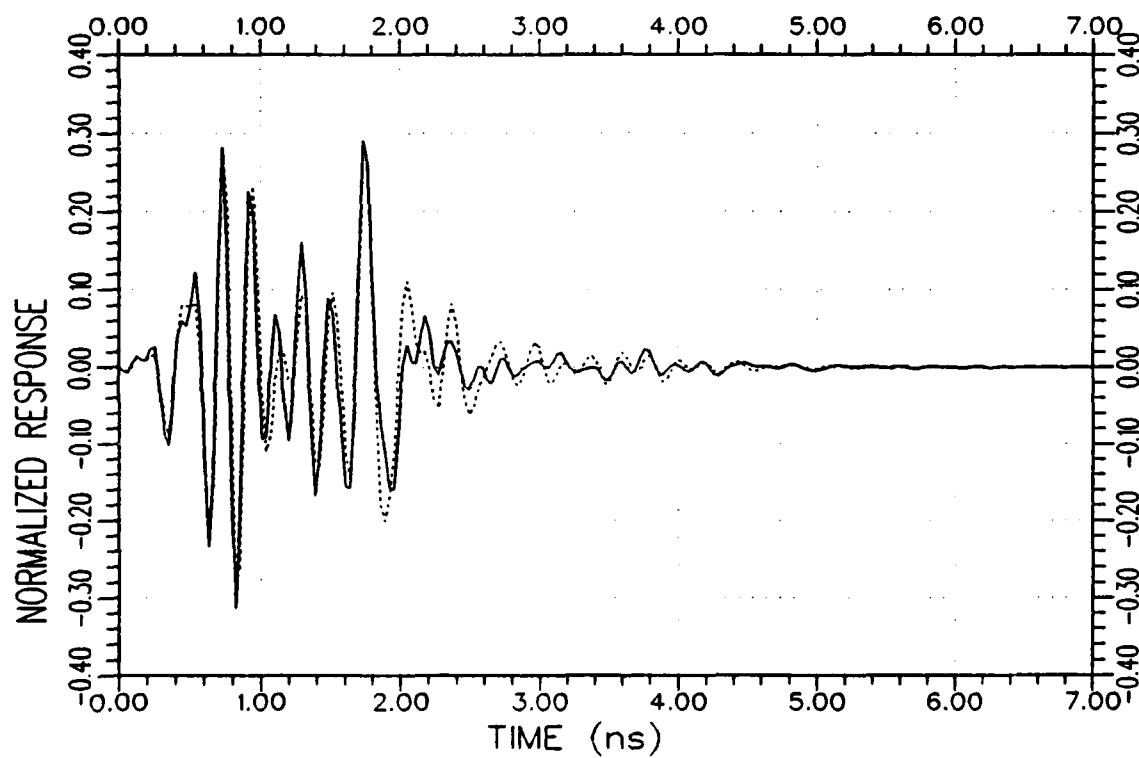
(a) Response waveforms

Figure 7.10. Normalized impulse response (.....) and K-pulse response (——) waveforms and their energy curves for aircraft A_2 at $0^\circ/VP$.



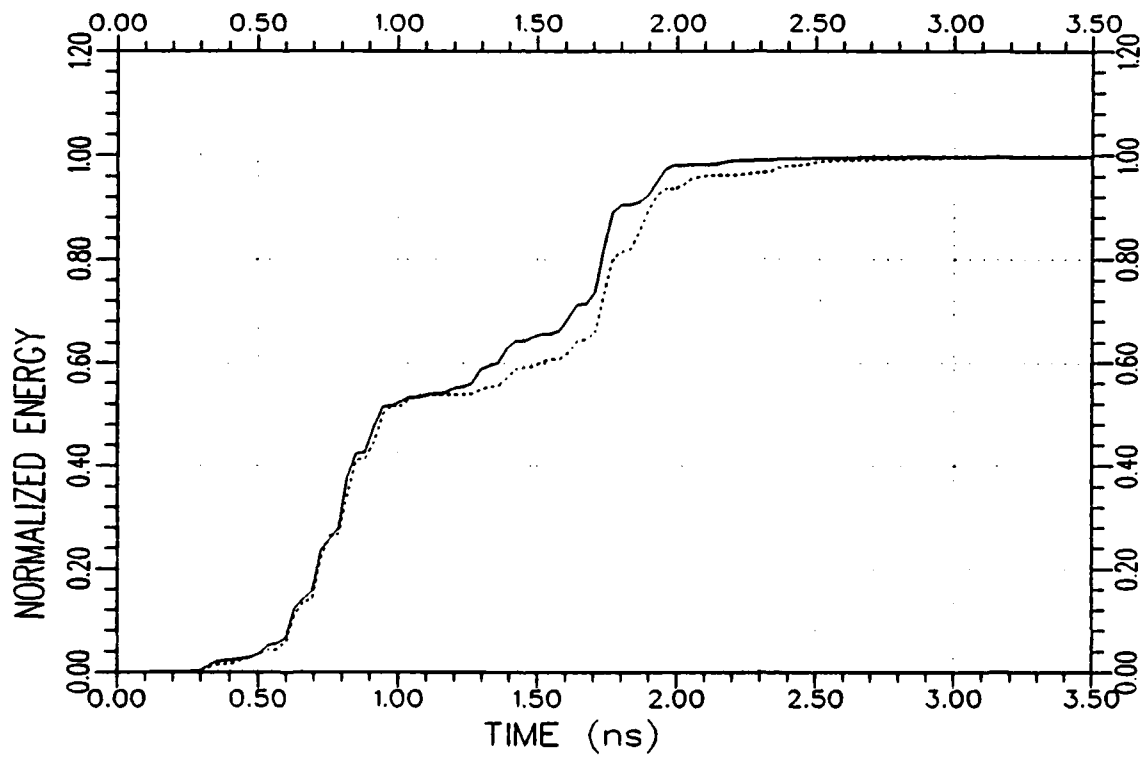
(b) Response energy curves

Figure 7.10. Continued.



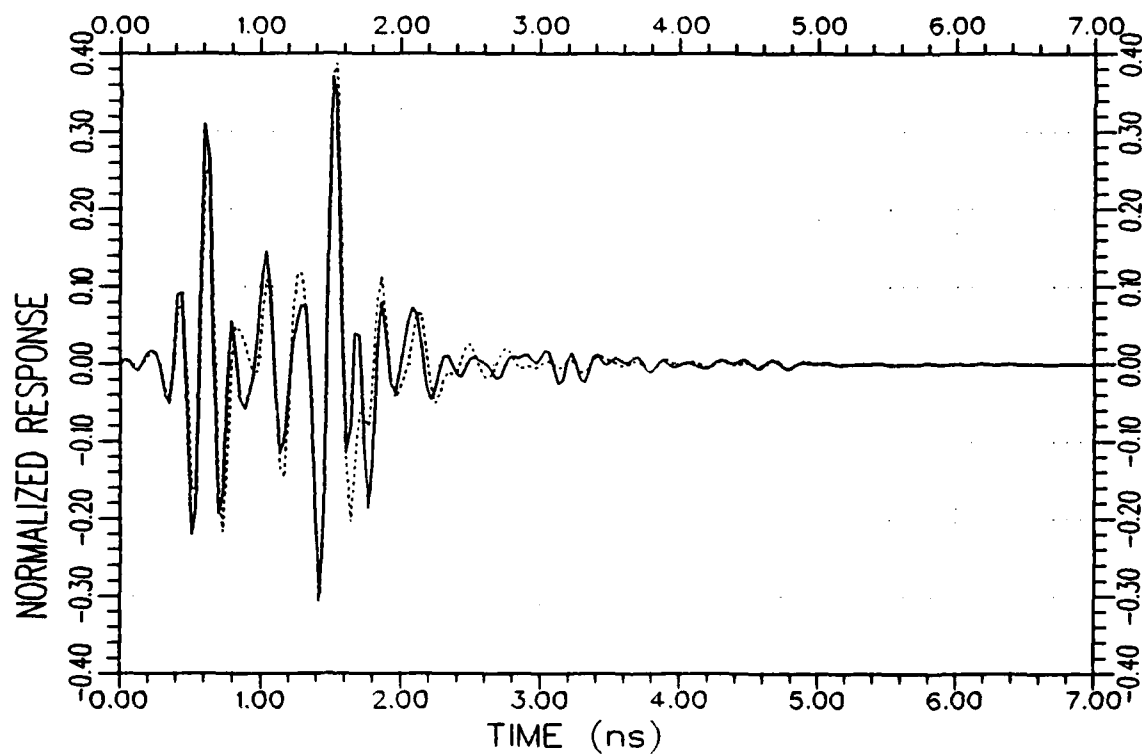
(a) Response waveforms

Figure 7.11. Normalized impulse response (·····) and K-pulse response (—) waveforms and their energy curves for aircraft A_2 at $45^\circ/VP$.



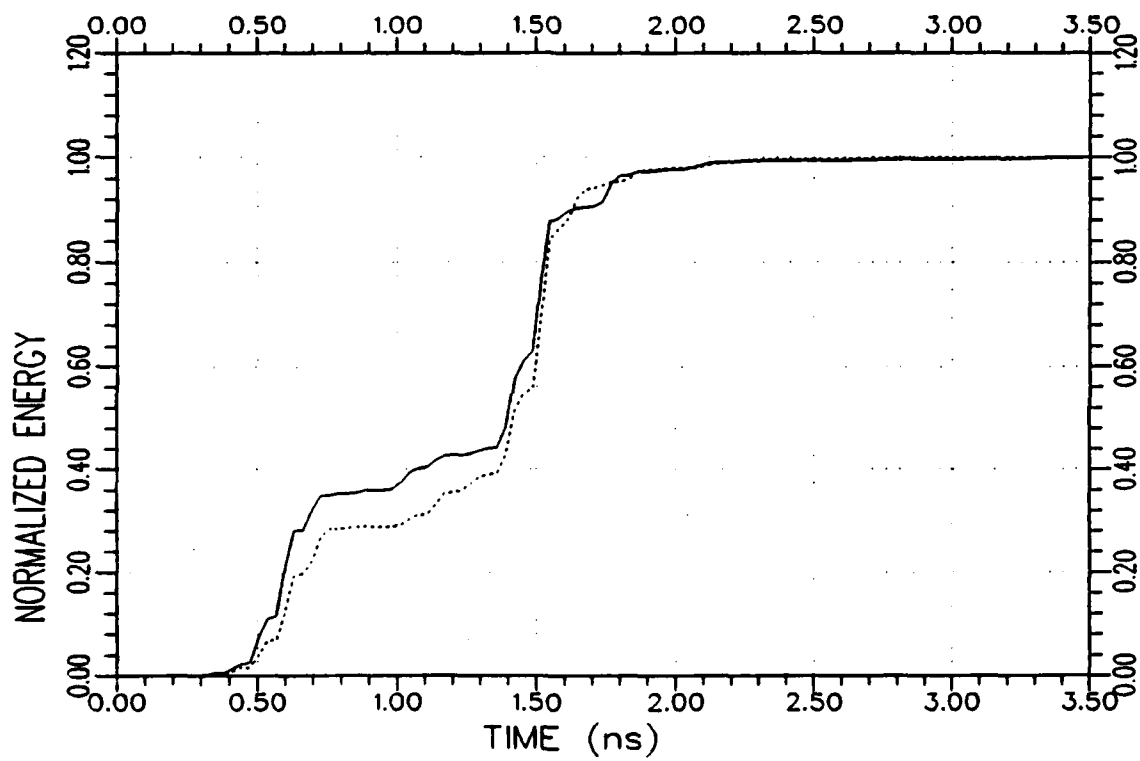
(b) Response energy curves

Figure 7.11. Continued.



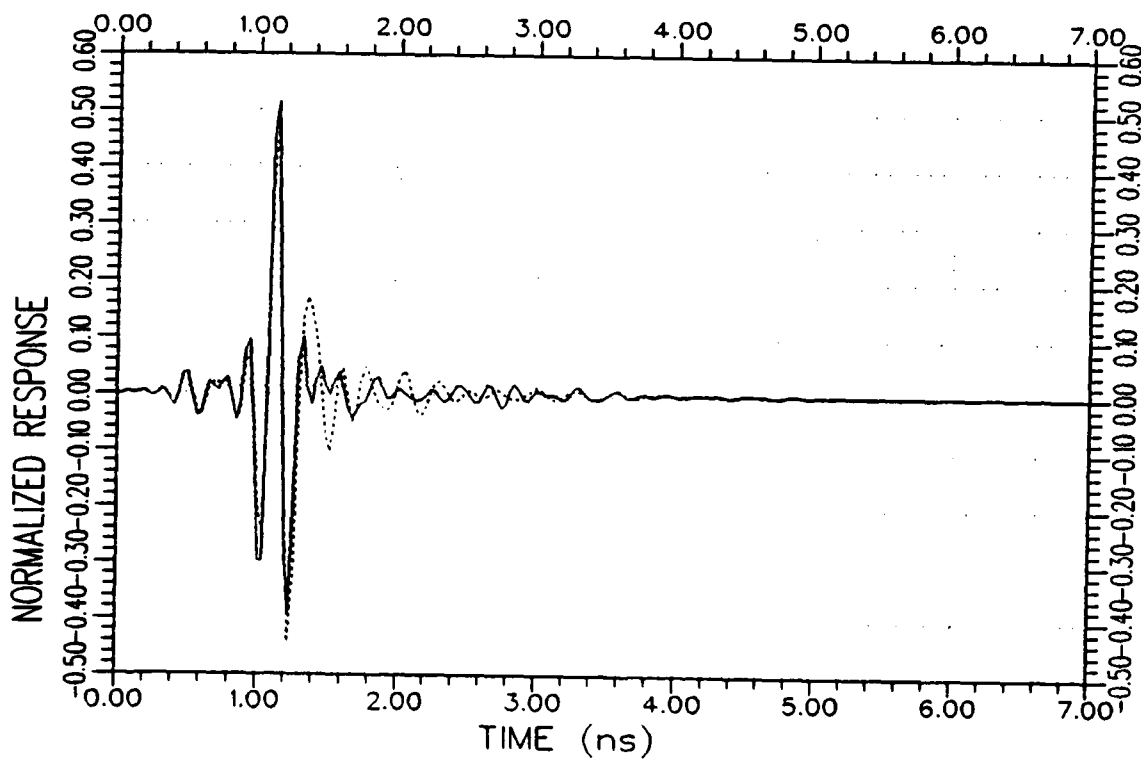
(a) Response waveforms

Figure 7.12. Normalized impulse response (.....) and K-pulse response (——) waveforms and their energy curves for aircraft A_2 at $60^\circ/VP$.



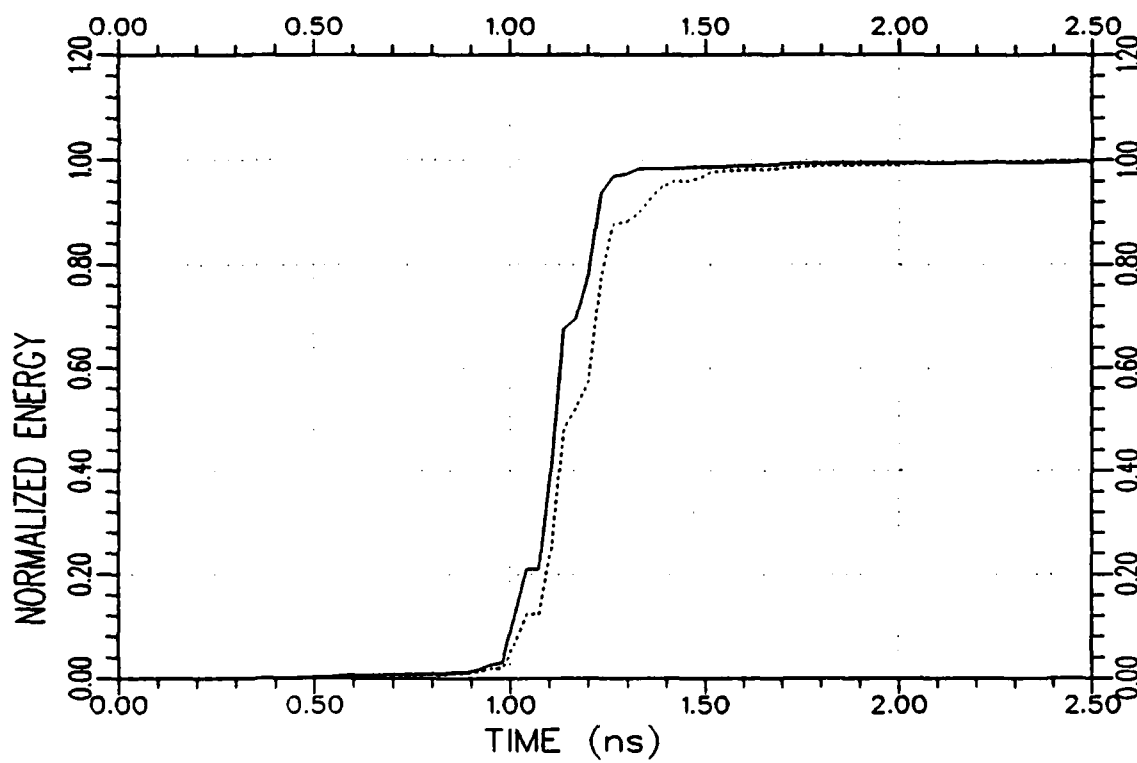
(b) Response energy curves

Figure 7.12. Continued.



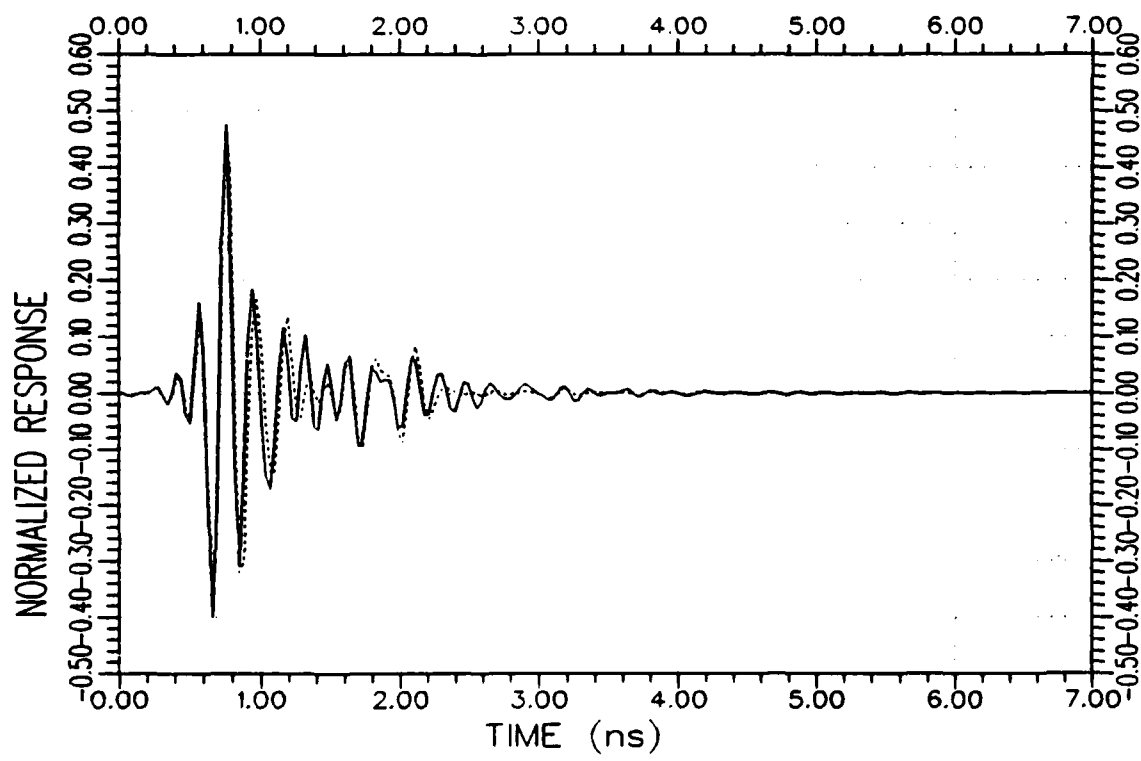
(a) Response waveforms

Figure 7.13. Normalized impulse response (.....) and K-pulse response (—) waveforms and their energy curves for aircraft A_2 at $90^\circ/VP$.



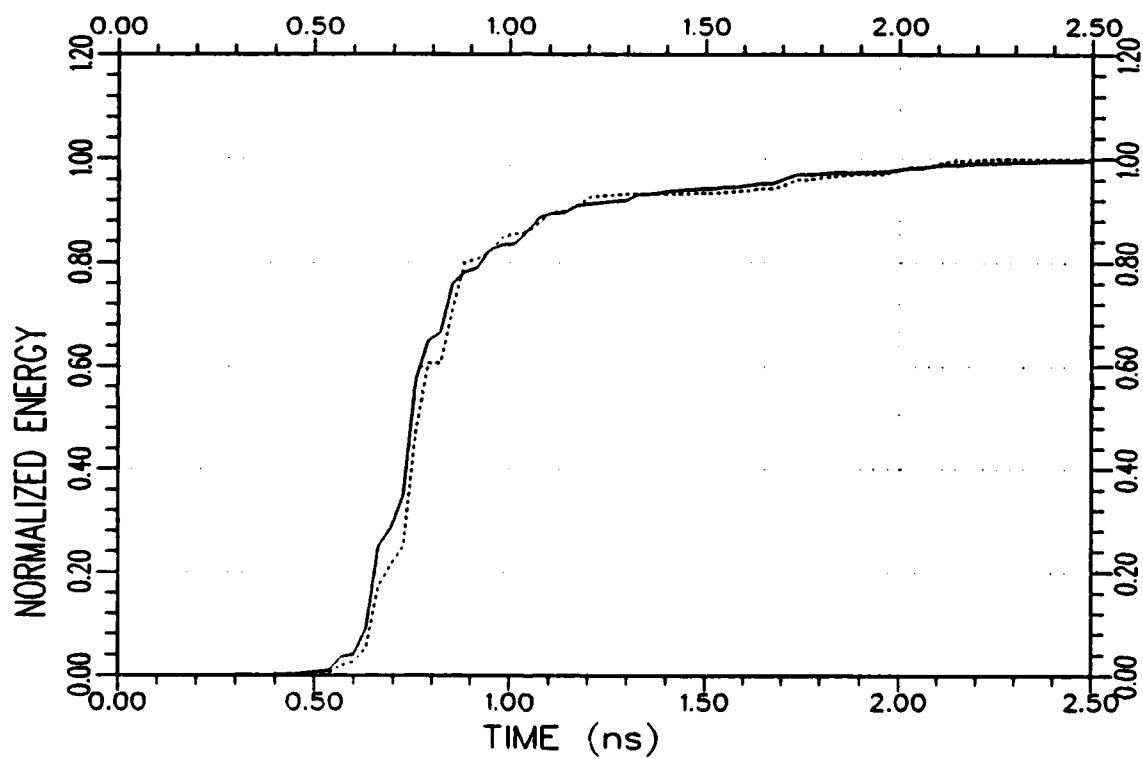
(b) Response energy curves

Figure 7.13. Continued.



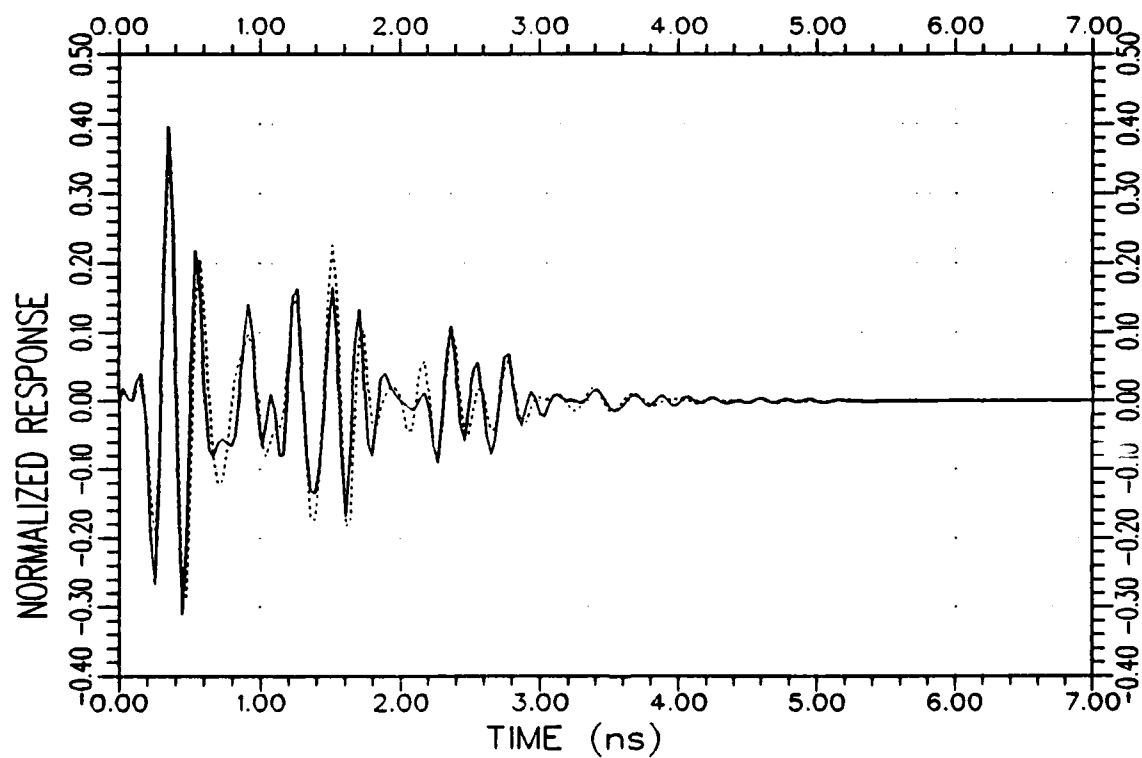
(a) Response waveforms

Figure 7.14. Normalized impulse response (.....) and K-pulse response (——) waveforms and their energy curves for aircraft A_2 at $120^\circ/VP$.



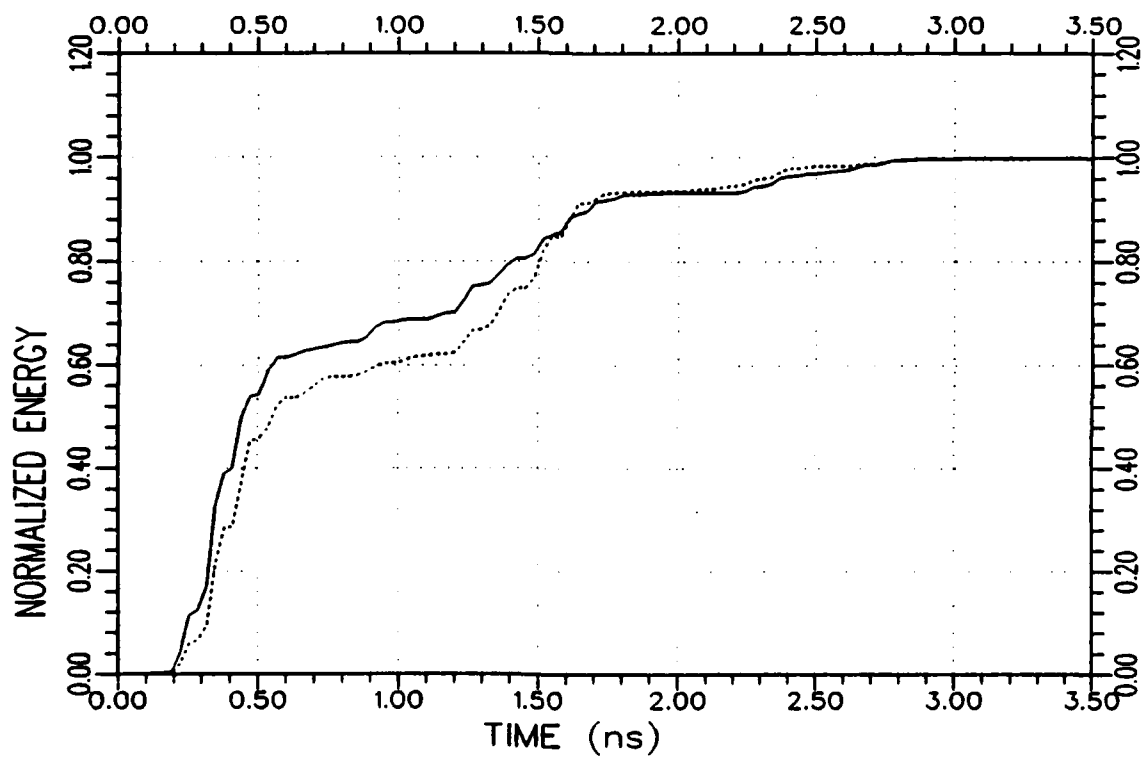
(b) Response energy curves

Figure 7.14. Continued.



(a) Response waveforms

Figure 7.15. Normalized impulse response (.....) and K-pulse response (—) waveforms and their energy curves for aircraft A_2 at $180^\circ/VP$.



(b) Response energy curves

Figure 7.15. Continued.

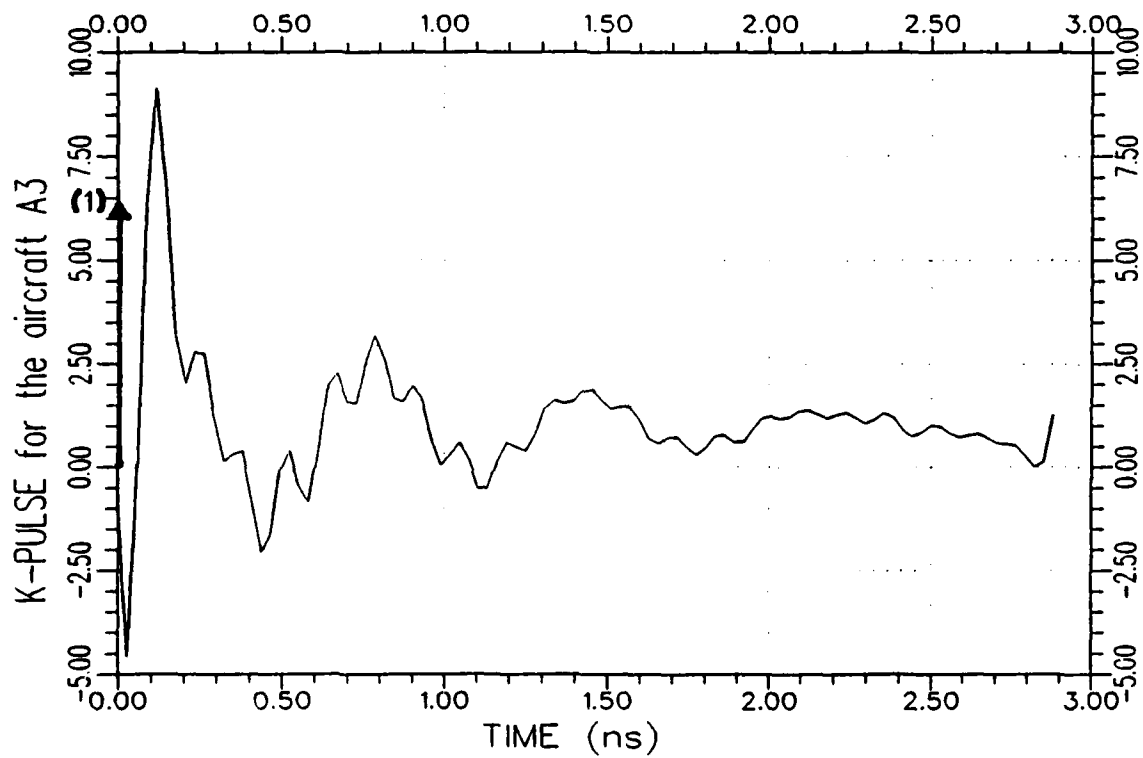
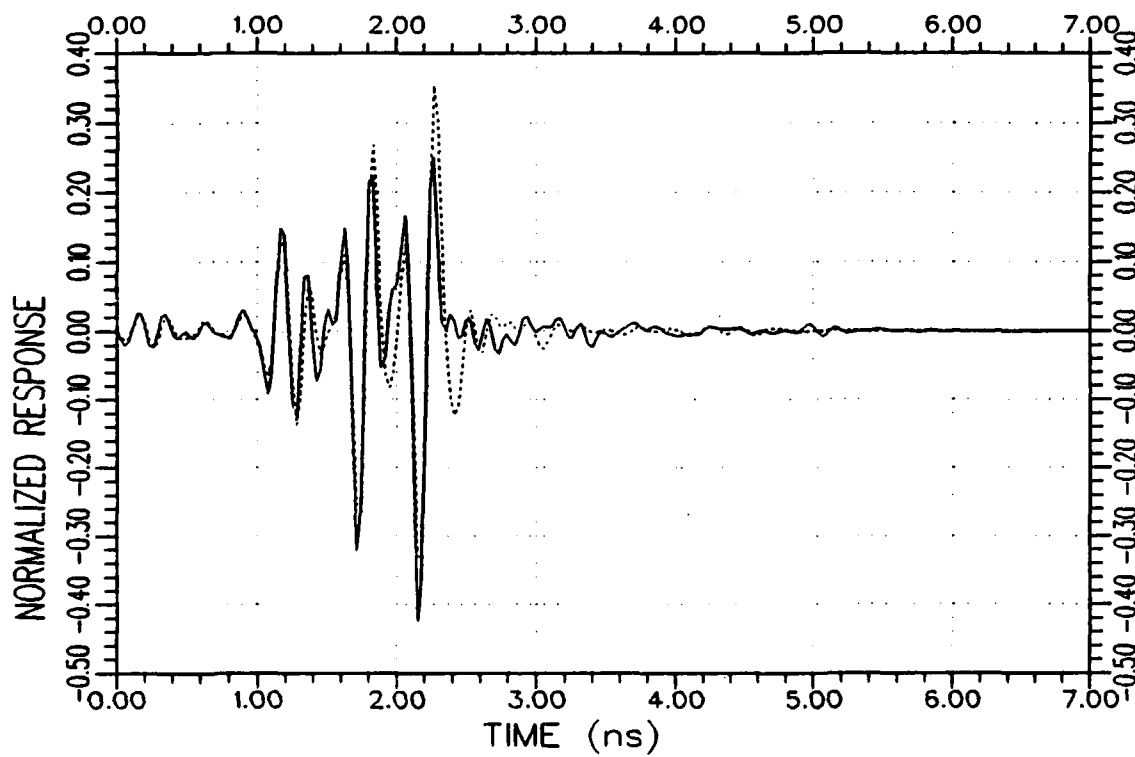
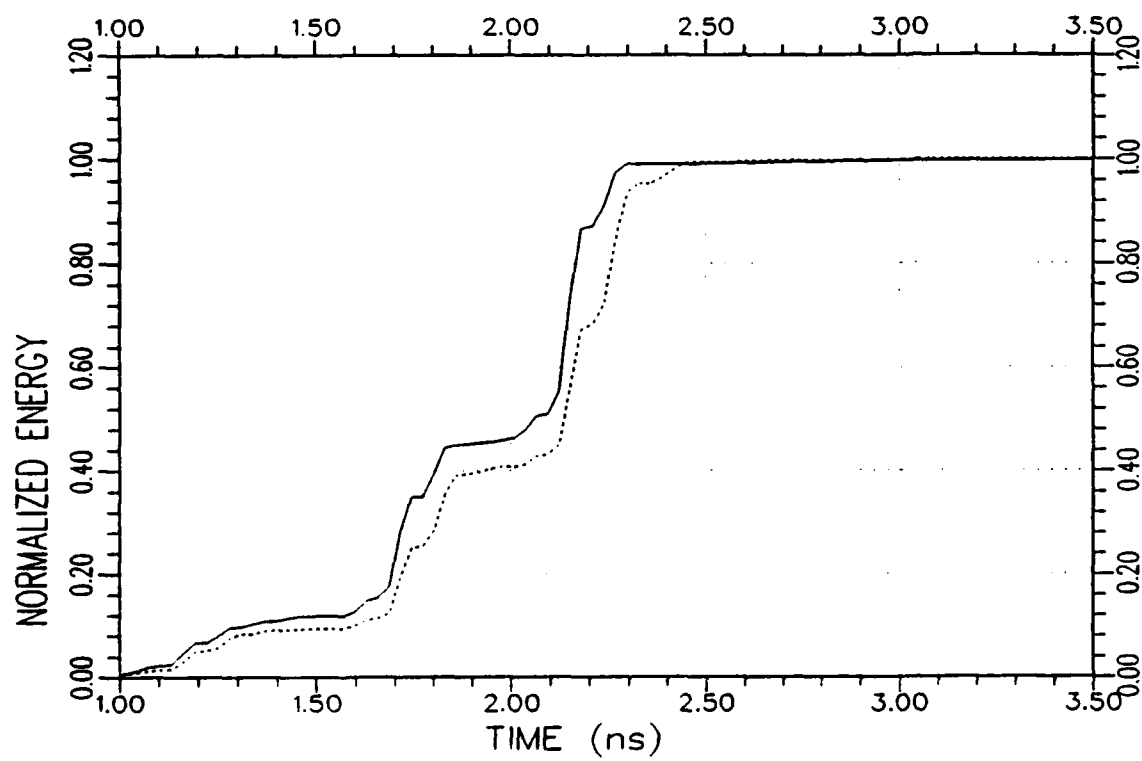


Figure 7.16. An approximate K-pulse waveform for the model aircraft A_3 estimated from the backscattered measurement data at $0^\circ/VP$ and $90^\circ/VP$ using a discrete representation for the continuous part of the K-pulse. (The $\delta(t)$ term of the K-pulse is symbolically shown by the arrow at $t=0$.)



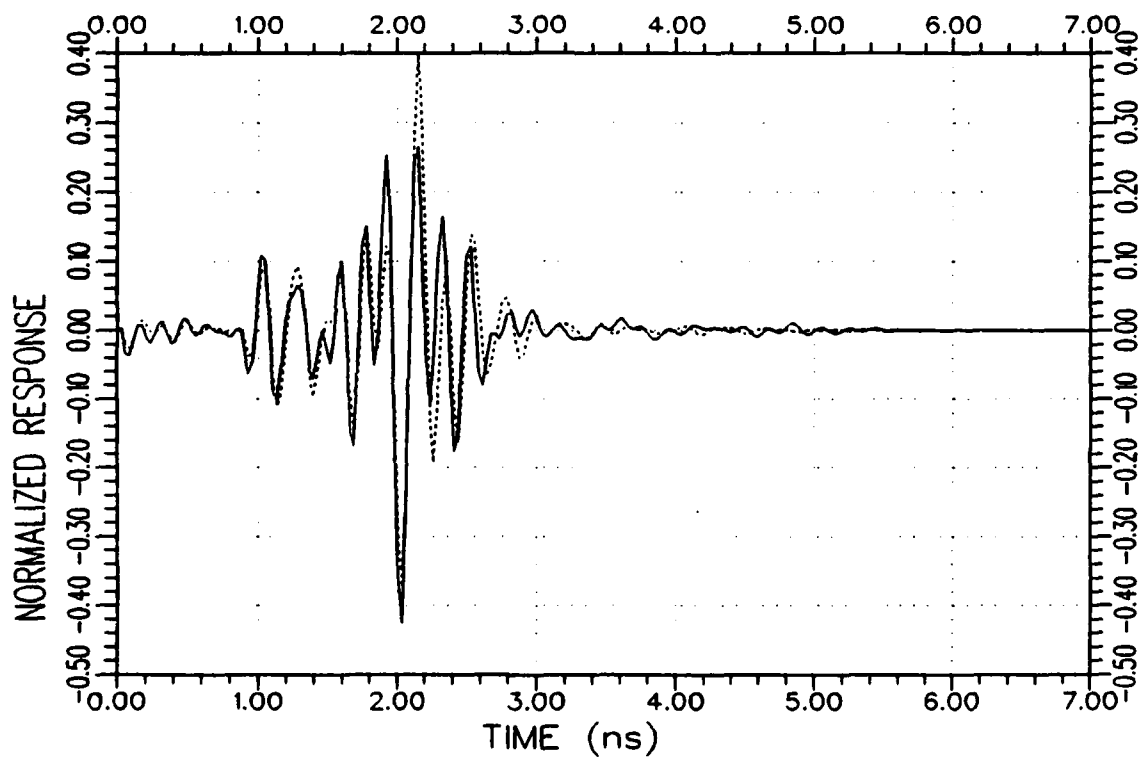
(a) Response waveforms

Figure 7.17. Normalized impulse response (.....) and K-pulse response (—) waveforms and their energy curves for aircraft A_3 at $0^\circ/VP$.



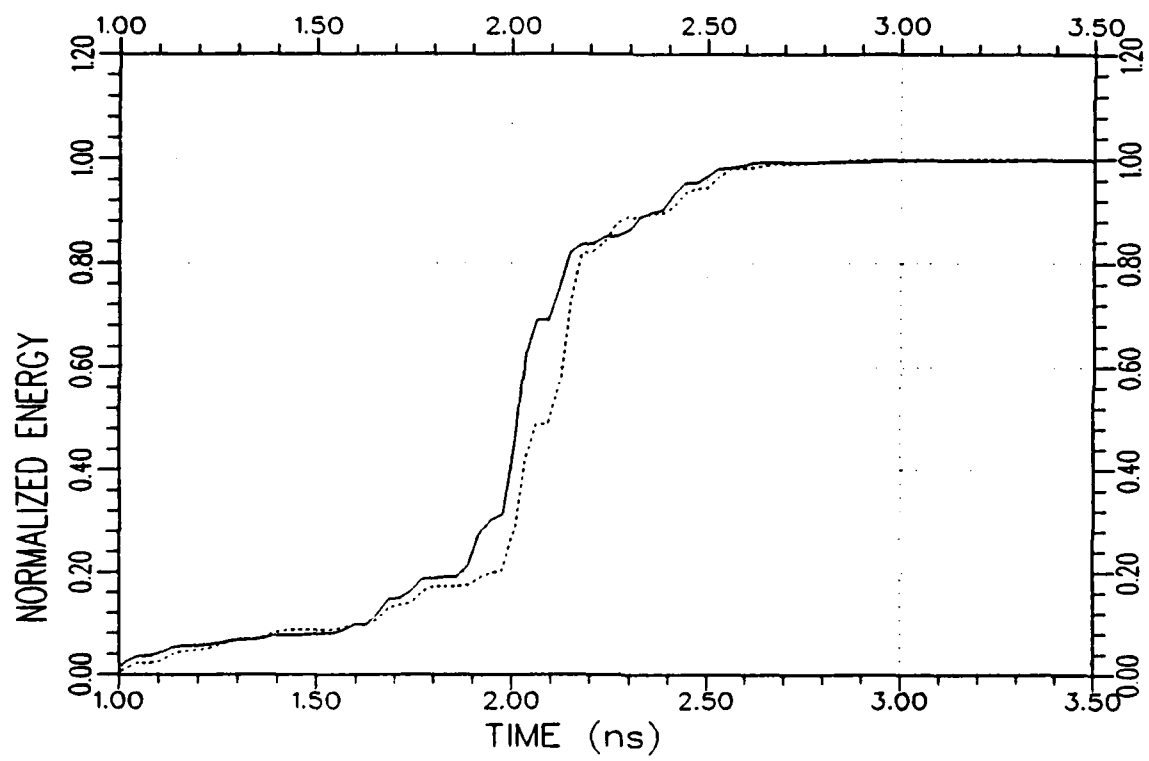
(b) Response energy curves

Figure 7.17. Continued.



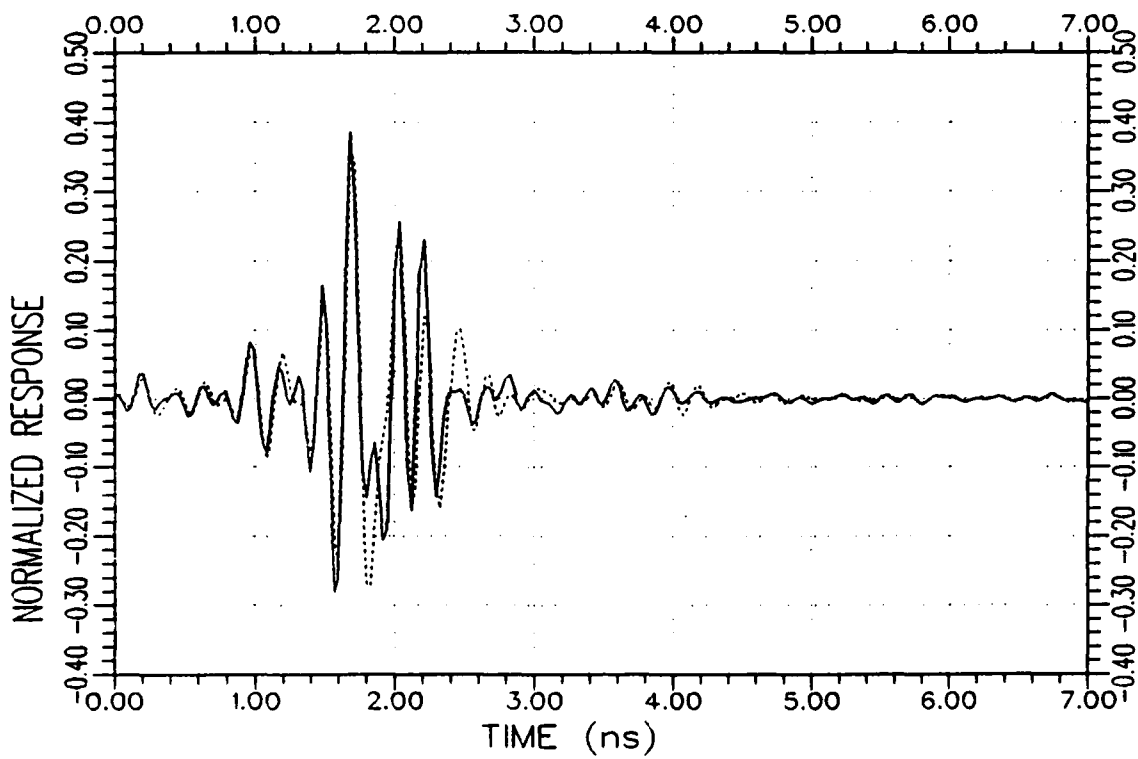
(a) Response waveforms

Figure 7.18. Normalized impulse response (.....) and K-pulse response (——) waveforms and their energy curves for aircraft A_3 at $30^\circ/VP$.



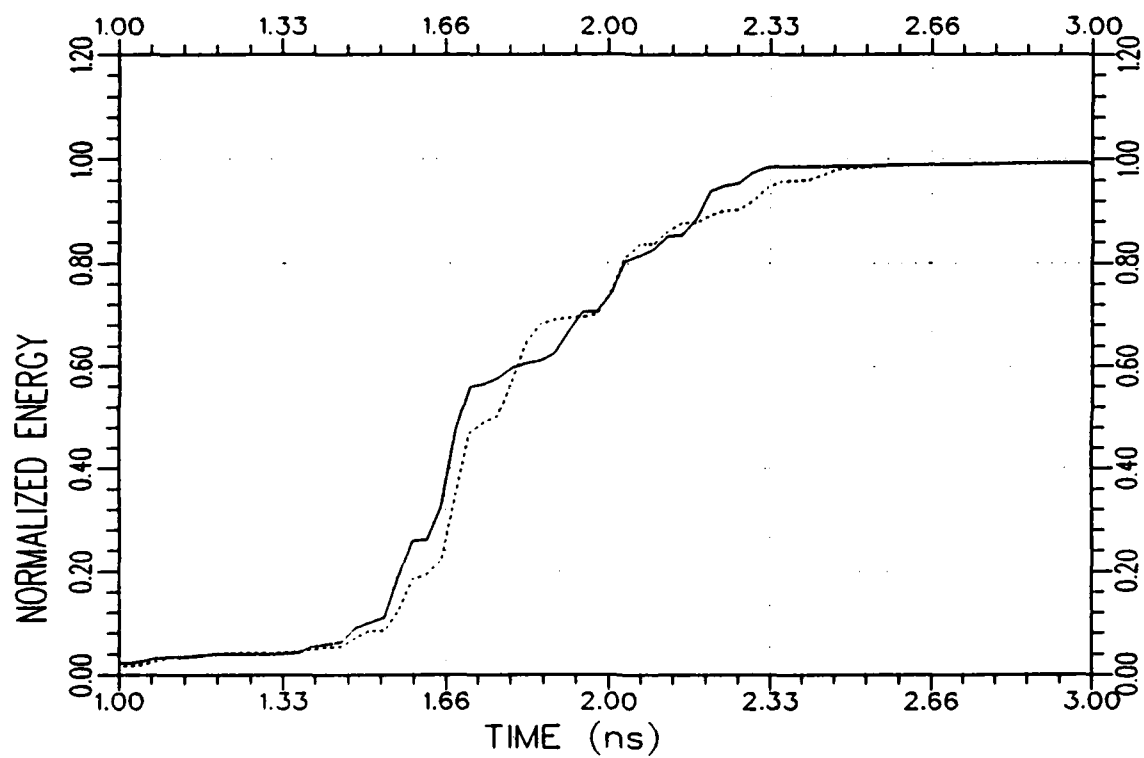
(b) Response energy curves

Figure 7.18. Continued.



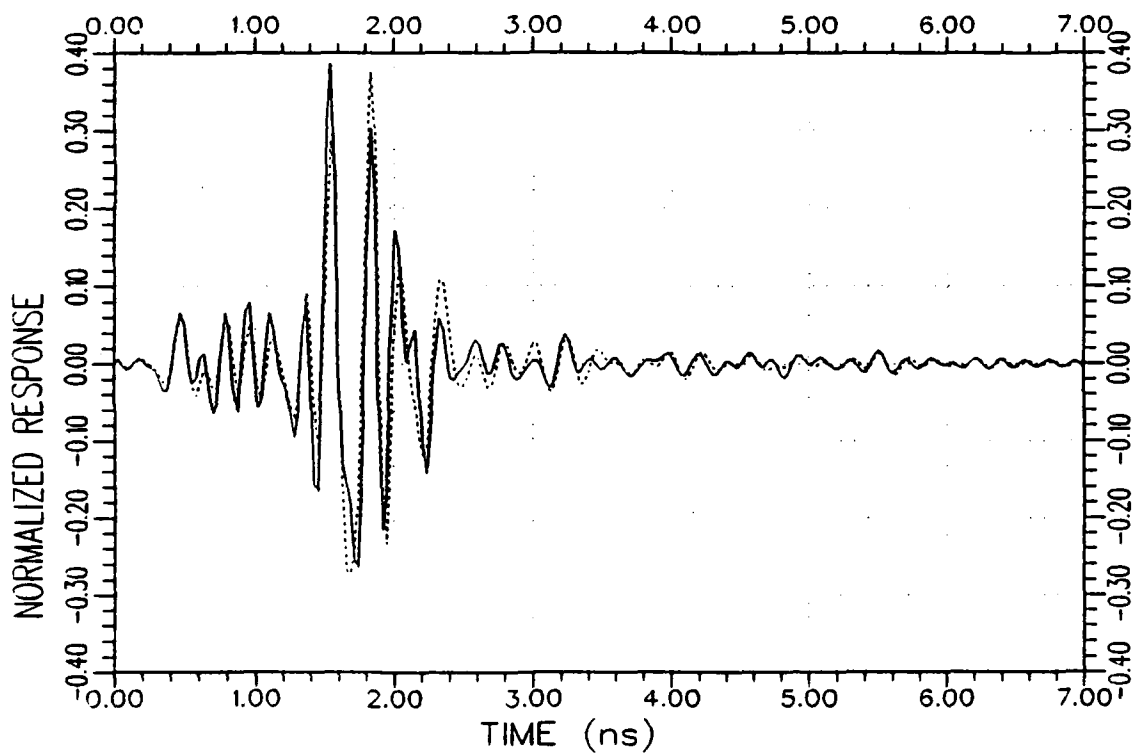
(a) Response waveforms

Figure 7.19. Normalized impulse response (.....) and K-pulse response (——) waveforms and their energy curves for aircraft A_3 at $45^\circ/VP$.



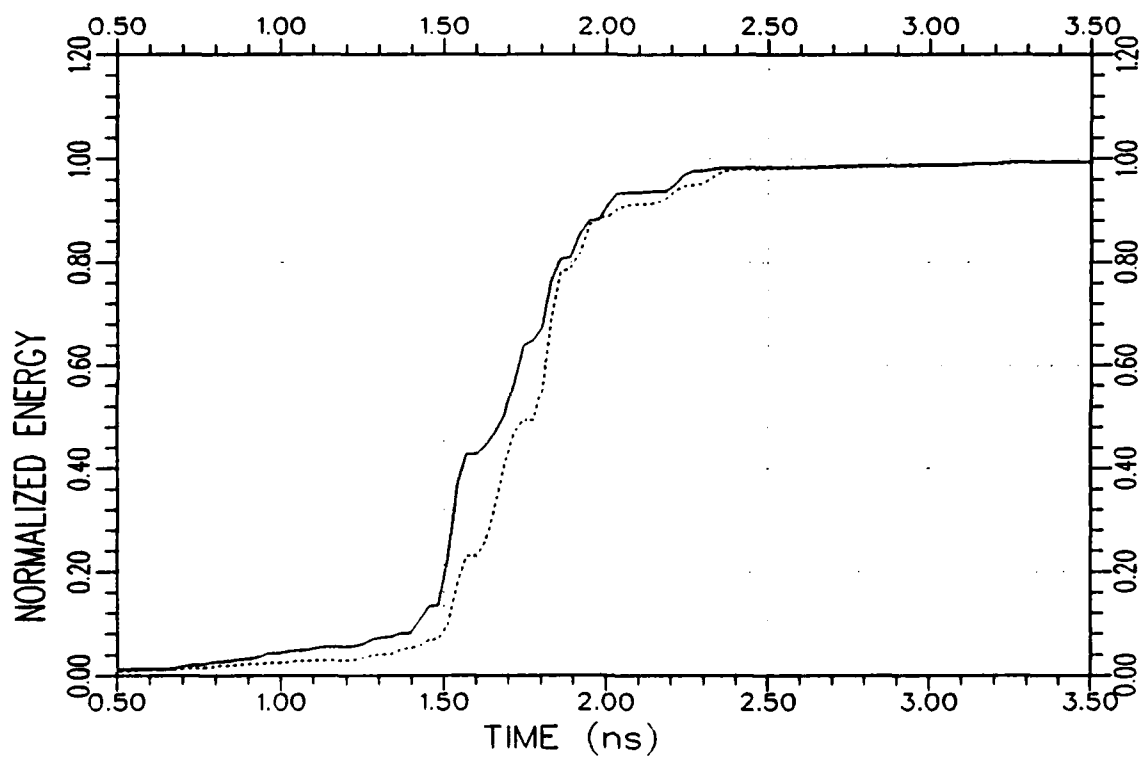
(b) Response energy curves

Figure 7.19. Continued.



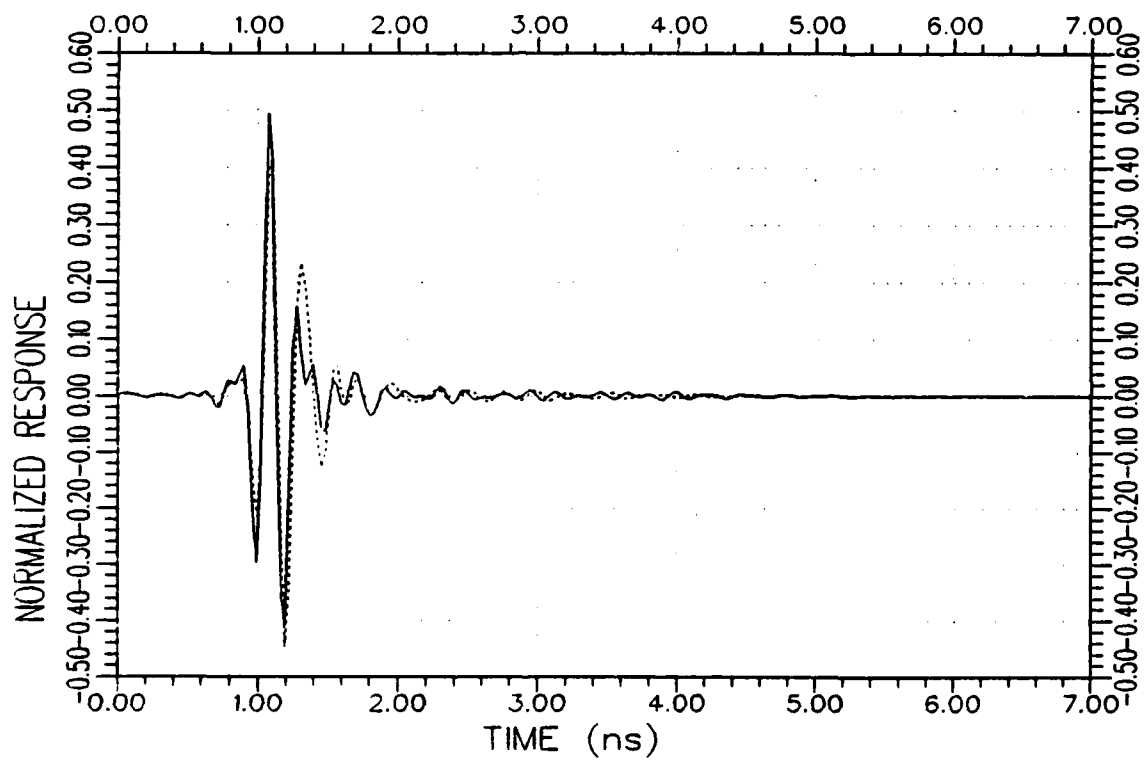
(a) Response waveforms

Figure 7.20. Normalized impulse response (.....) and K-pulse response (—) waveforms and their energy curves for aircraft A_3 at $60^\circ/VP$.



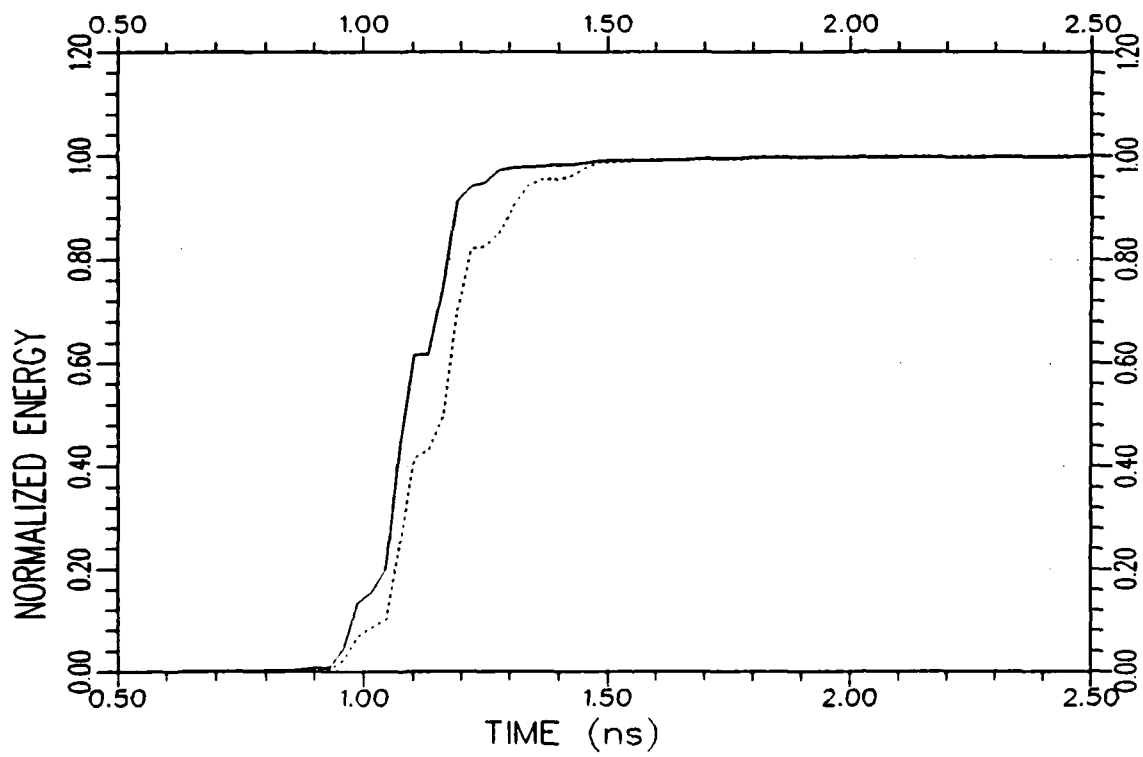
(b) Response energy curves

Figure 7.20. Continued.



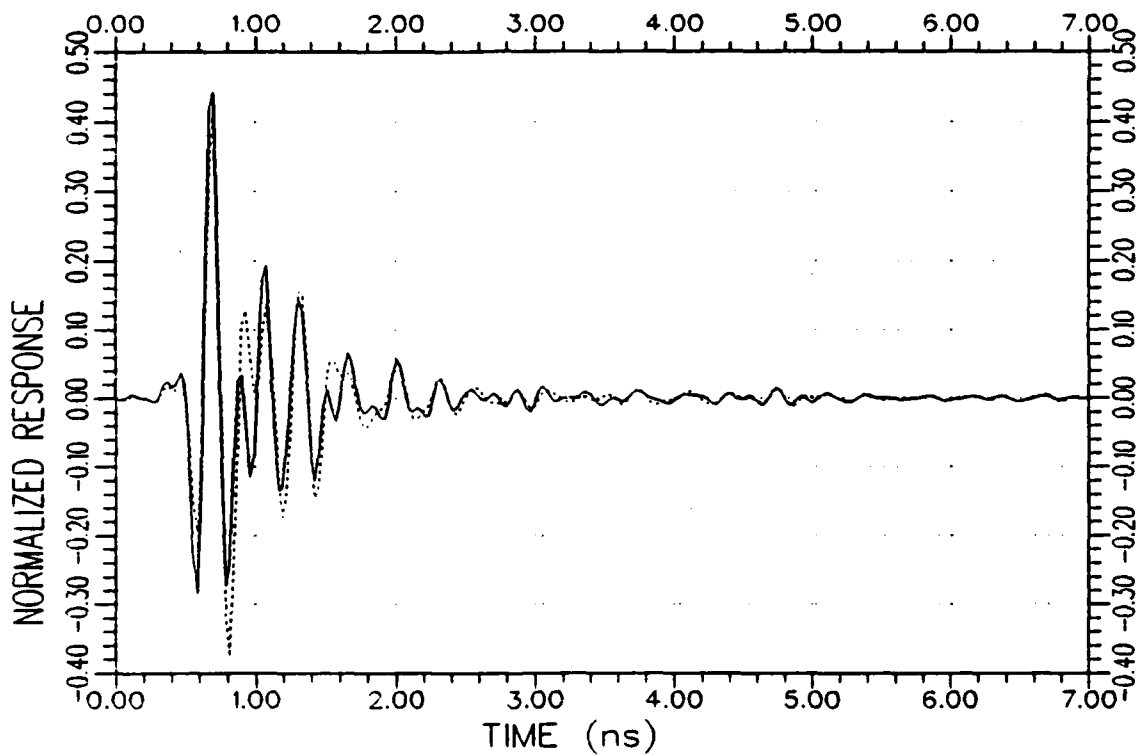
(a) Response waveforms

Figure 7.21. Normalized impulse response (.....) and K-pulse response (——) waveforms and their energy curves for aircraft A_3 at $90^\circ/VP$.



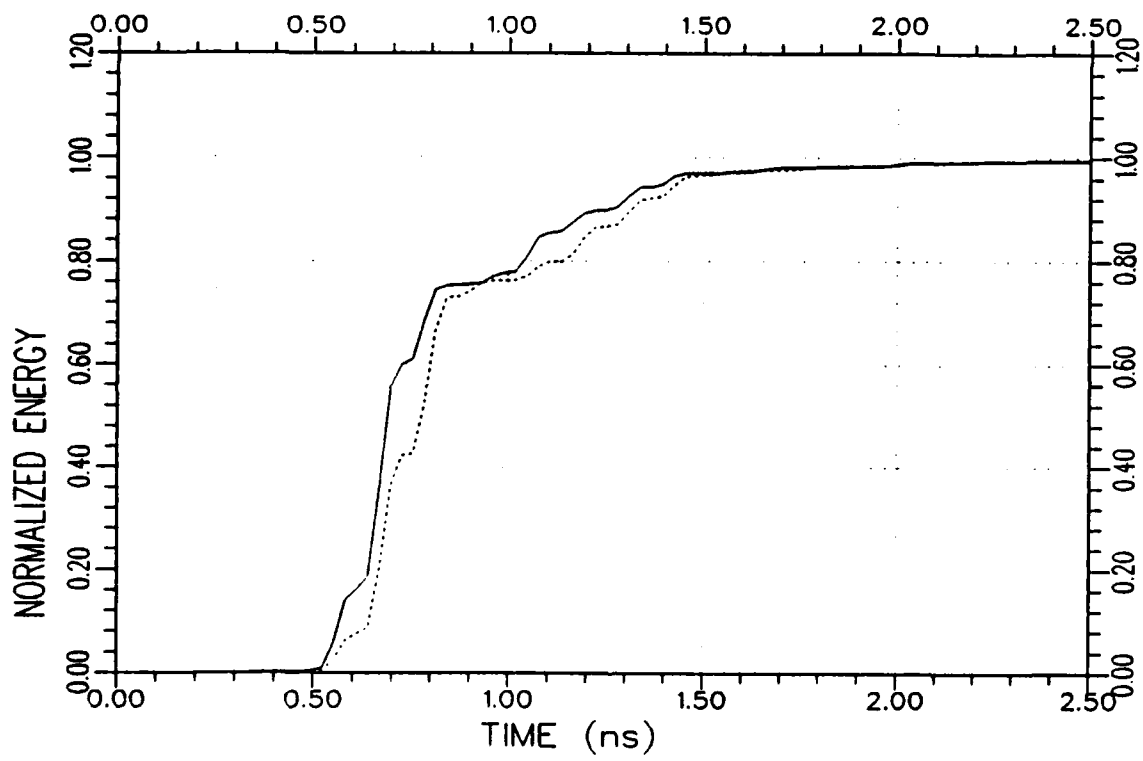
(b) Response energy curves

Figure 7.21. Continued.



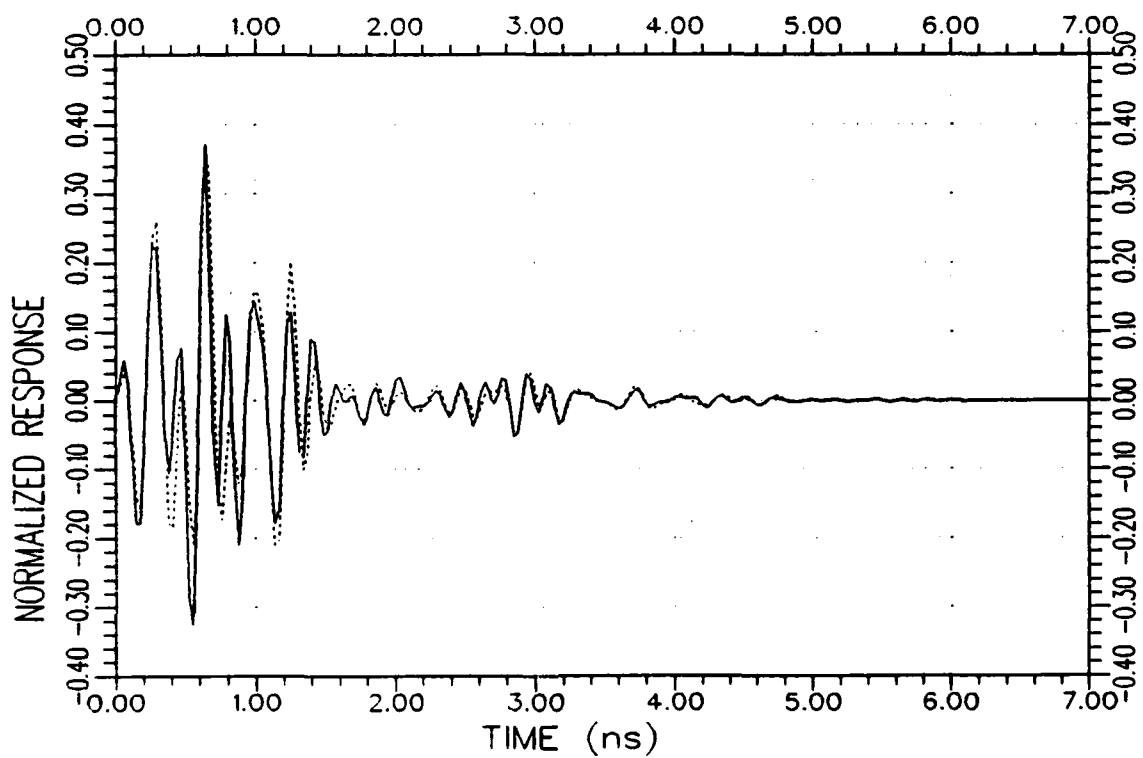
(a) Response waveforms

Figure 7.22. Normalized impulse response (.....) and K-pulse response (——) waveforms and their energy curves for aircraft A_3 at $120^\circ/VP$.



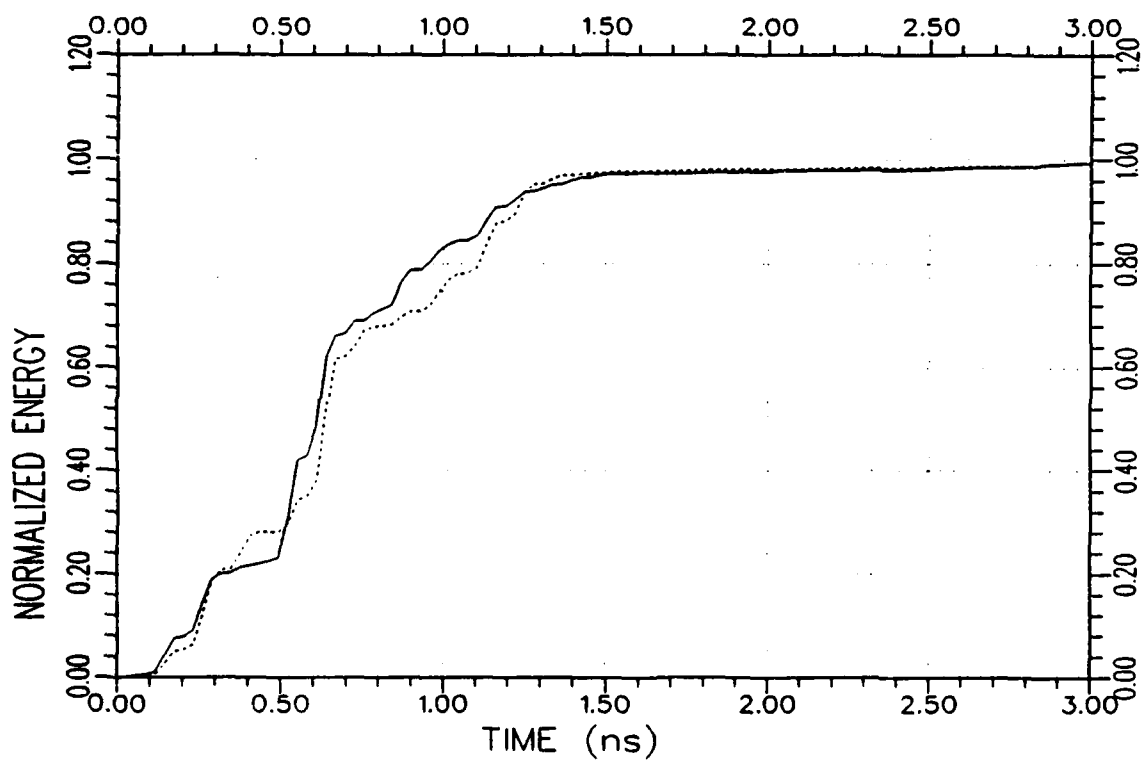
(b) Response energy curves

Figure 7.22. Continued.



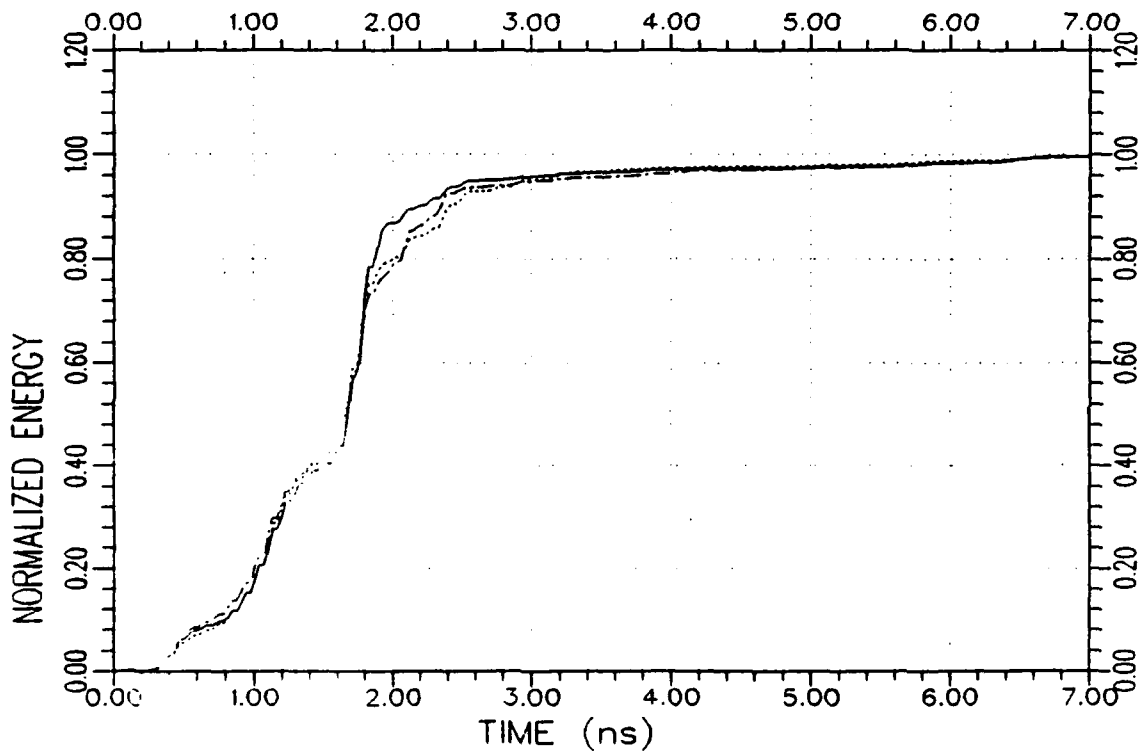
(a) Response waveforms

Figure 7.23. Normalized impulse response (.....) and K-pulse response (——) waveforms and their energy curves for aircraft A_3 at $180^\circ/VP$.



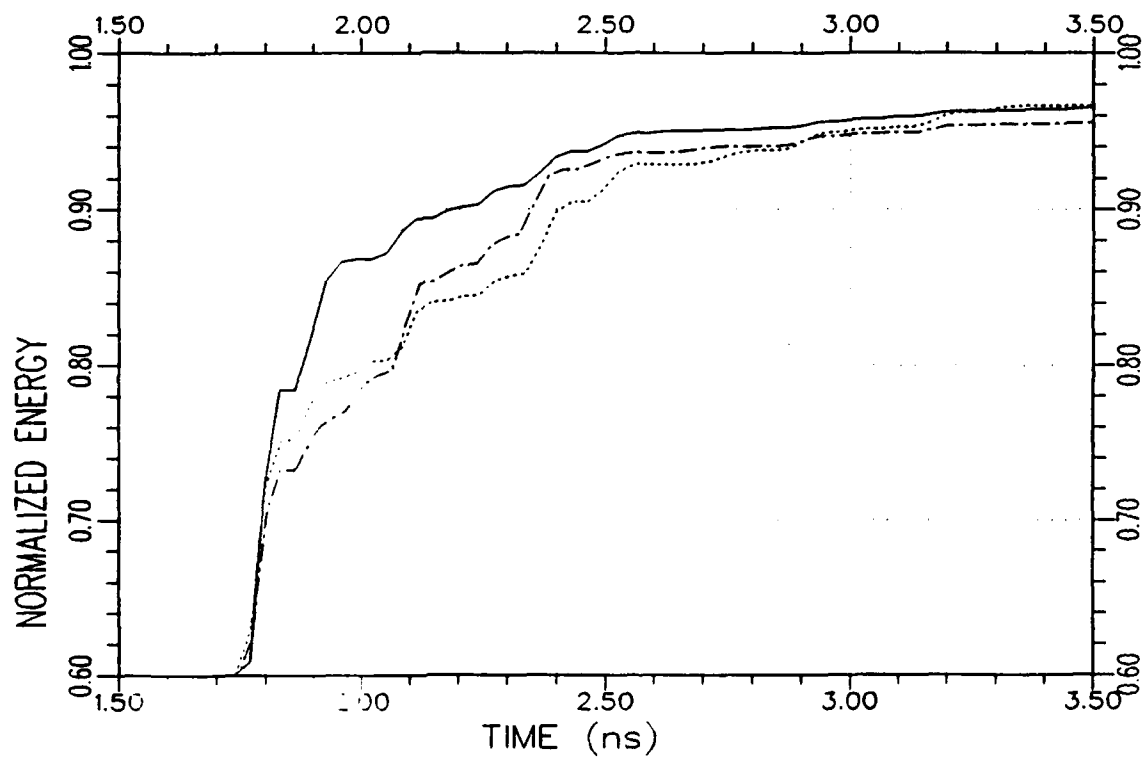
(b) Response energy curves

Figure 7.23. Continued.



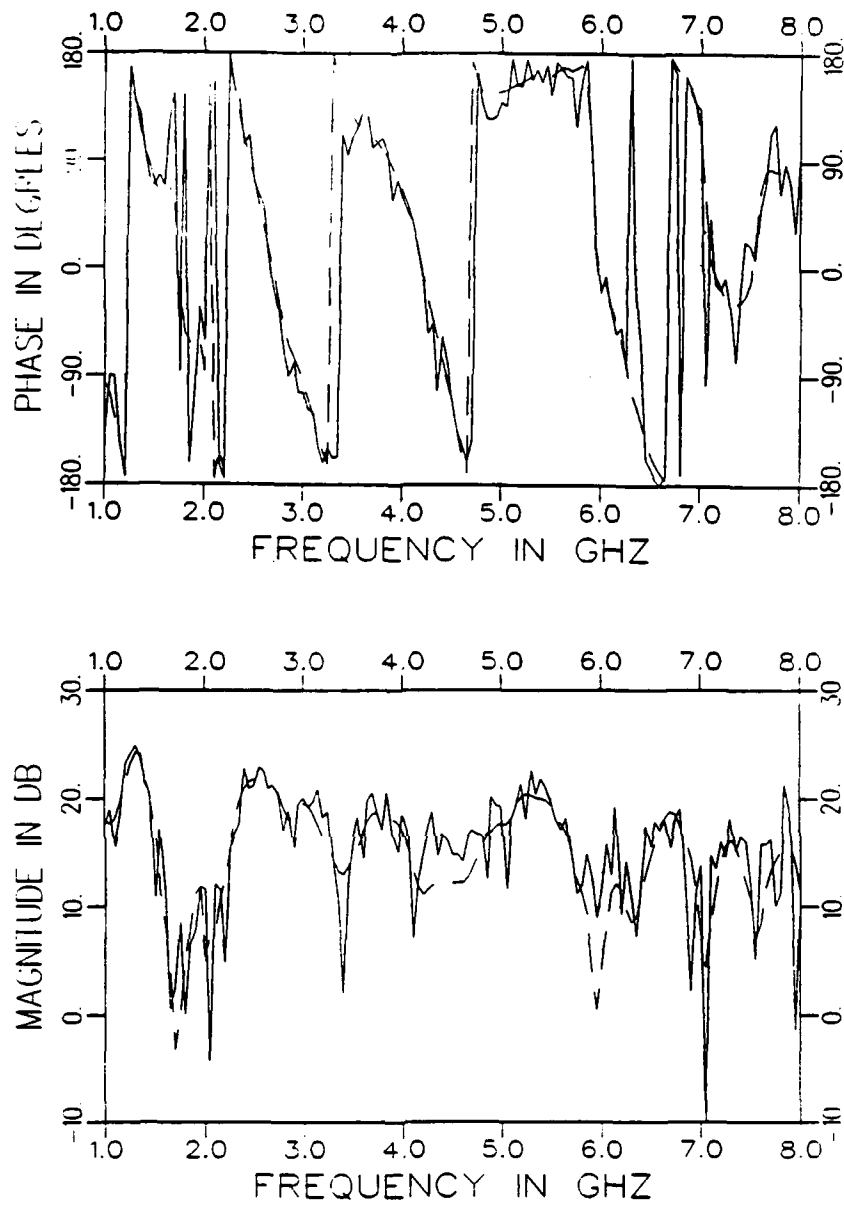
(a) A full-scale plot of the response energy curves

Figure 7.24. Normalized response energy curves of the test target A_1 produced by the K-pulses of the library targets A_1 (—), A_2 (·····) and A_3 (-·-·-) at $0^\circ/VP$ from a noisy backscattered data with SNR=11 dB.



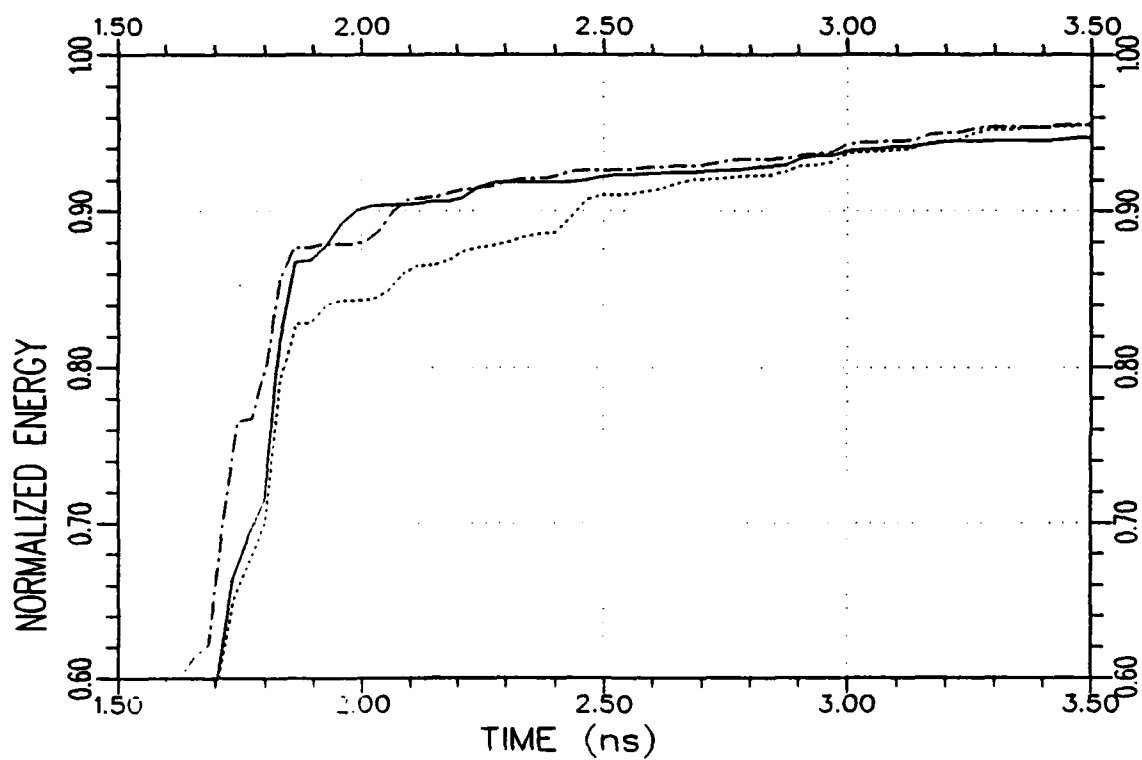
(b) A magnified version of part (a) showing only high energy level variations

Figure 7.24. Continued.



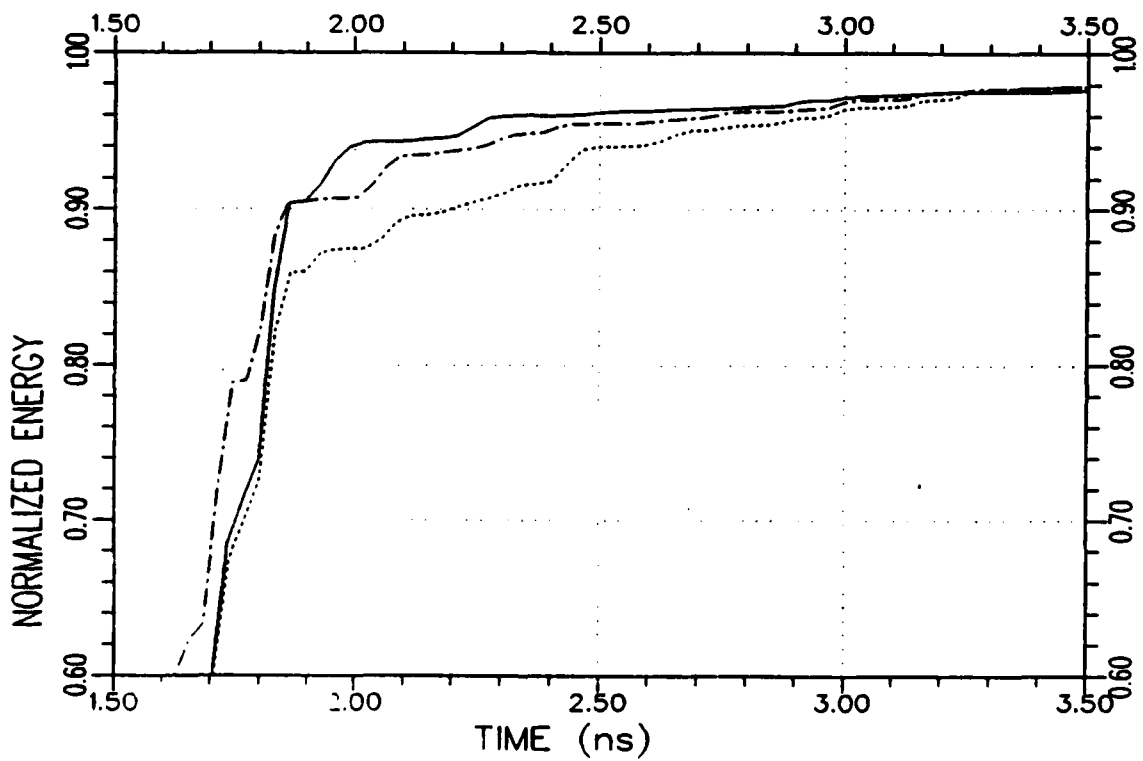
(c) The phase and magnitude plots for the noisy (—) and original (---) frequency domain data

Figure 7.24. Continued.



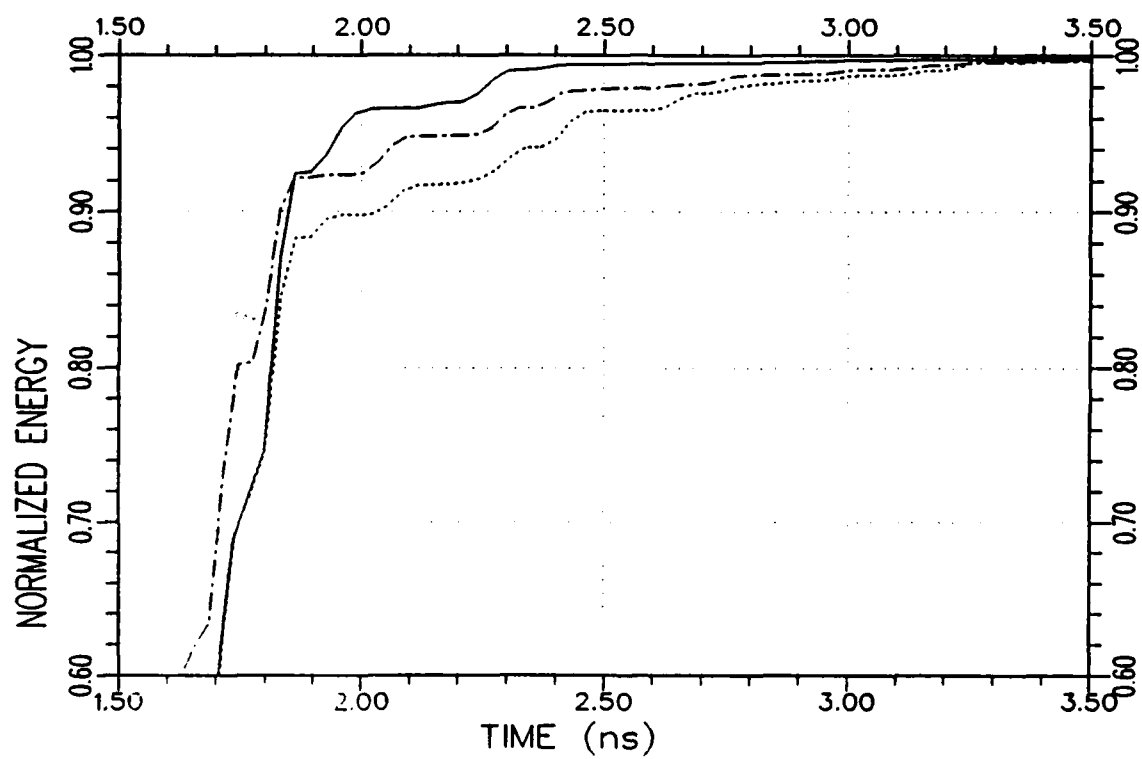
(a) for the SNR=11 dB

Figure 7.25. Normalized response energy curves (plotted on a magnified scale) of the test target A_1 produced by the K-pulses of the library targets A_1 (—), A_2 (····) and A_3 (-·-·-) at $30^\circ/VP$ for three different SNR levels.



(b) for the SNR=15 dB

Figure 7.25. Continued.



(c) for the $\text{SNR}=\infty$ (noise-free case)

Figure 7.25. Continued.

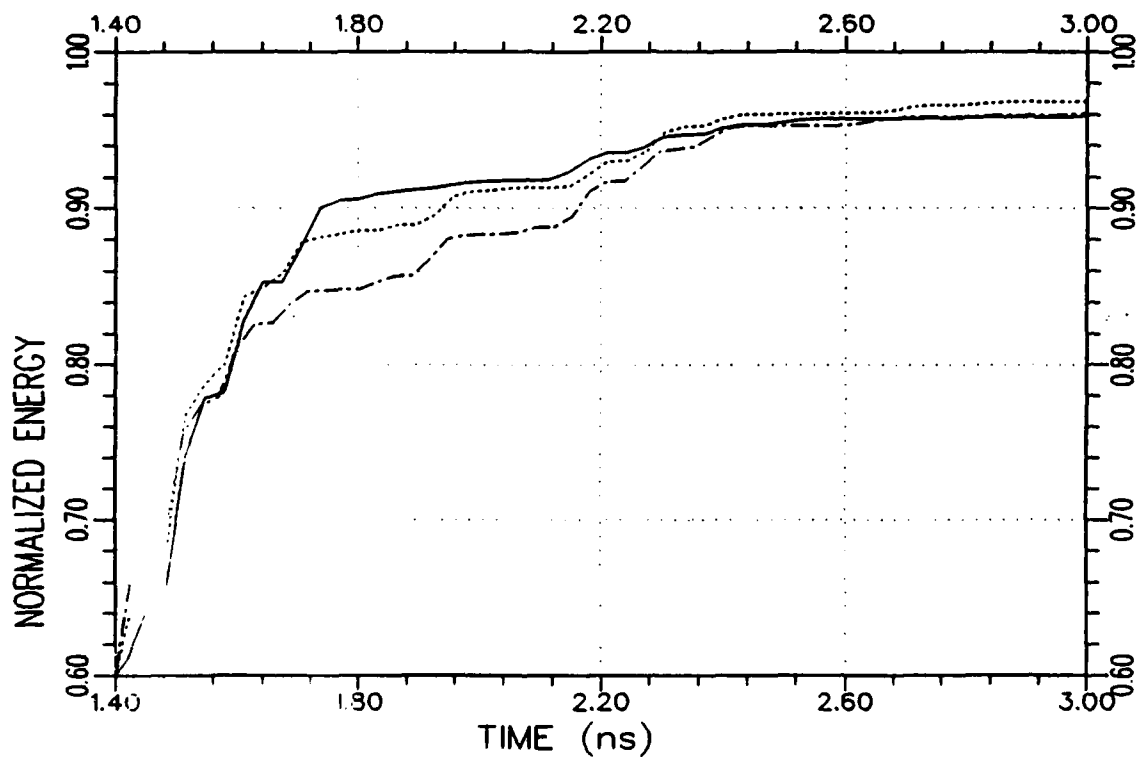
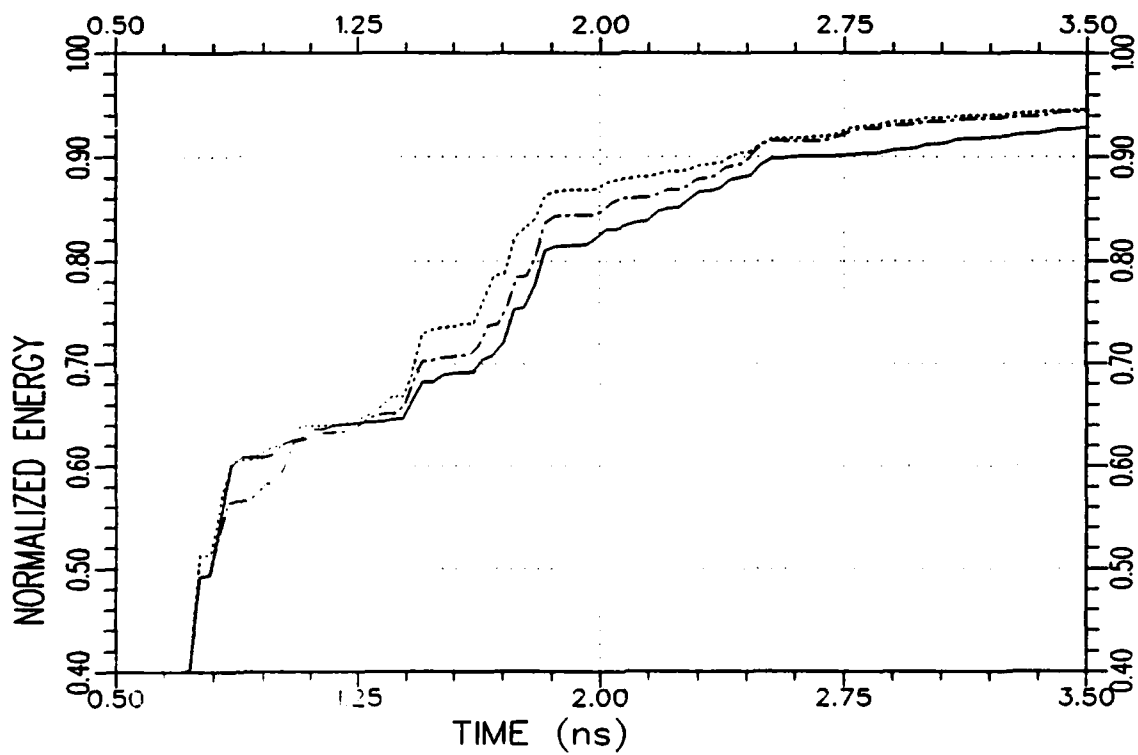
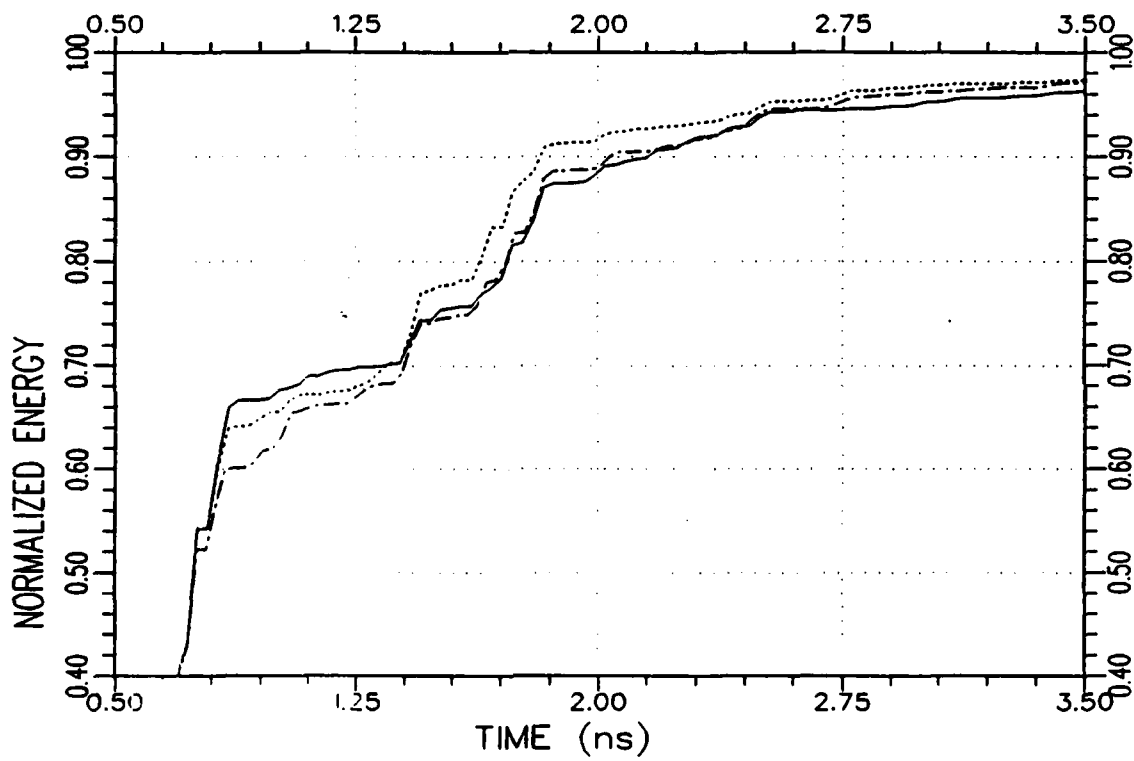


Figure 7.26. Normalized response energy curves (plotted on a magnified scale) of the test target A_1 produced by the K-pulses of the library targets A_1 (—), A_2 (·····) and A_3 (- - -) at $45^\circ/VP$ from a noisy backscattered data with $SNR=11$ dB.



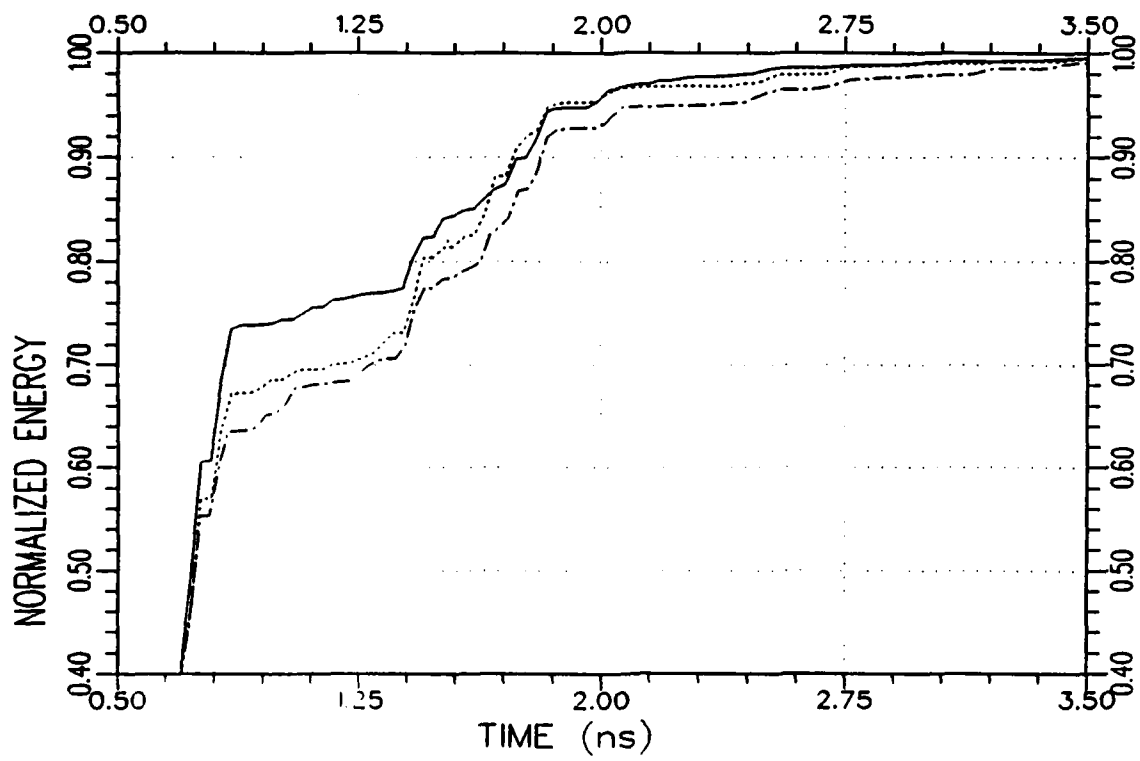
(a) for the SNR=11 dB

Figure 7.27. Normalized response energy curves (plotted on a magnified scale) of the test target A_1 produced by the K-pulses of the library targets A_1 (—), A_2 (·····) and A_3 (----) at $60^\circ/VP$ for three different SNR levels.



(b) for the SNR=15 dB

Figure 7.27. Continued.



(c) for the $\text{SNR}=\infty$ (noise-free case)

Figure 7.27. Continued.

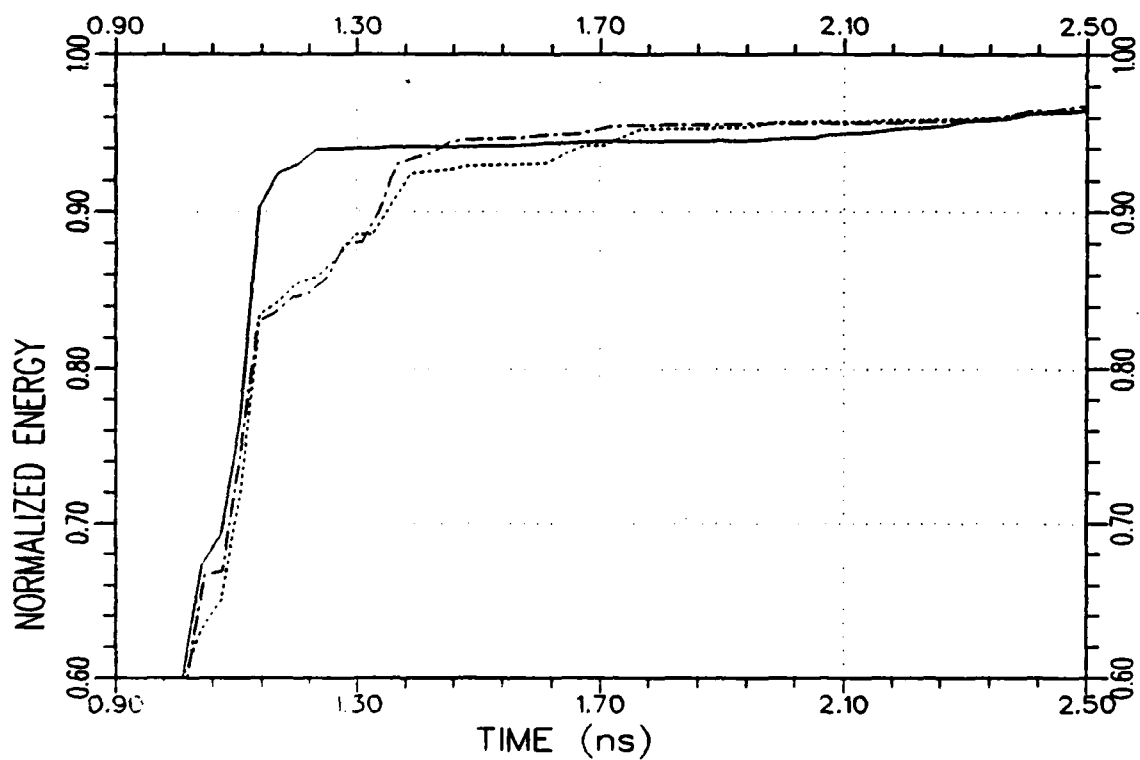


Figure 7.28. Normalized response energy curves (plotted on a magnified scale) of the test target A_1 produced by the K-pulses of the library targets A_1 (—), A_2 (·····) and A_3 (-·-·-) at $90^\circ/VP$ from a noisy backscattered data with $SNR=11$ dB.

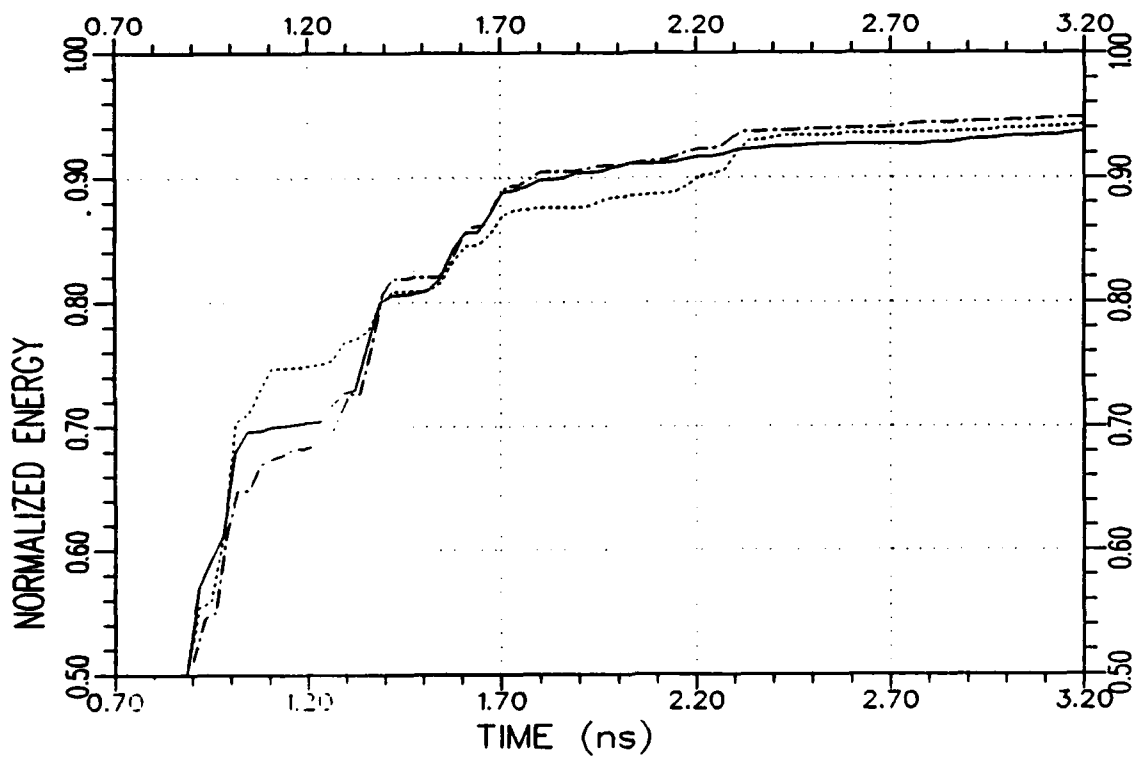
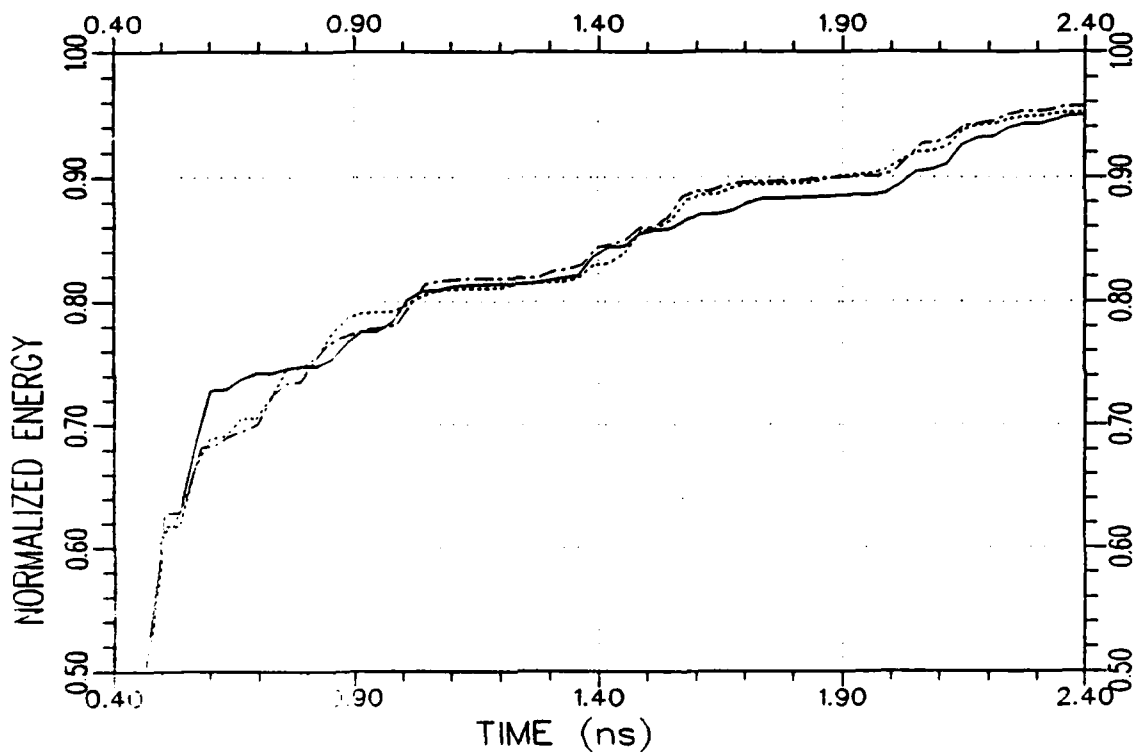
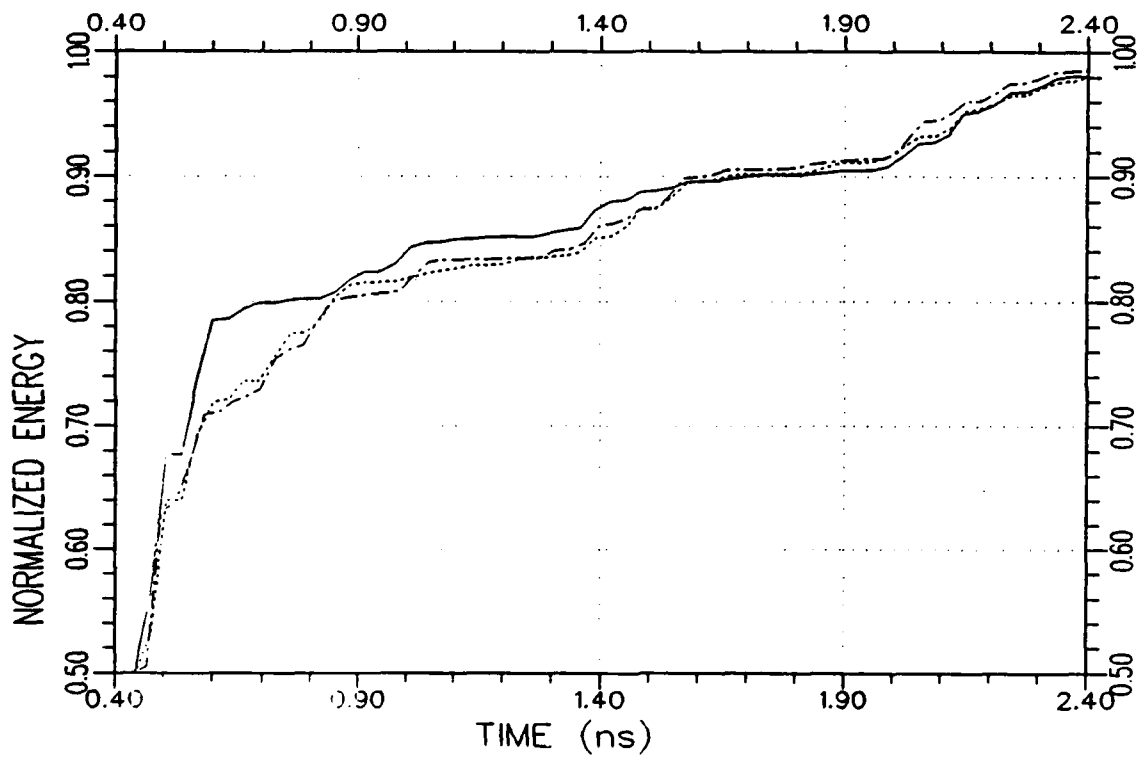


Figure 7.29. Normalized response energy curves (plotted on a magnified scale) of the test target A_1 produced by the K-pulses of the library targets A_1 (—), A_2 (·····) and A_3 (-·-·-) at $120^\circ/\text{VP}$ from a noisy backscattered data with $\text{SNR}=11$ dB.



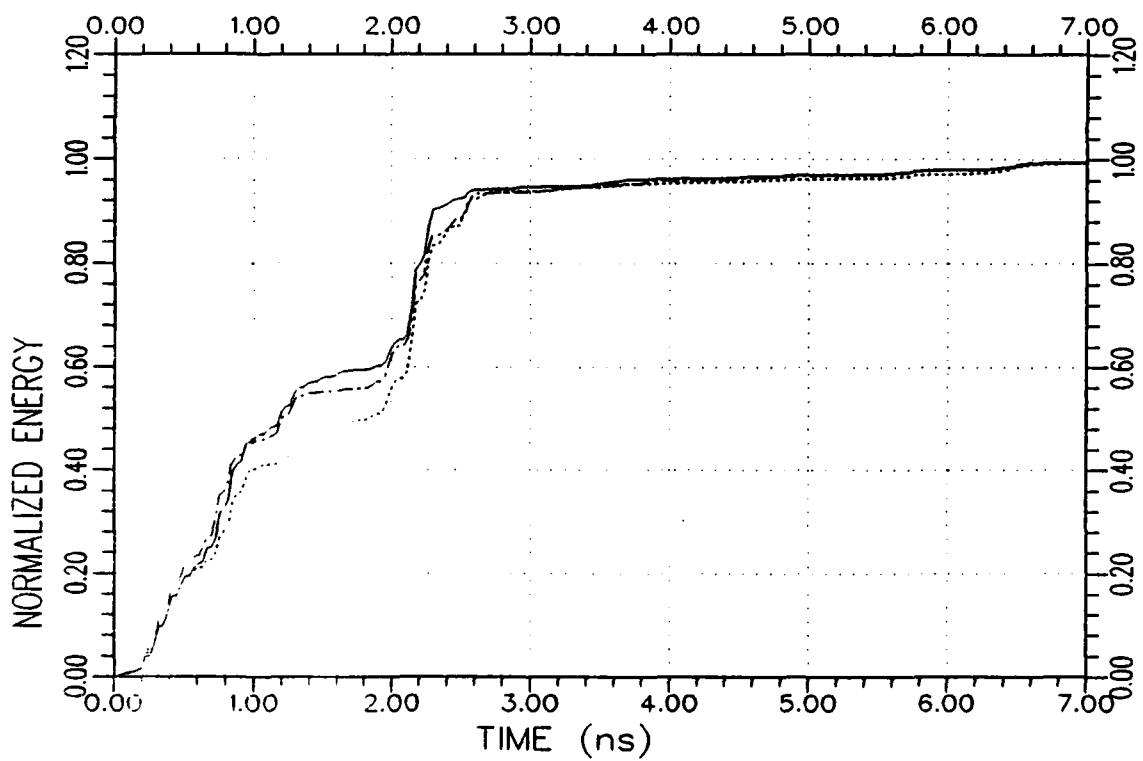
(a) for the SNR=11 dB

Figure 7.30. Normalized response energy curves (plotted on a magnified scale) of the test target A_1 produced by the K-pulses of the library targets A_1 (—), A_2 (·····) and A_3 (-·-·-) at $180^\circ/VP$ for two different SNR₂ levels.



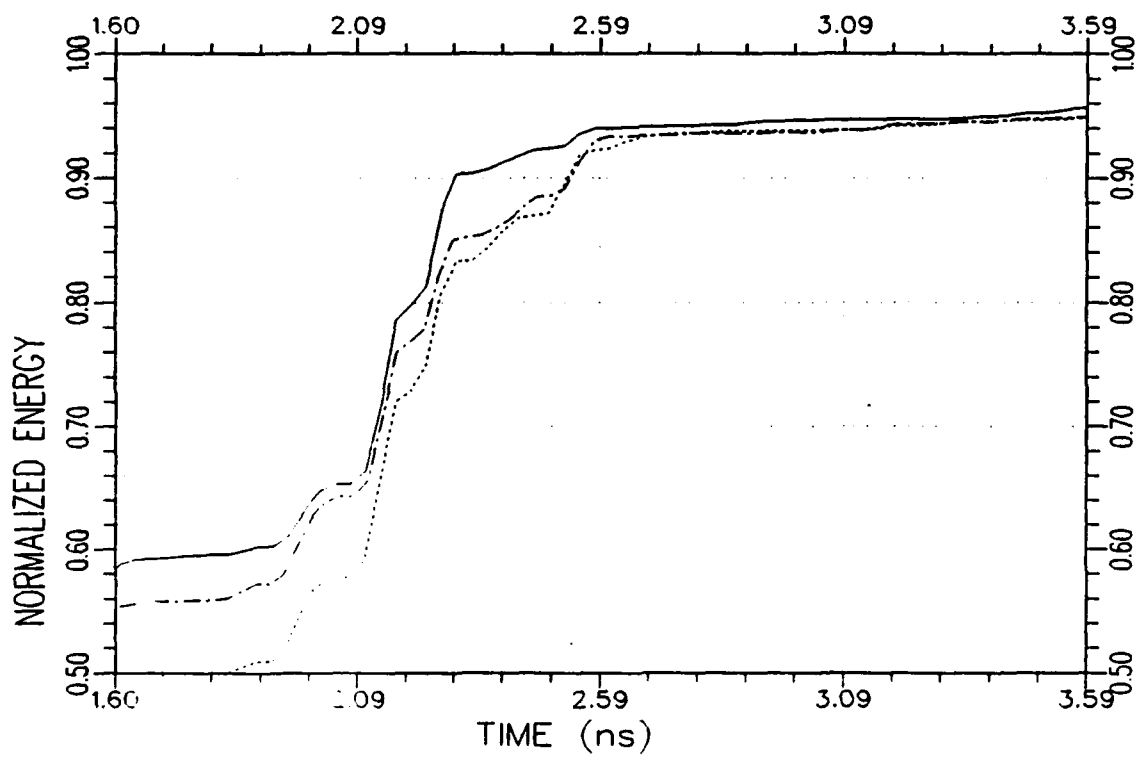
(b) for the SNR=15 dB

Figure 7.30. Continued.



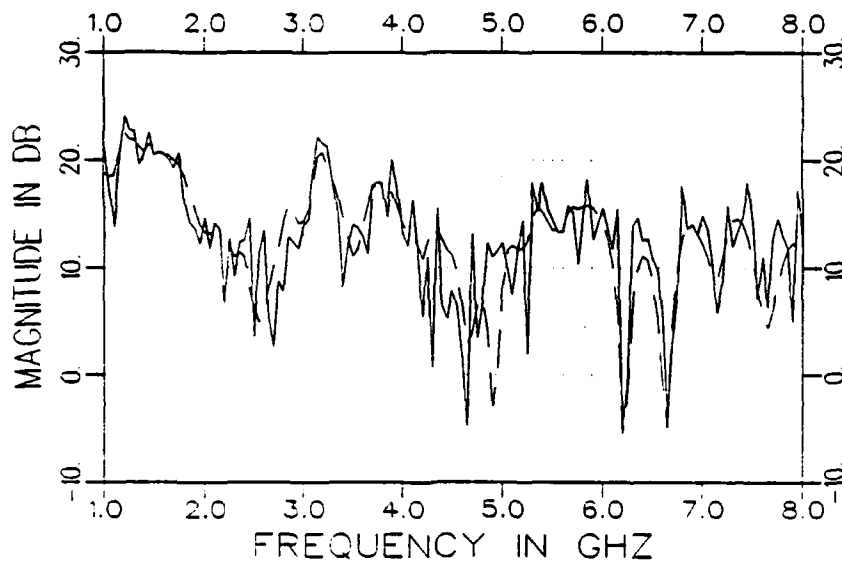
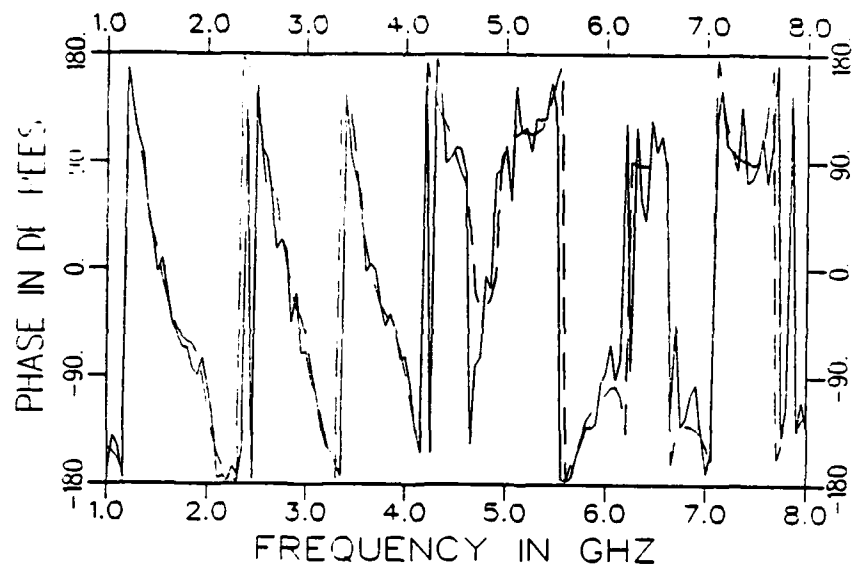
(a) A full-scale plot of the response energy curves

Figure 7.31. Normalized response energy curves of the test target A_2 produced by the K-pulses of the library targets A_1 ($\cdots\cdots$), A_2 (—) and A_3 ($-\cdot-\cdot-$) at $0^\circ/VP$ from a noisy backscattered data with $SNR=11$ dB.



(b) A magnified version of part (a) showing only high energy level variations

Figure 7.31. Continued.



(c) The phase and amplitude plots for the noisy (—) and original (---) frequency domain data

Figure 7.31. Continued.

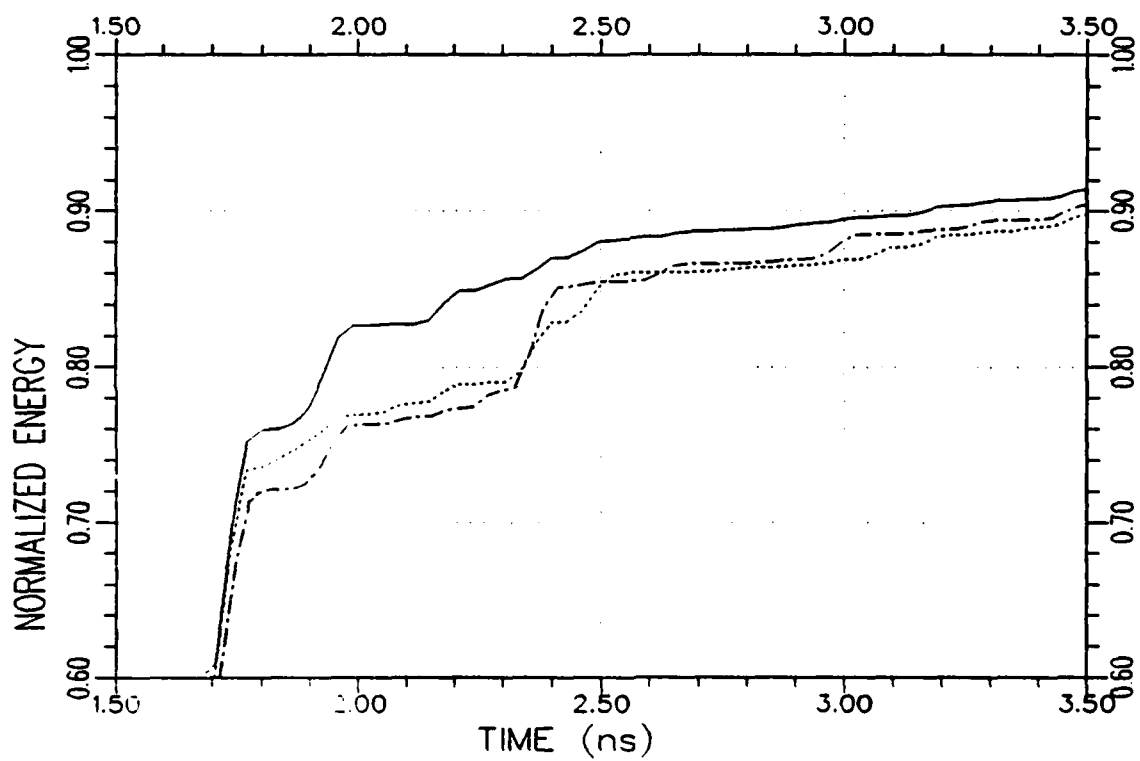
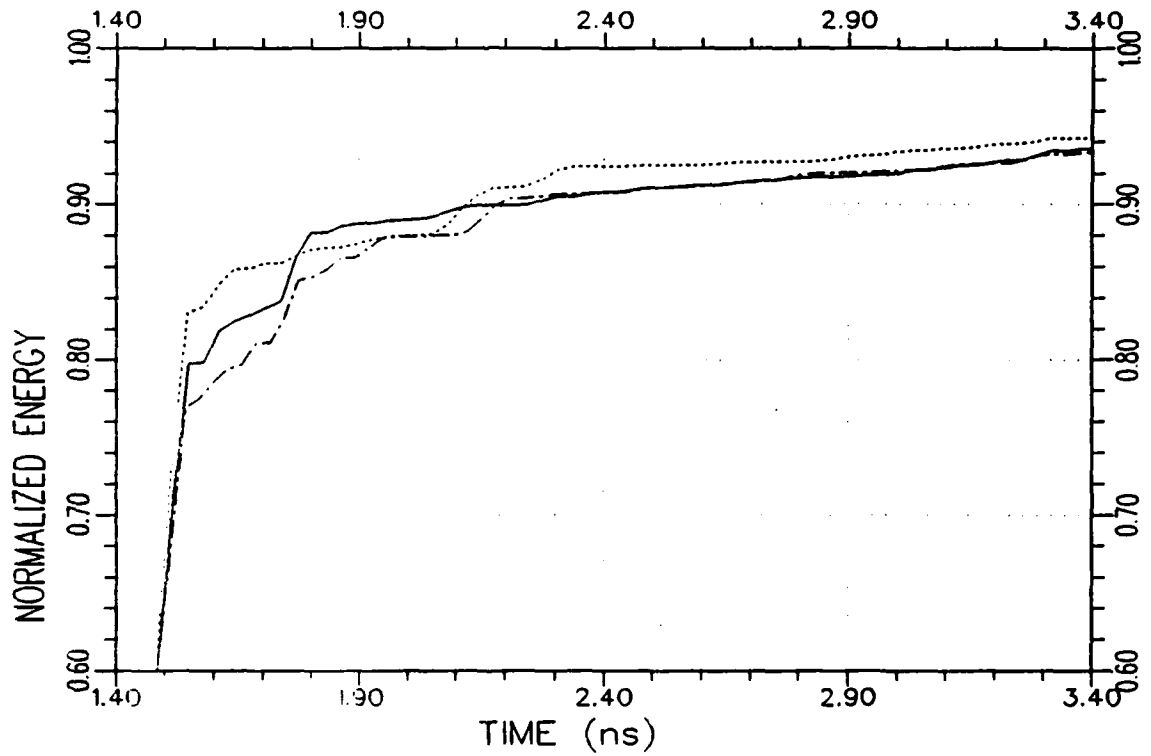
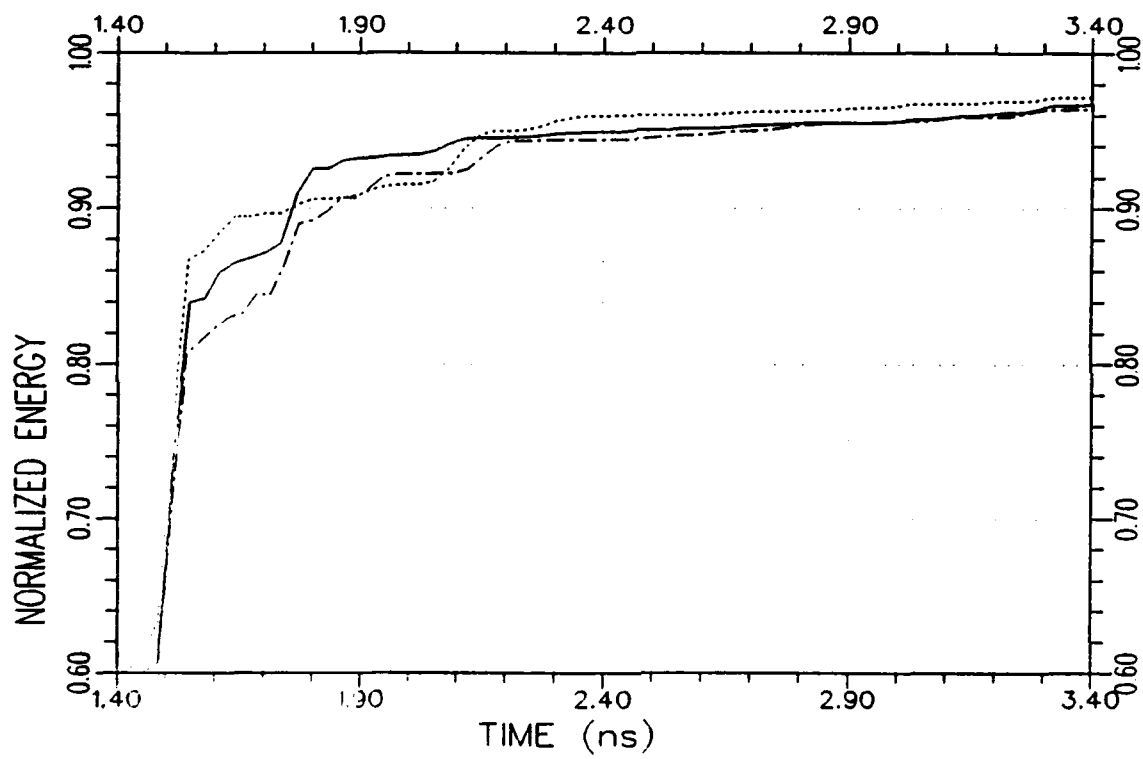


Figure 7.32. Normalized response energy curves (plotted on a magnified scale) of the test target A_2 produced by the K-pulses of the library targets A_1 ($\cdots\cdots$), A_2 (—) and A_3 (-·-·-) at $45^\circ/VP$ from a noisy backscattered data with SNR=11 dB.



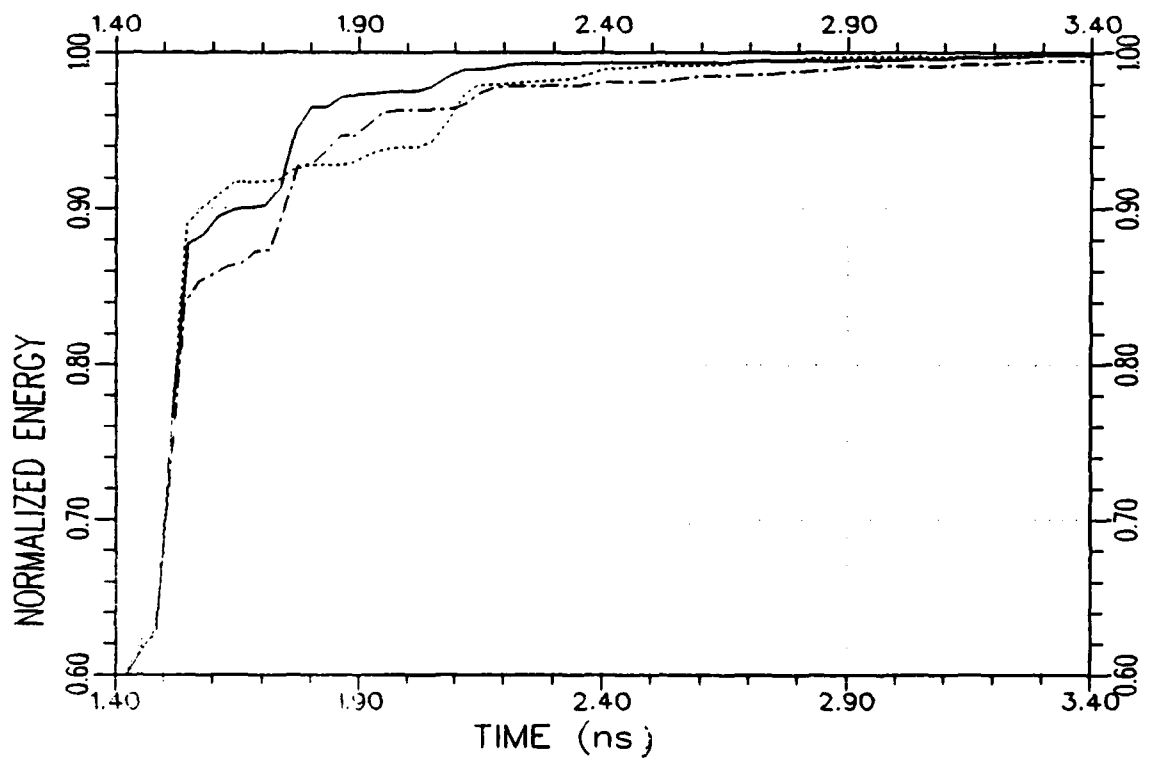
(a) for SNR=11 dB

Figure 7.33. Normalized response energy curves (plotted on a magnified scale) of the test target A_2 produced by the K-pulses of the library targets A_1 (·····), A_2 (—) and A_3 (----) at $60^\circ/VP$ for three different SNR levels.



(b) for SNR=15 dB

Figure 7.33. Continued.



(c) for $\text{SNR}=\infty$ (noise-free case)

Figure 7.33. Continued.

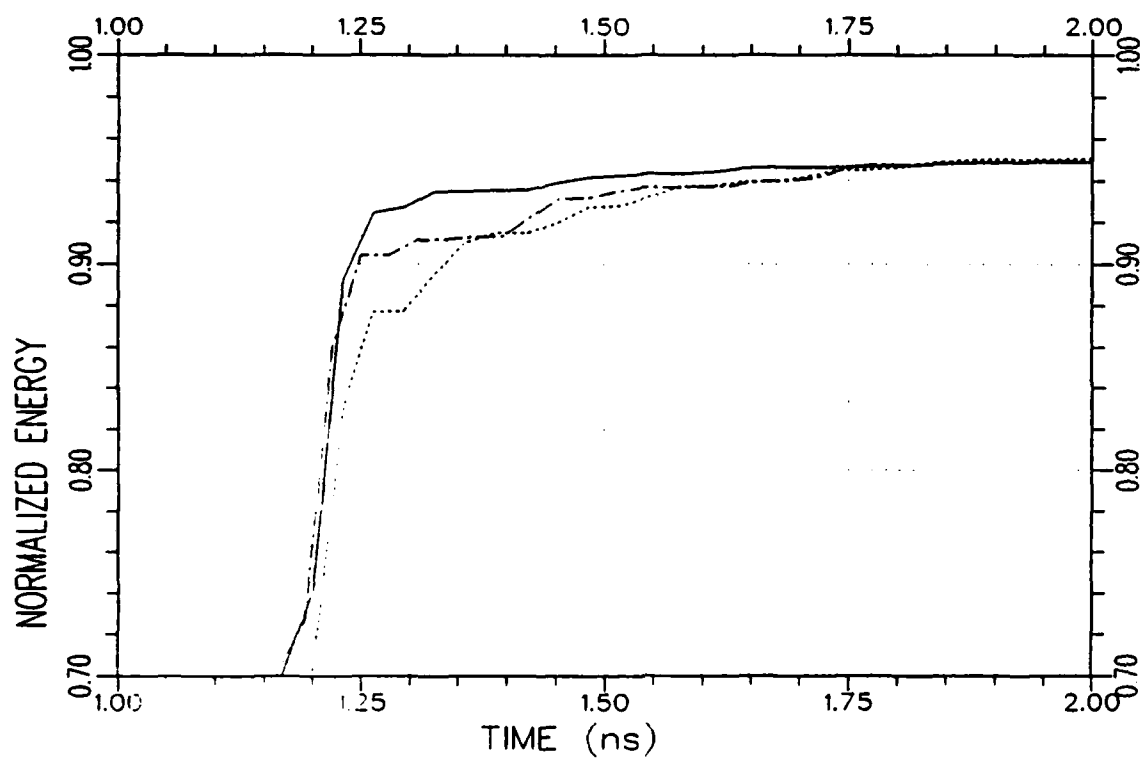


Figure 7.34. Normalized response energy curves (plotted on a magnified scale) of the test target A_2 produced by the K-pulses of the library targets A_1 ($\cdots\cdot\cdot$), A_2 (—) and A_3 ($\text{--}\cdot\text{--}$) at $90^\circ/\text{VP}$ from a noisy backscattered data with $\text{SNR}=11$ dB.

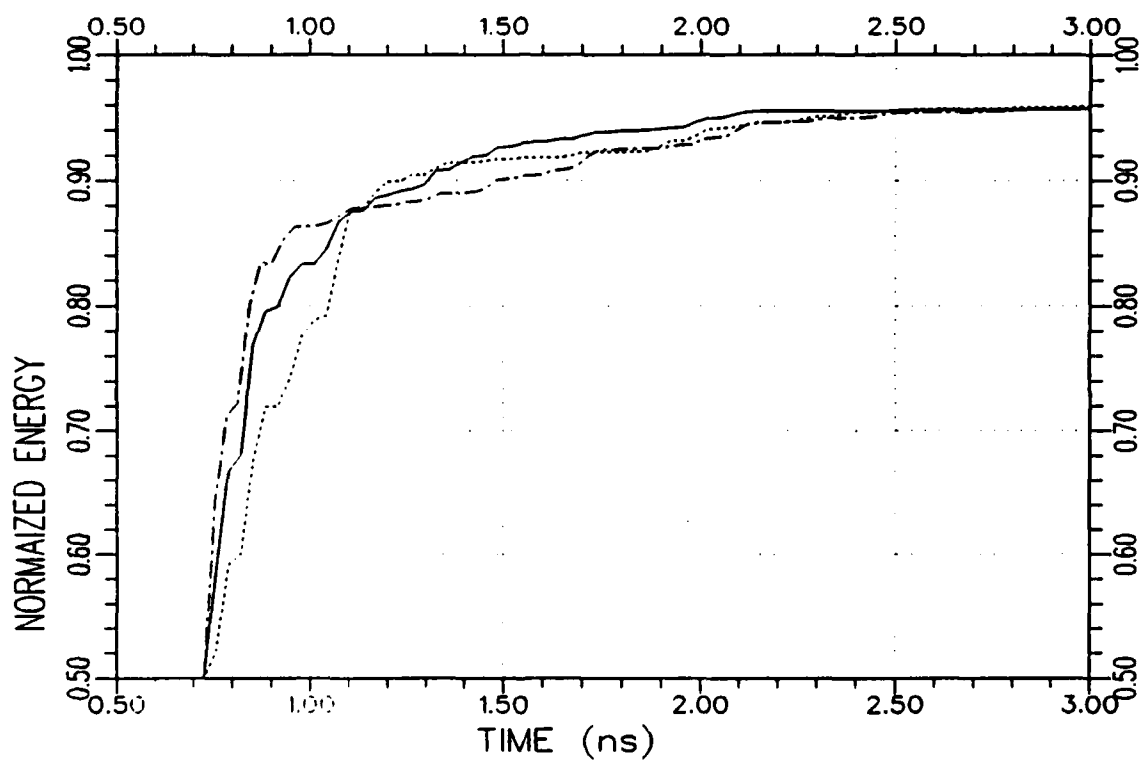
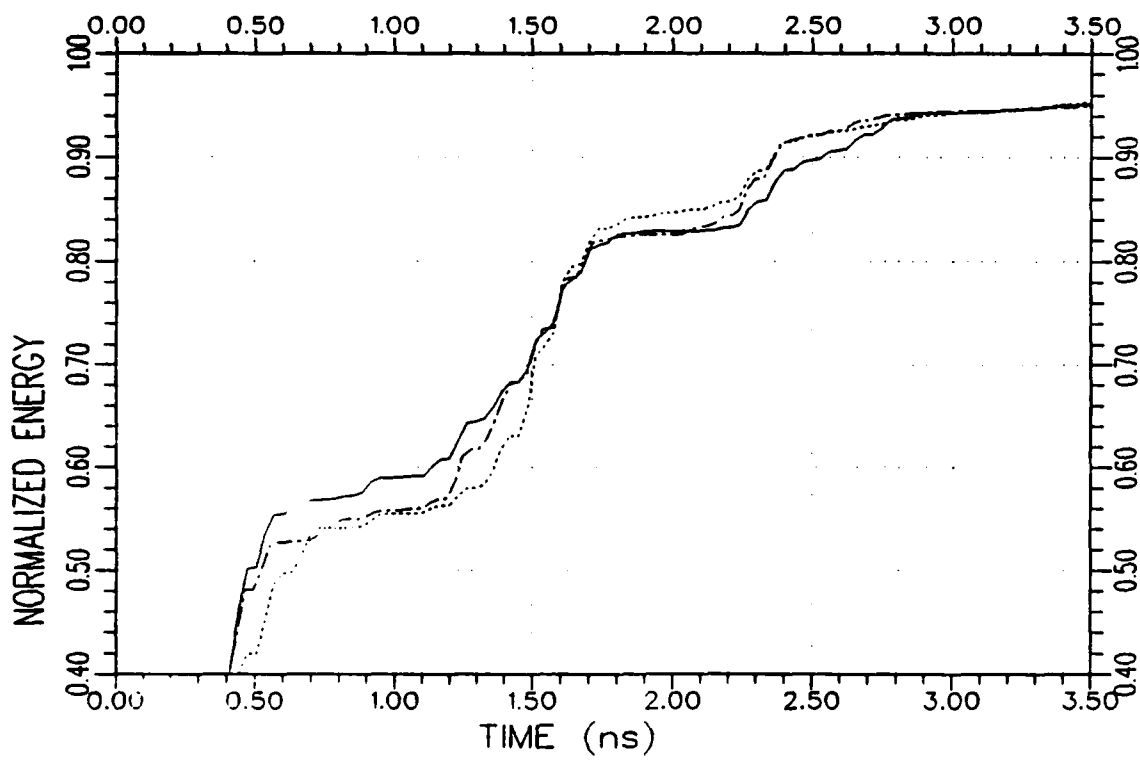
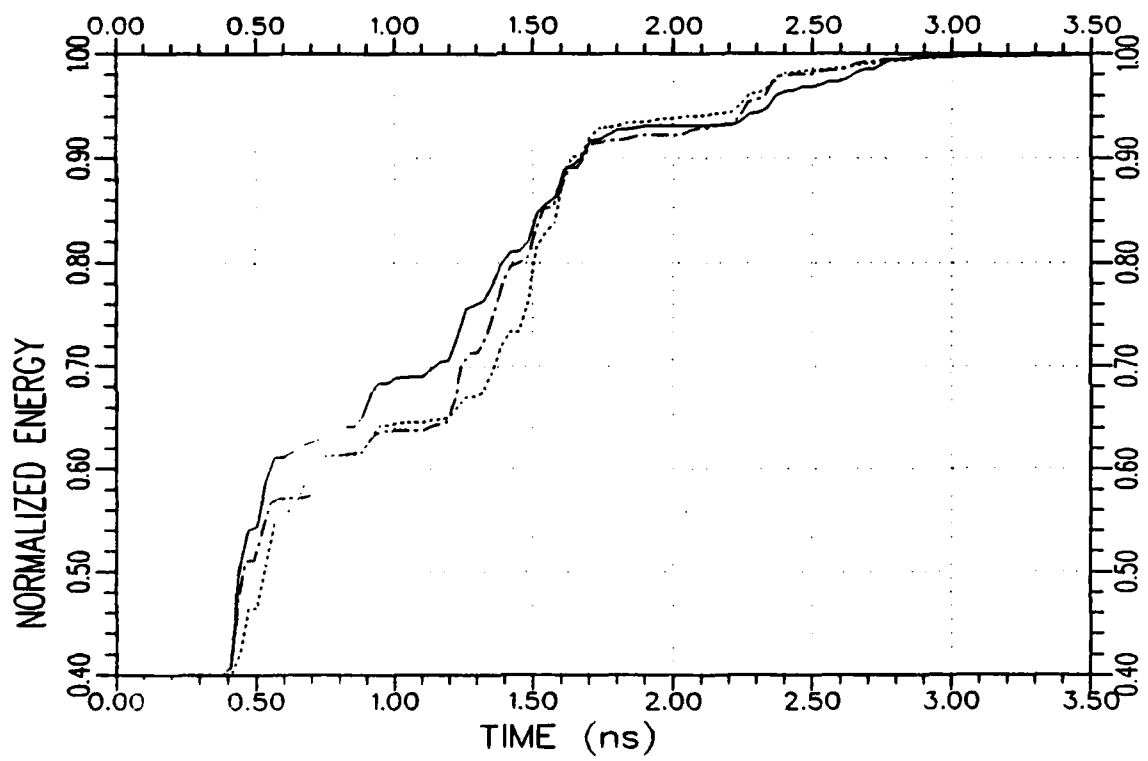


Figure 7.35. Normalized response energy curves (plotted on a magnified scale) of the test target A_2 produced by the K-pulses of the library targets A_1 ($\cdots\cdots$), A_2 (—) and A_3 (-·-·-) at $120^\circ/VP$ from a noisy backscattered data with SNR=11 dB.



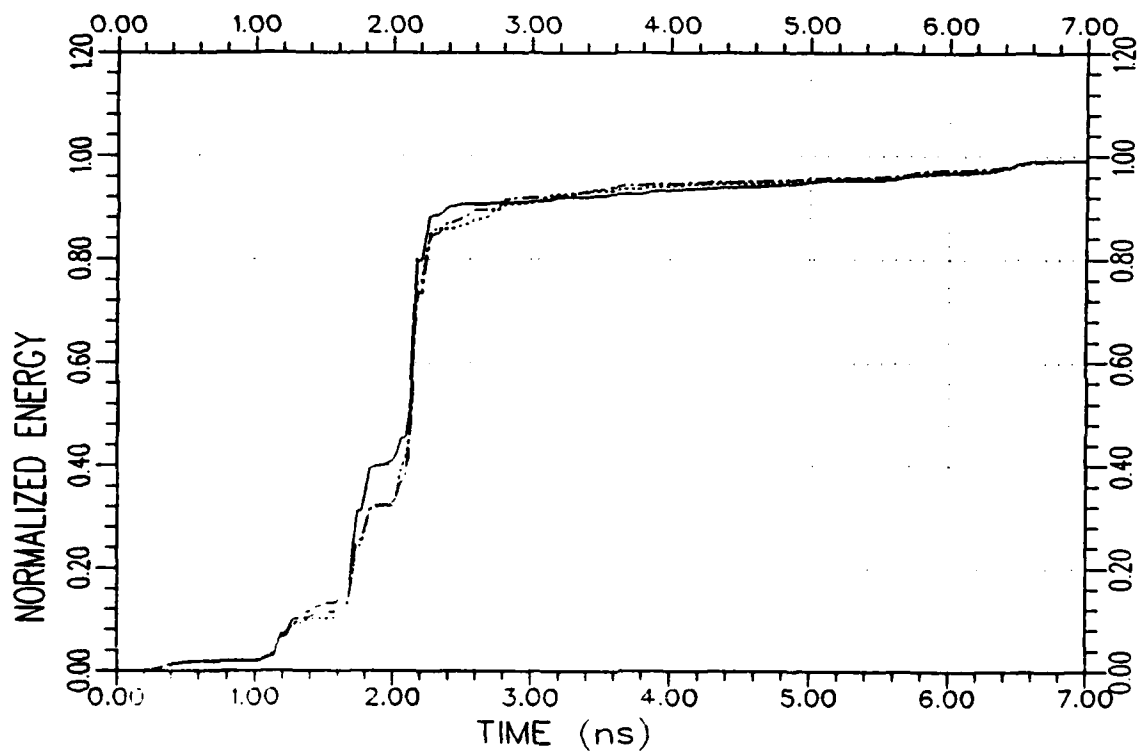
(a) for SNR=11 dB

Figure 7.36. Normalized response energy curves (plotted on a magnified scale) of the test target A_2 produced by the K-pulses of the library targets A_1 ($\cdots\cdots$), A_2 (—) and A_3 (---) at $180^\circ/\text{VP}$ for two different SNR levels.



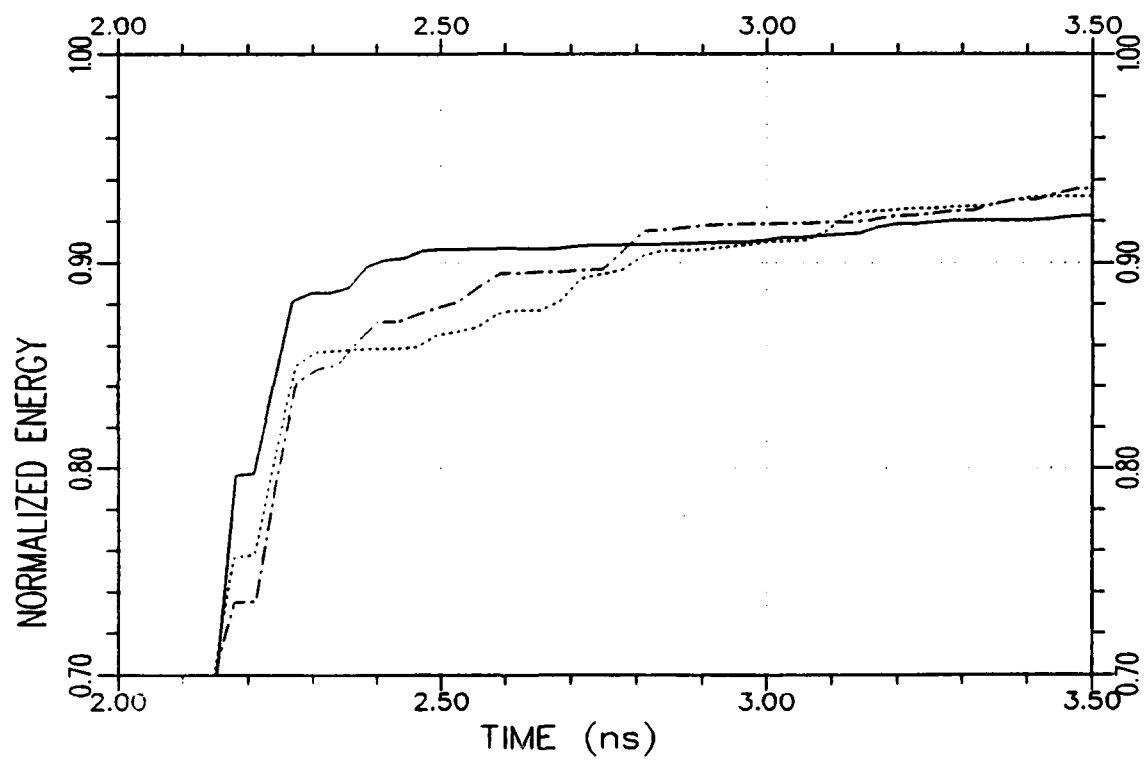
(b) for SNR=15 dB

Figure 7.36. Continued.



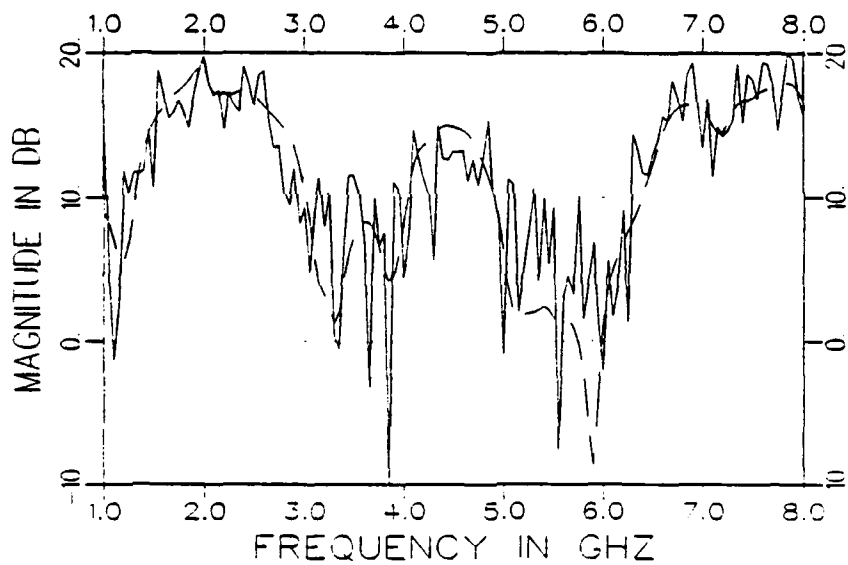
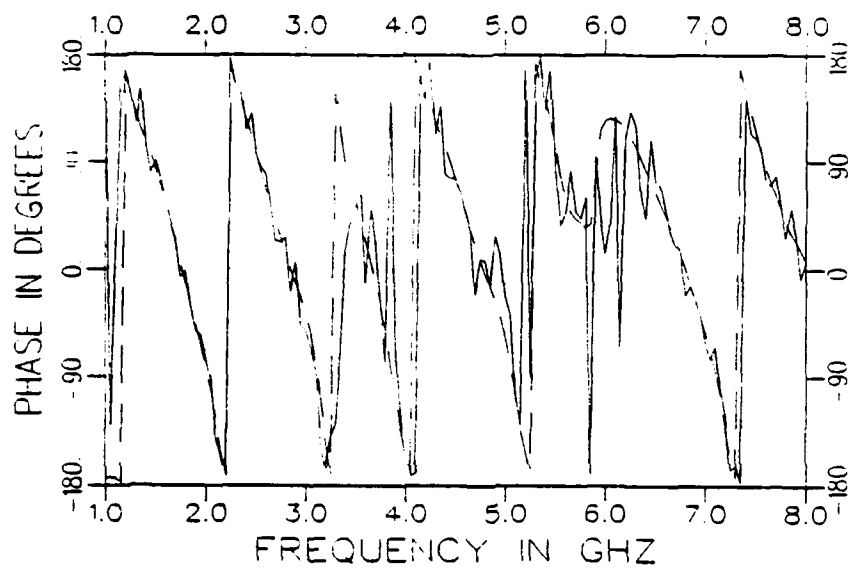
(a) A full-scale plot of the response energy curves

Figure 7.37. Normalized response energy curves of the test target A_3 produced by the K-pulses of the library targets A_1 (.....), A_2 (-·-·-) and A_3 (—) at $0^\circ/VP$ from a noisy backscattered data with SNR=11 dB.



(b) A magnified version of part (a) showing only high energy level variations

Figure 7.37. Continued.



(c) The phase and magnitude plots for the noisy (—) and original (---) frequency domain data

Figure 7.37. Continued.

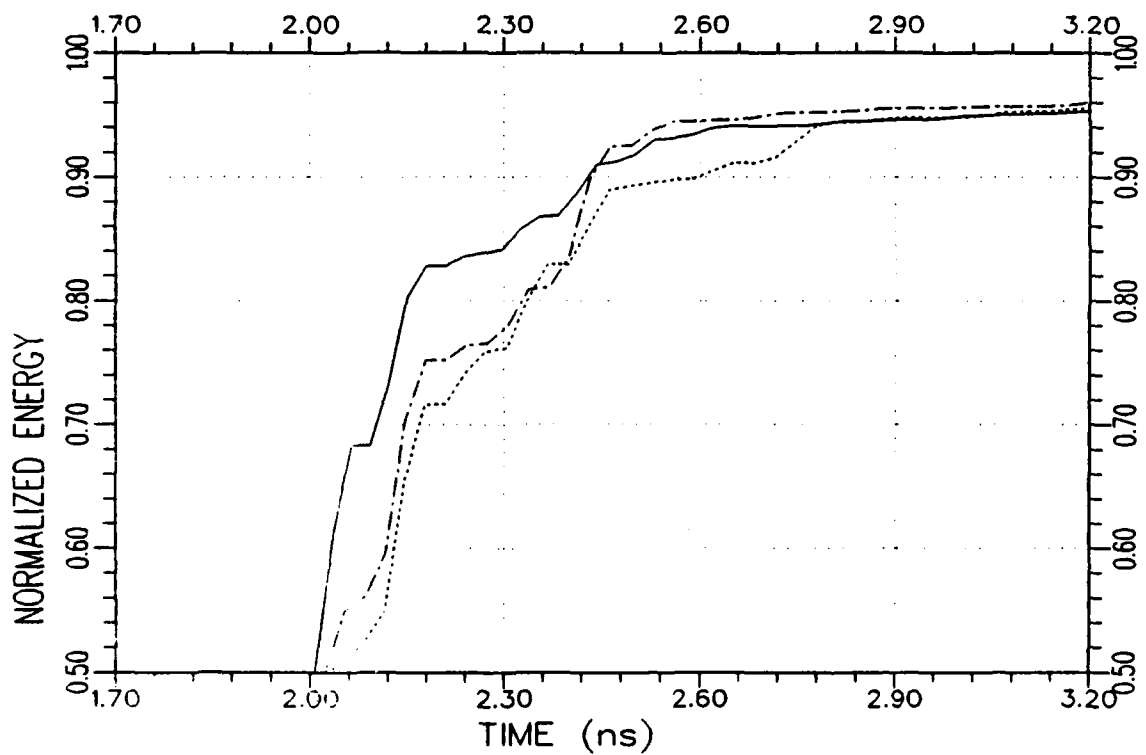


Figure 7.38. Normalized response energy curves (plotted on a magnified scale) of the test target A_3 produced by the K-pulses of the library targets A_1 (.....), A_2 (-·-·-) and A_3 (—) at $30^\circ/VP$ from a noisy backscattered data with SNR=11 dB.

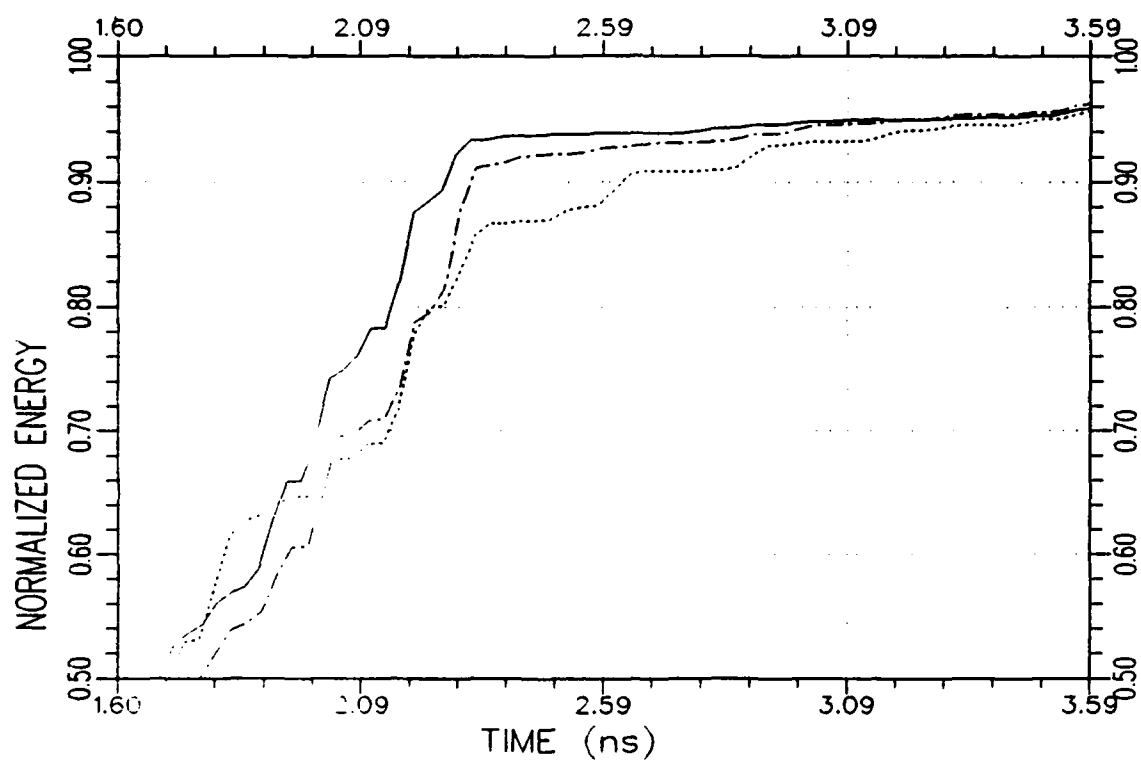


Figure 7.39. Normalized response energy curves (plotted on a magnified scale) of the test target A_3 produced by the K-pulses of the library targets A_1 ($\cdots\cdots$), A_2 ($- \cdot - \cdot -$) and A_3 (---) at $45^\circ/\text{VP}$ from a noisy backscattered data with $\text{SNR}=11$ dB.

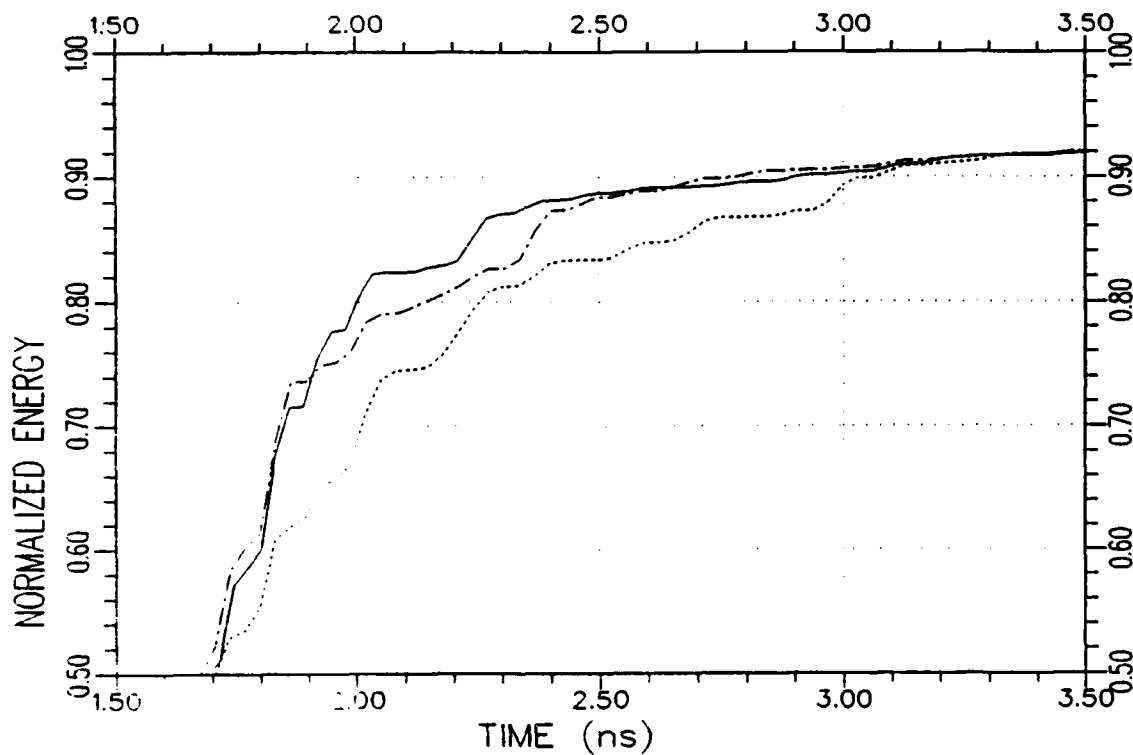


Figure 7.40. Normalized response energy curves (plotted on a magnified scale) of the test target A_3 produced by the K-pulses of the library targets A_1 ($\cdots\cdots$), A_2 ($- \cdot - \cdot -$) and A_3 (—) at $60^\circ/\text{VP}$ from a noisy backscattered data with SNR=11 dB.

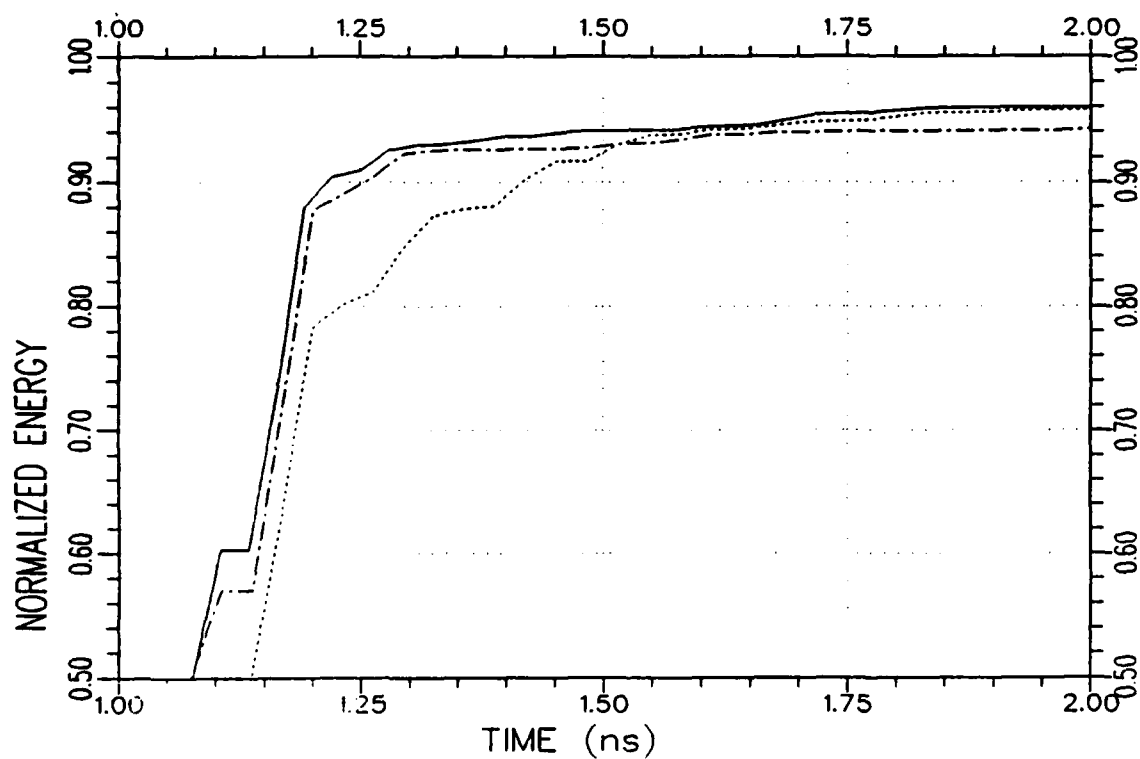


Figure 7.41. Normalized response energy curves (plotted on a magnified scale) of the test target A_3 produced by the K-pulses of the library targets A_1 ($\cdots\cdots$), A_2 ($- \cdot - \cdot -$) and A_3 (---) at $90^\circ/\text{VP}$ from a noisy backscattered data with $\text{SNR}=11$ dB.

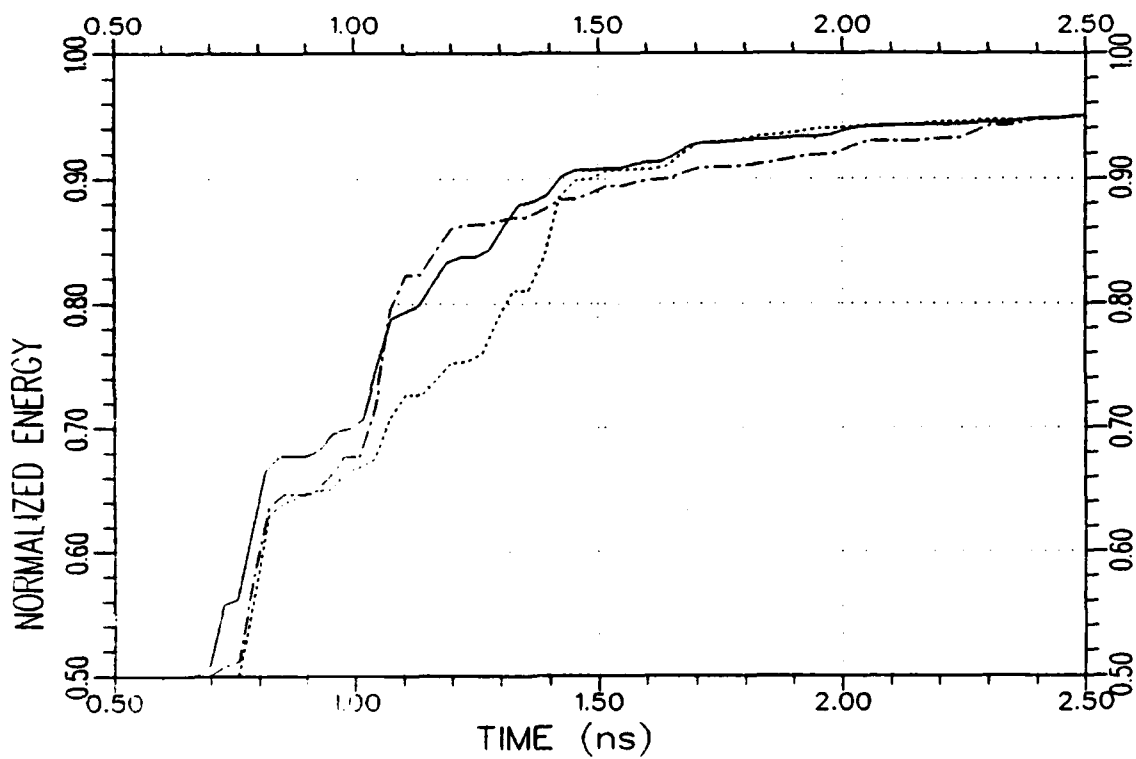
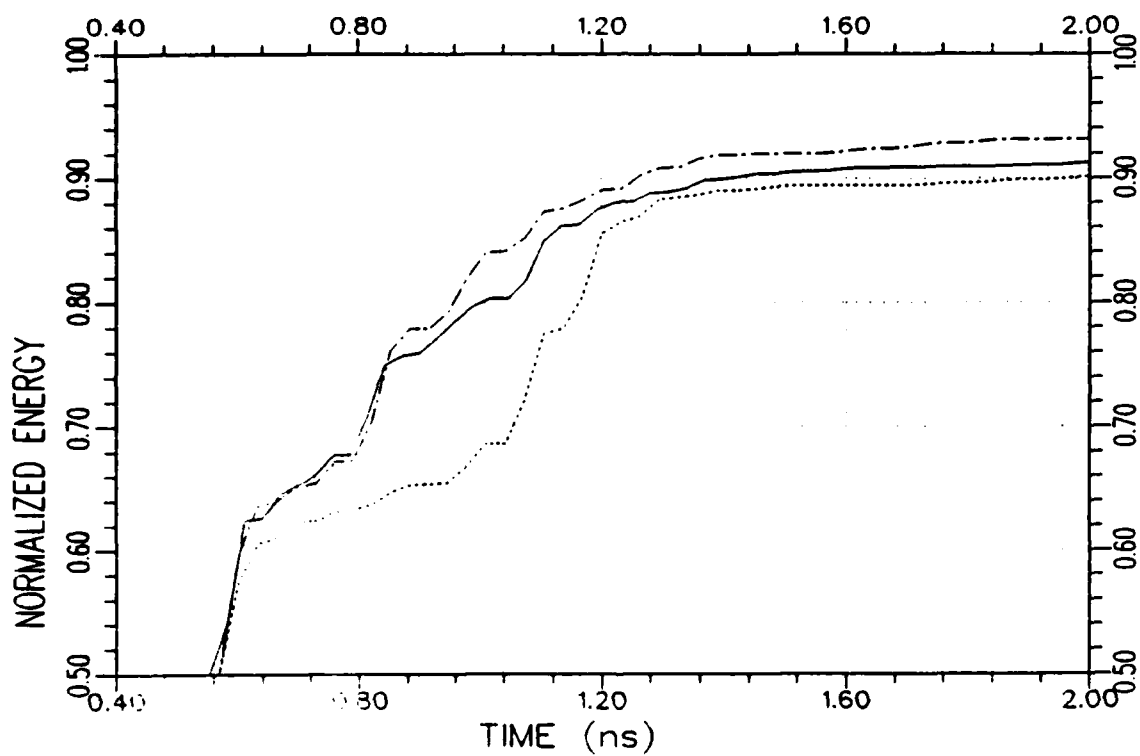
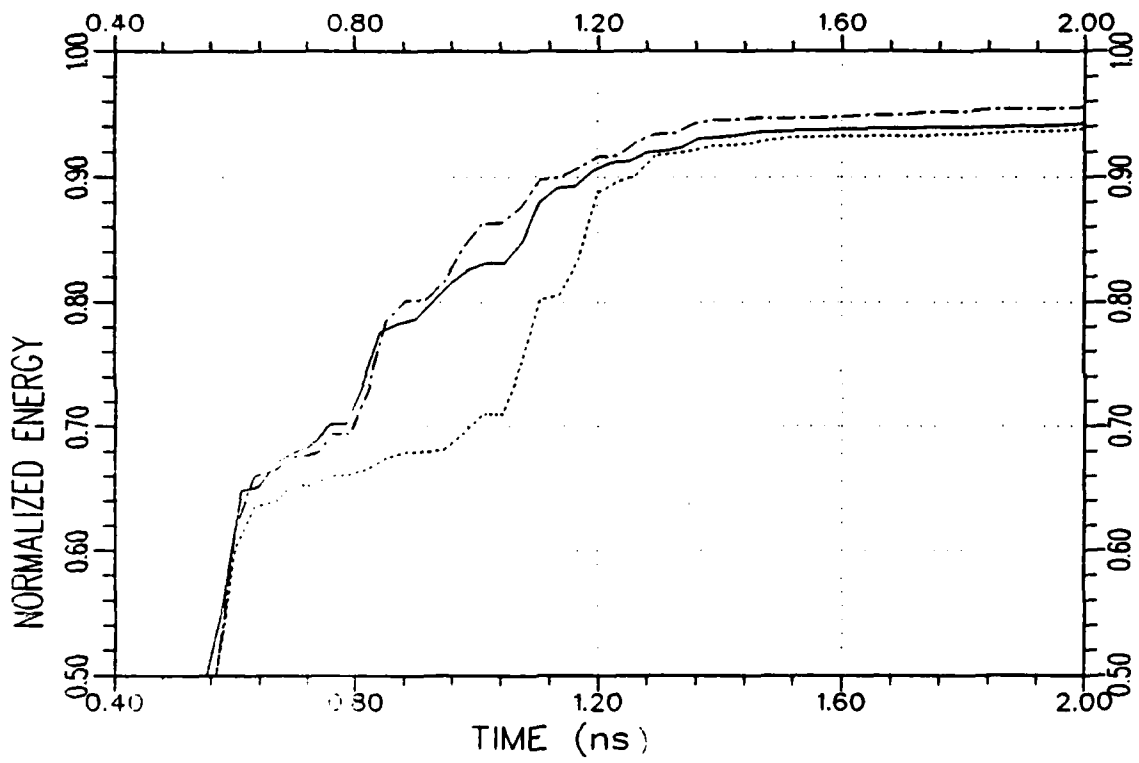


Figure 7.42. Normalized response energy curves (plotted on a magnified scale) of the test target A_3 produced by the K-pulses of the library targets A_1 ($\cdots\cdots$), A_2 ($- \cdot - \cdot -$) and A_3 (---) at $120^\circ/\text{VP}$ from a noisy backscattered data with $\text{SNR}=11$ dB.



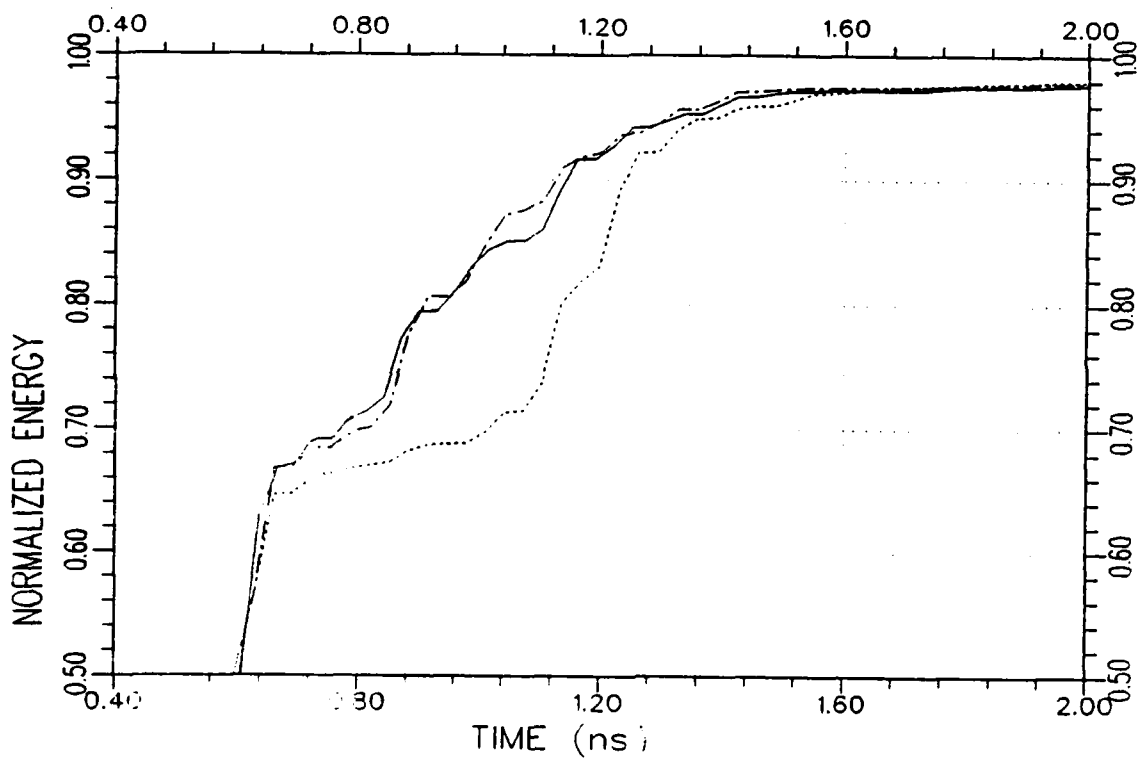
(a) for SNR=11 dB

Figure 7.43. Normalized response energy curves (plotted on a magnified scale) of the test target A_3 produced by the K-pulses of the library targets A_1 (·····), A_2 (-·-·-) and A_3 (—) at $180^\circ/VP$ for three different SNR levels.



(b) for SNR=15 dB

Figure 7.43. Continued.



(c) for $SNR = \infty$ (noise-free case)

Figure 7.43. Continued.

CHAPTER VIII

CONCLUSIONS

This report has presented a K-pulse estimation technique and a target identification scheme which can be applied to geometrically complicated and generally low-Q radar targets of tactical importance such as aircraft, surface ships and land vehicles. One of the basic features of the K-pulse estimation technique is that it is based, in principle, on the annihilation of the target's natural resonances under K-pulse excitation. This goal is achieved by minimizing the energy content of the target's natural response at sufficiently late-times. The technique is applicable to almost all target geometries since it does not require any a priori information on the system poles but only uses measured or theoretical (when available) band-limited scattered impulse response data of the target at several combinations of aspect and radar polarization. It should be stressed that use of multi-combinational data in K-pulse estimation, as suggested for the first time in this report, has a crucial impact on extending the K-pulse applications to realistically complicated problems.

The mathematical formulations of the K-pulse estimation technique are based on a general K-pulse waveform model which is composed of a unit strength impulse function at the initiation time of the waveform and then a continuous time function of finite duration. Two different approaches are utilized for the mathematical representation of the

continuous part of this K-pulse model, a discrete representation in terms of a basis which is a collection of equally-spaced discrete delta functions, and a continuous representation in terms of a basis of modified Legendre polynomials. While the former approach was originally introduced by Fok et al. [34,35], the latter one was suggested and formalized for the first time in this report. The discrete representation approach requires a rather simple mathematical formulation but a large number of optimization variables (equally-spaced sample values of the K-pulse waveform) involved in the energy minimization procedure. On the other hand, formulation of the Legendre polynomial approach is more complicated but usually leads to a much faster K-pulse synthesis algorithm with a smaller number of optimization variables (coefficients of a truncated Legendre polynomial expansion). Furthermore, in the case of a discrete representation, the K-pulse waveform needs to be interpolated between the sample points. A linear interpolation can be utilized if the sampling rate is sufficiently high. In the case of a Legendre polynomial representation, however, no interpolation is necessary since the basis functions themselves are continuous in time. Both of these representations are utilized to estimate the K-pulse waveforms of both simple and complicated target geometries with satisfactory results as demonstrated in Chapters IV through VII.

As previously indicated, the suggested K-pulse estimation technique utilizes the scattered impulse response data of the target in question. Most of the time, the original scattering data are available via band-limited measurements in the real-frequency domain and then the

corresponding band-limited impulse response is obtained using the standard inverse Fourier transformation technique. An important question is to be asked at this point: how wide the bandwidth of measurement data should be and which measurement frequency range would yield more useful K-pulse estimation results? In answering this question, it should be remembered that the K-pulse concept is built on the idea of natural resonance annihilation. Therefore, under ideal conditions, the frequency range of measurements should span the resonance region for the particular target in question. However, in many practical situations the measurement data may not be available at very low frequencies so that only the higher frequency portions of the resonance region can be utilized in K-pulse estimation. In the demonstrations of Chapters V through VII, it is shown that a useful K-pulse waveform can still be synthesized using such incomplete data. In some other practical cases, the available measurement frequency range may be well above the resonance region of the overall geometrical structure of the target. In such situations, the substructures of the target are important and the synthesized K-pulse waveform may still be useful in annihilating the natural resonances coming from the small substructures of the target rather than those caused by the major parts (such as the fuselage or wings of an aircraft) of the object. A pilot study for this case is demonstrated in Appendix F using a set of very narrow band full-scale radar measurement data from a real aircraft.

Another major concern in K-pulse synthesis is estimation of the K-pulse duration and minimization cut-off times. Although there is no straightforward way of guessing these parameters for complicated

geometries, the use of a multi-combinational analysis approach is shown to be quite useful in at least recognizing the errors coming from inaccurate estimations of these important parameters. Also, some rules of thumb that are found to be useful in intelligent guessing of K-pulse duration and cut-off times are given in Appendix A.

Also suggested for the first time in this report is a target identification scheme which is based on a normalized response energy concept. For the demonstrations in Chapters IV through VII, a K-pulse library is constructed for each class of targets. Each of these libraries is composed of the pre-synthesized K-pulse waveforms of the candidate targets which belong to the specific class in question. The unknown test target is identified as one of the library targets whose K-pulse waveform produces a normalized target response energy curve which reaches high energy levels earlier than the other normalized response energy curves produced by the rest of the library K-pulses using the same spectral data. It has been demonstrated that as the SNR of the scattering data decreases, the performance of this identification scheme deteriorates gracefully but not catastrophically. Even at SNR levels as low as 5 dB, the identification demonstrations produce satisfactory results. It should be pointed out that better identification results than those presented in this report can be expected if the library K-pulses are estimated more accurately by increasing the number of aspect and polarization combinations utilized in the K-pulse estimation procedure, allowing a higher number of iteration steps in the optimization algorithm and using a larger number of basis functions to represent the continuous part of the K-pulse. At

this stage of research, the main goal is to demonstrate the feasibility of a target identification approach based on the K-pulse theory. Therefore, the results of the identification demonstrations are discussed rather qualitatively without going into a detailed statistical analysis.

As indicated in Chapter III and Appendix C, target pole estimation is one of the by-products of the suggested K-pulse synthesis technique. It should be noted that the approximate pole-pairs extracted as the zeros of the estimated K-pulse spectra can be expected to be reliable only over the data frequency range utilized in the K-pulse synthesis procedure.

In summary, it was never the intent in Kennaugh's definition of the K-pulse that all singularities of a target be precisely cancelled except in principle. For the simple (geometrically) targets of his examples (wires, spheres), a simple zero model could approximately cancel an infinite string of simple poles. For geometrically complex targets, where numerous substructures ultimately contribute new strings of singularities, such models are not possible. Consequently, approximate K-pulses are in order which are no less useful but of less precise definition. The success of the K-pulse procedures when applied to the measured full-scale aircraft data (Appendix F) is a very significant step in the development of the K-pulse as a tool to be exploited for radar target identification. If one were to select one set of results from this report which clearly justifies continued research on the K-pulse as an identification algorithm, it would be those results shown in Appendix F.

We postulate that, ultimately, weighted K-pulses designed for specific contributions of substructures and/or aspects and/or polarizations will emerge. It is felt that the contents of this report will significantly contribute toward the development and application of such sophisticated K-pulses. New generations of radar systems will present very sophisticated diagnostic tools to radar applications. Hopefully, the K-pulse concept will make meaningful contributions to such studies.

APPENDIX A

ESTIMATION OF THE K-PULSE DURATION AND CUT-OFF TIMES

As indicated in Chapter III, the K-pulse duration (T_k) and the cut-off times (T_L^i , $i=1,2,\dots,I$) are the most important parameters involved in the K-pulse synthesis technique. More accurately, the better these parameters are pre-estimated, the more satisfactory are the results obtained. Unfortunately, there is no rigorous method of estimating these time durations for an arbitrary object. Especially for geometrically complicated and/or low-Q scatterers, the only viable approach appears to be a partially trial-and-error method; it is possible, however, to give several rules of thumb which work reasonably well in the case of simple K-pulse estimation problems and materially aid in making better initial guesses for the more complicated cases.

A. ESTIMATION OF K-PULSE DURATION

Estimation of K-pulse duration for various high-Q and low-Q objects with simple geometries was studied by Fok et al. [34-35] in detail. Observed was a very strong relationship between the K-pulse duration and the pole density of various objects such as conducting thin-wires, thin-loops, spheres and disks. For each of these objects, the difference between the imaginary parts of the successive pole values in a string is essentially constant. When the limit value of this almost constant difference (as the index of poles increases) is

denoted by $\Delta\omega$, in terms of radian frequency, the K-pulse duration can be estimated as

$$T_k = \frac{2\pi}{\Delta\omega} . \quad (A.1)$$

It was demonstrated in [34] that Equation (A.1) led to accurate K-pulse durations of $2L/c$ for a thin-wire of length L ; and $2\pi r/c$ for a thin circular loop, a sphere and a circular disk where r is the radius of these geometries. In all these cases, the K-pulse duration equals a closed path length around the object divided by the speed of light. This observation can be used as a rule of thumb in the estimation of K-pulse durations for more complicated geometries in the sense that while it does not guarantee a correct duration, especially in the case of complicated geometries, it at least provides a reasonable initial guess. As was also discussed by Fok [34], the K-pulse duration is approximately equal to the period of the dominant late-time oscillations of the object's impulse response. But such an estimation appears to be primarily limited to high-Q targets where natural impulse response components are not contaminated by forced response components over a sufficiently long time interval at the tail of the signal.

Most of the targets utilized in this report show low-Q features and have very complicated geometries. Therefore, neither of the rules of thumb summarized above are completely satisfactory. From experience, however, choosing the K-pulse duration in the range $\left[\frac{2L}{c}, \frac{3L}{c}\right]$ where L is the maximum line-of-sight dimensions of the target provides a useful initial guess for this parameter. If the pre-estimated

duration was less than the minimal K-pulse duration (of the theoretical unique K-pulse) either a serious convergence difficulty would be observed in the minimization of cost function, or the synthesized (so-called) K-pulse waveform would fail to reduce the late-time energy content of the target response at most of the aspects not used for K-pulse estimation. In such a case, the K-pulse synthesis procedure needs to be repeated for a longer K-pulse duration until a satisfactory result is obtained. On the other hand, if the pre-estimated K-pulse duration is longer than necessary, the resultant K-pulse waveform would be an acceptable approximation to the unique K-pulse except that its K-pulse spectrum would be zero at some additional complex frequency values different than the poles of the target in question. In this case, the approximate K-pulse waveform can be expressed as a convolution of two time functions as

$$k(t) = k^u(t) * a(t) , \quad (\text{A.2a})$$

for

$$t \in [0, T_k] , \quad (\text{A.2b})$$

where $k^u(t)$ is the "unique" K-pulse with the minimal K-pulse duration $T_k^u < T_k$; and $a(t)$ is an arbitrary function of duration T_a such that

$$T_k = T_k^u + T_a . \quad (\text{A.2c})$$

The Laplace domain counterpart of Equation (A.2a) is

$$K(s) = K^u(s) A(s) , \quad (A.3a)$$

and the solution of the non-linear equation

$$K(s) = 0 \quad (A.3b)$$

gives not only the zeros of the unique K-pulse component, i.e., the target poles, but also the zeros of the function $A(s)$. Since the primary concern here is target identification rather than pole extraction, estimating the K-pulse duration somewhat longer than necessary should not cause to a serious problem. In the K-pulse estimation for a conducting sphere (Chapter IV, Section B), the K-pulse duration is chosen about 6.4% longer than its actual value and it is observed that such a difference effected neither the extracted pole values nor the target identification performance drastically. As a matter of fact, no extra K-pulse spectrum zeros were detected as a result of this small perturbation.

B. ESTIMATION OF CUT-OFF TIMES

As indicated in Chapter III, a cut-off time, T_L^i , is an estimate of the target's forced response duration at an arbitrary aspect and polarization under the K-pulse excitation. The choice of a cut-off time directly effects the result of the K-pulse synthesis procedure since the minimization of late-time response energy content is performed for $t \geq T_L^i$. If the minimization is started before the forced response dies out, i.e., if the cut-off time is chosen earlier

than its correct value, the spectrum zeros of the synthesized K-pulse would be totally different from the target poles and most probably would be aspect and polarization dependent. Consequently, the synthesized waveform would be only a time-limited function but not a K-pulse. To avoid this basic problem, the cut-off time should be chosen as late as possible. Although this can be done in the case of a high-Q object whose natural response keeps ringing at late-times with sufficiently large amounts of energy to be minimized, the same precaution usually does not work for low-Q objects whose natural oscillations die out very quickly leaving a very small amount of late-time energy content for minimization. The only rule of thumb which can be suggested for an initial estimation of a cut-off time follows from the expression of K-pulse response

$$r^i(t) = h^i(t) * k(t) \tag{A.4a}$$

where the target's impulse response can be implicitly decomposed into the forced and natural components as

$$h^i(t) = h_f^i(t) + h_n^i(t) , \tag{A.4b}$$

then Equation (A.4b) can be rewritten as

$$r^i(t) = h_f^i(t) * k(t) + h_n^i(t) * k(t) , \tag{A.4c}$$

where from the time duration of the first term on the right hand side (the forced response component), the cut-off time, T_L^i , can be roughly estimated as

$$T_L^i \approx \frac{L}{c} + T_k \quad (\text{A.4d})$$

with L being the maximum line-of-sight dimension of the target. Starting with this initial guess, a better estimate of the cut-off time can be obtained via essentially a trial-and-error approach. As discussed by Felsen [56], a scattered field excited by an aperiodic short pulse can be interpreted as multiple wavefront arrivals not only during the early time interval but also at moderate subsequent times; and these incident wavefronts directly excite only the illuminated portion of a smooth convex object. The surface points on the geometrical shadow are rather excited by the creeping waves for the first time. Therefore, depending upon the geometry of the target, the actual forced response duration becomes different than the rough estimate given in Equation (A.4d). It should also be noted that the late-time energy minimization (beyond the cut-off time) approach utilized in this report is supported by the comments of Felsen [56] and Dudley [57] on the Singularity Expansion Method (SEM). They both pointed out that scattered fields should be expressed in the frequency domain as a superposition of two components, an entire function which characterizes the local information provided by ray-optic method and related to early-time content of the time-domain scattered field; and an expansion over the poles of a meromorphic function which contain the

function which contain the global information about the target and can be provided by the SEM at late-times in the time domain. It was also noted that contributions coming from these two separate scattering mechanisms interfere with each other at intermediate times. This interference causes the basic problem in the estimation of cut-off times during the K-pulse synthesis procedure especially for low-Q targets.

Before concluding this appendix, it should be pointed out that the "multi-combinational" analysis approach suggested for K-pulse estimation greatly reduces the risk of estimating K-pulse duration and the cut-off times incorrectly. When any of these parameters are pre-estimated improperly, the resultant K-pulse spectrum zeros may be useful in (partially) minimizing the target's late-time response at one aspect but not at the remaining ones. Consequently, the minimization procedure exhibits a very slow convergence rate or does not converge at all. Such a situation is a very useful warning signal that the pre-estimated values of K-pulse duration and/or cut-off times need to be readjusted. These adjustments call for a trial-and-error approach which may be time-consuming, but unfortunately appears to be the only viable approach at this stage of the K-pulse studies.

APPENDIX B

INTERPRETATION OF NORMALIZED ENERGY CURVES IN TARGET IDENTIFICATION

The basic idea behind using a normalized energy concept in target identification is explained in Chapter III and the related demonstrations are presented in Chapters IV through VII. The purpose of this appendix is to provide further discussion on how to interpret the relative differences of matched and mismatched normalized response energy curves in various situations in order to make an intelligent identification decision.

As mentioned previously, the normalized energy curve of a target's response to its own K-pulse (matched case) is expected to reach high energy levels earlier than the normalized response energy curves which correspond to the mismatched K-pulse waveforms of the K-pulse library. If the matched K-pulse is able to annihilate a significant amount of late-time natural response energy, the matched energy curve leads the mismatched energy curves not only at high energy levels but also at moderate or even very small energy levels. An example of this situation is observed in Figure 4.11b of Chapter IV for a conducting thin wire of length 12m at 60° aspect angle where the matched energy curve leads the mismatched ones very dominantly (since the targets are very high-Q objects) at all energy levels higher than about 65%. Another target identification example where the energy curves exhibit a similar behavior is shown in Figure 5.33 of Chapter V where the test

target is the model ship SH₂ and the mismatched library target is SH₁ at a 60°/VP combination. Since the targets of this example are relatively low-Q objects (as compared to conducting thin-wires of the previous example), the separation of the matched and mismatched energy curves is not very large. The target identification decision in the cases similar to these examples can be made without any uncertainty. In some cases, however, the matched and mismatched energy curves may exhibit such a variation that they arbitrarily lead or lag one another in some intermediate energy range but at high energy levels one of them starts leading substantially. An example of this situation is presented in Figure 5.25 of Chapter V for model ship SH₁ at 30°/VP where the other library target is SH₂. In this example, the mismatched energy curve leads the matched one up to about 70% energy level, then the matched curve reaches energy levels in the range 70% to 98% much earlier than the mismatched one. In such a case, the identification decision should be made in favor of the library target whose energy curve shows a better performance at high energy levels which are the main concern of the identification scheme. If one of the curves lags the other one at most of the energy levels but starts leading slightly at high energies, it is very difficult to make an identification decision with confidence. Such results are usually referred to as ambiguous ones in this report. Figure 5.29 of Chapter V shows an example of this case where the test target is model ship SH₁ at 170°/VP; and its matched energy curve leads the mismatched one only after 92% energy level by about 3% average energy difference only. Yet in some other cases, there may be no noticeable difference between

matched and mismatched energy curves as shown in Figure 7.41 of Chapter VII where the library targets are the model aircraft A_1 , A_2 and A_3 with A_3 being the test target at $90^\circ/VP$. In this example, the matched energy curve leads one of the mismatched energy curves (due to the K-pulse of target A_1) but shows about the same variations as the other mismatched energy curve (due to the K-pulse of target A_2) for almost all energy levels. Consequently, the library target A_1 can be eliminated easily as not being the "unknown target," but the rest of the identification decision is left to be ambiguous between targets A_2 and A_3 . Such a situation probably occurs either when the matched K-pulse of the test target does not work well enough at the combination of aspect and polarization being tested or when two library targets have a common (or at least close) pole pair excited strongly at that combination of aspect and polarization so that both the matched and mismatched K-pulses annihilate the natural resonances coming from that pole-pair equally well. In the former case, a better estimate for the matched K-pulse is called for but in the latter case, there is not much that one can do to improve the identification results since the uncertainty arises from the similar characteristics of the targets.

The performance of the identification scheme deteriorates under noisy conditions, as expected. The effect of noise energy is mostly observed at the tail of the normalized energy curves where the amount of noise energy is comparable to or even greater than the signal energy. As demonstrated in Figure 7.24 of Chapter VII, a correct identification decision can still be made at quite low SNR values (as low as 11 dB for this example and even lower for some other cases), if

the approximate library K-pulse associated with the "unknown" target annihilates the natural oscillations of the object sufficiently well under essentially noise-free conditions (see Figure 7.2 of Chapter VII). On the other hand, if the performance of the matched K-pulse is already poor at a particular aspect/polarization, it is more likely that the added noise will cause ambiguous or even false identification results as the SNR decreases. An example of this situation is given in Figure 7.27 of Chapter VII in conjunction with Figure 7.5 of the same chapter. Consequently, the success of identification scheme (either in noise-free or noisy cases) largely depends on the success of the K-pulse estimation procedure.

APPENDIX C

EXTRACTION OF TARGET POLES FROM THE K-PULSE

As explained in Chapter III, there should be a one-to-one correspondence between the poles (CNR frequencies) of a finite electromagnetic scatterer and the zeros of the Laplace transform of its "unique" K-pulse waveform. In practical cases, however, the Laplace domain zeros of an "approximate" K-pulse cannot satisfy such a strict condition; but they are expected to approximate a subset of the target's poles as close as possible. When a K-pulse waveform is estimated from some bandlimited theoretical or measurement data (without using a priori knowledge of the target poles), some of its spectrum zeros may not match to the actual target poles, or its Laplace transform may fail to be zero at certain target pole values over the frequency span utilized for K-pulse estimation.

The basic K-pulse synthesis technique formulated and utilized in this report estimates the discrete sample values of the continuous part of the K-pulse waveform. As discussed by Fok [34], if the time sampling increment is chosen to be sufficiently small, the continuous function, $k^c(t)$, can be well approximated by means of linear interpolation between the sampling points. Then, the derivative of $k^c(t)$ can be written as

$$\frac{d}{dt} k^c(t) = k_1 \delta(t) + \sum_{n=1}^N \frac{k_{n+1} - k_n}{\tau} P_{\tau/2} \left(t - (n - \frac{1}{2})\tau \right) - k_N \delta(t - T_k) \quad (C.1a)$$

where

$$k_n \stackrel{\Delta}{=} k^c(t) \Big|_{t=\tau(n-1)} \quad \text{for } n=1,2,\dots,N \quad (C.1b)$$

are discrete samples of the continuous part of the K-pulse waveform with N being the total number of samples; τ is the sampling step size and

$$P_{\tau/2}(t) = \begin{cases} 1 & \text{if } -\tau/2 \leq t \leq \tau/2 \\ 0 & \text{otherwise} \end{cases} \quad (C.1c)$$

is the rectangular pulse function.

The Laplace transform of the K-pulse waveform can be computed as

$$\begin{aligned} K(s) &= L\{\delta(t) + k^c(t)\} \\ &= 1 + K^c(s) \quad , \end{aligned} \quad (C.2a)$$

where

$$K^c(s) = \frac{1}{s} L\left\{\frac{d}{dt} k^c(t)\right\} \quad , \quad (C.2b)$$

or

$$K^c(s) = \frac{1}{s} \left[k_1 - k_N e^{-T_k s} + \sum_{n=1}^{N-1} \frac{k_{n+1} - k_n}{\tau} e^{-(n-\frac{1}{2})\tau s} L\{P_{\tau/2}(t)\} \right] \quad , \quad (C.2c)$$

with

$$L\{P_{\tau/2}(t)\} = \frac{e^{\tau s/2} - e^{-\tau s/2}}{s} \quad . \quad (C.2d)$$

After some algebraic manipulations, $K(s)$ can be obtained as

$$K(s) = 1 + \frac{k_1 - k_N e^{-T_1 k s}}{s} + \frac{e^{\tau s} - 1}{\tau s^2} \sum_{n=1}^{N-1} (k_{n+1} - k_n) e^{-n\tau s}, \quad (C.3a)$$

and the non-linear equation

$$K(s) = 0 \quad (C.3b)$$

can be solved to estimate the target poles (CNR frequencies). In this report, the complex roots of Equation (C.3b) are computed by using the Secant method [37]. It should be noted that the same pole extraction procedure was suggested earlier by Fok et al. in [34].

APPENDIX D

ORIGINAL AND MODIFIED LEGENDRE POLYNOMIALS

The purpose of this appendix is to summarize the basic definitions and the orthogonality properties of the original and modified (as used in this report) Legendre polynomials to clarify the derivations given in Section B of Chapter III.

The Legendre polynomials are originally defined [38] as

$$P_n(z) = \sum_{m=0}^n \alpha_{nm} z^m, \quad (D.1a)$$

for

$$z \in [-1, 1], \quad (D.1b)$$

where $n=0,1,2,\dots$ being the polynomial order and

$$\alpha_{nm} = \begin{cases} (-1)^{(n-m)/2} \frac{(n+m)!}{2^n m! \left(\frac{n+m}{2}\right)! \left(\frac{n-m}{2}\right)!} & \text{if } n \text{ and } m \text{ are} \\ & \text{of the same parity} \\ 0 & \text{otherwise} \end{cases} \quad (D.1c)$$

The infinite set of Legendre polynomials, $\{P_n(z)\}_{n=0}^{\infty}$, constitute a complete and orthogonal basis for the continuous functions over the interval $[-1,1]$. The well-known orthogonality property is stated as

$$\int_{-1}^1 P_n(z) P_m(z) dz = \begin{cases} \frac{2}{2n+1} & \text{if } n=m \\ 0 & \text{if } n \neq m \end{cases} \quad (\text{D.2})$$

The interval of definition required by the derivations of Section B of Chapter III is $[0, T_k]$ where T_k is the K-pulse duration. Therefore, using the transformation,

$$t = \frac{T_k}{2} (z+1) , \quad (\text{D.3a})$$

or equivalently,

$$z = \frac{2}{T_k} t - 1 , \quad (\text{D.3b})$$

the original interval $[-1,1]$ can be mapped onto the modified interval $[0, T_k]$. The resultant set of modified Legendre polynomials, $\{\bar{P}_n(t)\}_{n=0}^{\infty}$, are defined as

$$\bar{P}_n(t) = P_n(z) \Big|_{z=\frac{2}{T_k}t-1} , \quad (\text{D.4a})$$

or

$$\bar{P}_n(t) = \sum_{m=0}^n \alpha_{nm} \left(\frac{2}{T_k} t - 1 \right)^m , \quad (\text{D.4b})$$

for

$$t \in [0, T_k] . \quad (D.4c)$$

The orthogonality property for this new set of basis functions can easily be derived by using Equations (D.2), (D.3b), and (D.4b) as

$$\int_0^{T_k} \bar{P}_n(t) \bar{P}_m(t) dt = \begin{cases} \frac{T_k}{2n+1} & \text{if } n=m \\ 0 & \text{if } n \neq m \end{cases} . \quad (D.5)$$

APPENDIX E
SIMULATION OF NOISY DATA

The original data utilized in this report are either theoretically computed (Chapter IV) or measured on the Ohio State University compact measurement range [53] (in Chapters V-VII). In the former case, signal-to-noise ratio (SNR) of the data equals infinity; and in the latter case, it is finite but much larger than a typical SNR of a full scale radar measurement since the clutter type noise is minimized on the measurement range. The noisy data, which are essential for testing the noise performance of the proposed target identification scheme in Chapters IV through VII, are produced artificially by adding white Gaussian noise to the available data. Two uncorrelated Gaussian random processes [55] with zero means and equal standard deviations are generated from two different seeds (using the subroutine GAUSS in the IBM/360 Scientific Subroutine Package) and added to the real and imaginary parts of the original frequency spectra independently. The SNR of the resultant noisy signal is defined as

$$\text{SNR(dB)} = 10 \log_{10} \left[\sum_{i=1}^N |H_i|^2 / 2N\sigma^2 \right], \quad (\text{E.1})$$

where H_i is the complex value of the original signal spectrum at the sampling frequency f_i , N is the total number of samples used and σ is

the standard deviation of the random Gaussian processes. The factor 2 which appears at the denominator of Equation (E.1) is due to adding two different random noise processes to the real and imaginary parts of the signal spectrum separately.

APPENDIX F

K-PULSE ESTIMATION FOR A FULL-SCALE AIRCRAFT

In this appendix, the suggested K-pulse estimation technique is applied to a small jet aircraft, to be referred to as target A hereafter, using frequency domain backscattered data measured by a full-scale stepped-frequency radar system over the frequency range 3.1-(0.0048)-3.4024 GHz^{*}. At the lowest available measurement frequency, the ratio of the wavelength to the overall length of the aircraft is less than one percent and the data are recorded at only 64 sample frequencies. As far as the frequency range and bandwidth specifications are concerned, this demonstration is quite different than the others presented in Chapters IV through VII. In this specific problem, not only is the measurement bandwidth quite narrow but also the measurements are at very high frequencies so that the information provided by the scattered data can be best interpreted by means of high frequency techniques such as GTD. When it comes to K-pulse studies, it should be stressed that being able to estimate a useful K-pulse waveform under such realistic and highly restricted conditions is an

* These polarimetric backscattered data were provided to the ElectroScience Laboratory by Dr. D. Wiener of the Naval Ocean System Center.

ultimate goal which needs further research to solidify the outcomes reported in this report. However, the present K-pulse estimation technique as outlined in Chapter III can still be applied to this problem under the recognition that at such high measurement frequencies, only the dominant natural modes of sufficiently small substructures of the aircraft are strongly excited. Therefore, the pre-estimated K-pulse duration should be chosen much smaller than $2L/c$ where L is the overall length of the target. Before going into the details of the K-pulse estimation procedure, a major difficulty observed in synthesizing the impulse response of this full-scale aircraft from the available measurement data needs to be mentioned. As repeatedly indicated in the application chapters, the impulse response of the target is numerically synthesized from the frequency domain data using a standard IFFT (inverse fast Fourier transformation) algorithm which simply assumes zero values for the missing samples of the frequency spectrum between zero frequency and the starting frequency of the data. Consequently, when the available data are located at very high frequencies over a narrow bandwidth with a small number of samples, as is the case in this example, the numerical inversion technique introduces an important amount of error to the resultant impulse response waveform. Furthermore, the high frequency components exhibit very rapid variations in the impulse response making it almost useless for employment in the K-pulse estimation procedure. As a practical solution to these difficulties, the original frequency data of the aircraft A_4 are shifted by $\pm\omega_0$ where $\omega_0 = 2\pi f_0$ and f_0 is the chosen to be 3.09 GHz. Then the resultant composite data spectrum is

weighted by a band-pass Hanning window function eliminating the very high frequency components, which appear around ± 6 GHz, beyond ± 0.32 GHz. The relationship between the original data spectrum, $H(\omega)$, and the composite one, $\tilde{H}(\omega)$, can be expressed as

$$\tilde{H}(\omega) = [H(\omega - \omega_0) + H(\omega + \omega_0)] W(\omega) , \quad (\text{F.1})$$

where $H(\omega - \omega_0)$ and $H(\omega + \omega_0)$ are the right and left shifted versions of the originally measured spectrum and $W(\omega)$ is the window spectrum. Although the inverse Fourier transform of $\tilde{H}(\omega)$ is no longer simply the impulse response of the target, this composite frequency spectrum still contains the target pole information. As discussed in [56] and [57], the system function of an electromagnetic scatter can be expressed as

$$H(s) = A(s) + \frac{N(s)}{D(s)} \quad (\text{F.2})$$

where $A(s)$, $N(s)$ and $D(s)$ are all entire functions and the zeros of the denominator function $D(s)$ specify the simple poles of the system.

Using the complex-frequency counterpart of Equation (F.1) together with Equation (F.2) yields

$$\tilde{H}(s) = \left[A(s - s_0) + A(s + s_0) + \frac{N(s - s_0)D(s + s_0) + N(s + s_0)D(s - s_0)}{D(s - s_0)D(s + s_0)} \right] W(s) , \quad (\text{F.3a})$$

where

$$s_0 = j\omega_0 \quad (F.3b)$$

Obviously, the poles, \tilde{s}_n , of the equation

$$\tilde{H}(s) = 0 \quad (F.4a)$$

are located at

$$\tilde{S}(n) = s_n \pm j\omega_0 \quad (F.4b)$$

where the S_n 's denote the actual poles of the target. In the particular problem of this appendix, the shifted pole values would be essentially excited only over the frequency range 0.01 GHz to 0.3124 GHz as a result of the frequency gating effect introduced by the window function. In summary, the K-pulse estimation procedure demonstrated for target A annihilates the natural oscillations of a "composite impulse response" which is closely related to the target's actual impulse response as described by Equations (F.1) and (F.3).

An approximate (substructure-related) K-pulse waveform for aircraft A is synthesized from the data at $1^\circ/VP$ and $91^\circ/VP^*$ using a discrete representation for the continuous part of the K-pulse over the time interval [0,10.16 ns]. The initial guess for the K-pulse duration

* The aspect angles are calculated via a computer program using the values of range and azimuth angle which were measured while the aircraft was following an almost circular flight path.

was $2L/c \sim 80$ ns where L is the overall length of the aircraft, but this choice produced very unsatisfactory results as expected. After some preliminary trials (all smaller than 80 ns), a K-pulse duration of about 10 ns is found to lead to quite satisfactory results. The values of the K-pulse samples $k_1^c, k_2^c, \dots, k_N^c$ with $N=40$ are estimated by minimizing the cost function specified in Equation (3.9) for the cut-off times 160 ns and 110 ns at the synthesis aspect angles of 1° and 91° , respectively. The resultant K-pulse waveform is shown in Figure F.1. The Laplace domain zeros of this K-pulse are also numerically extracted and their shifted (by 3.09 GHz in the imaginary part) values are listed in Table F.1 as a set of approximate target poles for aircraft A. The composite impulse response and the corresponding composite K-pulse response waveforms are plotted together in parts (a) of Figures F.2 through F.9 at the aspect angles of $1^\circ, 30^\circ, 44^\circ, 60^\circ, 91^\circ, 119^\circ, 150^\circ$ and 179° , respectively for vertical polarization. (Each of these response waveforms is normalized such that its total energy is unity.) The corresponding normalized energy curves are also shown in parts (b) of the same figures. Similar results are provided in Figures F.10 through F.13 for the aspect angles of $1^\circ, 44^\circ, 75^\circ$ and 150° , respectively for horizontal polarization. The results shown for the aspect/polarization combinations of $1^\circ/VP, 30^\circ/VP, 44^\circ/VP, 91^\circ/VP, 1^\circ/HP, 44^\circ/HP$ and $75^\circ/HP$ are observed to be quite successful in the sense that the late-time energy content of the composite K-pulse response waveform is smaller than that of the composite impulse response waveform as a due to partial natural mode annihilation. The results at $60^\circ/VP, 119^\circ/VP, 150^\circ/VP$ and $150^\circ/HP$ while not excellent are

acceptable but the results at $179^\circ/VP$ turns out to be very poor. However, deterioration of the results at $179^\circ/VP$ can be explained by the fact that only two aspect angles, 1° and 91° which are both far from the aspect angle 179° , are utilized in the K-pulse estimation procedure. If the estimation procedure is repeated by using the aircraft data at some additional combinations of aspect and polarization including one or two more aspect angles in the range 90° to 180° and also including some horizontal polarization data, a better approximation for the K-pulse waveform can be expected. After demonstrating these pilot results on the K-pulse estimation for a full-scale aircraft from a real radar measurement data set, further research and possible improvements are left to be the subject of future K-pulse studies.

Table F.1

A Set of Approximate Target Pole-pairs
Estimated by Using the Laplace Domain Zeros
of the K-pulse Shown in Figure F.1

10^9 Nepers/s, GHz scale

.
. .
-0.0300 ± j 3.211
-0.0142 ± j 3.273
-0.0014 ± j 3.327
-0.0192 ± j 3.483
. .
. .
. .
. .

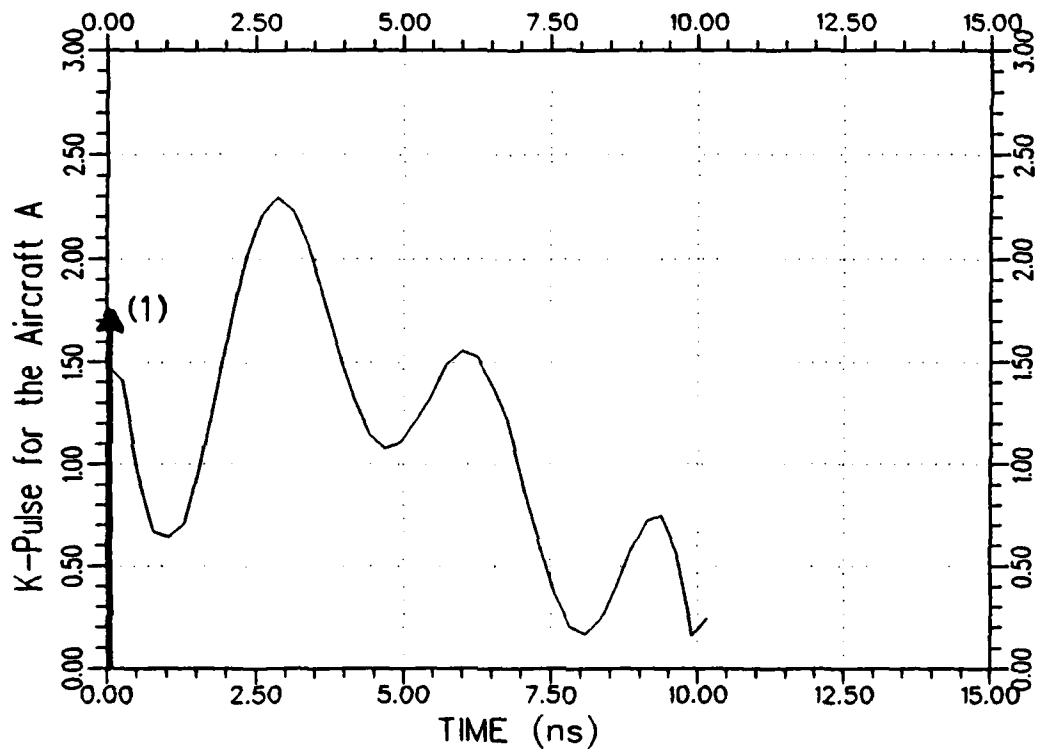
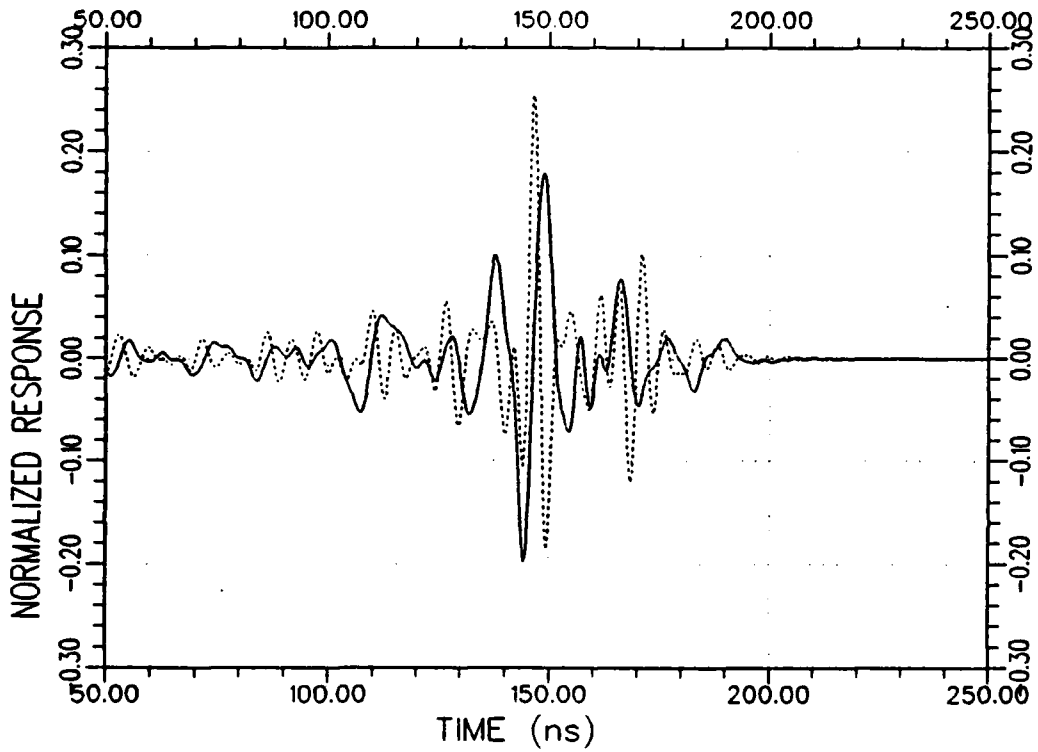
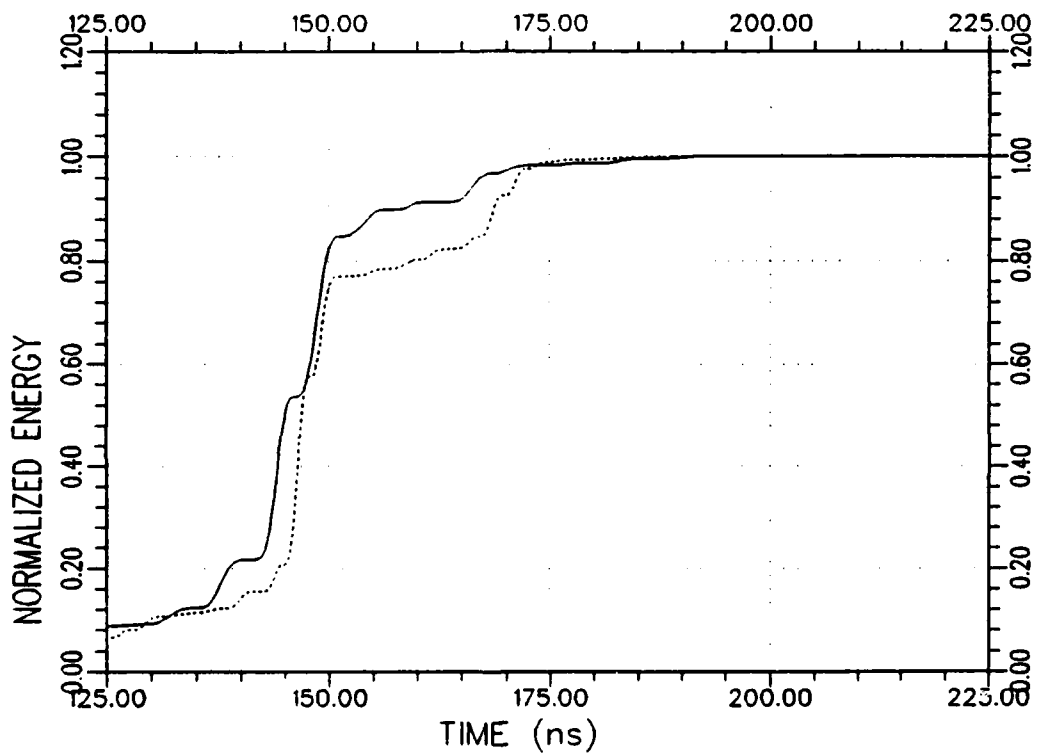


Figure F.1. An approximate K-pulse waveform for the aircraft A estimated from a set of narrow band (3.1 GHz to 3.4024 GHz) backscattered data at $1^\circ/\text{VP}$ and $91^\circ/\text{VP}$. (The $\delta(t)$ term of the K-pulse is symbolically shown by the arrow at $t=0$.)



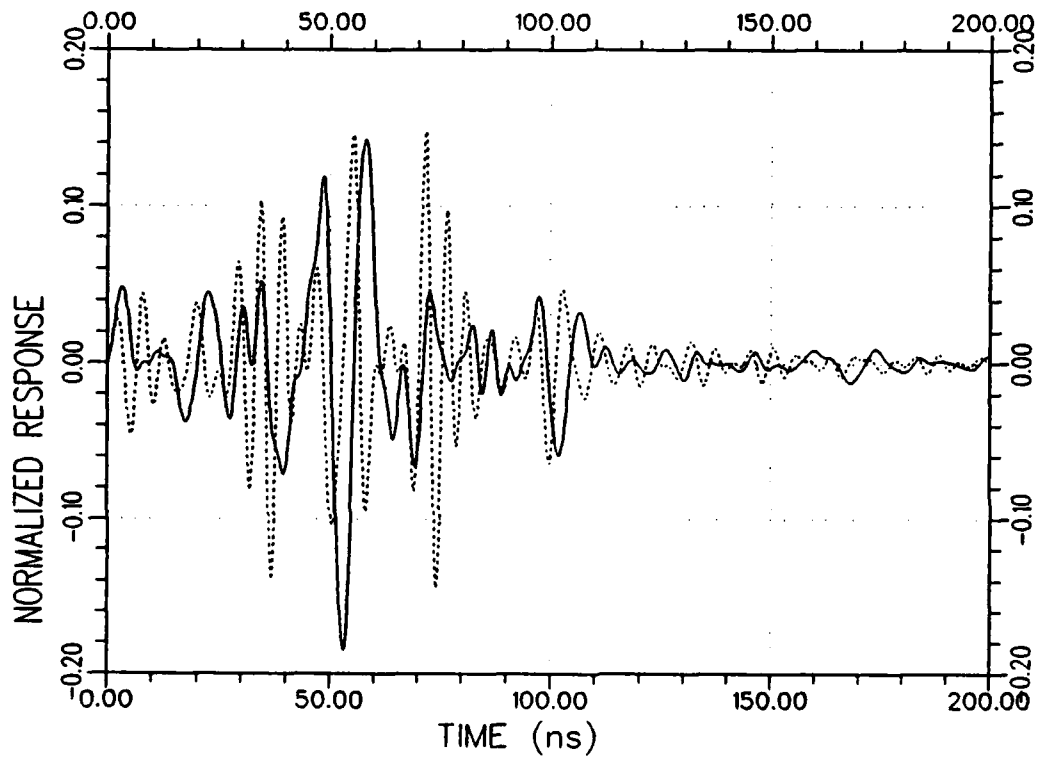
(a) Response waveforms

Figure F.2. Normalized composite impulse response (.....) and composite K-pulse response (——) waveforms and their energy curves for aircraft A at $1^\circ/\text{VP}$.



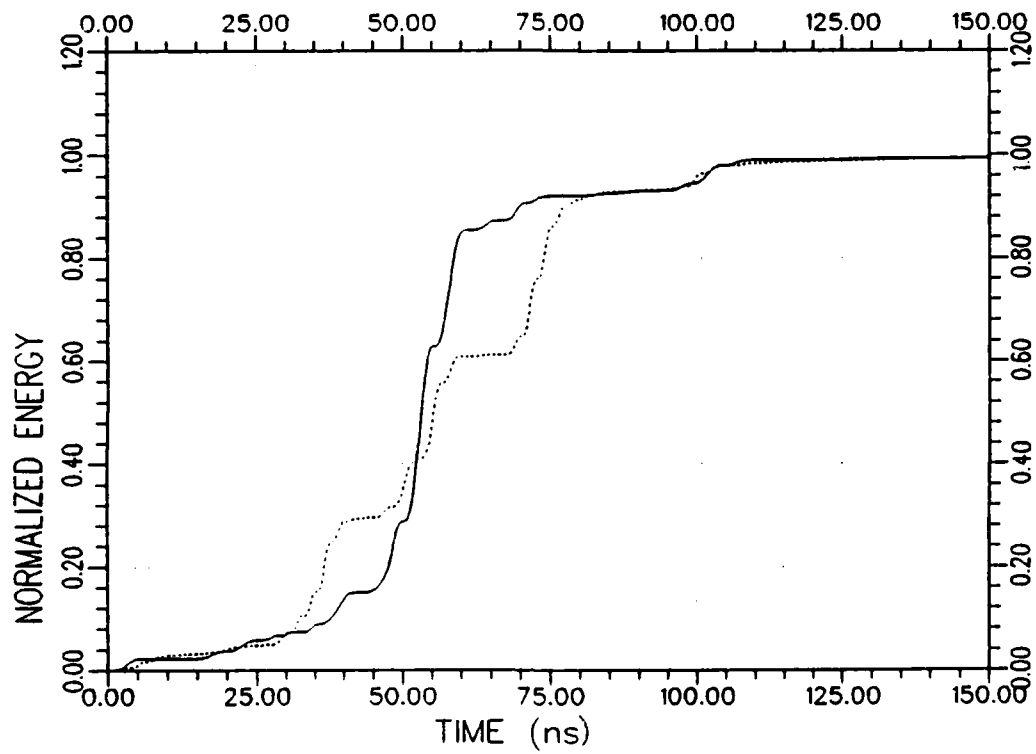
(b) Response energy curves

Figure F.2. Continued.



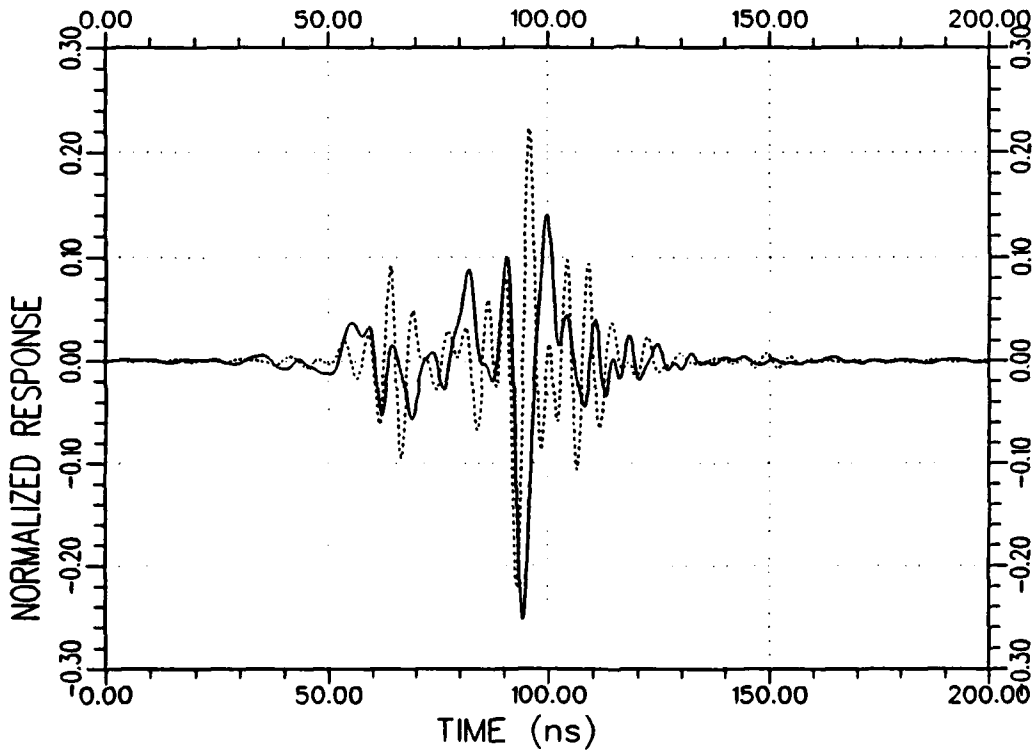
(a) Response waveforms

Figure F.3. Normalized composite impulse response (.....) and composite K-pulse response (——) waveforms and their energy curves for aircraft A at $30^\circ/\text{VP}$.



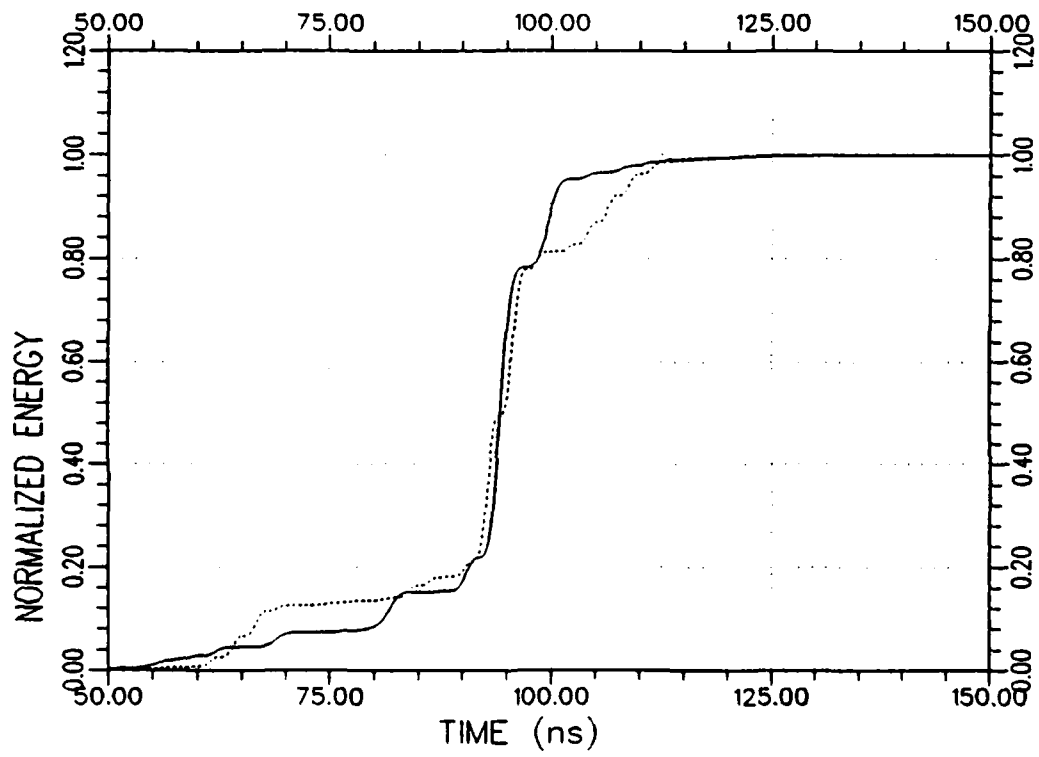
(b) Response energy curves

Figure F.3. Continued.



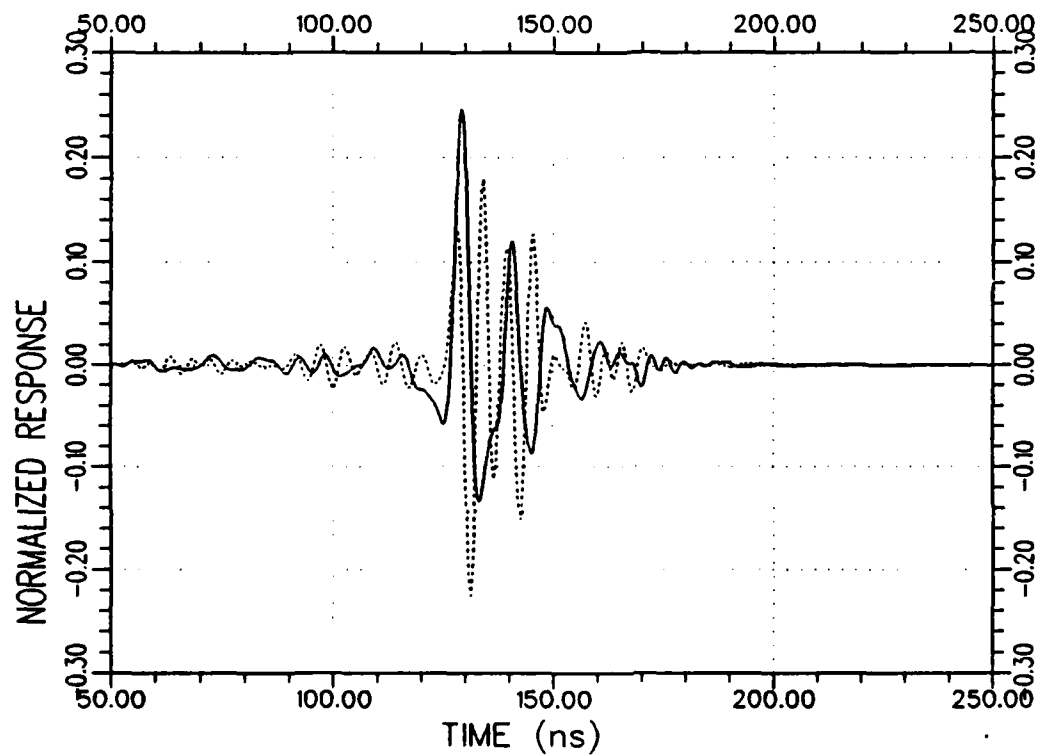
(a) Response waveforms

Figure F.4. Normalized composite impulse response (.....) and composite K-pulse response (——) waveforms and their energy curves for aircraft A at $44^\circ/VP$.



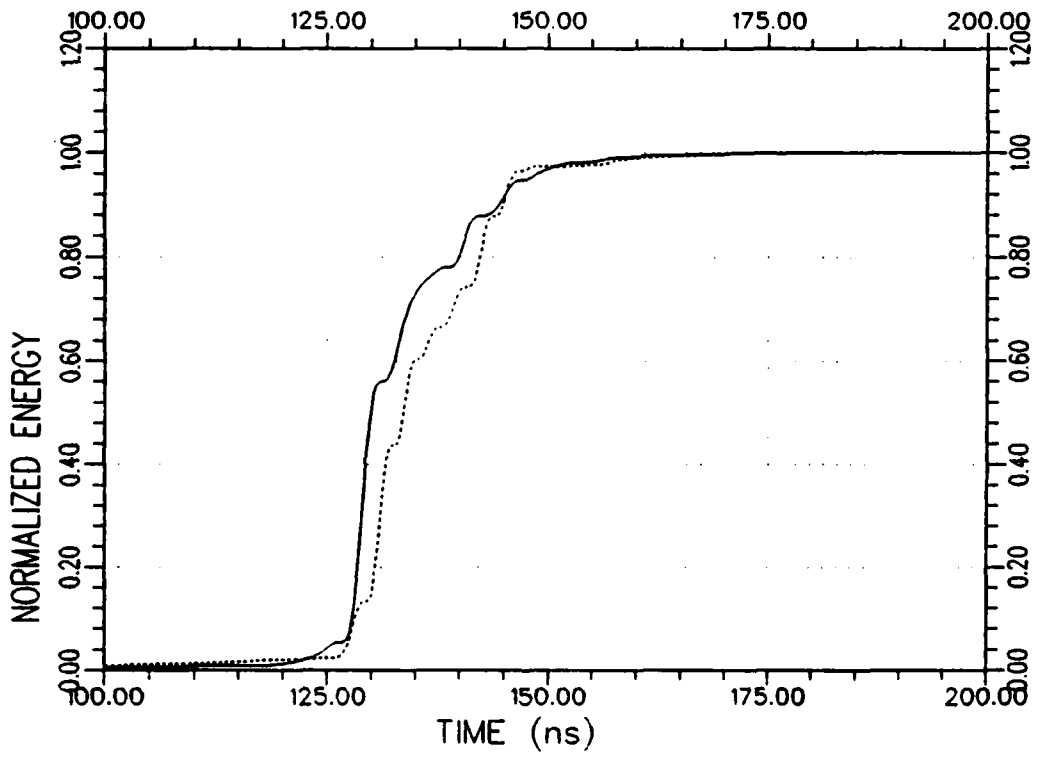
(b) Response energy curves

Figure F.4. Continued.



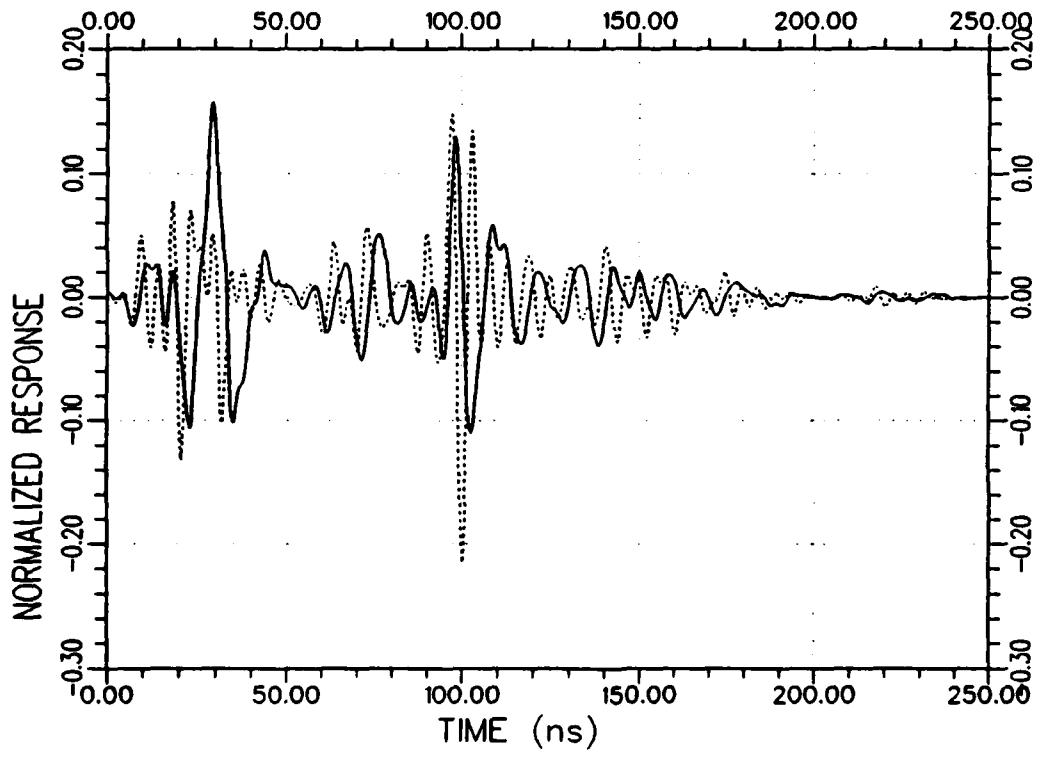
(a) Response waveforms

Figure F.5. Normalized composite impulse response (.....) and composite K-pulse response (——) waveforms and their energy curves for aircraft A at 60°/VP.



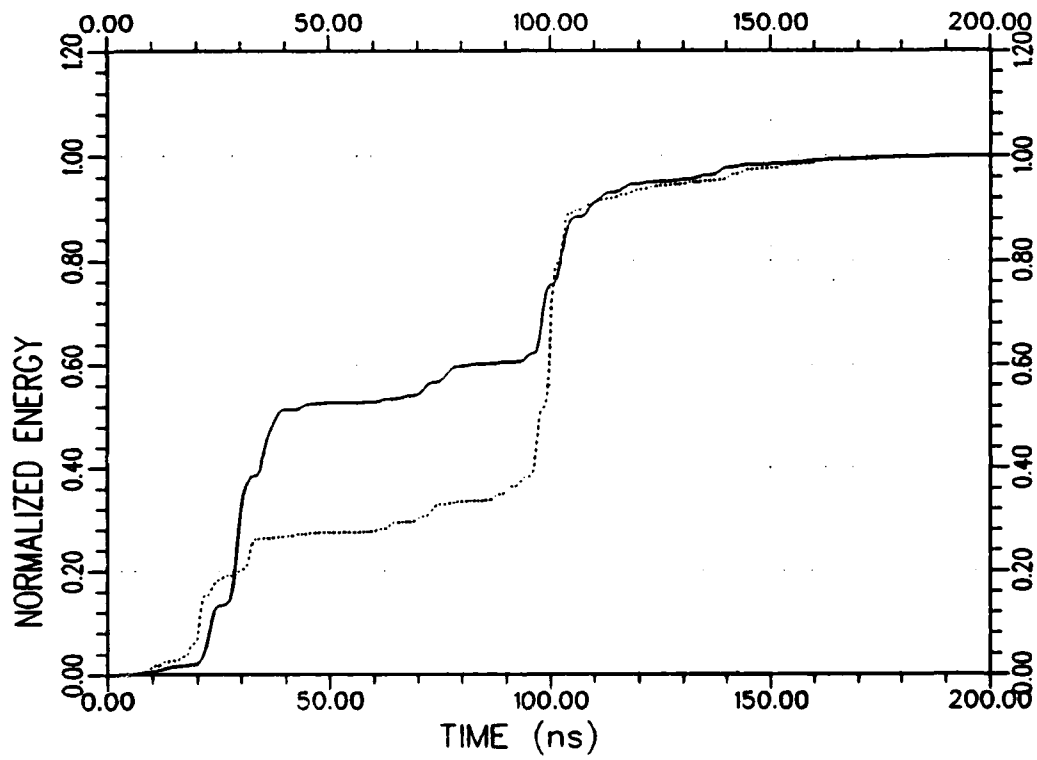
(b) Response energy curves

Figure F.5. Continued.



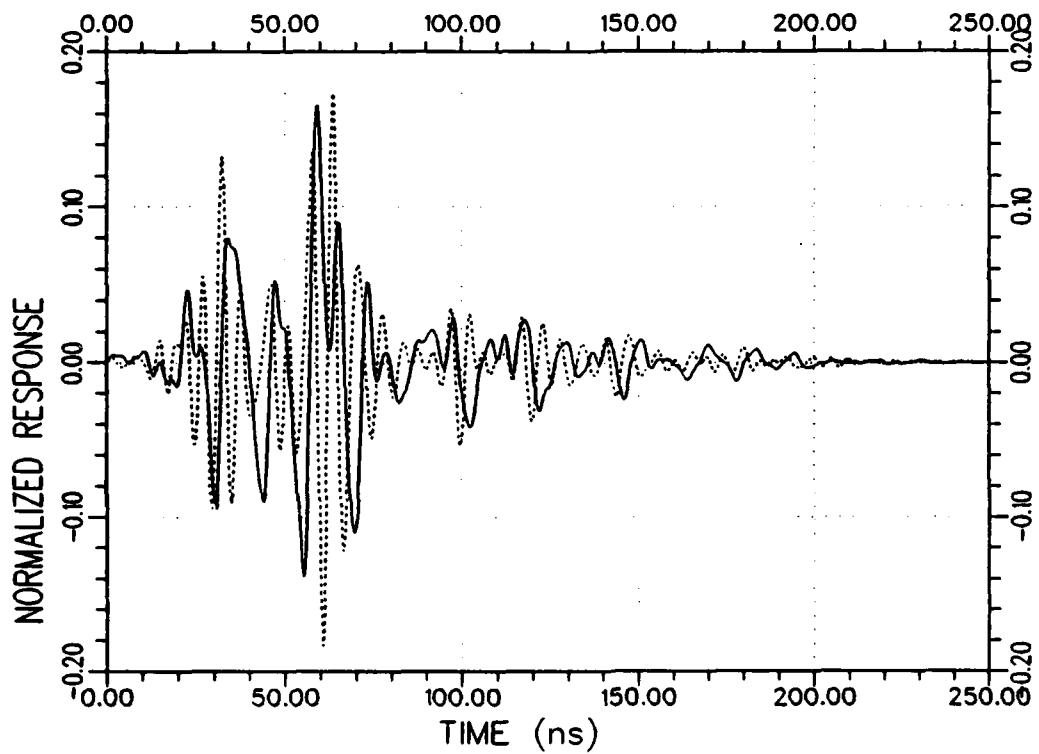
(a) Response waveforms

Figure F.6. Normalized composite impulse response (.....) and composite K-pulse response (——) waveforms and their energy curves for aircraft A at 91°/VP.



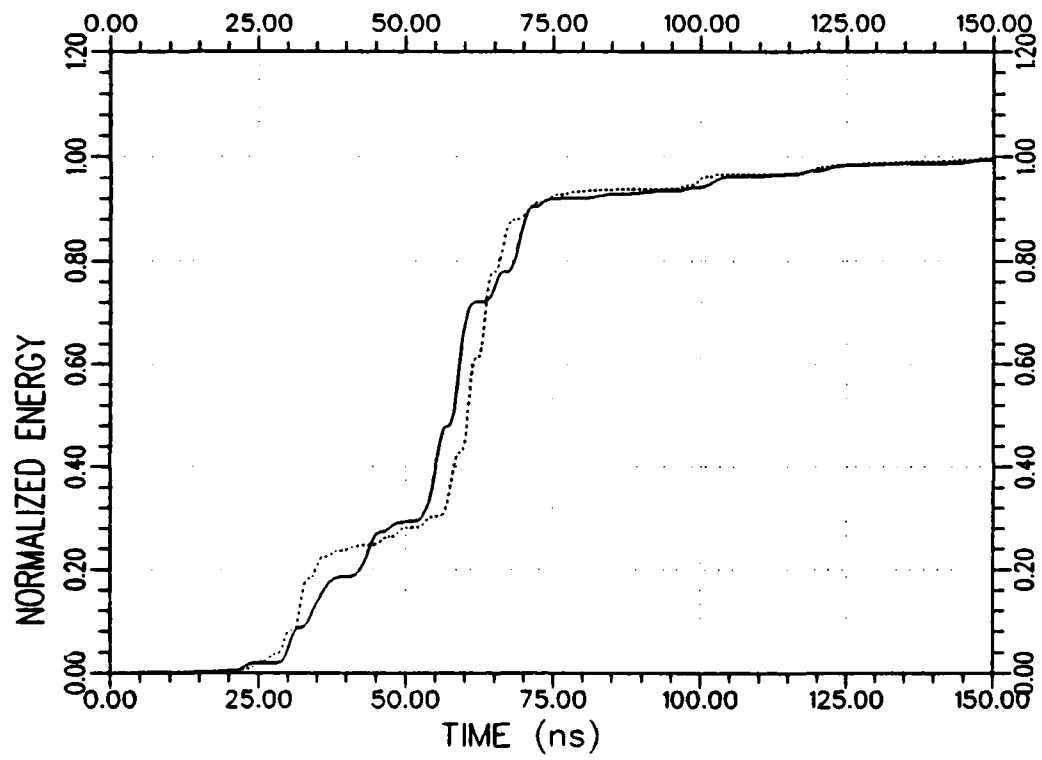
(b) Response energy curves

Figure F.6. Continued.



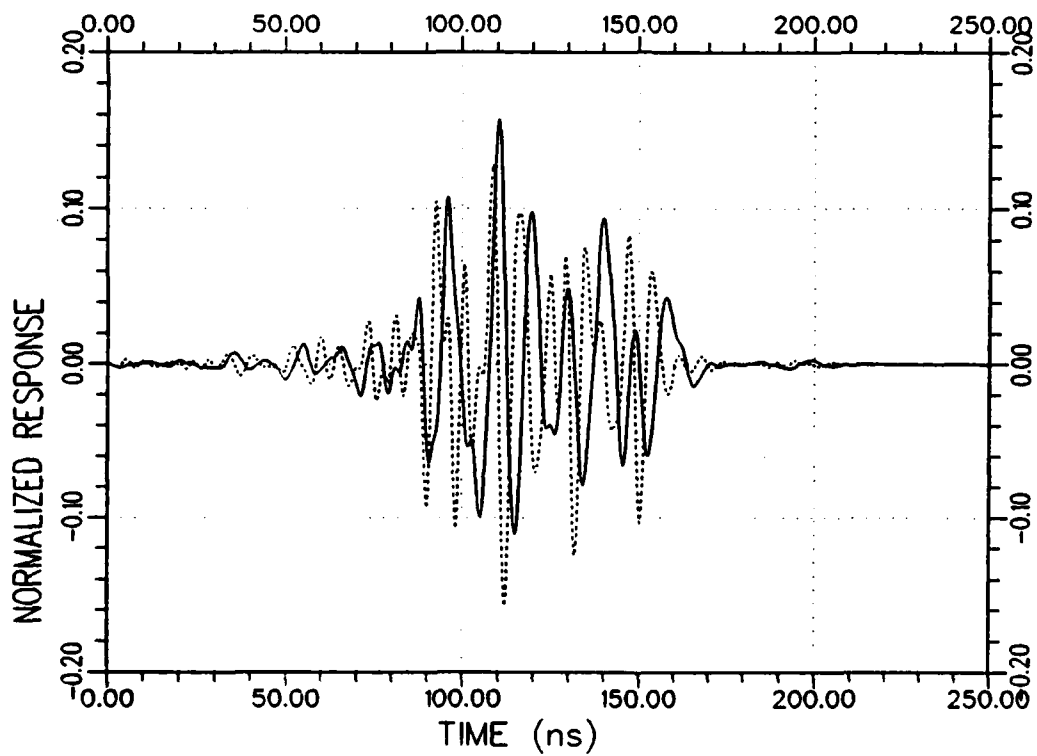
(a) Response waveforms

Figure F.7. Normalized composite impulse response (.....) and composite K-pulse response (——) waveforms and their energy curves for aircraft A at 119°/VP.



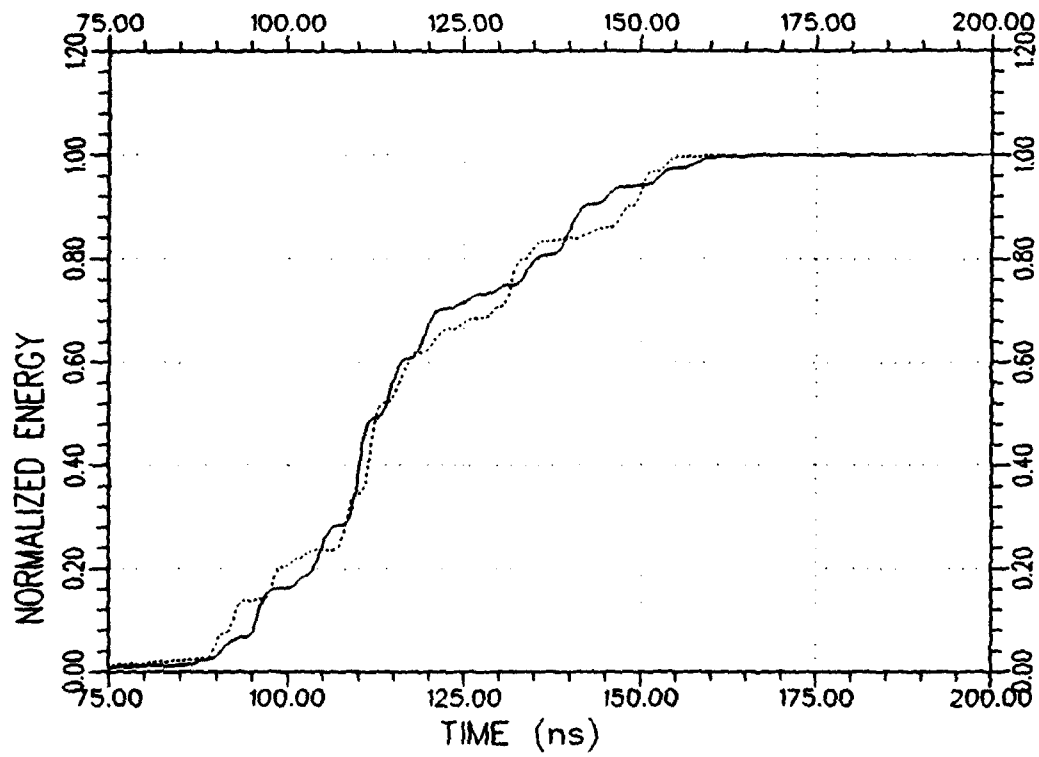
(b) Response energy curves

Figure F.7. Continued.



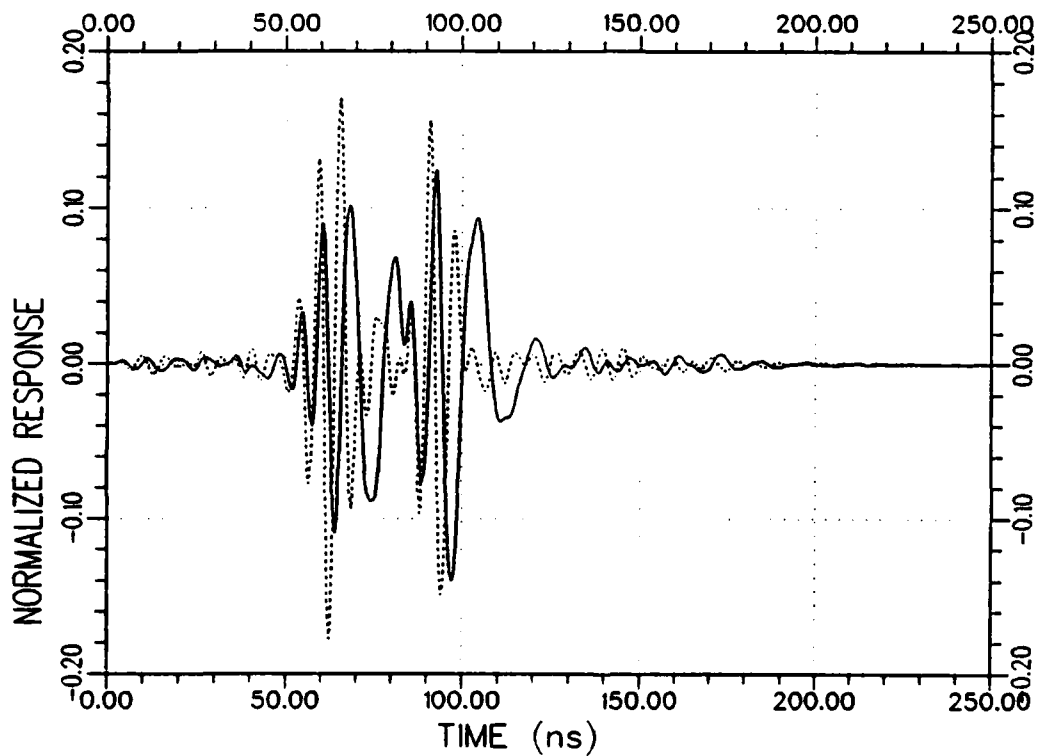
(a) Response waveforms

Figure F.8. Normalized composite impulse response (.....) and composite K-pulse response (——) waveforms and their energy curves for aircraft A at $150^\circ/\text{VP}$.



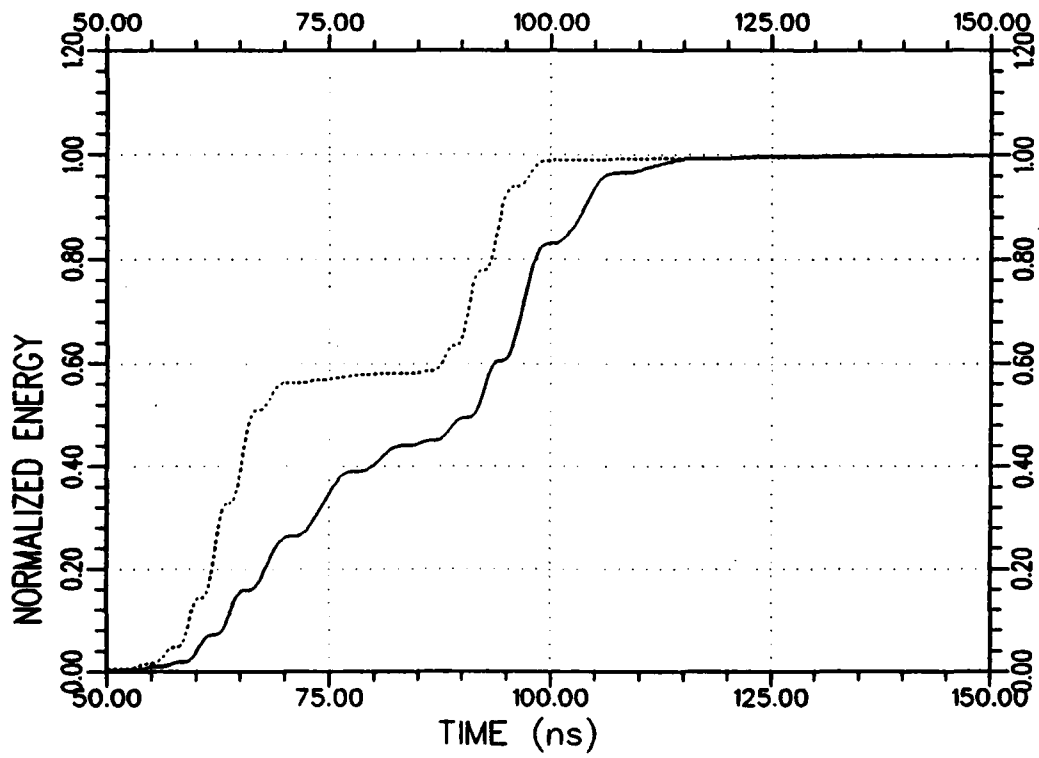
(b) Response energy curves

Figure F.8. Continued.



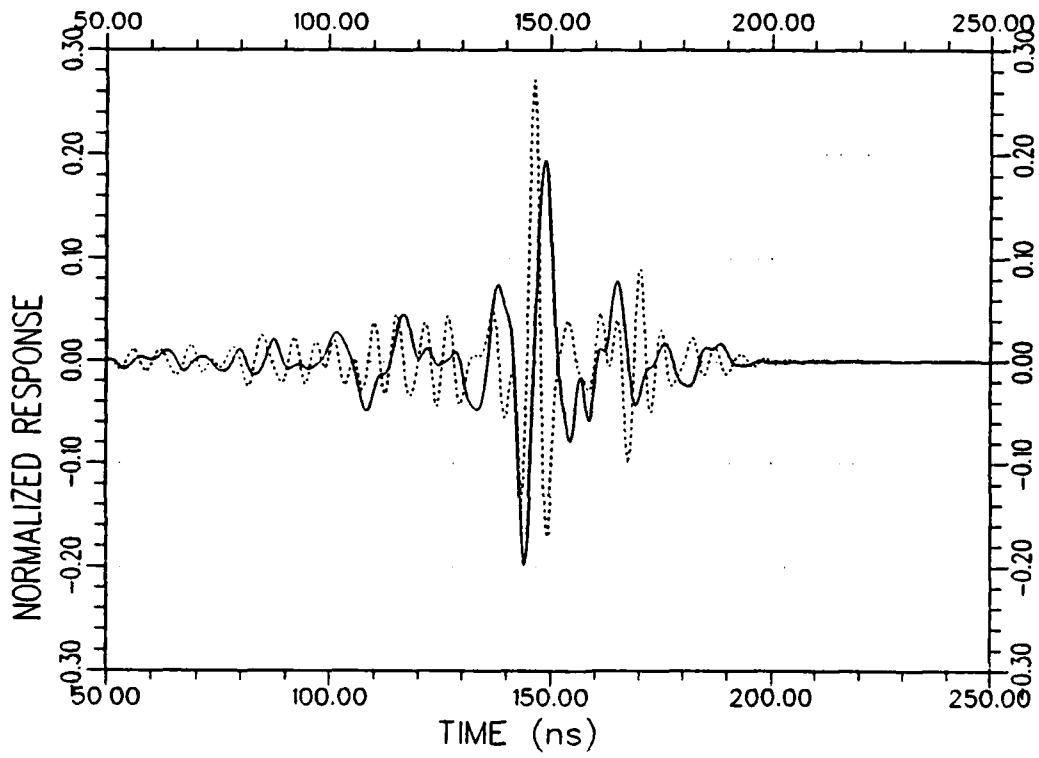
(a) Response waveforms

Figure F.9. Normalized composite impulse response (.....) and composite K-pulse response (——) waveforms and their energy curves for aircraft A at 179°/VP.



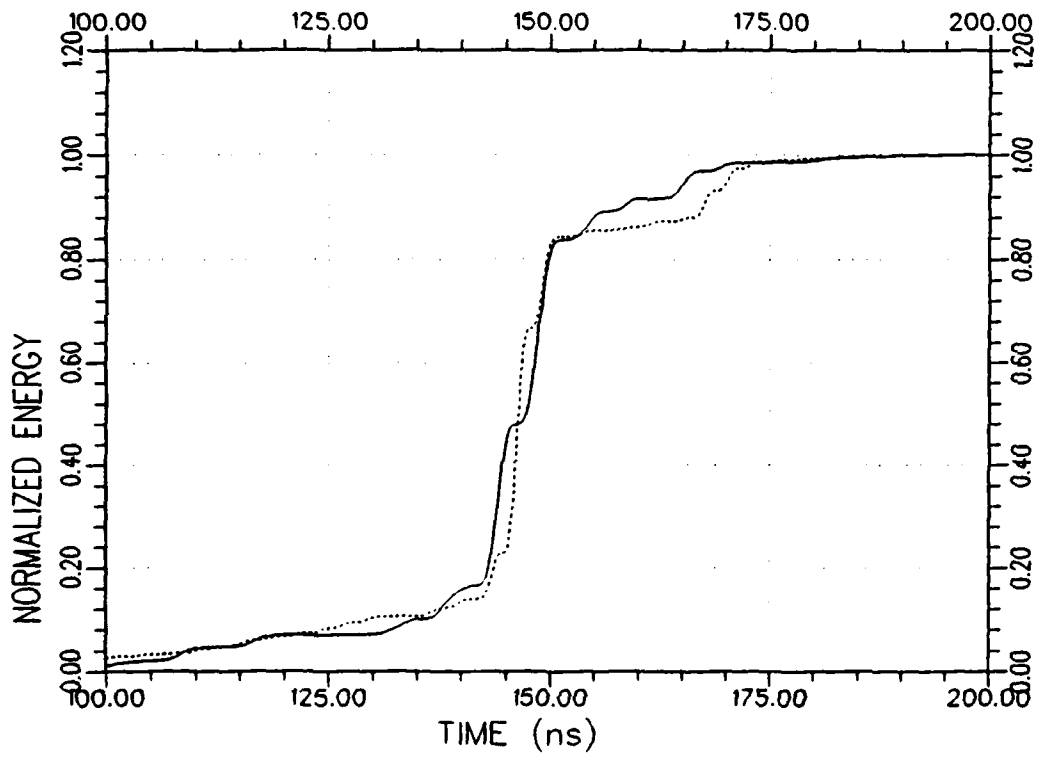
(b) Response energy curves

Figure F.9. Continued.



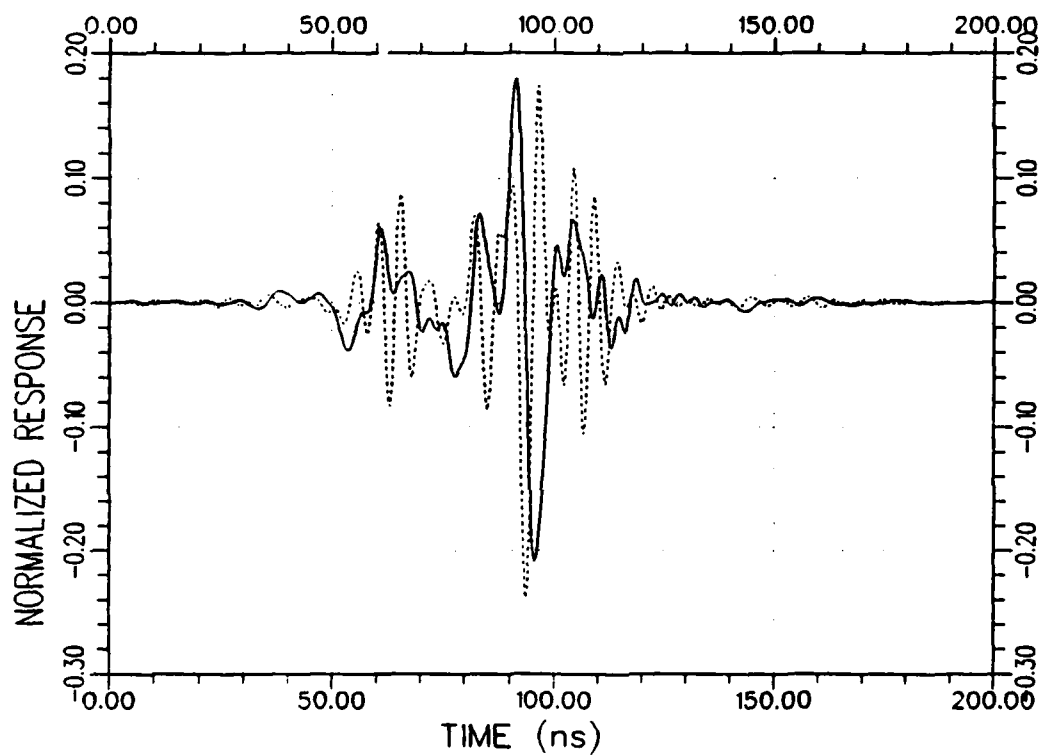
(a) Response waveforms

Figure F.10. Normalized composite impulse response (.....) and composite K-pulse response (——) waveforms and their energy curves for aircraft A at 1°/HP.



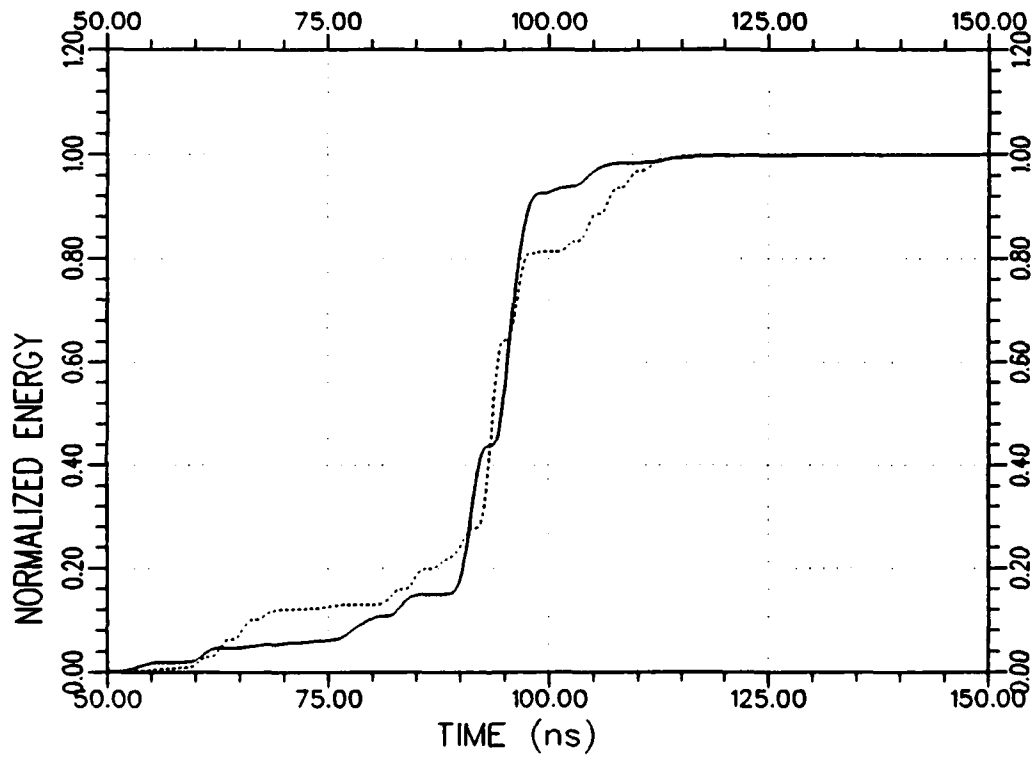
(b) Response energy curves

Figure F.10. Continued.



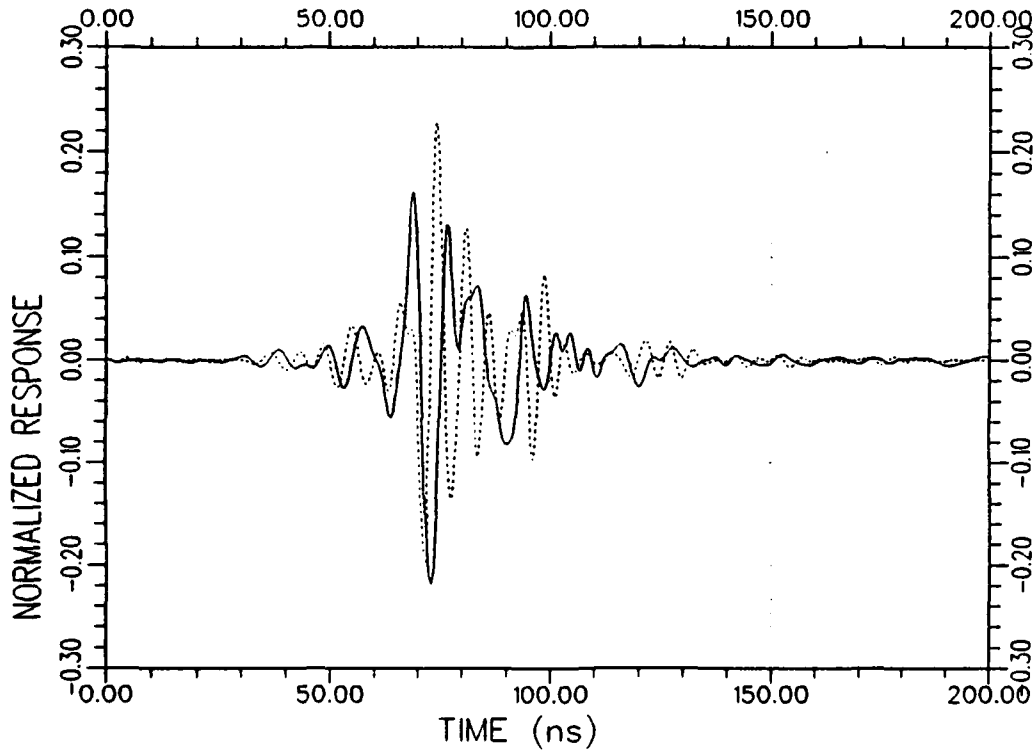
(a) Response waveforms

Figure F.11. Normalized composite impulse response (.....) and composite K-pulse response (——) waveforms and their energy curves for aircraft A at 44°/HP.



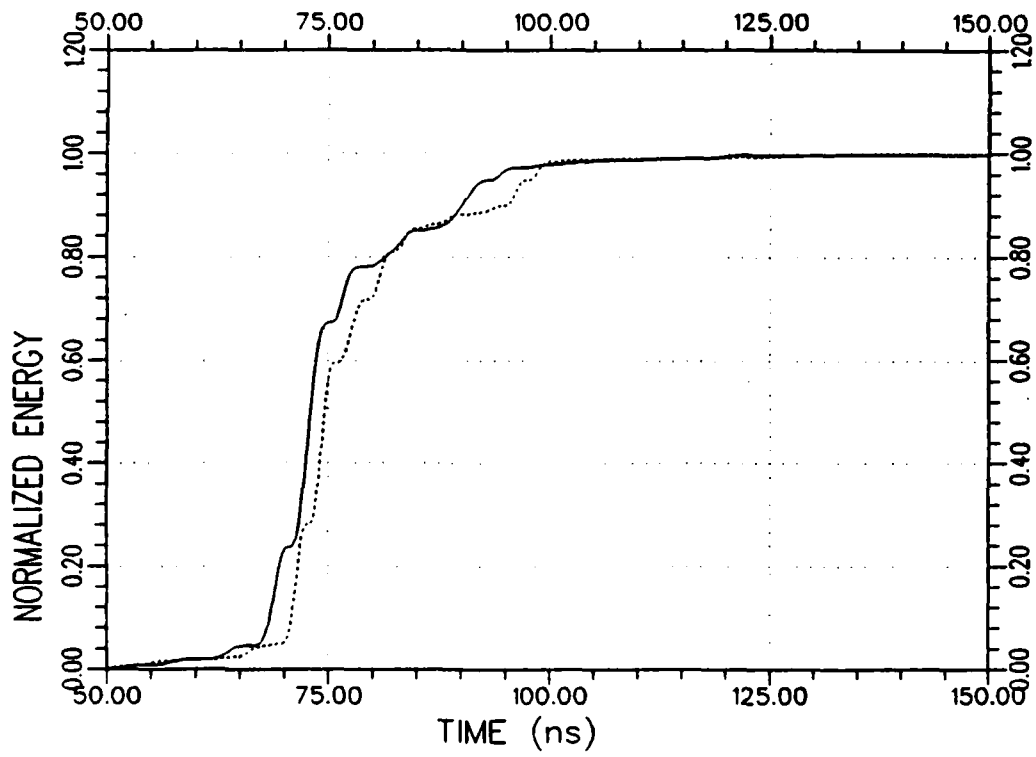
(b) Response energy curves

Figure F.11. Continued.



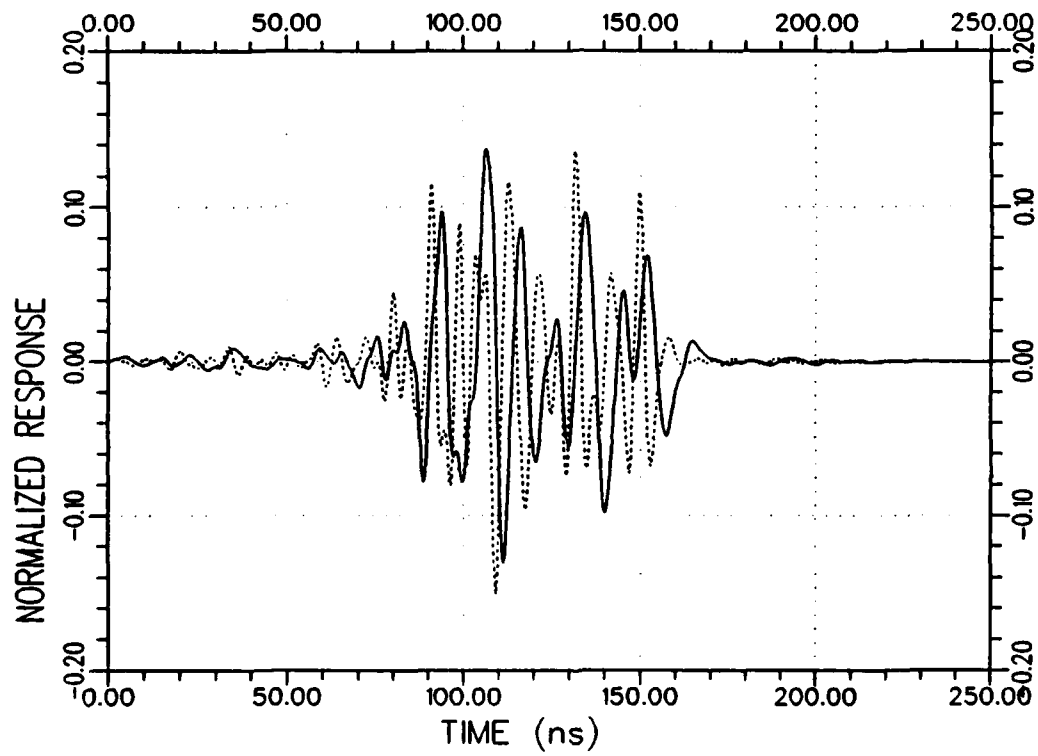
(a) Response waveforms

Figure F.12. Normalized composite impulse response (.....) and composite K-pulse response (——) waveforms and their energy curves for aircraft A at 75°/HP.



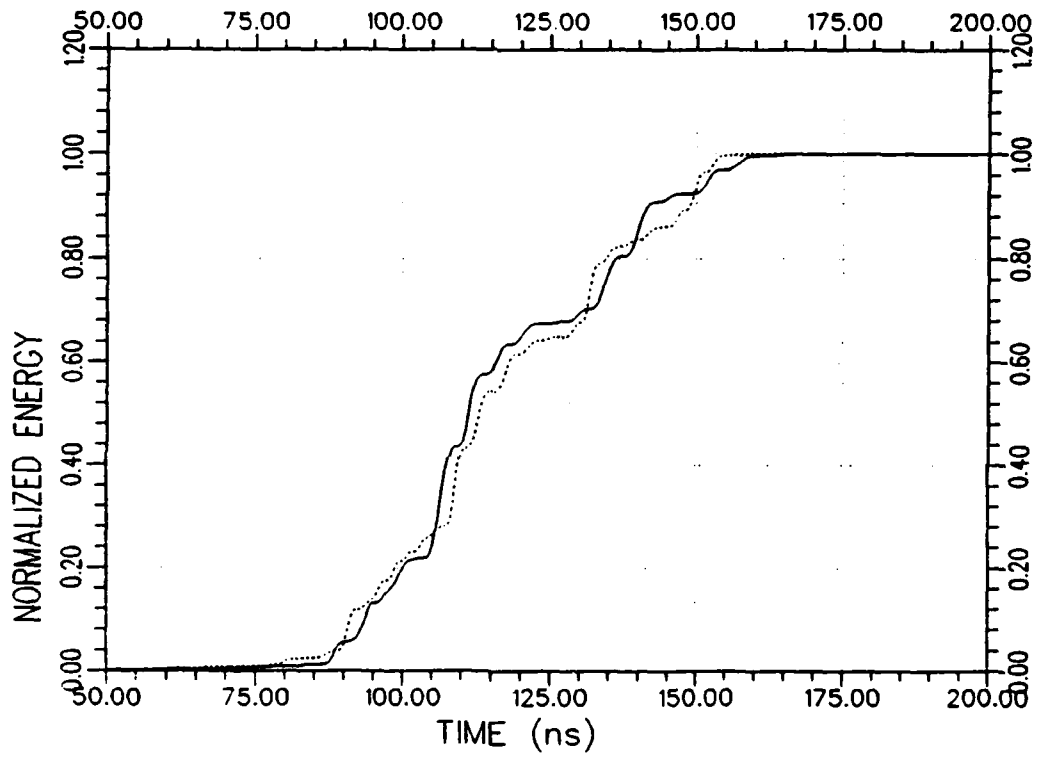
(b) Response energy curves

Figure F.12. Continued.



(a) Response waveforms

Figure F.13. Normalized composite impulse response (.....) and composite K-pulse response (—) waveforms and their energy curves for aircraft A at 150°/HP.



(b) Response energy curves

Figure F.13. Continued.

REFERENCES

- [1] Special Issue on Inverse Methods in Electromagnetics, IEEE Trans. on Antennas and Propagation, Vol. AP-29, No. 2, March 1981.
- [2] E.M. Kennaugh and R.L. Cosgriff, "The Use of Impulse Response in Electromagnetic Scattering Problems," 1958 IRE National Convention Record - Part 1, pp. 72-77.
- [3] E.M. Kennaugh and D.L. Moffatt, "Transient and Impulse Response Approximations," Proceedings of the IEEE, Vol. 53, No. 8, pp. 893-901, August 1965.
- [4] C.E. Baum, "The Singularity Expansion Method," in Transient Electromagnetic Fields, L.B. Felsen, ed., Springer-Verlag, New York, 1975.
- [5] C.E. Baum, "Toward an Engineering Theory of Electromagnetic Scattering: The Singularity and Eigenmode Expansion Methods," in Electromagnetic Scattering, P.L.E. Uslenghi, ed., Academic Press, New York, 1978.
- [6] D.L. Moffatt and R.K. Mains, "Detection and Discrimination of Radar Targets," IEEE Trans. on Antennas and Propagation, Vol. AP-23, No. 3, May 1975.
- [7] J.S. Bagby, "Natural Electromagnetic Oscillations: A Geometrical Theory," Master's Thesis, The Ohio State University, Department of Electrical Engineering, Columbus, Ohio, 1981.
- [8] M.L. Van Blaricum, "Techniques for Extracting the Complex Natural Resonances of a System Directly from its Transient Response," Ph.D. dissertation, Department of Electrical Engineering, University of Illinois at Urbana-Champaign, 1976.
- [9] C.W. Chuang and D.L. Moffatt, "Natural Resonances of Radar Targets Via Prony's Method and Target Discrimination," IEEE Trans. on Aerospace and Electronics Systems, Vol. AES-12, No. 5, September 1976.
- [10] T.C. Lee, "Approximate Methods for Obtaining the Complex Natural Electromagnetic Oscillations of an Object," Ph.D dissertation, The Ohio State University, Department of Electrical Engineering, Columbus, Ohio, 1983.
- [11] J.A. Stratton, Electromagnetic Theory, pp. 554-560, McGraw-Hill, New York, 1941.

- [12] D.P. Mithouard and D.B. Hodge, "Electromagnetic Scattering by a Disk," Technical Report 710816-3, The Ohio State University ElectroScience Laboratory, Department of Electrical Engineering, September 1979.
- [13] R.F. Harrington, Field Computation by Moment Methods, R.E. Krieger Publishing Company, Inc., Florida, 1968.
- [14] R.G. Kouyoumjian and P.H. Pathak, "A Uniform Geometrical Theory of Diffraction for an Edge in a Perfectly-Conducting Surface," *Proceedings of the IEEE*, Vol. 62, No. 11, pp. 1448-1461, November 1964.
- [15] E.M. Kennaugh, "The K-pulse Concept," *IEEE Trans. on Antennas and Propagation*, Vol. AP-29, No. 2, pp. 327-331, March 1981.
- [16] M.L. Van Blaricum and R. Mittra, "A Technique for Extracting the Poles and Residues of a System Directly from its Transient Response," *IEEE Trans. on Antennas and Propagation*, Vol. AP-23, No. 6, pp. 777-781, November 1975.
- [17] D.L. Moffatt and K.A. Schubert, "Natural Resonances Via Rational Approximants," *IEEE Trans. on Antennas and Propagation*, Vol. AP-25, No. 5, September 1977.
- [18] C.Y. Lai, "Improved Models for the Extraction and Application of Complex Natural Resonances to Target Identification," Ph.D dissertation, The Ohio State University, Department of Electrical Engineering, Columbus, Ohio, March 1986.
- [19] J.N. Brittingham, E.K. Miller and J. Willows, "Pole Extraction from Real-Frequency Information," *Proceedings of the IEEE*, Vol. 68, No. 2, pp. 263-273, February 1980.
- [20] J.R. Anton and M.L. Van Blaricum, "Investigation of Procedures for Automatic Resonance Extraction from Noisy Transient Electromagnetic Data," Vol. I-III, Final Report for Contract No. N00014-80-C-0299, Effects Technology, Inc., August 1981.
- [21] Unpublished notes from E.M. Kennaugh.
- [22] E.M. Kennaugh, "Transient Analysis of Radiation and Scattering Properties of a Thin Linear Antenna," an unsolicited proposal dated November 1975.
- [23] J. Gerst and J. Diamond, "The Estimation of Intersymbol Interference by Input Signal Shaping," *Proceedings of IRE*, Vol. 19, No. 7, pp. 1195-1203, July 1961.

- [24] J.B. Campbell, S.H. Chang, D.W. Fermental and N.T. Tsod-Wu, "Pulse Shaping by manipulating Transform Zeros," Scientific Report #1, Project 4610, Northeastern University, Boston, December 1964.
- [25] J.B. Campbell, "Design of Input Waveform to Yield Time-Limited Orthogonal Outputs," Technical Report #3, Project 4610, Northeastern University, Boston, MA, 1963.
- [26] J.S. Jones, Methods in Electromagnetic Wave Propagation, p. 834, Clarendon Press, Oxford, 1979.
- [27] B.J. Levin, Distribution of Zeros of Entire Functions, Translation of Mathematical Monographs, Vol. 5, American Mathematical Society, 1964, Thm. 11, p. 251.
- [28] H.T. Kim, N. Wang and D.L. Moffatt, "K-pulse for a Thin Circular Loop," IEEE Trans. on Antennas and Propagation, Vol. AP-33, No. 12, pp. 1403-1407, December 1985.
- [29] E.M. Kennaugh, D.L. Moffatt and N. Wang, "The K-pulse and Response Waveforms for Non-Uniform Transmission Lines," IEEE Trans. on Antennas and Propagation, Vol. AP-34, No. 1, pp. 78-83, January 1986.
- [30] E. Rothwell, K.M. Chen, Gharsallah and B. Drachman, "Frequency Domain E-Pulse Synthesis and Target Discrimination," presented at IEEE AP-S International Symposium, Vancouver, June 1985.
- [31] E. Rothwell, D.P. Nyquist, K.M. Chen and B. Drachman, "Radar Target Discrimination Using the Extinction-Pulse Technique," IEEE Trans. on Antennas and Propagation, Vol. AP-33, No. 9, pp. 929-936, September 1985.
- [32] K.M. Chan, D.P. Nyquist, L.L. Webb and B. Drachman, "Radar Target Discrimination by Convolution of Radar Return with Extinction-Pulses and Single Mode Extraction Signals," IEEE Trans. on Antennas and Propagation, Vol. AP-35, No. 7, pp. 896-904, July 1986.
- [33] F.Y.S. Fok and D.L. Moffatt, "The K-Pulse and E-Pulse," IEEE Trans. on Antennas and Propagation, Vol. AP-35, No. 11, pp. 1325, November 1987.
- [34] F.Y.S. Fok, "K-Pulse Estimation from the Impulse Response of a Target," Ph.D dissertation, The Ohio State University, Department of Electrical Engineering, Columbus, Ohio, 1986.
- [35] F.Y.S. Fok, D.L. Moffatt and N. Wang, "K-Pulse Estimation from the Impulse Response of a Target," IEEE Trans. on Antennas and Propagation, Vol. AP-35, No. 8, August 1987.

- [36] G. Turhan and D.L. Moffatt, "K-pulse Synthesis for Complex Geometries Using Incomplete Frequency Data," presented at IEEE AP-S/URSI Symposium, Blacksburg, Virginia, June 1987.
- [37] K.E. Atkinson, An Introduction to Numerical Analysis, John Wiley and Sons, New York, 1978.
- [38] R. Fletcher and M.J.D. Powell, "A Rapid Descent Method for Minimization," Computer Journal, Vol. 6, No. 2, pp. 163-168, 1963.
- [39] G. Turhan and D.L. Moffatt, "Expansion of K-Pulses in Terms of Legendre Polynomials for an Arbitrary Target," presented at IEEE AP-S/URSI Symposium, Philadelphia, June 1986.
- [40] G. Turhan, "Target Identification Using the K-Pulse Technique," FORUM 1988 Proceedings, pp. 59-67, Award Winning Paper in Engineering Sciences, The Ohio State University, Columbus, Ohio.
- [41] G. Turhan and D.L. Moffatt, "Estimation of the K-Pulse and Natural Resonance Frequencies Using Legendre Polynomial Expansions," presented at IEEE AP-S/URSI Symposium, Syracuse, 1988.
- [42] M. Abramowitz and J.A. Stegun, Handbook of Mathematical Functions, National Bureau of Standards, 1972.
- [43] R.F. Harrington, Time Harmonic Electromagnetic Fields, McGraw-Hill, New York, 1961.
- [44] E.M. Kennaugh, "The Scattering of Short Electromagnetic Pulses by a Conducting Sphere," Proc. of IRE, Vol. 49, p. 380, January 1961.
- [45] K. Chen and D. Westmoreland, "Impulse Response of a Conducting Sphere Based on Singularity Expansion Method," Proc. IEEE, Vol. 69, No. 6, pp. 747-750, June 1981.
- [46] G.C. Gaunard, H. Uberall and A. Nagl, "Complex-Frequency Poles and Creeping Wave Transients in Electromagnetic-Wave Scattering," Proc. IEEE, Vol. 71, No. 1, pp. 172-174, January 1983.
- [47] E.M. Kennaugh and D.L. Moffatt, "Comments on Impulse Response of a Conducting Sphere Based on SEM," Proc. IEEE, Vol. 70, No. 3, pp. 294-295, March 1982.
- [48] E.C. Jordan, Electromagnetic Waves and Radiating Systems, Prentice-Hall, Englewood Cliffs, NJ, 1950.
- [49] S.A. Schelkunoff and H.T. Friis, Antenna Theory and Practice, John Wiley and Sons, New York, 1952.

- [50] J.H. Richmond, "Computer Program for Thin Wire Structures in a Homogeneous Conducting Medium," Report NASA-CR-2399, June 1974.
- [51] D.F. Kimball, "Enhanced Techniques for Broadband Radar Backscatter Measurements," Technical Report #714190-4, The Ohio State University ElectroScience Laboratory, December 1983.
- [52] F.J. Harris, "On the Use of Windows for Harmonic Analysis with the Discrete Fourier Transform," Proc. IEEE, Vol. 66, No. 1, January 1978.
- [53] E.K. Walton and J.D. Young, "The Ohio State University Compact Radar Cross Section Measurement Range," IEEE Trans. on Antennas and Propagation, Vol. AP-32, No. 11, pp. 1218-1223, November 1984.
- [54] N.F. Chamberlain, "Surface Ship Classification Using Multipolarization, Multifrequency Sky-Wave Resonance Radar," Technical Report #714190-9, The Ohio State University ElectroScience Laboratory, October 1984.
- [55] A. Papoulis, Probability, Random Variables and Stochastic Processes, McGraw-Hill, New York, 1984.
- [56] L.B. Felsen, "Comments on Early Time SEM," IEEE Trans. on Antennas and Propagation, Vol. AP-33, No. 1, pp. 118-119, January 1985.
- [57] D.G. Dudley, "Comments on SEM and the Parametric Inverse Problem," IEEE Trans. on Antennas and Propagation, Vol. AP-33, No. 1, pp. 119-120, January 1985.